Alok K. Gupta
Somnath Dasgupta
(Editors)

# Physics and Chemistry of the Earth's Interior

## Crust, Mantle and Core

**Indian National Science Academy**
**A Platinum Jubilee Special Issue**

Indian
National
Science
Academy

Springer

# Physics and Chemistry of the Earth's Interior

## Crust, Mantle and Core

*Edited by*

Alok K. Gupta
Somnath Dasgupta

Indian National Science Academy
A Platinum Jubilee Special Issue

Editors:

Alok K. Gupta
National Centre of Experimental
Mineralogy and Petrology,
Allahabad University,
Allahabad, India

Somnath Dasgupta
Indian Institute of Science
Education and Research,
Kolkata,
India

**Gupta & Dasgupta: Physics and Chemistry of the Earth's Interior**
**Crust, Mantle and Core**

First Published 2009

ISBN 978-81-8489-196-6

This edition is published by Springer (India) Private Limited,
A part of Springer Science+Business Media, Registered Office: 906-907,
Akash Deep Building, Barakhamba Road, New Delhi – 110 001, India.

*Professor Kenzo Yagi (1915 – 2008)*

*This volume is dedicated to Professor Kenzo Yagi, for his remarkable achievements and contributions to the field of experimental mineralogy and petrology, particularly with reference to the genesis of alkaline rocks and volcanology.*

*Editors*

# Foreword

The Indian National Science Academy was established in January 1935 with the objective of promoting science in India and harnessing scientific knowledge for the cause of humanity and national welfare. In 1968 it was designated as the adhering organisation in India to the International Council for Scientific Union (ICSU) on behalf of the Government of India. Over the years, the Academy has published a number of journals, volumes, biographical memoirs, etc.

The year 2009–2010 will be specially celebrated to mark the Platinum Jubilee of the Academy. Many programmes are planned in different centres in India on this occasion. In addition, the Academy has decided to publish a number of special volumes on different subjects ranging from earth sciences to life sciences. This volume is on Physics and Chemistry of the Earth's Interior.

One of the main objectives of geophysicists is to establish the internal structure of the earth as revealed by seismic tomography. It is also their primary goal to correlate geophysical data to reveal thermal and chemical state of the crust, mantle and core of the earth. In order to interpret seismic velocities and associated density and elastic properties in terms of mineralogical and petrological models of the earth's interior, thermodynamic and high-pressure temperature data from mineral physics are essential. With the advent of different types of multi-anvil and laser-heated diamond anvil equipment, it is now possible to simulate conditions prevalent even in the lower mantle and core of the earth.

With high P-T experimental studies on essential mineral phases during the past three decades, it is now possible for mineral physicists to develop a clear picture about the earth's interior and dynamic processes associated with it. Seismological studies provide additional constraints on these models.

Leading national and international scientists have contributed to this special issue and I sincerely hope that this volume will throw further insight into our quest to understand how the earth works.

M. Vijayan

President, Indian National Science Academy, India

# Preface

During the past three decades, considerable amount of geophysical studies have been done towards establishing various seismological discontinuities from the surface to the core-mantle boundary of the earth. Two major discontinuities, one at 35–45 km below the continents (10–15 km below the oceans) and the other 2850 km below the surface, divide the earth into 1) crust, 2) mantle and 3) core. In most cases these discontinuities are associated with increase in density of the earth materials associated with velocity jumps as a function of depth. In some cases there is a sudden drop in the seismic velocity because of the presence of melt or occurrence of low-density materials subducted underneath.

Development of multi-anvil and laser-heated diamond anvil high-pressure equipment in recent years, have helped mineral physicists to establish different phase transformations of mantle minerals, which are associated with changes in the rheological properties, increase in density or variation in elastic constants of the earth materials.

The present volume encompasses several papers related to Physics and Chemistry of the crust, their metamorphic history as a function of pressure and temperature, mode of melt generation in the crust and their migration. There are also experiments related to the causes of orogenic events associated with plate tectonic processes in the upper part of the mantle. Another group of authors discusses about phase transformation of mantle minerals and their correlation with respect to various seismic discontinuities, the thermal state of the mantle and genesis of convective cycles.

Conservation of mass during metamorphic reactions is emphasised by *Sengupta* and *Dasgupta (Chapter 2)*, who use the singular value decomposition method to balance metamorphic reactions. Texturally-constrained metamorphic reactions from the Chilka Lake anorthosite complex are balanced to evaluate the nature of mobile elements during metamorphic reconstitutions. In the process they characterise the Pan-African thermal overprint in the Eastern Ghats Belt, India. The result has important implications on Indo-Antarctic correlation during Neoproterozoic.

*Mandal et al.* discuss geodynamic models pertaining to the development of large-scale fold belts (*Chapter 3*). In this paper they review some of the important models in context of the Himalayan-Tibetan system, which is believed to be the most spectacular collision type orogenic belt. The authors deal with theoretical and experimental models that address large-scale phenomena in orogens. Over the past two decades, geoscientists and geophysicists have extensively used wedge tectonic models to explain several tectonic processes in mountain chains, such as sequential thrusting, folding and rock upliftments. The wedge models pivot principally on two considerations: 1) choice of boundary conditions and 2) rheology of the crust.

*Brown* and *Korhonen (Chapter 4)* review the processes of melt generation during various types of metamorphism ranging from ultra-high-pressure to ultra-high temperature terranes. They discuss the source of heat to account for very high temperatures in the crust. Partially molten rocks invariably lose melt, but the nature of the melt escape channels varies with the volume of the melt produced. Bulk of the melt in the crustal rocks is produced by dehydration–melting. Melting and effect of melt loss are evaluated through quantitative phase equilibria modelling of two common crustal rock types, viz. pelites and aluminous greywackes.

*Ganguly* and *Tirone (Chapter 5)* address a fundamental problem related to retrieval of cooling history of rocks from mean closure temperature versus cooling age data of multiple geochronological systems. They discuss and review recent developments between the cooling age and cooling rate relations and show how cooling rate can be retrieved without knowledge of mean closure temperature. Further, mean closure temperature for a specific system, grain size and geometry can be retrieved from inferred cooling rate.

Estimation of pressure-temperature conditions of metamorphism remains a prime target for metamorphic petrologists. However, *Essene (Chapter 6)* argues that many of the geothermo-barometers suffer from severe inadequacies. This is particularly true for empirical thermo-barometers, and he cites several instances through a careful re-evaluation. He considers that the newly developed thermo-barometers in the system, Ca-Zr-Ti-Q, could be potentially usable, provided proper pressure corrections are employed for thermometers and activity of $TiO_2$ is correctly estimated.

*Santosh (Chapter 7)* argues that magmatic, metamorphic and metasomatic fluids play a pivotal role in the geochemical and tectonic evolution of the earth. The nature of fluids varies with tectonic settings. The fluid budget in the earth is controlled by various processes operative in the crust and mantle, and there could be significant crust-mantle interactions through fluid transport.

*Rai, Suryaprakasam* and *Gaur (Chapter 9)* discuss mantle discontinuities beneath India from the south Indian Archean cratons to the Himalayan subduction zone. Their results show presence of Lehmann discontinuity at a depth of 220–250 km beneath southern part of India. The 410 km discontinuity is sharp and at its normal depth beneath the Precambrian terrains and is elevated by 10–15 km in the Ganges basin and the Himalayas. They suggest that there was progressive cooling or thickening of the Indian lithosphere towards its northern margin. They also observe a 660 km discontinuity with a broad double peak beneath the Himalayas and southern India. They interpret this to be due to the presence of non-olivine component in the deep mantle. Apart from the above-mentioned global discontinuities, a velocity interphase is mapped at 475 km depth beneath Ladakh. The transition zone in the mantle show 10 km thickening beneath the Ganges basin, suggestive of the presence of relatively cold material within. The elevated 410 km discontinuity beneath the Ganges basin and the Himalaya is interpreted as the signature of north-east subducting the Indian slab and perhaps part of the Tethyan oceanic lithosphere in front of it.

*Singh (Chapter 10)* concludes that the present thermal structure of the crust can be constructed using the available heat flow and radiogenic heat data with steady state heat conduction models, which are temperature-dependent; and require thermal conductivity and depth-dependent radiogenic heat data. Thermal models are also needed to study the influences of heat, effect of additional materials to the crust, reordering of heat sources, temperature flux in the mantle, uplift and erosion-related events and fluid transport in the Indian crust. He summarises several thermal models useful in constraining above processes and emphasises that geological events leave behind signatures, which are embedded in the Indian crust.

*Manglik (Chapter 11)* thinks that solid state convection is the main heat transport mechanism in the earth's mantle because of significant temperature difference between the base of lithosphere and the core-mantle boundary. Mode of convective circulations in the mantle, induced by thermal heating, can be described using the fluid dynamical modelling approach. Initially some analytical models were developed to understand the process of convection in the mantle. However, the complexity of the structure, dependence of rock properties on pressure and temperature, grain-size effects, distribution of plate boundaries, presence of heterogeneous boundary layers, etc. have led to the development of numerical techniques to understand the dynamics of the mantle, plume-lithosphere interaction, flood basalt volcanism and ridge and subduction-related processes. Ever-increasing computing power has helped us in the development of more realistic models of the mantle dynamics. A brief overview of mathematical formulation and some of the applications of mantle convection modelling has been presented in this chapter.

We sincerely thank Dr. Mrigank M. Dwivedi and Mr. Soumitra Dasgupta for their herculean task in typesetting all the manuscripts in Springer-Verlag format. Thanks are also due to Ms. Alka Gupta for typing some of the manuscripts.

We also acknowledge the support and cooperation received from Dr. Priti Nanda, Senior Publishing Manager; Biplav Panda, Editorial Manager; Sangeeta P.C., Deputy Manager – Editorial; Amitava Dutta, Deputy Manager – Production; and Vivek Sharma, Associate – Production for improving the quality of content and for demonstrating great teamwork.

Alok K. Gupta

National Centre of Experimental Mineralogy and Petrology,
Allahabad University, Allahabad, India

Somnath Dasgupta

Indian Institute of Science Education & Research, Kolkata, India

# Contents

## 1

# Geophysical and Experimental Petrological Studies of the Earth's Interior

Alok K. Gupta, Mrigank Mauli Dwivedi and William S. Fyfe

**Abstract:** Seismo-tomographic studies, reveal the presence of two major discontinuities inside the earth: Mohorovicic discontinuity (occurring 35–45 km below the continents and 10–15 km below the ocean) and the other is Guttenberg-Reichert discontinuity, present 2860 km below the surface. These two discontinuities divide the earth into, a) crust, b) mantle and c) core. There is also a low velocity discontinuity (Conrad, 10–15 km below the continental crust; not globally observed). Drilling of up to 13 km in Kola Peninsula, Russia across Conrad, shows the presence of sub-parallel faults causing intense shearing and re-equilibration to lower grade metamorphic rocks. Phase equilibria studies on olivine, Mg-Fe pyroxenes, diopsides, garnet, (Mg, Fe)O under P-T conditions similar to upper and lower mantle conditions suggest that the discontinuity at 313 km can be correlated with orthopyroxene ⇔ high pressure clinopyroxene (Mg, Fe)$SiO_3$ phase transformation, but those at 410, 520 at 660 km have been attributed to structural changes of olivine ⇔ wadsleyite, wadsleyite ⇔ ringwoodite and akimotite ⇔ perovskite, respectively. The discontinuity at 720 and 1200 km are considered to be due to conversion of $MgSiO_3$ (majorite) to $MgSiO_3$ (perovskite) and stishovite (rutile structure) to a $SiO_2$ polymorph having $PbO_2$ or $CaF_2$-like structure. The discontinuity at 1700 km may be due to conversion of cubic Ca-perovskite to tetragonal Ca-perovskite structure, and that at 2740 km at the beginning of D" layer may be due to transformation of perovskite to post-perovskite structure. The ultra low velocity zone (ULVZ) below 2870 km is due to the presence of liquid iron core. Studies at megabar and high temperatures reveal that the solid iron core, has a hexagonal close-packed structure.

---

Alok K. Gupta (✉), Mrigank Mauli Dwivedi
National Centre of Experimental Mineralogy and Petrology, University of Allahabad, Allahabad - 211002, U.P., India
e-mail: ncempald@dataone.in

Mrigank Mauli Dwivedi
e-mail: mmdwivedi@gmail.com

William S. Fyfe
Department of Earth Sciences, University of Western Ontario, London, Ontario, N6A 5B7 Canada
e-mail: wsfyfe@ywo.ca

## 1.1 Introduction

Detailed mineralogical, petrological and geophysical knowledge about the earth's internal structure can be deciphered from the following: a) seismological observation, b) mean density of the earth, c) analogy with meteorites, d) mineralogy and chemistry of mantle xenoliths dragged to the surface by alkali basalts and kimberlitic magmas, and e) study of synthetic and natural minerals at mantle and core P-T conditions.

Seismic velocity versus depth profile of the earth's interior is presented in Fig. 1.1a, b, which also demonstrates that there are two major seismic discontinuities: one occurring 35–45 km below the surface (Mohorovicic or simply M-discontinuity) and the other one lying 2850 km below the M-discontinuity (core-mantle boundary, CMB). From the surface of the earth to the M-discontinuity is the crust of the earth. Between the moho and CMB lies the mantle, and from CMB to the centre of the earth, is the core. As the shear wave ($V_s^2 = \mu/\rho$) gets extinct below 2850 km ($\mu$ or coefficient of rigidity $\cong 0$), the outer part of the core is considered to be in a liquid state. The velocity [($V_p^2 = (1/\rho)$ (k + $4\mu/3$))] of the primary wave sharply decreases below CMB, but rises again up to the centre of the earth. The inner core is therefore, considered to be in a solid state.

Cavendish measured the gravitation constant (G) from his classical experiments with two lead spheres. He also determined the force of attraction between these spheres and the earth. Newton calculated the mean density of the earth (5.48 g/cm$^3$) based on the knowledge of G. This can also be calculated from the knowledge of earth's moment of inertia, which can be accurately determined from the data supplied by the artificial satellites, orbiting around the earth. The present accepted figure related to the mean density of the earth is 5.517 ± 0.004.

If m is the mass of a material within a sphere of radius r, and G is gravitation constant, then density of the material with respect to r can be calculated using Williamson-Adams equation:

$d\rho/dr = -Gm\rho/r^2 (V_p^2 - 4V_s^2/3)$

On the basis of the knowledge of average density of mantle xenoliths, if a value of upper mantle is assigned to the materials at a particular depth below the crust, new values of density over a certain distance of the mantle can be calculated by integrating, provided the knowledge of distribution of $V_p$, $V_s$, G and m are known. On the basis of such calculation, density distribution within the earth up to its core has been calculated by different geophysicists (Fig. 1.2a, b).

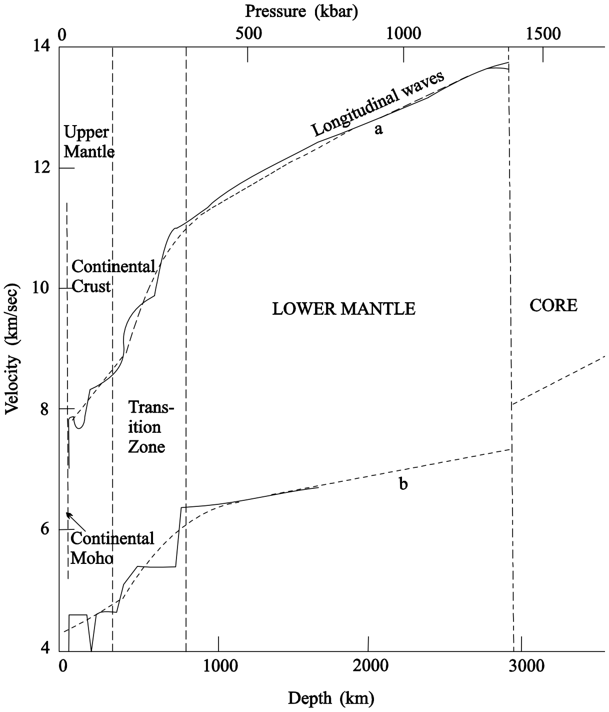

**Fig. 1.1** (a) Seismic velocity distribution in the mantle. P waves-solid lines: Johnson (1967, 1969). (b) S waves - solid line: Nuttli (1969). Broken line: Jeffrey (1937, 1939); From Ringwood, 1975, p. 327, with permission from McGraw-Hills, Inc.

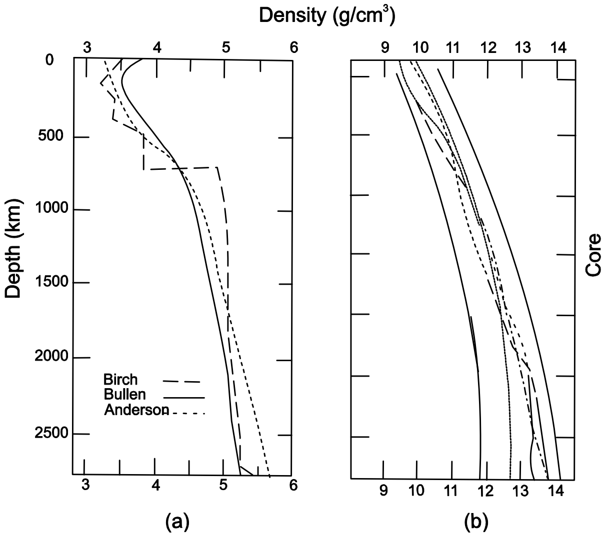

**Fig. 1.2** Density distribution of rocks in the (a) mantle and materials in the (b) core as a function of depth. (a) Density model of Anderson (1967) compared with the Bullen model (with the permission of the Academic Press). (b) Three plausible random density distribution obtained by Monte Carlo procedure, compared with Bullen model (Press, 1968, reprinted from Science 160, 1218–1221, with permission from the American Association for the Advancement of Science). Open circles represent Bullen's data

Meteorites are considered to be planetecimals, which are left over materials after the formation of the planets in the solar system. Their mineralogy and chemistry, therefore, throw light on the composition of the earth. Of the four different types of meteorites, siderite (comprising mainly Fe-Ni alloy) with density close to 12.8 gm/cc is considered to have density similar to that of core.

Based on composition of lherzolites from Kilbourne Hole (New Mexico, U.S.A), a chondritic meteorite (C-1, Ca: Al ratio = 1:1) is considered to have chemistry similar to that of the mantle of the earth. The mineralogy of such chondrites resembles lherzolitic xenoliths brought from the mantle to the surface of the earth by alkali basalts or kimberlitic magmas (Fig. 1.3). We have direct access to the crust as we live on its surface.

**Table 1.1** Average composition of crustal rocks

| | Earth's Crust | | Island Arcs | Kurile Islands |
|---|---|---|---|---|
| | 1 | 2 | 3 | 4 |
| | (Ronov and Yaroshevsky) | | McBirney (1969) | Markhinin (1968) |
| $SiO_2$ | 59.3 | 58.7 | 58.7 | 58.1 |
| $Al_2O_3$ | 15.9 | 17.3 | 17.4 | 17.1 |
| $TiO_2$ | 0.9 | 0.8 | 0.8 | 0.7 |
| FeO | 4.5 | 4.0 | 3.5 | 4.1 |
| $Fe_2O_3$ | 2.5 | 3.0 | 3.2 | 3.4 |
| MnO | 0.1 | 0.1 | 0.1 | 0.1 |
| MgO | 4.0 | 3.1 | 3.3 | 3.4 |
| CaO | 7.2 | 7.1 | 6.3 | 7.1 |
| $Na_2O$ | 3.0 | 3.2 | 3.8 | 2.8 |
| $K_2O$ | 2.4 | 1.3 | 2.0 | 1.2 |
| $P_2O_5$ | 0.2 | 0.2 | 0.2 | - |
| Total | 100.0 | 98.8 | 99.3 | 98.0 |

## 1.2 The Crust

The upper few kilometres of the earth is made up of a thin vineer of sediments and sedimentary rocks formed by erosion and transport of sediments into the basins. These are underlain by hard igneous and metamorphic rocks. The latter rock types are formed by re-crystallisation of igneous and sedimentary rocks.

### *1.2.1 The Continental Crust*

The upper few kilometres of the earth is made up of sediments or sedimentary rocks, deposited in sedimentary basins. The primary or P-wave velocity ($V_P$) in this region varies between 1.5 and 4.5 km/sec. The middle part of the continental crust between 5 and 30 km, the $V_p$ (5.8–6.3) corresponds to granodioritic crust. Granulitic rocks are formed at pressures of 6 to 8 kb (20–25 km below the surface) and temperatures of 550–800°C [$P(H_2O) < P(Total)$]. Granulites ($V_p$ = 6.3–7 km/sec) are exposed in different parts of the earth due to crustal erosion. South Indian granulitic terrain is an example of such an exposed lower crustal section. On the basis of estimation of a few kilometres of sediments and sedimentary rocks at the surface of the earth, followed successively by granite-granodioritic layer and then mafic granulites/gabbro, Ronov and Yaroshevsky (1969) calculated average composition of the crust (Table 1.1), which is not different from the composition of Island arcs (McBirney 1969) and Markhinin (1968).

It has been noted that certain regions of the earth's crust are characterised by low velocity zone (Conrad discontinuity, Ringwood 1975). Greise (1968) observed such a low velocity zone in the Alps near Lago-Lagorai (Fig. 1.4). Con-

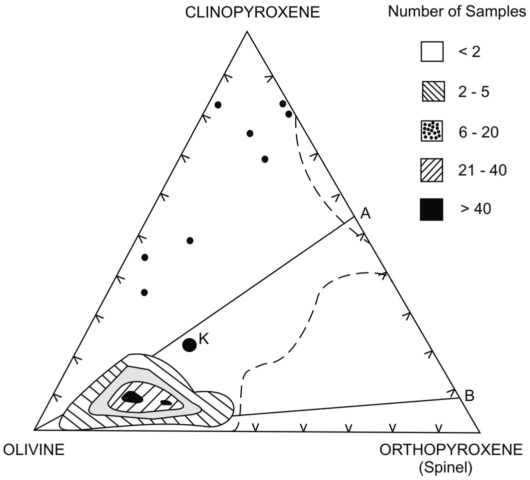

**Fig. 1.3** Composition of mantle xenoliths in a ternary diagram of olivine, orthopyroxene and clinopyroxene (after Cartar, 1970, Bull. Geol. Soc. Am., 81, 2021–2034, with permission)

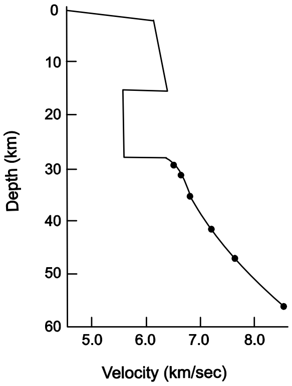

**Fig. 1.4** P-wave velocity-depth distribution in the Alps near Lago-Lagorai (after Greise, 1968, p. 89, with permission)

rad discontinuity has also been observed in the eastern part of India at Baliamba-Jagannathpur and at Konarak-Mukundapur section of Orissa (Kaila et al. 1987). Such a low velocity zone has also been detected in Kola peninsula, Russia. There are many other localities, where Conrad discontinuity has been found at depths of 10–15 km. Unlike Moho, this discontinuity has not been found to be distributed globally.

About 13 km of drilling was completed by the Russian earth scientist (Kola Superdeep project) at Zaporiliny in Kola peninsula. Thin section studies of mineral assemblages of the drill cores, collected from a depth of 1.4–4.9 km, reveal that there are rocks, which are essentially composed of mineral assemblages typical of pumpelyite-prehnite-quartzs subfacies of zeolite facies. Microscopic studies of rocks collected from depths between 9–6.5 km are characterised by the presence of chlorite, epidote and actinolite; this assemblage is typical of green-schist facies. Below 6–6.5 km hornblende appears and the rocks seemingly underwent metamorphism typical of almandine amphibolite facies. Below this depth sillimanite appears along with orthoclase, suggesting that these rocks attained P-T conditions similar to orthoclase-sillimanite subfacies of almandine-ampholite facies. There is a layer of biotite gneiss (2750 my old below 6–8 km) with hornblende and staurolite as associated minerals. A careful study of the drill cores across the so called Conrad discontinuity shows the presence of subparallel horizontal faults with evidence of shearing and mylonitisation. This might have lowered the density of rocks. Thus, in many localities, Conrad discontinuity may be related to the presence of a layer of lower density underlying higher grade rocks of greater density.

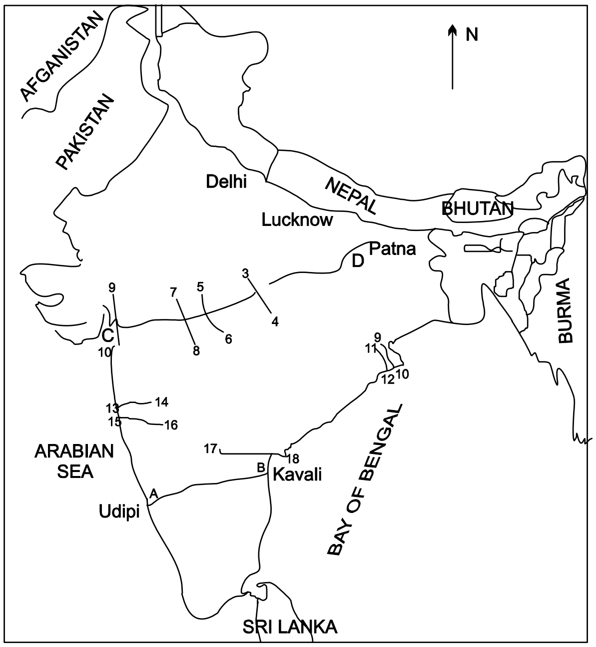

**Fig. 1.5** Map of India showing the location of various deep seismic profiles obtained by the scientists of the National Geophysical Research Institute. The Ujjain-Mahan and Propatheda-Patur profiles across Narmada-Son lineament are also shown (after Kaila et al. 1985, with permission from the Geological Society of India)

The thickness of the crust in such orogenic regions as the Andes (Fisher and Raith 1962), the Alps (Greise 1968) and the Himalayas (Kaila and Narain 1976) is 65 ± 5 km. Greater thickness of the crust in the orogenic regions, is caused by extra-masses of the mountains above the surface, which in turn have bigger root zones to counter isostatic adjustments. Kaila and his associates determined the crustal structure along different sections of India by using deep seismic sounding (DSS) technique.

Their results of DSS studies along the Kavali-Udipi profile (A-B, Fig. 1.5, Kaila et al. 1979) of the Cuddapah basin have been summarised by Kaila and Tewari (1985) in Fig. 1.6. In the eastern part of this section the Moho lies at a depth of 35–36 km, and below Dharmavaram it occurs at the same depth. In the western part, the Moho lies at a depth of 38 km, but occurs 41 km below Holalkere, and 36 km below Chennagiri.

Kaila et al. (1987) made deep seismic sounding along Hirapur-Mandla profile of central India. According to them along this region the Vindhyan sediments (maximum thickness 7 km, P-wave velocity 4.5–5.4 km/sec) overlie the crystalline basement rocks. The Moho discontinuity in this region lies 39.5 km below at Tikaria and 45 km below at Narsinghgarh.

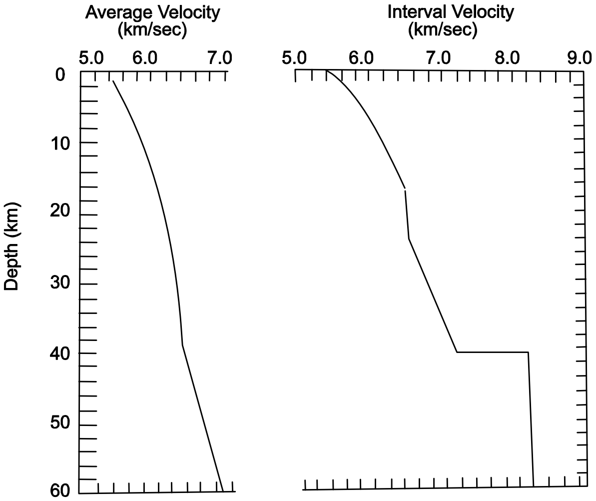

**Fig. 1.6** Average interval velocity versus depth profile in the Indian Peninsular shield (after Kaila et al. 1979, with permission from the Geological Society of India)

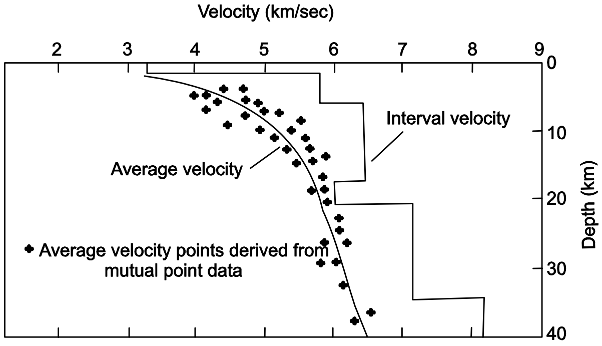

**Fig. 1.7** Average interval velocity versus depth profile along Baliamaba-Athgarh-Kendrapara-Jogonathpur, deep seismic sounding profile (after Kaila et al. 1987, with permission from the Geological Society of India)

Crustal structure of the Gondwana basin in the Mahanadi delta area of Orissa (Fig. 1.7) has been determined by Kaila et al. (1987) by using the DSS technique. The velocity versus depth profiles along Baliamaba-Athgarh-Kendrapara-Jagannathpur, and Konarak-Pratapnagar-Mukundpur sections are given in Fig. 1.7. In the case of both these sections a sudden drop in velocity from 6.5–6 km/sec may be observed below 20 km, suggesting the presence of the Conrad discontinuity. This is followed by an increase in the P-wave velocity to 7.1 km/sec. The thickness of the low velocity layer is about 3 km. The Moho discontinuity in this region lies at a depth of 34.5 km, across which the velocity increases to 8.1 km/sec.

The observations of the deep seismic sounding study of Kaila et al. (1985) across Narmada-Son lineament and central India along Ujjain-Mahan (Fig. 1.5) are summarised in Fig. 1.8, which shows the presence of Moho discontinuity at a depth of 40 km, but unlike the Gondwana basin of the Mahanadi delta area, the Narmada-Son region is devoid of any low velocity discontinuity. The depth versus velocity profiles along Ujjain-Dorwa, Dorwa-Mahan, Ahmedabad-Broach, Broach-Navasari, Saurashtra, Koyna and Peninsular shield show that a velocity of 8 km/sec, corresponding to M-discontinuity is reached at variable depths.

Kaila et al. (1984) determined the crustal structures of the region along Wular Lake-Gulmarg-Naushera across the Pir Panjal Range of the Himalayas (section 1–2, Fig. 1.9). The DSS profile of the section is given in Fig. 1.9. They observed that the Moho discontinuity lies at depths above 63–69 km, 78 km and 67 km north of Makum, the Greater Himalayan and the Nangaparbat region.

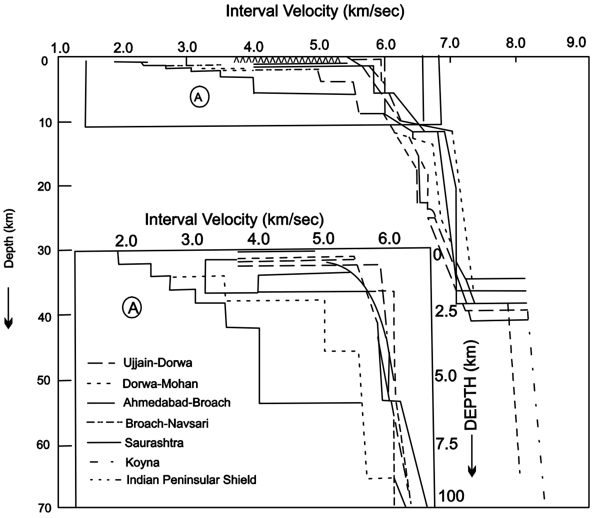

**Fig. 1.8** Velocity versus depth profile along Ujjain-Dorwa and Dorwa-Mahan sections of the Ujjain-Mahan deep seismic sounding profile. Inset shows the enlarged velocity-depth profile detailed in the shallower depth range 0–10 km. The interval velocity functions along the deep seismic sounding profile in India (Fig. 1.5) are shown for comparison (after Kaila et al. 1985, with permission from the Geological Society of India)

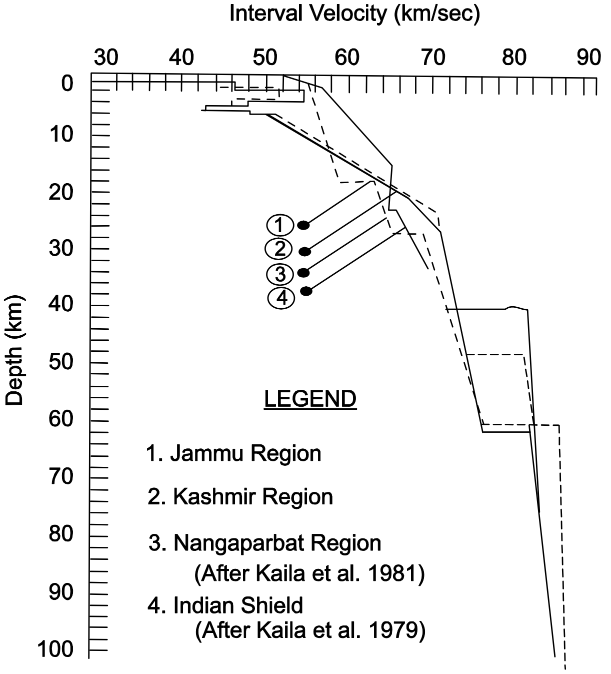

**Fig. 1.9** Interval velocity depth profile for the Jammu and Kashmir valleys determined from deep seismic sounding data. The interval velocity functions for the Indian Shield and Nangaparbat region, determined from the deep seismic sounding data, are shown for comparison. (Kaila et al. 1979, with permission from the Geological Society of India)

### 1.2.2 Oceanic Crust

On the basis of the studies of Hill (1957) and Raith (1963), a cross section of the oceanic crust may be as follows: the top is constituted of sea (4–5 km thick, $V_p = 1.5$ km/sec), followed by a layer of unconsolidated sediments (layer 1; 0.5 km thick, $V_p = 2$ km/sec), a layer of porous basaltic rocks (layer 2, $1.71 \pm 0.75$ km thick, $V_p = 5.07 \pm 0.63$ km/sec), lower part of which is intruded by mafic dykes and a $4.80 \pm 1.42$ km thick third layer has a P-wave velocity of $6.69 \pm 0.28$ km/sec. The S-wave velocity through this layer is 3.50 km/sec. Hess (1965) suggested that this third layer may be composed of serpentinised peridotite, but according to Ringwood (1975), such altered ultramafic rocks do not have the observed $V_p/V_s$ ratio of 1.8. He therefore, advocated that this layer at the base of the oceanic crust may be a mixture of anhydrous dolerite and gabbro along with assemblages typical of green-schist and amphibolite facies. A layer of such a composition has $V_p/V_s$ ration of 1.8.

A profile of the rocks in the Mid-Oceanic Ridge is shown in Fig. 1.10. Here, the layer of unconsolidated sediments is vanishingly small or missing and the basaltic layer is present below water. This layer of basalt is thicker than that of the oceanic crust in other areas. The third layer below basalt ($V_p = 4.86$ km/sec) is thin and the M-discontinuity between the mantle and the crust is poorly defined or absent. This region is characterised by basalt volcanism and hence, high heat flow. The Mid-Atlantic region is considered to be the region of ascending convection current.

The island arc regions are supposed to be regions of descending convection currents. The proposed structure across Puerto Rico is shown in Fig. 1.11. According to Morgan (1965), in the region of the arc-trench system, there is mass deficiency and negative gravity anomalies in the trench region, which may be related to dynamic processes (Ringwood 1975). He envisaged stress difference of the order of about half a kilobar. Rocks cannot support static stress of this magnitude. Thus, sinking of the lithosphere in this region appears to be very feasible. The subduction of the lithosphere is accompanied by the generation of earthquakes in the Benioff zone. The Moho discontinuity in the cases of some island arc subcrustal region may be missing. There is high heat flow toward the island arc side of the trench.

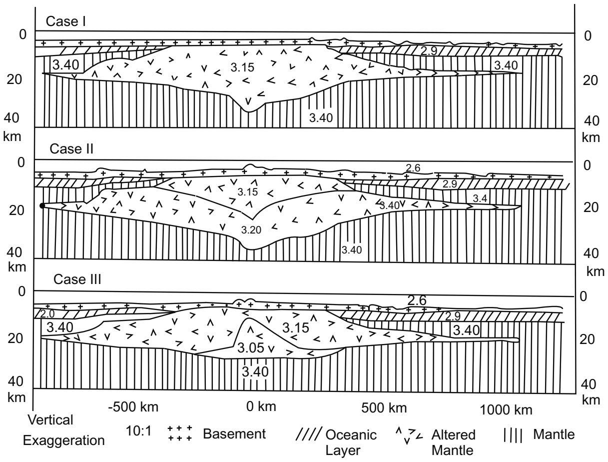

**Fig. 1.10** Three possible crustal models across north mid-Atlantic ridge which satisfy gravity anomalies and are in accordance with the seismic data. (from Talwani, Le Pichon and Ewing 1966, with permission of the American Geophysical Union)

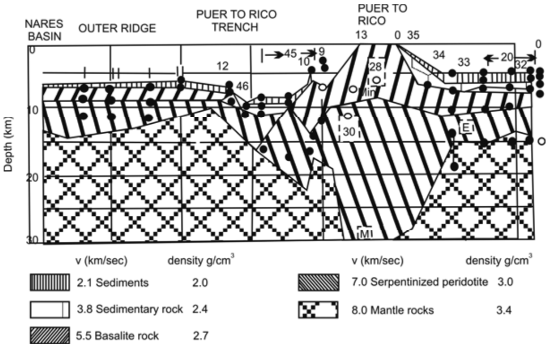

**Fig. 1.11** Crustal section across the Puerito Rico Trench from seismic refraction and gravity data. The points are from seismic refraction data and the position of the M-discontinuity has been obtained from gravity data in such a way that the computed free air anomaly matches with observed values (reproduced from Talwani, Sutton and Worgel 1959, with permission)

## 1.3 Mantle

The portion of the earth immediately below the crust is the mantle. With the development of multi-anvil and laser-heated diamond-anvil high pressure apparatus, the rock types supposedly present in this portion of the earth (e.g. peridotites), have been the subject of intensive experimental studies, related to phase transformation, variation in density, elastic and rheological properties so that the mysteries of the earth could be unfolded.

### 1.3.1 Peridotite with Compositions Similar to Chondritic Meteorite as a Possible Mantle Material

The density distribution within the first 400 km depth inside the earth is summarised in Fig. 1.12. Press (1969) used

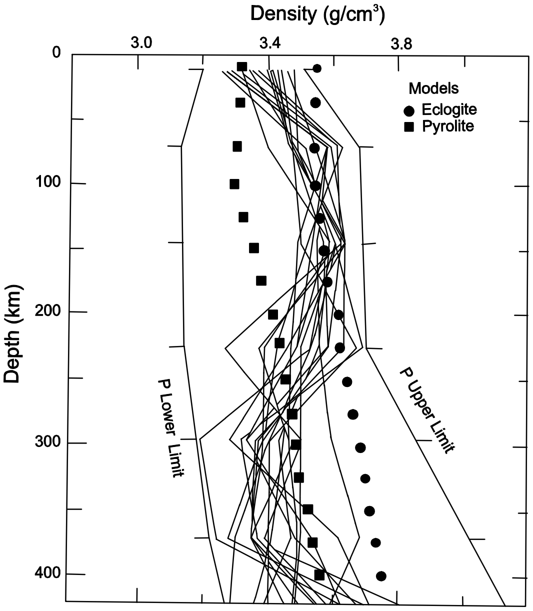

**Fig. 1.12** The observed values of density for peridotite and eclogite within the upper and lower limit of density as stipulated by the geophysicists for the density of mantle materials. Points show density values according to Clarke and Ringwood (1964) for pyrolite and eclogite models (after Press, 1969, reprinted from Science, with permission from the American Association for the Advancement of Science)

Monte Carlo statistical procedure and took into consideration many earth models. He used values for such mantle parameters as P- and S-wave velocities, density distribution (both upper and lower density limits as a function of depth), the mass of the earth, its moment of inertia and earth's free oscillation modes. Of various models generated by computers, two rock types appear to be the best candidates for mantle rocks: 1) peridotite and 2) eclogite.

With reference to Fig. 1.12, it may be observed that values of density for the above mentioned two rock types lie within the upper limit of density as stipulated by Press (1969).

The high P-T conversion of basalt to eclogite has been noted by Cohen et al. (Fig. 1.13a) and Gupta and Yagi (1979, Fig. 1.13b). Thus, complete melting of eclogitic mantle at depths should account for the generation of basaltic lavas, which have been observed to be a predominant lava type, throughout the history of the earth's evolution. This should however require large enthalpy of melting. Besides, experimental study on basalts suggest that conversion of basalt to eclogite (omphacite + pyrope-rich garnet) should require a depth of atleast 60 km (20 kb) and temperatures of more than 1000ºC.

In case of oceanic islands, the M-discontinuity defining crust-mantle boundary, occurs only below 8–10 km. Besides dredged samples from the ocean floor shows that below the oceanic islands, peridotite constitutes the mantle rocks.

Kushiro (1973) studied peridotites at pressures and temperatures equivalent to mantle depths. He observed that partial melting of peridotite accounts for the generation of basaltic magmas (Table 1.2). He further observed that at greater and greater pressure (e.g. 20 Kb or higher); partial melting of peridotites produced alkali basalts. Hence, peridotite may be accepted as one of the most possible rock type for the generation of basalts.

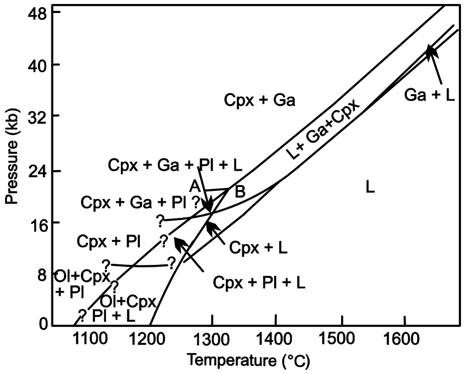

**Fig. 1.13a** High pressure-temperature projection on an anhydrous glass of olivine tholeiite composition, collected from Buffalo Butte, San Juan mountains, New Mexico, U.S.A. at variable temperatures and pressures. Cpx: clinopyroxene; Ga: garnet; Pl: plagioclase; Ol: olivine; L: liquid. Above curve AB, the assemblage clinopyroxene + garnet is representative of eclogite. The clinopyroxene is an omphacite and garnet has a composition similar to pyrope. (after Cohen, Ito and Kennedy, 1967; with permission from the American Journal of Science)

**Fig. 1.13b** P($H_2O$)-T diagram of a picritic basalt from wakuike (after Gupta and Yagi, 1979). Ga: garnet, Amph: amphibole, Cpx: clinopyroxene, Pl: plagioclase, Ht: magnetite; L: liquid; V: vapour. The assemblage above a-b is similar to that of eclogite. Reprinted from petrology and genesis of leucite bearing rocks; Gupta and Yagi, 1980, with permission from Springer-Verlag, Berlin

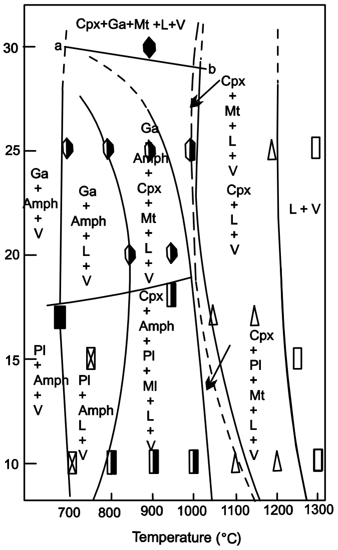

**Table 1.2** Compositions (wt%) of glasses formed by partial melting of a natural garnet lherzolite (Kushiro 1973)

| Oxides | Starting Material | 10 kbar, 1375ºC | 15 kbar, 1450ºC | 20 kbar, 1475ºC |
|---|---|---|---|---|
| $SiO_2$ | 44.54 | 50.3 | 51.4 | 50.3 |
| $Al_2O_3$ | 2.80 | 12.4 | 14.1 | 12.3 |
| $TiO_2$ | 0.26 | 1.07 | 1.24 | 1.10 |
| $Cr_2O_3$ | 0.29 | 0.44 | 0.31 | 0.38 |
| FeO | 10.24 | 10.5 | 10.0 | 10.4 |
| MnO | 0.13 | 0.19 | 0.21 | 0.18 |
| MgO | 37.94 | 9.62 | 8.07 | 9.97 |
| CaO | 3.32 | 12.5 | 11.2 | 12.0 |
| $Na_2O$ | 0.34 | 0.80 | 1.07 | 1.49 |
| $K_2O$ | 0.14 | 0.44 | 0.76 | 0.65 |
| NiO | n.d. | 0.07 | n.d. | 0.11 |
| Total | 100.00 | 98.3 | 98.4 | 98.8 |
| | | | | |
| Q | - | 2.02 | 3.97 | - |
| Or | 0.83 | 2.60 | 4.49 | 3.84 |
| Ab | 2.88 | 6.77 | 9.05 | 12.6 |
| An | 5.70 | 29.0 | 31.4 | 25.0 |
| Di | 8.54 | 27.1 | 19.8 | 28.3 |
| Hy | 12.59 | 28.2 | 26.8 | 21.5 |
| Ol | 68.54 | - | - | 4.96 |
| Cr | 0.43 | 0.65 | 0.46 | 0.56 |
| Il | 0.49 | 2.03 | 2.36 | 2.09 |
| Total | 100.00 | 98.37 | 98.33 | 98.95 |

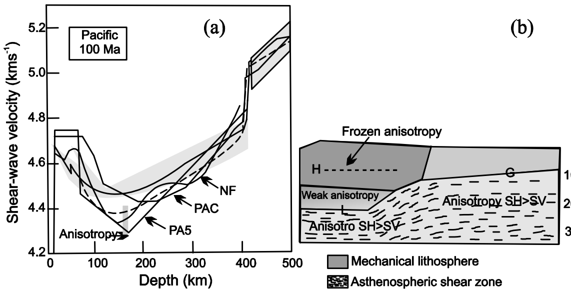

**Fig. 1.14** (a) The shear-wave velocity of pyrolite along a 100 Ma conductive cooling geotherm in the elastic limit, and including the effects of dispersion according to the seismological attenuation model QR 19 (Romanowicz 1998) and $\alpha = 0.25$ (bold dashed). Reprinted from "Seismic Properties of rocks and minerals and structure of the earth by Stixrude, 2007. In: Treatise on Geophysics, **2**, Mineral Physics; Past, Present and Future; ed: D. Price, with permission from Elsevier. (b) Sketch illustrating pattern of anisotropy found in a recent tomographic model in relation to lithospheric thickness and to the Lehmann (L) and Guttenberg (G) discontinuities. The Itales discontinuity (H) is also indicated. Global anisotropy and the thickness of continents. From Gung YC, Panning M and Bomanowicz B (Nature, 422: 707–711). Also see Stixrude, 2007; reprinted from Seismic Properties of Rocks and Minerals. In: Treatise on Geophysics, **2**, Mineral Physics; Past, Present and Future; ed: D. Price, with permission from Elsevier

## *1.3.2 Various Seismic Discontinuities within the Mantle*

Between Moho and the upper-lower mantle transition zone, there are discontinuities at following depths: 59 km (Hales), 77 km (Guttenberg), 230 km (Lehmann), 313 km, 410 km, 520 km and 660 km. Hales, Gutterberg and Lehmann (Fig. 1.14a and b) are discontinuities after the names of eminent geophysicists. The discontinuities at 410, 520 and 660 km depths are observed globally, and are related to phase transformation. The Lehmann discontinuity (L) near 200 km depth and the Gutenberg discontinuity (G) has been merged into one by Gung et al. (2003). These two discontinuities together with Hales discontinuity at 59 km (H) are considered to be related to anisotropy found in recent tomographic model in relation to lithospheric thickness.

The discontinuity at 520 km has been reported by Shearer (1990) and Revenaugh and Jordon (1991). Phase transformations of wadsleyite to ringwoodite and the evolution of Calcium perovskite from garnet (Ita and Stixrude, 1992) have been suggested. This could also be related to a subducting plate providing chemical heterogeneity.

In the lower mantle, there are discontinuities at following depths: 720 (global?), 900, 1200 (global?), 1700, 2640 (D" layer) and 2870 km (ULVZ). At the D" layer, the seismic wave speed becomes faster, whereas in the ultra-low velocity zone (ULVZ) the speed becomes slower. The terms fast and slow refer to regions of anomalously high and low wave speeds in tomographic models (Stixrude, 2007). The ULVZ (Garnero and Helmberger, 1996), which marks the beginning of the liquid core, is associated with 10% reduction in the wave speed. As many discontinuities are related to phase transformations of different minerals, experimental studies on important mantle minerals under variable P-T conditions are described below to correlate between different types of phase transformations at various depths with respect to various seismic discontinuities.

### 1.3.2.1 Investigation of the system $Mg_2SiO_4$ - $Fe_2SiO_4$ at high pressure and temperature: its significance with reference to 400 km discontinuity

The system $Mg_2SiO_4$ - $Fe_2SiO_4$ was investigated by Akimoto and Fujisawa (1966–1968) up to a pressure of 9.5 GPa. They presented phase diagrams of this system at 800, 1000 and 1200ºC. These are isothermal sections as a function of mole fraction of $Fe_2SiO_4$. Their study of the system $Mg_2SiO_4$ - $Fe_2SiO_4$ at variable pressures at 800ºC is summarised in Fig. 1.15, which shows that in presence of less than 84 mole% $Fe_2SiO_4$, orthorhombic olivine ($\alpha$) is stable up to 115 kb above which $(Mg, Fe)_2SiO_4$ with spinel struc-

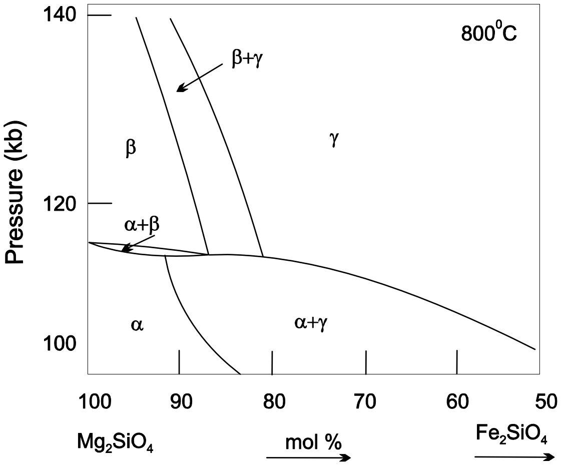

**Fig. 1.15** The system forsterite-fayalite at variable pressures and 800ºC: α: orthorhombic olivine; δ: spinel, (after Akimoto and Fujisawa, 1966, reprinted from Earth and Planetary Science Letters, with permission from Elsevier)

ture (β) is stable. With increase of $Fe_2SiO_4$ molecule α olivine is converted to a phase with inverse spinel (γ) structure.

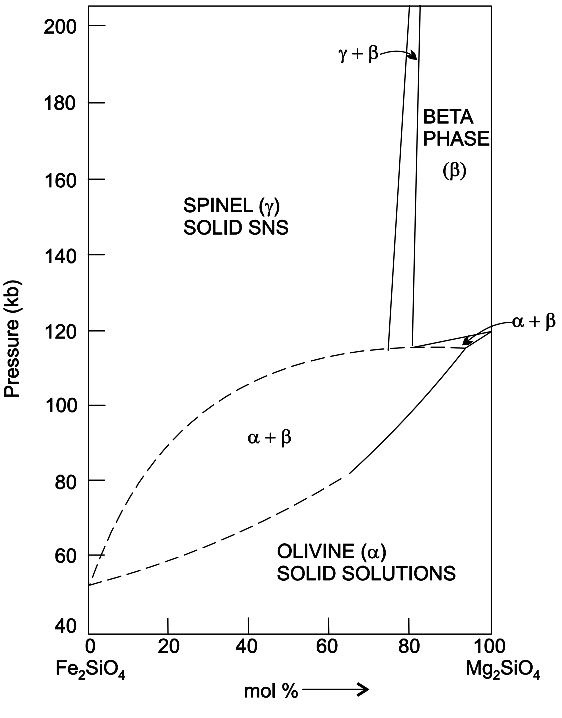

**Fig. 1.16** Phase relations in the system forsterite-fayalite at pressures between 50 and 200 kbars at 1000ºC (after Ringwood and Major, 1970, reprinted from Earth and Planetary Science Letters, with permission from Elsevier)

Ringwood and Major (1970, Fig. 1.16) investigated the same system between 5 and 20 GPa and at 1000ºC. They confirmed the findings of Akimoto and Fujisawa (1966). In case of β spinel, ($Mg^{2+}$ $Mg^{2+}$ $SiO_4$) both $Mg^{2+}$ occupy octahedral site, whereas $Si^{4+}$ is located in the tetrahedral site.

In case of the inverse spinel structure (γ phase) one of the $Mg^{2+}$ cation occupies the tetrahedral site whereas the other $Mg^{2+}$ and $Si^{4+}$ shares the octahedral site. The unit cell dimension of the β phase is related to those of the spinel (γ) phase having following cell dimensions: $a_\alpha = \sim a_\gamma$, $b_\beta = \sqrt{2}\, a_\gamma$ and $C_\beta = \sim a_\gamma \sqrt{2}$.

The join $Mg_2SiO_4$ - $Fe_2SiO_4$ was investigated later by Ito and Takahashi (1987), who found that above 24.5 GPa, $(Mg, Fe)_2SiO_4$ breaks down to three different assemblages with increasing Fe/Mg+Fe ratio (Fig. 1.17a, b).

Formation of assemblage, perovskite + wustite, could be explained by them according to following reaction:

$(Mg, Fe)_2SiO_4 \Leftrightarrow (Mg, Fe)SiO_3 + (Mg, Fe)O$
spinel perovskite magnesio-wustite

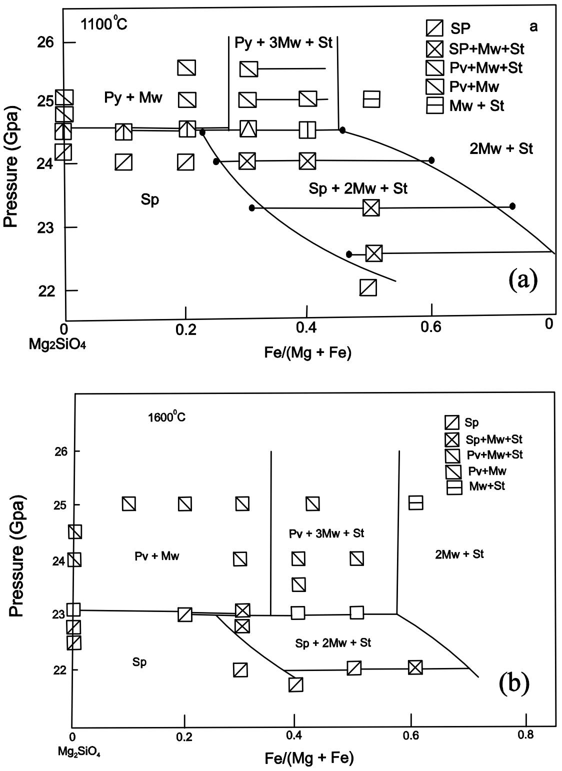

**Fig. 1.17** (a) Pseudobinary diagram in the system forsterite-fayalite at 1373 K: Pv: perovskite; Mw: magnesio wustite; St: stishovite; Sp: spinel, (after Ito and Takahashi, 1989. From the Journal of Geophysical Research, with permission). (b) Pseudobinary diagrams in the system forsterite-fayalite at 1873 K. Pv: perovskite; Mw: magnesio wustite; St: stishovite; Sp: spinel. (Ito and Takahashi, 1989, with permission of the American Geophysical Union)

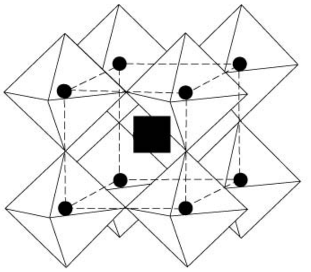

**Fig. 1.18** Idealised structure of perovskite $CaTiO_3$. A Ca atom is at the cube centre and the Ti-O octahedral are shown diagrammatically. (after Naray-Szabo, 1943). In the present case Mg occupies the position of Ca, whereas Si takes the place of Ti in the octahedral site

Formation of the assemblage (perovskite + magnesio wustite + stishovite) could be explained by the breakdown of spinel to perovskite, magnesio wustite and stishovite.:

$$2(Mg, Fe)_2SiO_4 \Leftrightarrow (Mg, Fe)SiO_3 + 3(Mg, Fe)O + SiO_2$$

spinel perovskite magnesio wustite stishovite

On the basis of their experimental studies and crystal-chemical consideration, Ringwood and Major (1971) concluded that the $CaSiO_3$ perovskite was stable above 100 kb at 1000ºC. It was suggested that the $Ca^{++}$ cation occupied a cubic close packed site, whereas the smaller cations comprising $Ti^{4+}$ and $Si^{4+}$ have octahedral coordination. Thus, in case of $MgSiO_3$ perovskite, $Mg^{2+}$ should be present in the site mentioned in Fig. 1.18. The large Ca atoms thus, occur in the cubic center whereas Ti is octahedrally coordinated with respect to oxygen.

Collerson et al. (2000) reported xenoliths and megacrysts from Malaita containing high pressure mineral assemblages apparently derived from the mantle transition zone between 400 and 670 km. These xenoliths and megacrysts, which occur in 34 Ma-old alnoite pipes and sills, intrude cretaceous Ontong, Java Plateau basalts on the island of Malaita, Southwest Pacific. Collerson et al. described occurrence of majorite, calcium and magnesium-perovskite, aluminous silicate phases and micro-diamond. Based on empirical barometer, majoritic garnets in these xenoliths record pressures of up to 22 GPa. These samples were brought to the surface at about 34 Ma ago by a potassic ultramafic magma, which presumably originated from the lower mantle.

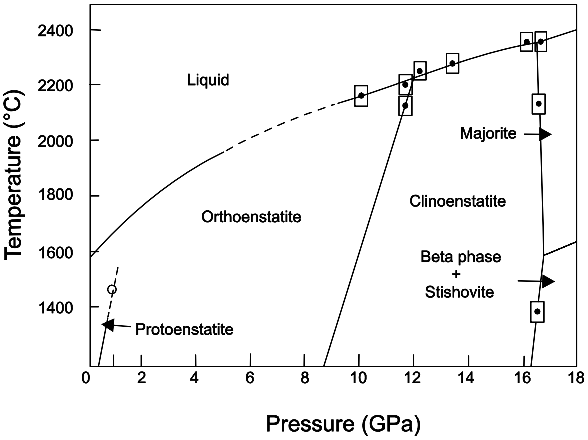

**Fig. 1.19** Phase diagram for the enstatite system (after Presnall and Gasparik, 1990; with permission from the Journal of Geophysical Research)

### 1.3.2.2 High pressure-temperature stability of $MgSiO_3$ system

The stability of $MgSiO_3$ at different temperatures up to 2400ºC and 20 GPa was studied by Kato and Kumazawa (1985). Presnall and Gasparik (1990) also investigated the same system in more detail at lower temperatures (Fig. 1.19). There is not much difference in the two studies, except for the fact that at lower temperatures, Presnall and Gasparik showed the presence of β-spinel and stishovite as a breakdown product of $MgSiO_3$ ($2MgSiO_3 \Leftrightarrow Mg_2SiO_4$, β-spinel) + $SiO_2$ (stishovite) at lower temperatures.

Wang et al. (2004) extended their study on the $MgSiO_3$ system at even higher pressure (Fig. 1.20). Their study was made particularly with reference to the stability of akimotite ($MgSiO_3$ ilmenite). Investigation of Wang et al. shows that above 16 ± 0.5 GPa with progressive increase of temperature high pressure clino-enstatite is converted to γ-spinel + stishovite (above EJ), β-$Mg_2SiO_4$ (spinel) beyond

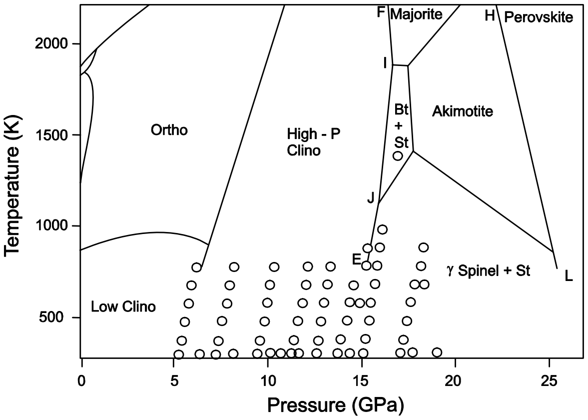

**Fig. 1.20** Phase diagram of $MgSiO_3$ system determined from quench experiments (Gasparik, 1990). Superimposed is a P-T path in the P-V-T measurements. Due to high temperatures nature of this phase, most P-V-T data are collected outside the stability field. Bt: wadsleyite; St: stishovite; Clino: clinoenstatite (reprinted from Wang, Uchida, Zhang, Rivers, Sutton, 2004. In: New Developments in High Pressure Mineral Physics and Applications to the Earth's Interior. D.C. Rubie, T.S. Deffy and E. Ohtani, eds.; with permission from Elsevier)

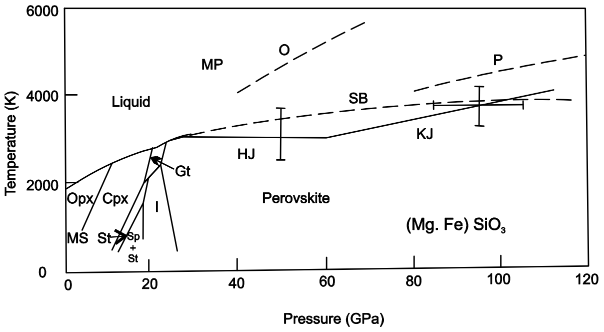

**Fig. 1.21** The P-T stability of enstatite (after Kato and Kumazawa, 1985; reprinted from Nature, with permission from Nature Group of Publishers)

JI and majorite garnet (above IF). With further increase of pressure and temperature, there is a field of akimotite ($MgSiO_3$ ilmenite). Beyond 23 GPa, above HL, perovskite is the stable phase.

The P-T stability of $MgSiO_3$ perovskite at different temperatures (up to 3500ºC) and pressures (up to 100 GPa, Fig. 1.21) has been discussed by Kato and Kumazawa (1985). The melting curve of (Mg, Fe)$SiO_3$ to 60 GPa was determined by Heinz and Jeanloz (1987). They showed that melting is independent of pressure above 30 GPa (Tm ~ 3000 K). Later studies by Bassett et al. (1988) support the results of Heinz and Jeanloz. Above 50 GPa, there is slight increase in the melting temperature of (Mg, Fe)$SiO_3$ (Knittle and Jeanolz, 1989). Subsequent studies by Ito and Katsura (1992) showed that melting of $MgSiO_3$ occurs at 2870 K, and between 21 and 25 GPa, the melting curve has a slope. Williams (1990) studied a composition $(Mg_{0.88}Fe_{0.12})SiO_3$ at 50–55 GPa using a laser-heated cell. His study shows that the quench glass was enriched in $SiO_2$ and magnesio-wustite was present as a liquidus phase. Further study of Ito and Katsura (1992) suggested that there is eutectic-type of melting relationship between magnesio-wustite and perovskite. They suggested that there may be incongruent melting of (Mg, Fe)$SiO_3$ at higher pressure.

Like (Mg, Fe)$SiO_3$, $CaSiO_3$ perovskite may also exist in the lower mantle as a separate phase, which could be present in relatively lesser amount than the ferro-magnesian silicates (perovskite and magnesio-wustite). According to Mao et al. (1991) a considerable enrichment of Ca in the form of $CaSiO_3$ perovskite should result in the increase of bulk modulus of earth's lower mantle. For example, $CaSiO_3$ has a higher bulk modulus than (Mg, Fe)$SiO_3$ (Mao et al. 1991). It has been suggested by Ita and Stixrude (1991, quoted in Hemeley and Cohen, 1992) that conversion of $CaSiO_3$ (pyroxenoid) to a mineral with perovskite-like structure is responsible for the seismic structure near 520 km; which corresponds to a transition zone (Shearer, 1990). As partitioning of REE could be controlled by the presence of cubic $CaSiO_3$ in the lower mantle, it may be considered as a reservoir of REE in the lower mantle.

On the basis of their studies on (Mg, Fe)$SiO_3$ (perovskite), Mao et al. (1977) suggested that such silicates with perovskite structure should be stable up to 60 GPa, whereas Knittle and Jeanolz (1987) concluded that Mg-rich perovskite may be stable up to 100 GPa. The breakdown of $MgSiO_3$ to oxides at P-T conditions similar to that existing in the D" layer is also expected.

Calcium perovskite ($CaSiO_3$) is stable at relatively lower pressure than magnesium perovskite (11–13 GPa, Mao et al. 1991). Perovskite ($CaSiO_3$) has a cubic structure and is considered to be stable to the mantle-core boundary. Experimental results by Tarrida and Richet (1989) and Yagi et al. (1989) showed that $CaSiO_3$ (perovskite) is stable to 94 GPa and 100 GPa, respectively.

### 1.3.2.3 The $MgSiO_3$ - $FeSiO_3$ system

Ringwood and Major added $FeSiO_3$ to see the effect of iron in the stability of $MgSiO_3$ polymorphs. Their results up to 20 GPa at 1000ºC are summarised in Fig. 1.22, which shows that with increase of $FeSiO_3$, β $(Fe, Mg)_2SiO_4$ coexist with stishovite. At the central part of the diagram spinel$_{ss}$, $MgSiO_3$ - clinopyroxene are stable to 20 GPa.

Fig. 1.23a shows polymorphic transformation of quartz, coesite and stishovite. The quartz ⇔ coesite transformation was established by Khitarov (1964), but coesite ⇔ stishovite univariant curve is based on the studies by host of investigators, Ringwood and Major (1966), Boettcher and Wyllie (1968) and Akimoto and Syno (1969).

In case of Coesite, $Si^{4+}$ has four-fold coordination with respect to oxygen, whereas stishovite has tetragonal symmetry. Octahedra of oxygen anions surround $Si^{4+}$ cation, and the structure is similar to that of rutile (Fig. 1.23b).

**Fig. 1.22** Phases observed in the system $MgSiO_3$ - $FeSiO_3$ at pressures up to 200 kbars and approximately 1000ºC.

○ Complete transformation to spinel + stishovite

⊙ Boundary determined by spinel composition obtained from lattice parameter.

←○ Experiment in three phase field

● Inferred points on boundary of pyroxene stability field.

Reprinted from Earth and Planetary Science Letters, with permission from Elsevier

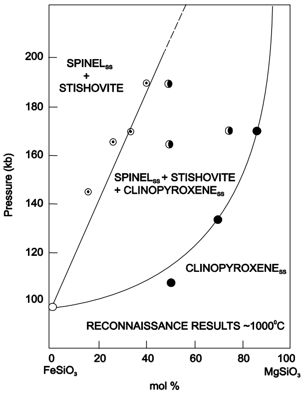

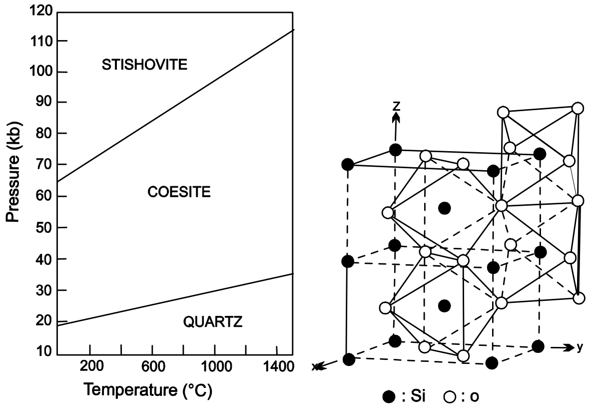

(a) (b)

**Fig. 1.23** (a) Quartz-coesite and coesite-stishovite equilibrium curves. The former is based upon the results of Khitarov (1964), Green, Ringwood, and Major (1966), and Boettcher and Wyllie (1968). The latter is based upon the results of Akimoto and Syno (1969) referred to the NBS pressure scale (after Ringwood, 1975; with permission from McGraw-Hills, Inc.). (b) The tetragonal structure of rutile showing the co-ordinating octahedral of oxygen anions around the titanium cations and the way in which these octahedra are linked in bands by sharing horizontal edges (Evans, 1966, with permission from the Cambridge University Press)

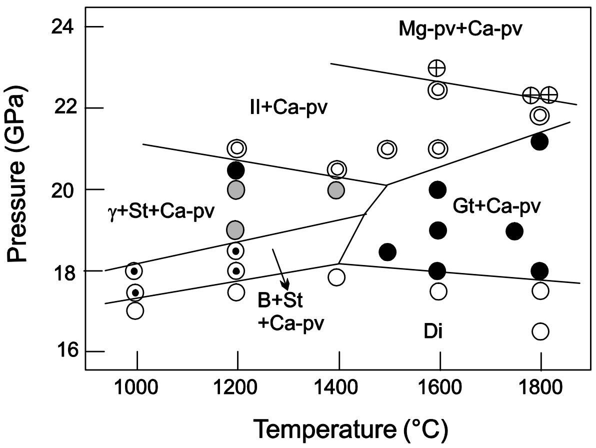

**Fig. 1.24** P-T Stability of diopside. Open and solid circles indicate product phases of diopside (Di) and of garnet (Gt) + Ca-perovskite (Ca-pv), respectively. Circles with a dot and those with lines represent β-phase + stishovite (St) + Ca-perovskite and γ–phase + stishovite + Ca-perovskite, respectively. Double circles and circles with cross indicate ilmenite (Il) + Ca-perovskite and Mg-perovskite (Mg-pv) + Ca-perovskite, respectively. (Reprinted from Akaogi, Yano, Tejima, Iijima and Kojitani (2004). In: New Developments in High Pressure Mineral. Physics and Application to the Earth's Interior (Eds.: D.C. Rubie, T. Duffy, E. Ohtani, with permission from Elsevier)

Whereas density of coesite is 2.91 gm/cm$^3$, that of stishovite is 4.28 g/cm$^2$. The large increase in density is associated with change of coordination of $Si^{4+}$ from four to six-fold co-ordination.

Post-stishovite structures at different pressures and temperatures was estimated by Karki et al. (1997), using pseudopotential method. They thought that at lower mantle, stishovite with rutile type of structure is changed to $CaCl_2$, $PbC_2$ and pyrite type structure at variable pressures in terms of volume changes.

Karki et al. (1997) estimated post-stishovite structures at different pressures and temperatures using pseudopotential method. They thought that at lower mantle, stishovite with rutile-type of structure is changed to $CaCl_2$, $PbC_2$ and pyrite type of structure at variable pressures in terms of volume changes.

### 1.3.2.4 Pressure-temperature phase relations in $CaMgSi_2O_6$

Phase transitions of $CaMgSi_2O_6$ diopside and $CaSiO_3$ wollastonite were studied by Akaogi et al. (2004) using a Kawai-type multi-anvil apparatus. The results of high pressure experiments on diopside are presented in Fig. 1.24. They observed that at 17–18 GPa diopside dissociates to $CaSiO_3$-perovskite and (Mg, Ca)$SiO_3$ garnet (Gt) above 1400ºC. They further noted that the solubilities of $CaSiO_3$ in garnet and $MgSiO_3$ in perovskite, increase with temperatures. Figure 1.24 further shows that at 17–18 GPa diopside dissociates to Ca-perovskite + $\beta Mg_2SiO_4$ + stishovite. Akaogi et al. (2004) noted that the Mg, Si phases co-existing with Ca-perovskite change to $\gamma Mg_2SiO_4$ + $SiO_2$ to ilmenite, and finally to Mg perovskite with increasing pressure. Figure 1.24 shows that wollastonite ($CaSiO_3$) transform to a phase with walstromite-like structure, and then further dissociates to $Ca_2SiO_4$ larnite + $CaSi_2O_5$ titanite at 9–11 GPa having a Clapeyron type slope. The assemblage larnite + titanite transforms to $CaSiO_3$ perovskite at 14.6 ± 0.6 GPa. Calcium perovskite ($CaSiO_3$) has tetragonal (I 4 / mcm) structure transforming to cubic Pm3m with increasing temperature (Stixrude et al. 2007).

Ringwood and Major (1968) synthesised a garnet at pressures between 20 and 30 GPa and thought that such a garnet may be present in the deeper part of earth's mantle. They called this as majorite garnet. The garnet synthesised by them had the following composition: $SiO_2$: 52.43%, $Al_2O_3$: 2.46%, $Cr_2O_5$: 0.62%, $Fe_2O_3$: 0.65%, FeO: 17.14%, Mg: 26.07 and $Na_2O$: 0.63%.

Ideally the composition of majorite ($MgSiO_3$) can be written in terms of garnet formula: $4MgSiO_3$ or $Mg_3$(Mg, Si) $Si_3O_{12}$. In this formula, one cation of $Mg^{2+}$ and one of $Si^{4+}$ presumably occupies octahedral site and three $Si^{4+}$ cations are present in the tetrahedral site.

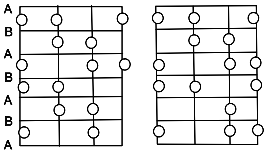

**Fig. 1.25** Diagrammatic comparison of the distribution of the metal atoms in corundum and ilmenite. The structures are viewed on (2 $\bar{1}$ $\bar{1}$ 0). Horizontal lines A, B indicate the positions of the close packed layers of O-atoms (after Wells, 1962. with permission from Oxford University Press)

Ito and Takahashi (1989) reported that in presence of iron, the pressure of conversion of akimotite ($MgSiO_3$ with ilminite structure) to perovskite takes place. The lower pressure-volume-temperature relations of akimotite up to 19 GPa and 1373 K at lower pressure, were studied by Wang et al. (2004), who observed that aluminium plays an important role in the akimotite stability field as pyrope has a complete solid solution relationship with $MgSiO_3$ (majorite garnet). This causes enlargement in the garnet field at the expense of akimotite. This is amply illustrated in Fig. 1.24 of Wang et al. It is observed that 10 mol% of pyrope in majorite field can enlarge the garnet field and can push the garnet-akimotite phase boundary downward by about 100 K and the pressure range is expanded by 1 GPa. According to Panero et al. (2006) $MgSiO_3$ perovskite dissolves about 15 mol% $Al_2O_3$ at 26 GPa and 1873 K.

Akimotite is isostructural with ilmenite, in which oxygen ions are nearly hexagonally close-packed and the cations occupy octahedral sites. The $SiO_6$ and $MgSiO_6$ octahedral sites form layers that lie half way between the close packed oxygen layers. In each layer, Mg or all Si alternate so that closest pairs are always Mg-Si atoms.

Ringwood (1975) considered ($MgSiO_3$ with ilmenite structure) to be similar to corundum structure, which is consisted of hexagonal closed packet array of oxygen atoms, with metal atoms occupying two-thirds of the octahedrally coordinated metal atoms (Fig. 1.25). In case of akomotite, $Mg^{2+}$ atoms occupy sites marked by solid circles.

### 1.3.2.5 Pressure-temperature stability of garnet

Pure pyrope ($Mg_3Al_2Si_3O_{12}$) breaks down to $MgSiO_3$ perovskite and $MgSiO_3$-$Al_2O_3$ solid solution at pressures above 26.5 GPa at 1723 K. They also reported that Al content in perovskite increases with increasing pressure and temperature.

Pyrope is transformed first to a polymorph with ilmenite structure at 21.5 GPa and 2400–3200 K and then is converted first to perovskite plus ilmenite at 24 GPa, and then to perovskite + corundum at 29 GPa. Finally this phase is transformed to perovskite with pyrope composition at 43 GPa (Serghiou et al. 1998). The isochemical nature of perovskite and pyrope was observed by Kesson et al. (1995).

Ahmed-Zaid and Madon (1995) made experimental studies on pyrope in a laser-heated diamond cell up to 40–50 GPa. They noted that natural pyrope broke down to perovskite and three alumina-rich phases depending on temperature and composition of the starting materials. These alumina-rich phases are (Ca, Mg)$Al_2SiO_6$ with an unknown structure (moderate temperature), $Al_2SiO_5$ with $V_2O_5$ structure (high temperature) and (Ca, Mg, Fe)$Al_2Si_2O_8$ with hollandite-like structure. The phase with hollandite-like structure formed from Fe-rich garnets.

Uchiyama et al. (1992) synthesised majorite at 20 GPa and 2200ºC and determined the bulk modulus of majorite, which is less than that of pyrope by 6%. A mixture of garnet and majorite (mixed in variable proportion) may therefore cause variation in the elastic properties of the mantle. O'Neill and Jeanolz (1994) studied P-T stability of Fe-rich garnet and found that garnet coexisting with perovskite was stable up to 50 GPa.

Miyajima et al. (1999, Fig. 1.26) studied garnet-perovskite transformation under P-T conditions similar to those of lower mantle. The three garnets used by them were collected from Dora-Maira massif, Western Alps (Pyd series), Checkoslovakia (Pyc) and Sakha Republic, Eastern Russia (Pys). In addition, they also used powdered materials of a garnet (Pysp). They noted that for all three py-

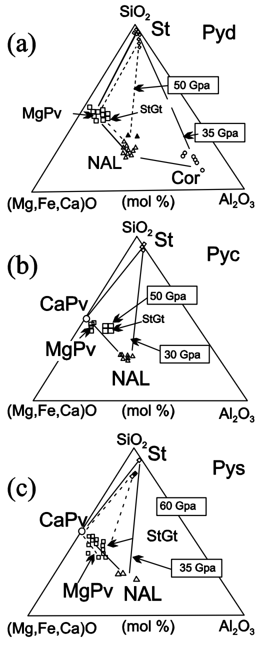

**Fig. 1.26** Compositions of starting materials and product phases projected on to the pseudo-ternary system of (Mg, Fe, Ca)O - $Al_2O_3$ - $SiO_2$. a) Pyd samples, b) Pyc samples, c) Pys samples. The product phases at lower phases pressures (open symbole) and higher pressures (hatched samples) are tied by solid and broken lines, respectively. Symbols: solid squares, starting materials garnets (St Gt); Squares, Mg-perovskites (Mg Pv); large circles, Ca-Perovskites (CaPv); small circles, corundum (Cor); diamonds, stishovite (St); triangle, a new Al-rich phase (NAL). Reprinted from, Physics of Earth and Planetary Interior, with permission from Elsevier

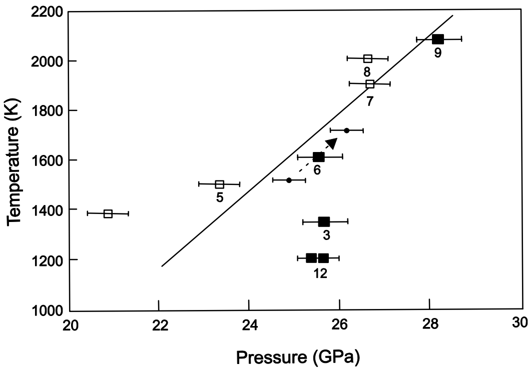

**Fig. 1.27** Reprinted from, "Post-garnet transition in a natural pyrope: a multi-anvil study based on in situ X-ray diffraction and transmission electron microscopy by. Oguri, Funamori, Uchida, Miyajima, Yagi and Fujino (2000). (Reprinted from Physics of Earth and Planetary Interior, with permission from Elsevier)

ropes, the dominant post-phase was Mg-rich orthorhombic silicate perovskite. They established that Al content of Mg-perovskite increased significantly with increasing pressure and temperature, and its chemical composition was closed to that of the starting material. Panero et al. (2006) however made first principle calculations in the $MgSiO_3$-$Al_2O_3$ system and predicted that $MgSiO_3$ perovskite can dissolve 15% $Al_2O_3$ at the top of the lower mantle (i.e. at a depth of 750–800 km) and is limited by coexistence of Al-rich ilmenite. They thought that the akimotite-corundum solid solution is nonideal with a symmetric regular solution parameter ($W_G$ = 66 kg/mol per formula unit) under P-T conditions similar to the top of the lower mantle. The critical temperature for the evolution of ilmenite is predicted to be 2000 K. They observed that Mg-perovskite with 25 mol% $Al_2O_3$ content quenched as a single phase orthorhombic perovskite with 25 mol% $Al_2O_3$ content at ambient conditions whereas Mg-perovskite with greater than 25 mol% $Al_2O_3$ content quenched as a single-phase orthorhombic perovskite at similar conditions.

Whereas Mg-perovskite with greater than 25 mol% $Al_2O_3$ content transformed into alternate lamellae of orthorhombic perovskite and another phase with lithium niobate-like structure; with further increase of alumina content the Mg-perovskite converted into a single-phase with lithium niobate-like structure having polysynthetic twinning on 1012 at ambient conditions. The high Al content may also induce stabilisation of $Fe^{3+}$ in the perovskite structure accompanied by metallic iron.

Miyajima et al. further established that at lower pressures, corundum and a new Al-rich phase (termed as NAL phase, Fig. 1.26) coexisted with Mg-perovskite. The composition of the NAL phase is close to $M_3Al_4Si_{1.5}O_{12}$ (M = Mg, Fe, Ca, Na and K). They thought that the diffraction pattern of the NAL phase was consistent with the space group of $P6_3/m$ or $P6_3$ with a = 8.85 (2) Å, C = 2.78 (2) Å, V = 188 (1) $Å^3$. This phase co-existed with stishovite.

Oguri et al. (2000) studied post-garnet transition in a natural pyrope with a composition $(Mg_{0.72}Fe_{0.17}Ca_{0.11})_3Al_2Si_3O_{12}$ under P-T conditions similar to that existing near 670 km discontinuity. The post-garnet transition boundary of the natural garnet is shown in Fig. 1.27. The equation of state related to the P-T curve was expressed by them as follows: P(GPa) = 14.4 + 0.0065T (K). The phases formed as a breakdown product were (Mg, Fe)$SiO_3$-$Al_2O_3$ perovskite, $CaSiO_3$ perovskite, stishovite and another phase ("NAL" phase) with composition close to $(Mg, Fe, Ca, Na, K)_3Al_4Si_{1.5}O_{12}$.

### 1.3.2.6 Phase transitions of (Mg, Fe)O

Phase transition of (Mg, Fe)O at megabar pressure and variable temperatures was performed by Kondo et al. (2004) using a diamond anvil cell and synchrotron radiation. Figures 1.28a and b summarise the experimental observation of Kondo et al. At high temperatures above 1500°C and megabar pressures, they observed a B1 phase with rock salt-like structure in all the samples [$(Mg_{0.20}Fe_{0.8})O$, $(Mg_{0.1}Fe_{0.9})O$,

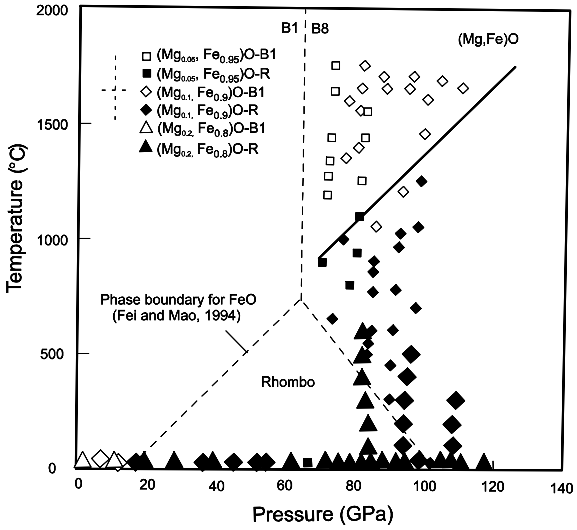

**Fig. 1.28a** Phase relations in (Mg, Fe)O system solid, and open symbols are the rhombohedral and B1 phases, respectively. Large triangles and diamonds below 600°C denote the results of external heating experiments in which no further transition was observed from the rhombohedral phase. Small symbols show laser heating experiments. The experimental errors in the external heating methods are within the symbol size. Broken lines represent phase boundaries in Wustite (Fei and Mao, 1994). The solid line indicate a tentative boundary. Reprinted from Kondo, Ohtani, Hirao, Yagi and Kikegawa (2004); Physics of Earth and Planetary Interior, with permission from Elsevier

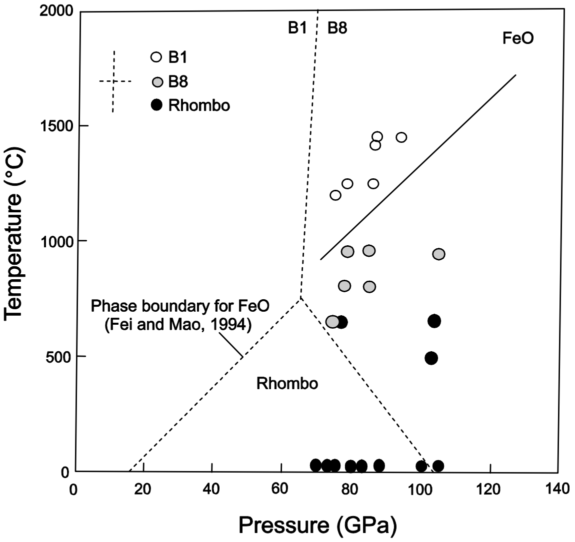

**Fig. 1.28b** Observed phases in Wustite, Solid, gray and open symbols are the rhombohedra, B8 and B1 phases respectively. All high temperature data were obtained from the laser heating experiments. Broken lines and the solid thick line are the same as shown in Fig. 1.27a. Reprinted from Kondo, Ohtani, Hirao, Yagi and Kikegawa (2004); Physics of the Earth and Planetary Interiors, with permission from Elsevier

($Mg_{0.05}$ $Fe_{0.95}$)O and FeO]. They did not find the B-8 (NiAs) structure in magnesio wustite samples, but they observed such a NiAs structure in case of FeO (wustite). Kondo et al. established that the diffraction pattern of B-8 phase was consistent with the calculated intensities for the inverse B-8 structure. Their results indicate that the stable phase of magnesio wustite should have a B-1 structure under lower most mantle condition.

It should be pointed out that Fei and Mao (1994) proposed transformation of magnesio wustite from a rock salt (B1) to NiAs structure at 74 GPa and 900 K. Such a transformation was observed in case of pure wustite but not for magnesio-wustite.

Mao et al. (2002) reported an increase of the transition pressure from 17 GPa (for FeO) to 20 GPa (for $Mg_{0.10}$ $Fe_{0.90}$)O under hydrostatic conditions indicating that the stability field of the B1 phase is extended to the high pressure region by adding MgO to FeO content. Kondo et al. however, found that the distortion from the B-1 phase starts always around 16 GPa up to the composition of ($Mg_{0.20}$ $Fe_{0.80}$)O. They conclude that rhombohedral distortion is strongly influenced by uniaxial stress in the sample (Mao et al. 1996). Therefore, the difference in the transition pressures for ($Mg_{0.10}$ $Fe_{0.90}$)O may be caused by nonhydrostatic effects. Kondo et al. also found that the molar volume of the B1 phase in ($Mg_{0.10}$ $Fe_{0.90}$)O was about 3% larger than that expected for FeO.

## *1.3.3 Experimental Studies on Peridotites and Meteorites*

As peridotites and their meteoritic counter parts are considered to constitute the mantle, they have been subjected to a lot of experimental studies.

### 1.3.3.1 Experimental study on a natural peridotite under high pressure and temperature

Takahashi (1986) studied a peridotite (KLB-1) of composition similar to that expected in the upper mantle. He observed that olivine is the liquidus phase at all pressures (Fig. 1.29). The second mineral to crystallise with increasing pressure is a Ca-orthopyroxene (up to 3 GPa), pigeonitic clinopyroxene (up to 7 GPa) and pyroxene-rich garnet (>7 GPa). The melting temperature interval of the peridotite is more than 600ºC wide at 1 atm but narrows to about 150ºC at 14 GPa. The partial melts along the peridotite solidus becomes increasingly more MgO-rich as pressure increases. At 5–7 GPa, the partial melts formed within 50ºC of the solidus contain more than 30 wt% MgO, and are similar to Al-depleted peridotitic komatiite, which are common in Archean volcanic terrains. Due to the increase of enstatite component in clinopyroxene solid solution at high pressure and temperature, the orthopyroxene liquidus field narrows, as pressure increases and disappears at 3–5 GPa. Harzburgites, are common in the peridotites from ophiolite suites. They may represent relicts after separation of the melts formed at depths lower than 100 km. He considered that lherzolites showing protogranular texture, might have been produced as single pyroxene peridotite residues formed by partial melting at relatively greater depths (>100 km). He also suggested a diapric model consistent with the genesis of a komatiitic magma formed by partial melting of a mantle peridotite at 150–200 depth. Takahashi (1986) made following observations: 1) convergence of the liqui-

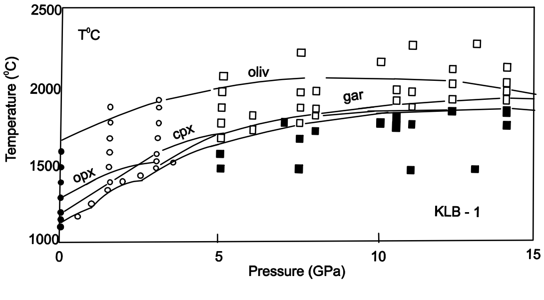

**Fig. 1.29** Phase relations on a peridotite (KLB-1) system at various pressures and temperatures (after Takahashi, 1986). Oliv.: olivine, gar: garnet, cpx: clinopyroxene, opx: orthopyroxene. (from the Journal of Geophysical Research, with permission)

dus and solidus of the peridotitites at pressure >14 GPa, 2) the near-solidus partial melt composition is very close to the bulk rock at 14 GPa and 3) change in the liquidus mineral from olivine to majorite garnet at pressures between 16 and 20 GPa.

Based on above conclusions he proposed that the upper mantle peridotite was generated originally as a magma (or magmas) formed by partial melting of the primitive earth at 400–500 km depth.

### 1.3.3.2 Experimental study of a chondrite up to 22 GPa and 2300ºC

Ohtani et al. (1986) studied a chondritic meteorite with following composition: $SiO_2$: 50.18, $Al_2O_3$: 3.62%, FeO: 7.16%, MgO: 36.18% and $CO_2$: 2.86%. The Mg, Si, Al and Ca contents are similar to those of chondrites with Fe/(Fe+Mg) ratio = 0.1. Their experimental results are summarised in Fig. 1.30, which show that below 13 GPa, olivine is the first phase to appear but above this pressure, majorite [(Mg, Fe)$SiO_3$; with garnet-like structure] is the liquidus phase. Their electron microprobe analyses of the liquid (in equilibrium with majorite) show that it is of peridotitic composition.

Ohtani et al. speculated that during thermal evolution of the earth the outer layer might have been in liquid state up to a depth of about 1000 km or more. The study of Ohtani et al. suggest that at pressure above 13 GPa (equivalent to a depth of 400 km), Fe-rich majorite will sink toward the lower part of the mantle and will leave behind a peridotitic liquid poorer in iron than that of a chondrite.

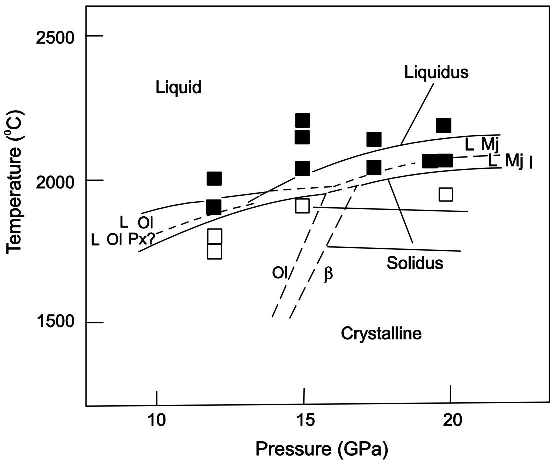

**Fig. 1.30** Phase equilibria study of Allende meteorite (CV-3) as a function of pressure and temperature (after Ohtani et al., 1986, 1987). Open squares: subsolidus, half-filled squares: crystal + liquid, filled square: super liquidus, L: liquid, Ol: olivine, Px: clinopyroxene, B: modified spinel, Mj: majorite. (Reprinted from Ohtani, Kato and Swamoto, 1986, with permission from the Nature Publishing Group

### 1.3.3.3 Study of Allende meteorites under lower mantle P-T condition

Phase relations of a carbonaceous chondrite at lower mantle conditions were studied by Asahara et al. (2004). The composition of the Allende meteorite as determined by Jarosewitch (1990) is as follows:

$SiO_2$: 34.23, $TiO_2$: 0.15, $Al_2O_3$: 3.29, $Cr_2O_3$: 0.52, FeO: 27.15, MgO: 24.62, MnO: 0.18, CaO: 2.61, $Na_2O$: 0.45, $K_2O$: 0.03, $P_2O_5$: 0.23, $H_2O$: <0.10, Fe: 0.17, Ni: 0.36, Co: 0.01, FeS: 4.03, C: 0.29, other 1.68. Total = 99.98.

They used a Kawai type of multi-anvil apparatus to study the meteorite. Phase relations established by them are shown in Fig. 1.31. The phase relations of Allende meteorite as determined by Asahara et al. (2004) showed that with increasing pressure, the liquidus phase changes from garnet to Mg-perovskite at about 24.5 GPa. They noted that magnesio-wustite crystallised as the second phase throughout the pressure range and the solidus curve coincided with the appearance of ringwoodite below 23 GPa, Mg-perovskite at 23–24 GPa and Ca-perovskite above 24 GPa. Immiscible silicate and metallic liquid phases were present in the entire melting range, and a single metallic liquid persisted below the solidus down to at least 1600ºC. They observed that the $K_D[(Fe/Mg)^{crystal/silicate\ liquid}]$ is well below un-

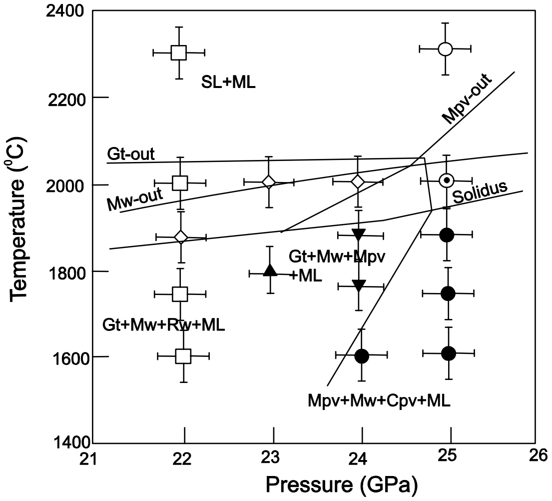

**Fig. 1.31** Phase relations of a carbonaceous chondrite under high pressure-temperature conditions. Sl: silicate liquid; Ml: metal liquid; Mw: magnesio-wustite; Mpv: magnesio perovskite; Gt: garnet; Rw: ringwoodite; Cpv: calcium perovskite. (Reprinted from Asahara, Tomoaki and Kondo 2004. In: New Developments in High Pressure Mineral Physics and Application to Earth's Interior (D.C. Rubie, T.S. Duffey and E. Ohtani, Eds.). Copyright 2004, with permission from Elsevier

ity for magnesio wustite (0.7–0.8), garnet (0.35–0.39) and Mg-perovskite (0.34). Asahara et al. found that Ni and S were strongly partitioned into metallic liquid and the Ni and Fe partition between metallic liquid and coexisting minerals were relatively constant with variation in pressure or temperature. They concluded that an important factor controlling $D^{\text{metal liquid/crystal}}$ of Fe and Ni is the oxygen fugacity. Their results provided further constraints on models for early earth differentiation and core formation. High P-T studies on the allende meteorite showed that if the mantle of the earth had composition similar to that of meteorites, then the assemblage of the mantle at depth might be represented by Mg and Ca-perovskite, magnesio-wustite and majorite ± ringwoodite in the transition zone between upper and lower mantle.

### *1.3.4 Mantle Heterogeneity*

Seismological evidence on heterogeneity in the upper mantle has been discussed by Nolet et al. (1994). Variation in seismological velocity propagation (long period and broad band observation) as a function of depth is summarised in Fig. 1.32. The seismic velocity versus depth profiles shown in Fig. 1.32 are from different sections of the United States, Northern Atlantic, Australia and Asiatic Russia. These upper mantle models from short period P-wave observations show a considerable variation in the interior structure of the earth. Early seismological studies established the presence of a low shear velocity zone (LVZ) between 150–200 km.

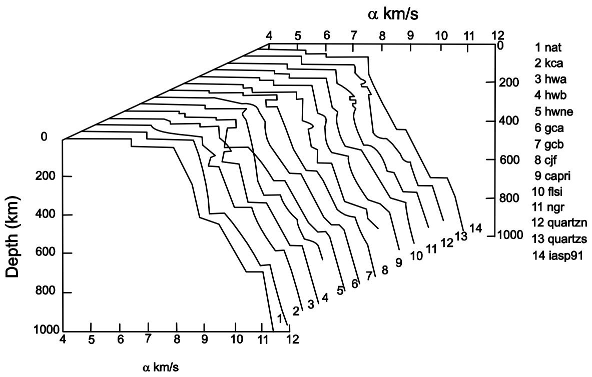

**Fig. 1.32** Upper mantle models derived from short-period P-observations show a considerable variation in structure. The upper mantle structure of iasp 91 (Kennett and Engdahi, 1991) was designed to provide a reasonable average of continental structure. Regional coverage: nat, North Atlantic, hwb, hwa, hwne, west-central united states: gca, gcb, cjf, western North America: Capri, fls, ngr, northern Australia, quartzn, quartzs, Asiatic Russia. Upper mantle models derived from short period P-waves observations show a considerable variation in structure (after Nolet et al., 1994, from the Journal of Geophysical Research, with permission)

The low velocity zone, as established by plotting shear wave velocity versus depth profile is shown in Fig. 1.32. This discontinuity has also been associated with the base of the lithosphere. The low velocity zone is often considered to be a layer characterised by partial melting of the mantle materials. Goroshkov (1958) concluded that the chamber under Kliuchevski volcano, Kamchatka was between 50 and 75 km deep, and he believed that its shape was that of a convex lens or possibly a triaxial ellipsoid. Fedotov and Tokarev (1974) indicated that the main zone of magma generation is probably located within the depth interval from 120 to 250 km.

A partially molten zone beneath Yellowstone National Park, Wyoming extend to about 100 km depth. This was established by Eaton et al. (1975). On the basis of 10% reduction in the velocity of P-wave.

Grand (1994) observed that the three shield areas of the three separate continents have higher than average velocities down to a depth between 320 and 400 km. Young tectonically active regions are very slow in the upper 250 km. Revenaugh and Jordan (1991) observed a discontinuity below 300–312 km depth. They also reported a discontinuity at 300 km beneath the shield region of Western Australia and 200 km below northern Australia. Woodland (1998) considered this to be related to transformation of orthorhombic $MgSiO_3$ to monoclinic high pressure clinopyroxene. The elastic constants of the monoclinic $MgSiO_3$ seem to confirm that this phase transformation may be responsible for this discontinuity (compare Fig. 1.14b and Fig. 1.20). According to Stixrude (2007), the proportion of orthopyroxene in a pyrolitic mantle is such that the magnitude of the velocity change should increase with decreasing temperature. This discontinuity is preferentially observed near subduction zones.

Rapid increase in seismic velocity at a depth of about 400 km has already been related to possible conversion of $(Mg, Fe)_2SiO_4$ from orthorhombic symmetry ($\alpha$-phase) to spinel type of structure ($\gamma$-phase, Jeffrey 1937). Jeffrey's prediction was based on Bernal's (1936) observation that $Mg_2GeO_4$ has two polymorphs, one with orthorhombic and the other with spinel type of symmetry. Bernal also suggested that transformation of olivine from $\alpha$ to $\gamma$ type will be accompanied by 9% increase in density.

The discontinuity around 450 km coincides with phase transformation of olivine to wadsleyite (see Fig. 1.15 and 16). This discontinuity has been observed globally (Dziewonski and Anderson 1981). As Fig. 1.14a shows this 450 km discontinuity is overlain by the low velocity zone. This low velocity zone may be associated with subduction of slab, providing water-rich fluid (Song et al. 2004). Study of Ito and Takahashi (1989) suggests that the transition is sharp as pressure of transformation is within 0.1 GPa.

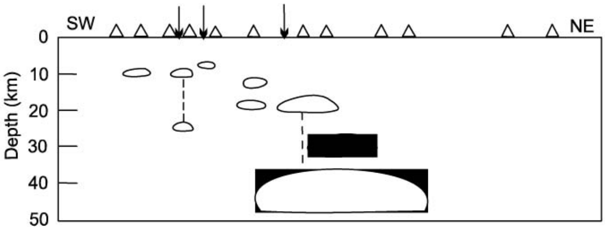

**Fig. 1.33** Vertical distribution of magma chambers (enclosed areas) and possible conduits (dashed lines) along the Katmai, Alaska, volcanic range according to Kubota and Berg (1967, p.202). The two deepest chambers outlined may consist of many smaller molten pockets, according to an alternative suggestion of Shimozuru (1963). Volcanoes (triangles) and seismic stations (arrows) are noted. The fourth seismic station is at Kodiak, about 150 km to the southeast of the range vertical and horizontal scales are about equal. (With permission of the Bulletin Volcanologique)

The 400 km discontinuity is a poorer reflector and spread over for more than 5 km depth. In certain regions the 400 km discontinuity reflect short period waves. There have been description of some secondary discontinuities, which are however, not so well constrained. A velocity jump has been noted at 300 km depth. Grand (1994) found lateral variation in shear velocity within the mantle beneath north and south America and their surrounding oceans and parts of Africa and Eurasia from travel time inversion of polarised sheared body waves. According to Grand the upper 400 km is dominated by lateral variations that correspond to surface tectonic environments.

The 660 km discontinuity has already been discussed in terms of phase transformation of akimotite ($MgSiO_3$ spinel) to perovskite. The temperature around this part of the mantle may be between 1000–2000ºC (Fig. 1.24). If relatively cold slab subducts in this part of the mantle, there may be relatively cold mantle phase transformation from $Mg_2SiO_4$ (spinel) + $SiO_2$ (Stishovite) to perovskite, If this part of the mantle is relatively hot, Fig. 1.24 suggests that the transition zone may be related to phase transformation of $MgSiO_3$ (majorite garnet) to Mg-perovskite.

Grand observed the presence of a high velocity layer in the transition zone beneath Western South America. This is probably related to a subducting slab. The velocity in the transition zone beneath the western and central part of north America is also faster than average. Grand (1994) considers that the lower mantle is dominated by large-scale sheets of higher than average velocity and more equidimensional regions of low velocity. He also found that from South America to Siberia, presence of sheet like high velocity anomalies extended from a depth of 750 km down to the CMB. Such a high velocity anomaly in the lower mantle was also observed beneath southern Eurasia. According to Grand (1994) such a high velocity lower mantle anomalies may be associated with subduction during the last 150 m.y.

Beyond the 660 km discontinuity, Revenaugh and Jordan (1991) reported a discontinuity which may or may not be global. The discontinuity at 720 km may be related to phase transformation of majorite garnet to $MgSiO_3$ perovskite. The discontinuity at 660 km, which separates upper mantle from the lower one is a good reflector with a near vertical 1-Hz P waves showing that transition zone has a width of 4 km or less. This suggests that the discontinuity is sharp (Vinnik, 1977).

Shearer (1990, also see Morelli et al. 1986) discussed about an inner core anisotropy with a symmetry axis roughly aligned with the rotation axis of the earth. It is estimated that there is nearly 3% anisotropy throughout much of the inner core. The P-wave velocity anomalies as large as 3% are rare in the deep earth and their existence in the inner core is therefore, intriguing. Proposed mechanism of inner core anisotropy may be associated with preferred alignments of hexagonal close-packed ($\alpha$) iron crystals (Jeanolz and Wenk, 1988).

A common feature of both short and long period refraction study showed that there is a relatively high gradient within the transition zone from 410–660 km depth.

The discontinuity reported by Kawakatsu and Niu (1994) may be due to subduction. The discontinuity at 1700 km, observed by Vinnik et al. (2001), may be related to phase transformation of cubic calcium perovskite to tetragonal $CaSiO_3$ perovskite. The question is how much $CaSiO_3$ as a breakdown product of diopside is expected to be present at this depth. The discontinuity at 2870 km, associated with extinction of S-wave, may be due to the presence of a liquid core.

### *1.3.5 Water Content in the Mantle*

Phase relations in the peridotite-water system, was studied by Ohtani et al. (2004) up to 35 GPa and 2500ºC. Their study reveals that a certain amount of water can be transported and stored by various hydrous minerals resulting in the formation of a hydrous transition zone. Litasov and Ohtani (2003) demonstrated that the maximum water solubility in wadsleyite at 15 GPa decreased with increased temperature from 2.0 wt% at 1000ºC to 0.5 wt% at 1600ºC. Ohtani et al. (2004) noted that water content in wadsleyite, further decreased to 0.3 wt% with increase of pressure to 18 GPa and 1600ºC. Thus, they concluded that in the deeper zone, there is a larger water storage potential than what was estimated earlier. The maximum water storage potentials of wadsleyite and ringwoodite are estimated to be 0.5–1 wt% along the normal mantle gradient. Ohtani et al. concluded that there is a layered structure in the water storage capacity in that the upper and lower mantle have relatively low water storage capacities, but the transition zone has a relativey higher water content. They further speculate that the water content in the transition zone might be even larger because the dehydrated water from the subducted slab together with primordial water in the lower mantle have been stored in the transition zone during geological time.

In a number of geophysical and geochemical processes water plays a significant role (Huang et al. 2005). For instance, in the melting behaviour of silicate rocks, plastic deformation, electrical conductivity and diffusion process, water plays a very important role.

Huang et al. (2005) determined the effects of water on electrical conductivity of Wadsleyite and ringwoodite. Their experimental results conducted at pressures between 14–16 GPa and variable temperatures are summarised in Fig. 1.34a, b, c, d. The influence of temperature and water content on electrical conductivity for wadsleyite and ringwoodite as determined by Huang et al. (2005) are shown in Fig. 1.35.

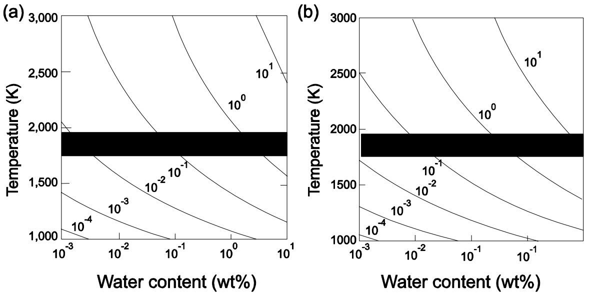

**Fig. 1.35** The influence of temperature and water content on electrical conductivity. **a.** wadsleyite; **b.** ringwoodite. The numbers on the curves represent electrical conductivity (in $Sm^{-1}$). The shaded areas represent temperatures of 1850 ± 100 K; the yellow shaded areas represent the electrical conductivity ranges in **a** the upper and **b** the lower, transition zone in the Pacific[4]; the black areas represent the range of temperature and water content that is consistent with the observations. The water content in the transition zone in the Pacific is ~0.1–0.2 wt% inferred from both wadsleyite and ringwoodite (after Huang et al. 2005; reprinted by permission of the Nature Publishing Group)

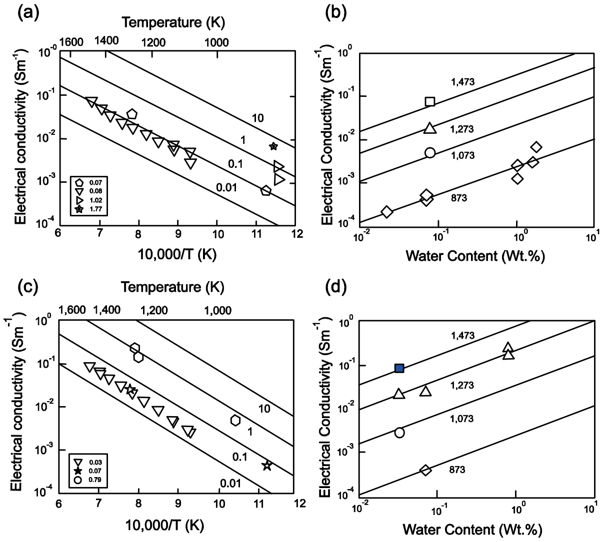

**Fig. 1.34** Measured electrical conductivity. **a.** Electrical conductivity of wadsleyiite as a function of temperature for several water contents; **b.** electrical conductivity of wadsleyiite as a function of water content for several temperatures; **c.** electrical conductivity of ringwoodite as a function of temperature for various water contents; **d.** electrical conductivity of ringwoodite as a function of water content for various temperatures. All data are at pressures P = 14–16 GPa. The lines in **b** and **d** are calculated for wadsleyiite and ringwoodite, respectively. In **a** and **c**, numbers present water content in wt%; In **b** and **d**, numbers present temperatures in K (after Huang et al., 2005; reprinted by permission of the Nature Publishing Group)

The electrical conductivity in the region between 410 and 660 km (i.e. the transition zone) varies between $10^{-2}$ $Sm^{-1}$ and ~1 $Sm^{-1}$ (Utada et al. 2005, Ichiki et al. 2006). The above values correspond to ~0.001 to ~0.4 wt% water. The conductivity in the transition zone for the upper mantle of the North Pacific Oceanic region was measured to be ~$10^{-1}$ to 5 x $10^{-1}$ $Sm^{-1}$ and the corresponding water content was estimated to be ~0.1–0.2 wt% for the temperature range of 1825–1900 K. These values of water content significantly exceed the estimated critical water content in the upper mantle. Huang et al. concluded that partial melting may indeed occur at 410 km depth, at least in the North Pacific region.

The electrical conductivity of synthetic polycrystalline olivine was measured at a pressure of 4 GPa in the temperature range of 873–1273 K by Huang et al. (2006). The samples contained 0.01–0.08 wt% water. Their results are summarised in Fig. 1.36a, b. The pressure of 4 GPa corresponds to 120 km depth which is equivalent to the top of the asthenosphere, although the temperature of 873–1273 K is lower than a typical temperature of the aesthenosphere (1600–1700 K). The electrical conductivity of the oceanic asthenosphere is typically $10^{-1}$ $Sm^{-1}$ (Evans et al. 2005) corresponding to water content of 0.8 x $10^{-2}$ wt%. This value agrees well with water content from the composition of mid-ocean ridge basalt. It should be pointed out however that electrical conductivity has a large regional variation.

Dwivedi and Gupta (2008) determined conductivity of diopside using a Hioki LCR-Z meter (model: 3522–50) OC, 1 mHz to 100 KHz. The conductivity measurement was performed at 4 and 7 GPa and different temperatures (773–1473 K). The water content of diopside crystals was equivalent to 220 ppm H/Si. The water content of the matrix crystals was 1400 ppm H/Si. The conductivity (S/m)

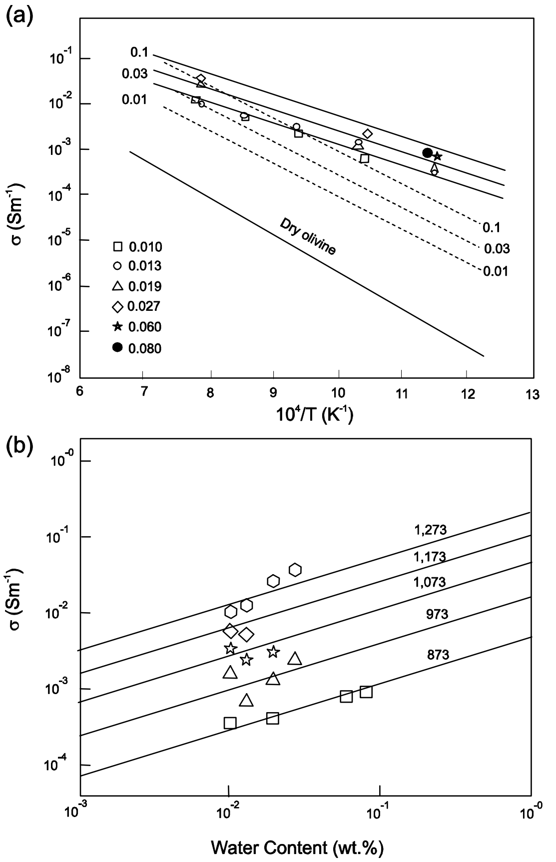

**Fig. 1.36** Electrical conductivity versus inverse temperature and water content. **a**. A plot of electrical conductivity (σ) versus inverse temperature. The numbers next to each line indicate the water content (in wt%). Solid lines with numbers are the results of multinear regression from all the data. Each symbol represents the data corresponding to a given water content (in wt%). The broken lines show the conductivity values calculated from water diffusion coefficients determined by Kohlstedt and Mackwell using the model by Karato, and the conductivity for 'dry' olivine. Both the magnitude and the slope from the present study are different from those of 'dry' olivine and the trend calculated using the Karato model, indicating that the charge carrier corresponding to the present study is different from those in the previous studies (neutral hydrogen-defect at M-sites for the Karato model, $Fe^{3+}$ for dry olivine). **b**. A plot of electrical conductivity versus water content. The fit of the data to a model equation yields r = 0.62 + 0.15. The numbers along each line represent the temperature in K. A relatively large error for r is due to the fact that only a narrow range of water content can be explored for olivine due to the relatively small hydrogen solubility, and to a large error in the estimate of water content from Ft-IR (see methods). Each symbol corresponds to the data for a given temperature (in K) (after Wang, Mukherjee, Xu and Karato 2006; reprinted by permission of the Nature Publishing Group)

versus inverse temperature (1000/T) diagram for diopside is shown in Fig. 1.37.

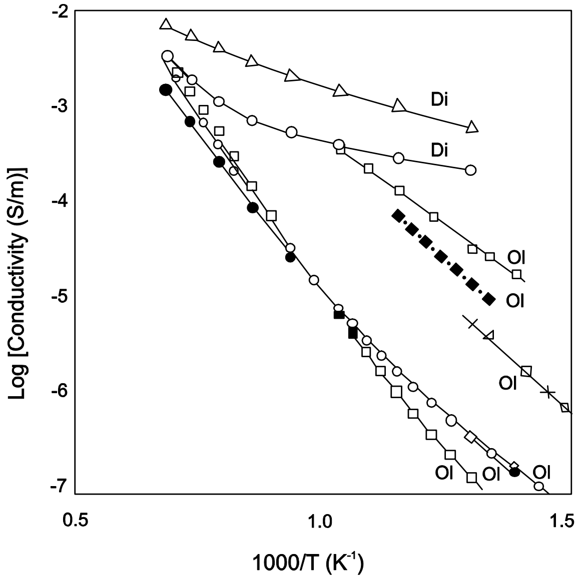

**Fig. 1.37** Electrical conductivity of diopside as a function of reciprocal temperature plotted in a similar diagram for hydrous olivine determine by Yoshino et al. The open triangle represents conductivity data of diopside determined under 7 GPa and that of open circle indicates conductivity data observed under 4 GPa. Open diamond, filled diamond with cross sign, and solid circles represent different crystallographic directions: Open square, filled square and filled diamonds represent different crystallographic directions: [100], [010] and [001], respectively. Solid dotted and dashed lines indicate the data fittings for [100], [010] and [001] respectively (after Dwivedi and Gupta 2008)

Electrical conductivity of diopside as a function of reciprocal temperature is plotted in a similar diagram for hydrous olivine (Yoshino et al. 2006) for comparison. The pressures of 4 and 7 GPa at which Dwivedi and Gupta measured electrical conductivity correspond to 120 and 210 km.

The electrical conductivity data in the continental upper mantle is close to $10^{-2}$ $Sm^{-1}$. The data of Dwivedi and Gupta (2008) are relevant to the conductivity data of the Continental mantle at a depth of 120–210 km.

### *1.3.6 The D" Layer*

According to Lay (2007), transformation of all mantle minerals to perovskite may be complete by 800 km, as the phase transformation for olivine, enstatite and garnet transforms to magnesium silicate [(Mg, Fe)$SiO_3$] occurs at this depth. Beyond 800 km, there is a smooth velocity gradient across lower mantle (Fig. 1.38). This explains smoothly increase in density of rocks up to the CMB. According to Lay

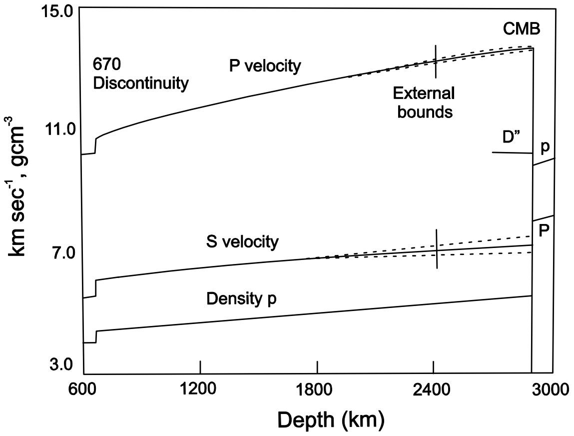

**Fig. 1.38** Variation in seismic velocity and density through the lower mantle for model PREM (Dziewonki and Anderson, 1981). The D" region is the lower most 200–300 km of the lower mantle overlying the CMB (reproduced from Lay, 1989. From Deep Earth Structure-Lower Mantle and D" (In: Treatise on Geophysics, Volume-2, Mineral Physics; Past Present and Future ; D.Price (ed.) with permission from Elsevier)

(2007 Fig. 1.38), below about 1600 km depth tomographic models show less coherence and relatively weak velocities anomalies (Grand et al. 1997). Variation in velocity increases in the lower most 300–500 km of the mantle particularly for shear waves (Fig. 1.38). Lateral variation of ± 4% for S-wave velocity and ± 1.5% for P-wave velocity are also observed.

Figure 1.38 shows that beyond the 720 km discontinuity the P- and S-wave velocity progressively rises as a function of depth, but then there is a sharp drop in the velocity at 2740 km. Steady rise in the density of lower mantle is also shown. This drop in velocity in the CMB, marks the occurrence of the D" zone. This is now assigned to phase transformation from perovskite to post-perovskite structure (Fig. 1.40). The ULVZ marks the beginning of a liquid core. Lay (2007) considers that it is most likely that a large amount of iron has separated from the mantle due to extensive melting associated with volatile depletion and chemical stratification.

The seismic velocities are not so consistent just 200–300 km above the CMB due to phase transformation of magnesium silicate perovskite to post perovskite phase (Murakeine et al. 2004). Because of this homogeinity in the structure of the lower few hundred kilometres of the mantle, this 200–300 km transition zone above the CMB is called the D" layer. This is a region of thermal and chemical in homogeneity.

In Fig. 1.39 the root mean square heterogeneity versus depth in the mantle as observed by various workers have been plotted by Lay (2007). The plots related to different workers include the data of the following workers: Masters et al. (2000), Gu et al. (2001), Megnin and Romanowicz

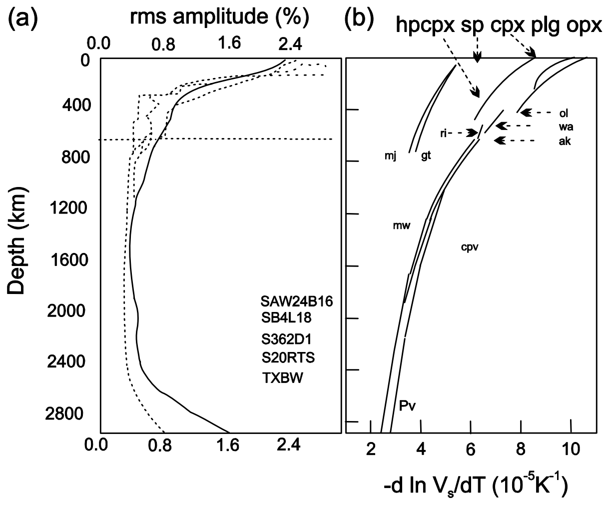

**Fig. 1.39** The amplitude of tomographic models as a function of depth (a) from (Romanowicz, 2003) as compared with the temperature derivative of the shear-wave velocity for mantle minerals along a typical isentrope (b) from Stixrude and Lithgow-Bertelloni, 2005. (In: Treatise on Geophysics, Volume-2, Mineral Physics; Past Present and Future; D.Price (ed.), with permission from Elsevier)

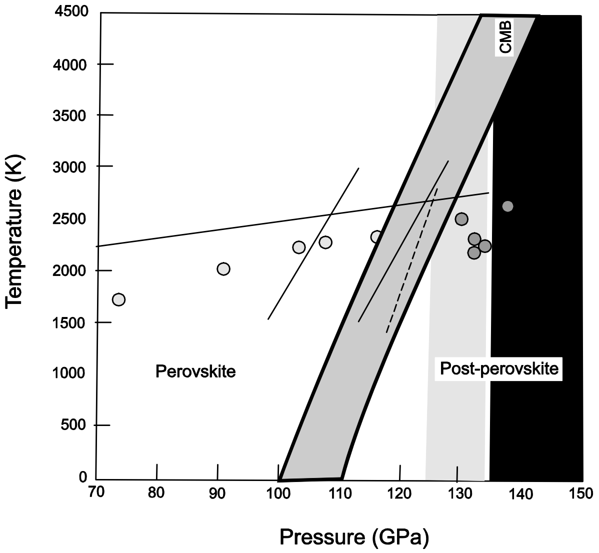

**Fig. 1.40** Post perovskite transition (after Tsuchiya et al. 2004 and Oganov and Ono; 2004) with lower and upper bound. CMB: Core-mantle boundary. Solid circle: post-pervoskite (ppv), open circle: pervoskite (pv). Conversion of pv to ppv is not sharp but associated with a zone (from L. Stixrude, 2007. In: Treatise on Geophysics, Volume-2, Mineral Physics; Past Present and Future; ed.: D.Price, with permission from Elsevier)

(2000), Ritsema and Van Heijst, 2000, Bolton (1996), Boschi and Dziewonski (1999), Zao (2001) and Karason and Van der Hilst (2001).

Stixrude (2007) concluded that of the five major cations of the mantle, iron has the largest influence on the density and elastic wave velocity. According to him the influence of iron content on the shear wave velocities, varies significantly among the major mantle minerals. This suggests that different bulk compositions (e.g. MORB, pyrolite, etc.) will have different sensitivities to lateral variations in iron contents (Fig. 1.39). Various phase transformations like olivine ⇔ wadsdeylite, wadsdeylite (wa) ⇔ ringwoodite (ri), akimotite (ak) ⇔ perovskite (pv), ringwoodite ⇔ perovskite + magnesio wustite, majorite garnet (gt) ⇔ perovskite (pv), etc. take place within 800 km of the mantle (Fig. 1.39).

The waveform studies indicate that the neighboring region within the D” layer is more distinct than had once been thought (Jeanolz and Lay, 1993). According to them several research groups investigating the CMB below northern Siberia observed that acoustic velocities vary so radically over a short distance that closely-spaced seismometers systematically recorded different waveforms.

This observation could be explained by the assumption that heterogeneities in seismic velocities is large in magnitude, and occur within few tens of kilometres and is difficult to resolve. According to Jeanoloz and Lay these reflections reveal that the thickness of the D” layer varies significantly. The D” layer at certain places can be very thin and may be undetectable, but it can span as much as 300 km. According to S.M. Flette (cited by Jeanoloz and Lay, 1993), the D” region appears to be quite ‘murky’ to seismic waves and probably contains heterogeneous features as small as 10 km in length and this layer possibly varies laterally in thickness.

Quoting the work of J.E. Vidale and H. Benz of the U.S. Geological Survey, Jeanolz and Lay (1993) observed that seismic waves arrived coherently across more than 900 stations in the array to suggest that the CMB is sharp.

E. Knittle (quoted in Jeanolz and Lay 1993) observed that perovskite, present in the lower mantle, reacts extensively with liquid iron existing at the outer core of the earth. She observed that products are a mixture of electrically insulating oxide minerals, $MgSiO_3$-perovskite, stishovite ($SiO_2$), metallic alloys, iron silicide (FeSi) along with wustite. Experimental studies of Knittle were conducted at 20–30 GPa. Such pressure are well below that existing in the CMB (136 GPa). It was therefore, concluded by Jeanoloz and Lay that the reaction probably persisted since the early history of the planet earth. They surmised that the lower mantle rocks have been, and is still dissolving liquid metal of the outer core. Because of such reaction the density of the outer core is nearly 10% lower than that of iron. They concluded that most possibly the core was never pure iron and perhaps contained Ni, S and other minor constituents as observed in iron-rich meteorites or siderites.

According to Birch (1964), the Geophysical properties of the outer core do not match those of pure liquid iron which is about 10% denser (Melchoir, 1956). The bulk modulus of pure iron is also greater than that of the core suggesting that in addition to Fe, the other associated components may be nickel, silicon, sulphur and oxygen. Experimental studies at the CMB (136 GPa) suggest substantial reaction between the core and mantle materials, and there is a possibility of incorporation of a large amount of Si and O in the metal (Knittle and Jeanolz, 1983).

Stacey (1977) used Lindemann’s Laws of fusion and estimated temperatures at different segments inside the earth, as follows:

| **Different Sites** | **Temperature (K)** |
|---|---|
| Centre of the Earth | 4286 |
| Inner - outer core boundary | 3947–4074 |
| Lower mantle - outer core | 2660–2840 |
| Upper mantle - lower mantle boundary | 2085 |
| Lower crust - upper mantle boundary | 550 |

The adiabatic temperature gradient is expressed by the following equation:

($\delta$ ln$T/\delta p$) = $\gamma$ / K. Thus, the temperature gradient is a function of $\gamma$ (Gunsen parameter) and the bulk modulus ($K_s$). On the basis of our knowledge of $K_s$ and $\gamma$ the temperature at the CMB is estimated to be 4000 K, in contrast to 2840 K estimated by Stacey (1977).

With reference to elastic properties of Fe, Steinle and Neumann (2001) estimated the temperature of the Earth’s centre to be 5000 K, which is 714 K more than that estimated by Stacey (1977).

According to Lay (2007), there is small scale variation in the D” layer with about 1% heterogeneities on a scale length of about 10 km. This is revealed by scattered P-wave signals. This small scale structure is suggested by analysis of diffracted coda (Bataille and Lund, 1996) waves and P KKP reflections (Earle and Shearer, 1997).

Anti-correlation in bulk and shear wave velocities cannot be explained by lateral variation in Fe content in $MgSiO_3$ perovskite, as velocities of both P- and S-waves decrease by addition of Fe in such minerals. Presence of $CaSiO_3$ perovskite can produce however, this observed anticorrelation as $CaSiO_3$ perovskite has a greater shear wave velocity, and lesser bulk sound velocity than that of $MgSiO_3$ perovskite.

There are suggestions that later variations in the lower mantle may also be associated with segregation of basalt by the process of subduction. According to Stixrude (2007) the insitu equation of State suggests that basalt under the P-T condition existing in the lower mantle should be denser than average mantle material. Lay (2007) suggested that, during the last 25 years, there have been second order features of seismological models, which suggest that the D” layer has been undergoing a large-scale dynamical process.

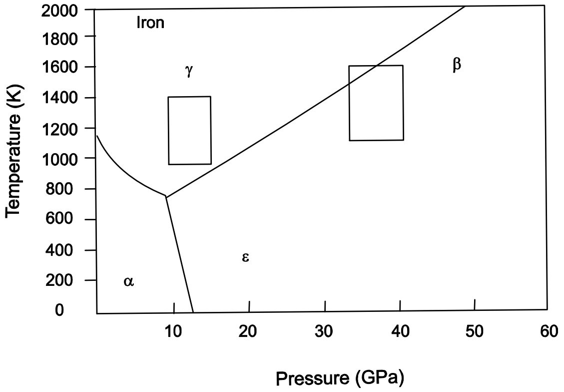

**Fig. 1.41** Part of the iron phase diagram showing the pressure-temperature fields. On laser heating, iron at lower pressures was largely converted to a fcc phase. At high pressures, iron shows a distinct phase transformation from hcp (hexagonal close packed) to possibly dhcp (double-layered hexagonal close-packed) form of iron, β-iron should be stable at 1400 K between 35 and 40 GPa. The δ phase is not shown. From Saxena, Dubrovinsky, Haggkvist, Cerenius, Shen, Mao 1995; reprinted from Science, with permission from American Association for Advancement of Science)

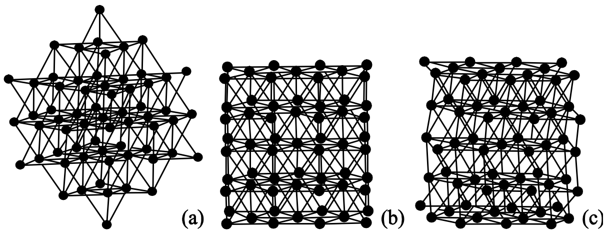

**Fig. 1.42** Phases of Iron: (A) γ (fcc); (B) ε (hcp); and (C) the four-layered phase (dhcp) (From Saxena, Dubrovinsky, Haggkvist, Cerenius, Shen, Mao 1995; reprinted from Science, with permission from American Association for Advancement of Science)

## 1.4 Core of the Earth

It has been observed that longitudinal waves travel a few percent faster along near-polar axis than in the equatorial plane, suggesting a lattice-preferred orientation of all crystalline phases of iron.

Experimental studies on iron by Saxena et al. (1995) have led to the understanding of phase relations related to various polymorphs of iron. They made synchrotron experiments with in situ laser heating of iron in a diamond-anvil cell. The phase diagram constructed by them is shown in Fig. 1.41. The melting curve of iron is now known to a pressure of nearly 2 Mbar, and it is believed that iron may occur in additional polymorphs. The crystal symmetry of the phases are as follows:

α (body-centered cubic), γ (face-centred cubic, fcc), ε (a polytype double layer hexagonal close packed β structure and δ (body centred cubic).

Reference to Fig. 1.41 shows that at higher pressures between 35 and 40 GPa, upon heating a new phase called β-iron could be detected by Saxena et al. Energy dispersive X-ray data showed that the new phase has a four-layered close-packed hcp (hexagonal closed packed) structure analogous to that of Ce and some other metals (Fig. 1.42).

The calculated lattice parameters (~38 GPa and 300 K) for the ε (hcp) phase is a = 2.396 Å and c = 3.814 Å. For the dhcp phase they calculated the lattice parameters be a = 2.427 Å and c = 7.66 Å. They also determined the molar volumes for ε and the dhcp.

Experimental studies on Fe-bearing system up to a pressure of 330 GPa and temperatures of 4800 K and above are required to learn about the processes taking place in the inner core-outer core boundary. However, melting studied on Fe polymorphs like face-centred cubic and hexagonal closed packed structure has been determined only up to 200 GPa using laser-heated diamond anvil cell (Boehler, 1993). The diagram of Boehler and Ross on melting relation of Fe

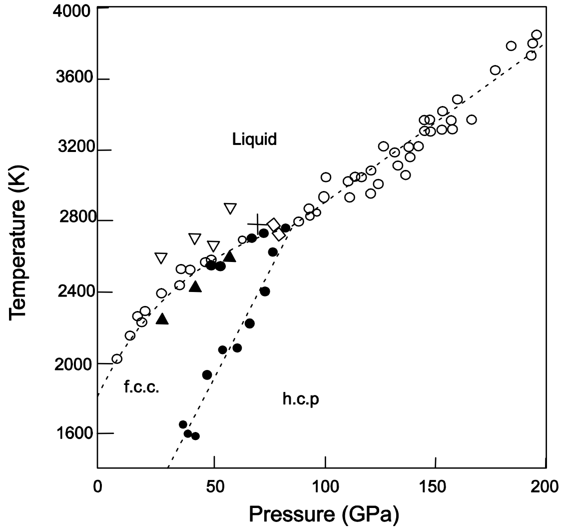

**Fig. 1.43** Iron phase diagram. Melting: open circles are from Boehler (1993); Triangles are from Shen et al. (2004); Open diamonds are measurement in an argon pressure medium. The fcc-hcp phase boundary: open squire and cross are data points of Mao et al. (1987) and Kubo et al. (1987). Diamonds are from Boehler (1993). Compiled by Boehler and Ross (2007). (In: Treatise on Geophysics, Volume-2, Mineral Physics; Past Present and Future; D.Price (ed.), with permission from Elsevier)

polymorphs is shown in Fig. 1.43. In obtaining these data between 220 and 240 GPa shown in Fig. 1.43, both diamond anvil cell and shock melting methods were employed. The diagram related to the f.c.c. - h.c.p phase boundary and the melting curve is based on the data of several investigators (for detail see Boehler and Ross 2007). These studies show that at ambient temperature, iron has a body centered cubic structure and transforms into hexagonal closed packed structure at 13 GPa (Boehler et al. 1990). The hexagonal closed packed phase is stable up to about 300 GPa (Mao et al. 1990). These authors think that the results from different laboratories using various methods are now in very good agreement. These data are important as the upper mantle is considered to be in liquid state. It is generally believed that the body-centred cubic phase is elastically unstable, a hexagonal close-packed structure is more favoured. The presence of light elements may help in the stabilisation of structure (Stixrude 2007).

## 1.5 References

Ahmed-Zaid I, Madon M (1995) Electron microscopy of high pressure phases synthesised from natural garnets in a diamond anvil cell: Implications for mineralogy of the lower mantle. Earth Planet Sci Lett 129: 233–247

Akaogi M, Yano M, Tejima Y, Iijima M, Kojitani H (2004) High-pressure transitions of diopside and wollastonite: phase equilibria and thermochemistry of $CaMgSi_2O_6$, $CaSiO_3$ and $CaSi_2O_5$ - $CaTiSiO_5$ system. In: Rubie DC, Duffy TS, Ohtani E (eds) New Developments in High-Pressure Mineral Physics and Applications to the Earth's Interior, Elsevier

Akimoto S, Fujisawa H (1966) Olivine-spinel solid solution equilibria in the system $Mg_2SiO_4$ - $Fe_2SiO_4$ at 800ºC. Earth Planet Sc Letters 1: 237–240

Akimoto S, Fujisawa H (1968) Olivine-spinel solid solution equilibria in the system $Mg_2SiO_4$ - $Fe_2SiO_4$. J Geophys Res 73: 1467–1479

Akimoto S, Syno Y (1969) Coesite-stishoivite transition. J Geophys Res 74: 1653–1659

Anderson DL (1969) Phase changes in the upper mantle. Science 157: 1165–1173

Asahara Y, Kubo T, Kondo T (2004) Phase relations of a carbonaceous chondrite at lower mantle conditions. In: Rubie DC, Duffy TS, Ohtani E (eds) New Developments in High-Pressure Mineral Physics and Applications to the Earth's Interior, Elsevier

Bataille K, Lund F (1996) Strong scattering of short period seismic waves by the CMB and the P-diffracted wave. Geophys Research Letters 18: 2413–2416

Bernal J D (1936) Discussion. Observatory 59: 268

Birch F (1964) Density and composition of the mantle and core. J Geophys Res 69: 4377–4388

Boehlar R, von Bargen N, Chopelas A (1990) Melting thermal expansion and phase transition of iron at high pressures. J Geophys Res 95: 21731–21736

Boehler R (1993) Temperatures in the Earth's core from melting-point measurements of iron at high static pressures. Nature 363: 534–536

Boehler R, Ross N (2007) Melting properties of lower mantle components. In: Price D G (ed) Treatise on Geophysics 2: Mineral Physics Past, Present and Future, Elsevier

Boettcher AL, Wyllie PJ (1968a) Jadeite stability measured in presence of silicate liquids in the system $NaAlSiO_4$-$SiO_2$-$H_2O$. Geochim Cosmochim Acta 32: 999–1012

Boettcher AL, Wyllie PJ (1968b) Melting of granite with excess water to 30 kilobars pressure. J Geol 76: 235–244

Bolton H (1996) Long Period Travel Times and the structure of the Mantle. PhD Thesis, Univ California, San Diego

Boschi L, Dziewonski AM (1999) High and low resolution images of the Earth's mantle - Implications of different approaches to tomographic modelling . J Geophys Res 104: 25567–25594

Brown JM, Shankland TJ (1981) Thermodynamic parameters in the Earth as determined from seismic prophiles. Geophys J Royal Astronom Soc 66: 579–596

Cohen LH, Ito K, Kennedy GC (1967) Melting and phase relations in an anhydrous basalt to 40 kb. Am J Sc 265: 475–518

Collerson KD, Hapugoda S, Kamber BS, Williams Q (2000) Rocks from the Mantle Transition Zone: Majorite-Bearing Xenoliths from Malaita, Southwest Pacific. Science 288: 1215–1223

Dwivedi MM, Gupta AK (2008) Electrical conductivity of diopside under 4 and 7 GPa at variable temperatures. Science and Culture 74: 5–6, 195–198

Dziewonski AM, Anderson DL (1981) Preliminary reference earth model. Phys Earth Planet Inter 25: 297–356

Earle PS, Shearer PM (1997) Observations of high frequency scattered energy associated with the core phase PKKP. Geophys Res Letters 25: 405–408

Earle PS, Shearer PM (1997) Observations of PKKP precursors used to estimate small-scale topography on the core-mantle boundary. Science 277: 677–680

Eaton JP, Christiansen RL, Iyer HM, Pitt AM, Mabey DR, Blank HR, Zietz JRI, Gettings ME (1975) Magma beneath Yellowstone National Park. Science 188: 787–796

Evans R (2005) Geophysical evidence from the MELT area for compositional control on oceanic plates. Nature 437: 249–252

Evans RC (1966) An Introduction to Crystal Chemistry, 2nd edn. Cambridge University Press, London

Fedotov SA, Tokarev PI (1974) Earthquakes, characteristics of the upper mantle under Kamchatka and their connection with volcanism (according to data collected up to 1971). Bull Volcanol 37: 245–257

Fei Y, Mao HK (1994) In situ determination of the Ni As phase of FeO at high pressure and temperature. Science 266: 1678–1680

Fisher RL, Raith W (1962) Topography and structure of Peru-Chile Trench. Deep Sea Res 9: 423–443

Flanagan MP, Shearer PM (1998) Global mapping of tomography on transition zone velocity discontinuity by stacking SS precursors. J Geophys Res Solid Earth 103: 2673–2692

Gaherty JB, Jordon TH (1995) Lehmann discontinuity as the base of an anisotropic layer beneath continents. Science 268: 1468–1471

Gaherty JB, Yankin W, Jordon TH, Weidner DJ (1999) Testing plausible upper-mantle compositions using time scale models of the 410 km discontinuity. Geophys Res Letters 26: 1641–1644

Garnero EJ, Helmberger DV (1995) A very slow basal layer underlying large-scale low velocity anomalies in the lower mantle beneath the Pacific: Evidence from core phases. Physics of the Earth and Planetary Interiors 91: 161–176

Garnero EJ, Helmberger DV (1996) Seismic detection of a thin laterally varying boundary layer at the base of the mantle beneath the Central-Pacific. Geophys Res Letters 23: 977–980

Gasparik T (1990) Phase relations in the transition zone. J Geophys Res 95: 15751–15769

Gasparik T (1996) Melting experiments on the enstatite-diopside join at 70–224 kbar, including the melting of diopside. Contrib Mineral Petrol 124: 139–153

Goroshkov GS (1958) On some theoretical problems of volcanology. Bull Volcanol 19: 103–113

Grand SP (1994) Mantle Shear structure beneath the Americas and surrounding oceans. J Geophys Res 99: 11591–11621

Grand SP, Van der Hilst RD, Widiyantoro S (1997) Global seismic tomography: A snapshot of convection in the Earth. GSA Today 7: 1–7

Graves RW, Helmberger DV (1988) Upper mantle cross section from Tonga to New Foundland. J Geophys Research Solid Earth and Planets 93: 4701–4711

Greise P (1968) Versuch einer gleiderung der erdkruste in nordichen Alpenvorland in den ostalapen und in teilen der westalpen mit hilfe characteristicher refractions laubzeit kurven sowie eine geologischedetung. Geophys. Abhand lungen. 1(2), 1–20, Inst Meteor Geophysik. Frei, Univ. Berlin

Gu YJ, Dziewnski AM, Ekstrom G (2001) Preferential detection of the Lehmann discontinuity beneath continents. Geophys Res Letters 28: 4655–4658

Gung YC, Panning M, Bomanowicz B (2003) Global anisotropy and the thickness of continents. Nature 422: 707–711

Gupta AK, Yagi K. (1979) Experimental study of two picrites with reference to the genesis of kimberlite. In: Boyd FR, Meyer H O A (eds) Kimberlites, diatremes and diamonds: Their Geology and Petrology and Geochemistry. Am Geophysical Union, Washington DC

Hess (1965) Mid-oceanic ridges and tectonics of seafloor. In: Whittard W D, Bradshaw R (eds) Submarine geology and Geophysics, Butterworth, London

Hill MN (1957) Recent exploration of the ocean floor. In: Ahrens L, Press F, Rankama K, Ruscorn S (eds) Physics and Chemistry of the earth, Pergamon Press, London

Huang X, Yousheng Xu, Karato S (2005) Water content in the transition zone from electrical conductivity of Wadsleyite and Ringwoodite. Nature 434: 746–749

Ichiki M (2001) Upper mantle conductivity structure of the back-arc region beneath north eastern China. Geophys Res Lett 28: 3773–3776

Ichiki M, Baba K, Obayashi M, Utada H (2006) Water content and geotherm in the upper mantle above the stagnant slab: Interpretation of electrical conductivity and seismic P-wave velocity models. Phys Earth Planet Inter 155: 1–15

Ita J, Stixrude L (1992) Petrology, elasticity and composition of the mantle transition zone. J Geophys Res 97: 6849–6866

Ito E, Takahashi E (1987) Ultra-high pressure transformation and the condition of the deep mantle. In: Manghanine MH, Syono Y (eds.) High pressure research in mineral physics. Amer Geophys Union, Washington DC

Ito E, Takahashi E (1989) Post spinel transformations in the system $Mg_2SiO_4$ - $Fe_2SiO_4$ and some geophysical implications. J Geophys Res Solid Earth and Planets 94: 10637–10646

Jarosewitch E (1990) Chemical analysis of meteorites: a compilation of stony and iron meteorite analysis. Meteoritics 25: 323–337

Jeanolz R, Lay T (1993) The core mantle boundary. Scientific American May: 48–65

Jeanolz R, Wenk HR (1988) Convection and anisotropy of the inner core. Geophys Res Letter 15: 72–75

Jeffrey H (1937) On the materials and density of the earth's crust. Mon Nat Roy Astron Soc Geophys Suppl 4: 50–61

Johnson L (1967) Array measurements of P velocities in the upper mantle. J Geophys Res 72: 6309–6325

Johnson L (1969) Array measurements of P velocities in lower mantle. Bull Seism Soc Am 59: 973–1008

Kaila KL, Narain H (1976) Evolution of the Himalayas based on seismotectonics and deep seismic sounding. Proc Himalayan Geol Sem Section II B: 1–39

Kaila KL, Reddy PR, Dixit MM, Kotesware Rao (1985) Crustal structure across the Narmada-Son lineament, central India from deep seismic soundings. Geol Soc Ind 26: 465–480

Kaila KL, Roychowdhury K, Reddy PR, Krishnan VG, Narain Hari, Subbotin SI, Sollogub VB, Chekunov AV, Kharetchko EG, Lazarenko MA, Ilchenko TV (1979) Crustal structure along Kavali-Udipi profile in the Indian peninsular shield from deep seismic sounding. Jour Geol Soc Ind 20: 367–333

Kaila KL, Tewari HC (1985) Deep seismic sounding and crustal tectonics. Assoc Explor Geophys Osmania Univ India 43–59

Kaila KL, Tiwari HC, Mall DM (1987) Crustal structure and delineation of Gondwana basin in the Mahanadi delta area, India, from Deep Seismic Soundings. J Geol Soc Ind 29: 293–308

Kaila KL, Tripathi KM, Dixit MM (1984) Crustal Structure along Wular Lake - Gulmarg. Aaoshera, profile across Pir Panjal Range of Himalayas from the seismic soundings. Geol Soc Ind 25: 706–719

Karason H, Van der Hilst RD (2001) Tomographic imaging of the lowermost mantle with differential times of reflected and diffracted core phases (PKP, Pdiff). J Geophys Res 106: 6569–6587

Karki BB, Warren MC, Stixrude L, Ackland GJ, Crain J (1997) Ab initio studies of high-pressure structural transformations in silica. Physical Review B 55: 3465–3471

Kato T, Kumazawa M (1985) Garnet phase of $MgSiO_3$ filling the pyroxene-ilmenite gap at very high temperature. Nature 316: 803–805

Kawakatsu H, Niu FL (1994) Seismic evidence for a 920 km discontinuity in the mantle. Nature 371: 301–305

Kennett BLN, Engdahi ER (1991) Travel times for global earthquake location and phase identification. Geophys J International 105: 429–465

Kesson SE, Fitz G, Shelley JW, Withers RL (1995) Phase relations structure and crystal chemistry of some aluminous silicate perovskites. Earth Planet Sci 134: 187–201

Khitarov NI (1964) New experimental work in the field of deep seated processes. Geochim Inter 3: 532–535

Kinbota S, Berg E (1967) Evidence for magma in the Katmai volcanic range. Bull Volcanol 31: 175–214

Knittle E, Jeanolz R (1987) Synthesis and equation of state of (Mg, Fe) $SiO_3$ perovskite to over 100 GPa. Science 235: 668–670

Knittle E, Jeanolz R (1991) Earth's core-mantle boundary: Results of experiments at high pressures and temperatures. Science 251: 1438–1443

Kondo T, Ohtani E, Hirao N, Yagi T, Kikegawa T (2004) Phase transitions of (Mg, Fe)O at megabar pressures. In: Rubie DC, Duffy TS, Ohtani E (eds) New Developments in High-Pressure Mineral Physics and Applications to the Earth's Interior, Elsevier

Kubota S, E Berg (1967) Evidence for magma in the Katmai volcanic range. Bull Volcanol 31: 175–214

Kushiro (1973) Partial melting of garnet lherzolites from kimberlite at high pressures. In: Nixon PH (ed) Lesotho kimberlites. Lerotho National Development Corporation, Maseru, Lesotho

Lay T (2007) Deep Earth Structure-Lower Mantle and D". In: Price DG (ed) Treatise on Geophysics 2: Mineral Physics Past, Present and Future, Elsevier

Lay T, Willams Q, Granero EJ, Kellogg L, Wysession ME (1998b) Seismic wave anisotropy in the D" region and its implications. In: Gurnis M, Wysession, ME, Knittle E and Buffett BA (eds) The

Core-Mantle boundary Regions. Am Geophys Union, Washington DC

Lay T, Young CJ (1989) Waveform complexity in teleseismic broadband SH displacements: Slab diffractions or deep mantle reflections? Geophys Res Lett 16: 605–608

Mao HK, Wu Y, Chen LC, Shu JF, Jephocat AP (1990) Static compression of iron to 300 Gpa and Fo $_{0.8}$Ni$_{0.2}$ alloy to 260 Gpa: Implications for compression of the core. J Geophys Res 95: 21737–21742

Mao HK, Yagi T, Bell PM (1977) Mineralogy of the earth's deep mantle: Quenching experiments on mineral compositions at high pressure and temperature. Carnegie Inst Wash Yb 76: 502–504

Mao HR, Hemley RJ, Chao ECT (1987b) The application of micro-Raman spectroscopy to analysis and identification of minerals in thin sections. Scanning microscopy 1: 495–501

Mao WL, Mao HK, Goncharov AF, et al. (2002) Hydrogen clusters in clathrate hydrate. Science 297

Markhinin EK (1968) Volcanism as an agent of formation of the Earth's crust. In: Knopoff L, Drake CL and Hart PJ (eds) The Crust and Upper Mantle of the Pacific Area. Geophysical Monograph 12, Am Geophys Union, Washington DC

Masters G, Laske G, Bolton H, Dziewonski A (2000) The relative behavior of shear velocity, bulk sound speed and compressional velocity in the mantle: Implications for chemical and thermal structure. In: Karato Sl, Forte A, Liebermann R, Masters G and Stixrude L (eds) Earth's deep Interior: Mineral Physics and Tomography from Atomic to the Global Scale. Am Geophys Union, Washington DC

McBirney AR (1969) Compositional variations in Cenozoic calc-alkaline suites of Central America. In: Oregon Dep. Geol Mineral Ind Bull 65: 185–189

Mechie J, Egorkin AV, Fuchs K, Ryberg T, Solodilov L, Wenzel F (1993) P-wave mantle velocity structure beneath northern Eurasia from long-range recordings along the profile. Phys Earth Planet Inter 79: 269–286

Megnin C, Romanowicz B (2000) The three-dimensional shear velocity structure of the mantle from the inversion of body, surface and higher-mode waveform. Geophys J Int 143: 709–728

Megnin C, Romanowicz B (2008) The three-dimensional shear velocity structure of the mantle from the inversion of body, surface and higher mode wave form. Geophys J Internet 143: 709–728

Melchior P (1986) The physics of the Earth's core. Pergman press,Oxford.

Miyajima N, Fujino K, Kondo N, Yagi T (1999) Garnet-perovskite transformation under conditions of the earth's lower mantle: an analytical transmission electron microscopy study. Phys Earth Planet Int 116: 117–131

Morelli A, Dzieworksi AM, Woodhouse JH (1986) Anisotropy of the inner core inferred from PKIP travel times. Geophys Res Letter 13: 1545–1548

Morgan WR (1965) Gravity anomalies and convection currents: The Puerto Rico Trench and the Mid Atlantic rise. J Geophys Res 6189–6204

Murakami M, Hirose K, Kawamura K, Sata N, Ohishi Y (2004) Post perovskite phase transition in $MgSiO_3$. Science 304: 855–858

Naray-Szabo STV (1943) Der Structure type des perovskits ($CaTiO_3$). Naturewiss 31: 202–203

Nishimura CE and Forsyth DW (1989): The anisotropic structure of the upper mantle in the Pacific. Geophys J Oxford 96: 203–229

Nolet G, Grand SP, Kennet BLN (1994) Seismic heterogeneity in the upper mantle J Geophys Res 99: 23753–23766

Nuttli OW (1969) Travel times and amplitude of S waves from nuclear explosion in Nevada. Bull Seism Soc Am 59: 385–398

O'Neill B, Jeanloz R (1994) $MgSiO_3$-$FeSiO_3$-$Al_2O_3$ in the Earth's lower mantle: perovskite and garnet at 1200 km depth. J Geophys Res 99: 19901–19915

Oganov AR, Ono S (2004) Theoretical and experimental evidence for a post perovskite phase of $MgSiO_3$ in Earth's D" layer. Nature 430: 445–448

Oguri K, Funamori N, Takeyuki U, Nobuyoshi M, Yagi T, Fujino K (2000) Post-garnet transition in a natural pyrope: A multi-anvil study based on in situ X-ray diffraction and transmission electron microscopy. Physics of the Earth and Planetary Interiors 122: 175–186

Ohtani E, Kato T, Sawamoto H (1986) Melting of model chondritic mantle to 20 GPa. Nature 322: 352–354

Ohtani E, Litasov K, Hosoya T, Kubo T, Kondo T (2004) Water transport into the deep mantle and formation of a hydrous transition zone. In: Rubie DC, Duffy TS, Ohtani E (eds) New Developments in High-pressure Mineral Physics and Applications to the Earth's interior. Elsevier

Ohtani E, Sawamoto H (1987) Melting experiment on a model chondrite mantle composition at 25 GPa. Geophys Res Letter 14: 733–736

Panero W, Knutson R, Akbar S, Stixrude L (2006) $Al_2O_3$ incorporation in $MgSiO_3$ perovskite and ilmenite, Earth and Planetary Science Letters 252: 152–161

Presnall DC, Gasparik T (1990) Melting enstatite ($MgSiO_3$) from 10 to 16.5 GPa and the forsterite ($Mg_2SiO_4$) - Majorite ($MgSiO_3$) eutectic at 16.5 GPa: implications for the origin of the mantle. J Gephys Res 95: 15. 771–15. 777

Press F (1969) The suboceanic mantle. Science 165: 174–176

Raith R (1963) The crustal rocks. In: M.N. Hill (ed.) The Sea. Wiley Inter Science, New York

Revenaugh JS, Jordan TH (1991) Mantle layering from seismic reverberations, 2. The transition zone. J Geophys Res 96: 19763–19780

Ringwood AE (1974) The petrological evolution of island arc systems. J Geol Soc London 183–204

Ringwood AE (1975) Composition and petrology of the earth's mantle. McGraw-Hill Book Company, USA

Ringwood AE, Major A (1966) Synthesis of $Mg_2SiO_4$ - $Fe_2SiO_4$ solid solutions. Earth and Planet Sc Letters 1: 241–245

Ringwood AE, Major A (1968) High pressure transformations of spinels. 1. Earth and Planet Sc Letters 5: 245–250

Ringwood AE, Major A (1971) Olivine-spinel transformations in $MgMnGeO_4$, $FeMnGeO_4$ and $CoMnGeO_4$. J Phys Chem Solids 31: 2791–2793

Ringwood AF, Major A (1970) The system $Mg_2SiO_4$-$Fe_2SiO_4$ at high pressures and temperatures. Phys Earth Planet Interior 3: 89–108

Ritsema J, van Heijst HJ (2000) Seismic imaging of structural heterogeneity in the Earth's mantle: Evidence for large-scale mantle flow. Science Progress 83: 243–259

Ritsema J, Van Heijst HJ (2002) Constraints on the correlation of P and S wave velocity homogeneity in the mantle from P, PP, PPP and PKPab travel times. Geophys J Internat 149: 482–489

Romanowicz B (1998) Attenuation tomography of the earth's mantle. A review of current status. Pure and Applied Geophys 153: 257–272

Romanowicz B (2003) Global mantle tomography Progress status in the past 10 years. Annual Review of Earth and Planet Sci 31: 303–328

Ronov AB, Yaroshevsky AA (1969) Chemical composition of the Earth's Crust. In: Hart PJ (ed) The Earth's Crust and Upper Mantle, Geophysical Monograph 13, Am Geophysical Union, Washington DC

Saxena SK, Dubrovinsky LS, Haggkvist P, Cerenius G Shen, Mao HK (1995) Synchrotron X-ray Study of Iron at High Pressure and Temperature. Science 269: 1703–1704

Serghiou G, Zerr A, Chopelas A, Boehler R (1998) The transition of pyrope to perovskite. Phys Chem Miner 25: 193–196

Shearer PM (1990) Seismic imaging of upper mantle structure with new evidence for a 520 km discontinuity. Nature 344: 121–126

Shen GY, Prakopenka VB, River ML, Sutton SR (2004) Structure of liquid iron at pressures up to 58 GPa. Physical Review Letters 92: 1–4

Shidorin I, Gurnis M, Helmberger DV (1999) Evidence for a ubiquitons seismic discontinuity at the base of the mantle. Science 286: 1326–1331

Shimozuru D (1963) Geophysical evidence for suggesting the existence of molten pockets in the earth's upper mantle. Bull Volcanol 26: 181–195

Stacey FD (1977) A thermal model of the earth. Phys Earth Planet Int 15: 341–348

Steinhart JS, Meyer RP (1961) Explosion studies of continental structure. Carnegie Inst Wash Pub 62: 409

Steinle-Neumann G, Stixrude L, Cohen RE, Gleseren O (2001) Elasticity of iron at the temperature of the Earth's inner core. Nature 413: 57–60

Stixrude L (2007) Properties of Rocks and Minerals-Seismic Properties of Rocks and Minerals and Structure of the Earth. In: Price DG (ed) Treatise on Geophysics 2: Mineral Physics Past, Present and Future, Elsevier

Stixrude L, Lithgow-Bertelloni C (2005) Mineralogy and elasticity of the oceanic upper mantle: Origin of the low velocity zone. J Geophys Res Solid Earth 110 B03204. doi: 10. 1029/2004 JB002965

Takahashi E (1986) Melting of dry peridotite KLB–1 up to 14 GPa, Implications of the origin of the peridotitic upper mantle. J Geophys Res 91: 9367–9382

Takida M, Richet P (1989) Equation of state of $CaSiO_3$ perovskite to 96 GPa. Geophys Res Lett 16: 1351–1354.

Talwani M, Pichon X Le, Ewing M (1966) A crustal section across Puetrico Trench. J Geophys Res 70: 341–352

Talwani M, Sutton GH, Worzel JL (1959) A crustal section across the Puero Rico Trench. J Geophys Res 64: 1545–1555

Tsuchiya T, Tsuchiya J, Ummemoto K, Wentzcovitch RM (2004) Phase transition in $MgSiO_3$ perovskite in Earth's lower mantle. Earth and Planet Science letters 224: 241–248

Uchiyama Y, Yagi T, Akaogi M, Ito E (1992) Technical report of the institute of solid state physics. The University of Tokyo, Japan

Utada H, Koyama T, Shimazu H, Chane AD (2003) A seismiglobal reference model for electrical conductivity in the mid-mantle beneath the north Pacific region. Geophys Res Lett. 30,10.1029/2002 GL016092

Utada H, Koyama T, Shimizu H, Chave AD (2003) A semi-global reference model for electrical conductivity in the mid-mantle beneath the north Pacific region. Geophys Letter 30. 1194. doi: 10.1029/2002 GL 016902

Vinnik L, Kato M, Kawakatsu H (2001) Search for seismic discontinuities in the lower mantle. Geophys J Internat 147: 41–56

Vinnik LP (1977) Detection of waves converted from P to SV in the mantle. Phys Earth Planet Inter 15: 39–45

Wang D, Mookherjee M, Youshang Xu, Karato S (2006) The effect of water on the electrical conductivity of olivine. Nature 443: 977–980

Wang Y, Uchida T, Zhang J, Rivers ML, Sutton SR (2004) In: Rubie D, Duffy TS and Ohtani E (eds) New Developments in High Pressure Mineral Physics and Application to the Earth's Interior, Elsevier

Wells AF (1962) Structural Inorganic Chemistry, 2nd edn. Clarendon, Oxford

Woodland AB (1998) The orthorhombic to high-monoclinic phase transition in Mg-Fe pyroxenes: Can it produce a seismic discontinuity? Geophys Res Letters 25: 1241–1244

Yagi T, Kusanagi S, Tsuchida Y, Fukai Y (1989) Isochemical compression and stability of perovskite-type $CaSiO_3$. Proceeding Japan Acad. B-Physics 65: 129–132

Yoshino T, Matsuzaki T, Yamashita S, Katsura T (2006) Hydrous olivine unable to account for conductivity anomaly at the top of the asthenosphere. Nature 443: 973–976

Zao D (2001) Seismic structure and origin of hotspots and mantle plumes. Earth and Planet Sci Letters 192: 251–265.

## 2

# Modelling of Metamorphic Textures with *C-Space*: Evidence of Pan-African High-grade Reworking in the Eastern Ghats Belt, India

Pulak Sengupta and Somnath Dasgupta

**Abstract:** The polymetamorphic Eastern Ghats Belt, India is an important component of models predicting Indo-Antarctic correlation in the Precambrian. However, the metamorphic signatures developed during the Pan-African orogeny are hardly known. Here we address this issue through modelling of reaction textures developed in a massif-type anorthosite from Chilka Lake area using the programme *C-Space*. We have explained the metamorphic textures in terms of balanced chemical reactions, which revealed at least two stages of mineral reconstitutions during the Pan-African event.

---

Pulak Sengupta (✉)
Department of Geological Sciences, Jadavpur University, Kolkata - 700032
e-mail: pulaksg@cal3.vsnl.net.in

Somnath Dasgupta
Indian Institute of Science Education & Research, HC-VII, Sector 3, Salt Lake, Kolkata - 700106, India
e-mail: somnathdasg@gmail.com

## 2.1 Introduction

Matrix operation is an important technique in linear algebra that is frequently used to solve diverse problems in science and engineering (Press et al. 1989). The different methods of this technique are routinely employed to derive values of unknown parameters that are linked by linear equations. In different branches of geology, many problems can be expressed in the form of a set of linear equations that can be solved with the methods of matrix operation (e.g. Fisher 1989, 1993, Spear 1993). In orogenic belts, changing physico-chemical conditions leave their mark in the textures of rocks. One of the main goals of metamorphic petrology is to interpret these reaction textures to decipher the P-T-fluid regimes of the extinct orogenic belts (Ague 2003, Das et al. 2008, Lang et al. 2004, Spear 1993, Sengupta et al. 1999 among other). Construction of balanced chemical reactions integrating textural relations and mineral compositions forms the basis of all energy and mass balance calculations that are performed on the rocks of ancient orogenic belts (Ague 2003, Lang et al. 2004, Spear 1993).

In this paper we have demonstrated as to how the computer programme *C-Space* (Torres-Roldan et al. 2000) that employs the singular value decomposition (SVD) method of matrix operation can be applied to model the reaction textures of metamorphic rocks. This procedure has been applied on two samples of a meta-anorthosite from the Chilka Lake complex, Eastern Ghats Belt (EGB) to characterise the metamorphic reconstitution of the Grenvillian massif-type anorthosite during the Pan-African orogenesis in this region. A rationale for selecting these samples for modelling is to document the nature of tectonothermal reworking of broadly Pan-African age in the EGB, which was hitherto poorly characterised.

## 2.2 The Chilka Lake Anorthosite Complex (CLAC)

The CLAC represents one of the massif-type anorthosite complexes that intruded the granulite basements of the EGB (Dobmeier and Raith 2003, Dasgupta and Sengupta 2003). Barring a few tens of metres at the contact with the host rocks, the anorthosite is massive and is dominated by saccaroidal aggregates of off-white colour plagioclase grains. With in the sea of plagioclase dark streaks rich in pyroxenes and Fe-Ti oxides occur. In places, laterally continuous to discontinuous layers rich in oxides and mafic minerals were observed (Fig. 2.1a). At the marginal part, the anorthosite developed a pervasive foliation and a prominent sub-horizontal lineation defined by aggregates of pyroxene, amphibole and biotite (Fig. 2.1b). Anorthosite and the adjoining rocks of the CLAC have been studied by a number of workers. Detail information on the geological evolution of the rocks of CLAC can be obtained from Bhattacharya et al. (1994), Bhattacharya et al. (1998), Krause et al. (2001), Sengupta et al. (2008) and Simmat and Raith (2008). The evolutionary history of the CLAC can be summarised as follows. The hot (>1000ºC) parental magma of the massif-type anorthosite of CLAC was emplaced into a suite high-grade rocks consisting of metapelites, calc-silicate, felsic and mafic granulites (reviewed in Sengupta et al. 2008). The enclosing pelitic and calc-silicate rocks underwent ultra-high temperature contact metamorphism at the mid crustal depth (corresponding to 7 ± 1 kbar pressure) (Sengupta et al. 2008). These rocks were subsequently repeatedly deformed, metamorphosed and chemically altered due to influx of fluids from an external source. Quantitative geothermobarometry on the metamorphic assemblages that were developed in anorthosite, constrains pressure and temperature in the range of ~6 ± 1 kbar and 650 ± 50ºC (Sengupta et al. 2008). Based on U-Pb dating of zircon from a ferrodiorite that was deemed to be co-genetic with the anorthosite, Krause et al. (2001) placed the time of emplacement of the anorthosite at ca 0.79 Ga. An age of ~0.66–0.69 Ga has been attributed to the metamorphism and deformation of the CLAC (Dobmeier and Simmat 2002, Simmat and Raith 2008). In a recent geochronological study, Chatterjee et al. (2008) obtained U-Pb zircon date of ~0.98 Ga which was interpreted as the time of emplacement of the anorthosite magma of the CLAC. This should also be considered as the age of ultra-high temperature metamorphism that was observed in the calc-silicate rocks occurring at the contact of anorthosite body (Sengupta et al. 2008). Chatterjee et al. (2008) also recorded metamorphic recrystalisations of the Grenvillian anorthosite and the adjoining rocks of the CLAC during the Pan-African tectonothermal events (~0.72 Ga and also 0.64–0.69 Ga). Therefore, the mineral reconstitutions in the anorthosite occurred during the Pan-African orogeny.

In this study two samples (#2K-28 and #CM10-2b) from an anorthosite body that are exposed near the town of Rambha, Orissa, India (85º06'E, 19º28'N), have been chosen for detail textural modelling . Sample #2K-28 was taken from the centre of the anorthosite body and was least chemically altered during the Pan-African metamorphism. The other sample, #CM10-2b, occurs at the most deformed marginal part of the anorthosite body and developed retrograde minerals in profusion. A pink coloured granite that veined the sample #CM10-2b was also deformed and disintegrated into lenticles of quartz and feldspar. The geological evolution of the rocks of the studied area has been described in Sengupta et al. (2008).

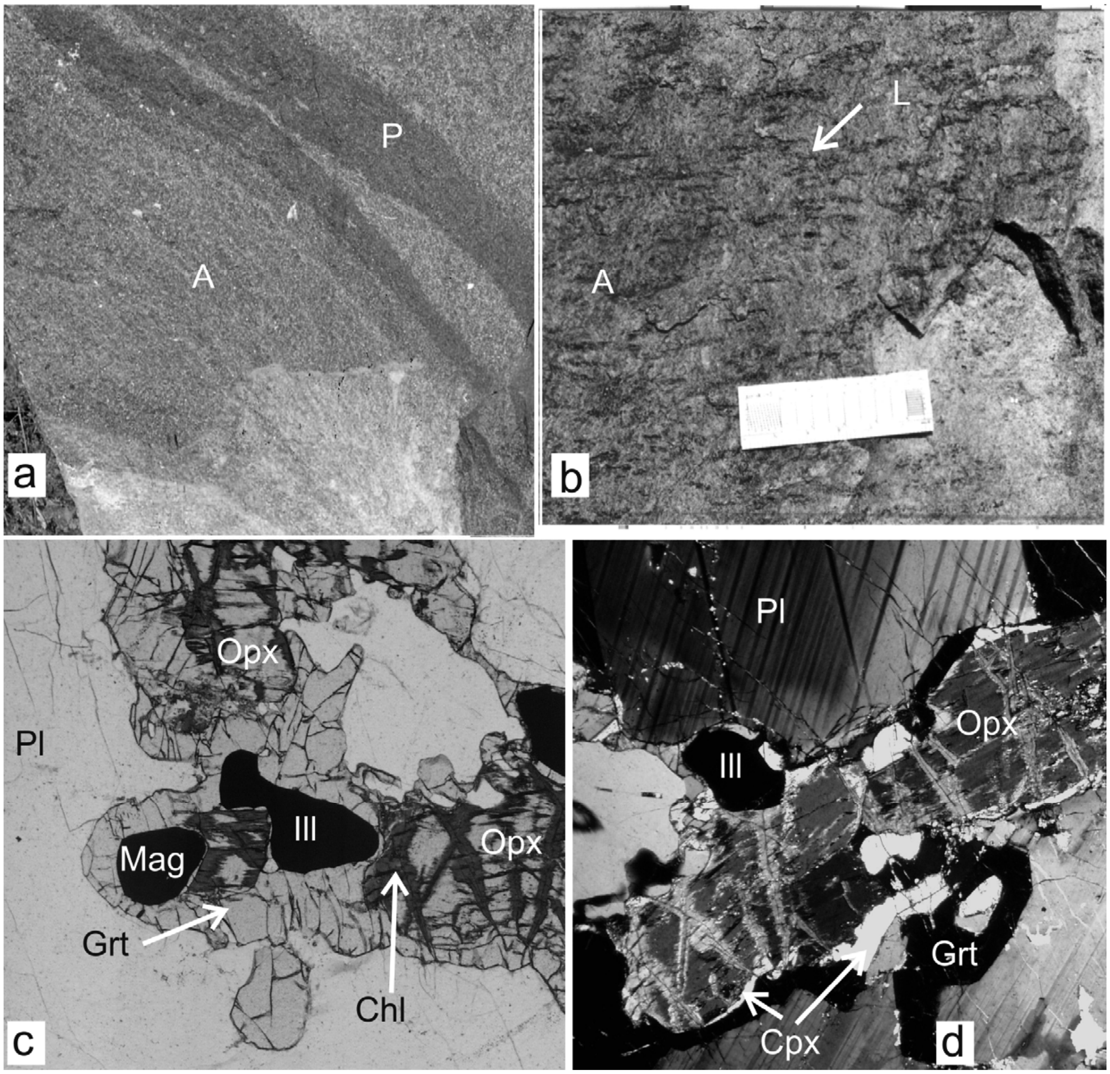

**Fig. 2.1** a. Pyroxene (P)-rich layers in anorthosite (A). b. Sub-horizontal mineral aggregate (amphibole + biotite) lineations (L) in anorthosite (A). c. Coronal garnet (Grt) along the junctions of orthopyroxene (Opx), ilmenite (Ill), magnetite (Mag) and plagioclase (Pl). Note that the coronal garnet preferentially dedelop on plagioclase. Orthopyroxene grains are veined by chlorite (Chl). d. Same as Fig. 2c but note the compound corona of clinopyroxene (Cpx) and garnet at the interface of orthopyroxene and plagioclase.

## 2.3 Reaction Textures and Phase Compositions

In this section, the textural features of the two samples that are suitable for textural modelling will be described. Representative compositions of the minerals of the two samples are presented in Tables 2.1 and 2.2. The mineral compositions were obtained with a CAMECA electron probe micro analyser (CAMEBAX) at the Mineralogy and Petrology Institute, University of Bonn, Germany. The details of operating conditions, standards used and the ZAF correction procedures of the raw data are described in Sengupta et al. (1999).

### *2.3.1 Sample #2K-28*

Grains of orthopyroxene, clinopyroxene, ilmenite, magnetite and plagioclase that presumably represent the magmatic precursor of the anorthosite were recrystallised during the superimposed deformation and produced a granoblastic fabric in this rock. The most conspicuous reaction texture in this rock is the growth of thick to thin garnet coronae along the interfaces of plagioclase, orthopyroxene, ilmenite and magnetite (Fig. 2.1c). In places, orthopyroxene and Fe-Ti oxides are separated from the adjoining plagioclase grains by compound coronae of clinopyroxene and garnet

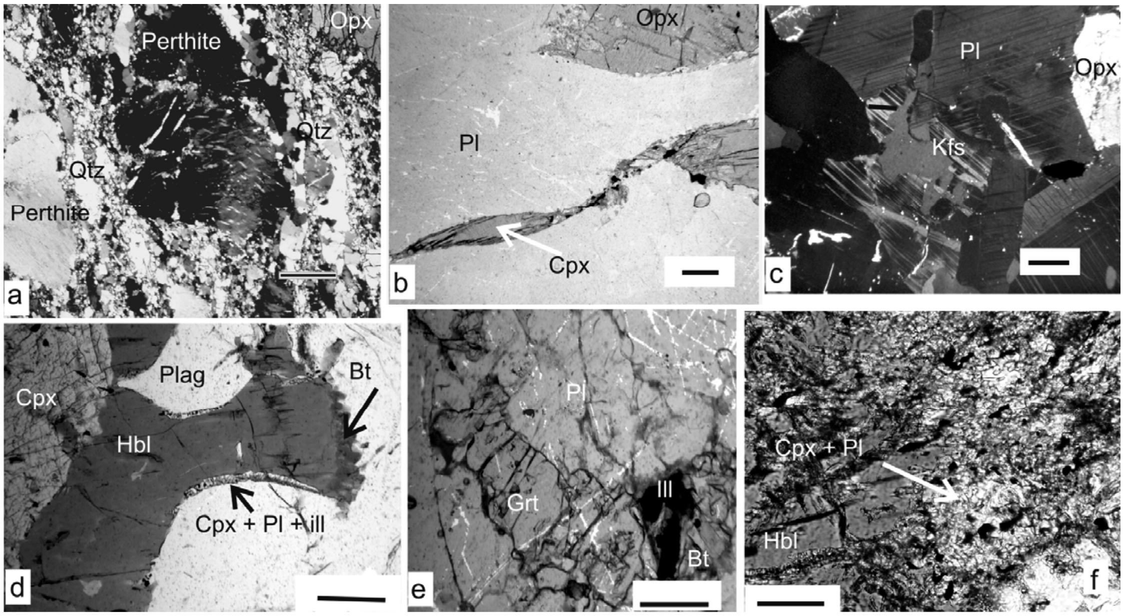

**Fig. 2.2** a. Marginal recrystalisation of perthite and quartz of the granite veins in marginal part of anorthosite. Also note the deformed orthopyroxene (Opx). b. Stretched grains of clinopyroxene (Cpx) and orthopyroxene (Opx) in the matrix of plagioclase (Pl) grains in anorthosite. Note that the clinopyroxene porphyroclasts have tails defined by small and recrystallised grains of this mineral c. K-feldspar (Kfs) veins replacing recrystallised plagioclase grains (Pl) of anorthosite. d. Clinopyroxene (Cpx) porphyroclast is replaced successively by amphibole (Hbl) and biotite (Bt). Note that a symplectic intergrowth of clinopyroxene + plagioclase + ilmenite replacing amphibole along the margin. e. Garnet (Grt) on plagioclase (Pl) grains close to the domain shown in d. Also note the ilmenite (Ill) and biotite (Bt) grains close by. f. Coarse amphibole (Hbl) is replaced by a granular aggregates of clinopyroxene + plagioclase and ilmenite. The length of the scale bars in all the diagrams measures 100 microns.

(Fig. 2.1d). Coronal garnet is always developed more on the grains of plagioclase than the coexisting pyroxene and Fe-Ti oxides (Figs. 2.1c and 2.1d). This feature is consistent with (a) immobile nature of Al during the growth of coronal garnet and (b) the fact that garnet consumed more plagioclase than the adjoining orthopyroxene or Fe-Ti oxides. Quartz and rutile are conspicuous by their absence. Orthopyroxene porphyroclasts are veined by retrograde chlorite (Figs. 2.1c and 2.1d).

The coarse orthopyroxene ($X_{Mg}$ = 0.36, $Al_2O_3$ = 0.72 wt%), coronitic clinopyroxene ($X_{Mg}$ = 0.53, $Al_2O_3$ = 1.33 wt%) and garnet ($X_{Prp}$ = 0.09, $X_{Sps}$ = 0.04, $X_{Grs}$ = 0.21) are compositionally homogeneous (Table 2.1). Plagioclase grains, irrespective of the presence of garnet, show normal zoning. At the contact with the aforesaid coronal garnet, the plagioclase shows ~ 7 mol% decrease in anorthite towards the rim (Table 2.1).

### 2.3.2 Sample #CM10-2b

Clinopyroxene, orthopyroxene, plagioclase, ilmenite and magnetite represent the magmatic minerals in this sample. Amphibole, biotite, quartz and garnet developed during metamorphism. Where veined by granite, the rock shows abundant pertihite and quartz (Fig. 2.2a). Sphene and dolomite are the common accessory minerals in the rock. In contrast, sample #CM10-2b shows intense post-crystalline deformation manifested by (a) elliptical grains of magmatic clino- and orthopyroxene grains, (b) bending, undulose extinction and marginal recrystalisation of the grains of perthite and quartz in granite veins (Figs. 2.2a and 2.2b), and (c) recrystalisation of the magmatic pyroxene and plagioclase grains into polygonal aggregates showing triple point junctions (Fig. 2.2c). Some of the plagioclase grains were veined by K-feldspar (Fig. 2.2c). Pyroxene was replaced successively by amphibole and biotite (Fig. 2.2d). Garnet developed on plagioclase grains close to these retrograde hydrous phases (Fig. 2.2e). Amphibole is commonly rimmed by a symplectic intergrowth of clinopyroxene and plagioclase in sub-equal proportion (Fig. 2.2d). The biotite corona that formed around the amphibole did not replace the symplectite. In places, amphibole grains were partially replaced by granular aggregates of clinopyroxene, plagioclase and ilmenite (Fig. 2.2f). Similar to the symplectic intergrowth, clinopyroxene and plagioclase also occur in roughly equal volume proportion in the granular aggregates.

**Table 2.1** Representative compositions of minerals in the sample #2K-28

| | Grt cr | Cpx cr | Opx | Pl r | Pl c | Ill |
|---|---|---|---|---|---|---|
| $SiO_2$ | 37.84 | 50.3 | 49.58 | 51.48 | 49.88 | 0.03 |
| $TiO_2$ | 0.04 | 0.18 | 0.08 | 0.01 | 0.00 | 50.52 |
| $Al_2O_3$ | 21.37 | 1.33 | 0.72 | 31.53 | 32 | 0.01 |
| $Cr_2O_3$ | 0.03 | 0.00 | 0.00 | 0.00 | 0.00 | 0.01 |
| FeO | 29.94 | 15.42 | 36.84 | 0.16 | 0.21 | 48.3 |
| MnO | 1.78 | 0.25 | 0.7 | 0.00 | 0.00 | 0.42 |
| MgO | 2.23 | 9.79 | 11.83 | 0.01 | 0.01 | 0.55 |
| CaO | 7.58 | 22.99 | 0.73 | 13.47 | 15.3 | 0.03 |
| $Na_2O$ | 0.00 | 0.28 | 0.01 | 3.85 | 3.25 | 0.00 |
| $K_2O$ | 0.01 | 0.00 | 0.01 | 0.14 | 0.11 | 0.00 |
| Total | 100.82 | 100.54 | 100.5 | 100.65 | 100.76 | 99.87 |
| Oxygen p.f.u. | 24 | 6 | 6 | 8 | 8 | 3 |
| Si | 5.99 | 1.94 | 1.98 | 2.32 | 2.27 | 0.00 |
| Ti | 0.00 | 0.01 | 0.00 | 0.00 | 0.00 | 0.97 |
| Al | 3.99 | 0.06 | 0.03 | 1.68 | 1.71 | 0.00 |
| Cr | 0.00 | 0.00 | 0.00 | 0.00 | 0.00 | 0.00 |
| Fe | 3.96 | 0.50 | 1.23 | 0.01 | 0.01 | 1.03 |
| Mn | 0.24 | 0.01 | 0.02 | 0.00 | 0.00 | 0.01 |
| Mg | 0.53 | 0.56 | 0.70 | 0.00 | 0.00 | 0.02 |
| Ca | 1.29 | 0.95 | 0.03 | 0.65 | 0.74 | 0.00 |
| Na | 0.00 | 0.02 | 0.00 | 0.34 | 0.29 | 0.00 |
| K | 0.00 | 0.00 | 0.00 | 0.01 | 0.01 | 0.00 |
| $X_{Prp}$ | 0.09 | – | – | – | – | – |
| $X_{Alm}$ | 0.66 | – | – | – | – | – |
| $X_{Sps}$ | 0.04 | – | – | – | – | – |
| $X_{Grs}$ | 0.21 | – | – | – | – | – |
| $X_{Mg}$ | – | 0.53 | 0.36 | – | – | – |
| An% | – | – | – | 0.65 | 0.72 | – |

All abbreviations are after Kretz (1983). c = core, r = rim, cr = corona

Representative compositions of the minerals of this sample are presented in Table 2.2. Barring the plagioclase, compositions of all other phases are virtually homogeneous. Similar to the other sample (#2K-28), plagioclase grains show normal zoning (54 mol% and 49 mol% anorthite in core and rim of the porphyroblastic plagioclase respectively). The composition of the symplectic plagioclase (50 mol% anorthite) is similar to that of the rim composition of the porphyroblastic plagioclase. Compositions of the porphyroblastic orthopyroxene ($X_{Mg}$ = 0.49, $Al_2O_3$ = 0.79 wt%) and clinopyroxene ($X_{Mg}$ = 0.58, $Al_2O_3$ = 1.5 wt%) are more magnesian compared to that of the sample #2K-28.

## 2.4 Modelling of Reaction Textures with *C-Space* Programme

*C-Space* programme is applied to meta-anorthosite of the CLAC, sample number #2K-28 and #CM10-2b.

### *2.4.1 Theory*

A set of linearly independent relations,

$$a_{11}X_1 + a_{12}X_2 + a_{13}X_3 + \ldots + a_{1n}X_n = Y_1$$
$$a_{21}X_1 + a_{22}X_2 + a_{23}X_3 + \ldots + a_{2n}X_n = Y_2$$
$$a_{31}X_1 + a_{32}X_2 + a_{33}X_3 + \ldots + a_{3n}X_n = Y_3$$
$$\ldots\ldots\ldots\ldots\ldots\ldots\ldots\ldots\ldots\ldots\ldots\ldots\ldots\ldots$$
$$a_{m1}X_1 + a_{r2}X_2 + a_{r3}X_3 + \ldots + a_{mn}X_n = Y_m$$

can be expressed in the following matrix form:

$$A.X = Y \qquad (2.1)$$

Where **A, X and Y** are expressed as,

$$\begin{pmatrix} a_{11} & a_{12} & a_{13} & \ldots & a_{1n} \\ a_{21} & a_{22} & a_{23} & \ldots & a_{2n} \\ a_{31} & a_{32} & a_{33} & \ldots & a_{3n} \\ \ldots & \ldots & \ldots & \ldots & \ldots \\ a_{m1} & a_{m2} & a_{m3} & \ldots & a_{mn} \end{pmatrix} = A \begin{pmatrix} X_1 \\ X_2 \\ X_3 \\ \ldots \\ X_m \end{pmatrix} = X \begin{pmatrix} Y_1 \\ Y_2 \\ Y_3 \\ \ldots \\ Y_m \end{pmatrix} = Y$$

Where m and n represent the rows and columns of a given matrix. There exists a number of techniques e.g. Gauss-Jordon elimination, SVD etc. to solve the equation (2.1) (Press et al. 1989). The SVD is a powerful technique in many matrix operations for a number of reasons. It is very robust to numerical errors. In many cases where other methods fail to give satisfactory results, the SVD diagnoses the problem and provide a solution (Press et al. 1989). SVD also helps solve most linear least-squares problems. In general terms the SVD method states that any m × n matrix A, where m and n are the number of rows and columns of the matrix A (m ≥ n), can be expressed as the product of an m × n column-orthogonal matrix U, an n × n diagonal matrix W with positive or zero elements, and transpose of an n × n orthogonal matrix V.

$$A = U.W.V \qquad (2.2)$$

For details of the SVD procedures the readers are referred to Press et al. (1989).

Combining the relations (2.1) and (2.2), we have,

$$U.W.V.X = Y \qquad (2.3)$$

The relation (2.3) can be recast into the form,

$$W.z = d \qquad (2.4)$$

Where, $z = V^T.X$ and $d = U^T.Y$

The relation (2.4) can be solved to obtain the values of the unknowns $X_1$ to $X_n$.

**Table 2.2** Representative mineral compositions in the sample #CM10-2b

| | Grt | Opx | Amph | Bt | Pl sy | Pl r | Pl c | Cpx | Cpx sy | Ill | Sph |
|---|---|---|---|---|---|---|---|---|---|---|---|
| $SiO_2$ | 37.55 | 49.99 | 39.18 | 35.44 | 55.82 | 55.39 | 55.28 | 51.83 | 51.24 | 0.02 | 30.26 |
| $TiO_2$ | 0.18 | 0.05 | 2.58 | 4.92 | 0.26 | 0.06 | 0.06 | 0.21 | 0.19 | 50.28 | 35.61 |
| $Al_2O_3$ | 20.64 | 0.79 | 13.3 | 14.76 | 26.40 | 26.85 | 28.72 | 1.50 | 1.61 | 0.01 | 2.71 |
| $Cr_2O_3$ | 0.02 | 0.00 | 0.06 | 0.10 | 0.00 | 0.00 | 0.00 | 0.03 | 0.00 | 0.04 | 0.03 |
| FeO | 28.9 | 30.37 | 18.7 | 21.21 | 0.46 | 0.81 | 0.13 | 13.02 | 12.43 | 46.14 | 0.92 |
| MnO | 3.19 | 0.65 | 0.32 | 0.05 | 0.02 | 0.07 | 0.03 | 0.47 | 0.54 | 1.12 | 0.08 |
| ZnO | 0.00 | 0.00 | 0.00 | 0.00 | 0.00 | 0.00 | 0.00 | 0.00 | 0.00 | 0.00 | 0.00 |
| MgO | 2.11 | 16.13 | 7.36 | 9.31 | 0.12 | 0.30 | 0.01 | 10.27 | 10.33 | 0.43 | 0.00 |
| CaO | 7.41 | 0.77 | 11.74 | 0.01 | 10.24 | 10.17 | 11.55 | 23.75 | 22.46 | 0.07 | 27.83 |
| $Na_2O$ | 0.03 | 0.05 | 1.61 | 0.00 | 5.45 | 5.68 | 5.38 | 0.39 | 0.42 | 0.00 | 0.00 |
| $K_2O$ | 0.01 | 0.00 | 2.38 | 9.83 | 0.29 | 0.28 | 0.24 | 0.00 | 0.05 | 0.00 | 0.00 |
| NiO | 0.00 | 0.00 | 0.00 | 0.00 | 0.00 | 0.00 | 0.00 | 0.00 | 0.00 | 0.00 | 0.00 |
| Total | 100.04 | 98.8 | 97.23 | 95.63 | 99.06 | 99.61 | 101.4 | 101.47 | 99.27 | 98.11 | 97.44 |
| Oxygen p.f.u. | 24 | 6 | 23 | 11 | 8 | 8 | 8 | 6 | 6 | 3 | 5 |
| Si | 6.01 | 1.97 | 6.07 | 2.74 | 2.54 | 2.52 | 2.47 | 1.95 | 1.97 | 0.00 | 1.01 |
| Ti | 0.02 | 0.00 | 0.30 | 0.29 | 0.01 | 0.00 | 0.00 | 0.01 | 0.01 | 0.98 | 0.90 |
| Al | 3.90 | 0.04 | 2.43 | 1.34 | 1.42 | 1.44 | 1.51 | 0.07 | 0.07 | 0.00 | 0.11 |
| Cr | 0.00 | 0.00 | 0.01 | 0.01 | 0.00 | 0.00 | 0.00 | 0.00 | 0.00 | 0.00 | 0.00 |
| Fe | 3.87 | 1.00 | 2.42 | 1.37 | 0.02 | 0.03 | 0.00 | 0.41 | 0.40 | 1.00 | 0.03 |
| Mn | 0.43 | 0.02 | 0.04 | 0.00 | 0.00 | 0.00 | 0.00 | 0.02 | 0.02 | 0.02 | 0.00 |
| Zn | 0.00 | 0.00 | 0.00 | 0.00 | 0.00 | 0.00 | 0.00 | 0.00 | 0.00 | 0.00 | 0.00 |
| Mg | 0.50 | 0.95 | 1.70 | 1.07 | 0.01 | 0.02 | 0.00 | 0.58 | 0.59 | 0.02 | 0.00 |
| Ca | 1.27 | 0.03 | 1.95 | 0.00 | 0.50 | 0.49 | 0.55 | 0.96 | 0.92 | 0.00 | 1.00 |
| Na | 0.01 | 0.00 | 0.48 | 0.00 | 0.48 | 0.50 | 0.47 | 0.03 | 0.03 | 0.00 | 0.00 |
| K | 0.00 | 0.00 | 0.47 | 0.97 | 0.02 | 0.02 | 0.01 | 0.00 | 0.00 | 0.00 | 0.00 |
| Ni | 0.00 | 0.00 | 0.00 | 0.00 | 0.00 | 0.00 | 0.00 | 0.00 | 0.00 | 0.00 | 0.00 |
| $X_{Prp}$ | 0.08 | – | – | – | – | – | – | – | – | – | – |
| $X_{Alm}$ | 0.64 | – | – | – | – | – | – | – | – | – | – |
| $X_{Sps}$ | 0.07 | – | – | – | – | – | – | – | – | – | – |
| $X_{Grs}$ | 0.21 | – | – | – | – | – | – | – | – | – | – |
| $X_{Mg}$ | – | 0.49 | 0.41 | 0.44 | – | – | – | 0.58 | 0.60 | – | – |
| An% | – | – | – | – | 50 | 49 | 54 | – | – | – | – |

c = core, r = rim, sy = symplectite

Now compositions of the m number of minerals or chemical species that are linked by a chemical reaction can be expressed in terms of n number of system components to generate an m × n matrix as in **A** of equation (2.1). Solution of this matrix can be done with the SVD methods using the relation (2.4). Torres-Roldàn et al. (2000) published a computer programme, *C-Space*, that solves an m × n matrix with the SVD technique and outputs all the possible balanced chemical reactions involving a given set of mineral compositions or chemical species. Out of the possible balanced chemical reactions, those explain the textural relations (i.e. reactant and product appear on two sides of a reaction, the predicted and observed proportion of product or reactant phases should match closely) should be used for mass and energy balance calculations for a given metamorphic assemblage. The *C-Space* programme, which is based on the algorithm published by Fisher (1989, 1993) is, therefore, an elegant tool to model reaction textures that may help decipher the physico-chemical conditions, which a given rock might have evolved through (Lang et al. 2004, Sengupta et al. in review). The SVD of a compositional matrix developed for the garnet-bearing assemblage of sample #2K-28 and the possible chemical reactions involving the minerals are demonstrated in Appendix 1 and 2.

### *2.4.2 Application of the C-Space Programme to Meta-anorthosite of the CLAC*

The SVD technique described above was applied to the mineral assemblages in the two chosen samples from the meta-anorthosite to obtain a set of balanced chemical reactions that are consistent with the observed textural relations. This will be elaborated in the following sections.

#### 2.4.2.1 Reaction modelling in sample #2K-28

The *C-Space* programme outputs the following balanced reactions for mineral compositions of this sample:

*I. Without clinopyroxene*

1. 3.4845 Opx + 4.6463 Mag + 75.3158 Pl (c) + 1.9303 $SiO_2$ + 1.0000 Mn = 66.1866 Pl (r) + 3.5707 Ca + 2.9665 $O_2$ + 4.6022 Grt
2. 3.4845 Opx + 4.6463 Mag + 52.6302 Pl (c) + 1.0000 Mn = 42.9576 Pl (r) + 3.0437 Ca + 1.0867 Na + 3.2096 $O_2$ + 4.6022 Grt
3. 3.4845 Opx + 10.6774 Pl (c) + 6.9694 $Fe_2O_3$ (Ill) + 1.0000 Mn = 2.0689 Ca + 3.0965 Na + 4.8209 $O_2$ + 3.5698 $SiO_2$ + 4.6022 Grt
4. 3.4845 Opx + 460.4466 Pl (c) + 18.4494 Na + 6.9694 $Fe_2O_3$ (Ill) + 34.7010 $SiO_2$ + 1.0000 Mn = 460.5421 Pl (r) + 12.5187 Ca + 4.6022 Grt
5. 3.4845 Opx + 52.6302 Pl (c) + 6.9694 $Fe_2O_3$ (Ill) + 1.0000 Mn = 42.9576 Pl (r) + 3.0437 Ca + 1.0867 Na + 4.3712 $O_2$ + 4.6022 Grt

*II. With clinopyroxene*

6. 7.2178 Opx + 4.3952 Mag + 81.2406 Pl (c) + 3.3193 $SiO_2$ + 1.0342 Mn = 4.2580 Cpx + 71.1360 Pl (r) + 1.0000 $O_2$ + 5.0340 Grt
7. 6.9791 Opx + 78.5543 Pl (c) + 6.3748 $Fe_2O_3$ (Ill) + 3.2096 $SiO_2$ + 1.0000 Mn = 4.1172 Cpx + 68.7838 Pl (r) + 2.0294 $O_2$ + 4.8675 Grt

The balanced chemical reactions that are presented above provide valuable information about the chemical environments that led to the growth of garnet in the studied anorthosite sample. Some salient features are described below:

- Formation of garnet corona in this sample was a complex function of several parameters namely, the nature of the oxide phase, behavior of Ca and Na, redox potential of the system etc. Depending upon the variation of the magnitudes of these parameters, quartz can be produced or consumed during the garnet forming reactions (McLelland and Whitney 1977, Ellis and Green 1985). The studied anorthosite did not contain any primary quartz. Therefore, garnet formation at the expanse of orthopyroxene, magnetite and plagioclase by reaction 2, which doesn't involve free silica, seems to be a good option. However, textural features demonstrated that ilmenite and clinopyroxene were also involved in the garnet-forming reactions. To drive the garnet-forming reactions 1, 4, 6 and 7 some source of $SiO_2$ was, therefore, necessary. The coefficients of the participating phases of reactions 6 and 7 indicate that significant amount of silica (more than 60% of the moles of garnet produced) was added to the domains where the compound corona of garnet and clinopyroxene were formed. Much higher amount of $SiO_2$ (about 7 times the moles of garnet produced) was required to drive reaction 4. The $SiO_2$ that was required for the garnet formation in the sample was either supplied by reaction 4 ('closed system') or was metasomatically introduced ('open system').
- In domains where garnet grew without clinopyroxene, either Ca or Na or both must be mobile (reactions 1–5). No new Ca or Na-bearing phases were found in or proximal to the garnet-bearing domains of the rock. This then follows that the Ca and Na that were released by the garnet-forming reactions, were carried away by fluid. Presence of compositionally zoned plagioclase in garnet-free domains further supports the involvement of fluid during metamorphic recrystalisation of the studied anorthosite. The existence of fluid, which apparently left no trace on the mineralogy of the rock, can be inferred from the balanced reactions 1–5. This metasomatic fluid could also supply $SiO_2$ to augment the growth of garnet (reactions 1, 4, 6 and 7) in the rock.
- Barring reaction 4, coefficients of the participating phases in all other garnet-forming reactions required consumption orthopyroxene and plagioclase in the volume ratios that varied from ~1:4 (without clinopyroxene) to ~1:2.23 (with clinopyroxene) (molar volume data of orthopyroxene and garnet were taken from Holland and Powell 1998, updated in 2004 at the estimated peak metamorphic conditions of 6 kbar and 650ºC). This calculation explains why garnet grew preferentially on plagioclase relative to orthopyroxene or Fe-Ti oxide (Fig. 2.2e). Formation of garnet by reaction 4, on the other hand, consumes more orthopyroxene than plagioclase and hence, is not likely to have operated in this rock.

#### 2.4.2.2 Reaction modelling in sample #CM10-2b

The textural relations in this sample attest to a number of retrograde reactions involving amphibole, biotite and symplectic clinopyroxene and plagioclase. The algebraic analyses of the compositions of these minerals with the *C-Space* programme identified the following balanced chemical reactions:

*I. Amphibole forming reactions*

8. 73.9035 Cpx (c) + 2270.7557 Pl (c) + 113.9957 Na + 33.4186 K + 20.1319 $H_2O$ + 15.0782 Ill + 288.0756 Qtz

= 19.4914 Hbl + 2348.2189 Pl (r) + 131.2305 Ca + 1.0000 Mn

9. 19.5495 Cpx (c) + 143.9573 Pl (c) + 7.1389 Na + 6.0774 K + 9.9858 $H_2O$ + 2.8122 Ill + 2.2144 Grt + 4.7683 Opx = 9.9858 Hbl + 141.1844 Pl (r) + 12.2468 Ca + 1.0000 Mn

10. 19.9914 Cpx (c) + 219.3244 Pl (c) + 11.7984 Na + 5.7646 K + 7.4061 $H_2O$ + 2.0225 Ill + 1.9906 Grt + 16.3820 Qtz = 7.4061 Hbl + 223.8513 Pl (r) + 18.2193 Ca + 1.0000 Mn

It is evident from above that although textural features are equivocal about the relative timing of growth of garnet and amphibole, the constructed reactions indicate that the former phase was developed prior to the formation of retrograde amphibole. In view of low ($\leq$ 10 vol%) modal volume of garnet, it seems reasonable to infer that bulk of the amphibole was produced from pyroxenes, plagioclase and ilmenite by reaction 8. Reactions 8–10 further demonstrate that the magmatic protolith of the anorthosite was chemically altered during the growth of retrograde amphibole. Quantitatively, ~ 1.3–7.5 moles of Na + K and ~2.5–15 moles of $SiO_2$ (excepting the reaction 9) were consumed and ~1.2–6.7 moles of Ca were released in producing one mole of amphibole in the rock. Coefficients of the reactant (core) and product (rim) plagioclase in the constructed reactions indicate that barring the garnet-absent reaction 8, volume of plagioclase remained virtually constant during the formation of amphibole. Operation of reaction 8, on the other hand, consumed larger amount of plagioclase (approximately 4 moles of plagioclase/mole of amphibole).

*II. Biotite forming reaction*

Modelling of the observed reaction textures with *C-Space* identifies following biotite-forming reaction:

11. 25.2224 Hbl + 38.3020 K + 18.4731 $H_2O$ = 6.6698 Kfs + 44.2125 Bt + 49.9673 Ca + 12.2996 Na + 1.2289 Ill + 16.9292 Qtz + 1.0000 Mn

Reaction 11 explains the replacement of amphibole by biotite and plagioclase by K-feldspar (Fig. 2.2d). Replacement of clinopyroxene successively by amphibole and biotite can be explained by gradual increase in $\mu_k$ of the infiltrating fluids that augmented the reactions 8–11.

*III. Formation of clinopyroxene + plagioclase symplectite*

Textural modelling with *C-Space* identifies the following reactions to explain the formation of the clinopyroxene and plagioclase symplectite after amphibole:

12. 23.5015 Hbl + 7.2980 Ca + 8.4922 Na + 26.9348 Sph + 56.0825 Qtz + 1.0000 Mn = 66.8165 $Cpx_{sy}$ + 37.0163 $Pl_{sy}$ + 10.3061 K + 23.5015 $H_2O$ + 30.1830 Ill

13. 51.1009 Hbl + 9.6406 Ca + 23.4049 Na + 69.9071 Sph + 3.4931 Grt + 123.8035 Qtz + 1.0000 Mn = 150.2002 $Cpx_{sy}$ + 90.4736 $Pl_{sy}$ + 22.2080 K + 51.1009 $H_2O$ + 77.1023 Ill

Reaction 12 doesn't involve garnet and produces clinopyroxene and plagioclase in the volume ratio of 1.2:1 (molar volume data from Holland and Powell 1998 up dated in 2004). The other reaction involves garnet as a reactant phase and produces clinopyroxene and plagioclase almost in equal volume ratio. In view of the textural observations, it can be inferred that the clinopyroxene + plagioclase symplectite was formed by the garnet-consuming reaction 13. A portion of the Na and Ca that were required to drive the reaction 12 could be derived from the biotite-forming reaction 11. This explains the decomposition of the same grain of amphibole to biotite and clinopyroxene + plagioclase symplectite (Fig. 2.2f).

## 2.5 Discussion

The foregoing analysis demonstrates that modelling of 'frozen-in' reaction textures with the *C-Space* programme can provide a wealth of information about the intricate chemical processes that eventually shape the mineralogy and textures of metamorphic/metasomatic rocks. Mobility of elements during metamorphism/metasomatism can also be predicted from the balanced chemical reactions that are consistent with the textural observations. In extreme cases, *C-Space* modelling of reaction textures can also track down the subtle fluid-rock interaction whose existence cannot otherwise be established from petrographic study or from the chemographic projections of mineral compositions in simple chemical systems.

*C-Space* modelling of reaction textures of two samples from the Chilka Lake anorthosite has revealed complex geological history. Subsequent to the emplacement of their magmatic protolith at ca 0.98 Ga, the anorthosite underwent superposed deformation and metamorphism during the globally extensive Pan-African orogenesis (~0.6–0.69 Ga, Dobmeier and Simmat 2002, Chatterjee et al. 2008). At the earliest stage, the magmatic assemblages (orthopyroxene, clinopyroxene, ilmenite and magnetite) underwent granulite facies metamorphism and developed garnet through a number of chemical reactions. During this event the rocks were open, at least partially, to external fluid that helped transport of Ca, Na and possibly $SiO_2$. Subsequent to the Pan-African high-grade event, the anorthosite was infiltrated by fluids particularly at or close to its contact with the adjoining lithologies. These fluids supplied significant amount of K, Na and $SiO_2$ to the host anorthosite to augment the growth of retrograde amphibole, biotite, carbonates and chlorite. Extant experimental studies have shown that brine-rich aqueous fluids can dissolve and transport large amounts of alkali elements and $SiO_2$ (Aranovich et al. 1998, Harlov and Forster 2002, Newton and Manning 2000).. By virtue of low dihedral angle subtended by brine molecules with the solid grains, these fluids pass through the pore spaces of the rocks more easily and thus, metasomatise wall rocks more efficiently than what the low saline fluids do (Aranovich et al. 1998). In view of these observations, it is presumed that the alkali and silica metasomatism of the deformed anorthosite (#CM10-2b) was caused by infiltration of highly saline fluids. At the terminal part of this retrograde event, amphibole broke down into a symplectic intergrowth of clinopyroxene + plagioclase. *C-Space* modelling of this texture indicates that garnet was also a reactant phase in the reaction that led to the formation of the symplectic clinopyroxene and plagioclase.

Incidentally, the studied area only document the Pan-African high-grade overprint on the Grenvillian granulite crust from the whole of the EGB. This has important implications on transcontinental correlation in the late Proterozoic, particularly with respect to Indo-Antarctic correlation. The EGB was presumably juxtaposed against east Antarctica from where Pan-African high-grade metamorphism has been previously described (Harley, 2003).

Finally, as a note of caution, it must be mentioned that construction of chemical reactions using the SVD technique are strongly sensitive to the input phase compositions. A small change in the input phase compositions may have dramatic effect on the coefficients of participating phases in the output reactions (Lang et al. 2004). Additionally, for successful modelling of reaction textures, *a priory* knowledge about the behaviour of elements or chemical species i.e. mobile or immobile, is a prerequisite. In spite of these caveats, textural modelling with *C-Space* can be a potential tool for deciphering the metamorphic processes that were operative in the extinct orogenic belts.

**Acknowledgements** We acknowledge financial assistance from the Department of Science and Technology (DST), New Delhi. SDG acknowledges financial support through J.C. Bose Fellowship from the DST. The chemical data used in this study were generated when PS was visiting the Mineralogy Petrology Institute, University of Bonn, Germany as a Humboldt Fellow (2002–2003, 2006). PS thanks Profs. M.M. Raith and C. Ballhaus and the staff members of this institute for their help. Prof. M.M. Raith is specially thanked for many stimulating scientific discussions on the evolution of the EGB. We also thank Mr. N.R. Dutta, Ms Aparajita Dutta and Ms Sushmita Sarkar for their help during our field visit.

## 2.6 References

Ague JJ (2003) Fluid infiltration and transport of major, minor, and trace elements during regional metamorphism of carbonate rocks, Wepawaug Schist, Connecticut, USA: Am J Sci 303: 753–816

Bhattacharya A, Raith M, Hoernes S, Banerjee D (1998) Geochemical evolution of the massif-type anorthosite complex at Bolangir in the Eastern Ghats Belt of India. J Petrol 39: 1169–1195

Bhattacharya S, Sen SK, Acharya A (1994) The structural setting of the Chilka Lake granulite-migmatite-anorthosite suite with emphasis on the time relation of charnockites. Precam Res 66: 393–409

Chatterjee N, Crowley JL, Mukherjee A, Das S (2008) Geochronology of the 983 Ma Chilka Lake Anorthosite, Eastern Ghats Belt, India: implications for pre-Gondwana tectonics. J Geol 116: 105–118

Das S, Nasipuri P, Bhattacharya A, Swaminathan S (2008) The thrust-contact between the Eastern Ghats Belt and the adjoining Baster craton (Eastern India): Evidence from mafic granulites and tectonic implications. Precam Res 162: 75–80

Dasgupta S, Sengupta P (2003) Indo-Antarctic correlation: a perspective from the Eastern Ghats Granulite Belt, India. In: Yoshida M, Windley BF, Dasgupta S (eds) Proterozoic East Gondwana: Supercontinent Assembly and Breakup. Geological Society, London

Dobmeier C, Simmat R (2002) Post-grenvillian transpression in the Chilka Lake area, Eastern Ghats Belt—implications for the geological evolution of peninsular India. Precam Res 113: 243–326

Dobmeier CJ, Raith MM (2003) Crustal architecture and evolution of the Eastern Ghats Belt and adjacent regions of India, In: Yoshida M, Windley BF, Dasgupta S (eds) Proterozoic East Gondwana: Supercontinent Assembly and Breakup. Geological Society, London

Ellis DJ, Green DH (1985) Garnet-forming reactions in mafic granulites from Enderby Land, Antarctica—implications for geothermometry and geobarometry. J Petrol 26: 633–662

Fisher GW (1989) Matrix analysis of metamorphic mineral assemblages and reactions. Contrib Mineral Petrol 102: 69–77

Fisher GW (1993) An improved method for algebraic analysis of metamorphic mineral assemblages. Amer Min 78: 1257–1261

Harley SL (2003) Archaean crustal development of east Antarctica: Metamorphic characteristics and tectonic implications. In: Yoshida M, Windley BF, Dasgupta S (eds) Proterozoic East Gondwana: Supercontinent Assembly and Breakup. Geological Society, London

Harlov EH, Forster HJ (2002) High-grade Fluid Metasomatism on both a Local and a Regional Scale: the Seward Peninsula, Alaska, and the Val Strona di Omegna, Ivrea-Verbano Zone, Northern Italy. Part I: Petrography and Silicate Mineral Chemistry. J Petrol 43: 769–799

Holland TJBH, Powell R (1998) An internally consistent thermodynamic data set for phases of petrological interest. J Met Geol 16: 309–343

Krause O, Dobmeier C, Raith MM, Mezger K (2001) Age of emplacement of massif-type anorthosites in the Eastern Ghats Belt, India: constraints from U-Pb zircon dating and structural studies. Precam Res 109: 25–38

Kretz R (1983) Symbols for rock forming minerals. Amer Min 68: 277–279

Lang HM, Lee AJ, Peterson, Ryan JG (2004) Coexisting clinopyroxene/spinel and orthopyroxene/spinel symplectites in metatroctolite from the Buck Creek ultramafic body, North Carolina Blue Ridge, USA. Amer Min 89: 20–30

McLelland JM, Whitney PR (1980) A generalised garnet-forming reaction for metaigneous rocks in the Adirondacks. J Geol 72: 111–122

Newton RC, Manning CE (2000). Quartz solubility in H2O-NaCl and H2O-CO2 solutions at deep crust-upper mantle pressures and temperatures: 2–15 kbar and 500–900°C. Geochim Cosmochim Acta 64: 2993–3005.

Newton RC, Aranovich LYa, Hansen EC, Vandenheuvel BA (1998) Hypersaline fluids in Precambrian deep-crustal metamorphism. Precam Res 91: 41–63

Press WH, Flannery BP, Teukolsky SA, Vetterling WT (1989). Numerical recipes: The art of scientific computing. Cambridge University Press

Simmat R, Raith MM (2008) U-Th-Pb monazite geochronometry of the Eastern Ghats Belt, India: Timing and spatial dispositions of poly-metamorphism. Precam Res 162: 16–39

Sengupta P, Sen J, Dasgupta S, Raith MM, Bhui UK, Ehl J (1999) Ultrahigh temperature metamorphism of metapelitic granulites from Kondapalle, Eastern Ghats Belt: Implications for the Indo-Antarctic correlation. J Petrol 40: 1065–1087

Sengupta P, Dasgupta S, Dutta NR, Raith MM (2008) Petrology across a calcareous rock-anorthosite interface from the Chilka Lake complex, Orissa: Implications for Neo-Proterozoic crustal evolution of the northern Eastern Ghats Belt. Precam Res 162: 40–58

Torres-Roldán RL, García-Casco A, García-Sanchez PA (2000) C-Space: An integrated workplace for the graphical and algebraic analysis of phase assemblages on 32-bit Wintel platforms. Computers and Geosciences 26: 779–792

# Appendix 1

Result of the matrix operation using SVD technique on the assemblage Grt-Opx-Cpx-Ill-Qtz-Pl in the anorthosite:

INPUT MATRIX:

| Cpx | Opx | Pl r | Pl c | Ca | Na | $O_2$ | $Fe_2O_3$ | Qtz | Grt | Mn | |
|---|---|---|---|---|---|---|---|---|---|---|---|
| 1.94 | 1.98 | 2.3 | 2.27 | 0 | 0 | 0 | 0 | 1 | 5.99 | 0 | Si |
| 0.06 | 0.03 | 1.67 | 1.71 | 0 | 0 | 0 | 0 | 0 | 3.99 | 0 | Al |
| 0.01 | 0 | 0 | 0 | 0 | 0 | 0 | 0 | 0 | 0 | 0 | Ti |
| 0.5 | 1.23 | 0 | 0 | 0 | 0 | 0 | 2 | 0 | 3.96 | 0 | Fe |
| 0.56 | 0.7 | 0 | 0 | 0 | 0 | 0 | 0 | 0 | 0.53 | 0 | Mg |
| 0.95 | 0.03 | 0.7 | 0.74 | 1 | 0 | 0 | 0 | 0 | 1.29 | 0 | Ca |
| 0.02 | 0 | 0.33 | 0.29 | 0 | 1 | 0 | 0 | 0 | 0 | 0 | Na |
| 6 | 6 | 8 | 8 | 0 | 0 | 2 | 3 | 2 | 24 | 0 | O |
| 0.01 | 0.03 | 0 | 0 | 0 | 0 | 0 | 0 | 0 | 0.24 | 1 | Mn |

MATRIX U:

| | | | | | | | | | | |
|---|---|---|---|---|---|---|---|---|---|---|
| −0.2459 | 0.2778 | −0.4469 | 0.0009 | −0.2677 | −0.7146 | 0.2682 | 0.0217 | 0.0886 | 0 | 0 |
| −0.1473 | 0.2828 | 0.7772 | 0.0036 | 0.3109 | −0.4265 | 0.0047 | −0.0368 | 0.1193 | 0 | 0 |
| −0.0001 | 0.0003 | −0.004 | 1 | 0.0013 | 0.0023 | −0.0028 | 0.0001 | 0 | 0 | 0 |
| −0.1331 | −0.8802 | 0.1107 | 0.0013 | −0.067 | −0.4043 | −0.1537 | 0.0256 | −0.0553 | 0 | 0 |
| −0.0242 | −0.0795 | −0.3922 | −0.0024 | 0.9091 | −0.0965 | 0.0535 | 0.0243 | 0.0044 | 0 | 0 |
| −0.0578 | 0.2122 | −0.1634 | −0.003 | −0.013 | −0.1353 | −0.9482 | 0.019 | 0.084 | 0 | 0 |
| −0.0061 | 0.127 | 0.0478 | 0.0002 | 0.0176 | −0.1014 | −0.0386 | 0.3706 | −0.9122 | 0 | 0 |
| −0.9466 | −0.004 | −0.001 | −0.0008 | 0.008 | 0.3197 | 0.0077 | −0.0147 | −0.036 | 0 | 0 |
| −0.0072 | −0.0241 | 0.0328 | 0 | −0.01 | 0.0619 | 0.0317 | 0.9268 | 0.3665 | 0 | 0 |
| 0 | 0 | 0 | 0 | 0 | 0 | 0 | 0 | 0 | 1 | 0 |
| 0 | 0 | 0 | 0 | 0 | 0 | 0 | 0 | 0 | 0 | 1 |

MATRIX V:

| | | | | | | | | | | |
|---|---|---|---|---|---|---|---|---|---|---|
| −0.2118 | 0.0932 | −0.677 | 0.5935 | 0.0381 | 0.1675 | −0.3259 | 0.0129 | 0.003 | 0 | 0 |
| −0.2136 | −0.2221 | −0.5972 | −0.5237 | 0.277 | −0.1063 | 0.3405 | 0.0306 | −0.0854 | 0.087 | 0.233 |
| −0.2833 | 0.4714 | 0.0967 | −0.081 | −0.1211 | 0.1029 | 0.0086 | 0.0066 | −0.1228 | −0.541 | 0.589 |
| −0.2833 | 0.4738 | 0.118 | −0.0831 | −0.0552 | 0.1071 | −0.0292 | −0.0096 | −0.0823 | 0.795 | 0.138 |
| −0.0019 | 0.0788 | −0.0967 | −0.5132 | −0.0445 | −0.1884 | −0.8105 | 0.019 | 0.0811 | −0.064 | −0.125 |
| −0.0002 | 0.0471 | 0.0283 | 0.0389 | 0.0603 | −0.1412 | −0.033 | 0.3708 | −0.8806 | −0.052 | −0.234 |
| −0.0636 | −0.003 | −0.0012 | −0.2702 | 0.0551 | 0.8904 | 0.0132 | −0.0294 | −0.0695 | −0.114 | −0.328 |
| −0.1044 | −0.6581 | 0.1292 | 0.0459 | −0.3766 | 0.2098 | −0.2429 | 0.0071 | −0.211 | 0.174 | 0.466 |
| −0.0719 | 0.1002 | −0.2655 | −0.1261 | −0.8623 | −0.1046 | 0.2424 | −0.0077 | 0.016 | −0.044 | −0.287 |
| −0.8537 | −0.2091 | 0.253 | 0.0645 | 0.0944 | −0.1674 | 0.0127 | −0.0083 | 0.1182 | −0.114 | −0.308 |
| −0.0002 | −0.0089 | 0.0194 | −0.0057 | −0.0343 | 0.0861 | 0.0271 | 0.9273 | 0.3538 | 0.025 | 0.066 |

SINGULAR VALUES W:

| | | | | | | | | | | |
|---|---|---|---|---|---|---|---|---|---|---|
| 29.7469 | 2.6935 | 1.6908 | 0.0059 | 0.2918 | 0.7182 | 1.1698 | 0.9995 | 1.0359 | 0 | 0 |

All abbreviations are after Kretz (1983). c = core, r = rim, $Fe_2O_3$ refers to the same in ilmenite.

## Appendix 2

Balanced chemical reactions produced by the operation of the SVD technique on the INPUT matrix of the Appendix-1. All abbreviations are after Kretz (1983). $Fe_2O_3$ refers to the $Fe_2O_3$ component in ilmenite. The reactions R6 and R7 are supported by the metamorphic textures of the anorthosite (see text).

R1. 93.2961 Pl (c) + 4.4693 Na + 1.0000 $O_2$ + 7.9385 Qtz = 95.5307 Pl (r) + 2.1676 Ca

R2. 3.4845 Opx + 5.0841 Pl (r) + 5.7122 Pl (c) + 6.9694 $Fe_2O_3$ + 1.0000 Mn = 1.9536 Ca + 3.3343 Na + 4.8741 $O_2$ + 3.9922 Qtz + 4.6022 Grt

R3. 95.5307 Pl (r) + 2.1676 Ca = 93.2961 Pl (c) + 4.4693 Na + 1.0000 $O_2$ + 7.9385 Qtz

R4. 3.4845 Opx + 10.6774 Pl (c) + 6.9694 $Fe_2O_3$ + 1.0000 Mn = 2.0689 Ca + 3.0965 Na + 4.8209 $O_2$ + 3.5698 Qtz + 4.6022 Grt

R5. 3.4845 Opx + 10.9332 Pl (r) + 6.9694 $Fe_2O_3$ + 1.0000 Mn = 1.8209 Ca + 3.6079 Na + 4.9353 $O_2$ + 4.4783 Qtz + 4.6022 Grt

R6. 78.3724 Pl (c) + 7.3623 Na + 5.7754 $O_2$ + 11.1470 Qtz + 4.6022 Grt = 3.4845 Opx + 91.1827 Pl (r) + 6.9694 $Fe_2O_3$ + 1.0000 Mn

R7. 3.4845 Opx + 75.3158 Pl (c) + 6.9694 $Fe_2O_3$ + 1.9303 Qtz + 1.0000 Mn = 66.1866 Pl (r) + 3.5707 Ca + 4.1280 $O_2$ + 4.6022 Grt

R8. 3.4845 Opx + 460.4466 Pl (c) + 18.4494 Na + 6.9694 $Fe_2O_3$ + 34.7010 Qtz + 1.0000 Mn = 460.5421 Pl (r) + 12.5187 Ca + 4.6022 Grt

R9. 93.2961 Pl (c) + 4.4693 Na + 1.0000 $O_2$ + 7.9385 Qtz = 95.5307 Pl (r) + 2.1676 Ca

R10. 42.9576 Pl (r) + 3.0437 Ca + 1.0867 Na + 4.3712 $O_2$ + 4.6022 Grt = 3.4845 Opx + 52.6302 Pl (c) + 6.9694 $Fe_2O_3$ + 1.0000 Mn

R11. 95.5307 Pl (r) + 2.1676 Ca = 93.2961 Pl (c) + 4.4693 Na + 1.0000 $O_2$ + 7.9385 Qtz

R12. 93.2961 Pl (c) + 4.4693 Na + 1.0000 $O_2$ + 7.9385 Qtz = 95.5307 Pl (r) + 2.1676 Ca

# 3

# Orogenic Processes in Collisional Tectonics with Special Reference to the Himalayan Mountain Chain: A Review of Theoretical and Experimental Models

Nibir Mandal, Atin Kumar Mitra and Santanu Bose

**Abstract:** With advent of the plate tectonic theory geoscientists have taken a new turn in order to interpret the evolution of orogenic belts. As a consequence, a large volume of geodynamics models have emanated in recent times. In this paper we review some of the important models in context of the Himalayan-Tibetan system, which is believed to be the most spectacular collision-type orogenic belt. Studies on this system trend in diverse directions, covering surface topography to deep-crustal processes. Here we deal with theoretical and experimental models that address large-scale phenomena in orogens. Over the last two decades, geoscientists and geophysicists have extensively used wedge tectonic models to explain several tectonic processes in mountain chains, like sequential thrusting, folding and rock upliftments. The wedge models pivot principally on two considerations: 1) choice of boundary conditions and 2) rheology of the crust. In this review we classify the models into three rheological classes: Coulomb, plastic and viscous, and present the model results as a function of the boundary conditions.

---

Nibir Mandal (✉)
Indian Institute of Science Education and Research, HC-7, Salt Lake, Kolkata - 700106, India
e-mail: nibirmandal@yahoo.co.in

Atin Kumar Mitra
Department of Geology, J. K. College, Purulia - 723101, West Bengal, India

Santanu Bose
Department of Geology, University of Calcutta, 35 Ballygunge Circular Road, Kolkata - 700019, India

## 3.1 Introduction

Orogens are landmark features in the evolving continental crust. Large cratons, e.g. Indian craton, show mosaics of smaller continents separated by a number of orogenic belts of varying geological ages (Fig. 3.1). Geologists earlier invoked different conceptual tectonic models, e.g. geosynclines, and explained them entirely in terms of gravity forces (Marshall 1951; Belousov and Gzovsky 1965; Philip 1977; Ramberg 1981). Bucher (1956) in his famous wax experiments demonstrated that elevated crustal masses can flow in the foreland direction under its own gravity, and cause folding of strata in orogens. Advent of the plate tectonic theory turned the study in new directions (Hess 1962; Vine and Matthews 1963; Wilson 1965). Active mountain chains were shown to be an expression of convergent plate boundaries, where the crustal masses undergo intense deformations by horizontal contraction.

Orogenic chains can occur in a variety of convergent tectonic settings, such as continent-continent collisions, continent-island arc collision, continent-island arc collision, and subduction of an oceanic plate beneath a continent. In some cases they develop away from the active plate boundaries, e.g. the Tien Shan in central Asia (Avouac et al. 1993). The present review will be concerned with orogenic processes taking place in collision tectonics. The Himalaya-Tibetan plateau system is probably the best representative of the collision-type of mountains on the earth. A large number of geologists and geophysicists have been working on this system over the decades (England and Houseman 1986; Molnar 1988 and references therein; Avouac and Tapponnier 1993; England and Molnar 1997; Willett 1999; Yin 2006; Beaumont et al. 2001; DeCelles et al. 2002; Bilham et al. 2001; Mitra et al. 2005; Copley and McKenzie 2007; Groome et al. 2008). This review attempts to discuss different theoretical and experimental models describing crustal deformations and flow in collisional tectonic settings and their relevance to the Himalaya-Tibet system. A line of modelling deals with surface velocities in active mountain belts, using available GPS data, and addresses several geological issues. For example, the topographic dynamics of the Himalaya-Tibet system is interpreted to be a result of deep-crustal processes. Field observations reveal extensional deformations and associated structures, e.g. normal faults. There is a range of possibilities of lower crustal processes, such as flow of weak lower crust (Beaumont et al. 2001), Rayleigh-Taylor instability in the lower lithosphere (Houseman et al. 1981; England and Houseman 1986) and thermally controlled rheological and thickness changes of the crust and lithosphere (Jimenez-Munt and Platt 2006), which might have governed the toporgraphy and the deformation in Tibet. Orogens thus evolve through a complex kinematic history, and its understanding demands appropriate geophysical modelling .

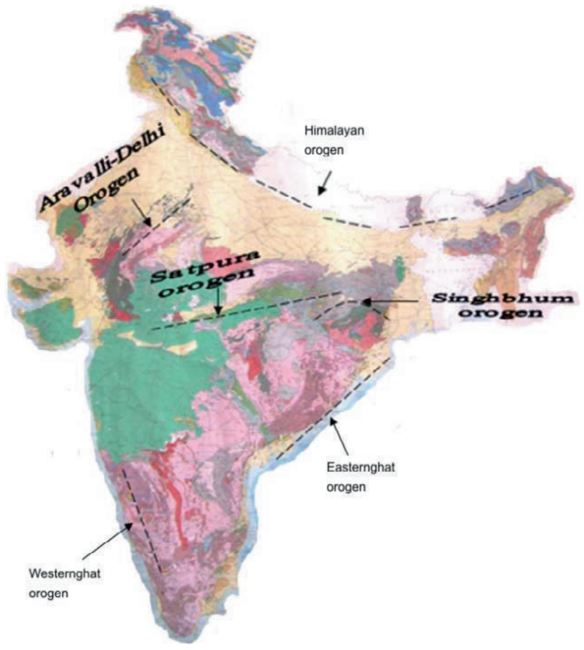

**Fig. 3.1** Distribution of orogenic belts in Indian craton (after GSI published geological maps, with permission from Geological Survey of India)

Higher-order orogenic processes, such as thrusting and shear zone localisation, play an important role in forming the orogen architecture, especially in shallow crustal levels. In the Himalayan mountain belt, for example, a set of large-scale foreland-vergent thrusts splay from a basal thrust, called the Main Himalayan Thrust (MHT). This type of thrust sequences occur virtually in all phanerozoic orogenic belts. Geodynamicists have developed different types of tectonic models to understand their mechanics. A line of models involves the critically-tapered wedge theory, which is based on Coulomb rheology of the crust (Chapple 1978; Davis et al. 1983; Dahlen 1984; Mulugeta 1988**)**. The models explain the growth of orogenic wedges and the process of sequential thrusting, which has been tested in sandbox experiments (Boyer and Elliot 1982; Davis et al. 1983; Liu et al. 1992; Dixon and Liu 1992; Mulugeta and Koyi 1987; Mandal et al. 1997; Marques and Cobbold 2002; Gulick et al. 2004). Recent experimental studies demonstrate that surface erosion can greatly influence the event of frontal thrust progression and the exhumation process in mountain belts (Konstantinovskaia and Malavieille 2005).

Many orogens show a characteristic structural style, indicating spatially varying ductile strain. Coulomb wedge or sandbox models are not suitable in studying such penetrative ductile strains. Workers generally employ viscous models, considering a proper scaling of the model parameters, e.g. viscosity, density and strain rate. Different experimental techniques, such centrifuge modelling , have been adopted to perform physical experiments with viscous models. These models give valuable insights into our field observations.

We present our review in the following manner. The next section deals with a general description of orogens and their topography. In this section we also discuss in detail penetrative and non-penetrative deformational structures, and their relation to orogenic strain fields. We then show the first-order crustal flow in orogens, considering the Himalaya-Tibetan plateau as an example. In recent times a variety of wedge models have been used to interpret large-scale orogenic processes, such as sequential thrusting. We classify these models into three broad rheological classes: Coulomb, plastic and viscous, and describe them separately. The review finally presents a critical discussion on existing orogenic models in view of what we actually observe in the field.

## 3.2 Orogens and Their Tectonic Structures

### *3.2.1 Orogen Topography*

In convergent tectonic regimes, the crustal materials undergo intense deformations, and extrude up dominantly in the vertical direction, forming linear topographic reliefs on the earth surface. The topography can vary widely depending upon the nature of lithospheric plate collision and the evolution of convergent tectonic zones. For example, there may be collision between two fore-arc island crustal masses, forming an orogenic relief between two oceanic plates. On the other hand, crustal reliefs can develop in continent-continent collisional tectonic settings, such as India-Eurasia (Fig. 3.2). The topography of orogens, in general, is characterised by an axial zone of highest elevation, which is flanked by mountain belts showing overall slopes in the foreland directions. Orogens, however, show a wide variation in their topographic profiles, as illustrated in Fig. 3.3 (Molnar 1988).

The Himalayan-Tibet system shows a unique topography, which consists of a flat-lying elevated terrain with an average elevation of about 5 km, forming a plateau (called Tibetan plateau) (Figs. 3.3, 3.4a). The Tibetan plateau covers a width of about 1000 km in the N-S direction. There is a sharp drop in elevation on either side of the plateau. Digital elevation maps reveal that the mountain system has a regional variation of its elevation in the E-W direction. The western and the central parts have higher topographic elevations relative to that in its eastern flank (Copley and McKenzie 2007; Jimenez-Munt and Platt 2006). The maximum elevation in the west reaches close to 7 km, whereas it is < 5 km in the eastern side. Topographic evolution of

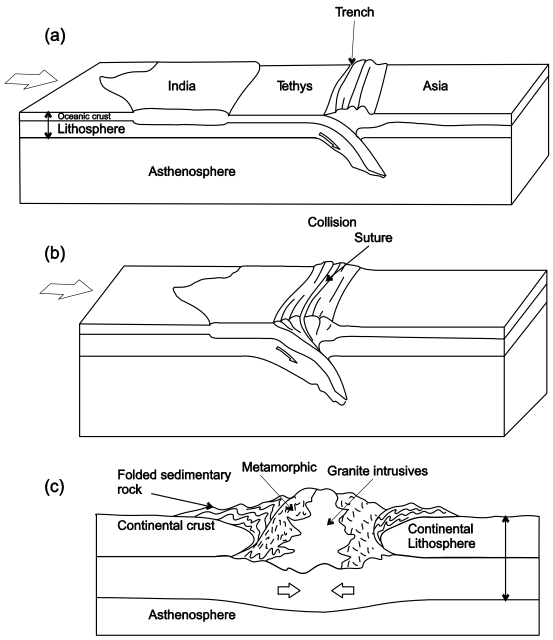

**Fig. 3.2** (a) and (b) Cartoon diagrams illustrating the evolution of India-Asia collision zones. (c) Principal geological units of an accreted crustal mass between two colliding continents (after Harold and Levin 2007)

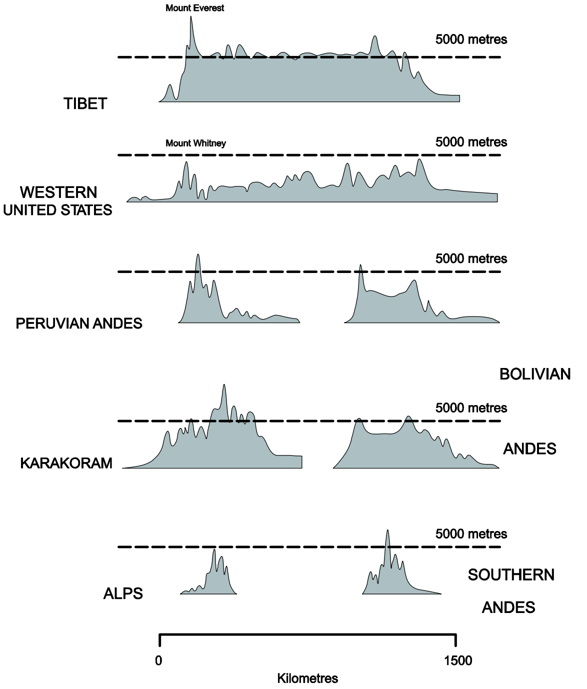

**Fig. 3.3** Toprgraphic profiles of different orogenic belts (after Molnar 1988, with permission from Philosophical Transaction, Royal Society of London)

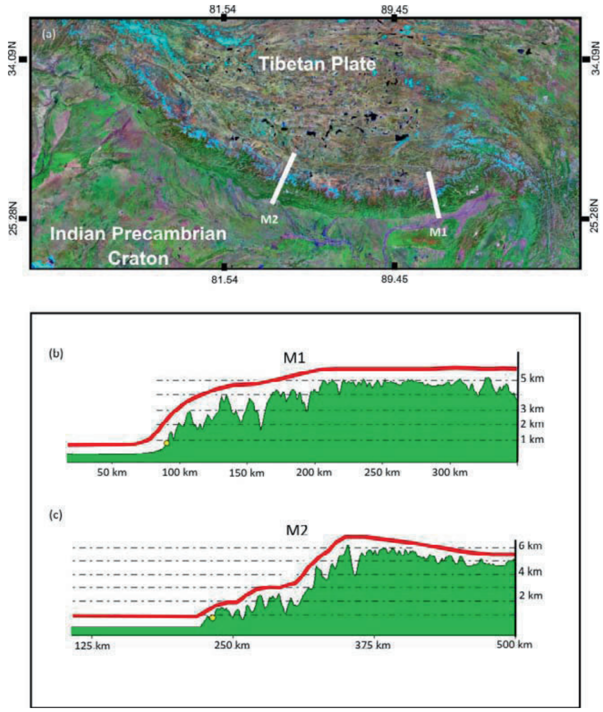

**Fig. 3.4** (a) A panoramic view of the Himalaya-Tibet mountain system. (b) and (c) Topographic profiles (prepared from a digital elevation map) of the Himalayan belt lying the Indo-Tsango stuture zone and the Indo-Gangetic Alluvium Plain. Location of these sections are shown in (a)

the Himalayan-Tibetan orogenic system is a subject of great interest in geodynamics. A number of tectonic models prevail in the literature, which we will discuss in a later section.

The Himalayan mountain belt shows wedge-like topographic profiles, consisting of two parts: a flat hinterland terrain and a mountain front, meeting the Indo-Gangetic plain in the foreland. The orogenic wedge slopes generally about 4° towards S (Avouac 2007). The hinterland topography varies from west to east (Fig. 3.4b, c). In the western Himalaya, the hinterland terrain slopes gently in the north direction. On the other hand, this is horizontal and flat in the central transect. In some sections the hinterland is not flat, but shows varying topography.

### *3.2.2 Geological Setting*

A collisional orogen consists of a number of geological units that are systematically disposed from the mountain front to the interior hinterland parts (Fig. 3.5). To describe this, we compared them with that observed in the Himalayan belt. Most of the orogens show a distinct belt of syn-orogenic sediment deposits in their fronts, e.g. the Indo-Gangetic Alluvium Plain (IGAP) between the Himalaya and the Indian craton. The IGAP-craton boundary is considered to be the *hinge line*, that demarcates the location of lithospheric bending. The evolution of these alluvial plains keeps a dynamic balance with the orogenic growth. There occurs a narrow belt of flat-lying sedimentary rocks forming the mountain fronts, which are described as *foredeep* (Fig. 3.5) According to the plate tectonic model, subducting lithospheric plates in collisional zones undergo flexure bending due to overloading, resulting in linear sedimentary basins running parallel to the orogen (Turcotte and Schubert 2001). Detailed description of the mechanics of foredeep basin formation is outside the scope of this review. In the Himalaya, the Siwalik group of rocks constitutes the foredeep. Most of the orogens contain thrust and fold sequences in an external belt, known as *fold-and-thrust belt* (FTB). FTBs are characterised by systematically arranged foreland and hinterland vergent thrusts, and thrust-

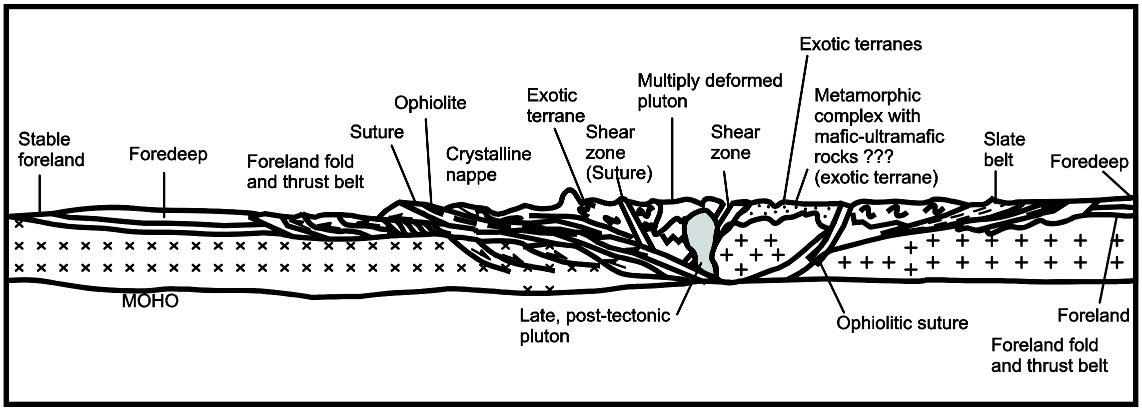

**Fig. 3.5** Dispositions of major geological components in a continent-continent collision-type orogen (after Twiss and Moores 2007, with permission from W. H. Freeman and Company)

controlled fold structures, such fault bend folds and fault propagation folds. The mechanics of FTBs has been dealt mostly with wedge tectonic models, which are presented separately in section 3.4. Several workers have described FTB structures from the western (e.g. Mukhopadhyay and Misra 2005) and the eastern (e.g. Acharyya 1994, 1999; Mukul 2000) parts of the Himalaya.

The FTB sequences are followed by a *metamorphic belt* (Fig. 3.5). In the Himalaya, this terrain shows increasing grade of metamorphism with increasing topographic elevations. Gansser (1964) divided the metamorphic belt into two: low-grade and high-grade terrains, which are separated by the Main Central Thrust (MCT). There are, however, differences in views on the nature of their transition (i.e. sharp or gradual) as well as the location of MCT. Recently, it has been shown from petrological evidence that the grade of metamorphism increases continuously without any break and the metamorphic belt appears to be coherent from the petrological point of view (Dasgupta et al. 2008 and references therein). The rocks in the metamorphic belt are multiply deformed, and consist of a variety of small-scale structures, resulting from intense ductile strain. The Himalayan metamorphic belt contains syn-orogenic plutons. These are strongly deformed, developing penetrative gneissic foliations. Several workers have interpreted the granite plutons as an evidence of partial melting in the lower crustal levels (Nelson 1996; Beaumont et al. 2001; Dasgupta et al. 2008). Partially molten lower crustal rocks beneath the Tibetan plateau are believed to have flowed southward and finally exhume up to the higher Himalayas. We will elaborate these tectonic models separately in a later section.

Collisional orogens contain a *suture zone* that marks the line of amalgamation of colliding crustal masses (Fig. 3.5). The suture zones may be in multiple in number, giving rise to composite nature of the orogen (Twiss and Moores 2007). For example, the Himalayan-Tibet system consists of two major suture zones, namely *Indus-Tsangpo suture zone* (ITS) and *Bangong-Nujiang suture zone* (BNS) (Jimenez-Munt and Platt 2006). The suture zones are generally associated with *ophiolitic belts*. In the Himalaya, there is a narrow belt of arc granite following the ITS zone (Fig. 3.6). Some exotic geological units can occur in the deformed and metamorphosed terrain of orogens. The high-grade metamorphic terrain lying between the MCT and ITS, contains Tethyan sedimentary rocks as outliers. Similarly, on the north of ITS there are discrete bodies of fore-arc sediments.

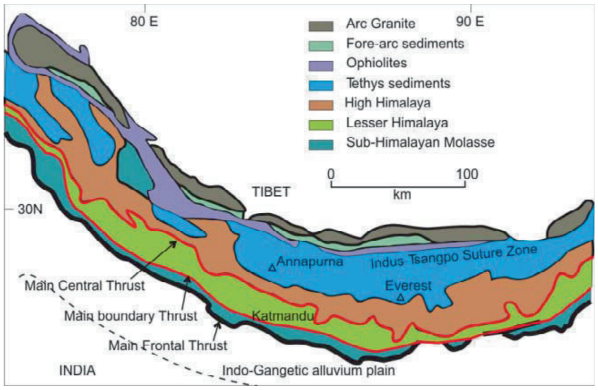

**Fig. 3.6** A generalised map showing the principal tectonic divisions and different geological units of the Himalayan mountain belt (after Avouac 2007, with permission from Elsevier)

### 3.2.3 Ductile Deformational Structures and Strain

Rocks in any orogen contain abundant small-scale deformational structures (Fig. 3.7), which are produced by penetrative ductile tectonic strain. Analysis of these structures enable us to interpret spatio-temporal variations of the regional as well as local strain fields, and help in developing appropriate tectonic models. Ductile structures observed in geologically old and modern orogenic belts suggest a common pattern of spatially varying regional strain. For example, rocks in the frontal Himalaya are weakly deformed, containing virtually no macroscopic tectonic fabrics (Fig. 3.7a). The finite deformations on a regional scale become increasingly intense in the hinterland direction, and the deformation episodes multiply in number (Fig. 3.7b). This type of variation occurs in old mobile belts, like the Cuddapah (Narayanswamy 1966; Mitra et al. 2008). The regional scale variations can be perturbed by local strain fields due to several geological factors, such as lithology and discontinuities like faults and shear zones. In this discussion we thus consider structures developing under three types of ductile

**Fig. 3.7** Field examples of ductile deformational structures from the Darjeeling-Sikkim Himalaya. (a) Hinterland-dipping weakly deformed sandstone of Lower Siwalik. (b) Superposition of later upright folds on earlier subhorizontal schistosity in Daling Group. (c) Intra-folial tight and isoclinals folds in Daling. (d) Pinch-and-swell structures in Gneissic rocks, west Sikkim

strain field: 1) *global strain field*, 2) *structure-bound strain field* and 3) *shear zone-related strain field*.

### 3.2.3.1 Global strain field

Penetrative linear (e.g. stretching lineation) and planar tectonic fabrics (e.g. cleavage and schistosity) develop in the rocks, tracking the principal extension (X-axis) and the plane (XY plane) normal to principal shortening of ductile strain. Their varying orientations suggest a heterogeneous global strain field. Mitra et al. (2008) have recently shown the structural styles in the Cuddapah mobile belt. The rocks in this belt contain a foreland-vergent steeply-dipping continuous cleavage in the western margin. The cleavage dip decreases continuously in the hinterland direction, indicating a heterogeneous strain field (Fig. 3.8). Such a strain field has been demonstrated in physical models (see section 3.4, Willett 1999; Chattopadhyay and Mandal 2002). Similar structural variations are noticed on N-S transects in the eastern Himalaya. Upper Siwalik rocks in the mountain front are virtually underformed, and show sub-horizontal primary layers. The strata progressively steepen its dip in the north direction, suggesting influence of ductile strain. The rocks contain a conspicuous shape fabric defined by flattened quartz grains (Fig. 3.9a). Using Fry method, the finite strain is estimated (Fig. 3.9b). The planar fabrics verge mostly in the foreland direction. The rocks strata show gentle upright or foreland-vergent, small-scale buckle folds. Foreland-vergent folds occur also in the low-grade metamorphic belt. The fold styles progressively vary further in the hinterland (Dixon and Liu 1992). They occur as tight or isoclinals intrafolial folds (Fig. 3.7c), and the primary layers become parallel to the schistose foliation, implying larger magnitudes of finite strain in the rocks. Boudinage structures are a common variety of extensional structures (Fig. 3.7d). They indicate the bulk stretching direction perpendicular to the boudin axes.

Based on observations from different orogenic belts, Fyson (1971) presented a generalised scheme for spatial and

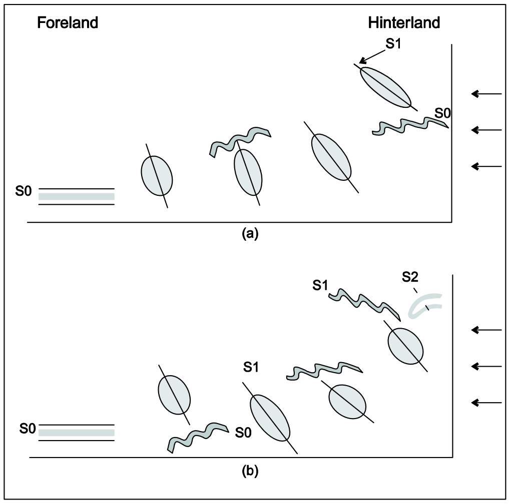

**Fig. 3.8** Schematic sketches illustrating the spatial variation of schistosity dip in relation to strain ellipse, and superposition of a second-generation schistosity in the hinterland part

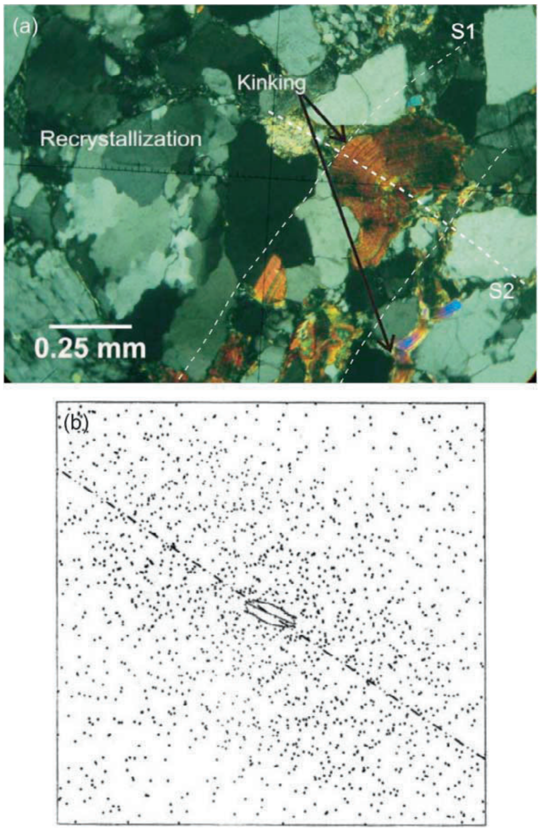

**Fig. 3.9** (a) Micro-scale tectonic fabrics in Siwalik rocks. Note superposition of folds on the fabric. (b) Estimation of strain, based on the Fry Method for Lower Siwalik rocks

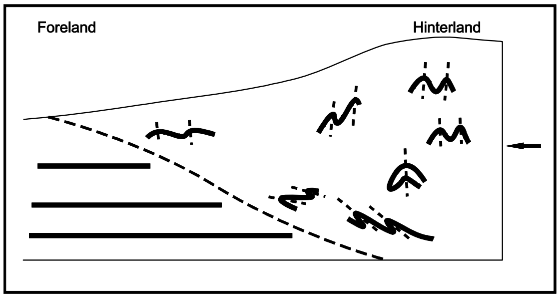

**Fig. 3.10** A generalised scheme of fold styles in orogens (after Chattopadhyay and Mandal 2002)

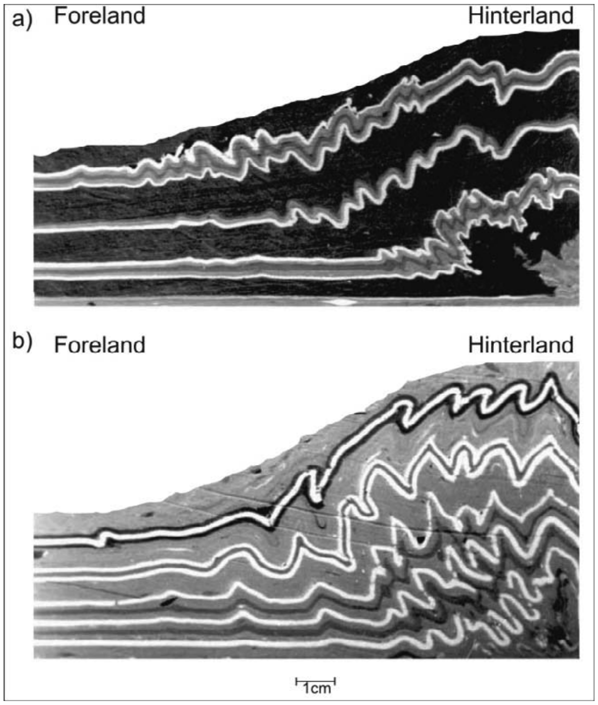

**Fig. 3.11** Fold styles in analogue models. (a) Initial and (b) advanced stages of orogenic growth (after Chattopadhyay and Mandal 2002)

temporal variations in folds styles (Fig. 3.10). He has shown that folds formed in shallow crustal levels are upright, and those formed in deeper parts of the crust are mostly recumbent. During upliftment of deep-crustal rocks the recumbent folds can be superimposed by later upright folds. Using analogue experiments Chattopadhyay and Mandal (2002) investigated the fold styles developed in the global orogenic strain (Fig. 3.11). Fyson's scheme appears to be valid only in specific conditions. Their experimental results suggest that the fold styles depend on the stage of orogenic growth (see section 3.4 for details). The folds developed in the initial stage follow a style predicted in the Fyson's scheme (Fig. 3.11a). With progressive evolution of orogens, the fold styles turn to be different. Experiments show development of hinterland vergent folds (back folds) and recumbent folds in the shallow levels (Fig. 3.11b).

Structural superpositions are a characteristic feature of deformed rocks in the metamorphic belts of orogens, reflecting a temporal variation in the global strain field. This takes place in diverse styles. Several workers have reported overprinting of hinterland-vergent foliations on the earlier foreland-vergent foliation (Brown et al. 1986; Macaya et al. 1991). Similarly, back folds can be superposed on foreland-vergent folds. These hinterland-vergent structures are geometrically similar to back thrusts. There are several tectonic models for back-vergent structures, which we will discuss separately in section 3.4. Analogue experiments suggest that the convergence movement can give rise to top-to-hinterland shear component in the hinterland, which probably causes back folding in orogens (Chattopadhyay and Mandal 2002). The hinterland ward shear is found to be most active during the stabilisation and subsequent phases of gravity collapse in the orogen.

The Himalayan metamorphic belts show superposition of late recumbent folds on the earlier penetrative schistose or gneissic foliations (Fig. 3.12). Different kinematic models have been employed to explain the origin of late recumbent folds. One of the possibilities is that earlier upright or inclined folds might have rotated their axial planes in response to horizontal shear, and turned to be recumbent (Fig. 3.13). However, this model is not applicable to fold systems in the Himalayan rocks, as their axial plane cleavages are regionally sub-horizontal. The recumbent folds seem to have developed in a strain field with a vertical shortening component, as observed in physical experiments (Chattopadhyay and Mandal 2002).

**Fig. 3.12** (a) Recumbent folds in gneissic rocks and (b) superposition of upright folds on earlier recumbent folds (north Sikkim)

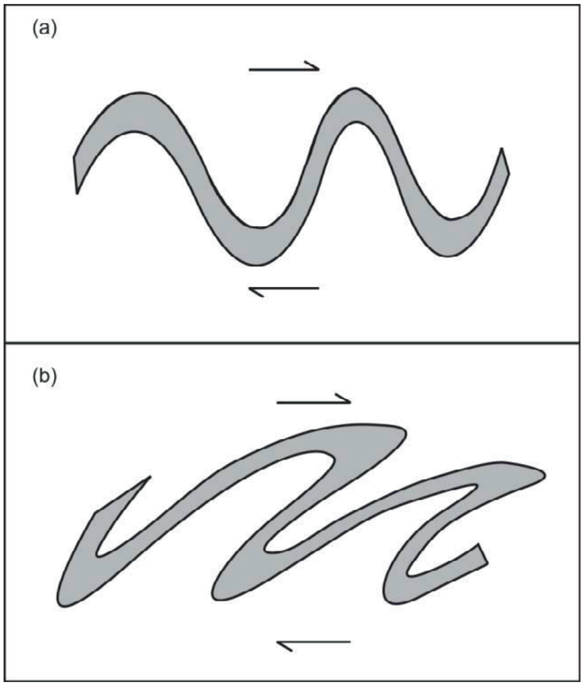

**Fig. 3.13** Development of recumbent folds by passive rotation of early upright folds due to horizontal shear

### 3.2.3.2 Ductile structures in thrust sheets

Orogenic belts show localisation of ductile structures within thrust sheets. These structures form by penetrative ductile strain in a thrust sheets during its movement (Rowan and Kligfield 1992; Casey and Dietrich 1997). The Himalayan mountain belt consists of three major large-scale thrust sheets separated by four principal faults: 1) Main Frontal Thrust (MFT), 2) Main Boundary Thrust (MBT), 3) MCT and 4) south Tibetan Detachment zone (STDZ). In the literature, thrust sheets with large displacements, say hundreds of kilometres are described as *thrust nappes*. Spectacular nappes, e.g. Pennine nappe, Helvetic nappe, have been reported from the Alpine orogen (Fig. 3.14a).

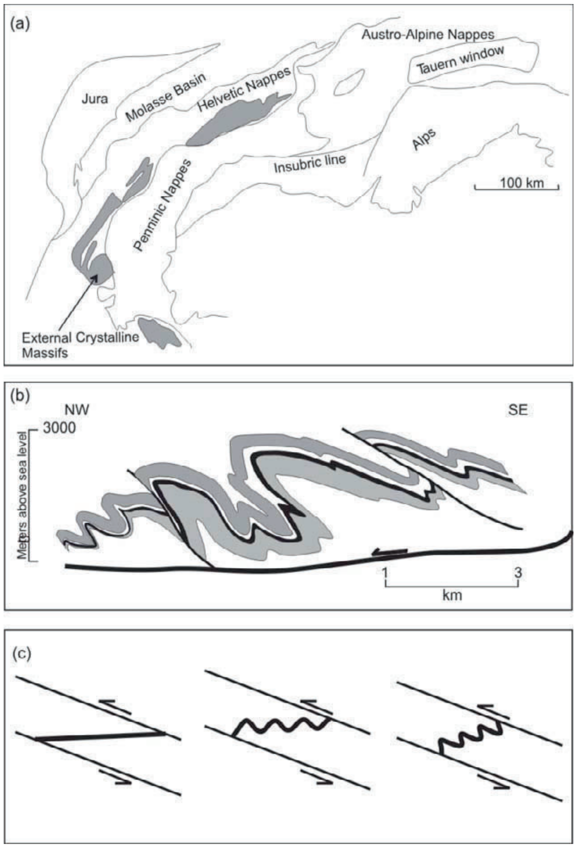

**Fig. 3.14** (a) Thrust nappes of the Alpine orogen (after Twiss and Moores 2007, with permission from W.H. Freeman and Company). (b) Large-scale asymmetric folds in the Helvetic nappe, with permission from Chapmen and Hall, London and (c) Kinmeatic model of asymmetric folding in a thrust sheet (after Rowan and Kligfield)

Thrust nappes contain penetrative deformational structures different from those formed under the global strain in orogens. To discuss this point, we consider large-scale asymmetric folds within the Helvetic nappe (Fig. 3.14b). These asymmetric folds were not produced by the global strain. It has been shown that the thrust sheet has undergone simple shear deformation during thrusting (Rowan and Kligfield 1992). The primary strata within the sheet were buckled under that shear, producing a set of symmetric upright folds. The upright folds progressively turn to be inclined and asymmetric in the course of thrust-parallel shearing (Fig. 3.14c). Thrust sheet deformations can take place in other ways. The front of a thrust sheet moving over a ramp deforms by a combination of flexural bending and thrust-parallel shearing. Horizontal layers within the thrust sheet develop large-scale bending folds and at the same time buckle folds in response to thrust-parallel shear. The shear may be heterogeneous, resulting in further accentuation of large-scale fold structures (Fig. 3.15).

The internal deformations of thrust sheets can be strongly heterogeneous, resulting in varying orientations of penetrative fabrics within the thrust sheets. It has been shown that a ductile thrust sheet experience larger shear at the basal detachment, and the amount of shear decreases away from the basal surface. This type of heterogeneous shear is reflected in varying orientations of the penetrative planar fabric that develop tracking the XY planes of finite strain (Fig. 3.16).

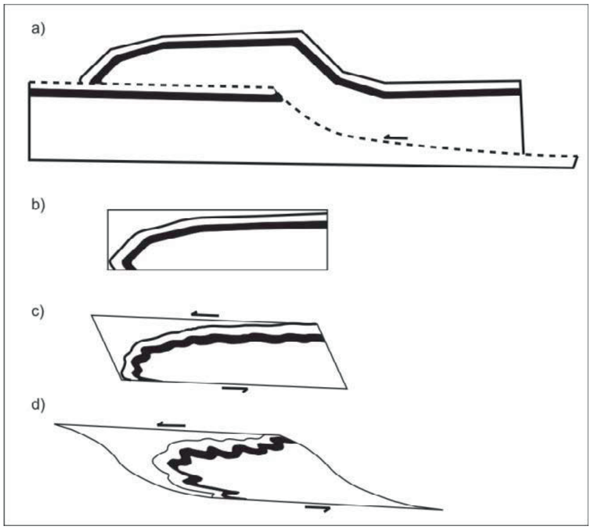

**Fig. 3.15** Development of folds in a thrust sheet riding on a ramp (after Ramsay 1992)

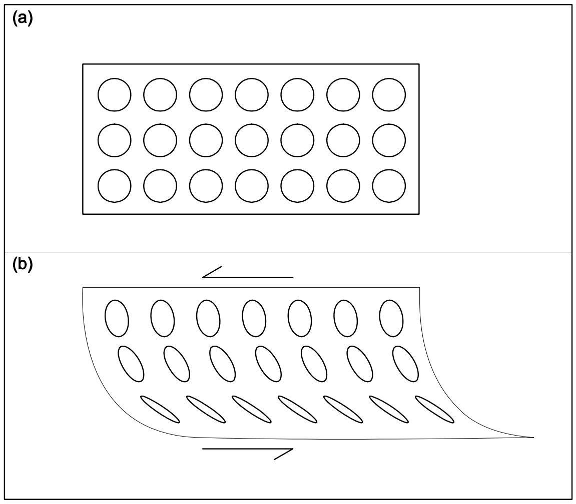

**Fig. 3.16** Heterogeneous strain distribution in a thrust sheet undergoing shear deformation

### 3.2.3.3 Ductile deformation in shear zones

Large amounts of crustal shortening in orogenic belts are partitioned in ductile shear zones of varying scales. These shear zones are marked by larger strain localisation relative to the global strain (Fig. 3.17). There have been a large volume of work on the kinematics and structures of shear zones, the detailed discussion of which is outside the scope of this paper. In this review we will briefly describe them in context of the regional kinematics in orogens. Thrust-type ductile shear zones is the most common variety, as it accommodates horizontal shortening and allows the crust to thicken in collisional tectonic zones. In this section we address an important issue – how much horizontal crustal shortening a thrust-type ductile shear zone can accommodate. It may be noted that this can occur in two modes: 1) simple shear movement and 2) transpressive movement (Fig. 3.18). There is no mechanical constraint for simple shear movement. On the other hand, transpressive movement can occur in particular geological conditions, as it involves extrusion of materials or volume loss. Theoretical studies suggest that, under constant volume conditions the ratio of transpression and shear rates follows (Mandal et al. 2001)

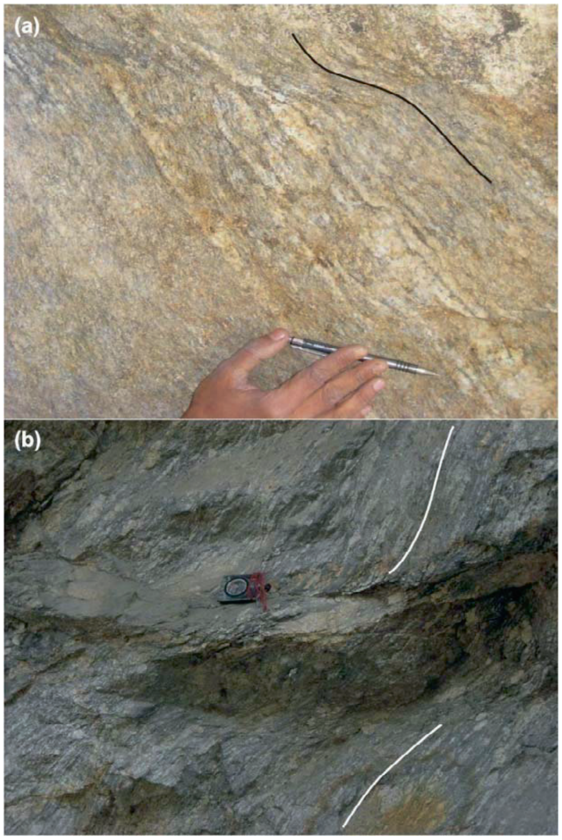

**Fig. 3.17** Ductile gently-dipping thrust-type ductile shear zones in the high-grade metamorphic rocks of the Himalaya (north Sikkim)

$$S_{\gamma} = \frac{\varepsilon}{\gamma} = \frac{10}{24 + 5D^2} \cot 2\alpha \tag{3.1}$$

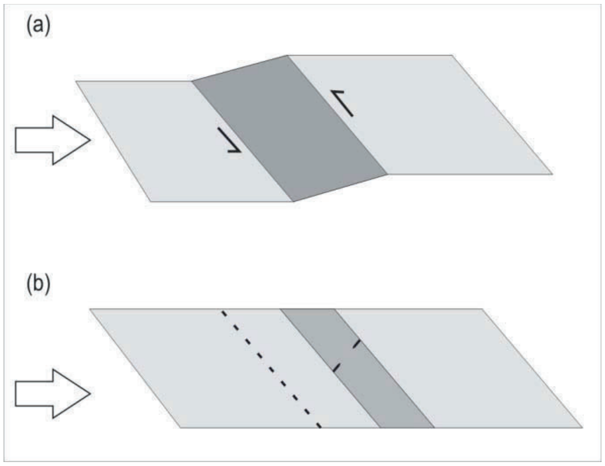

**Fig. 3.18** Thrust-type ductile shear zones with (a) simple shear and (b) transpression movements

$D$ is the length to thickness ratio of shear zone and $\alpha$ is the angle of shear zone normal with the principal compression direction. The kinemaical vorticity number can be expressed as (Ghosh 1987)

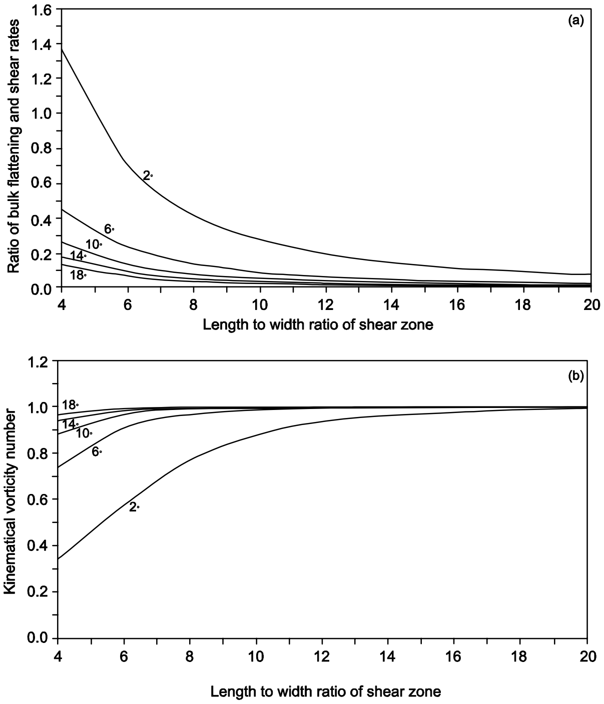

**Fig. 3.19** Plots of (a) the flattening to shear rate ratio and (b) bulk vorticity as a function of length to thickness ratio of shear zones

$$W_k = 1 \Big/ \sqrt{1 + 4\left(\frac{\varepsilon}{\gamma}\right)^2} \tag{3.2}$$

A shear zone with bulk simple shear motion will have $W_k = 1$ and $\varepsilon/\gamma = 0$. Using equations 3.1 and 3.2 it can be shown that $W_k$ increases steeply, and then asymptotically tends to be 1, as the inclination of shear zone normal $\alpha$ increases (Fig. 3.19). For large values of $D$, $W_k$ becomes nearly 1 even for small values of $\alpha$. The plots imply that long shear zones are likely to accommodate horizontal crustal shortening mostly by simple shear movement. There cannot be any significant amount of transpression. This is also evident from $S_r$ values (Fig. 3.19). According to this analysis, thrust-type shear zones are unlikely to partition horizontal shortening by transpression if a constant volume condition prevails there. Natural shear zones, however, can undergo synkinematic volume changes. Considering relative enrichment of immobile elements, such as $Fe^{3+}$, Ti, Ni, Mohanty and Ramsay (1994) have shown that there can be more than 70% volume loss during shearing movement. Such a volume reduction can result in transpressive movement across ductile shear zones (Ramsay and Graham 1970; Ramsay 1980). Considering homogeneous shear and transpression, the total horizontal shortening ($S$) possible across a ductile shear zone is

$$S = \left(\Delta + \gamma \cos^2 \theta\right) \sec \theta t \tag{3.3}$$

$\Delta$ and $\gamma$ are the volume and the shear strains in shear zones. $\theta$ and $t$ are the dip and the thickness of shear zones.

Convergent tectonic regimes can be associated with extensional deformation zones, which occur mostly in the hinterland of an orogen. These zones show abundant extensional shear zones in micro- to macro-scale (Fig. 3.20). In the Himalayan range, the high-grade metamorphic rocks lying north of the MCT show shear zones containing extensional crenulation cleavages (ecc). The vergence of ecc indicates that the shear zones are extensional (Fig. 3.21). Extensional shear zones indicate that the high-grade metamorphic terrain has undergone extensional deformations in the horizontal direction. This is also evident from the STDZ showing the kinematics of a normal fault (Fig. 3.21). In sec-

**Fig. 3.20** Extensional shear bands in high-grade rocks (west Sikkim)

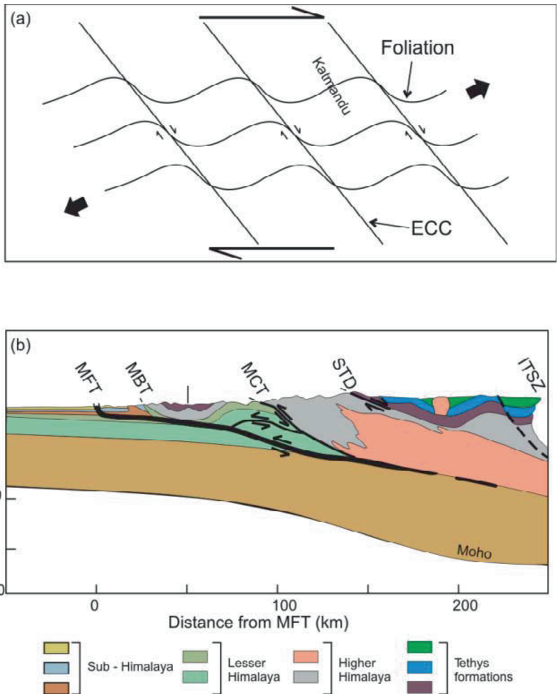

**Fig. 3.21** (a) Foreland-vergent extensional crenulation cleavage developed under top-to-hinterland horizontal shear. (b) Large-scale hinterland-dipping extensional zone (STDZ) in the hinterland part of the Himalayan orogen (after Avouac 2007, with permission from Elsevier)

tion 3.4 we will deal with existing tectonic models that provide probable explanations for extensional deformations in the Himalayan-Tibetan plateau system.

### *3.2.4 Large-scale Fault Systems*

Crustal deformations take place dominantly in brittle modes above the brittle-ductile transition zone at a depth about 12 km. Collisional tectonics thus produce numerous brittle faults in orogenic systems. A number of faults can develop in a region under the same kinematic and dynamic framework, which can be called a *fault system*. Contrasting types of fault systems can occur in the same orogenic belt. Seismic profiles of the Himalayan-Tibetan systems reveal a large-scale thrust system lying over the MHT. This section shows a sequence of foreland-vergent crustal-scale thrusts: MFT, MBT and MCT splaying from the MHT (Fig. 3.21b). This type of imbricate thrust system is quite common in orogenic fronts. The mechanics of sequential thrusting has been explained using critically-tapered wedge models (see section 3.5 for details). According to this model, the crustal wedge section lying on the detachment surface, e.g. MHT in the Himalaya, tends to slide and becomes on the verge of failure, forming a thrust when the wedge attains a critical taper. With progressive convergence movement the orogenic front propagates in the foreland direction developing successive new frontal thrusts. However, the process of thrusting in orogenic systems can be more complex compared to that predicted from physical or theoretical models. During progressive convergence earlier thrusts can reactive or some faults can form as *out-of-sequence thrusts*.

Collisional mountain belts also develop strike-slip faults transverse to the orogenic trend. According to the dynamics of faulting, this type of faults is likely to form in contraction tectonic regimes with horizontal extension and vertical restrictions. In the eastern flank of the Himalaya-Tibetan plateau system there are sets of large-scale strike-slip faults (Fig. 3.22). The fault system resembles to that produced in physical experiments producing an extrusion tectonic setting. We shall see in the next section that the Himalayan collision belt show eastward crustal flow in its eastern flank.

Normal faults occur in convergent tectonic settings. In the Himalayan belt the STDZ represents a large-scale nor-

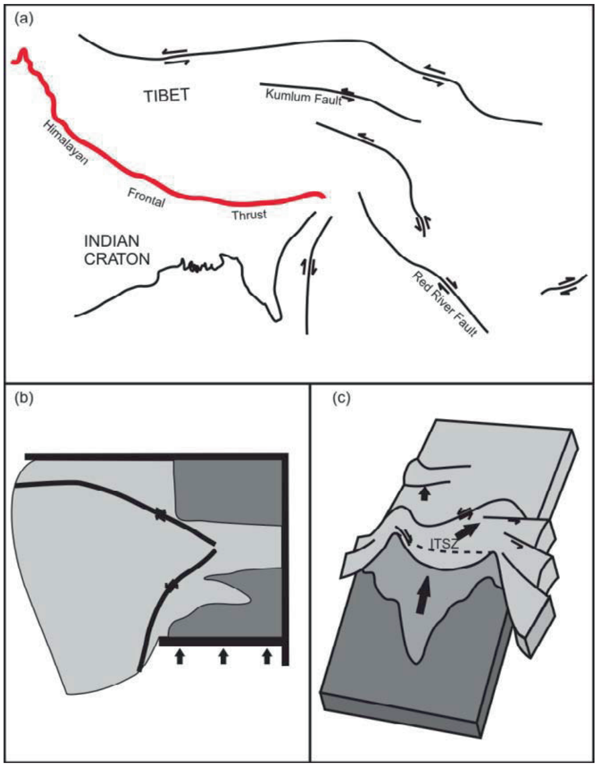

**Fig. 3.22** (a) Major strike-slip faults in the Himalaya-Tibet system (after Molnar et al. 1981). (b) Formation of strike-slip faults associated with lateral extrusion tectonics in models. (c) A schematic sketch of strike-slip movement on the eastern flank of the Tibetan plateau (after Avouac 2007, with permission from Elsevier)

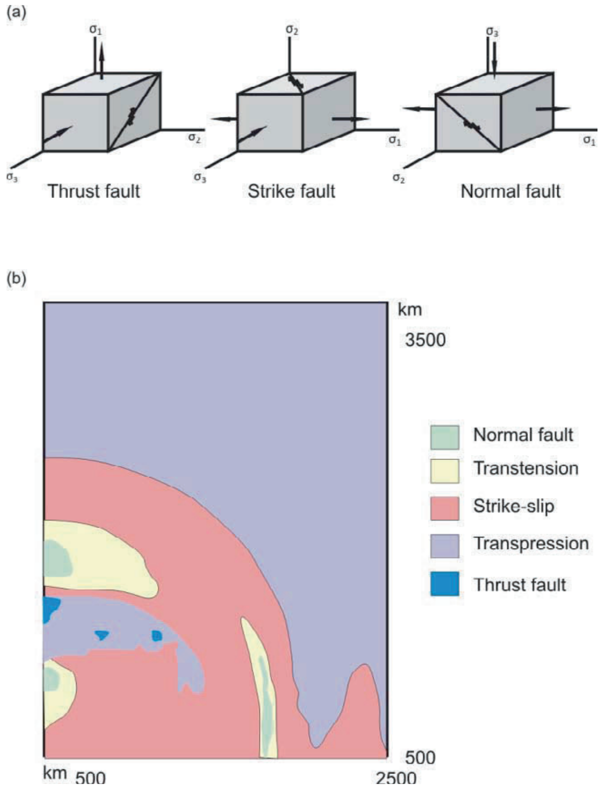

**Fig. 3.23** (a) Stress conditions for thrust, strike-slip and normal faulting in the crust. (b) Distribution of different types of faults in the Himalaya-Tibet system predicted from finite difference numerical model (after Jimenez-Munt and Platt 2006, with permission from Elsevier)

mal fault. The fault dips in the north direction (Fig. 3.21b).

The three types of faults described above form in three different stress fields (Fig. 3.23a). Their presence in the Himalayan belt indicates that the lithospheric stress must be spatially heterogeneous. Using a finite element method Jimenez and Platt (2006) derived a possible map of heterogeneous stress distribution in the Himalaya-Tibet convergent zones. Based on this map, they have shown the distribution of different fault systems (Fig. 3.23b).

## 3.3 Crustal Flow in Orogens

On a crustal scale, collisional mountain belts can be considered as a deforming continuum medium sandwiched between two relatively rigid blocks. During collisional movement, the orogenic materials deform and flow in response to the dynamic condition prevailing in the convergent zone. Several workers have modeled the flow in collisional tectonics with the approach of a thin viscous layer lying on relatively stiff lithospheric plates (e.g. England and Molnar 1997; Jimenez-Munt and Platt 2006; Copley and McKezie 2007). In this review we will deal with crustal flow models on the Himalaya-Tibetan plateau system. In the following two sections, we present models describing horizontal movements on the ground surface and vertical deep-crustal flow respectively.

### *3.3.1 Surface Velocity*

In recent times, earth scientists have mapped the surface velocities in the India-Tibet collisional zone by using GPS techniques (Wang et al. 2001; Jade et al. 2004; Zhang et al. 2004). The maps reveal that the Indian craton presently moves northward at a velocity of 40–50 mm/yr relative to the Eurasia. The surface velocity in the Himalaya-Tibetan crustal masses varies strongly both along and across the orogenic belt. In the central Himalayan range the movement is taking place northward at a velocity of 4 cm/yr. However, the displacement trajectories strongly curve, showing eastward movement on the eastern side of the Tibetan plateau. The crustal flow finally trends southward in the region between Szecwan basin and the Indo-Burman range (Fig. 3.24). The flow pattern resembles that obtained laterally extruding convergent tectonic settings. In the western Tibetan plateau, the relative crustal movement occurs mostly in the north direction. The rate of movement decreases fast northward.

The crustal scale movement in the Himalaya-Tibet system described above indicates that the collision between the Indian and the Eurasian plates has taken place by a combination of crustal thickening and lateral extrusion. This kind of complex crustal flow has been modeled considering deformation of either a Coulomb layer or a viscous layer in the convergent tectonic zone. It can be shown from analo-

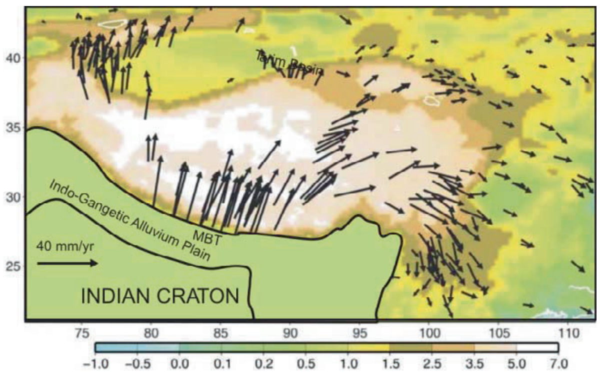

**Fig. 3.24** Surface velocity pattern in the Himalaya-Tibet convergent zone. The velocity is relative to the Eurasian plate (after Wang et al. 2001, with permission from American Association of Advancement of Science)

gue model experiments that, in case of Coulomb rheology (e.g. sand layer) the crustal shortening takes place entirely by large-scale thrusting, resulting in crustal thickening and rise of mountains. This process is concurrently associated with strike-slip faulting, which lead to lateral extrusion taking place in the eastern flank of the Himalayan-Tibetan system (Fig. 3.22, Molnar et al. 1981; Avouac 2007). On the other hand, several workers have followed a thin viscous layer approach to analyse the crustal deformation and associated flow patterns. Recently, Jimenez-Munt and Platt (2006) have used numerical models employing a finite difference method. In their analysis they have taken a vertically averaged viscosity, and local isostasy of the lithosphere. Considering a vertical integration of the lithospheric plate, they reduced the three-dimensional problem in a two-dimensional framework. Their model configurations are illustrated in Fig. 3.25a. The model covers an initial area with horizontal dimensions of 4000 km on east-west and 6000 km on north-south directions. The Indian craton is considered to be a virtually rigid block with a viscosity in the order of $10^{25}$ PaS, moving northward with a velocity of 5 cm/yr relative to the northern boundary of the Tibet. This modelling takes into account the effect of removal of mantle lithosphere beneath the Tibet. The kinematic conditions at the model boundaries are shown in Fig. 3.25a. The model runs reveal curvilinear crustal flow in the Himalaya-Tibet system, showing eastward lateral surface velocities (Fig. 3.25b), as obtained from the GPS data. Their model also presents a map delineating the zones of crustal thickening and thinning. There are localisation of maximum thickening and thinning rates in two discrete arcuate zones located in the southern fringe and at the centre of the plateau. Their estimates show that the crustal thinning takes place at rates between 2 and 10 × $10^{-16}$/s. On the other hand, the crustal thickening rate at the India-Tibet contact is in the order of 1 × $10^{-16}$/s.

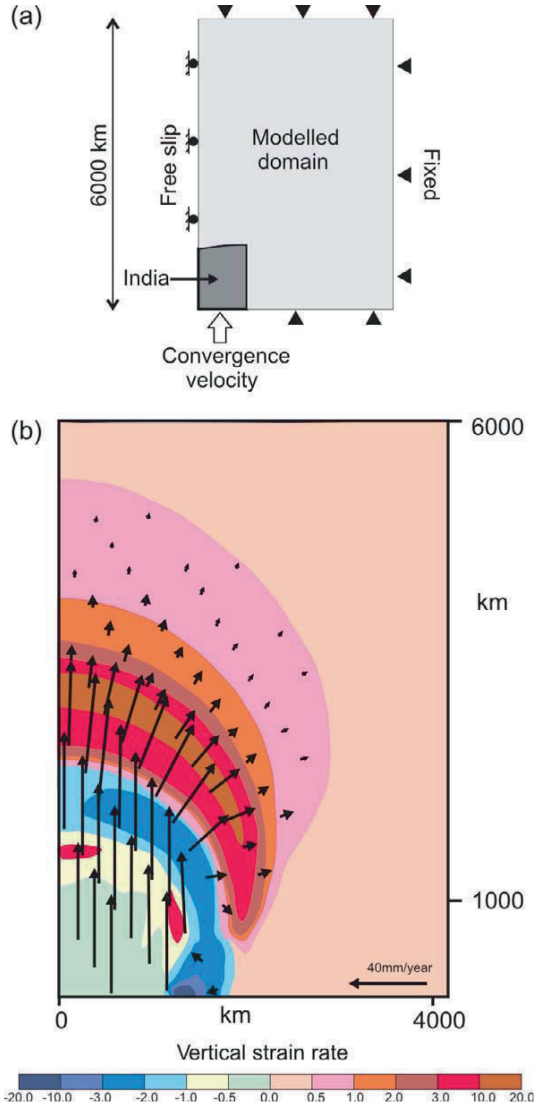

**Fig. 3.25** Consideration of boundary conditions for crustal flow modelling using finite difference method (after Jimenez-Munt and Platt 2006, with permission from Elsevier) (b) Model results showing flow pattern in the Himalaya-Tibet system

With the help of a thin viscous layer approach Copley and McKenzie (2007) has explained the surface velocities in the India-Asia collision zone. Their model shows the velocity field as fluid flows driven entirely by the topographically controlled pressure gradients. In this model a “stress-free” condition is adopted, implying that there is no shear stress on the layer boundary and that there is no restriction to the horizontal velocity. They have modeled the crustal flow in the different parts of the collision zone using different boundary conditions. For modelling of crustal flow over India from Tibet and the Indo-Burmese range, the upper surfaces are considered as stress-free, while the lower boundary is rigid, but deformable (i.e. horizontal velocity = 0 and vertical velocity $\neq$ 0). This type of boundary conditions is employed considering the presence of a rigid (high viscosity) lithospheric plate beneath the Tibetan plateau. Model results based on this boundary conditions and viscosity in the order of $10^{20}$ PaS show surface velocities in the south Tibet that match well with that obtained from the GPS data (Fig. 3.26a). Models with the same condition produce velocity field in the south-eastern Tibet, showing large misfits with the GPS data (Fig. 3.26b). In contrary, models with stress-free conditions at basal and upper boundaries give rise to crustal velocities more consistent with the GPS data when the flow is assumed to be confined between rigid walls (the Szechwan basin and the low land near the syntaxis). The stress-free basal condition appears to be valid, as there is no evidence of rigid lithospheric substrate in the region between the Szechwan basin and the eastern syntaxis. It has been shown that the best-fit velocity field is obtained for crustal viscosity of this region in the order of $10^{22}$ PaS. Based on the thin viscous sheet approach, the topographically controlled surface velocity pattern in the Himalaya-Tibet is illustrated in Fig. 3.26c.

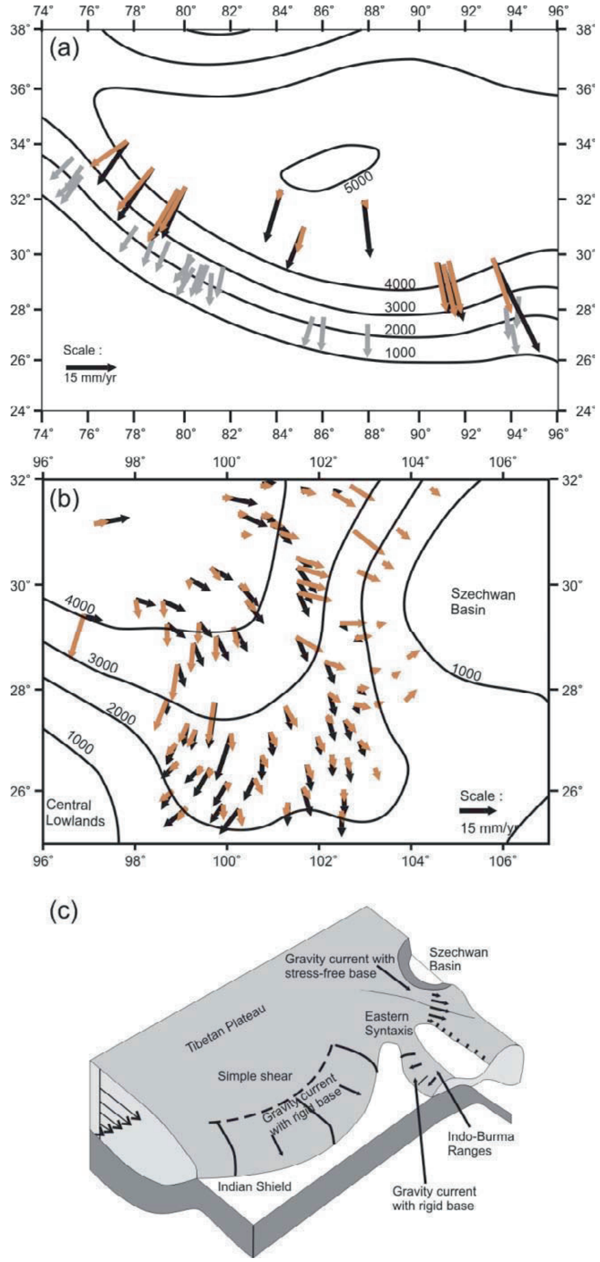

**Fig. 3.26** Modelling of topography-driven crustal flow under topography controlled pressure gradients in (a) south Tibet and (b) south-eastern Tibet. Black and brown arrows show velocity from GPS data and model results respectively. Gray shaded arrows indicate motion obtained from fault slip data. (c) An overall view of topography controlled flow in the Himalaya-Tibet system. (after Copley and McKenzie 2007, with permission from Blackwell Scientific)

### *3.3.2 Deep-crustal Flow*

In collisional zones, the subducting litospheric plate induces complex flows in both the mantle and the crustal materials sandwiched between the two colliding lithospheric plates. Understanding these flow processes is essential for resolving many geological phenomena, such as rock uplift rates in metamorphic terrains, deformation history, recycling of crustal materials and crust-mantle interactions. In recent times there have been discrete attempts to enumerate the rate of rock uplift using structural and petrological information. For example, Ganguly et al. (2000) have estimated that exhumation in the north-eastern Himalaya took place at a rate of 1.5 cm/yr up to a depth of 15 km, which decreased down to 0.2 cm/yr when the rocks were uplifted to a depth of 5 km. However, compared to the surface velocity patterns described above, we have little quantitative data for deep-crustal flows in orogens. Our understanding is mostly based on different flow models in recent studies. In this section we present some of these models.

Most of the crustal flow models employ a viscous rheology approach to study large-scale (first order) flow patterns in convergent tectonic boundaries. Several workers have used the corner flow theory of fluid mechanics (Cowan and Silling 1978; Cloos 1982, 1984; Mandal et al. 2002). The theory describes the velocity field in a fluid medium confined between two converging rigid plates, where one plate moves against the other, setting in a viscous flow (Batchelor 1967). Considering a polar coordinate system

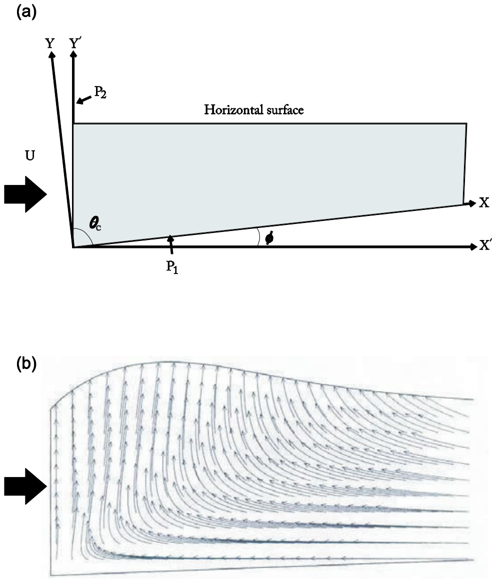

**Fig. 3.27** (a) Theoretical modelling of viscous flow between two converging plates. The plate $P_1$ subducts against the plate $P_2$. (b) Particle paths of flow obtained from the corner flow theory

(Fig. 3.27a), the velocity components of fluid flow can be expressed as

$$u_r = A\cos\theta - B\sin\theta + C(\sin\theta + \theta\cos\theta) + D(\cos\theta - \theta\sin\theta) \qquad (3.4a)$$

$$u_\theta = -(A\sin + B\cos\theta + C\theta\sin\theta + D\theta\cos\theta) \qquad (3.4b)$$

where *A, B, C* and *D* are constants, the expression of which are as follows.

$$A = (U/\sin^2\theta_c)[\cos^2\theta_c \cos\ \ \ - K(\theta_c + \sin\theta_c \cos\theta_c)]$$

$$B = U \sin$$

$$C = UK$$

$$D = -[\cos\ \ \ + (1/\sin^2\theta_c)\{\cos^2\theta_c \cos\ \ \ - K(\theta_c + \sin\theta_c \cos\theta_c)\}U]$$

$$K = [\theta_c - \sin\theta_c \cos\theta_c \{(1-\theta_c)^2 \cos\ \ \ + \theta_c^2\} + \sin^2\theta_c\{\theta_c\{\cos\ \ \ - 1) + \sin\ \ \ \}]/(\theta_c - \sin^2\theta_c)$$

*U* is the relative velocity of one plate moving against the other one. $\phi$ is the dip of the moving plate, and $\theta_c$ is the angle between two plates. This velocity function can be used to crustal flow sandwiched between the subducting and the overriding lithospheric plates in subduction zones. However, the flow pattern derived from the velocity function is somewhat simplistic (Fig. 3.27b), as it does not take into account the effect of gravity. Furthermore, the actual crustal flow is likely to be more complicated due to the effects of additional factors, such temperature, fluid activity and density variation. Workers therefore use different numerical methods, such as finite element method and finite difference method, to study the flow patterns considering different geological factors. A few examples are presented below.

Numerical simulations based on a finite difference method reveal that the crustal materials in subduction zones continuously churn itself in the form of large-scale vortex (Fig. 3.28a). The pattern is quite different from that obtained from the corner flow theory. These models also explain several geological phenomena, such as multiple metamorphic events, P-T-t paths and exhumation of deep crustal rocks in high-pressure metamorphic belts (Gerya et al. 2002). The flow pattern can be further complex depending upon the geological settings. The deep-crustal flow in the Himalayn-Tibet is thought to be controlled by a combined effect of surface processes, such erosional denudation and deep-crustal processes, such as partial melting and lowering in viscosity. Beaumont et al. (2001) has demonstrated from numerical models that the lower crustal segment lying below the Tibet has undergone partial melting, and that partially molten flow in the south direction. The crustal flow converges into a channel-like passage between the MCT and the STD, which appears to be the location of maximum denudation. They have used three models (Model 1, 2 and 3). Model 1 considers a condition of no crustal subduction and a basal velocity of 2 cm/yr. With the help of this model the velocity fields corresponding to the basal movement and the gravity forces were derived separately, and added to obtain the total velocity field. Model results show that the gravity forces play a dominant role in governing the channel flow. Model 2 takes a subduction process of the pro-lithosphere at a rate of 5 cm/yr with advancement of the subduction zone at a rate of 2.5 cm/yr. The two models yield similar thermal tectonic styles, implying relative insensitivity to the choice of boundary conditions. In Model 3 they have considered an upper weak crust and variable denudation rate. The overall flow pattern is illustrated in Fig. 3.28b.

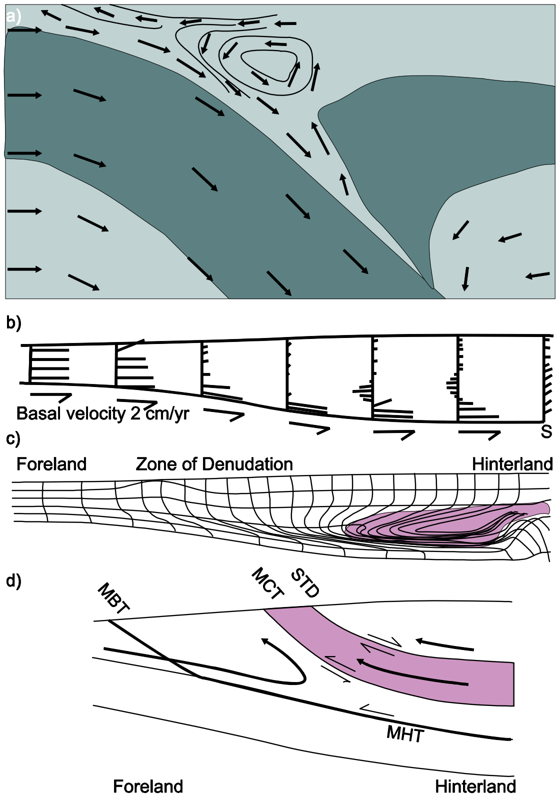

**Fig. 3.28** (a) Numerical models showing the crustal flow pattern in a subduction zone (after Gerya et al. 2002, with permission from American Geophysical Union). (b)-(c) Numerical simulation of lower crustal flow beneath the Tibetan plateau and (d) Exhumation of low-viscous deep-crustal rocks (pink shaded) in the form of channel in the higher Himalaya (after Beaumont et al. 2001, with permission from Nature Group of Publishers)

Beaumont et al. (2001) model show that the exhumation process in the high-grade metamorphic terrain has taken place in the form of channel, as discussed by several workers. The mechanics of channel flow is similar to that for fluid flow between two rigid plates under a pressure gradient ($dp/dx$). The velocity of plate-parallel fluid flow can be obtained from the following equations:

$$u = \frac{1}{2\eta}\frac{dp}{dx}\left(y^2 - \frac{h^2}{4}\right) \tag{3.5}$$

where $\eta$ and h are the fluid viscosity and the channel width respectively. The channel flow can be complex if the boundary plates move relative to each other (Jaeger 1969). The plates can approach to each other or slide one another. The velocity field for a channel flow can be described in terms of a general equation as

$$u = \frac{1}{2\eta}\frac{dp}{dx}\left(y^2 - \frac{h^2}{4}\right) + \dot{\gamma}y + 3V_0 x\frac{h^2 - y^2}{2h^3} \tag{3.6}$$

$$v = V_0 y\frac{y^2 - 3h^2}{2h^3} \tag{3.7}$$

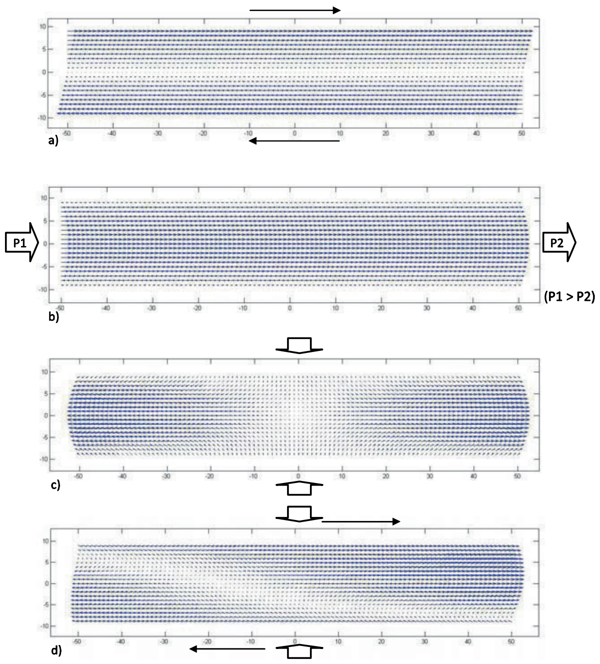

**Fig. 3.29** Patterns of channel flow in response to (a) simple shear movement on walls, (b) pressure difference between the two ends of channel, (c) walls approaching each other, and (d) a combined effect of simple shear, pressure gradient and wall-normal movement

$\dot{\gamma}$ and $V_0$ are the shear rate and the approaching velocity between two plates. Fig. 3.29 shows different possible patterns of channel flow as a function of boundary conditions.

Geological evidence supports that the crust can behave as a visco-elastic layer, the stress relaxation of time of which has been estimated in the order of $10^{10}$ s. Finite element models, based on Maxwell visco-elastic rheology, reveal that the flow pattern can vary with the subduction rate (Fig. 3.30). The pattern resembles that predicted from the corner flow theory when the rate is high, e.g. more than 6 cm/yr. With decreasing subduction rate there occurs a flow separation in the hinterland of orogen, forming vortex-like motion in the deeper level and forelandward flow along hyperbolic paths in the shallow levels. The flow pattern de-

**(a) $V_s$=2 cm/yr**

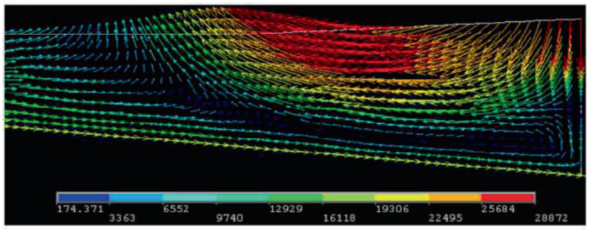

**(b) $V_s$=4 cm/yr**

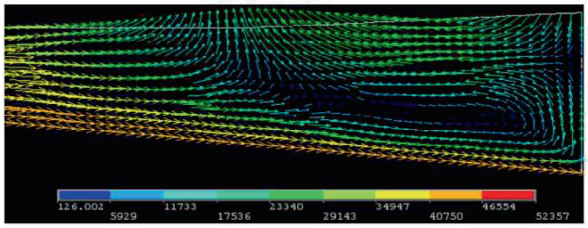

**(c) $V_s$=6 cm/yr**

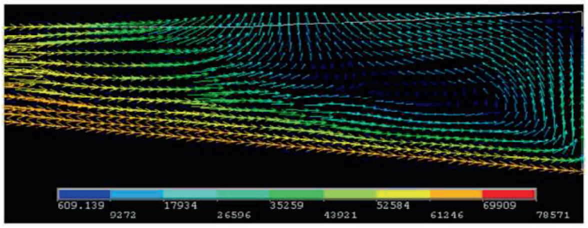

**(d) $V_s$=8 cm/yr**

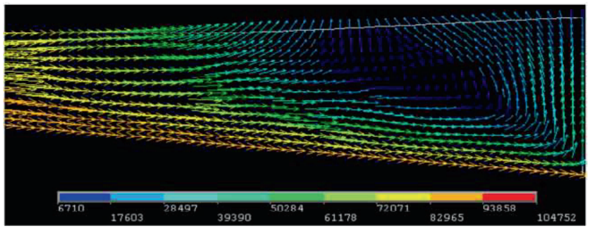

**Fig. 3.30** Finite element models showing flow patterns in convergent zones as a function of subduction rate ($V_s$)

scribes a narrow zone where deep-level materials extrude up, which resemble a channel flow.

## 3.4 Orogenic Wedge Models

### 3.4.1 Preamble

Most of the orogenic belts show a wedge-shaped section, containing intensely deformed rocks lying over a relatively undeformed base. A variety of wedge models has been applied to explain the deformation kinematics in orogenic wedges. These models differ from one another either the choice of boundary conditions or rheology. The boundary conditions can be grouped into three categories: 1) crustal layer segment lying on a base with a velocity discontinuity, 2) crustal segment lying on a kinematic base and entirely confined by vertical based and 3) condition same as in 2) but not entirely confined by the backstop (Fig. 3.31). The three boundary conditions give rise to contrasting model results. Models with the second boundary condition produce mono-vergent wedges, whereas those with the first and the third boundary conditions develop bi-vergent wedges. Rheologically, wedge models can be classified again into three types: 1) Coulomb models, 2) plastic models and 3) viscous models, that are described separately in the following sections.

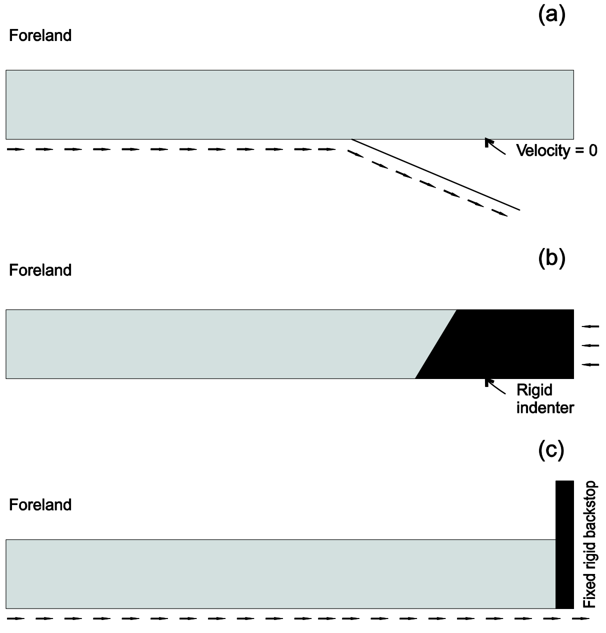

**Fig. 3.31** Three types of model set-up for simulation of orogenic wedges

### 3.4.2 Coulomb Wedge Models

Coulomb wedge models have been widely used both for studying the evolution of FTBs in orogens. Davis et al. (1983) introduced the concept of critically tapered wedge, leading to instability and shear failure in non-cohesive materials. Later workers have advanced the model considering cohesive materials (Dahlen et al. 1984). According to the critically-tapered wedge model, an accretionary wedge deforms internally and increases its taper angle, and at a critical taper the wedge develops internal stresses, leading the system on the verge failure everywhere. In this dynamic state the basal shear stresses also reach a value required for frictional sliding at the basal detachment (Davis et al. 1983; Boyer and Elliot 1982; Chappel 1978). The critically tapered wedge thus tends to slide stably along its base, giving rise to a new thrust in the wedge. The critical taper is found to be a function of basal friction as:

$$\alpha + \beta = \left(\frac{1-\sin\phi}{1+\sin\phi}\right)\mu_b \tag{3.8}$$

$\alpha$ and $\beta$ are topographic and basal slopes respectively. $\mu_b$ is the basal friction and $\phi$ is the material friction. The wedge section lying above in the Himalayan belt show a surface slope about 4°, suggesting a low basal friction (Avouac 2007).

The development of Coulomb wedges is associated with formation of successive frontal thrusts, such as MCT, MBT and MFT. Both experiments and theory, show that frontal thrusts develop sequentially maintaining a spacing which can be shown as a function of thickness of the crustal segments ($h$) and basal friction ($\mu_b$). Mandal et al. (1997) derived a mathematical relation for thrust spacing (a) as

$$a = \left[\frac{n}{\mu_b} - \frac{1}{2}\left(\frac{M - N\mu_b}{L\mu_b} + \frac{1}{m_t}\right)\right]h \tag{3.9}$$

where

$$L = \mu_m \sin^2\theta_t - \frac{1}{2}\sin 2\theta_t$$

$$M = \mu_m \cos^2\theta_t + \frac{1}{2}\sin 2\theta_t$$

$$N = \cos 2\theta_t - \mu_m \sin 2\theta_t$$

$\mu_m$ and $\theta_t$ are the co-efficient of material friction and thrust dip respectively. Equation shows that thrust spacing is inversely proportional to basal friction, as also seen in physical experiments and field. In a recent study it has been

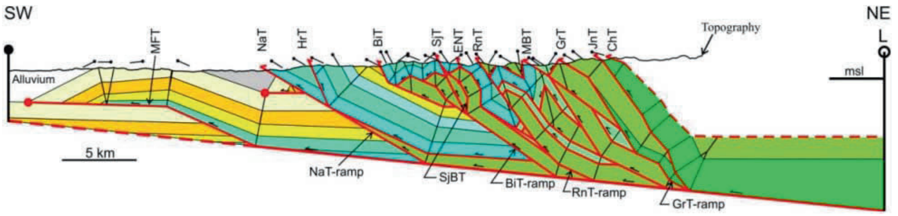

**Fig. 3.32** Imbricate thrust sequence in Nahan Salient, western Himalaya (Mukhopadhyay and Mishra 2005, with permission from Elsevier)

shown that thrust spacing may remain constant or vary during the orogenic growth. Coulomb wedges with high basal friction develop successive thrusts with strongly increasing spacing when they do not involve significant surface erosion. On the other hand, the spacing remains steady when the basal friction is low (Bose et al. 2008).

There have been a large volume of experimental studies on the evolution of thrust wedges. In this review we will highlight only major outcomes of these studies. Mono-vergent thrust wedges develop thrust sequences propagating continuously in the foreland direction, as observed in the frontal Himalaya (Figs. 3.32, 3.33a). High basal friction conditions lead to formation of mainly foreland-vergent thrust, and individual thrusts show large displacement (Fig. 3.33b). In contrast, low basal friction conditions show development of foreland-vergent thrusts in coupled with back thrusts, and the thrust sequences appears to be relatively complex (Fig. 3.33c). Coulomb wedges with low basal friction have tendency to form out-of-sequence thrusts in the hinterland.

The evolution of bi-vergent thrust wedges is much different from that of mono-vergent wedges. In describing bi-vergent wedges, we need to consider thrust progression against (called pro-wedge progression) and towards (called retro-wedge) the seduction direction, forming wedges called *pro-wedge* and *retro-wedge* respectively (Fig. 3.34). The evolution of bi-vergent wedges has been successfully demonstrated in physical experiments (Persson and Sokoutis 2002; Storti et al. 2000). Using the first boundary condition (velocity discontinuity at base) it has been shown that a pair of foreland-vergent and back thrusts first forms at the point of velocity discontinuity (Storti et al. 2000; Fig. 3.34). With progressive horizontal shortening the back-thrust becomes more active, resulting in dominance of the retro-wedge, where a number of closely spaced foreland-vergent thrusts form, giving rise to pro-wedge with a relatively gentle surface slope. The pro-wedge propagates foreland ward through successively formation of frontal thrusts, whereas

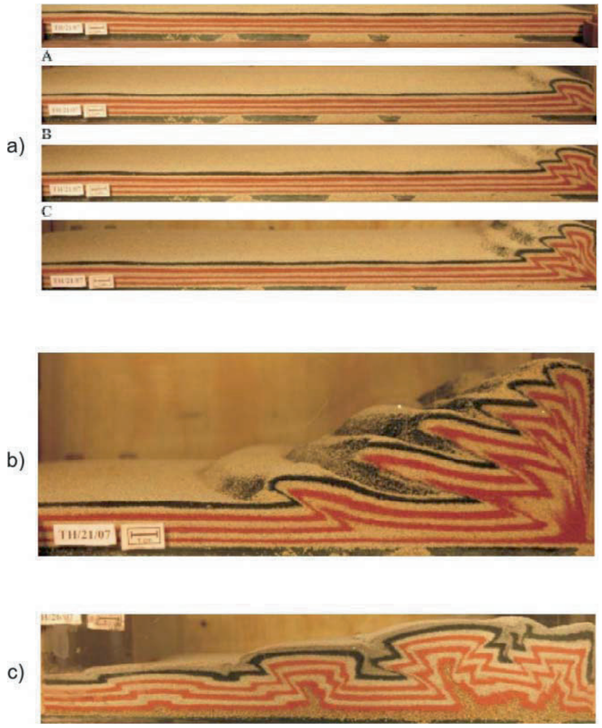

**Fig. 3.33** (a) Sequential thrusting in sandbox experiments. (b) and (c) Thrust wedges with high basal (0.46) and low (0.3) basal friction

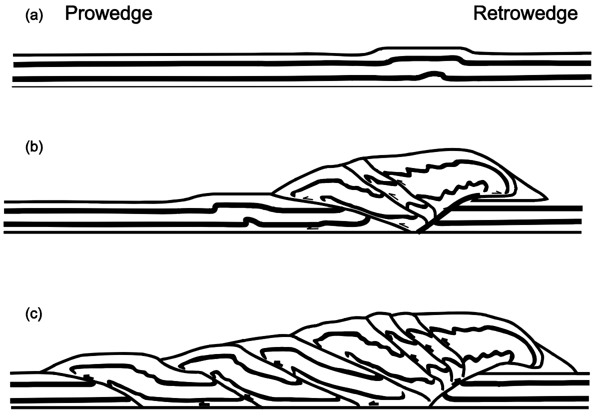

**Fig. 3.34** Sequential thrusting and growth of a bi-vergent wedge in a model with velocity discontinuity at the base (after Storti and Salvini 2000, with permission from American Geophysical Union

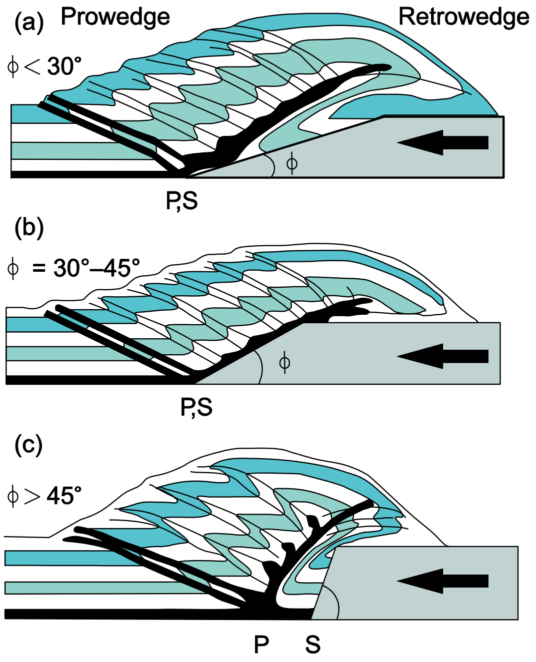

**Fig. 3.35** Development of a bi-vergent Coulomb wedge against a rigid indentor (after Persson and Sokoutis 2002, with permission from Elsevier)

the retro-wedge shows a limited lateral propagation, but grows vertically by active movement on the back thrusts. The bi-vergent wedge finally assumes a strongly asymmetrical geometry. Model experiments with the second boundary conditions (unconfined backstop) also show a similar evolution history of bi-vergent wedges. In these experiments brittle layers are deformed by moving a rigid indentor (Fig. 3.35). The architecture of pro-wedge and retro-wedge thrusts depends on the geometry of indentors (Persson and Sokoutis 2002). In case of indentors with large face slopes (>60º), the back thrust propagates from a basal point located away from the toe of the indentor, and define a triangular zone, that acts an *effective indentor*. On the other hand, for smaller face slopes (<45º) the point is located at the toe. A bi-vergent wedge contains a frontal thrust and a back thrust that meet at this point, which does not shift with progressive deformation. A frontal thrust forms at this point, and remains active for a period of time and then turn to be passive. The thrust then rides over the back thrust, and a new thrust form at the toe. The pro-wedge thrusts finally lie over the back thrusts (Fig. 3.35). There is an overall difference between bi-vergent wedges produced in the two boundary conditions. In case of the first boundary condition, the pro-wedges propagate foreland, as new frontal thrusts form successively away from the back thrust. On the other hand, the second boundary condition develops pro-wedges with a frontal most thrust always meeting the toe of the back thrust.

A variety of numerical methods have been adopted to design benchmark experiments for studying the development of thrust wedges. Recently, several workers have used discrete element method to simulate sandbox experiments. For example, Egholm et al. (2007) have used a stress-base discrete element method (SDEM). The basic approach to this modelling is to treat rocks as granular masses that can be considered an aggregate of grains. In their models the grains are circular disc or spherical elastic particles, interacting in pairs at the contact points. The inter-particle forces at the contacts are calculated from the stress tensors as

$$(f_i)^{ab} = \left(R_a \sigma_{ij}^{a} + R_b \sigma_{ij}^{b}\right) n_j^{ab} \tag{3.10}$$

$R_a$ and $R_b$ are the radii of particles a and b respectively; $\sigma^{a}_{ij}$ and $\sigma^{b}_{ij}$ are tensors corresponding to the two particles. $n_j^{ab}$ is the unit vector denoting the line joining the centre of the particles. The total force acting on each particle at an instant can be obtained by taking summation of the gravity force and the forces at the contact points, the expression of which follows

$$F_i^{ab}(t) = \sum\nolimits_a f_i^{ab}(t) + m_a g_i \tag{3.11}$$

Particles will tend to slide over the other as the forces overcome the frictional resistance. Using this technique, sandbox experiments can be successfully simulated. The development of thrust wedges that are observed in sandbox experiments can be exactly replicated in this type of experiments based on DEM. An example is illustrated in

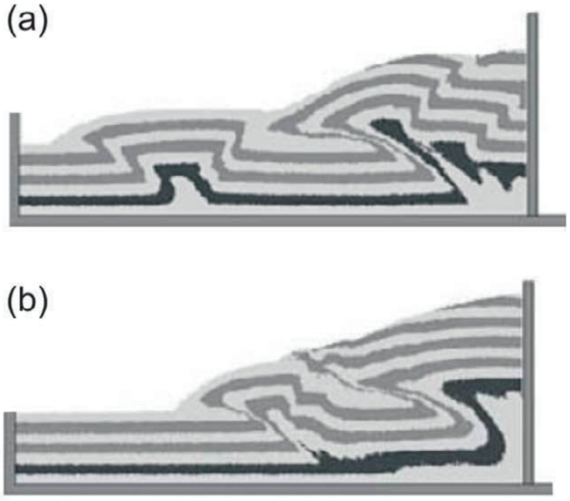

**Fig. 3.36** Thrust wedges simulated in discrete element models. (a) Low and (b) high basal friction (after Egholm et al. 2007, with permission from American Geophysical Union)

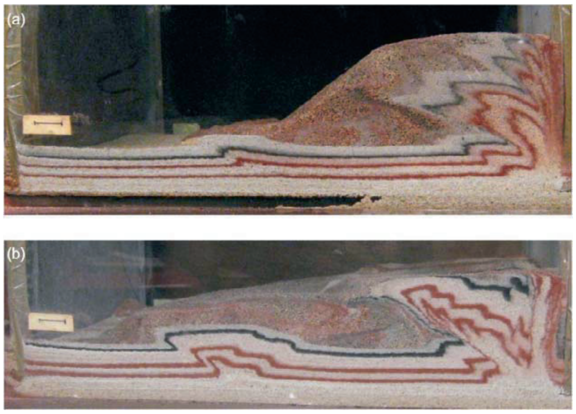

**Fig. 3.37** Effects of surface erosion on localisation of exhumation in experimental thrust wedges. (a) High and (b) low basal friction

Fig. 3.36. The models can be efficiently used for studying thrust structures in convergent tectonic belts.

Geological findings suggest that surface and deep-crustal processes can mutually influence one another. Recently, several workers have performed sandbox experiments to investigate the effects of surface erosion on the evolution of Coulomb wedges. One of the most significant effects of surface is concerned with the exhumation process in orogenic belts. In no erosion conditions, a Coulomb wedge develops successive frontal thrusts, and propagate foreland, without showing any localised exhumation zone of deeper materials. On the other hand, the wedge develops a distinct zone of exhumation localisation beneath the surface undergoing erosion. Such erosion-controlled exhumation localisation is intense when the basal friction is low (Fig. 3.37).

### 3.4.3 Plastic Models

Plastic rheological models have also been used to study strain localisation in rocks. Experiments show that rocks under stresses deform elastically, and begin to deform permanently, developing permanent strain at a critical stress (called *yield stress*). This represents typically an elastic-plastic rhelogy of solids. However, in modelling large-scale crustal deformation other types of plastic rheology, such as Coulomb-plastic and viscous-plastic, appear to be appropriate. We will present studies dealing with modelling of wedges based on Coulomb-plastic rhelogy. The behaviour can be understood in a way that the stress in this case is determined by the frictional properties of rocks, and causes yielding when it reaches the yield stress. The yield condition can be defined by using the Mises criterion, which takes into account the second invariant of the deviatoric stress tensor $S'_{ij}$ :

$$J'_2 = \frac{1}{2} S'_{ij} S'_{ij} \qquad (3.12)$$

The yield will take place when $J'_2$ is equal to the yield strength. However, rocks at low temperatures show dominantly frictional behaviour. Thus, to characterise the yield, Coulomb criterion would be more appropriate. This can be expressed in two dimensions with the first and the second stress invariants as:

$$\left(J'_2\right)^{\frac{1}{2}} = c\cos\phi + \frac{1}{3} J_1 \sin\phi \qquad (3.13)$$

Using finite element method the development of bi-vergent thrust wedges have been studied with Coulomb plastic models. The models show formation of pro-wedge and retro-wedge thrusts in a system with a basal velocity discontinuity (condition 1). They propagate laterally at more or less at equal rates, accompanying formation of conjugate thrusts (Fig. 3.38).

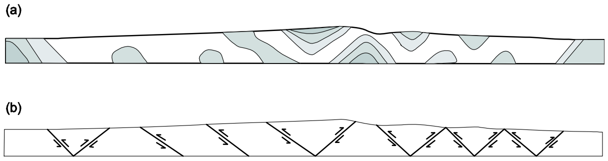

**Fig. 3.38** Numerical simulation of bi-vergent wedges in plastic models containing a basal velocity discontinuity (after Willett 1999, with permission from Elsevier)

### 3.4.4 Viscous Wedge Model

Typical Coulomb or plastic materials under stresses develop shear fractures or high-strain zones without any significant amount of global permanent strains. However, ductile structures, such as penetrative fabrics, folds, described in section 3.2.3 indicate that the crustal deformations produce a global ductile strain in orogenic belts. Experiments also show that rocks at relatively high temperatures can undergo dislocation-controlled or diffusion-controlled creep. In order to model such creep behaviour earth scientists use different types of models based on linear or power-law viscous rheology.

Considering the first basal condition (section 3.4.2), Willett (1999) has shown the development of a bi-vergent wedge in a viscous layer lying on a rigid base. The models

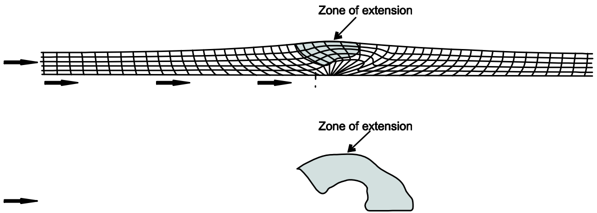

**Fig. 3.39** Numerical simulation of bi-vergent wedges in viscous models containing a basal velocity discontinuity (after Willett 1999, with permission from Elsevier)

give the pattern of strain distribution in the wedge (Fig. 3.39). Mapping of the horizontal strain rate component delineate localisation of horizontal extension in a zone between the pro-wedge and retro-wedge. His analysis involves a number of normalised parameters: Argand number *Ar*, time $t^*$ and strain rate $\dot{\varepsilon}$, the expression of which follow

$$Ar = \frac{\rho g h^2}{\eta V_P},\ t^* = \frac{V_p t}{h} \text{ and } \dot{\varepsilon}^* = \frac{\dot{\varepsilon} h}{V_p}$$

where $\rho$, $g$ and $h$ are density, gravity acceleration and layer thickness. It may be noted that *Ar* is a measure of viscosity. Lower values of *Ar* imply larger viscosities of the system, when all the parameters remain constant. Model results show that the extensional zone localise at highest elevation of the wedge for $Ar = 10$, which tends to localise in two discrete locations on the flanks of either side of the wedge when $Ar = 0.1$.

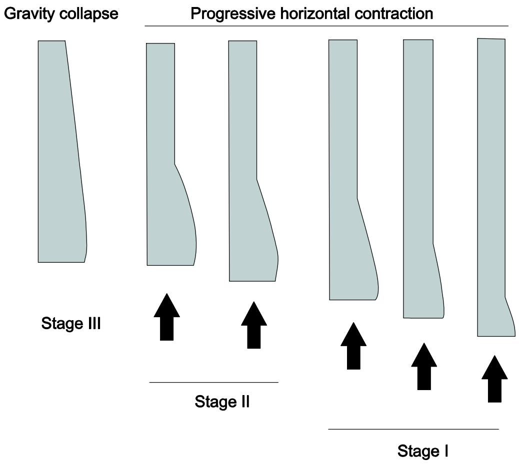

**Fig. 3.40** Three stages of wedge growth in orogens. Stage I: vertical growth. Stage II: lateral migration of wedge maintaining a stable elevation. Stage III: Gravity collapse of wedge following tectonic relaxation (after Chattopadhyay and Mandal 2002, with permission from Elsevier)

Viscous models have also been used in physical experiments to study the evolution of strain in a growing wedge. Chattopadhyay and Mandal (2002) has shown three principal stages of viscous wedges from pitch models (Fig. 3.40). In the first stage (Stage I) wedges grow dominantly in the vertical direction. With progressive shortening they tend to attain a stable elevation. In this second stage (Stage II) the wedges propagate in the foreland direction. There occurs gravity collapse following relaxation in horizontal shortening (Stage III). Each stage is characterised by the strain distribution and the flow pattern (Fig. 3.41). The hinterland strain is strongly heterogeneous, and show extension in the shallow level. Stage III develop strong top-to-hinterland (back) shear in the hinterland.

Viscous models have also been used to investigate the surface topography in a deforming wedge. Rossetti et al. (2000) developed a paraffin wax model in an experimental set-up in a controlled temperature condition. In the model the temperature varied from the back to front and the surface to the base of wedge by maintaining a constant gradient. The experiments show that the mode of wedge deformation is sensitive to the strain rate. Models with a strain

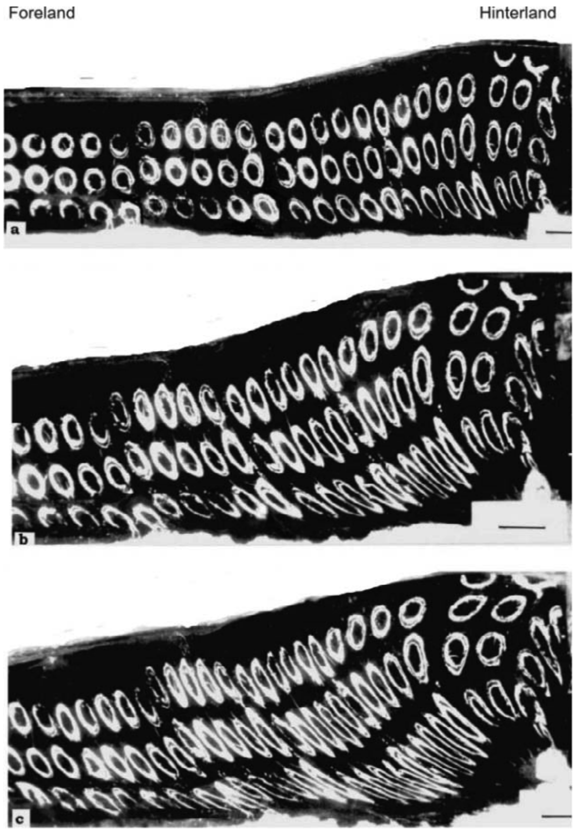

**Fig. 3.41** Strain distribution in the three stages of viscous orogenic wedges in experiments (after Chattopadhyay and Mandal 2002, with permission from Elsevier)

rate of 5 × $10^5$/s developed steep wedge slopes with narrow deformed zone in the form of a single antiform. On the other hand, models with slower strain rates ($10^5$/s) produced relatively lower surface slopes and wider deformed zones with multiple antiforms that developed successively in the course of progressive horizontal shortening.

## 3.5 Discussion

### *3.5.1 Orogenic Structures and Tectonic Modelling*

In the previous sections we have seen that orogens contain both brittle and ductile deformational structures of varying scales. Their styles vary continuously from the foreland to hinterland. Furthermore, deformed rocks show superposed structures that occur regionally, and reflect a temporal variation in the strain field. Such structural superpositions are noticed over a large area in a terrain, and needs to be looked in terms of regional strains. Several workers have reported even more than two phases of deformations. For example, the Daling group of rocks lying in frontal belts of the Himalaya show imprints of repeated ductile deformations. Different mechanical models have evolved in recent times, which have been discussed in section 3.4. Barring a few studies, most of the models deal with either a first-order structure, such as orogen topography and crustal flow or very large-scale deformations, such as thrusts. These models provide an overall picture of tectonic styles in orogens. Analysis of spatial and temporal variations of penetrative ductile strain in relation to the bulk kinematics of orogens is required to interpret the structural history. In order to elaborate this discussion, consider an example from the Himalaya. Field observations in Daling group show superstition of buckle folds on early extensional structures, such as stretching lineation or boudinaged layers in foliated rocks. The superposed structures suggest that the rocks underwent extensional deformations in one stage, which were followed contraction along the principal extension direction of the early deformation. This type of strain history is difficult to explain with a single, progressive movement with a constant kinematic framework. We therefore need to develop more refined models to reveal the pattern of multiple deformations as a function of both space and time.

Critically-tapered Coulomb wedge models are commonly employed to describe structures, such as thrust array and their kinematics (e.g. thrust upliftment) in the Himalayan belt. According to this model, the crustal shortening is partitioned in spaced shear zones or thrusts, leaving intact rocks in between them. In contrary, field studies on a N-S transect shows that the rocks lying from the mountain front to the MCT do not show sequentially disposed undeformed rocks separated by intensely deformed zones. Rather, one can find increasing intensity of penetrative deformations in the north direction. In order to explain both penetrative structures and relatively lower-order strain localisation, Coulomb wedge models with temporally steady and spatially homogenous rheology would probably be over simplification. Thus, we need to formulate orogenic models with rheology satisfying the conditions for development of small-scale structures observed in orogens.

In the Himalayan belt, the architecture of crustal-scale thrust sequences lying on MHT show some differences with that obtained in Coulomb wedge model experiments. Considering the topographic slope of the mountain front and the dip of MHT (~ 4°), and internal friction of 0.85, the effective friction has been estimated in the order of 0.12 (Cattin and Avouac 2000). However, calculations based on the whole Himalayn wedge shows relative higher values (0.25). In section 3.4.2, we have seen that wedges with high basal friction contain foreland-vergent thrusts with little or no hinterland-vergent (back) thrusts, which tend to be abundant with decreasing basal friction. Sandbox experiments performed with a basal friction of 0.35 produce simultaneous development of back thrusts and foreland-vergent thrusts during forelandward propagation of the Coulomb wedge. The back thrusts occur even in the extreme frontal part of the wedge, which are virtually absent in the Himalayan thrust wedge, even it is considered to have very low basal friction. Moreover, the spatial arrangement of splaying three major thrusts, MCT, MBT and MFT, is somewhat different from that obtained in typical experimental Coulomb wedges (Figs. 3.21, 3.33–3.37). These issues probably need to be looked into in view of models considering actual structural dispositions in orogens.

### *3.5.2 Problem of Basement Shortening*

All the orogenic wedge models described in the previous section are based on thin-skin crustal deformations in collisional regimes. Coulomb wedge models consider deformation of a brittle layer lying on a moving rigid base. In sandbox experiments one side of the rigid base moves beneath the sand layer, forming thrust wedges at its terminal point. It may be noted that this modelling approach do not take any account of the basal part. The results obtained from this kind of wedge models are applied to explain thrust wedges in the orogenic belts. A basic question – does the boundary conditions that we impose in theoretical or experimental Coulomb wedge models replicate the actual condition in orogens? It is a long standing problem what is happening to the base. For example, the frontal Himalayan thrust sequences-MFT, MBT and MCT are considered to splay out from the basal thrust-MHT. The geological cross-sections indicate that the crustal segment has undergone a large amount of crustal shortening. The lower crustal part decoupled from the upper part by the MHT acts as based of the frontal thrust sequences. In modelling the base is completely decoupled from the overlying layer, and does not interact with the latter with progressive shortening any more. On other hand, the decoupled lower crust does not subduct entirely, but accrete and interact with the overlying orogenic mass, as reflected from the occurrences of deep-crustal metamorphic rocks in the Himalaya. We therefore need to understand how the basement accommodates horizontal shortening. Some workers have suggested that pre-existing normal in the basement can reactivate as thrusts to accommodate the shortening. However, the distributions of seismicity in the Himalayan do not unequivocally favour such a mechanics. Alternatively, the lower crust (basement) is likely to be increasing ductile as it moves into deeper levels. The frontal part of the basement below the thrust sequence can deform in a ductile manner to accommodate horizontal shortening. Evidently, deforming basement will give rise to deformation patterns in the overlying orogenic wedges quite different from that obtained from typical Coulomb wedge models. We therefore need a new type of mechanical models with a better approximation of the rheological and boundary conditions.

### 3.5.3 *Exhumation Processes and Orogenic Models*

One of the major issues in orogenic studies is concerned with the exhumation mechanics of deep-crustal materials. Ultra-high pressure (UHP) rocks exposed in the Himalaya indicate that the crustal materials have journeyed from a depth of around 90 km. The problem is of two folds: 1) how a buoyant crustal material could travel a large distance, and reach a depth of 100 km for UHP metamorphism, and 2) what is the mechanics of rock uplift and exhumed back to the surface by unroofing the overlying materials. In this discussion we like to elaborate the second issue in view of tectonic models that have been presented in earlier sections.

Consider first different orogenic wedge models that are characterised by a basal detachment surface. According to the present tectonic setting of the Himalaya, the MHT acts as the basal detachment, and allow the overlying Himalayan crustal wedge to shortening in the N-S direction. It has been shown from sandbox experiments that the surface erosion can greatly promote localisation of the exhumation. Erosion-controlled exhumation is found to be more intense in wedges with low basal friction, which is true for the MHT. However, this process is likely to be important in much upper level crustal sections, as the depth penetration of MHT never go beyond 30 km. It may be recalled that rocks under a long-time scale field behaves in a ductile manner below the brittle-ductile transition zone at a depth of 12–14 km. Coulomb wedge models therefore cannot explain exhumed high-grade granulites rocks in the metamorphic belts, the petrological evidence of which suggests burial to a depth more than 30 km.

The channel flow mechanics has recently gained much popularity in explaining the exhumed metamorphic rocks lying between the MCT and STD. This probably gives a convincing account for flow of lower crustal materials beneath Tibet, focusing into a channel to the surface of the higher Himalaya. One of the basic premises in this mechanical model that the flowing material is much weaker than the surrounding medium, and the contrast in the upper section is so large that the rocks on either side of the channel behaves virtually like rigid walls. According to this model, isotherms strongly convex upward, giving rise to temperatures much higher than that expected from the general geothermal gradient. This probably allows the material remain viscous to a much shallower depth, and fulfils the requirement of channeling of lower crustal materials to the surface. Several geological consequences need to be overviewed in applying this model. On the footwall of the MCT (southern wall of channel), one can find Daling group of rocks in the Darjeeling-Sikkim Himalaya, which are mostly phyllitic and show evidence intense multiple episodes of ductile deformations. Petrological studies suggest that the rocks have undergone upper green schist metamorphism corresponding to a depth of 14 km. It is a question how such a ductile rock might have acted as a stiff wall for the channel. Secondly, seismic sections show MCT as a typical thrust with a very large displacement, which is difficult to explain in a high-temperature environment.

## 3.6 Concluding Remarks

Orogen building is one of the most important planetary processes, which govern the growth of continental land masses. Earth scientists have designed a variety of tectonic models to understand many complex orogenic processes, like sequential thrusting, metamorphism and deformations. However, we should cautiously use these models of different rheological considerations. For example, Coulomb wedge models have gained a significant importance in the literature on mountain tectonics. The models would ideally work only when the material flow is governed by frictional resistance. Secondly, Coulombs wedge models produce only localised deformation. In contrary, rocks exposed in the mountain show intense ductile deformations that are penetrative in nature, and appear to have undergone power-law flow. Finally, theoretical or experimental orogenic models should be designed considering deformational structures actually observed in mountain rocks.

**Acknowledgement:** We sincerely thank Prof. A. K. Gupta for giving us a guideline in preparing the manuscript. We are grateful to Prof. G. V. R. Prasad for critically reading an early version of the manuscript. Mr. Amiya Baruah helped in making diagrams.

## 3.7 References

Acharyya SK (1994) The Cenozoic foreland basin and tectonics of the eastern Sub-Himalaya: Problems and prospects, In: Kumar R, Ghosh S, Phadtare NR (eds) Siwalik foreland basin of Himalaya. Him Geol

Acharyya SK (1999) Tectonic evolution of the eastern Himalayan Tertiary basin, In: Jain AK, Manickavasagam RM (eds) Geodynamics of NW Himalaya. Gond Res Mem 6: 263–271

Avouac JP (2007) Dynamic Processes in Extensional and Compressional Settings-Mountain Building: From Earthquakes to Geological Deformation. In: Watts AB (ed) Treatise on Geophysics. Vol 6, Elsevier

Avouac JP, Tapponnier P (1993) Kinematic model of active deformation in central Asia. Geophys Res Lett 20: 895–898

Avouac JP, Tapponnier P, Bai M, You H, Wang G (1993) Active thrusting and folding along the northern Tien-Shan and Late Cenozoic rotation of the Tarim relative to Dzungaria and Kazakhstan. J Geophys Res (Solid Earth) 98: 6755–6804

Batchelor, GK (1967) An Introduction to fluid dynamics. The University Press, Cambridge

Beaumont C, Jamieson RA, Nguyen MH, Lee B (2001) Himalayan tectonics explained by extrusion of a low-viscosity crustal channel coupled to focused surface denudation. Nature 414: 738–742

Belousov VV, Gzovsky MV (1965) Experimental tectonics. In: Ahrens LH, Press F, Runcorn SK, Urey HC (eds) Phy Chem of the Earth. Pergamon Press, Oxford

Bilham R, Gaur VK, Molnar P (2001) Himalayan Seismic Hazard. Science 293: 1442–1444

Boyer S, Elliot D (1982) Thrust systems. Bull Am Ass Petrol Geol 66: 1196–1230

Brown RL, Jouneay JM, Larry SL, Murphy DC, Ree CJ (1986) Obduction, backfolding and piggyback thrusting in the metamorphic hinterland of the south-eastern Canadian Cordillera. J Struct Geol 8: 255–268

Bucher WH (1956) Role of gravity in orogenesis. Geol Soc Am Bull 67: 1295–1318

Casey M, Dietrich D (1997) Overthrust shear in mountain building. In: Sengupta S (ed) Evolution of Geological Structures in Micro-to-Macro-scales. Chapman and Hall

Chapple WM (1978) Mechanics of thin-skinned fold-and-thrust belts. Geol Soc Am Bull 89: 1189–1198

Chattopadhyay A, Mandal N (2002) Progressive changes in strain patterns and fold styles in a deforming ductile orogenic wedge: an experimental study. J Geodyn 33: 353–376

Cloos M (1982) Flow melanges: Numerical modelling and geologic constrants on their origin in the Franciscan subduction complex, California. Geol Soc Am Bull 93: 330–345

Cloos M (1984) Flow melanges and the structural evolution of accretionary wedges. Geol Soc Am Spl paper 198: 71–79

Copley A, McKenzie Dan (2007) Models of crustal flow in the India–Asia collision zone. Geophys J Int 169: 683–698

Cowan DS, Silling RM (1978) A dynamic, scaled model of accretion at trenches and its implications for the tcctonic evolution of subduction complexes. J Geophys Res 83: 5389–5396

Dahlen FA, Suppe J, Davis D (1984) Mechanics of fold-and-thrust belts and accretionary wedges: Cohesive Coulomb theory. J Geophys Res 89: 10,087–10,101

Dahlen FA (1984) Noncohesive critical Coulomb wedges: An exact solution. J Geophys Res 89: 10125–10133

Dasgupta S, Chakraborty S, Neogi S (2008) Petrology of an inverted Barrovian sequence of metapelites in Sikkim Himalaya, India: constraints on the tectonics of inversion. Am J Sc (In press)

Davis D, Suppe J, Dahlen FA (1983) Mechanics of fold-and-thrust belts and accretionary wedges. J Geophys Res 88: 1153–1172

DeCelles P, Robinson D, Zandt G (2002) Implications of shortening in the Himalayan fold-thrust belt for uplift of the Tibetan plateau Tectonics 21. doi: 10.1029/2001TC001322

Dixon JM, Liu S (1992) Centrifuge modelling of the propagation of thrust belts. In: McClay KR (ed) Thrust Tectonics. Chapman & Hall, London

Egholm DL, Sandiford M, Clausen Ole R, Nielsen SB (2007) A new strategy for discrete element numerical models: 2. Sandbox applications. J Geophys Res 112, B05204. doi: 10.1029/ 2006JB004558

England P, Molnar P (1997) Active deformation of Asia: from kinematics to dynamics. Science 278: 647–650

England PC, Houseman GA (1986) Finite strain calculations of continental deformation. 2. Comparison with the India-Asia collision zone. J Geophys Res 91: 3664–3676

Fyson WK (1971) Fold attitudes in metamorphic rocks. Am J Sc 270: 373–382

Ganguly J, Dasgupta S, Cheng W, Neogi S (2000) Exhumation history of a section of the Sikkim Himalaya, India: records in the metamorphic mineral equilibria and compositional zoning of garnet. Earth Planet Sc Lett 183: 471–486

Gansser A (1964) Geology of the Himalaya. London: Interscience Publishers, New York

Gerya TV, Stoeckhert B (2002) Exhumation rates of high pressure metamorphic rocks in subduction channels: the effect of rheology. Geophys Res Lett 29: 102-1–102-4

Ghosh SK (1987) Measure of non-coaxiality. J Struct Geol 9: 111–113

Groome WG, Koons PO, Johnson SE (2008) Metamorphism, transient midcrustal rheology, strain localisation and the exhumation of high-grade metamorphic rocks. Tectonics 27, TC1001. doi: 10.1029/2006TC001992

Gulick SPS, Bangs NLB, Shipley TH, Nakamura Y, Moores G, Kuramoto S (2004) Three-dimensional architecture of the Nankai accretionary prism's Imbricate thrust zone of Cape Muroto, Japan: Prism reconstruction via en echelon thrust propagation. J Geophys Res 109, B02105. doi: 10.1029/2003JB002654

Hess HH (1962) History of ocean basins. In: Engel AEJ and others (eds) Petrologic studies – a volume in honor of A. F. Buddington. Geol Soc Am

Houseman GA, McKenzie DP, Molnar P (1981) Convective instability of a thickened boundary layer and its relevance for the thermal evolution of continental convergence belts. J Geophys Res 86: 6115–6132

Jade S, Bhatt BC, Yang Z, Bendick R, Gaur VK, Molnar P, Anand MB, Kumar D (2004) GPS measurements from the Ladakh Himalaya, India: Preliminary tests of plate-like or continuous deformation in Tibet. GSA Bull 116: 1385–1391

Jaeger JC (1969) Elasticity, fracture and flow: with engineering and geological applications. Science paperbacks, Chapman and Hall

Jimenez-Munt I, Platt JP (2006) Influence of mantle dynamics on the topographic evolution of the Tibetan plateau: Results from numerical modelling . Tectonics 25, TC6002. doi: 10.1029/2006TC001963

Konstantinovskaia E, Malavieille J (2005) Erosion and exhumation in accretionary orogens: Experimental and geological approaches. Geochem Geophys Geosys 6, Q02006. doi: 10.1029/2004GC000794

Liu H, McClay KR, Powell D (1992) Physical models of thrust wedges. In: McClay KR (ed) Thrust Tectonics. Chapman and Hall, London

Macaya J, Gonzalez-Lodeiro F, Martinez-Catalan JR, Alvarez F (1991) Continuous deformation, ductile thrusting and backfolding of cover and basement in the Sierra de Guadarrama, Hercynian Orogen of central Spain. Tectonophys 191: 309–321

Mandal N, Chakraborty C, Samanta SK (2001) Flattening in shear zones under constant volume: a theoretical evaluation. J Sruct Geol 23: 1771–1780

Mandal N, Chattopadhyay A, Bose S (1997) Imbricate thrust spacing: experimental and theoretical analyses. In: Sengupta S (ed) Evolution of Geological Structures in Micro- to Macro-Scales. Chapman & Hall, London

Mandal N, Samanta SK, Chakraborty C (2002) Flow and strain patterns at the terminations of tapered shear zones. J Struct Geol 24: 297–309

Marques FO, Cobbold PR (2002) Topography as a major factor in the development of arcuate thrust belts; insights from sandbox experiments. Tectonophysics 348: 247–268

Marshall K (1951) north American Geosyncline. Geol Soc Am Mem 48

Mitra AK, Mahmoud M, Sarkar S, Mandal N (2008) Spatial and temporal variations of the strain fields in orogenic belts: An analysis based on kinematic model. International Conference Volume on Geology: Indian Scenario and Global Context, Indian Statistical Institute (In Press)

Mitra S, Priestley K, Bhattacharyya AK, Gaur VK (2005) Crustal Structure and earthquake focal depths beneath north-eastern India and southern Tibet. Geophys J International 160: 227–248

Mohanty S, Ramsay JG (1994) Strain partitioning in ductile shear zones: an example from a Lower Pennine nappe of Switzerland. J Sruct Geol 16: 663–676

Molnar P (1988) A review of Geophysical constraints on the deep structure of the Tibetan plateau, the Himalaya and the Karakoram, and their tectonic implications. Phil Trans R Soc Lond A 326: 33–88

Molnar P, Tapponnier P, Chen WP (1981) Extensional tectonics in central and eastern Asia: A brief summary. Phil Trans R Soc Lond A 300: 403–406

Mukhopadhyay DK, Misra P (2005) A balanced cross section across the Himalayan frontal fold-thrust belt, Subathu area. Himachal Pradesh, India: thrust sequence, structural nevolution and shortening. J Asian Earth Sc 25: 735–746

Mukul M (2000) The geometry and kinematics of the Main Boundary Thrust and related neotectonics in the Darjiling Himalayan fold-and-thrust belt, West Bengal, India. J Struct Geol 22: 1261–1283

Mulugeta G (1988) Modelling the geometry of Coloumb thrust wedges. J Struct Geol 10: 847–859

Mulugeta G, Koyi H (1987) Three-dimensional geometry and kinamatics of experimental piggyback thrusting. Geology 15: 1052–1056

Narayanswamy S (1966) Tectonics of the Cuddapah Basin. J Geol Soc Ind 7: 33–50

Nelson KD, et al. (1996) Partially molten middle crust beneath southern Tibet: a synthesis of Project INDEPTH results. Science 274: 1684–1688

Persson KS, Sokoutis D (2002) Analogue models of orogenic wedges controlled by erosion. Tectonophysics 356: 323–336

Philip KB (1977) The Evolution of north America. Revised edition, Princeton University Press

Ramberg H (1981) Gravity, Deformation and the Earth's crust in theory, experiments and geological application. (2nd ed) Academic Press, London

Ramsay JG, Graham RH (1970) Strain variation in shear belts. Can J Earth Sci 7: 786–813

Ramsay JG (1980) Shear zone geometry: a review. J Struct Geol 2: 83–99

Rossetti F, Feccenna C, Ranalli G, Storti F (2000) Convergence rate-dependence growth of experimental viscous orogenic wedges. Earth Planet Sc Lett 178: 367–372

Rowan MG, Kligfield R (1992) Kinamatics of large-scale asymmetric buckle folds in overthrust shear: an example from the Helvetic nappes. In: McClay KR (ed) Thrust Tectonics. Chapman & Hall, London

Storti F, Salvini F, McClay K (2000) Synchronous and velocity-partitioned thrusting and thrust polarity reversal in experimentally produced, doubly-vergent thrust wedges: Implications for natural orogens. Tectonics 19: 378–396

Turcotte DL, Schubert G (2001) Geodynamics. Wiley, New York

Twiss RJ, Moores EM (2007) Structural Geology (2nd ed) WH Freeman and company, New York

Vine FD, Matthews DH (1963) Magnetic anomalies over ocenic ridges. Nature 199: 947–949

Wang Q, Zhang PZ, Freymueller JT, et al. (2001) Present-day crustal deformation in China constrained by global positioning system measurements. Science 294: 574–577

Willett SD (1999) Rheological dependence of extension in wedge models of convergent orogens. Tectonophysics 305: 419–435

Wilson JT (1965) A new class of faults and their bearing on continental drift. Nature 207: 343–347

Yin A (2006) Cenozoic tectonic evolution of the Himalayan orogen as constrained by along-strike variation of structural geometry, exhumation history, and foreland sedimentation. Earth Science Reviews 76: 1–131

Zhang PZ, et al. (2004) Continuous deformation of the Tibetan plateau from global positioning system data. Geology 32: 809–812

## 4

# Some Remarks on Melting and Extreme Metamorphism of Crustal Rocks

Michael Brown and Fawna J Korhonen

**Abstract:** Typically melting occurs during decompression in ultra-high-pressure terranes, along the evolution from peak pressure to peak temperature in medium-temperature eclogite-high-pressure granulite terranes and by simple prograde heating in granulite facies and ultra-high-temperature (UHT) metamorphic terranes. The source of heat must be due to one or more processes among thickening and radiogenic heating, viscous dissipation, and heat from asthenospheric mantle. Melt-bearing rocks become porous at a few vol% melt initiating an advective flow regime. As the melt volume approaches and exceeds the melt connectivity transition (~ 7 vol% melt), melt may be lost from the system in the first of several melt-loss events. In migmatites and residual granulites, a variety of microstructures indicates the former presence of melt at the grain scale and leucosome networks at outcrop scale record melt extraction pathways. This evidence supports a model of focused melt flow by dilatant shear failure at low melt volume as the crust weakens with increasing melt production. Melt ascent is initiated as ductile fractures but continues in dykes that propagate as brittle fractures. Crustal rocks undergo melting via a sequence of reactions beginning with minimal melt production at the wet solidus (generally < 1 vol% melt, unless there is influx of $H_2O$-rich fluid). The major phase of melt production is related to hydrate-breakdown melting (perhaps > 50 vol% melt, depending on the fertility of the protolith composition and the intensive variables). At temperatures above the stability of the hydrate, assuming significant melt loss by this point, low-volume melt production continues by consumption of feldspar(s) and quartz at UHT conditions (generally < 10 vol% melt at peak UHTM conditions). Significant melt loss is a contributory factor to achieving UHTs because dehydration of the system limits the progress of heat-consuming melting reactions among the residual phases in the source.

---

Michael Brown (✉)
Laboratory for Crustal Petrology, Department of Geology, University of Maryland, College Park, MD 20742-4211, USA
e-mail: mbrown@umd.edu; phone: +1 301 405 4080; fax: +1 301 314 7970

Fawna J. Korhonen
Laboratory for Crustal Petrology, Department of Geology, University of Maryland, College Park, MD 20742-4211, USA
e-mail: korhonen@umd.edu; phone: +1 301 405 8653; fax: +1 301 314 7970

## 4.1 Introduction

The processes of high-grade crustal metamorphism and melting and differentiation of the continental crust are intimately connected (Brown and Rushmer 2006). Reactions that produce high-grade mineral assemblages in the deep crust typically generate melt, the loss of which yields a refractory lower crust, whereas the ascent and emplacement of this melt to form plutons at shallower levels creates an enriched upper crust (Brown 2007b). Thus, high-grade metamorphic rocks comprise a high proportion of anhydrous minerals formed in association with melt, and since $H_2O$ strongly partitions into the melt there is no free $H_2O$-rich volatile phase attending high-grade metamorphism. Although loss of melt is important for the preservation of these anhydrous mineral assemblages during exhumation (Powell 1983), a small amount of residual melt commonly remains along grain boundaries (Holness and Sawyer 2008). This residual melt facilitates a limited development of retrograde mineral assemblages that are critical to constraining the overall form of *P-T* paths (e.g. Raith and Brown 1996; Raith et al. 1997). Whether the *P-T* paths retrieved from granulite terranes are clockwise or counter clockwise is important in constraining the tectonics of high-grade metamorphic belts (e.g. Brown 2003).

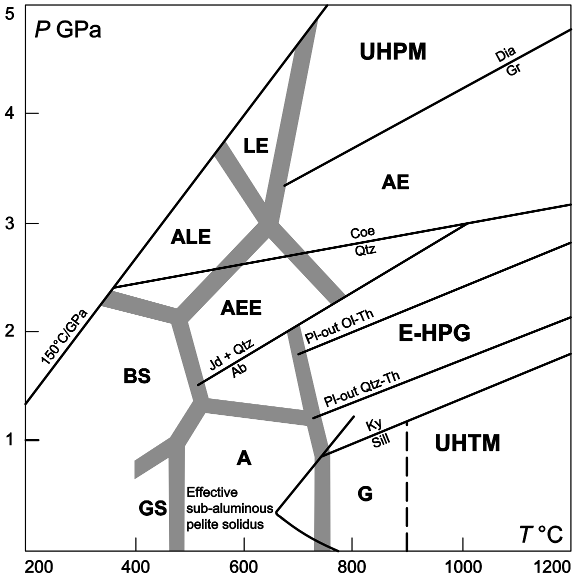

**Fig. 4.1** *P-T* diagram to show the principal metamorphic facies in *P-T* space and the *P-T* ranges of different types of extreme metamorphism. HP-UHP metamorphism includes the following – BS = blueschist, AEE = amphibole-epidote eclogite facies, ALE = amphibole lawsonite eclogite facies, LE = lawsonite eclogite facies, AE = amphibole eclogite facies, UHPM = ultra-high-pressure metamorphism; GS = greenschist facies and A = amphibolite facies; E-HPG = medium temperature eclogite – high-pressure granulite metamorphism; and, G = granulite facies, whereas UHTM = the ultrahigh-temperature metamorphic part of the granulite facies.

In this chapter, we first outline melting at the extremes of the metamorphic *P-T* realm and evaluate possible sources of heat to achieve the temperatures required by high-grade crustal metamorphism, which is critical given the strongly endothermic nature of melting. Next, we briefly summarise those microstructures in residual high-grade metamorphic rocks that indicate the former presence of melt, and we consider in a brief but comprehensive manner the mechanism of melt extraction and ascent in continental crust. We follow this review with an analysis of the melting process in crustal rocks, including the initiation of melting, wet melting and hydrate-breakdown melting, and a discussion of the implications of the melting process for the trace element chemistry of melts, and for zircon and monazite chronology in high-grade metamorphic rocks. Then we investigate the processes of melting and melt loss using phase equilibria modelling of average pelite and aluminous greywacke compositions. To finish we evaluate the importance of melt loss in achieving the extreme conditions of ultra-high-temperature metamorphism (UHTM), and we suggest some directions for future research.

## 4.2 Melting at the Extremes of the Metamorphic *P-T* Realm

Traditionally metamorphic petrologists have divided the field of *P-T* conditions recorded by crustal rocks into mineral facies represented by a common group of mineral assemblages that occur repeatedly and that we infer register equilibration within a limited range of *P-T* conditions (Fig. 4.1). The success of the mineral facies concept demonstrates that peak mineral assemblages are potentially robust recorders of metamorphic *P* and *T*, particular at high *P-T* conditions. Even where significant retrogression has occurred, the preservation of prograde, peak and retrograde mineral assemblages as inclusions in refractory minerals such as garnet and zircon enables the facies associated with peak metamorphism to be determined. This robustness reflects prograde dehydration (up to middle amphibolite facies and during low d*T*/d*P* metamorphism) and melt loss (at upper amphibolite and granulite facies), which produces nominally anhydrous mineral assemblages that are difficult to retrogress or overprint without an influx of hydrous fluid. These peak mineral assemblages show that the extremes of *P* and *T* recorded by crustal rocks are much higher than we previously thought (e.g. Turner 1968).

Some granulite facies rocks record temperatures >900°C at pressures of 0.6–1.3 GPa (UHTM, Fig. 4.1; e.g. Harley 1998a, 2008; Brown 2007a; Kelsey 2008) and some eclogite facies rocks record pressures above the quartz to coesite reaction, >2.5–3.0 GPa, possibly up to 10 GPa at temperatures of 600–1000°C (UHPM, Fig. 4.1; e.g. Chopin 2003; Brown 2007a; Liu et al. 2007). The field of transitional $P$-$T$ conditions between these two extreme facies is referred to as medium-temperature eclogite-high-pressure granulite metamorphism (E-HPGM, Fig. 4.1; e.g. O'Brien and Rötzler 2003; Brown 2007a). The name of this field reflects the overlap between plagioclase-bearing and plagioclase-absent assemblages in rocks of basaltic composition at $T > 650°C$ and at pressures between the sillimanite to kyanite and the quartz to coesite reactions (Fig. 4.1). Based on the temperature ranges of extreme metamorphism we may anticipate that crustal rocks are likely to have melted in many cases. In some high-temperature UHPM terranes melting is likely close to peak temperatures and in many UHPM terranes melting may occur during exhumation (e.g. Hermann and Green 2001; Hermann 2002; Vielzeuf and Schmidt 2001; Schmidt et al. 2004; Auzanneau et al. 2006; Lang and Gilotti 2007; Osanai et al. 2008; Xia et al. 2008). In most E-HPGM terranes melting is likely to occur along the evolution from peak $P$ to peak $T$ (e.g. Rushmer 1993; O'Brien and Rotzler 2003). In all UHTM terranes melting will occur simply by prograde heating (e.g. Vielzeuf and Holloway 1988; Waters 1988; Vielzeuf and Montel 1994; Montel and Vielzeuf 1997; Carrington and Harley 1995; Brown and Raith 1996; Raith et al. 1997; Harley 1998b, 2008; White et al. 2001; Moraes et al. 2002; Guernina and Sawyer 2003; Baldwin and Brown 2008).

## 4.3 Sources of Heat for High-grade Crustal Metamorphism and Melting

The processes that generate the heat necessary to drive high-grade metamorphism and crustal melting in a specific metamorphic belt remain obscure in many cases, although the heat must be due to one or more processes among thickening and radiogenic heating, viscous dissipation and heat from asthenospheric mantle. Radiogenic heating is important and sometimes may be sufficient, particularly if time for thermal equilibration is available after crustal thickening (Le Pichon et al. 1997; Gerdes et al. 2000; Jamieson et al. 2002; Andreoli et al. 2006; McLaren et al. 2006; McKenzie and Priestley 2008). The observation that regional metamorphic belts typically contain abundant crust-derived intrusive rocks at shallow levels in the crust leads to the postulate that intracrustal magmatism increases the regional thermal gradient at shallow levels. This postulate is consistent with observations from several metamorphic belts that medium-pressure regional metamorphism grades with decreasing crustal depth into regional-scale contact metamorphism (e.g. Brown and Solar 1999). In addition, in accretionary orogenic systems ridge subduction may introduce hot asthenospheric mantle to the base of the overriding plate to generate anomalous high-temperature conditions in the forearc leading to anatexis at shallow crustal levels (Brown 1998a, 1998b; Groome and Thorkelson 2008).

Heating by viscous dissipation is likely to be important in subduction-to-collision orogenic systems (Leloup and Kienast 1993; Kincaid and Silver 1996; Stüwe 1998; Leloup et al. 1999; Burg and Gerya 2005; Hobbs et al. 2007; Stüwe 2007), although to be an effective mechanism requires the lithosphere is initially strong (e.g. a differential stress of 100–300 MPa). There is a positive correlation in thermo-mechanical models between the overall intensity of viscous heating in crustal rocks and the instantaneous convergence rate (Burg and Gerya 2005). This correlation suggests that viscous heating makes an important contribution ($> 0.1\ \mu Wm^{-3}$) to the heat budget in the crust when the convergence rate exceeds 1 cm/yr especially if the lower crust is strong. On this basis, it is plausible that heating by viscous dissipation may be a dominant heat source early in subduction-to-collisional orogenesis if convergence rates are fast (e.g. the Himalayas), in which case it will also control the mode of deformation (Burg and Schmalholz 2008).

Apparent thermal gradients that significantly exceed 750°C/GPa are retrieved from UHTM terranes (Brown 2007b), but these gradients cannot be sustained to mantle depths in overthickened crust without exceeding the peridotite solidus. There are two alternative ways to interpret this observation. First, we may infer that the asthenosphere was close to the Moho, which could lead to transient thermal gradients up to the conductive limit (1000°C/GPa, potentially higher over a plume head; Stüwe 2007). Such a scenario is plausible if convective instability removes a lithosphere root (Platt and England 1994; Platt et al. 1998, 2003) or if a subducting slab breaks off (Davies and von Blanckenburg 1995). Second, we may infer that there was sufficient heat advected into the crust with mantle-derived magma (e.g. Sandiford and Powell 1991; Stüwe 2007), for which, unfortunately, evidence is generally scarce (e.g. Harley 2004; Baldwin and Brown 2008). An example occurs in the Bohemian Massif, where there appears to be a genetic relationship between the late-Variscan ultrapotassic magmatism and UHTM in the Moldanubian zone (Janousek and Holub 2007; Leichmann et al. 2007), although the heat in this case is due to asthenospheric upwelling following delamination. Underplating by basaltic magma is commonly invoked to provide heat (e.g. Dewey et al. 2006), but the temporal relations between extension, crustal melting and emplacement of basic magma sometimes are ambiguous (e.g. Barboza et al. 1999; Peressini et al. 2007). Modelling studies suggest that heating by multiple intraplating of dykes and sills may be effective at melting the lower crust in continental arcs (e.g. Jackson et al. 2003; Dufek and Bergantz 2005; Annen et al. 2006).

Currently, the major mountain belts of the circum-Pacific orogenic systems are located in former subduction zone backarcs. These areas have high heat flow for continental crust with average radiogenic heat production of

69–85 ± 16 mWm$^{-2}$ (Hyndman et al. 2005; Currie and Hyndman 2006; Currie et al. 2008). Geophysical data summarised by Currie and Hyndman (2006) indicate Moho temperatures of 800–900°C in backarcs, uniformly high temperatures in the shallow mantle (~ 1200°C) and a thin lithosphere (~ 60 km thick over backarc widths of 250 to >900 km) in comparison with Moho temperatures of 400–500°C and lithosphere 200–300 km thick for cratons. The difference results in backarc lithosphere being at least an order of magnitude weaker than cratons. These heat flow values for circum-Pacific orogenic systems are similar to the average value of 65 ± 10 mWm$^{-2}$ for Variscan crust of the Iberian mainland (Fernandez et al. 1998) but lower than the range of 90–150 mWm$^{-2}$ for a limited number of measurements from Tibet (Francheteau et al. 1984). The reason subduction zone backarcs are hot may be principally due to thin lithosphere and shallow convection in the asthenosphere of the mantle wedge. Convection is inferred to result principally from a reduction in viscosity induced by water from the underlying subducting plate (Currie and Hyndman 2006, 2007; Currie et al. 2008; Schellart 2007). The high temperatures associated with circum-Pacific orogenic systems decay over a timescale of about 300 Ma following termination of subduction by collision (Currie and Hyndman 2006). This timescale means that most circum-Pacific mountain belts are broad zones of long-lived tectonic activity because they remain sufficiently weak to deform by the forces developed at plate boundaries.

## 4.4 Microstructures Indicative of the Former Presence of Melt in Residual High-grade Metamorphic Rocks

Microstructures in natural anatectic systems provide evidence of the former presence of melt in grain-scale pores (e.g. Brown et al. 1999; Sawyer 1999; Brown 2001a, 2001b; Albertz et al. 2005). Melting may be inferred using the following criteria: mineral pseudomorphs after grain-boundary melt films and pockets [in contact migmatites (e.g. Rosenberg and Riller 2000; Marchildon and Brown 2001, 2002; Holness and Sawyer 2008), in regional migmatites (e.g. Marchildon and Brown 2003; Holness and Sawyer 2008) and in granulites (e.g. Sawyer 1999, 2001; Brown 2002; Guernina and Sawyer 2003; Holness and Sawyer 2008)]; magmatic rims on subsolidus cores of grains [e.g. rational faces, overgrowths of different compositions (e.g. Marchildon and Brown 2001, 2002; Sawyer 2001)] or magmatic microstructures in leucosomes (e.g. Vernon and Collins 1988; Brown 2002); spatial distribution of like and unlike phases [i.e., mineral phase distribution (Ashworth and McLellan 1985)]; sub-parallel intra-granular fractures (e.g. feldspar-filled fractures in quartz; Rosenberg and Riller 2000); and, annealed microfractures (e.g. in quartz; Watt et al. 2000; Marchildon and Brown 2001, 2002).

## 4.5 The Mechanism of Melt Extraction and Ascent in Continental Crust

The processes of melt extraction and ascent occur through a depth interval of crust that is unlikely to be < 10 km and may be several times larger (Brown 2004; 2007b, 2008). The anatectic front (the wet solidus) at the top of the anatectic (or suprasolidus) zone is a dynamic surface; it shallows during the later stages of syn-deformational prograde heating and deepens during early retrograde cooling. As a result, there may be variations of melt production in three dimensions and in the volume of material transported through any particular point within the suprasolidus volume (Brown 2004). These variations give rise to a zonal arrangement beneath a level of pluton emplacement in the orogenic crust, whereby a zone of migmatite commonly overlies a zone of residual granulite (Brown and Solar 1999; Brown 2004).

Migmatites that characterise the upper part of the anatectic (suprasolidus) zone tend to be complex and polygenetic, suggesting that this crustal level may be a zone of both melting and melt transfer, with possible interactions between the ascending and locally produced melts. This upper part of the anatectic (suprasolidus) zone is also the first part to stagnate during exhumation and cooling. In contrast, the higher temperatures and larger melt proportions generated in the lower part of the anatectic zone enable efficient melt loss with consequent dehydration generating residual granulites with minimal leucosome. In the migmatites of the upper part of the anatectic (suprasolidus) zone as well as in the deeper residual granulites, leucosome may have cumulate or fractionated compositions; only rarely does the leucosome represent a sample of the original anatectic melt. Furthermore, granite in dykes that traverse the migmatites may be polyphase, recording multiple pulses of melt transport through the anatectic (suprasolidus) zone.

Based on field observations of migmatites and residual granulite facies metamorphic complexes, melt extraction at the outcrop scale is inferred to occur by lateral melt flow in melt-induced deformation band networks to ductile opening-mode fractures that evolve to dykes. The deformation band networks form by linking among shear bands, compaction bands and dilation bands; they allow melt accumulation and form a reservoir for melt storage as well as providing the mechanism for deformation-assisted melt transport to dykes (Brown and Marchildon 2003; Brown 2004, 2005). The dykes form by opening-mode failure along zones of localised porosity increase or by pore growth and coalescence or they may propagate from shear bands (Regenauer-Lieb 1999; Eichhubl et al. 2001; Simakin and Talbot 2001; Du Bernard et al. 2002; Eichhubl and Aydin 2003; Brown 2004, 2005). These ductile fractures grow until they reach a critical length, at which point brittle fracture processes will dominate to allow magma transport through the subsolidus crust (Brown 2008). Interaction among dykes may focus magma flow into a smaller number of more widely spaced dykes during ascent (Ito and Martel 2002).

Regional-scale crustal melting is a process that occurs in response to crustal thickening and exhumation or due to the input of mantle heat. Heat generally will be the principal rate control at the crustal scale, whereas deformation due to regional stress will be the mechanism enabling segregation and extraction (Brown 1994, 2007b). For a pelite protolith it is likely that 80–90% of melt generated is extractable with < 20% remaining on grain boundaries. Segregation by intragranular porous flow probably occurs on a similar time scale to melting, but migration of segregated melt by channel flow in veins is faster. Gravity-driven and/or shear-enhanced compaction of the solid matrix is likely to be rate controlling at the outcrop scale (Rutter 1997; Rutter and Mecklenburg 2006). Rates of ascent vary according to the mechanism of ascent, but there is consensus that some form of conduit flow is likely the dominant mechanism and that the time scale for ascent is short (Brown 2007b). Emplacement of individual melt batches occurs on a similar time scale to ascent—hundreds to thousands of years—whereas pluton construction may take hundreds of thousands to several millions of years and require hundreds to thousands of batches of melt.

## 4.6 The Melting Process in Crustal Rocks

Earth's continental crust is composed of a diversity of rocks that neither melt equally for a particular *P-T* condition or temperature interval nor behave uniformly in response to stress. Common crustal rocks may melt at temperatures as low as 650°C, if $H_2O$-rich fluid is present [wet melting (high $a_{H2O}$ melting)]. However, 'fluid-absent' melting reactions [hydrate-breakdown melting (moderate-to-low $a_{H2O}$ melting)] are responsible for the production of most crust-derived granite (*sensu lato*) melts and significant melt volumes require temperatures above 750–800°C. The amount of $H_2O$-undersaturated melt produced varies according to protolith composition and mineralogy, particularly the hydrous mineral species and mode, the depth of melting (pressure) and heat input (temperature), and the length of time at temperatures above the solidus. Common crustal protoliths yield 10–50 vol% of $H_2O$-undersaturated leucogranite, trondhjemite, granodiorite or tonalite melt at temperatures attainable during orogenesis (e.g. Clemens 2006).

### 4.6.1 The Initiation of Melting

Under equilibrium conditions in an isotropic crust, melting begins at multiphase grain junctions that include quartz and feldspar, and a hydrate phase. However, earth's crust is anisotropic and in a state of stress, and variations in bulk composition and grain size influence the sites at which melting begins. Thus, differential stress varies within any particular volume of crust and variations in differential stress give rise to pressure gradients throughout this volume of crust. It follows that equilibrium conditions cannot be modelled using hydrostatic thermodynamics, and in using modelling based on hydrostatic thermodynamics, we should acknowledge this simplification.

Melting may begin at sites of lower or higher resolved normal stress, once the initial thermal overstep is close to that required to overcome the activation energy for the particular melting reaction. For wet melting (solidus with negative *dP/dT*), the start of reaction is more likely at sites of higher resolved normal stress, whereas for hydrate-breakdown melting (solidus with positive *dP/dT*), the start of reaction is more likely at sites of lower resolved normal stress (Brown and Solar 1998, pp. 212–213). Deformation leads to dissipation of energy as heat, which may be significant in determining possible sites of initial melting in addition to the resolved normal stress, but this control has not been investigated for suprasolidus rocks (Hobbs et al. 2007).

Once melting begins, within the first few volume percent melt of melt production the melt reaches the melt connectivity transition in all common crustal protoliths in both non-deforming and deforming environments (Laporte et al. 1997). As melting progresses beyond the melt connectivity transition, the development of permeability and gradients in melt pressure allow melt to flow down pressure. The formation of gradients in melt pressure implies that melt pressure and confining stress are not equal. Thus, there will be differences in stress at melt-solid (lower stress) and solid-solid (higher stress) interfaces. To investigate the implications of these stress differences in relation to melting requires the application of non-hydrostatic thermodynamics. In non-hydrostatic thermodynamics, the local resolved normal stress at an interface or surface controls the chemical potentials, which will lead to important feedbacks as melting develops at sites of higher or lower resolved normal stress. However, these implications have not yet been evaluated for suprasolidus rocks.

### 4.6.2 Wet Melting

At a regional scale, there is only a small amount of free hydrous phase in high-grade rocks immediately below the solidus in the middle and lower crust (<1 vol%). Melting at the wet solidus immediately consumes this small volume of free hydrous phase. Two generalised examples of fluid-consuming reactions for metapelites are Ms + Pl (±Kfs) + Qtz + $H_2O$ = Liq and Ms + Bt + Pl + Qtz + $H_2O$ = Liq [mineral abbreviations are from Kretz (1983), plus Liq for melt].

Once fluid-consuming melting reactions have used up the available water, further melting proceeds by fluid-conserving (hydrate-breakdown) melting reactions that produce progressively more water-undersaturated liquid with increasing temperature. The negative slope of the solidus for wet melting limits vertical migration of the melt (it will crystallise during limited decompression to the solidus) whereas this is not the case for water-undersaturated melting (because hydrate-breakdown melting reactions have positive slopes in *P*-*T* space at crustal pressures).

Inconsistency between the observed volume of (apparently) locally derived leucosome and the maximum expected for the calculated peak *P*-*T* conditions assuming no melt loss may be indicative of infiltration of hydrous fluid to promote extensive wet melting. For example, local introduction of water may occur in the inner zone of contact aureoles around granites and mafic intrusions (Pattison and Harte 1988; Symmes and Ferry 1995; Johnson et al. 2003). In addition, water may infiltrate from adjacent units that have a higher solidus or along zones of localised high-strain deformation or regionally (Sibson 1986; Wickham and Taylor 1987; McCaig et al. 1990; Upton et al. 1995; Selbekk et al. 2000; Johnson et al. 2001; Connolly and Podladchikov 2004; Slagstad et al. 2005; White et al. 2005; Berger et al. 2008; Florian et al. 2008).

Given the limited porosity of high-grade subsolidus crust, deformation-enhanced dynamic permeability is likely required to facilitate fluid infiltration and pervasive melt migration (e.g. Upton et al. 1995; Connolly and Podladchikov 2004; Hasalová et al. 2008a, 2008b). Zones of regional-scale transpressive deformation may be particularly important in promoting fluid-enhanced melting and melt flow [e.g. the St. Malo migmatite belt, France (Brown 1995; Milord et al. 2001) and the Tumbledown and Weld anatectic domains in Maine, USA (Brown and Solar 1999; Solar and Brown 2001)].

In convergent tectonic settings in general, relaxation of the yield stress developed in the brittle portion of the crust may result in a depth interval below the brittle-ductile transition characterised by an inverted pressure gradient (Petrini and Podladchikov 2000; Stüwe et al. 1993; Stüwe and Sandiford 1994). At depths where this inverted pressure gradient is less than the hydrostatic gradient of an interstitial fluid, a hydrous fluid that is subject to the confining pressure will migrate downward and stagnate where the rock pressure gradient equals the hydrostatic fluid gradient (Connolly and Podladchikov 2004). This condition defines a depth of tectonically induced neutral buoyancy that also acts as a barrier to upward fluid flow. In combination with dynamic downward propagation of the brittle-ductile transition during the early stages of orogenic thickening, this phenomenon provides a mechanism to sweep upper crustal hydrous fluids into the lower crust to promote melting as prograde heating evolves to peak temperatures.

Alternatively, recycling the hydrous fluid exsolved during melt ascent removes the need for hydrous fluid influx. Evidence to support recycling of hydrous fluid comes from metamorphic core complexes of the Canadian Rockies where there is a remarkable uniformity of mineral $\delta^{18}O$ values in the middle continental crust beneath detachment faults (Holk and Taylor 2000). These zones of pervasive homogenisation in $^{18}O$-$^{16}O$ are interpreted to result from exchange with magmatic or metamorphic hydrous fluid, and this same hydrous fluid appears to have promoted crustal melting. Holk and Taylor (2000) suggest that melting of metapelites and greywackes beneath the Canadian Rockies began at *P*-*T* of ~ 0.8 GPa and ~ 750°C in response to influx of hydrous fluid. They infer derivation of the hydrous fluid from dehydration reactions deeper in the crust and muscovite breakdown locally. As the resulting $H_2O$-rich melt ascends adiabatically through the crust it will exsolve $H_2O$. This $H_2O$ is available to exchange oxygen with subsolidus rocks and catalyse melting. Melting at deeper levels and $H_2O$ exsolution at shallower levels occurs simultaneously in different parts of the crustal section during exhumation, until final crystallisation of leucogranite in plutons occurred at much shallower levels in the crust where the stage of exsolution of $H_2O$ during final crystallisation enabled $^{18}O$-$^{16}O$ exchange with the subsolidus country rocks.

### 4.6.3 Hydrate-breakdown Melting

Hydrate-breakdown melting occurs over a range of temperature after an initial insignificant wet melting step that generates minimal melt from the small amount of free water (<1 vol%) at the water saturated solidus. With increasing temperature, the crust progressively encounters muscovite and biotite breakdown in metasedimentary and (leuco-) granite protoliths, biotite with or without hornblende breakdown in quartzo-feldspathic (e.g. calc-alkaline) plutonic rocks and hornblende breakdown in amphibolites (e.g. White et al. 2004; Clemens 2006). Generalised examples of hydrate-breakdown melting reactions are Ms + Pl + Qtz = Als + Kfs + Liq, Bt + Als + Qtz = Grt/Crd + Kfs + Liq, Bt + $Pl_1$ + Als + Qtz = Grt/Crd + $Pl_2$ (± Kfs) + Liq, Bt + Pl + Qtz = Opx (± Cpx ± Grt) + Liq and Hbl + Qtz = Pl + Opx + Cpx (± Grt) + Liq.

Crustal rocks are complex multicomponent systems, in which the melting reactions are multivariant. Hydrate-breakdown melting has been investigated by experiments on natural and synthetic samples, reviewed by Clemens (2006), and by phase equilibria modelling, as discussed by Holland and Powell (2001), White et al. (2001, 2004, 2007), White and Powell (2002), White (2008). The experimental and modelling approaches are complementary to each other, as demonstrated by Johnson et al. (2008).

In phase equilibria modelling, we investigate the phase relations and chemography of melting for a range of bulk compositions using calculated suprasolidus equilibria in a simplified model system. For example, metasedimentary rock compositions typically have been modelled in the NCKFMASHTO model system ($Na_2O$, CaO, $K_2O$, FeO, MgO, $Al_2O_3$, $SiO_2$, $H_2O$, $TiO_2$, $Fe_2O_3$, sometimes with MnO). Phase topologies and mole proportions of phases are calculated using an internally consistent thermodynamic dataset (Holland and Powell 1998), a thermodynamic model for silicate melt (Holland and Powell 2001; extended by White et al. 2001), appropriate *a-x* models for the phases of interest (e.g. White et al. 2007) and the software THERMOCALC (Powell et al. 1998). Examples of this approach include White and Powell (2002), Johnson et al. (2003), Johnson and Brown (2004) and White et al. (2004, 2005, 2007).

A modelling study typically involves constructing a *P-T* grid for a simple model chemical system (e.g. KFMASH) to identify the main invariant and univariant phase equilibria that control the more complex high variance phase equilibria in natural rocks (e.g. White et al. 2007; White 2008). The natural rocks are modelled using the most complete model chemical system possible, and the high variance equilibria are visualised using *P-T* pseudosections (equilibrium phase diagrams for a fixed bulk composition), *T-X* and *P-X* diagrams or projections that use conjugate thermodynamic variables as appropriate (e.g. White and Powell 2002; Johnson et al. 2004; Powell et al. 2005).

The volume of melt produced varies as a function of *P*, *T*, *t* and hydrate mode in the protolith, but common rock types (metapelites and metagreywackes, and some calc-alkaline plutonic rocks and amphibolites) may yield 10–50 vol% of water-undersaturated melt at attainable crustal temperatures (Vielzeuf and Vidal 1990; Brown and Rushmer 2006). The compositions of the melts may range from leucogranite to trondhjemite and granodiorite to tonalite, depending on the chemistry and mineralogy of the source rocks and the temperature of melting.

Peraluminous (leuco-) granites are the common product of crustal melting in collisional orogenic systems and in experiments on melting crustal protoliths (e.g. Patiño-Douce 1999). However, the chemistry of many granites *sensu lato*, particularly the more mafic 'S-type' granites is not matched by experimental melt compositions and dissolution of entrained residue or peritectic products of melting is required to match their chemistry (e.g. Sawyer 1996; Stevens et al. 2007).

In general, the solid products of hydrate-breakdown reactions (e.g. orthopyroxene, garnet and cordierite in metasedimentary protoliths and pyroxene in basaltic protoliths) have difficulty nucleating. Thus, it is energetically favourable for diffusion-controlled melting to continue at initially established sites and for the solid products to continue to grow at these sites (Waters 1988; Powell and Downes 1990; Brown 1994, 2004; Brown and Dallmeyer 1996; White et al. 2004).

The common occurrence of pristine to only weakly-retrogressed residual granulites suggests melt has been lost from the lower crust (e.g. White and Powell 2002; Guernina and Sawyer 2003), removing the dissolved water, consistent with the widespread occurrence of (leuco-) granites in the upper crust and partitioning of water into the melt. In a closed system, cooling potentially will lead to retrogression by reaction between melt and/or exsolved water and residue, unless segregation has separated them sufficiently (Brown 2002).

### 4.6.4 Implications for the Trace Element Chemistry of Melts, and for Zircon and Monazite Chronology in High-grade Metamorphic Rocks

The stability of various rock-forming minerals exerts a strong control on melt chemistry as the phase assemblages evolve along a prograde *P-T* path, particularly with respect to some of the petrogenetically significant trace element concentrations (Harris and Inger 1992; Inger and Harris 1993). In addition, the stability of the ferromagnesian rock-forming minerals commonly controls the availability of those elements necessary to form zircon or monazite as the phase assemblages evolve along a retrograde *P-T* path (Fraser et al. 1997; Bingen and von Breemen 1998; Bingen et al. 2001; Degeling et al. 2001). Finally, accessory phases such as zircon, monazite and apatite host a large proportion of the trace element budget for granite melts (Watt and Harley 1993; Bea 1996; Bea and Montero 1999). These accessory phases commonly are preferentially associated with the ferromagnesian rock-forming minerals, either along the grain edges or as inclusions. As a result, the range of stability of these phases under suprasolidus conditions likely will control the availability of accessory phases to contribute to the chemistry of the melt (Brown 2007b), although kinetic constraints also play a critical role in dissolution rates (Watson 1996; Hanchar and Watson 2003).

Biotite is stable at low-to-moderate pressures and ordinary granulite facies temperatures (< 900°C), although F will tend to stabilise it to UHTs in nature. Since biotite commonly may include accessory phases such as zircon and monazite, the stability of biotite is likely to exert a strong control on the trace element chemistry of the melt as well as the degree of inheritance in zircon in leucosomes and upper crustal granites. In contrast, garnet is stable at moderate-to-high pressures and moderate-to-UHTs. The development of garnet as a peritectic product of biotite-breakdown melting exerts a strong control on the rare earth element (REE) chemistry of the melt (Brown 2007b). Furthermore the presence of garnet exerts a strong control on the REE chemistry of phases that may grow in equilibrium with it during cooling and on those phases that may replace it along the retrograde *P-T* evolution (Rubatto 2002; Hermann and Rubatto 2003; Clarke et al. 2007).

Zircon and monazite incorporate elements that make them suitable for dating crystallisation as well as determining the environment of growth (Williams 2001; Williams and Jercinovic 2002; Watson 1996; Montel et al. 1996; Harley et al. 2007; Harley and Kelly 2007). In granulites, rather simplistic interpretations of zircon ages in relation to the *P-T* evolution are common and follow an assumption that the ages retrieved date the peak of metamorphism. Then these metamorphic ages have been used to constrain geodynamic interpretations.

However, recent advances have enabled links to be made between the age retrieved and the *P-T* point or segment along the prograde or retrograde evolution where zircon or monazite crystallisation occurred. These advances include the use of trace element partitioning between coeval zircon and garnet or zircon and orthopyroxene (Rubatto 2002; Rubatto and Hermann 2003; Möller et al. 2003; Rubatto et al. 2006; Möller et al. 2007), and accessory phase trace element thermometry (Watson et al. 2006; Baldwin et al. 2007; Ferry and Watson 2007). In addition, the thermodynamic modelling of accessory phase stability by Kelsey et al. (2008) has provided a framework to understand differences in zircon and monazite ages as a function of cooling rate. As a result, the simplistic interpretation of zircon and monazite ages as dating the peak of metamorphism is no longer acceptable, and it has been shown that many zircon ages record an event along the retrograde *P-T* path (e.g. Kelly and Harley 2005; Harley and Kelly 2007; Baldwin and Brown 2008).

This approach is particularly useful in dating accessory phases located in leucosome in residual granulites and migmatites or in retrograde reaction microstructures, where the age and temperature of crystallisation provide a data point along the retrograde *P-T* path (Tompkins et al. 2005). These advances have significantly improved the utility of accessory phase dating in granulites and UHT metamorphic rocks (e.g. Whitehouse and Platt 2003; Harley and Kelly 2007). As a result, we can be more confident in the use of these ages in the characterisation of high-temperature processes and in constraining tectonic models (Fitzsimons et al. 1997; Cocherie et al. 1998; Crowley and Ghent 1999; Schaltegger et al. 1999; Williams et al. 1999; Hoskin and Black 2000; Rubatto et al. 2001, 2006; Möller et al. 2002; Kelley et al. 2006; Baldwin and Brown 2008).

## 4.7 Phase Equilibria Modelling of Pelite and Aluminous Greywacke

For most ordinary granulites the *P* of metamorphism around peak *T* is in the range 0.4–1.0 GPa, clustering around 0.8 GPa (Pattison et al. 2003; Brown 2007a), whereas for UHTM rocks the *P* of metamorphism around peak *T* is in the range 0.7–1.4 GPa, clustering around 1.0 GPa (Brown 2007a). In nature it is likely that melt loss will occur at the melt connectivity transition around 7 vol% melt, and that there will be periodic melt loss in a cyclic fashion as melt volume increases to the melt connectivity transition several times (Brown 2007b). For the modelling, we will consider the suprasolidus part of the prograde evolution to occur at $P = 0.9$ GPa, and melt loss to occur as a single event at the biotite-out line at a $P = 0.9$ GPa. For alternative scenarios of melt loss along a *P-T* path the interested reader is referred to White and Powell (2002).

### *4.7.1 Methodology*

In this section, we use calculated pseudosections for an average amphibolite facies pelite (Table 4.1; Ague 1991, his Table 2, amphibolite) and a peraluminous greywacke (Table 4.1; Sawyer 1986, his sample ES36) to investigate the process of melting and the effects of melt loss on the formation and preservation of high-grade metamorphic assemblages in migmatites and residual granulites. The calculations were undertaken using THERMOCALC 3.26 (Powell and Holland 1988; updated August 2007) and the internally consistent thermodynamic dataset of Holland and Powell (1998; dataset tcds55, created in November 2003). The calculations were undertaken in the chemical system $Na_2O$ - CaO - $K_2O$ - FeO – MgO - $Al_2O_3$ - $SiO_2$ - $H_2O$ - $TiO_2$ -$Fe_2O_3$ (NCKFMASHTO).

We used the most recently available *a-x* models as follows: for biotite and melt, White et al. (2007); for orthopyroxene and spinel-magnetite, White et al. (2002); for garnet, Dienier et al. (2008); for orthoamphibole, Dienier et al. (2007); for cordierite, Holland and Powell (1998); for K-feldspar and plagioclase, Holland and Powell (2003); for white mica, Coggon and Holland (2002); and, for ilmenite-hematite, White et al. (2000). The aluminosili-

**Table 4.1** Bulk compositions used in the construction of pseudosections

| | | | | | | wt% | | | | | |
|---|---|---|---|---|---|---|---|---|---|---|---|
| Figure | Protolith | $H_2O$ | $SiO_2$ | $Al_2O_3$ | CaO | MgO | $Fe_2O_3$* | MnO | $K_2O$ | $Na_2O$ | $TiO_2$ | $Fe^{3+}/Fe^{2+}$ |
| Fig. 4.2 | Pelite | 3.02 | 56.25 | 20.18 | 1.54 | 3.23 | 5.58 | 0.18 | 4.02 | 1.80 | 1.05 | 0.33 |
| Fig. 4.5 | Greywacke | 1.45 | 67.58 | 14.66 | 2.81 | 2.48 | 5.07 | 0.07 | 2.28 | 3.57 | 0.50 | - |

| | | | | | | Normalised mol% | | | | |
|---|---|---|---|---|---|---|---|---|---|---|
| Figure | Protolith | $H_2O$ | $SiO_2$ | $Al_2O_3$ | CaO | MgO | FeO | $K_2O$ | $Na_2O$ | $TiO_2$ | O |
| Fig. 4.2 | Pelite | 5.65 | 60.38 | 12.77 | 1.77 | 5.17 | 7.53 | 2.76 | 1.87 | 0.84 | 1.25 |
| Fig. 4.3 | Pelite | 0.23 | 54.73 | 15.23 | 2.18 | 8.41 | 12.25 | 1.92 | 1.54 | 1.41 | 2.10 |
| Fig. 4.4 | Pelite | 0.00 | 41.23 | 16.81 | 2.31 | 13.13 | 18.92 | 0.44 | 1.38 | 2.32 | 3.45 |
| Fig. 4.5 | Greywacke | 2.75 | 71.17 | 9.10 | 3.17 | 3.90 | 4.02 | 1.53 | 3.64 | 0.40 | 0.12 |
| Fig. 4.6 | Greywacke | 0.18 | 72.18 | 9.37 | 3.67 | 4.58 | 4.50 | 1.12 | 3.76 | 0.49 | 0.15 |
| Fig. 4.7 | Greywacke | 0.00 | 72.10 | 9.42 | 3.97 | 4.87 | 4.19 | 0.82 | 3.91 | 0.56 | 0.17 |

Pelite protolith composition (wt%) taken from Ague (1991, average amphibolite facies pelite). Greywacke protolith composition (wt%) is sample ES36 from Sawyer (1986; total iron as $Fe_2O_3$ (wt%), $Fe^{3+}/Fe^{2+}$ ratio not reported); the normalised mol% composition is taken from Johnson et al. (2008). MnO is not included in the phase equilibria modelling and therefore is not included in the normalised mol%.

cates, quartz, and aqueous fluid ($H_2O$) are pure end-member phases. The mineral abbreviations are as follows (after Kretz 1983): Bt – biotite; Crd – cordierite; Ged – gedrite; Grt – garnet; $H_2O$ – aqueous fluid; Ilm – ilmenite (hematite proportion < 0.5); Kfs – K-feldspar; Ky – kyanite; Liq – silicate liquid/melt; Mag – magnetite; Ms – white mica; Opx – orthopyroxene; Pl – plagioclase; Qtz – quartz; Sil – sillimanite; Spl – spinel. At UHT conditions the miscibility between magnetite and spinel results in an aluminous spinel (*sensu lato*), which is simply labelled spinel (Spl) on the pseudosections.

Modelled $H_2O$ contents in the protolith bulk compositions were adjusted to just saturate the solidus with hydrous fluid contents < 1 mol% at $P = 0.9$ GPa. Given the decrease in solubility of $H_2O$ in melt with decreasing $P$, this will result in overestimation of melt vol% in the phase assemblages at lower pressures than 0.9 GPa.

The NCKFMASHTO system is currently the most realistic approximation of rock compositions within which modelling at suprasolidus conditions can be undertaken (White et al. 2003, 2007). Table 4.1 lists the two protolith bulk compositions in oxide wt% and the protolith and residual compositions after the melt loss events in normalised mol% NCKFMASHTO components. The modelling does not include MnO, which is negligible in the protolith bulk compositions considered (< 0.2 wt%, Table 4.1). Other minor components, such as F and Cl in biotite or ZnO and $Cr_2O_3$ in spinel-magnetite also are not included in the modelling. Sapphirine was not considered in the modelling, as the current *a-x* model for sapphirine (Kelsey et al. 2004) does not include $Fe^{3+}$. Therefore, the results of our calculations for the pelite composition may yield metastable phase equilibria within the stability field of sapphirine at UHT conditions (> 1000ºC).

### *4.7.2 Modelling Melting of a Pelite Protolith Composition*

First, we discuss the pelite composition. Figure 4.2 is a *P-T* pseudosection calculated for this composition at suprasolidus conditions. The heavy dashed line between 660 and 740°C is the wet solidus, whereas the dashed lines between the wet solidus and the heavy solid line represent contours of mol% melt assuming a system closed to melt loss. The heavy solid line is the biotite-out line. A prograde evolution around 0.9 GPa yields minimal production of melt up to the muscovite-out line around 750°C. Melt production increases to about 40 mol% around 900°C, with the appearance of peritectic garnet around 820°C.

Around 900°C biotite is completely consumed and we model melt loss at this point, retaining 1 mol% of the melt produced. This is equivalent to ~ 3 vol% in a natural rock, which is within the range of observations of low volume percent melt (as pseudomorphs of a mineral different from that of the pore walls) retained along grain boundaries in residual granulites and hornfelses (Sawyer 2001; Marchildon and Brown 2002; Holness and Sawyer 2008). Melt loss changes the bulk composition of the system [although in nature there will be a flux of melt through the system, so the change in nature is more difficult to quantify (Brown 2007b, 2008)] and the pseudosection in Fig. 4.2 is no longer appropriate for a discussion of the prograde evolution into the UHTM field after this first melt loss event.

Figure 4.3 is a *P-T* pseudosection calculated for the residual composition after the melt loss event around 900°C at 0.9 GPa. The composition of the residue and the topology of the pseudosection do not change significantly if the pressure of the melt loss event is in the range 0.8–1.0 GPa,

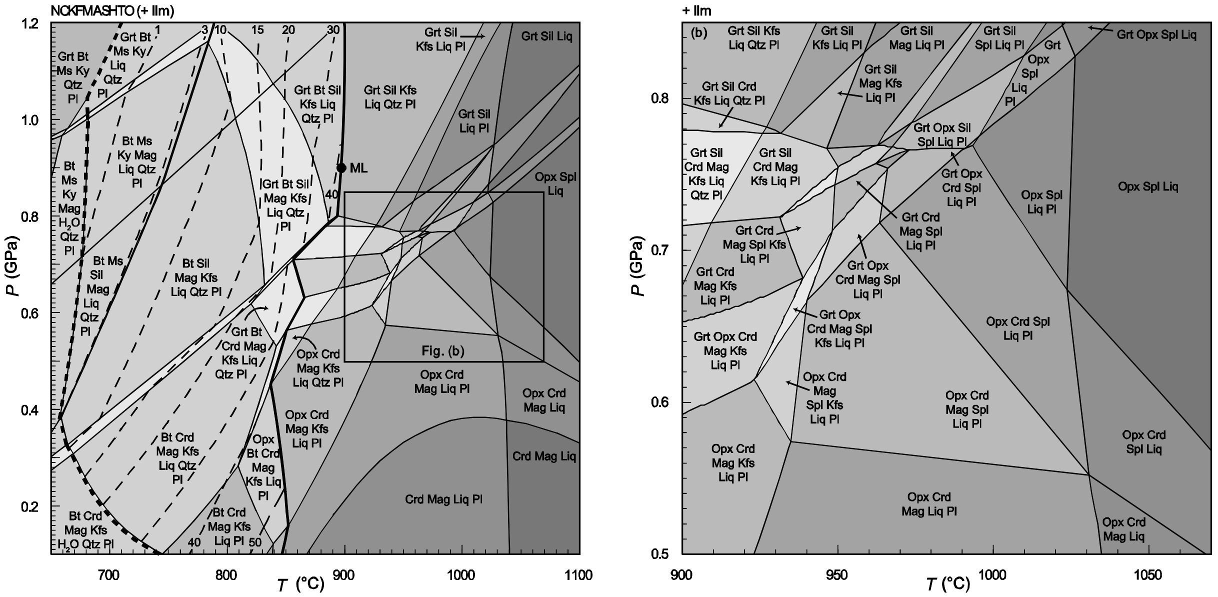

**Fig. 4.2** *P-T* pseudosection (isochemical phase diagram) calculated for an average amphibolite facies pelite composition (Table 4.1) in the system NCKFMASHTO. For clarity, the lower diagram (Fig. 4.2b) shows an expansion of the moderate-P-high-T part of the upper diagram where there are a large number of small multivariant phase assemblage fields. At *T* > 1000°C the phase assemblages shown may be metastable with respect to sapphirine (see text). This diagram is drawn for a fixed composition, which means that processes such as melt loss cannot be considered in relation to this diagram but require calculation of a new pseudosection for the residual composition after an imposed melt loss event. A melt loss event is imposed along a prograde *P-T* path that crosses the biotite-out line at 0.9 GPa (black circle labelled 'ML'). The pseudosection is contoured for melt mol% up to the biotite-out line for a rock saturated in $H_2O$ at 0.9 GPa at the wet solidus. Due to the different amount of $H_2O$ required to saturate the rock in a $H_2O$ fluid at different pressures along the wet solidus, the amount of fluid present at the low-P part of the solidus is an over-estimation, and consequently the amount of melt produced at low pressures is overestimated. The heavy dashed line represents the wet solidus, the dashed lines represent contours of mol% melt, and the heavy solid line is the biotite-out line.

because the biotite-out line is essentially isothermal above 0.8 GPa in Fig. 4.2. However, as pressure increases above 1.0 GPa changes in the composition of the melt and in the amount of melt produced, and the proportion lost become more significant, which will affect the topology at higher pressures.

The composition represented in Fig. 4.3 is less fertile so the solidus is located at higher temperatures (heavy dashed line), and the assemblages stable below the solidus are more refractory in comparison with those below the biotite-out line in the fertile composition represented in Fig. 4.2 (e.g. no muscovite, lower mol% biotite and garnet stable to lower *T*). Continued heating at 0.9 GPa leads to an increase in melt production to ~ 4 mol% at 1000°C, ~ 7 mol% at 1050°C and > 40 mol% at 1100°C (Fig. 4.3). Temperatures as high as 1100°C generally are not recorded by exposed residual UHTM rocks (Brown 2007b; Harley 2008). Over the interval 900–1100°C the melt becomes progressively drier as a high proportion of the anhydrous phases dissolve with increasing temperature. If temperatures approach 1100°C in nature, perhaps at levels of the crust not generally exposed, then the melt proportion likely will exceed the melt connectivity transition above 1050°C and melt loss is likely to have occurred for crust above 1050°C. This represents a second melt loss event.

Figure 4.4 is an isobaric $T$-$X_{melt\ loss}$ diagram at 0.9 GPa that allows us to investigate the effects of the two melt loss events on the formation and preservation of metamorphic assemblages. In nature, the phase assemblage evolution relates to the original protolith composition, the number of melt loss events, the *P-T* of each melt loss event and the proportion of melt retained after each of these events. In the discussion below, the scale of melt migration is not considered and melt loss simply refers to a scale greater than the equilibration volume at the *P-T* conditions of interest.

The original protolith composition is represented at $X_{melt\ loss} = 0$ (left side of the diagram) up to 900°C where the first melt loss event occurs. The heavy bar along the melt loss axis around 0.5 overall melt loss fraction represents the residual composition used for Fig. 4.3. The prograde evolution to 1100°C after the first melt loss event is represented by the vertical grey line, and complete melt loss at any *T* > 1050°C is represented by $X_{melt\ loss} = 1$ (right side of the diagram), although this is unlikely in nature.

A notable feature of this diagram is the increase in solidus temperature with increasing melt loss from ~ 680°C

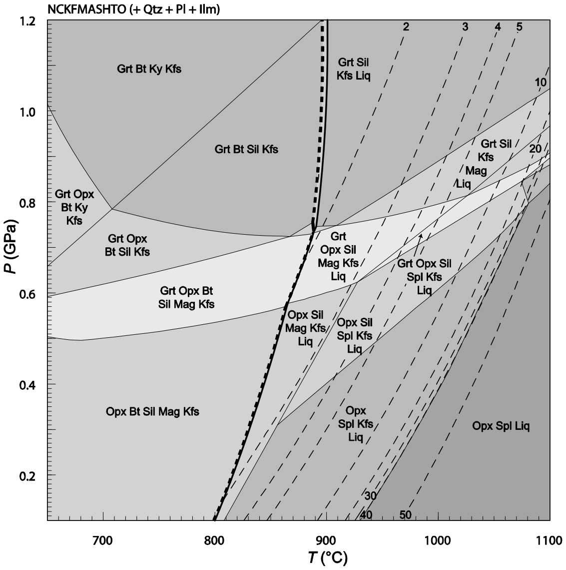

**Fig. 4.3** *P-T* pseudosection (isochemical phase diagram) calculated for the residual composition derived from the average amphibolite facies pelite composition after a melt loss event at the biotite-out line at 0.9 GPa (Table 4.1) in the system NCKFMASHTO. Because the biotite-out line is essentially isothermal above 0.8 GPa (Fig. 4.2), neither the composition of the residue nor the topology of the pseudosection in Fig. 4.3 varies much if the pressure of the melt loss event is in the range 0.8–1.0 GPa. The pseudosection is contoured for melt mol% at suprasolidus conditions, and demonstrates that the residual composition is less fertile than the protolith composition. This diagram is appropriate for considering the evolution at UHTM (> 900°C) conditions following the initial melt loss event (black circle labelled 'ML' on Fig. 4.2). The heavy dashed line represents the solidus and the dashed lines represent contours of mol% melt.

at $X_{melt\ loss} = 1$ to ~ 1090°C at $X_{melt\ loss} = 1$. The melt volume and the dissolved $H_2O$ limit the potential for retrograde reaction—the larger the volume of melt retained, the greater is the potential for retrograde reaction down temperature to the solidus. In general, we expect the melt volume retained in deep residual granulites of the lower anatectic zone to be less than the melt connectivity transition (7–10 mol% melt). Significant retrograde reaction below the solidus is unlikely in these deep residual granulites, because the $H_2O$ that exsolves from the crystallising melt is limited and the mineral assemblage at the solidus is likely to survive mostly intact.

For isobaric cooling in which equilibrium is maintained after near complete melt loss at $T > 1050$°C (i.e. overall $X_{melt\ loss} > 0.925$, Fig. 4.4 this requires deformation-enhanced melt loss in nature to achieve such a low-melt-volume state), the residual assemblage at the solidus will be Grt-Sil-Spl-Kfs (+Pl, +Ilm). Partial subsolidus equilibration to Grt-Bt-Sil-Mag-Kfs (+Pl, +Ilm) and Grt-Bt-Ky-Mag-Kfs (+Pl, +Ilm) may be possible if $H_2O$ is available below the solidus. However, in nature the volume of $H_2O$ that exsolves from the low volume percent of crystallising residual melt after near complete melt loss at $T > 1050$°C is insignificant and the mineral assemblage at the solidus is likely to survive intact unless there is an influx of hydrous fluid along a syn-metamorphic zone of localised high-strain deformation.

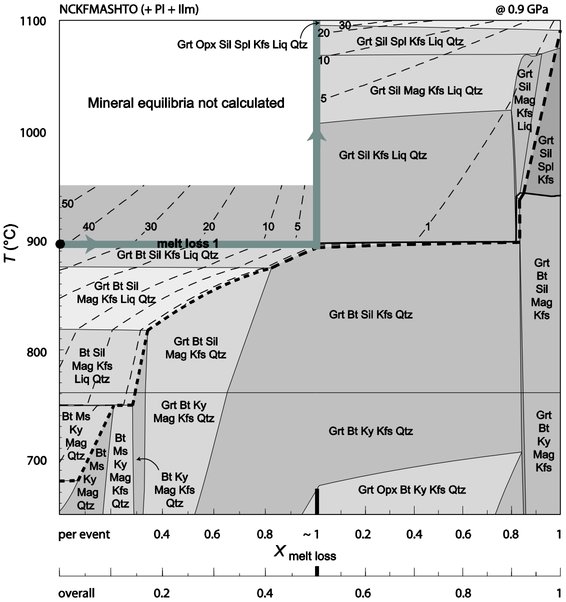

**Fig. 4.4** Calculated *T*-$X_{melt\ loss}$ pseudosection showing the effects of two melt loss events for a protolith composition of average amphibolite facies pelite (Fig. 4.2; Table 4.1) at $P = 0.9$ GPa. The original protolith composition is represented at overall $X_{melt\ loss} = 0$ (left side of the diagram) up to 900°C where the first melt loss event occurs (black circle labelled 'ML' on Fig. 4.2). The residual composition after the first melt loss event (Fig. 4.3) is represented by the heavy bar at overall $X_{melt\ loss} = 0.5$. The prograde evolution after the first melt loss event to 1100°C is represented by the vertical grey arrow, and complete melt loss at any $T > 1050$°C is represented by overall $X_{melt\ loss} = 1$ (right side of the diagram). This diagram is appropriate for an isobaric prograde evolution with near complete melt loss at the biotite-out line at 0.9 GPa, followed by additional melt loss at UHTM conditions. The heavy dashed line represents the solidus and the dashed lines represent contours of mol% melt.

Next consider isobaric cooling if the proportion of melt lost after the first melt loss event is lower (i.e. overall $X_{melt\ loss} > 0.5$ but $< 0.925$, Fig. 4.4) or if the peak temperature does not exceed 1050°C so that most of the melt generated above the biotite-out line is retained. This second scenario is analogous to many exposed UHTM terranes, where peak *T* was in the range 900–1050°C (Brown 2007b; Harley 2008) and loss of melt generated above the biotite-out line is unlikely to have occurred because the amount of melt was less than the melt connectivity transition (7–10 mol% melt). In this case, the residual assemblage at the solidus will be Grt-Bt-Sil-Kfs-Qtz (+Pl, +Ilm). Partial subsolidus equilibration to Grt-Bt-Ky-Kfs-Qtz (+Pl, +Ilm) and Grt-Opx-Bt-Ky-Kfs-Qtz (+Pl, +Ilm) may be possible if $H_2O$ is available below the solidus, but reaction progress will be determined by the amount of hydrous fluid. If this evolution occurred, for example associated with an influx of hydrous fluid in a syn-metamorphic zone of localised high-strain deformation, it has the consequence of producing orthopyroxene as a subsolidus retrograde phase. In addition, it is clear from Fig. 4.3 that any component of decompression during cooling is likely to lead to the widespread development of retrograde orthopyroxene since this phase becomes stable above the solidus at lower pressure.

For ordinary granulites in which some melt loss occurs during the prograde evolution to peak $T < 900$ºC, the subsolidus assemblage evolution during isobaric cooling in which equilibrium is maintained is a function of the proportion of melt that is lost. For close to complete melt loss at $T$ close to 900°C, the residual assemblage at the solidus will be Grt-Bt-Sil-Kfs-Qtz (+Pl, +Ilm), as shown in Fig. 4.4. If only half the melt generated at 900°C is lost the residual assemblage at the solidus will be Grt-Bt-Sil-Mag-Kfs-Qtz (+Pl, +Ilm), as shown in Fig. 4.4. At lower peak $T$ without significant melt loss or if the source retains a lot more melt the residual assemblage at the solidus may include muscovite (Fig. 4.4, for the first melt loss event $X_{melt\ loss} < 0.2$). In all cases, the mineral assemblage at the solidus is likely to survive mostly intact even if grain boundaries retain the $H_2O$ exsolved from the last melt crystallised at the solidus to allow minor retrogression to a subsolidus assemblage, unless there is an influx of hydrous fluid along a syn-metamorphic zone of localised high-strain deformation.

The dynamic nature of the orogenic environment means that an isobaric retrograde evolution is unrealistic for many regional metamorphic terranes, and decompression (exhumation) is likely to accompany cooling. In addition, melt generated deeper in the anatectic zone will transfer through the overlying crust, which means that additions of melt are possible at any level in the crust, both suprasolidus and subsolidus, as it is exhumed. These melts may be trapped or they may pass through, but they have the potential at shallower levels in the high-grade crust to increase the amount of exsolved $H_2O$ available locally or to generate gradients in $a_{H2O}$ locally to promote subsolidus retrograde recrystallisation (Baldwin et al. 2005).

### 4.7.3 *Modelling Melting of a Peraluminous Greywacke Protolith Composition*

Second, we discuss the peraluminous greywacke composition. Figure 4.5 is a $P$-$T$ pseudosection calculated for this composition at suprasolidus conditions. The heavy dashed line between 665 and 750°C is the wet solidus, whereas the dashed lines between the wet solidus and the heavy solid line represent contours of mol% melt assuming a system closed to melt loss. The heavy solid line is the biotite-out line. Orthopyroxene is stable throughout the pressure range at high temperature (from ~ 740°C at low $P$ to ~ 920°C at high $P$), and garnet is stable from ~ 740°C at moderate $P$ to ~ 700°C at high $P$. A prograde evolution around 0.9 GPa yields minimal production of melt up to ~ 800°C. Melt production increases to about 20 mol% around 890°C.

Around 890°C biotite is completely consumed and we allow melt loss to occur at this point, retaining 1 mol% of the melt produced. This is equivalent to ~ 5 vol% in a natural rock, which is within the range of observations in nature

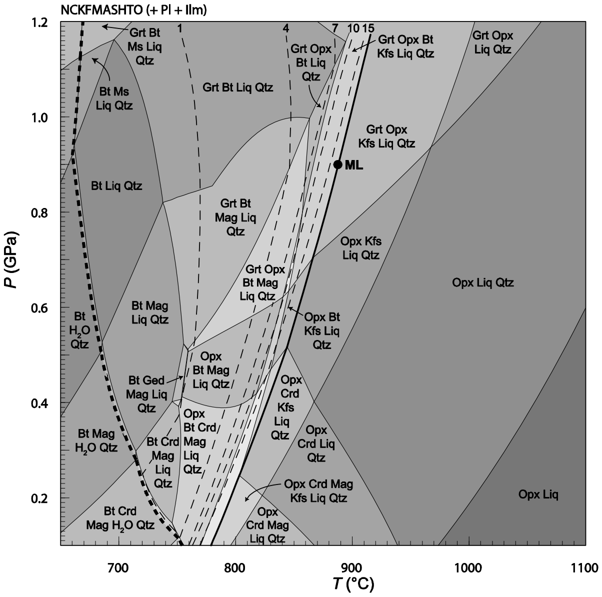

**Fig. 4.5** $P$-$T$ pseudosection (isochemical phase diagram) calculated for a greywacke composition (Table 4.1) in the system NCKFMASHTO. This diagram is drawn for a fixed composition, which means that processes such as melt loss cannot be considered in relation to this diagram but require calculation of a new pseudosection for the residual composition after an imposed melt loss event. A melt loss event is imposed along a prograde $P$-$T$ path that crosses the biotite-out line at 0.9 GPa (black circle labelled 'ML'). The pseudosection is contoured for melt mol% up to the biotite-out line for a rock saturated in $H_2O$ at 0.9 GPa at the wet solidus. Due to the different amount of $H_2O$ required to saturate the rock in a $H_2O$ fluid at different pressures along the wet solidus, the amount of fluid present at the low-$P$ part of the solidus is an overestimation, and consequently the amount of melt produced at low pressures is overestimated. In comparison to the metapelite in Fig. 4.2, the pseudosection is dominated by higher variance equilibria defining large fields in $P$-$T$. The dominance of high variance equilibria is due to the limited occurrence of K-feldspar and the absence of sillimanite and muscovite from most of the $P$-$T$ range shown. The heavy dashed line represents the wet solidus, the dashed lines represent contours of mol% melt, and the heavy solid line is the biotite-out line.

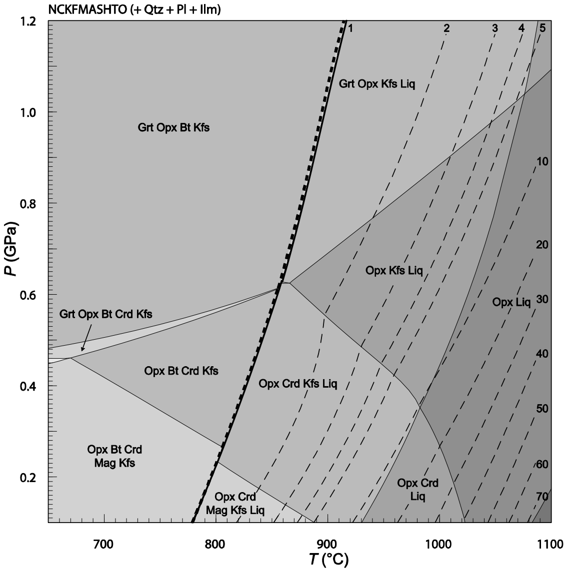

**Fig. 4.6** *P-T* pseudosection (isochemical phase diagram) calculated for the residual composition derived from the greywacke composition after a melt loss event at the biotite-out line at 0.9 GPa (Table 4.1) in the system NCKFMASHTO. The pseudosection is contoured for melt mol% at suprasolidus conditions, and demonstrates that the residual composition is less fertile than the protolith composition. This diagram is appropriate for considering the evolution at UHTM (>900°C) conditions following the initial melt loss event (black circle labelled ‘ML’ on Fig. 4.5). The heavy dashed line represents the solidus and the dashed lines represent contours of mol% melt.

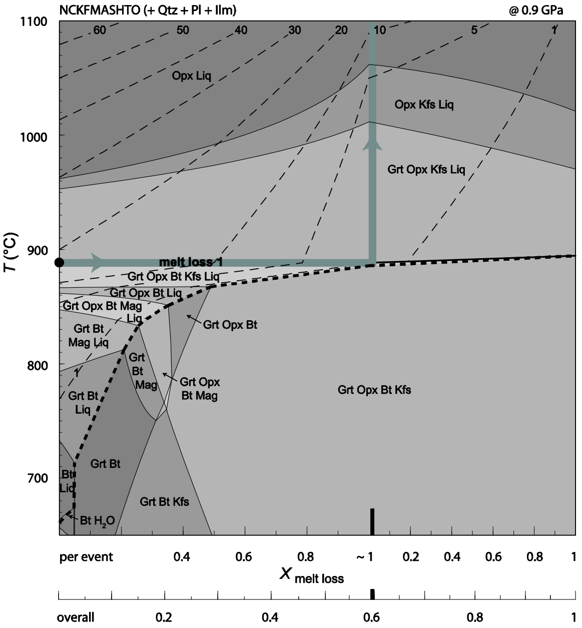

**Fig. 4.7** Calculated $T$-$X_{melt\ loss}$ pseudosection (isochemical phase diagram) showing the effects of two melt loss events for the greywacke composition (Fig. 4.5; Table 4.1) at $P$ = 0.9 GPa. The original protolith composition is represented at overall $X_{melt\ loss}$ = 0 (left side of the diagram) up to 890ºC where the first melt loss event occurs (black circle labelled ‘ML’ on Fig. 4.5). The residual composition after the first melt loss event (Fig. 4.6) is represented by the heavy bar at overall $X_{melt\ loss}$ = 0.6. The prograde evolution after the first melt loss event to 1100°C is represented by the vertical grey arrow, and complete melt loss at $T$ = 1100°C is represented by overall $X_{melt\ loss}$ = 1 (right side of the diagram). This diagram is appropriate for an isobaric prograde evolution with near complete melt loss at the biotite-out line at 0.9 GPa, followed by additional melt loss at UHTM conditions. The heavy dashed line represents the solidus and the dashed lines represent contours of mol% melt.

of low volume percent melt (as pseudomorphs of a mineral different from that of the pore walls) retained along grain boundaries in residual granulites and hornfelses (Sawyer 2001; Marchildon and Brown 2002; Holness and Sawyer 2008). Melt loss changes the bulk composition of the system [although in nature there will be a flux of melt through the system, so the change in nature is more difficult to quantify (Brown 2007b, 2008)] and the pseudosection in Fig. 4.5 is no longer appropriate for a discussion of the prograde evolution into the UHTM field after this first melt loss event.

Figure 4.6 is a *P-T* pseudosection calculated for the residual composition after the melt loss event around 890°C at 0.9 GPa. Because the biotite-out line has a high *dP/dT* (~ 1 GPa $100°C^{-1}$) and the melt isopleths are nearly parallel to it, neither the composition of the residue nor the topology of the pseudosection in Fig. 4.6 varies much if the pressure of the melt loss event is higher or lower by, for example 0.2 to +0.3 GPa. The composition now is less fertile so the solidus is located at higher temperatures (heavy dashed line), and the assemblages stable below the solidus are more refractory than those below biotite-out in Fig. 4.5 (e.g. no muscovite at high *P*, less mol% biotite and garnet stable to lower *T*). Continued heating at 0.9 GPa leads to an increase in melt production to close to 3 mol% at 1000°C and ~ 13 mol% at 1100°C (Fig. 4.6), temperatures not generally recorded by exposed residual UHTM rocks. If temperatures higher than this are achieved in nature, perhaps at levels of the crust not generally exposed, then melt loss may occur close to 1100°C where the melt proportion likely will exceed the melt connectivity transition.

Figure 4.7 is an isobaric $T$-$X_{melt\ loss}$ diagram at 0.9 GPa. The original protolith composition is represented at $X_{melt\ loss}$ = 0 (left side of the diagram) up to 890°C where the first melt loss event occurs. The residual composition used for Fig. 4.6 is now represented by the heavy bar along the melt loss axis around 0.6 overall melt loss fraction, whereas the prograde evolution to 1100°C after the first melt loss event is represented by the vertical grey line. Complete melt loss is represented by $X_{melt\ loss}$ = 1 (right side of the diagram). A notable feature of this diagram is the increase in solidus temperature with increasing melt loss from ~ 660°C at $X_{melt\ loss} = 1$ to ~ 900°C at $X_{melt\ loss} = 1$.

For any protolith composition where the peak $T$ exceeds ~ 890°C at 0.9 GPa, melt loss is likely (at > 7–10 mol% melt, above the melt connectivity transition). In these cases, an isobaric evolution maintaining equilibrium down temperature will produce a mineral assemblage of Grt-Opx-Bt-Kfs (+Qtz, +Pl, +Ilm) at the solidus. In contrast, consider any isobaric cooling path starting > 20°C below $T \sim 890°C$ at 0.9 GPa, where the volume of melt produced is < 7–10 mol% melt, which is below the melt connectivity transition, making melt loss unlikely. The phase assemblage progressively equilibrates through the various steps along the $X_{melt\ loss} = 0$ side of the diagram to the solidus at ~ 665°C, where the final assemblage is Bt-$H_2O$ (+Qtz, +Pl, +Ilm). One consequence of retrogression starting from a metamorphic peak much below $T \sim 890°C$ is that potentially ordinary granulites ($T \ll 900°C$) derived from a greywacke protolith composition at 0.9 GPa ultimately may contain very little orthopyroxene. For any isobaric cooling path starting at peak $T \sim 890°C$ at 0.9 GPa, assuming melt above the melt connectivity transition at < 7–10 mol% melt is lost, then $X_{melt\ loss}$ is ~ 0.5 or less and the phase assemblage progressively equilibrates through the various steps to the solidus in the low $T$ - low $X_{melt\ loss}$ corner of Fig. 4.7. In all cases, the mineral assemblage at the solidus is likely to survive mostly intact even if grain boundaries retain the $H_2O$ exsolved from the last melt crystallised at the solidus to promote minor subsolidus growth of biotite.

Phase relations for melting and melt loss at pressures lower than 0.9 GPa will be different than those presented in Figs. 4.5, 4.6 and 4.7. Johnson et al. (2008) modelled the same peraluminous greywacke composition and investigated melt loss at 0.7 GPa. As $P$ is reduced the solidus moves to lower $T$ and higher $X_{melt\ loss}$, expanding the area in which retrogression above the solidus produces biotite. At temperatures above the solidus mol% isopleths for biotite (mol% increasing with decreasing $T$) and orthopyroxene (mol% decreasing with decreasing $T$) have shallow slopes but change to steep slopes below the solidus (Johnson et al. 2008, their Fig. 6a). This feature implies that significant retrograde replacement of orthopyroxene by biotite in the presence of melt is likely but subsolidus retrograde reaction of orthopyroxene to biotite is unlikely regardless of the $H_2O$ exsolved from the crystallising melt.

### *4.7.4 Limitations of the Modelling*

It is important to remember that there are limitations to phase equilibria modelling. Limitations intrinsic to phase equilibria modelling include the use of a simplified chemical system (no matter how complete we make it), an internally consistent thermodynamic dataset with uncertainties (there will always be uncertainties on the experimental data used in the dataset), and imperfect *a-x* models for solid solutions (no matter how sophisticated we make them). For these reasons, it is important to take care in interpreting the results of any phase equilibria modelling. For example, since the model is not complete and cannot be perfect one should avoid too literal an interpretation of the mole proportions of phases at any point in a phase diagram in relation to the mode of the natural rock under investigation.

It is critical to identify correctly the variable of interest if the modelling is to lead to a better understanding of the process being investigated (e.g. Powell et al. 2005). The protolith composition is always an important variable, but an investigation of the effects associated with differences in protolith composition is beyond the scope of this chapter. However, the interested reader is referred to studies of pelites at granulite facies conditions in the literature for comparative information. Examples of such studies include those by Johnson et al. (2003, 2004), Johnson and Brown (2004) and White et al. (2002, 2003, 2004). For consideration of high-grade metamorphism and melting of greywackes of variable composition, we refer the interested reader to the recent study by Johnson et al. (2008).

For this modelling study, we adjusted the $H_2O$ contents in the protolith bulk compositions to just saturate the solidus with hydrous fluid contents < 1 mol% at $P = 0.9$ GPa. However, due to the variation in the amount of $H_2O$ required to saturate a rock just below the solidus at different pressures (lower at lower $P$), the mol% melt calculated in the models at low $P$ is overestimated.

There are many variables associated with where and how melt loss occurs and on what scale, which require simplifying assumptions to be made for the modelling to become tractable. In this chapter, we have taken a very simple approach to melt loss in the pelite composition, simply deferring melt loss until the biotite-out line. In nature it is likely that melt loss will occur at the melt connectivity transition around 7 vol% melt, and that there will be periodic melt loss in a cyclic fashion as melt volume increases to the melt connectivity transition multiple times (Brown 2007b, 2008). However, our purpose above was to gain an understanding of the processes involved in the retrograde evolution after melt loss rather than presenting multiple *P-T* pseudosections for the prograde evolution and a more complex isobaric *T-X* diagram to mimic more closely the natural process. White and Powell (2002) discuss the issue of scale of melt migration in some detail. For our purpose in this chapter, the widespread occurrence of pristine to only weakly retrogressed granulite facies terranes throughout the geological record demonstrates that the deep crust typically undergoes substantial melt loss (Brown 2007b).

A bigger issue concerns the use of isobaric $T$- $X_{melt\ loss}$ diagrams to investigate retrograde processes in regional high-grade metamorphic terranes. Such diagrams generally are appropriate to investigate melting, melt loss and retrograde phase assemblage evolution in contact metamorphic aureoles (e.g. Johnson et al. 2003, 2004), and they might be appropriate to investigate retrograde processes in metamorphic belts that follow a counter clockwise *P-T* path, if the retrograde path is close to isobaric (White and Powell 2002). However, these diagrams are inappropriate for many of the metamorphic belts that follow a clockwise *P-T* path (Brown 2002; White and Powell 2002), where the reactions that occur during retrogression may differ from those predicted in an isobaric $T\text{-}X_{melt\ loss}$ diagram. For terranes where the retrograde path is stepped with a close-to-isothermal segment followed by a close-to-isobaric segment (e.g. Raith et al. 1997; Johnson and Brown 2004), the post peak-*P* evolution could be investigated using a combination of an isothermal *P-X* diagram and an isobaric *T-X* diagram.

## 4.8 Importance of Melt Loss for Achieving Temperatures of UHTM

Crustal melting is multivariant, which means that melting occurs over some temperature interval, and strongly endothermic, which means that the rate of temperature increase during prograde heating is buffered by the melting reactions. Melting occurs via a sequence of three types of multivariant reactions: wet melting at the solidus; hydrate-breakdown melting at moderate-to-high suprasolidus temperatures; and, anhydrous melting at ultra-high suprasolidus temperatures. The latent heat of fusion is lowest for wet melting and highest for anhydrous melting. Furthermore, both hydrate-breakdown and anhydrous melting are non-linear processes, with a tendency for a larger mol% melt production as the hydrate-out line or as the liquidus is approached. These features are similar for both the pelite and greywacke compositions investigated herein (Figs. 4.2, 4.3, 4.5 and 4.6). The fertility of the pelite composition is about twice that of the greywacke composition. In addition, the melt production per increment of temperature along the prograde path to the biotite-out line is four and five times greater for the pelite and greywacke compositions, respectively, than the melt production per increment of temperature above the biotite-out line (Figs. 4.2, 4.3, 4.5 and 4.6).

### *4.8.1 The Effect of Melt Loss on the Thermal Evolution*

It is likely that significant loss of melt generated along the prograde path up to the biotite-out line around 900°C facilitates the crust reaching UHTs (> 900°C). Melt loss dehydrates the system, which limits the progress of heat-consuming melting reactions among the residual phases in the source and enables the temperature to increase into the UHTM field (Martignole 2008). We quantify this effect as follows.

Taking the latent heat of fusion of the crust as 320 kJ/kg and the specific heat capacity of the crust as 0.8–1.0 $\mathrm{J g^{-1} K^{-1}}$ yields a retardation in the temperature increase for complete crustal melting of 320–400°C. For the pelite, which achieves > 40 mol% melt at the biotite-out line (Fig. 4.2), melting from the wet solidus to the biotite-out line at 0.9 GPa requires an increase in *T* of ~ 240°C and consumes heat equivalent to an additional 128–160°C. For the greywacke, which achieves > 20 mol% melt at the biotite-out line (Fig. 4.5), melting from the wet solidus to the biotite-out line at 0.9 GPa requires an increase in *T* of ~ 230°C and consumes heat equivalent to an additional 64–80°C. For the residual pelite composition, an increase in temperature of 150°C above the biotite-out line (to 1050°C, Fig. 4.3) produces an additional ~ 8 mol% melt and consumes heat equivalent to only an additional ~ 30°C. For the residual greywacke composition, an increase in temperature of 160°C above the biotite-out line (to 1050°C, Fig. 4.6) produces an additional ~ 4 mol% melt and consumes heat equivalent to only an additional ~ 15°C. For both rock compositions, more heat is required to pass through the granulite field along a prograde *P-T* path than to achieve peak temperatures in the UHTM field, assuming melt loss occurs along the prograde *P-T* path (in this chapter modelled as a single melt loss event at the biotite-out line).

Nonetheless, to achieve UHTM conditions requires maintenance of elevated orogenic heat flow; if the elevated orogenic heat flow diminishes before the rock crosses the biotite-out line, then attaining UHTM conditions is unlikely. For a regional metamorphic terrane with a length scale of up to 10 km, the normal diffusive thermal time constant is up to ~ 1 Ma (Stüwe 2008). Taking the thickness of a section of crust at $T > 900$°C to be < 10 km, then the diffusive thermal time constant to achieve UHTM conditions may increase by up to 20–40% for the protolith compositions modelled due to the buffering effect of melting reactions. However, any advective component of heat transport will reduce the time taken to achieve peak conditions through the crustal section considered.

### *4.8.2 An Example: Interpretation of UHT Metamorphic Rocks from the Basement of the Peruvian Andes*

We apply the generic modelling described above to illustrate aspects of the *P-T* evolution of the regional-scale

Grenville-age UHTM of the Mollendo-Camana block in the basement of the Peruvian Andes (Martignole and Martelat 2003). The UHTM rocks comprise migmatites, non-migmatitic aluminous gneisses and sub-aluminous (sillimanite-absent) gneisses. The sub-aluminous gneisses are less common than the migmatites.

A pelite protolith is probable for the migmatites (Martignole and Martelat 2003). They comprise leucosome (dominant) and melanosome (subordinate) layers. The leucosomes consist of mesoperthite, perthitic orthoclase or microcline (up to 60 vol%), quartz (up to 50 vol%) and plagioclase (10–20 vol%), with minor and variable amounts of orthopyroxene, sillimanite, oxides, biotite and traces of sapphirine. The associated melanosomes consist of sillimanite (55–75 vol%), orthopyroxene (0–15 vol%), garnet (0–10 vol%), cordierite (0–20 vol%), magnetite and ilmenite (2–10 vol%), biotite (0–10 vol%), and sapphirine and spinel (0–10 vol%). The occurrence of peritectic orthopyroxene in leucosomes together with sillimanite in melanosomes and only minor garnet in the mode indicates that the average pelite used in our study is not an appropriate composition for study of these migmatites.

The sub-aluminous gneisses consist of quartz (15–30 vol%), feldspars (orthoclase and plagioclase; 50–60 vol%), orthopyroxene (0–10 vol%), garnet (0–10 vol%), magnetite and ilmenite (0–5 vol%), biotite (0–2 vol%) and spinel (0–10 vol%). Microstructures that record arrested retrograde reactions are common in the gneisses. These microstructures involve garnet, cordierite, orthopyroxene, sapphirine, sillimanite, oxides, quartz and plagioclase. Examples include cordierite rims around garnet and sapphirine-bearing pseudomorphs after garnet or sapphirine-cordierite intergrowths at the contacts between sillimanite and orthopyroxene. We explain these features using the generic model for the aluminous greywacke composition.

The range of peak $P$-$T$ conditions estimated by Martignole and Martelat (2003) is $T$ = 960–1060°C at $P$ = 1.15 GPa. For these $P$-$T$ conditions, from the modelling we estimate the peak assemblage (in mol%) will be between Qtz ~ 27 + Kfs ~ 7 + Pl ~ 45.5 + Opx ~ 13.5 + Grt ~ 4.5 + Ilm ~ 1.5 + Liq ~ 1.5 at 960°C and Qtz ~ 26.5 + Kfs ~ 2.5 + Pl ~ 49 + Opx ~ 15 + Grt ~ 2 + Ilm ~ 1.5 + Liq ~ 3.5 at 1060°C. These values (1 mol% is approximately equivalent to 1 vol%) compare favourably with the modal proportions estimated by Martignole and Martelat (2003), except that Opx is higher in the model. Exhumation with cooling will allow retrograde formation of cordierite at $T$ < 880°C at $P$ < 0.63 GPa at the expense of garnet and orthopyroxene. If the $H_2O$ exsolved from residual melt crystallising at the solidus is retained along grain boundaries, then production of minor amounts of biotite is possible immediately subsolidus at $T$ < 860°C and $P$ < 0.6 GPa.

For the migmatites, Martignole and Martelat (2003) use the KFMASH grid of Carrington and Harley (1995) and the FMAS grid of Harley (1998a) to estimate $P$ of 0.9–0.8 GPa for retrograde cooling after decompression from peak $P$. However, Baldwin et al. (2005, their Fig. 1) have shown that the FMAS grid of Harley (1998a) is probably a constant $a_{H2O}$ section in the FMASH system. Based on the petrographic information given by Martignole and Martelat (2003), and the discussion by Baldwin et al. (2005), we suggest the $P$ of retrograde cooling in the migmatites could be as low as 0.65 GPa, which is consistent with the $P$ estimated above for the retrograde formation of cordierite and minor biotite in the sub-aluminous gneisses.

## 4.9 Directions for Future Research

By discussing the limitations on the modelling, we have identified some directions for future research, and others and we are currently making progress with several of these topics. Studies that investigate a wider range of appropriate values for each of the variables will be useful, as demonstrated by the investigation of variations in composition in greywackes by Johnson et al. (2008). For example, it is worth investigating processes involving melt loss using multiple isobaric $T$-$X_{melt\ loss}$ diagrams at well-chosen pressures and using combinations of isothermal $P$-$X_{melt\ loss}$ diagrams with isobaric $T$-$X_{melt\ loss}$ diagrams. In this chapter, we have taken a very simple approach to melt loss events, whereas in nature it is likely that there will be multiple melt loss events along the prograde evolution requiring calculation of multiple $P$-$T$ pseudosections and a more complex series of isobaric $T$- $X_{melt\ loss}$ diagrams to mimic the natural process. Although White and Powell (2002) discuss the issue of scale of melt migration in some detail there is scope for more studies on this issue. For studies of metasedimentary protoliths at UHT metamorphic conditions, a new *a-x* model for sapphirine that includes $Fe^{3+}$ is required. Finally, there is a need to develop complete thermodynamically based forward models that allow for investigation of the growth of zircon and monazite and other Zr- and REE-bearing minerals in high-grade metamorphic rocks as a function of evolving $P$-$T$-$X$ variables (Kelsey et al. 2008). These models will provide a better quantitative framework for investigating the growth of zircon and monazite, which will improve our interpretation of chronologic data from high-grade metamorphic terranes

## 4.10 References

Ague JJ (1991) Evidence for major mass-transfer and volume strain during regional metamorphism of pelites. Geology 19: 855–858

Albertz M, Paterson SR, Okaya D (2005) Fast strain rates during pluton emplacement: Magmatically folded leucocratic dikes in aureoles of the Mount Stuart Batholith, Washington, and the Tuolumne Intrusive Suite. California. Geol Soc Am Bull 117: 450–465

Andreoli MA, Hart RJ, Ashwal LD, Coetzee H (2006) Correlations between U, Th content and metamorphic grade in the western Namaqualand Belt, South Africa, with implications for radioactive heating of the crust. J Pet 47: 1095–1118

Annen C, Blundy JD, Sparks RSJ (2006) The genesis of intermediate and silicic magmas in deep crustal hot zones. J Pet 47: 71–95

Ashworth JR, McLellan EL (1985) Textures. In: Ashworth JR (ed) Migmatites. Blackie Son Ltd., Glasgow

Auzanneau E, Vielzeuf D, Schmidt MW (2006) Experimental evidence of decompression melting during exhumation of subducted continental crust. Contrib Mineral Petrol 152: 125–148

Baldwin JA, Brown M (2008) Age and duration of ultrahigh-temperature metamorphism in the Anapolis-Itaucu Complex, Southern Brasilia Belt, central Brazil-constraints from U-Pb geochronology, mineral rare earth element chemistry and trace-element thermometry. J Meta Geol 16: 213–233

Baldwin JA, Brown M, Schmitz MD (2007) First application of titanium-in-zircon thermometry to ultrahigh-temperature metamorphism. Geology 35: 295–298

Baldwin JA, Powell R, Brown M, Moraes R, Fuck RA (2005) Mineral equilibria modelling of ultrahigh-temperature metamorphism: an example from the Anápolis-Itauçu Complex, central Brazil. J Meta Geol 23: 511–531

Barboza SA, Bergantz GW, Brown M (1999) Regional granulite facies metamorphism in the Ivrea zone: Is the Mafic Complex the smoking gun or a red herring? Geology 27: 447–450

Bea F (1996) Residence of REE, Y, Th and U in granites and crustal protoliths; implications for the chemistry of crustal melts. J Petrol 37: 521–552

Bea F, Montero P (1999) Behavior of accessory phases and redistribution of Zr, REE, Y, Th, and U during metamorphism and partial melting of metapelites in the lower crust: An example from the Kinzigite Formation of Ivrea-Verbano, NW Italy. Geochim Cosmochim Acta 63: 1133–1153

Berger A, Burri T, Alt-Epping P, Engi M (2008) Tectonically controlled fluid flow and water-assisted melting in the middle crust: An example from the Central Alps. Lithos 102: 598–615

Bingen B, van Breemen O (1998) U-Pb monazite ages in amphibolite- to granulite-facies orthogneiss reflect hydrous mineral breakdown reactions: Sveconorwegian Province of SW Norway. Contrib Mineral Petrol 132: 336–353

Bingen B, Austrheim H, Whitehouse M (2001) Ilmenite as a source for zirconium during high-grade metamorphism? Textural evidence from the Caledonides of western Norway and implications for zircon geochronology. J Petrol 42: 355–375

Brown M (1994) The generation, segregation, ascent and emplacement of granite magma: The migmatite-to-crustally-derived granite connection in thickened orogens. E Sci Rev 36: 83–130

Brown M (1995) The late-Precambrian geodynamic evolution of the Armorican segment of the Cadomian belt (France): Distortion of an active continental margin during south-west directed convergence and subduction of a bathymetric high. Géol France 3: 3–22

Brown M (1998a) Unpairing metamorphic belts: *P-T* paths and a tectonic model for the Ryoke Belt, southwest Japan. J Meta Geol 16: 3–22

Brown M (1998b) Ridge-trench interactions and high-T-low-P metamorphism, with particular reference to the Cretaceous evolution of the Japanese Islands. In: Treloar PJ, O'Brien PJ (eds) What drives metamorphism and metamorphic reactions. Geol Soc Spec Pub 138: 131–163

Brown M (2001a) Crustal melting and granite magmatism: key issues. Phys Chem Earth (A) 26: 201–212

Brown M (2001b) Orogeny, migmatites and leucogranites: a review. Proceed Indian Acad Sci 110: 313–336

Brown M (2002) Prograde and Retrograde Processes in Migmatites Revisited. J Meta Geol 20: 25–40

Brown M (2003) Hot orogens, tectonic switching, and creation of continental crust: Comment and Reply. Geology: On-Line Forum June 2003, doi: 10.1130/0091–7613 (2003) 31

Brown M (2004) Melt extraction from lower continental crust. Trans R Soc Edinburgh: Earth Sci 95: 35–48

Brown M (2007a) Metamorphic conditions in orogenic belts: A record of secular change. Internat Geol Rev 49: 193–234

Brown M (2007b) Crustal melting and melt extraction, ascent and emplacement in orogens: Mechanisms and consequences. J Geol Soc London 163: 709–730

Brown M (2008) Granites, migmatites and residual granulites: Relationships and processes. In: Sawyer EW, Brown M (eds) Working with Migmatites. Mineralogical Association of Canada Short Course Series 38, Quebec City, Quebec

Brown M, Dallmeyer RD (1996) Rapid Variscan exhumation and role of magma in core complex formation: Southern Brittany metamorphic belt, France. J Meta Geol 14: 361–379

Brown M., Raith M (1996) First evidence of ultrahigh-temperature decompression from the granulite province of southern India. J Geol Soc 153: 819–822

Brown M, Solar GS (1999) The mechanism of ascent and emplacement of granite magma during transpression: a syntectonic granite paradigm. Tectonophysics 312: 1–33

Brown M, Rushmer T (2006) Evolution and Differentiation of the Continental Crust. Cambridge University Press

Brown MA, Brown M, Carlson WD, Denison C (1999) Topology of syntectonic melt flow networks in the deep crust: inferences from three-dimensional images of leucosome geometry in migmatites. Amer Mineral 84: 1793–1818

Burg JP, Gerya TV (2005) The role of viscous heating in Barrovian metamorphism of collisional orogens: thermomechanical models and application to the Lepontine Dome in the Central Alps. J Meta Geol 23: 75–95

Burg JP, Schmalholz SM (2008) Viscous heating allows thrusting to overcome crustal-scale buckling: Numerical investigation with application to the Himalayan syntaxes. Earth Planet Sci Lett 274: 189–203

Carrington DP, Harley SL (1995) Partial melting and phase-relations in high-grade metapelites – An experimental petrogenetic grid in the KFMASH system. Contrib Mineral and Petrol 120: 270–291

Clarke GL, White RW, Lui S, Fitzherbert JA, Pearson NJ (2007) Contrasting behaviour of rare earth and major elements during partial melting in granulite facies migmatites, Wuluma Hills, Arunta Block, central Australia. J Meta Geol 25: 1–18

Chopin C (2003) Ultrahigh-pressure metamorphism: tracing continental crust into the mantle. Earth Plan Sci Lett 212: 1–14. doi: 10.1016/S0012-821X (03) 00261-9

Clemens JD (2006) Melting of the continental crust: fluid regimes, melting reactions, and source-rock fertility. In: Brown M, Rushmer T (eds) Evolution and Differentiation of the Continental Crust. Cambridge University Press

Cocherie A, Legendre O, Peucat JJ, Kouamelan AN (1998) Geochronology of polygenetic monazites constrained by in situ electron microprobe Th-U total lead determination: Implications for lead behaviour in monazite. Geochim Cosmochim Acta 62: 2475–2497

Coggon R, Holland TJB (2002) Mixing properties of phengitic micas and revised garnet-phengite thermobarometers. J Meta Geol 20: 683–696

Connolly JAD, Podladchikov YY (2004) Fluid flow in compressive tectonic settings: Implications for midcrustal seismic reflectors and downward fluid migration. J Geophys Res 109: B04201. doi: 10.1029/2003JB002822

Crowley JL, Ghent ED (1999) An electron microprobe study of the U-Th-Pb systematics of metamorphosed monazite: the role of Pb diffusion versus overgrowth and recrystallisation. Chem Geol 157: 285–302

Currie CA, Hyndman RD (2006) The thermal structure of subduction zone back arcs. J Geophys Res 111: B08404. doi: 10.1029/2005JB004024

Currie CA, Hyndman RD (2007) Reply to comment by W.P. Schellart on "The thermal structure of subduction zone back arcs". J Geophys Res – Solid Earth 112: B11408. doi: 10.1029/2007JB005415

Currie CA, Huismans RS, Beaumont C (2008) Thinning of continental backarc lithosphere by flow-induced gravitational instability. Earth Planet Sci Lett 269: 435–446

Davies JH, Von Blanckenburg F (1995) Slab breakoff: a model of lithosphere detachment and its test in the magmatism and deformation of collisional orogens. Earth Planet Sci Lett 129: 1–4

Dewey JF, Robb L, Van Schalkwyk L (2006) Did Bushmanland extensionally unroof Namaqualand? Precam Res 150: 173–182

Degeling H, Eggins S, Ellis DJ (2001) Zr budgets for metamorphic reactions, and the formation of zircon from garnet breakdown. Mineral Mag 65: 749–758

Diener JFA, Powell R., White RW, Holland TJB (2007) A new thermodynamic model for clino-and orthoamphiboles in the System $Na_2O$-CaO-FeO-MgO-$Al_2O_3$-$SiO_2$-$H_2O$-O. J Meta Geol 25: 631–656

Diener JFA, White RW, Powell R (2008) Granulite facies metamorphism and subsolidus fluid-absent reworking, Strangways Range, Arunta Block, central Australia. J Meta Geol 26: 603–622

Du Bernard X, Eichhubl P, Aydin A (2002) Dilation bands: A new form of localised failure in granular media. Geophys Res Lett 29: doi: 10.1029/2002GL015966

Dufek J, Bergantz GW (2005) Lower crustal magma genesis and preservation: a stochastic framework for the evaluation of basalt-crust interaction. J Pet 46: 2167–2195

Eichhubl P, Aydin A (2003) Ductile opening-mode fracture by pore growth and coalescence during combustion alteration of siliceous mudstone. J Struct Geol 25: 121–134

Eichhubl P, Aydin A, Lore J (2001) Opening-mode fracture in siliceous mudstone at high homologous temperature – effective of surface forces. Geophys Res Lett 28: 1299–1302

Ferry JM, Watson EB (2007) New thermodynamic models and revised calibrations for the Ti-in-Zircon and Zr-in-rutile thermometers. Contrib Mineral Petrol 154: 429–437

Fernandez M, Marzan I, Correia A, Ramalho E (1998) Heat flow, heat production, and lithospheric thermal regime in the Iberian Peninsula. Tectonophysics 291: 29–53

Fitzsimons ICW, Kinny PD, Harley SL (1997) Two stages of zircon and monazite growth in anatectic leucogneiss: SHRIMP constraints and the duration and intensity of Pan-African metamorphism in Prydz Bay, East Antarctica. Terra Nova 9: 47–51

Florian G, Bussy F, Epard JL, Baumgartner L (2008) Water-assisted migmatisation of metagraywackes in a Variscan shear zone, Aiguilles-Rouges massif, western Alps. Lithos 102: 575–597

Francheteau J, Jaupart C, Shen XJ, Kang WH, Lee DL, Bai JC, Wei HP, Deng HY (1984) High heat-flow in southern Tibet. Nature 307: 32–36

Fraser G, Ellis E, Eggins S (1997) Zirconium abundance in granulite-facies minerals, with implications for zircon geochronology in high-grade rocks. Geology 25: 607–610

Gerdes A, Worner G, Henk A (2000) Post-collisional granite generation and HT-LP metamorphism by radiogenic heating: the Variscan South Bohemian Batholith. J Geol Soc London 157: 577–587

Groome WG, Thorkelson DJ (2008) The three-dimensional thermo-mechanical signature of ridge subduction and slab window migration. Tectonophysics doi: 10.1016/j.tecto.2008.07.003

Guernina S, Sawyer EW (2003) Large-scale melt-depletion in granulite terranes: An example from the Archean Ashuanipi Subprovince of Quebec. J Meta Geol 21: 181–201

Hanchar JM, Watson EB (2003) Zircon saturation thermometry. Rev Mineral Geochem 53: 89–112

Harley SL (1998a) On the occurrence and characterisation of ultrahigh-temperature (UHT) crustal metamorphism. In: Treloar PJ, O'Brien PJ (eds) What drives metamorphism and metamorphic reactions? Geol Soc Spec Publ

Harley SL (1998b) Ultrahigh-temperature granulite metamorphism (1050 degrees C, 12 kbar) and decompression in garnet (Mg70) - orthopyroxene-sillimanite gneisses from Rauer Group, East Antarctica. J Meta Geol 16: 541–562

Harley SL (2004) Extending our understanding of ultrahigh-temperature crustal metamorphism. J Mineral Petrol Sci 99: 140–562

Harley SL (2008) Refining the *P-T* records of UHT crustal metamorphism. J Meta Geol 26: 125–154, DOI: 10.1111/j.1525-1314.2008.00765.x

Harley SL, Kelly NM (2007) The impact of zircon-garnet REE distribution data on the interpretation of zircon U-Pb ages in complex high-grade terrains: An example from the Rauer Islands, East Antarctica. Chem Geol 241: 62–87

Harley SL, Kelly NM, Moeller A (2007) Zircon behaviour and the thermal histories of mountain chains. Elements 3: 25–30

Harris NBW, Inger S (1992) Trace-element modelling of pelite-derived granites. Contrib Mineral Petrol 110: 46–56

Hasalova P, Schulmann K, Lexa O, et al. (2008a) Origin of migmatites by deformation-enhanced melt infiltration of orthogneiss: a new model based on quantitative microstructural analysis. J Meta Geol 26: 29–53

Hasalova P, Stipska P, Powell R, et al. (2008b) Transforming mylonitic metagranite by open-system interactions during melt flow. J Meta Geol 26: 55–80

Hermann J (2002) Experimental constraints on phase relations in subducted continental crust. Contrib Mineral Petrol 143: 219–235

Hermann J, Green DH (2001) Experimental constraints on high pressure melting in subducted crust. Earth Planet Sci Lett 188: 149–168

Hermann J, Rubatto D (2003) Relating zircon and monazite domains to garnet growth zones: age and duration of granulite facies metamorphism in the Val Malenco lower crust. J Meta Geol 21: 833–852

Hobbs B, Regenauer-Lieb K, Ord A. (2007) Thermodynamics of folding in the middle to lower crust. Geology 35: 175–178

Holk GJ, Taylor HP (2000) Water as a petrologic catalyst driving O-18/O-16 homogenisation and anatexis of the middle crust in the metamorphic core complexes of British Columbia. Internat Geol Rev 42: 97–130

Holland TJB, Powell R (1998) An internally consistent thermodynamic data set for phases of petrological interest. J Meta Geol 16: 309–343

Holland TJB, Powell R (2003) Activity-composition relations for phases in petrological calculations: an asymmetric multicomponent formulation. Contrib Mineral Petrol 145: 492–501

Holland TJB, Powell R (2001) Calculation of phase relations involving haplogranite melts using an internally consistent dataset. J Pet 42: 673–683

Holness MB, Sawyer EW (2008) On the pseudomorphing of melt-filled pores during the crystallisation of migmatites. J Pet 49: 1343–1363, doi: 10.1093/petrology/egn028

Hoskin PWO, Black LP (2000) Metamorphic zircon formation by solid-state recrystallisation of protolith igneous zircon. J Meta Geol 18: 423–439

Hyndman RD, Currie CA, Mazzotti SP (2005) Subduction zone backarcs, mobile belts, and orogenic heat. GSA Today 15: 4–10

Inger S, Harris N (1993) Geochemical constraints on leucogranite magmatism in the Langtang Valley, Nepal Himalaya. J Petrol 34: 345–368

Ito G, Martel SJ (2002) Focusing of magma in the upper mantle through dike interaction. J Geophys Res 107: B10, 2223, doi: 10.1029/2001JB000251

Jackson MD, Cheadle MJ, Atherton MP (2003) Quantitative modelling of granitic melt generation and segregation in the continental crust. J Geophys Res-Solid Earth 108: Art. No. 2332

Jamieson RA, Beaumont C, Nguyen MH, Lee B (2002) Interaction of metamorphism, deformation and exhumation in large convergent orogens. J Meta Geol 20: 9–24

Janousek V, Holub FV (2007) The causal link between HP-HT metamorphism and ultrapotassic magmatism in collisional orogens: case study from the Moldanubian Zone of the Bohemian Massif. Proc Geol Assoc 118: 75–86

Johnson T, Brown M (2004) Quantitative Constraints on Metamorphism in the Variscides of Southern Brittany—a Complementary Pseudosection Approach. J Pet 38: 1237–1259

Johnson TE, Hudson NFC, Droop GTR (2001) Melt segregation structures within the Inzie Head gneisses of the northeastern Dalradian. Scottish J Geol 37: 59–72

Johnson TE, Hudson NFC, Droop GTR (2003) Evidence for a genetic granite-migmatite link in the Dalradian of NE Scotland. J Geol Soc 160: 447–457

Johnson TE, Brown M, Solar GS (2003) Low-pressure subsolidus and suprasolidus phase equilibria in the MnNCKFMASH system: Constraints on conditions of regional metamorphism in western Maine, northern Appalachians. Amer Mineral 88: 624–638

Johnson TE, Gibson RL, Brown M, Buick IS, Cartwright I (2003) Partial melting of metapelitic rocks beneath the Bushveld Complex, South Africa. J Pet 44: 789–813

Johnson T, Brown M, Gibson R, Wing B (2004) Spinel-cordierite symplectites replacing andalusite: Evidence for melt-assisted diapirism in the Bushveld Complex, South Africa. J Meta Geol 22: 529–545. doi: 10.1111/j.1525-1314.2004.00531.x

Johnson TE, White RW, Powell R (2008) Partial melting of metagreywacke: a calculated mineral equilibria study. J Meta Geol 26: 837–853

Kelly NM, Harley SL (2005) An integrated microtextural and chemical approach to zircon geochronology: refining the Archaean history of the Napier Complex, east Antarctica. Contrib Mineral Petrol 149: 57–84

Kelly NM, Clarke GL, Harley SL (2006) Monazite behaviour and age significance in poly-metamorphic high-grade terrains: A case study from the western Musgrave Block, central Australia. Lithos 88: 100–134

Kelsey DE (2008) On ultrahigh-temperature crustal metamorphism. Gondwana Res 13: 1–29

Kelsey DE, White RW, Holland TJB, Powell R (2004) Calculated phase equilibria in $K_2O$-FeO-MgO-$Al_2O_3$-$SiO_2$-$H_2O$ for sapphirine-quartz-bearing mineral assemblages. J Meta Geol 22: 559–578

Kelsey DE, Clark C, Hand M (2008) Thermobarometric modelling of zircon and monazite growth in melt-bearing systems: examples using model metapelitic and metapsammitic granulites. J Meta Geol 26: 199–212

Kincaid C, Silver P (1996) The role of viscous dissipation in the orogenic process. Earth Planet Sci Lett 142: 271–288

Kretz R (1983) Symbols for rock-forming minerals. Amer Mineral 68: 277–279

Lang HM, Gilotti JA (2007) Partial melting of metapelites at ultrahigh-pressure conditions, Greenland Caledonides. J Meta Geol 25: 129–147

Laporte D, Rapaille C, Provost A (1997) Wetting angles, equilibrium melt geometry, and the permeability threshold of partially molten crustal protoliths. In: Bouchez JL, Hutton DHW, Stephens WE (eds.) Granite: From segregation of melt to emplacement fabrics. Kluwer Academic Publishers, The Netherlands

Leichmann J, Novak M, Burianek D, Burger D (2007) High-temperature to ultrahigh-temperature metamorphism related to multiple ultrapotassic intrusions: evidence from garnet-sillimanite-cordierite kinzigite and garnet-orthopyroxene migmatites in the eastern part of the Moldanubian Zone (Bohemian Massif). Geol Carpathica 58: 415–425

Leloup PH, Kienast JR (1993) High-temperature metamorphism in a major strike-slip shear zone—the Ailao-Shan-Red River, Peoples Republic of China. Earth Planet Sci Lett 118: 213–234

Leloup PH, Ricard Y, Battaglia J, Lacassin R (1999) Shear heating in continental strike-slip shear zones: model and field examples. Geophys J Internat 136: 19–40

Le Pichon X, Henry P, Goffe B (1997) Uplift of Tibet: From eclogites to granulites – Implications for the Andean Plateau and the Variscan belt. Tectonophysics 273: 57–76

Liu L, Zhang J, Green HW, Jin Z, Bozhilov KN (2007) Evidence of former stishovite in metamorphosed sediments, implying subduction to >350 km. Eos, Trans Amer Geophys Union 86: V51E-08

Marchildon N, Brown M (2001) Melt segregation in late syn-tectonic anatectic migmatites: an example from the Onawa Contact Aureole, Maine, U.S.A. Phys Chem Earth (A) 26: 225–229

Marchildon N, Brown M (2002) Grain-scale melt distribution in two contact aureole rocks: Implication for controls on melt localisation and deformation. J Meta Geol 20: 381–396

Marchildon N, Brown M (2003) Spatial distribution of melt-bearing structures in anatectic rocks from Southern Brittany: implications for melt-transfer at grain- to orogen-scale. Tectonophysics 364: 215–235

Martignole J (2008) Is the dehydration of migmatites by melt extraction a precursor to UHT metamorphism? Québec 2008, GAC-MAC-SEG-SGA, Abstracts Vol 33: 105

Martignole J, Martelat JE (2003) Regional-scale Grenville-age UHT metamorphism in the Mollendo-Camana block (basement of the Peruvian Andes). J Meta Geol 21: 99–120

McCaig AM, Wickham SM, Taylor HP (1990) Deep fluid circulation in Alpine shear zones, Pyrenees, France - Field and oxygen isotope studies. Contrib Mineral Petrol 106: 41–60

McKenzie D, Priestley K (2008) The influence of lithospheric thickness variations on continental evolution. Lithos. doi: 10.1016/j.lithos.2007.05.005

McLaren S, Sandiford M, Powell R, Neumann N, Woodhead J. (2006) Palaeozoic intraplate crustal anatexis in the Mount Painter province, South Australia: timing, thermal budgets and the role of crustal heat production. J Pet 47: 2281–2302

Milord I, Sawyer EW, Brown M (2001) Formation of diatexite migmatite and granite magma during anatexis of semi-pelitic metasedimentary rocks: an example from St Malo, France. J Pet 42: 487–505

Möller A, O'Brien PJ, Kennedy A, Kroner A (2002) Polyphase zircon in ultrahigh-temperature granulites (Rogaland, SW Norway): constraints for Pb diffusion in zircon. J Meta Geol 20: 727–740

Moller A, Hensen BJ, Armstrong RA, Mezger K, Ballevre M (2003) U-Pb zircon and monazite age constraints on granulite-facies metamorphism and deformation in the Strangways Metamorphic Complex (central Australia). Contrib Mineral Petrol 145: 406–423

Möller A, Hellebrand E, Moraes R, Mocek B (2007) REE distribution between zircon and orthopyroxene in granulites as a link between petrology and geochronology. Geochim Cosmochim Acta 71: A680–A680

Montel JM, Foret A, Veschambre M, Nicollet C, Provost A (1996) Electron microprobe dating of monazite. Chem Geol 131: 37–53

Montel JM, Vielzeuf D (1997) Partial melting of metagreywackes. 2. Compositions of minerals and melts. Contrib Mineral Petrol 128: 176–196

Moraes R, Brown M, Fuck RA, Camargo MA, Lima TM (2002) Characterisation and *P-T* evolution of melt-bearing ultrahigh-temperature granulites: an example from the Anápolis-Itauçu Complex of the Brasília Fold Belt, Brazil. J Pet 43: 1673–1705

O'Brien PJ, Rötzler J (2003) High-pressure granulites: formation, recovery of peak conditions and implications for tectonics. J Meta Geol 21: 3–20

Osanai Y, Nakano N, Owada M, Nam TN, Miyamoto T, Thi Minh N, Van Nam N, Van Tri T (2008) Collision zone metamorphism in Vietnam and adjacent South-eastern Asia: Proposition for Trans Vietnam Orogenic Belt. J Mineral Petrol Sci 103: 226–241

Patiño-Douce AE (1999) What do experiments tell us about the relative contributions of crust and mantle to the origin of granitic magmas? In: Castro A, Fernández C, Vigneresse J-L (eds) Understanding Granites: Integrating New and Classical Techniques. Geol Soc London Spec Publ 168: 55–75

Petrini K, Podladchikov Y (2000) Lithospheric pressure-depth relationship in compressive regions of thickened crust. J Meta Geol 18: 67–77

Pattison DRM, Harte B (1988) Evolution of structurally contrasting migmatites in the 3-kbar Ballachulish aureole, Scotland. J Meta Geol 6: 475–494

Peressini G, Quick JE, Sinigoi S, Hofmann AW, Fanning M (2007) Duration of a large mafic intrusion and heat transfer in the lower crust: a SHRIMP U-Pb zircon study in the Ivrea-Verbano Zone (Western Alps, Italy). J Pet 48: 1185–1218

Platt JP (1998) Thermal evolution, rate of exhumation, and tectonic significance of metamorphic rocks from the floor of the Alboran extensional basin, western Mediterranean. Tectonics 17: 671–689

Platt JP, England PC (1994) Convective removal of lithosphere beneath mountain belts – thermal and mechanical consequences. Am J Sci 294: 307–336

Platt JP, Whitehouse MJ, Kelley SP, Carter A, Hollick L (2003) Simultaneous extensional exhumation across the Alboran Basin: Implications for the causes of late orogenic extension. Geology 31: 251–254

Powell R (1983) Processes in granulite facies metamorphism. In Atherton MP, Gribble CD (eds) Migmatites, melting and metamorphism. Shiva, Nantwich

Powell R, Downes J (1990) Garnet porphyroblast-bearing leucosomes in metapelites: Mechanisms, phase diagrams and an example from Broken Hill. In: Ashworth JR, Brown M (eds) High temperature metamorphism and crustal anatexis. Unwin Hyman, London

Powell R, Holland TJB (1988) An internally consistent dataset with uncertainties and correlations. 3. Applications to geobarometry, worked examples and a computer-program. J Meta Geol 6: 173–204

Powell R, Holland T, Worley B (1998) Calculating phase diagrams involving solid solutions via non-linear equations, with examples using THERMOCALC. J Meta Geol 16: 577–588

Powell R, Guiraud M, White RW (2005) Truth and beauty in metamorphic phase equilibrias: Conjugate variables and phase diagrams. Can Mineral 43: 21–33

Raith M, Karmakar S, Brown M (1997) Ultrahigh-temperature metamorphism and multi-stage decompressional evolution of sapphirine granulites from the Palni Hill Ranges, Southern India. J Meta Geol 15: 379–399

Regenauer-Lieb K (1999) Dilatant plasticity applied to Alpine collision: Ductile void growth in the intraplate area beneath the Eifel volcanic field. J Geodyn 27: 1–21

Rosenberg CL, Riller U (2000) Partial-melt topology in statically and dynamically recrystallised granite. Geology 28: 7–10

Rubatto D (2002) Zircon trace element geochemistry: partitioning with garnet and the link between U-Pb ages and metamorphism. Chem Geol 184: 123–138

Rubatto D, Williams IS, Buick IS (2001) Zircon and monazite response to prograde metamorphism in the Reynolds Range, central Australia. Contrib Mineral Petrol 140: 458–468

Rubatto D, Hermann J, Buick IS (2006) Temperature and bulk composition control on the growth of monazite and zircon during low-pressure anatexis (Mount Stafford, central Australia. J Petrol 47: 1973–1996

Rushmer T (1993) Experimental high-pressure granulites - some applications to natural mafic xenolith suites and Archean granulite terranes. Geology 21: 411–414

Rutter EH (1997) The influence of deformation on the extraction of crustal melts: A consideration of the role of melt-assisted granular flow. In: Holness MB (ed) Deformation-enhanced fluid transport in the Earth's crust and mantle. Chapman and Hall, London

Rutter EH, Mecklenburg J (2006) The extraction of melt from crustal protoliths and the flow behavior of partially molten crustal rocks: an experimental perspective. In: Brown M, Rushmer T (eds) Evolution and Differentiation of the Continental Crust. Cambridge University Press

Sandiford M, Powell R (1991) Some remarks on high-temperature-low-pressure metamorphism in convergent orogens. J Meta Geol 9: 333–340

Sawyer EW (1986) The influence of source rock type, chemical-weathering and sorting on the geochemistry of clastic sediments from the Quetico Meta-Sedimentary Blet, Superior Province, Canada. Chem Geol 55: 77–95

Sawyer EW (1996) Melt segregation and magma flow in migmatites: implications for the generation of granite magmas. Trans R Soc Edinburgh: Earth Sci 87: 85–94

Sawyer EW (1999) Criteria for the recognition of partial melting. Phys Chem Earth (A) 24: 269–279

Sawyer EW (2001) Melt segregation in the continental crust: Distribution and movement of melt in anatectic rocks. J Meta Geol 18: 291–309

Schaltegger U, Fanning CM, Gunther D, Maurin JC, Schulmann K, Gebauer D (1999) Growth, annealing and recrystallisation of zircon and preservation of monazite in high-grade metamorphism: conventional and in-situ U-Pb isotope cathodoluminescence and microchemical evidence. Contrib Mineral Petrol 134: 186–201

Schellart WP (2007) Comment on "The thermal structure of subduction zone back arcs. J Geophys Res - Solid Earth 112: Bll407. doi: 10.1029/2007/JB005287

Schmidt MW, Vielzeuf D, Auzanneau E (2004) Melting and dissolution of subducting crust at high pressures: the key role of white mica. Earth Planet Sci Lett 228: 65–84

Selbekk R, Skjerlie KP, Pedersen RB (2000) Generation of anorthositic magma by H2O-fluxed anatexis of silica-undersaturated gabbro: an example from the north Norwegian Caledonides. Geol Mag 137: 609–621

Sibson RH (1986) Earthquakes and rock deformation in crustal fault zones. An Rev Earth Planet Sci 14: 149–175

Simakin A, Talbot C (2001) Transfer of melt between microscopic pores and macroscopic veins in migmatites. Phys Chem Earth 26: 363–367

Slagstad T, Jamieson RA, Culshaw NG (2005) Formation, crystallisation, and migration of melt in the mid-orogenic crust: Muskoka domain migmatites, Grenville Province, Ontario. J Pet 46: 893–919

Solar GS, Brown M (2001) Petrogenesis of migmatites in Maine, USA: Possible source of peraluminous leucogranite in plutons? J Petrol 42: 789–823

Stevens G, Villaros A, Moyen JF (2007) Selective peritectic garnet entrainment as the origin of geochemical diversity in S-type granites. Geology 35: 9–12

Stüwe K (1998) Heat sources of Cretaceous metamorphism in the Eastern Alps – a discussion. Tectonophysics 287: 251–269

Stüwe K (2007) Geodynamics of the lithosphere. Springer

Stüwe K, Sandiford M (1994) Contribution of deviatoric stresses to metamorphic *P-T* paths – an example appropriate to low-P, high-T metamorphism. J meta. Geol 12: 445–454

Stüwe K, Sandiford M, Powell R (1993) Episodic metamorphism and deformation in low-pressure, high-temperature terranes. Geology 21: 829–832

Symmes GH, Ferry JM (1995) Metamorphism, fluid-flow and partial melting in pelitic rocks from the Onawa contact aureole, Central Maine, USA. J Pet 36: 587–612

Tomkins HS, Williams IS, Ellis DJ (2005) In situ U-Pb dating of zircon formed from retrograde garnet breakdown during decompression in Rogaland, SW Norway. J Meta Geol 23: 201–215

Turner FJ (1968) Metamorphic Petrology. McGraw-Hill

Watson EB (1996) Dissolution, growth and survival of zircons during crustal fusion: Kinetic principles, geological models and implications for isotopic inheritance. Trans R Soc Edinburgh-Earth Sci 87: 43–56

Watson EB, Wark DA, Thomas JB (2006) Crystallisation thermometers for zircon and rutile. Contrib Mineral Petrol 151: 413–433

Watt GR, Harley SL (1993) Accessory phase controls on the geochemistry of crustal melts and restites produced during water-undersaturated partial melting. Contrib Mineral Petrol 114: 550–566

Upton P, Koons PO, Chamberlain CP (1995) Penetration of deformation-driven meteoric water into ductile rocks: Isotopic and model observations from the Southern alps, New Zealand. New Zealand J Geol Geophys 38: 535–543

Vernon RH, Collins WJ (1988) Igneous microstructures in migmatites. Geology 16: 1126–1129

Vielzeuf D, Holloway JR (1988) Experimental-determination of the fluid-absent melting relations in the pelitic system - consequences for crustal differentiation. Contrib Mineral Petrol 98: 257–276

Vielzeuf D, Montel JM (1994) Partial melting of metagreywackes. 1. Fluid-absent experiments and phase-relationships. Contrib Mineral Petrol 117: 375–393

Vielzeuf D, Schmidt MW (2001) Melting relations in hydrous systems revisited: application to metapelites, metagreywackes and metabasalts. Contrib Mineral Petrol 141: 251–267

Vielzeuf D, Vidal Ph (1990) Granulites and Crustal Evolution. Kluwer Academic Publishers

Waters DJ (1988) Partial melting and the formation of granulite facies assemblages in Namaqualand, South Africa. J Meta Geol 6: 387–404

Watt GR, Oliver NHS, Griffin BJ (2000) Evidence for reaction-induced microfracturing in granulite facies pelitic migmatites. Geology 28: 331–334

White RW (2008) Insights gained from the petrological modelling of migmatites: Particular reference to mineral assemblages and common replacement textures. In: Sawyer EW, Brown M (eds) Working with Migmatites. Mineralogical Association of Canada Short Course Series 38, Quebec City, Quebec

White RW, Powell R (2002) Melt loss and the preservation of granulite facies mineral assemblages. J Meta Geol 20: 621–632

White RW, Powell R, Holland TJB, Worley BA (2000) The effect of $TiO_2$ and $Fe_2O_3$ on metapelitic assemblages at greenschist and amphibolite facies conditions: Mineral equilibria calculations in the $K_2O$-FeO-MgO-$Al_2 0_3$-$SiO_2$-$H_2O$-$TiO_2$-$Fe_2O_3$. J Meta Geol 18: 497–511

White RW, Powell R, Holland TJB (2001) Calculation of partial melting equilibria in the system $Na_2O$-CaO-$K_2O$-FeO-MgO-$Al_2O_3$-$SiO_2$-$H_2O$ (NCKFMASH). J Meta Geol 19: 139–153

White RW, Powell R, Clarke G (2002) The interpretation of reaction textures in Fe-rich metapelitic granulites of the Musgrave Block, central Australia: constraints from mineral equilibria calculations in the system $K_2O$-FeO-MgO-$Al_2O_3$-$SiO_2$-$H_2O$-$TiO_2$-$Fe_2O_3$. J Meta Geol 20: 41–55

White RW, Powell R, Clarke G (2003) Prograde metamorphic assemblage evolution during partial melting of metasedimentary rocks at low pressures: Migmatites from Mt. Stafford, central Australia. J Petrol 44: 1937–1960

White RW, Powell R, Halpin JA (2004) Spatially-focused melt formation in aluminous metapelites from Broken Hill, Australia. J Meta Geol 22: 825–845

White RW, Pomroy NE, Powell R (2005) An in situ metatexite-diatexite transition in upper amphibolite facies rocks from Broken Hill, Australia. J Meta Geol 23: 579–602

White RW, Powell R, Holland TJB (2007) Progress relating to calculation of partial melting equilibria for metapelites. J Meta Geol 25: 511–527

Wickham SM, Taylor HP (1987) Stable isotope constraints on the origin and depth of penetration of hydrothermal fluids associated with Hercynian regional metamorphism and crustal anatexis in the Pyrenees. Contrib Mineral Petrol 95: 255–268

Williams IS (2001) Response of detrital zircon and monazite, and their U-Pb isotopic systems, to regional metamorphism and host-rock partial melting, Cooma Complex, southeastern Australia. Aus J Earth Sci 48: 557–580

Williams ML, Jercinovic MJ (2002) Microprobe monazite geochronology: putting absolute time into microstructural analysis. J Struct Geol 24: 1013–1028

Williams ML, Jercinovic MJ, Terry MP (1999) Age mapping and dating of monazite on the electron microprobe: Deconvoluting multistate tectonic histories. Geology 27: 1023–1026

Xia QX, Zheng YF, Zhou LG (2008) Dehydration and melting during continental collision: Constraints from element and isotope geochemistry of low-T/UHP granitic gneiss in the Dabie orogen. Chem Geol 247: 36–65.

5

# Closure Temperature, Cooling Age and High Temperature Thermochronology

Jibamitra Ganguly and Massimilano Tirone

**Abstract:** The concept and analytical formulations of mean closure temperature ($\overline{T}_c$) and closure temperature profile in cooling geochronological systems have been reviewed along with a discussion of their limitations. The conventional approach of retrieving the average cooling rate of a rock from $\overline{T}_c$ vs cooling age data of multiple geochronological systems, which are applied to the same sample, suffers from the problem of circular logic in that the $\overline{T}_c$ of a given decay system itself depends on the cooling rate, especially when it falls below 10°C/Myr for many systems. It is, however possible to retrieve cooling rate of a sample, without any knowledge of $\overline{T}_c$, directly from (a) the extent of resetting of average mineral age during cooling and (b) the difference between the average ages of a central segment of a mineral grain and the bulk grain itself, as determined by a specific decay system. On the other hand $\overline{T}_c$ for a specific system, grain size and geometry can be retrieved from the inferred cooling rate. These recent developments between the cooling age and cooling rate relations are reviewed in this paper.

---

Jibamitra Ganguly (✉)
Department of Geosciences, University of Arizona, Tucson, AZ 85721, USA
e-mail: ganguly@email.arizona.edu

Massimilano Tirone
Department of Earth Sciences, Florida International University, Miami, FL 33199, USA

## 5.1 Introduction

In a broad sense thermochronology refers to determination or constraining the thermal history of rocks within a framework of absolute time that is determined by dating rocks and minerals. Most thermochronological studies deal with relatively low temperature geological and planetary processes, typically below ~500°C. A recent volume of Reviews of Mineralogy and Geochemistry, edited by Reiners and Ehlers (2005), provides a thorough overview of the subject of low-temperature thermochronology and its wide ranging applications.

It is fair to say that quantitative thermochronological studies began with a seminal paper by Dodson (1973), which formally introduced the concept of closure temperature ($T_c$) of a cooling geochronological system and provided a mathematical formulation for calculating the closure temperature on the basis of the geometry and size of the mineral grains used for dating, cooling rate of the host rock and diffusion kinetic properties of the geochronological system in the mineral of interest. The age of a mineral as determined by mineral-whole rock age or internal mineral isochron, is effectively the time lapse since the closure temperature of the mineral for the specific decay system. The mineral ages are, thus often referred to as cooling ages.

Since Dodson's paper, numerous studies have sought to constrain cooling rates of rocks on the basis of a $T_c$ vs age plot in which the different combinations of $T_c$ and age, as determined by different decay systems in different minerals are collected together and fitted to obtain the average rate of change of temperature during cooling. An example of such approach is illustrated in Fig. 5.1 which is taken from Spear and Parrish (1996). An inherent circularity in this approach is that cooling rate is retrieved by assigning a $T_c$ to a specific system in a mineral while $T_c$ itself depends on cooling rate. Despite this circularity, cooling rate retrieved from closure temperature diagrams may provide a good first order approximation of the true cooling rate within the temperature interval encompassed by the closure temperatures, provided that several decay systems have been used to constrain it, the cooling is relatively rapid (>10°C/Myr) and sufficient uncertainties are assigned to the $T_c$ values to reflect their variability in natural environments as function of different parameters that affect them, as discussed below. Ideally the $T_c$ of each decay system should be recalculated using the initial value of the cooling rate and the process should be repeated until there is no significant change of the calculated $T_c$ values for the different systems.

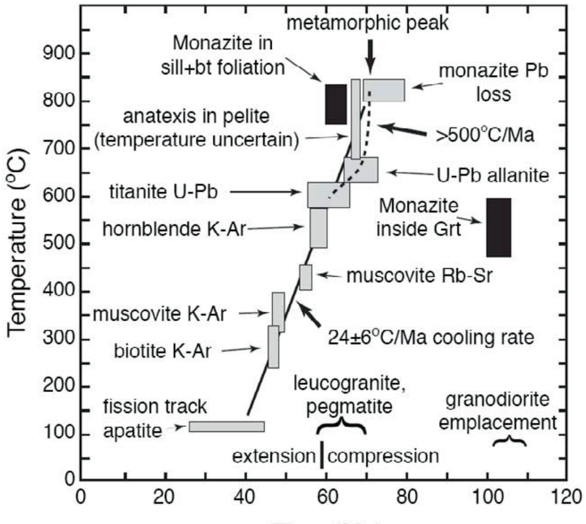

**Fig. 5.1** Mineral closure temperature vs cooling age plot of a number of geochronological systems for samples from the Valhalla complex, British Columbia. The data are fitted to obtain an average cooling rate of 24 ± 6°C/Ma. From Spear and Parrish (1995). With permission from J Pet (Oxford University Press)

There are several simplifying assumptions in the Dodson (1973) formulation of closure temperature. One of the assumptions is that there is sufficient diffusive loss of the daughter product from the mineral so its concentration even at the core of the mineral is different from that at the peak thermal condition. For many geologically important systems, this "memory loss" condition is not satisfied. For example diffusivities of elements in minerals like garnet and pyroxene are too slow to affect the composition at the core during cooling unless the cooling rate is very slow and/or the grain size is very small (Ganguly et al. 1998). Ganguly and Tirone (1999) extended the Dodson formulation to include systems that did not suffer complete "memory loss" and also developed methods of determining cooling rate from cooling ages of minerals, without requiring any knowledge of their closure temperatures.

The purpose of this review is to provide a simple exposition of the concept of closure temperature in a cooling geochronological system and the methods by which one can retrieve cooling rate from knowing the average age loss of a decay system or its spatial variation within a single crystal. Within the framework of assumptions of the Dodson (1973) formulation of closure temperature, there is no formal restriction on the temperature range of application of these methods as long as the cooling is monotonic and follows a specific form. However if the average age loss is determined by such decay systems as Sm-Nd, Lu-Hf, Rb-Sr for which the parent and daughter nuclides effectively cease to diffuse at relatively high temperatures (>500°C), then one obtains cooling rates at temperatures between the peak temperature and the closure temperature of diffusion of the geochronological system. Thus the methods reviewed in this paper may be used to complement those of low temperature thermochronology that typically yield cooling rates below 500°C.

## 5.2 Closure Temperature and Mineral Age

### 5.2.1 General Concept

The concept of closure temperature is illustrated in Fig. 5.2 with a numerical simulation of the spatial variation of the compositional change during cooling in a spherical mineral surrounded by a homogeneous matrix of fixed composition. The mineral is assumed to have a radius of 1 mm and to have cooled from a peak temperature ($T_o$) of 900°C following an asymptotic form given by the relation (Fig. 5.2a)

$$(1/T) = (1/T_0) + \eta t \tag{5.1a}$$

so that

$$(dT/dt) = -\eta T^2 \tag{5.1b}$$

where η is a cooling time constant with the dimension of $K^{-1}t^{-1}$. It is assumed to have a value of $9.6 \times 10^{-6}$ $Myr^{-1}K^{-1}$. As the mineral cools, a species *i* tends to diffuse into the mineral to maintain equilibrium with the matrix. It is assumed that the diffusion coefficient of *i* as a function of temperature is given by the Arrhenian relation $D = D_o e^{-E/RT}$, where $D_o = 7.22 \times 10^{-4}$ $cm^2/s$ and E (activation energy) = 266 kJ/mol.

The surface composition ($C_s$) of the mineral is assumed to maintain equilibrium with the matrix at all time following a prescribed relation, $C_s/C_o = 0.65e^{500/T}$, where $C_o$ is the initial concentration, which is homogeneous at $T_o$. However the compositional change within the interior of the grain progressively lags behind that required to maintain equilibrium with the matrix. Figure 5.2b shows the compositional change of the species within the crystal as a function of radial distance. At any given distance, the change of composition of *i* follows the equilibrium path up to a certain temperature, then falls off the equilibrium relation and ultimately quenches below a temperature ($T_q$) where the diffusion coefficient is too small relative to the length scale of diffusion to cause any significant gain of the diffusing species (note that D decreases exponentially with temperature). The temperature corresponding to the projection of the quenched composition on to the line for equilibrium change of composition (given by $C_s$ vs T relation) has been defined by Dodson (1973) as the closure temperature ($T_c$) (Fig. 5.2b). It is different from $T_q$, but as long as the time interval between $T_c$ and $T_q$ is small, substitution of $T_c$ for $T_q$ does not cause any significant problem.

In the numerical simulation presented in Fig. 5.2, $T_c$ varies as a function of the radial distance within the crystal in-

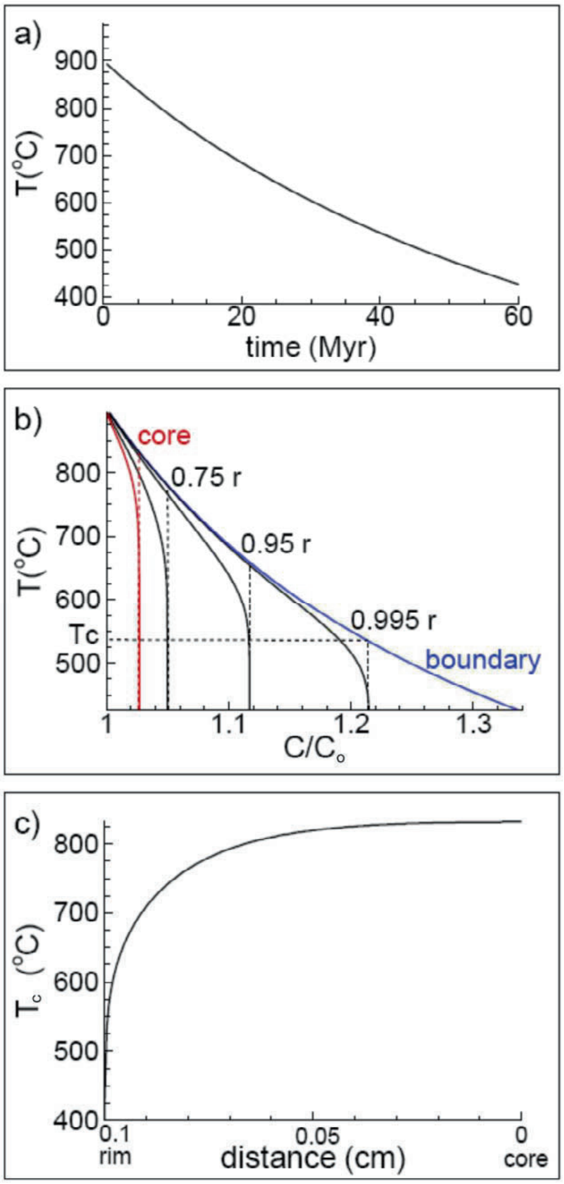

**Fig. 5.2** Numerical simulation of (a) cooling of a system following an asymptotic T-t relation (Eq. 5.1a) with $\eta = 9.6 \times 10^{-6}$ $Myr^{-1}K^{-1}$, (b) spatial variation of change of concentration of a species during cooling within a spherical grain of 1 mm radius and (c) corresponding closure temperature profile within the crystal. The diffusion coefficient of the species is given by $D = 7.22 \times 10^{-4}\exp(-E/RT)$ with E(activation energy) = 266 kJ/mol. The panel (b) illustrates the formal definition of closure temperature ($T_c$) at any radial distance within the crystal. $C_o$ stands for the initial concentration that is established at the peak temperature

creasing smoothly towards the center (Fig. 5.2c). Thus instead of a discrete closure temperature, there is a closure temperature profile, $T_c(x)$. The magnitude of change of $T_c(x)$ as function of distance depends on the factors that control the diffusive loss of the species of interest from the mineral, namely D, grain size, $T_o$ and cooling rate. One can also speak of mean closure temperature, $\overline{T}_c$ which represents a weighted average of $T_c(x)$.

If the diffusing species represent the parent and daughter nuclides of a decay system (e.g. Sm-Nd system), hen the age of a mineral effectively represents the elapsed time since the average closure temperature, $\overline{T}_c$ of the system in the mineral. If there is significant variation of closure temperature as function of distance within a mineral, then there is also a corresponding age profile, in which case the age of a mineral determined by thermal ionisation mass spectrometry represents its average age.

### 5.2.2 Dodson Formulation

Dodson (1973) derived an expression for the weighted average of the closure temperatures, $\overline{T}_c$ of a geochronological system as

$$\frac{\mathrm{E}}{\mathrm{R}\overline{\mathrm{T}}_{\mathrm{c}}} = \ln\left(-\frac{AR\overline{T}_c D_o}{Ea^2\left(dT/dt\right)_{@\overline{\mathrm{T}}_{\mathrm{c}}}}\right) \tag{5.2}$$

where a is a characteristic grain dimension (radius for sphere and cylinder, and half-length for a plane sheet), R is the gas constant, $D_o$ is the pre-exponential factor in the Arrhenian expression of diffusion coefficient and A is a geometric factor that is given by

$$\mathrm{A} = \mathrm{e}^{\mathrm{G}} \tag{5.2'}$$

where G = 4.0066 for sphere, 3.29506 for cylinder and 2.15821 for plane sheet.

It is, however often overlooked that the cooling rate in the above expression refers to that at $\overline{T}_c$. It can be replaced by cooling rate at any other temperature, T′, by replacing $\overline{T}_c$ with T′ on the right hand side. (According to Eq. 5.1b) the cooling rates (CR) at any two temperatures, say $T_o$ and T′ are related according to the square of their ratio, e.g. $(CR)_{@T_o}/(CR)_{@T'} = (T_o/T')^2)$. Subsequently Dodson (1986) derived an expression of closure temperature profile, which is discussed below along with a modification of his formulation.

The important assumptions underlying Dodson's formulations of closure temperature (Dodson 1973, 1986), which is restricted to minor or trace components (a condition that is satisfied by a geochronological system) are:

(a) The mineral of interest has a homogeneous distribution of the parent and daughter nuclides at the peak thermal condition

(b) It is surrounded by a sufficiently large mass of fast diffusing matrix so that the composition of the matrix remains effectively homogeneous and fixed

(c) The surface composition of the mineral is in equilibrium with the matrix during cooling and changes uniformly with time

(d) The cooling is monotonic and follows the form of Eq. 5.1

(e) The mineral is isotropic with respect to diffusion and, as mentioned above

(f) The mineral has suffered a complete "memory loss" of its concentration of radiogenic daughter product established at To.

The last assumption makes the closure temperature independent of $T_o$. This critical assumption underlying Dodson (1973, 1986) formulation has, however been overlooked in numerous applications of his formulation (Eq. 5.2) to calculate $\overline{T}_c$ of a geochronological system.

In order to discuss further developments, it is convenient at this stage to introduce a dimensionless parameter, M, the square root of which may be viewed as the diffusion distance within a grain, normalised by the grain size. The original expression of M given by Dodson (1973) may be recast in the following form (Ganguly and Tirone, 1999).

$$M = -\frac{RD(T_o)T^2}{Ea^2\left(dT/dt\right)_{@T}} = \frac{RD(T_o)}{E\eta \mathrm{a}^2} \tag{5.3}$$

where $D(T_o)$ is the diffusion coefficient at $T_o$.

The closure temperature formulation of Dodson (1973) is valid only for a sufficiently large value of M so that the original concentration of the daughter product at the peak temperature is not preserved even at the core of the mineral grains. Ganguly and Tirone (1999) showed that the threshold values of M are ~0.3 for sphere, ~0.5 for cylinders and ~1.1 for plane sheet. Thus one needs to evaluate if the system has an M value greater or equal to the appropriate threshold value if the average closure temperature is to be determined from Eq. 5.2. Also, in as much as the common practice is to determine cooling rate from $\overline{T}_c$ vs cooling age data of multiple geochronological systems applied to the same rock (Fig. 5.1), one should at least evaluate M from the retrieved cooling rate to test if it has a value greater than the appropriate threshold value given above, if $\overline{T}_c$ values are calculated according to Eq. 5.1.

### *5.2.3 Extension of Dodson Formulation by Ganguly and Tirone*

When the concentration of a species established at $T_o$ is preserved within a mineral grain, which is a quite common situation both in terrestrial and planetary samples, the classic Dodson formulation would yield erroneously high value of $\overline{T}_c$. As stated by Dodson (personal communication) "... calculated closure temperatures which come out close to the peak metamorphic temperatures are bound to be in error to some extent." Many closure temperature calculations in the literature are indeed erroneously too high because these were calculated on the basis of Dodson (1973) formulation without regard to the condition of critical diffusive loss of the daughter product, as discussed above.

Ganguly and Tirone (1999) modified the Dodson (1973) formulation so that it becomes applicable to any system regardless of the extent of diffusive loss of daughter products. They showed that the desired modification results in the replacement of the geometric term A in Dodson's formulation (Eq. 5.2) by A′ that is given by $A' = e^{G+g}$. The term g, which we would refer to as a "memory function", depends on both M and the shape or geometry of the mineral grains (Fig. 5.3). In other words g depends on size and geometry of the grain, cooling rate, $T_o$ and the volume diffusion property of the species of interest. In terms of M, one can express the closure temperature at a given position within a mineral grain, $T_c(x)$ (Fig. 5.2), according to Ganguly and Tirone (1999),

$$E/[RT_c(x)] = \ln M + (E/RT_o) + G(x) + g(x) \qquad (5.4)$$

where G(x) and g(x) are respectively, a spatially dependent geometric term called "closure function" by Dodson (1986) and a spatially dependent "memory function". Values for G(x) within a single crystal as function of distance normalised by the grain size, as well as their mean values, are given by Dodson (1986) for spherical, plane sheet and cylindrical geometries. Note from the last expression that incorporation of the "memory effect" has introduced a dependence of $T_c$ on $T_o$, which is unlike the expression of $T_c$ in the classic Dodson (1973) formulation (Eq. 5.2). The expression of $T_c(x)$ derived by Dodson (1986) is the same as the last expression except that it does not have the g(x) term.

If the mean value of the "memory function" is negligible, then combination of Eqs. (5.3) and (5.4) and substitution of mean G for G(x) yield the general form of the classic Dodson (1973) expression for $\overline{T}_c$ (Eq. 5.2). In this case, the cooling rate on the right is defined at any arbitrary temperature, T′ that appears in the right hand numerator instead of $\overline{T}_c$. Dodson (1973) specialised the general expression by substituting $\overline{T}_c$ for T′.

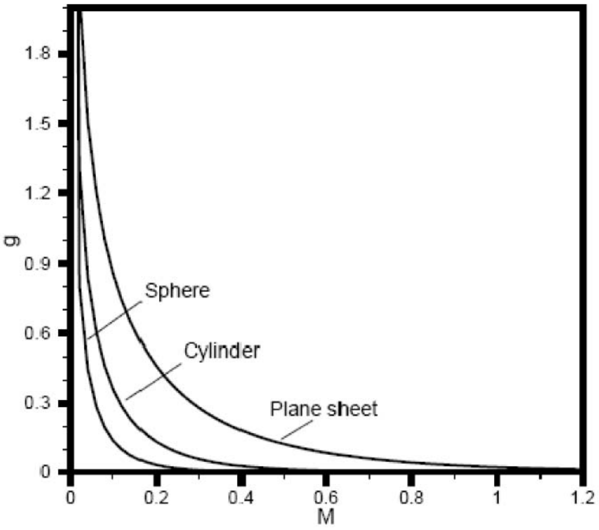

**Fig. 5.3** Variation of the "memory function" g used in the modification of Dodson (1973) formulation of closure temperature as function of the dimensionless parameter M (Eq. 5.3) and grain geometry. From Ganguly and Tirone (1999). With permission from EPSL (Elsevier)

Ganguly and Tirone (1999) derived an analytical expression for g(x). Using that formulation, Ganguly and Tirone (2001) calculated values of g(x) that are averaged over normalised distances of 0.25, 0.5 and 1.0 from the center of a crystal of a specific geometry (sphere, cylinder and plane sheet) and presented the data in tabular form as function of M.

Figure 5.4a shows $\overline{T}_c$ vs grain size for a cooling rate of 10°C/Myr (at $\overline{T}_c$) for Pb diffusion on monazite, as calculated by Cherniak et al. (2004) using both Dodson (1973) formulation, and its extension by Ganguly-Tirone (1999), which may be referred to as Dodson-Ganguly-Tirone or DGT formulation. Figure 5.4b shows a comparison of the $\overline{T}_c$ - s of spherical grains according to the two formulations as function of the dimensionless variable M (Ito and Ganguly, 2005). From the latter diagram one can calculate $\overline{T}_c$ for any geochronological system for any combination of grain size and cooling rate, provided that the $T_o$ values correspond to those used in the calculations.

To reiterate, in general $T_c$ depends on $T_o$. However $T_c$ becomes independent of $T_o$ (Fig. 5.4a) when the system has suffered a critical amount of diffusive loss of the daughter product. In Fig. 5.4, the domain of validity of the Dodson (1973) formulation is restricted to grain size or M values below those marking the points of its divergence from the modified formulation by Ganguly and Tirone (1999). Note

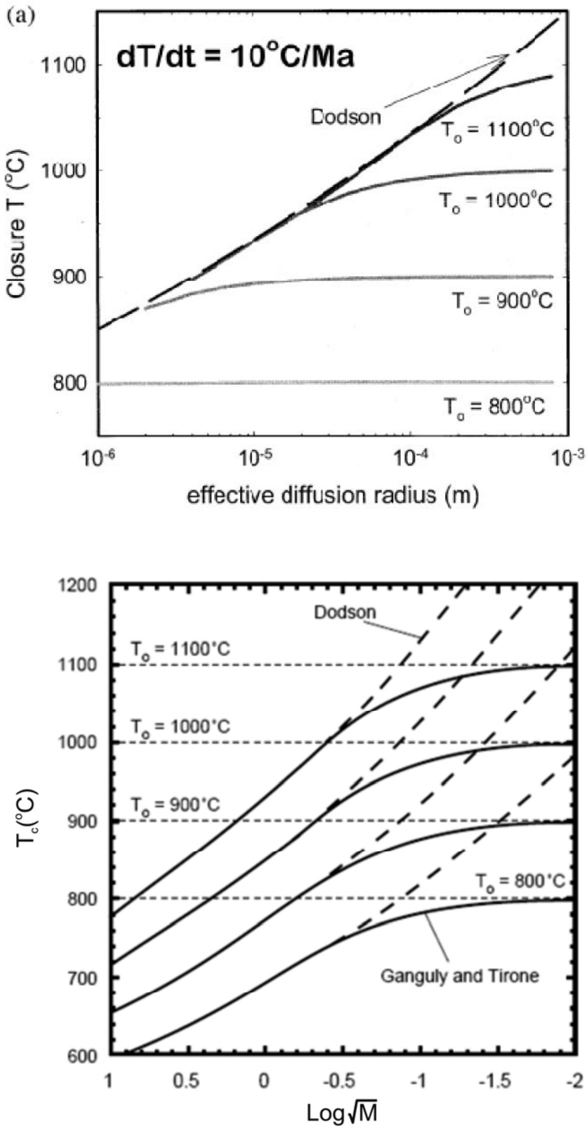

**Fig. 5.4** Comparison of average closure temperatures according to the conventional Dodson (1973) formulation with the modified formulation by Ganguly and Tirone (1999). (a) Pb diffusion in monazite for a fixed cooling rate of 10°C/Myr and different initial temperatures, $T_o$ (from Cherniak et al. 2004); (b) $T_c$ vs the dimensionless variable, M (Eq. 5.3) (from Ito and Ganguly, 2006). The domain of validity of the Dodson (1973) formulation is restricted to (a) grain size or (b) M values marking the point of divergence from the modified formulation by Ganguly and Tirone (1999). With permission from EPSL (Elsevier)

that the Dodson closure temperatures exceed $T_o$ at grain size and M values somewhat above the threshold values. Values of $T_c$ greater than $T_o$ were erroneously calculated by some workers in the literature (Ganguly and Tirone 2001, for discussion of the results of Göpel et al. 1994).

### 5.2.4 *Effects of Modal Abundance and Nature of Matrix Phase*

As stated above the closure temperature formulation of Dodson (1973) and its subsequent modification by Ganguly and Tirone (1999, 2001) assume that the matrix is homogeneous and effectively infinite. Analytical formulation of $\overline{T_c}$ under condition of a homogeneous but finite matrix (i.e. matrix of limited mass but sufficiently rapid diffusion property so that it changes composition during cooling, but remains homogeneous) has not been developed yet. However Jenkin et al. (1995) explored the problem numerically for a biotite-plagioclase assemblage and showed that the $\overline{T_c}$ for the Rb-Sr system changes non-linearly between the Dodson $\overline{T_c}$ - s of the two minerals as function of their modal abundances (Fig. 5.5). Since the system consists of only two minerals, there is only one $\overline{T_c}$, denoted as $T_{app}$, since both minerals must close simultaneously (in a binary system, the composition of a mineral cannot change if the other phase is closed). In the limits of biotite surrounded by a semi-infinite matrix of plagioclase ($V_{biotite}$ ~0) and the reverse ($V_{biotite}$ ~1), $T_{app}$ approaches $\overline{T_c}$ (biotite) and $\overline{T_c}$ ( plagioclase) of Dodson (1973), respectively.

The expected effect of the nature of matrix phase on closure temperature has been demonstrated by Burton et al. (1995) in their geochronological study of a garnet bearing coronite from Gaupås in the Bergen Arcs, western Norway.

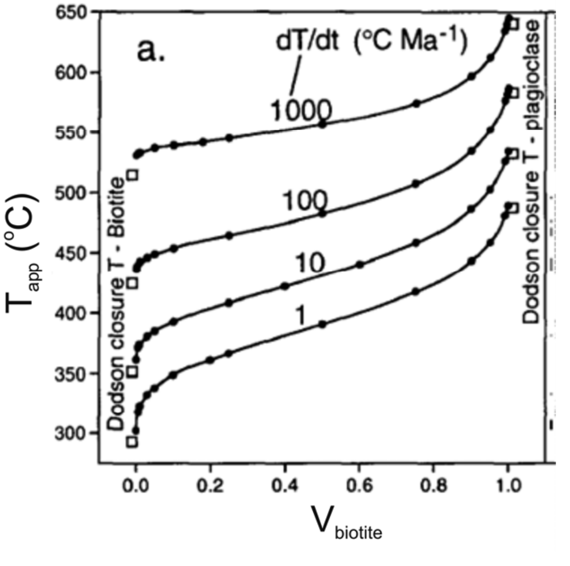

**Fig. 5.5** Variation of Rb-Sr closure temperature in an assemblage consisting of biotite and plagioclase as function volume fraction of biotite, $V_{biotite}$ and cooling rate, as calculated numerically by Jenkin et al. (1995)

They showed that the Sm-Nd ages of different parts of a garnet crystal are different, depending on the nature of the adjacent matrix phases, which implies that closure temperature for Nd diffusion within garnet depends on the nature of matrix phase, as expected.

### 5.2.5 *Effect of Diffusion Anisotropy*

Diffusion in non-cubic minerals is expected to be anisotropic and has indeed been found to have significant dependence on crystallographic orientation of diffusion direction in a number of anisotropic minerals (e.g. Chakraborty [1997]; Ito and Ganguly [2004, 2006]; Ganguly et al. [2007]). Ito and Ganguly (2006) and Ganguly et al. (2007) have shown variation of closure temperature as a function of crystallographic orientation of the direction of diffusive loss in olivine and orthopyroxene, respectively. In general, however the Dodson (1973) or the DGT (1999, 2001) formulation is inadequate to treat the problem of bulk closure temperature for minerals with significant diffusion anisotropy. It is anticipated that such a formulation would not only involve grain size, but also an aspect ratio. Diffusion may be very fast in one direction compared to that in other directions, but the diffusive loss in the fast direction may be small because of relatively much larger length scale for diffusive loss along that direction.

## 5.3 Thermochronology

### 5.3.1 *Resetting of Bulk Mineral Age*

Equation (5.4) enables one to calculate cooling rate of a mineral from knowledge of the difference between

(a) Its bulk cooling age, as determined by a specific decay system, and age at the peak thermal condition (Ganguly et al. [1998]; Ganguly and Tirone [2001]) or

(b) Its core and bulk ages (Ganguly and Tirone [2001]; Ducea et al. [2003]).

These methods, which have been developed by Ganguly and Tirone (1999, 2001) are presented below. As noted above, these methods are not restricted to any particular range of temperature, and thus may be used to fill the gap of thermochronological methods in the high temperature domain if these are used for decay systems with relatively slow diffusion property.

From Eq. 5.4, we have

$$\frac{E}{R}\left(\frac{1}{\overline{T}_c}-\frac{1}{T_o}\right)=\ln M+G+g \tag{5.5}$$

where the geometric term G and the "memory function" g, are for the bulk crystals of specific geometries. The bulk values of G for crystals of three different geometries, namely, spherical, cylindrical and plane sheet are given above (Eq. 5.2'), whereas those of g for the bulk crystal are given by Ganguly and Tirone (2001) as function of M for the same geometrical shapes.

If Δt represents the extent of resetting of a bulk mineral age (i.e. the time lapse between $T_o$ and $\overline{T}_c$), as determined by a specific decay system, then we can write Δt = Age since $T_o$ – Age since $\overline{T}_c$. Thus using Eq. 5.1a, the above expression may be written as

$$\Delta t = R/\eta E\,[\ln M + G + g] \tag{5.6}$$

Note that M is a function of the cooling time constant η (Eq. 5.3), whereas g is a function of M. If the peak temperature, $T_o$, grain size and diffusion kinetic properties determining the closure of the decay system in the mineral of interest are known, then both M and g can be determined by specifying η and crystal geometry, according to Eq. 5.3 and the tabulation of bulk g values as function of M and grain geometry given by Ganguly and Tirone (2001). If Δt for a specific decay system and mineral is known (e.g. for Sm-Nd age of garnet in a given rock), then one can determine η numerically by varying its value until the right hand side of the above equation yields the estimated value of Δt. This method has been applied (e.g. Ganguly et al. [1998]; Ito and Ganguly [2006]; Ganguly et al. [2007]; Shearer et al. [2000]) to determine the cooling rates of both terrestrial and planetary samples at relatively high temperatures. In this approach, one needs to know the age since the peak temperature from either whole rock age or mineral age by using another geochronological system, such as U-Pb system, that is characterised by very slow diffusion kinetic property leading to its closure at nearly the peak thermal condition.

### 5.3.2 *Spatial Variation of Age Within a Crystal*

In the absence of any knowledge of age since $T_o$, one can retrieve the cooling rate from the spatial variation of age or age profile, within a single crystal. The assumptions behind this approach are the same as for Dodson (1973, 1986) formulations, as summarised above, except that it does not require the condition of critical "memory loss" (condition (f)). An example of such age profiles as function of the dimensionless parameter M in crystals with spherical and plane sheet geometries (Ganguly and Tirone, 1999), is

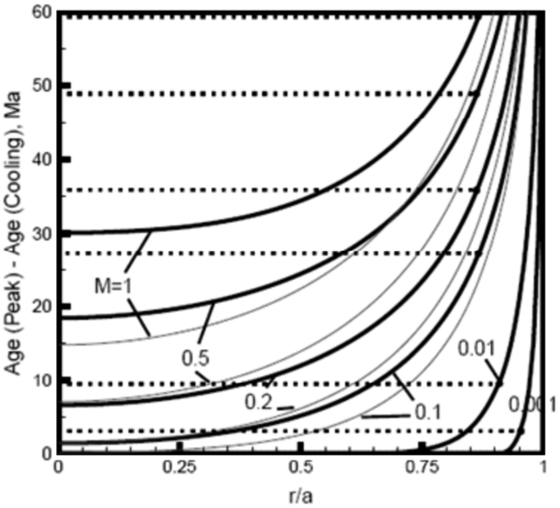

**Fig. 5.6** Simulated cooling age profiles within single crystals of spherical (heavy black lines) and plane sheet (light blue lines) geometries as function of the dimensionless variable, M (Eq. 5.3) and normalised distance from the center. The cooling age profiles are relative to the age at the thermal peak. From Ganguly and Tirone (1999). With permission from EPSL (Elsevier)

shown in Fig. 5.6. The activation energy (E) for diffusion is assumed to be 260 kJ/mol, which is approximately that for Nd diffusion in garnet (Ganguly et al. 1998). The mean ages corresponding to different age profiles for spherical geometry are shown by horizontal dashed lines.

If it is possible to determine age profile within a mineral grain, then one can calculate the value of M corresponding to the observed profile, and from that the cooling rate according to Eq. 5.3. However determination of age profile within a mineral does not seem to be a realistic goal within foreseeable future. It is more practical to determine the average age of a central segment and the average bulk age of a mineral using a single geochronological system. These ages can be used to derive cooling rate of a mineral as follows. Indeed Dodson (1986) suggested this possibility, but required a knowledge of E and $\overline{T}_c$. However as discussed below, the cooling rate can be determined from the difference between average core and average bulk ages without any knowledge of $\overline{T}_c$.

From Eqs. (5.1) and (5.5), the difference between the average central segment and bulk ages, ΔΓ, is given by (Ganguly and Tirone, 2001)

$$\Delta\Gamma = -(R/\eta E)\,(\Delta G + \Delta g) \qquad (5.7)$$

where Δ stands for the difference of the specified quantity between its weighted average value at a central domain of known dimension and for the bulk crystal (e.g. ΔΓ = average Age [central segment] – average Age [bulk grain]). The values of G and g, averaged over specified central dimensions and for the bulk crystal of different geometries (sphere, cylinder and plane sheet), are given by Ganguly and Tirone (2001). As for Eq. 5.6, the above equation is solved for η by successive approximations so that the right hand quantity equals the observed difference between the central and bulk age of a single crystal, as determined by a single geochronological system.

Ducea et al. (2003) applied the above method to determine the cooling rate of the granulite facies rocks from the metamorphic core complex in Valhalla, British Columbia. The cooling rate of these rocks were determined earlier by Spear and Parrish (1996) using the conventional $\overline{T}_c$ vs mineral age relations of multiple geochronological systems (Fig. 5.1). Ducea et al. (2003) selected a large garnet crystal and drilled from it a circular central segment of normalised radius of 0.4 for mass spectrometric analyses of $^{147}Sm/^{144}Nd$ and $^{143}Nd/^{144}Nd$ isotopic ratios. The data, which are illustrated in Fig. 5.7, yield a central segment-whole rock age of 67.3 (±2.3 Ma). In contrast, the rim-whole rock and bulk crystal-whole rock Sm-Nd ages were found to be 59.8 (±2.0) and 60.9 (±2.1) Ma, respectively. Using the difference between the central segment-whole rock and bulk crystal-whole rock ages (6.4 ± 3.1 Myr) and the appropriate data for the spatially averaged values of ΔG and Δg from Ganguly and Tirone (2001), $T_o$ = 820°C, as determined from geothermometry (Spear and Parrish, 1996)

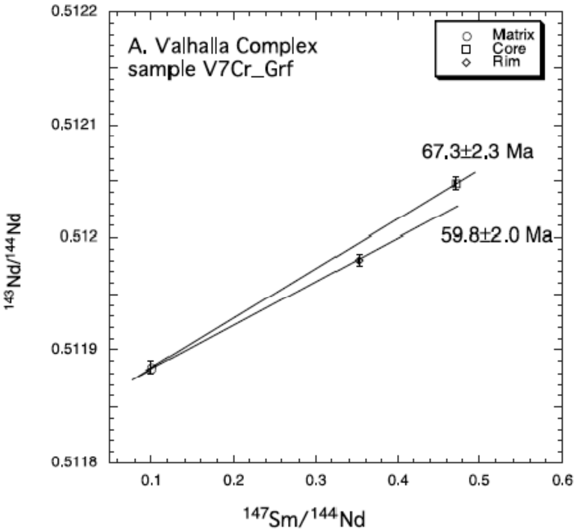

**Fig. 5.7** Whole rock matrix, core and rim Sm-Nd ages of a garnet single crystal from the Valhalla complex, British Columbia (From Ducea et al. 2003). With permission from EPSL (Elsevier)

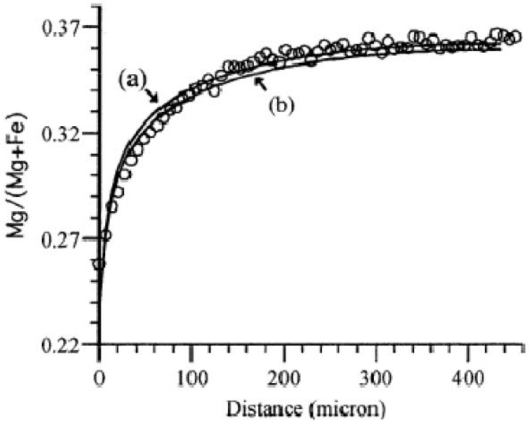

**Fig. 5.8** Compositional zoning (circles) of Mg in a garnet crystal from the Valhalla complex, British Columbia, which was subjected to core-rim Sm-Nd dating (Fig. 5.7). The solid lines are fits to the measured zoning profile assuming that the profiles developed during cooling from a peak temperature of 830°C at 8 kbar pressure. Curve (a) is an optimised fit to the data according to the numerical solution of the diffusion equation incorporating the effect of changing interface equilibrium during cooling, and assuming a non-linear cooling model (Eq. 5.1). The curve (b) is calculated by forcing the profile to better fit the data near the interface. With permission from EPSL (Elsevier)

and Nd diffusion data in almandine garnet (Ganguly et al. 1998), Ducea et al. (2003) solved Eq. 5.7 to obtain a value of $\eta = (5.1–8.3) \times 10^{-6}\ K^{-1}Myr^{-1}$. Using Eq. 5.1 and assuming a monotonic cooling, one can now calculate a T-t path or cooling rate as a function of temperature. The initial cooling rate is found to be 6–10°C/Myr.

Ducea et al. (2003) also determined the cooling rate of the sample by modelling the retrograde Fe-Mg zoning that developed in the same garnet crystal (Fig. 5.8). They found that the measured zoning profiles could be fitted very well using $\eta = (3.6–4.8) \times 10^{-6}\ K^{-1}Myr^{-1}$ that yields initial cooling rate of 4–6°C/Myr. These results are in agreement with the cooling rate retrieved from the Sm-Nd age data of the garnet crystal.

The numerical programme used to fit the data allows for the effect of changing interface equilibrium during cooling. In addition, the programme allows for the effect of crystallisation/resorption of the mineral during cooling through an interlinked optimisation programme that permits variation of crystal size during cooling, along with a prescribed uncertainty of the initial composition of the crystal, which is assumed to be homogeneous. It is found that the best match to the observed retrograde profile is obtained with a fixed crystal size and initial concentration given by the quenched core composition of the garnet crystal.

Using an error of ±30°C for $T_o$, the range of initial cooling rate inferred from the core and bulk Sm-Nd age data of garnet expands to 4–13°C/Myr, whereas that inferred from retrograde zoning to 2–13°C/Myr. These cooling rates are slower than that (24 ± 6°C/Myr) deduced by Spear and Parrish (1996) from the closure temperature vs cooling age relations (Fig. 5.1). These workers have also discussed the tectonic implication of the relatively rapid cooling rate that they have deduced. As suggested by Ducea et al. (2003), a consensus temperature of 15–20°C/Myr would seem to roughly satisfy the cooling rates inferred by Ducea et al. (2003) and Spear and Parrish (1996), and would not affect the tectonic scenario presented by Spear and Parrish (1996). However in view of good agreement between the relatively slower cooling rates derived by two independent methods, namely spatial variation of Sm-Nd age of garnet and retrograde Fe-Mg zoning of the same crystal, further study of the cooling rate of Valhalla complex seems warranted.

## 5.4 Selection of Mineral Grains for Dating

For constraining cooling rate from mineral ages, whether it is from the conventional $T_c$ vs cooling relation (Fig. 5.1) or from the thermochronological methods described above, one must ensure that (a) the mineral had a homogeneous composition of the daughter product at the peak temperature, (b) the only process significantly affecting the mineral age was cooling and (c) there was no significant growth/resorption or recrystallisation of the mineral grains. Conventional age determination by isotopic analyses of crushed mineral grains in a thermal ionisation mass spectrometer cannot, however serve these objectives. However the crystallisation/resorption history of the mineral may be understood by taking compositional profiles of major (Fig. 5.8) and/or minor elements in an electron microprobe. If the compositional maps show complex compositional patterns of the elements forming a decay system, or of major elements when mapping of the desired minor elements is not feasible, then the crystals may not be suitable for the determination of cooling age that can be related to a closure temperature, as calculated from the Dodson (1973) formulation or its extension (Ganguly and Tirone, 1999).

Geochronologists should keep track of the size of the mineral grains that are used to determine average mineral ages. The closure temperature must always be calculated from the average grain size of the minerals. Geochronologists should also carefully examine the nature and abundance of the matrix phases of the target mineral that is being dated.

In summary, age determination should be preceded by a careful examination of the target mineral and its surroundings by optical microscope and electron microprobe. In this connection it should be noted that even if a target mineral is not surrounded by minerals with very fast volume diffusion properties, the condition of a fast diffusing matrix may be satisfied when the matrix phases are fine grained because of rapid grain boundary diffusion and small length scale of volume diffusion required for the homogenisation of the matrix grains (e.g. Liermann and Ganguly, 2001; Ganguly et al. 2001).

## 5.5 Conclusions

For minerals that have not suffered a critical amount of diffusive loss of the daughter product, which needs to be determined from calculation of the dimensionless parameter, M, as discussed above, calculation of closure temperature according to the classic Dodson (1973) formulation would yield erroneously high values (Fig. 5.4), the extent of which depends on the value of the dimensionless variable, M (Eq. 5.3), and crystal geometry (Ganguly and Tirone [1999, 2001]).

In addition to cooling rate, grain size and diffusion kinetic property of the decay system, which have been considered explicitly in the Dodson formulation, the bulk closure temperature of a mineral also depends on the nature and modal abundance of the matrix phases, and diffusion anisotropy in non-cubic minerals.

The cooling rate of a rock can be deduced from the cooling age of a mineral without requiring any knowledge of its closure temperature, thus avoiding the circular logic inherent in the use of $\overline{T}_c$ vs cooling age data to retrieve cooling rate. The cooling rates can be determined from the bulk cooling age of a mineral if the age since the peak temperature of the rock is known or from the difference between average core and bulk ages of a single crystal, as determined by a single decay system. However using Eq. 5.1a, the closure temperature of a sample for a decay system may be calculated from the cooling rate data and resetting of age of the decay system during cooling. In this procedure, one needs to simply replace T by $T_c$ and t by $\Delta t$ (i.e. time lapse between $T_o$ and $T_c$) in Eq. 5.1a and solve for $T_c$ using the inferred $\eta$ value.

It is important to carry out careful optical microscopic examination of the rock sample and electron microprobe analysis of the target mineral to ensure that various assumptions that underlie the closure temperature and thermochronology formulations are approximately satisfied.

**Acknowledgements:** We acknowledge the support of NASA Cosmochemistry programme, specifically grant No. NNG04GG26G, for continued support of our research on diffusion kinetics and thermochronology. Thanks are due to Sumit Chakraborty for helpful suggestions and Somnath Dasgupta for inviting us to contribute a chapter to the present volume.

## 5.6 References

Burton KW, Kohn MJ, Cohen AS, O'Nions RK (1995) The relative diffusion of Pb, Nd, Sr and O in garnet. Earth Planet Sci Let 133: 199–211

Chakraborty S (1997) Rates and mechanisms of Fe-Mg interdiffusion in olivine. J Geophys Res 102(B6): 12317–12331

Cherniak DJ, Watson EB, Grove M, Harrison TM (2004) Pb diffusion in monazite: A combined RBS/SIMS study. Geochim Cosmochim Acta 68: 829–840

Dodson MH (1973) Closure temperature in geochronological and petrological systems. Contrib Mineral Petrol 40: 259–274

Dodson MH (1986) Closure profiles in cooling geological systems. In: Dennis PF, Freer R (ed) Kinetics and transport in silicate systems: Materials Science Forum 7, Min. Soc., U.K.

Ducea MN, Ganguly J, Rosenberg EJ, Patchett PJ, Cheng W, Isachsen C (2003) Sm-Nd dating of spatially controlled domains of garnet single crystals: a new method of high temperature thermochronology. Earth Planet Sci Let 213: 31–42

Ganguly J, Tirone M, Hervig RL (1998) Diffusion kinetics of samarium and neodymium in garnet, and a method for determining cooling rates of rocks. Science 281: 805–807

Ganguly J, Tirone M (1999) Diffusion closure temperature and age of a mineral with arbitrary extent of diffusion: theoretical formulation and applications. Earth Planet Sci Let 170: 131–140

Ganguly J, Tirone M (2001) Relationship between cooling rate and cooling age of a mineral: Theory and applications to meteorites. Meteoritics Planet Sci 36: 167–175

Ganguly J, Hensen B, Cheng W (2001) Reaction texture and Fe-Mg zoning in granulite garnet from Søstrene Island, Antarctica: Modelling and constrain on the time scale of metamorphism during Pan-African collisional event. Proc Indian Acad Sci, Earth Plane Sci 110: 305–312

Ganguly J, Ito M, Zhang X-Y (2007) Cr diffusion in orthopyroxene: Experimental determination, $^{53}$Mn-$^{53}$Cr thermochronology, and planetary applications. Geochim Cosmochim Acta 71: 3915–3925

Göpel C, Manhès G, Allègre C (1994) U-Pb systematics of phosphates from equilibrated ordinary chondrites. Earth Planet Sci Let 121: 153–171

Ito M, Ganguly J (2004) Potassium diffusion in melilite: experimental studies and constraints on the thermal history and size of planetesimals hosting CAIs. Meteor Planet Sci 39: 1911–1919

Ito M, Ganguly J (2006) Diffusion kinetics of Cr inn olivine and $^{53}$Mn-$^{53}$Cr thermochronology of early solar system objects. Geochim Cosmochim Acta 70: 799–809

Jenkin GWT, Rogers G, Fallick AE, Farrow CM (1995) Rb-Sr closure temperatures in bi-mineralic rocks: a mode effect and test for different diffusion models. Chem Geol 122: 227–240

Liermann H-P, Ganguly J (2001) Compositional properties of coexisting orthopyroxene and spinel in some Antarctic meteorites: Implications for thermal history. Meteoritics Planet Sci 36: 155–166

Reiners PW, Ehlers TA (2005) Low-temperature thermochronology: Techniques, interpretation and applications. Reviews in Mineralogy and Geochemistry, Mineralogical Soc America & Geochem Soc, v. 58

Scherer EE, Cameron KL, Blichert-Toft J (2000) Lu-Hf garnet geochronology: Closure temperature relative to Sm-Nd system and the effects of trace mineral inclusions. Geochim Cosmochim Acta 64: 3413–3432

Spear FS, Parrish RR (1996) Petrology and cooling rates of the Valhalla Complex, British Columbia. J Petrol 37: 733–765.

# 6

# Thermobarometry Gone Astray

Eric J. Essene

**Abstract:** Quantitative thermobarometers require selection of a univariant reaction, consideration of dilutions in all phases and application to fully buffered systems. Empirical thermobarometers include $Al^{IV}$ in chlorite, Al in hornblende, Ti in biotite, phengite barometry and various clay and organic transformations. For the most part they were not evaluated with univariant reactions, buffering phases or corrections for solid or fluid solutions and as a result they are not adequately calibrated.

Recently proposed thermometers in the system $CaO$-$ZrO_2$-$TiO_2$-$SiO_2$ (CazrtiQ) include Ti in zircon, Ti in quartz, Zr in rutile and Zr in sphene. Most of the original calibrations assumed that pressure (P) had no influence on the thermometer despite a significant volume change in buffering reactions. The Zr in sphene was calibrated as a thermobarometer, the P dependence of Ti in zircon and Zr in rutile has now been evaluated and Ti in quartz probably has a P dependence as well. Recent work indicates that zircon thermometer has a -80° to -90°C temperature (T) correction when applied to high level granitic intrusions crystallised at 1–2 kbar and that these are minima in the absence of rutile. Calculations of $a(TiO_2)$ from ilmenite-magnetite in the Bishop tuff gives $0.4 \pm 0.02$, suggesting that granitoids may have a lower $a(TiO_2)$ than previously thought, which will shift T back by +30 to +80°C if the zircon can be shown to have equilibrated with the oxides. Combination of thermobarometers in CazrtiQ offers a new set of phase equilibria potentially of wide use in metamorphic and igneous rocks.

---

Eric J. Essene (✉)
Department of Geological Sciences, University of Michigan, Ann Arbor, MI 48109 - 1005, USA
e-mail: essene@umich.edu

## 6.1 Introduction

Quantitative evaluation of the pressure-temperature (P-T) paths that rocks follow during metamorphic events is essential to models of the extent and duration of tectonothermal conditions. In high-grade rocks, peak metamorphic conditions and multiple thermal events are seldom preserved even in robust minerals. Elements that are used to determine metamorphic T (e.g. exchange reactions involving partitioning of Fe vs Mg) are often easily mobilised with increasing T due to high diffusion rates (Tracy 1982). In granulite and eclogite facies rocks, little or no evidence of the prograde history is preserved and only a portion of the retrograde P-T path can be recovered (e.g. Essene 1989; Frost and Chacko 1989; Anovitz and Essene 1990). Sometimes a ferromagnesian mineral such as ilmenite (Hayob et al. 1993) or biotite (Donohue and Essene 2005) can be found as an inclusion in quartz or plagioclase porphyroblasts preserving shielding it from retrograde Mg/Fe exchange and preserving T closer to peak metamorphic conditions. The retrograde P-T path contains valuable information about the uplift and tectonic history of deep-seated granulites (e.g. Harley 1989) and eclogites (e.g. Newton 1986). However the often-cryptic prograde P-T path records the early path of deep-seated and high-grade metamorphic terranes and may indicate whether subduction or thrusting was involved in early burial (Page et al. 2003, 2007a).

Most successful thermometers applied to igneous and metamorphic rocks involve calibration of univariant equilibria corrected for solid solutions (Essene 1989). This paper will emphasise calibrations and applications of the last two decades to minimise repetition of materials in that early review. A recent review of modern thermobarometry emphasising the computational approach including use of fixed bulk compositions and pseudosections is available for the interested reader (Powell and Holland 2008). Empirical calibrations derived from yet other previously established thermobarometers have had a long and storied history in studies of metamorphic petrology. The approach of empirical calibration of necessity assumes equilibration in both sets of thermobarometers, increasing the chances of miscalibration, particularly in low temperature metamorphic systems yet to obtain full equilibration and also in high temperature metamorphic systems in which re-equilibration is rampant (Edwards and Essene 1988). Empirical calibration can only be as good as the thermobarometer on which it was based and systematic errors are often involved that were left unevaluated by the original authors.

One of the early empirical thermometers was calibration of the Mg/$Fe^{2+}$ exchange thermometer for garnet-biotite based on the stable isotope partition of $^{18}O/^{16}O$ between magnetite and quartz (Goldman and Albee 1977). From today's perspective one might turn around that empirical exchange and consider calibration of partitioning of $^{18}O/^{16}O$ for magnetite vs quartz based on garnet-biotite thermobarometry. In addition the occurrence of garnet that is strongly zoned in Mg and Fe from metapelites certainly raises questions about the calibration. In addition the authors did not consider the systematic effect $Fe^{3+}$ of in biotite on the empirical thermometer and the effect of retrogression on the $d^{18}O$ of magnetite, which often exsolves ilmenite as it cools, at least in higher grade rocks (Bohlen and Essene 1977). Essene (1982) discussed other concerns about the calibration of Goldman and Albee (1977). In retrospect, it is surprising that their thermometer compared so well with Thompson (1976) and Ferry and Spear (1978). Subsequent to these early works garnet-biotite thermometry has repeatedly been addressed (e.g. Holdaway 2000), with recent calibrations addressing additional components such as variable Al and Ti in biotite, as well as Ca and Mn in garnet (Dasgupta et al. 1991; Kleemann and Reinhardt 1994; Wu and Cheng 2006). The garnet-biotite thermometer has serious problems of resetting during both continued prograde and early retrograde metamorphism and it is not recommended as a reliable thermometer unless great care is taken to evaluate these issues.

## 6. 2 Empirical Thermobarometers

Empirically calibrated thermobarometers that are still being used widely include the $Al^{IV}$-in-chlorite thermometer, the Al-in-hornblende barometer and the phengite barometer. They are followed by brief commentary on other empirical thermobarometers that continue to be used. Emphasis will be placed on works completed after the review of Essene (1989) whenever possible to minimise duplication.

### *6.2.1 Chlorite Thermometry*

Tetrahedral aluminum and vacancy substitutions in chlorite have been used to construct empirical chlorite thermometers based on variation of chlorite compositions with temperature (T) in geothermal systems (Cathelineau and Nieva 1985; Cathelineau 1988). Chlorite thermometry is still used for low-grade chlorite from a variety of geological occurrences despite critical papers on the basis of the thermometer (de Caritat et al. 1993; Jiang et al. 1994a; Essene and Peacor 1995). The detailed underpinning of the Cathelineau thermometer is in part constructed from data that likely have submicroscopic intergrowths below 300°C. Different reactions control change in $Al^{IV}$ of chlorite with different buffering systems and the treatment as a single mineral thermometer is not warranted.

#### 6.2.1.1 Basis of the chlorite thermometer

Despite the lack of a buffering reaction, chlorite thermometry has retained its popularity for the last two decades. It was based in part on work by McDowell and Elders (1980, 1983), who analysed chlorite in studies of active geothermal deposits in Salton sea sandstones. They found authigenic chlorite from 170–360°C with variable excess $Al^{VI}$ (solid dots in Figs. 6.1, 6.2). They used energy dispersive spectroscopy (EDS) for analyses because they thought it provided a smaller analytical volume and worked better on rough surfaces than wavelength dispersive spectroscopy (WDS), but these assumptions are not correct. They obtained low analytical totals that they attributed to a contribution from epoxy, down to 60 wt%, which should have perturbed the Bence-Albee corrections and therefore the quality of their analytical data is questionable. McDowell and Elders (1980) did not give analytical data in oxide wt% and normalised their analyses to 10 cations rather than the more conventional 14 oxygens on an anhydrous basis (data recalculated to 14 O in Figs. 6.1, 6.2).

Cathelineau and Nieva (1985) based the original $Al^{IV}$-in-chlorite thermometer on chlorite data from altered andesites on the active Los Azufres geothermal field. Direct thermometry was compared to the $Al^{IV}$ content in chlorite. Their samples have chlorite-epidote-quartz ± Kfeldspar between 200°C and 300°C. The analyses were obtained with a point beam at 6 nA and 15 kV, but only for 6 s, which should have produced large imprecision. Analyses from the 700 and 120 m depths in their Table 2 do not match with sample depths in their Fig. 2 or average analyses in their Table 3. They assumed that the electron microprobe (EMP) analyses of chlorite samples were single-phase chlorite even though many of the analyses from 130–215°C in Table 3 (but strangely, few from 700 and 1240 m in Table 2) contain relatively high CaO (0.2–0.8 wt% CaO), $K_2O$ (0.2–0.5 wt%) and/or $Na_2O$ (0.2–0.3 wt%). No buffered reaction controlling the $Al^{IV}$ in chlorite was proposed to explain why chlorite compositions vary with T. Cathelineau and Nieva (1985) excluded the chlorite at 170°C from their graph of $Al^{IV}$ vs T without comment: it lies well off of their trend. They also added a point at 300°C from Walshe and Solomon (1981) from a different lithology and field area. Pandarinath et al. (2006) conducted an X-ray diffraction (XRD) study of the bulk mineralogy and clay separates from three more drill cores from the Los Azufres field. They found no epidote but noted abundant chabazite persisting to 250–290°C in two of the drill cores. Smectite was present at 120–260°C in different cores, with the clay assemblage of illite-chlorite persisting to the bottom of the cores at 300°C. Two chlorite analyses of Cathelineau and Nieva (1985) at 130 and 180°C dictate the slope of the chlorite Al thermometer and likely contain submicroscopic smectite.

Cathelineau (1988) combined chlorite analyses of Cathelineau and Nieva (1985) with some new data from Los Azufres and the data of McDowell and Elders (1980) from

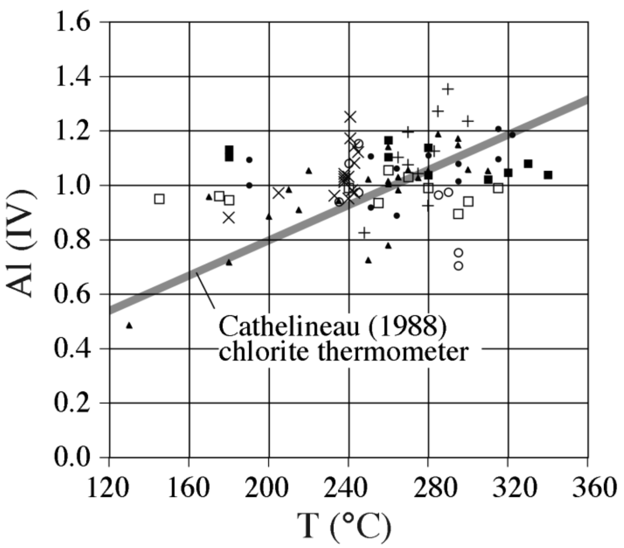

**Fig. 6.1** Geothermal chlorite $Al^{IV}$ vs T. Recalculated data of McDowell and Elders (1980), Cathelinieu and Nieva (1985), Cho et al. (1988), Lonker et al. (1990, +), Lonker et al. (1993, o), Martinez-Serrano and Dubois (1997, ), Mas et al. (2006, x), Ruggieri et al. (2006, △). Cathelineau's (1988) fit of the data from McDowell and Elders (1980) and Cathelinieu and Nieva (1985) is the solid line. Note its failure with the expanded data set

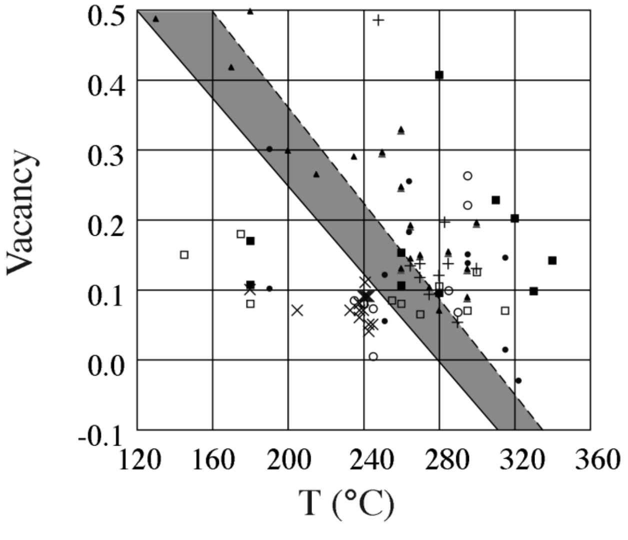

**Fig. 6.2** Geothermal chlorite vacancy vs T. Recalculated data of McDowell and Elders (1980), Cathelinieu and Nieva (1985), Cho et al. (1988), Lonker et al. (1990, +), Lonker et al. (1993, o), Martinez-Serrano and Dubois (1997, ), Mas et al. (2006, x), Ruggieri et al. (2006, △). The dashed line is from Cathelinieu and Nieva (1985), the solid line is the writer's best fit to their recalculated data and the shaded area represents the range between. Note the failure of the fits to the expanded data set

the Salton sea for a revised thermometer for $Al^{IV}$ in chlorite, referred to in this paper as the Cathelineau chlorite thermometer. He rejected two analyses of McDowell and Elders (1980) at 190°C because they may have inherited the chemistry of original detrital chlorite and were from a dolomite-bearing sandstone rather than the deeper calcite-bearing sandstones in the Salton sea cores. This is the first mention of a lithological control on the Cathelineau chlorite thermometer and it is an odd concern when otherwise combining data without comment from altered andesites at Los Azufres with illite-rich sandstones at Salton sea. Cathelineau (1988) also excluded the chlorite analyses of Cathelineau and Nieva (1985) at 210°C, 220°C, 250°C and 260°C without comment and added two more analyses at 310°C from Los Azufres. The Cathelineau chlorite thermometer rests on uncertain data involving different bulk compositions from two field areas. The Cathelineau thermometer is shown as a shaded line for the $Al^{iv}$ vs T in Fig. 6.1. Cathelineau and Nieva (1985) fit to the variation of chlorite vacancies vs T is a dashed line in Fig. 6.2 (the shading shows the range of the original data as calculated in this study). The equation provided by Cathelineau and Nieva (1985) for vacancies does not correspond with the line shown in their plot. Workers subsequently have applied the Cathelineau chlorite thermometer to a wide range of lithologies: metabasalts, metakomatites, chloritites and alteration zones in ore deposits and hydrothermal settings.

Walshe and Solomon (1981) evaluated chlorite solid solutions in a volcanic-hosted copper deposit at Mt. Lyell, Tasmania and generated a six-component mixing model for chlorite. Walshe (1986) used the compositions of the coexisting minerals in Salton sea assemblages and a model of ideal ionic mixing on each site to extract thermodynamic data for $Mg_6Si_4O_{10}(OH)_8$ and $Al_4Si_4O_{10}(OH)_8$ components in chlorite. He used a dioctahedral chlorite end-member, $Al_4\ {}_2Si_4O_{10}(OH)_8$ where the vacancy is indicated by the  , to explain the excess $Al^{VI}$ in low-grade chlorite. However an ideal ionic mixing model is not likely to provide a realistic a/X relations in chlorite for multisite, multivalent exchanges such as $(Al)^{VI}{}_{-1}(Al)^{VI}{}_{-1}Mg_1Si_1$ or $(Al)^{VI}{}_{-2}(Mg)^{VI}{}_3$. Moreover the $Al^{VI}$ atoms of chlorite are systematically partitioned into the two VI 2:1 sites relative to $Mg^{VI}$ and $Fe^{VI}$ atoms, which prefer the brucite layer. Extensive short range order of Al vs Si occurs in tetrahedral sites of monoclinic clinochlore (Welch et al. 1995). The amount of the dioctahedral $Al_4\ {}_2Si_4O_{10}(OH)_8$ component in low-grade chlorite in bulk EMP analyses such in Cathelineau and Nieva (1985) may be confused with submicroscopic intergrowths with corrensite, smectite and/or illite and trends of chemical change with grade may result from variable admixture of clays (Velde et al. 1991; de Caritat et al. 1993; Jiang et al. 1994a). Walshe (1986) used equilibrium constants for six chlorite species in the SUPCRT computer programme with an ideal site-by-site mixing model. He calculated chlorite oxidation-dehydration reactions of ferri-daphnite, $Fe^{2+}{}_5Fe^{3+}{}_2Si_3O_{10}(OH)_8$ to form magnetite, quartz and $H_2O$ and showed that the amount of Fe in the chlorite depends on P, $fO_2$ and $fS_2$. Although the applications of Walshe (1986) to chlorite equilibria in various mineralised deposits are of interest, in many cases the chlorites formed at <300°C and may contain submicroscopic clay admixtures that may have perturbed the analytical data.

### 6.2.1.2 Additional data on geothermal chlorite

Several investigations of chlorite from geothermal areas have appeared since the calibration of the chlorite thermometer by Cathelineau (1988). The new data have been included in updated plots of chlorite thermometers (Figs. 6.1, 6.2). Cho et al. (1988) analysed chlorite from the chlorite-calcite zone to the biotite zone in additional drill cores of Salton sea sediments. Their data call into question the assumption that chlorite shows systematic patterns of change with T at Salton sea. Major studies of systematic mineralogical and chemical changes down core were undertaken in the Broadlands geothermal system of New Zealand (Lonker et al. 1990) and on the Reykjanes and Svartsengi systems of Iceland (Lonker et al. 1993). They found large variations in $Al^{IV}$ (0.1–0.2) of chlorite at the same grade. Schiffman and Fridleifsson (1991) conducted an XRD and EMP study of the smectite-chlorite transition in the Nesjaveller geothermal field Iceland. They found chlorite-smectite intergrowths forming at 200–270°C and their EMP analyses of those samples indeed have high CaO (0.8–2.4 wt%). Martíñez-Serrano and Dubois (1998) analysed hydrothermal chlorite from the Los Humeros geothermal field of Mexico and Mas et al. (2006) analysed chlorite from the Bouillante geothermal field Guadeloupe. Each of the above studies concluded that the $Al^{IV}$ of chlorite do not show systematic variations with T. Plotting all the geothermal analyses of chlorite together shows that trends of $Al^{IV}$ and vacancies in chlorite with T are weak and should not be used as a thermometer (Figs. 6.1, 6.2). They likely register variations in buffer assemblages from sample to sample and different field areas and variable chlorite/smectite, especially at lower T. The amount of $Fe^{3+}$ in the chlorite is not known but it should not be assumed to be negligible, especially in more oxidised geothermal systems. The measured T has diminished over time leading to retrogression in some geothermal systems, which may not have been recognised elsewhere (Fulignati et al. 1975).

### 6.2.1.3 TEM studies of low T "chlorite"

Peacor and coworkers undertook systematic transmission electron microscope (TEM) studies of diagenetic sheet silicates from the Salton sea and elsewhere. Ahn and Peacor (1985) examined diagenetic chlorite from the CWRU Gulf

Coast #6 well in the Gulf Coast at depths of 2450 and 5500 m, the first two above the illite-smectite transition and the last below it. Packets of mixed layer illite-smectite are intergrown with the 2450 m well, whereas only minor amounts of 7 Å septichlorite are coherently interlayered with 14 Å chlorite at 5500 m and 165°C (Hower et al. 1976). Renormalisation of their analytical electron microscope (AEM) analyses of 14 Å chlorite from 5500 m depth to 14 O showed $Al^{IV}$ of 1.1 ± 0.2 and   of 0.3 ± 0.1 (cf. Peacor 1992a for a description of AEM). It is not clear whether AEM analyses have sufficient precision for meaningful determinations of $Al^{IV}$ and vacancies of chlorite. In well IID2 from the Salton sea, Yau et al. (1988) showed packets of illite intergrown with chlorite at 170°C and 260°C, whereas at 330°C the chlorite forms undisturbed packets with only a few layer terminations and edge dislocations. Shau et al. (1990) studied chlorite and corrensite from slates associated with prehnite-pumpellyite greenstones in the Hsuehshan Range near Jungua in Taiwan and showed that low-grade "chlorite" is an ordered intergrowth called corrensite or is a mixture of chlorite and smectite. The corrensite and smectite increases the apparent dioctahedral component of presumed chlorite and influences chlorite thermometry using EMP analyses.

Jiang and Peacor (1994) examined pelitic sediments from Ordovician pelites in the Gaspé Peninsula of Quebec with TEM and AEM. They identified corrensite in the diagenetic zone to low anchizone and chlorite from the diagenetic zone to the epizone and analysed both with AEM. Temperature estimates for this sequence are in the range estimated as 80–260°C (Jiang et al. 1994a). Jiang and Peacor (1994) found no variation in the tetrahedral aluminum content of chlorite (ave. $Al^{IV}$ of 1.3) and no sudoite component in the chlorite with changes in metamorphic grade. For corrensite, the average $Al^{IV}$ is 0.7 and the vacancy level is 0.3 when normalised as chlorite. The EMP analysis of chlorite-corrensite mixtures assuming they are chlorite would yield $Al^{IV}$ close to 1 with ca 0.1 vacancies. Jiang et al. (1994a) compared Gaspé chlorite with that in drill cores from the Gulf Coast of Texas estimated to have formed at 140–170°C. They identified corrensite and illite intergrown with chlorite in samples from the Gaspé Peninsula and mixtures of 7 Å chamosite and 14 Å daphnite from the Gulf Coast. They analysed chlorite packets that were ca. 200 Å wide with AEM, but none had authigenic crystals wide enough for meaningful EMP analyses. The AEM analyses of chlorite showed little or no octahedral site vacancies within error (i.e. 0 ± 10% sudoite solid solution) when renormalised to 14 O. In contrast the AEM analyses of chlorite (Ahn and Peacor 1985) from 5500 m depth in the Gulf Coast have an average of 30% sudoite (15% Al chlorite). It seems possible that AEM analyses do not have the precision needed for identifying sudoite content. The Gulf Coast samples were from grades where EMP analyses of chlorite from geothermal deposits produced apparent VI site vacancies (Cathelineau 1988), as was also predicted from thermodynamic modelling of chlorite in equilibrium with quartz and $H_2O$ (Vidal et al. 2001). Jiang et al. (1994a) noted that EMP analyses of chlorite-smectite have Na+K+2Ca correlated directly with apparent VI vacancies and inversely with $Al^{IV}$. They concluded that chlorite from the Salton sea and Los Azufres included variable amounts of smectite and that chlorite has limited sudoite (0–10%) in the absence of smectite contamination. Thus EMP analyses of chlorite in their samples include contributions from other minerals and they questioned the use of conventional $Al^{IV}$ or vacancy chlorite thermometry based on EMP analyses. Giorgetti et al. (2003) made TEM observations of sheet silicates from Salton sea sediments and observed detrital and authigenic chlorite intergrown submicroscopically with illite. Collectively the TEM observations indicate that chlorite and illite formed below 300°C is often a submicroscopically intergrown mixture in hot springs deposits and diagenetic sediments (Peacor 1992b).

### 6.2.1.4 Phase equilibria for the chlorite thermometer

Essene and Peacor (1995, 1997) noted that the tetrahedral Al content of chlorite is buffered differently for different low-grade assemblages. They proposed six reactions buffering the Al content of chlorite:

$$\text{clinochlore + calcite + quartz = Mg chlorite + clinozoisite} + CO_2 + H_2O \tag{6.1}$$

$$6Mg_5AlSi_3AlO_{10}(OH)_8 + 8CaCO_3 + 14SiO_2 = 5Mg_6Si_4O_{10}(OH)_8 + 4Ca_2Al_3Si_3O_{10}(OH) + 8CO_2 + 2H_2O$$

$$\text{Mg chlorite + clinozoisite} + H^+ = \text{clinochlore + quartz} + H_2O + Ca^{2+} \tag{6.2}$$

$$5Mg_6Si_4O_{10}(OH)_8 + 4Ca_2Al_3Si_3O_{10}(OH) + 16H^+ = 6Mg_5AlSi_3AlO_{10}(OH)_8 + 14SiO_2 + 6H_2O + 8Ca^{2+}$$

$$\text{Mg chlorite + clinozoisite + quartz = actinolite + clinochlore + quartz} + H_2O \tag{6.3}$$

$$25Mg_6Si_4O_{10}(OH)_8 + 12Ca_2Al_3Si_3O_{10}(OH) + 14SiO_2 = 18Mg_5AlSi_3AlO_{10}(OH)_8 + 12Ca_2Mg_5Si_8O_{22}(OH)_2 + 19H_2O$$

$$\text{Mg chlorite + quartz} + Ca^{2+} = \text{actinolite} + H_2O + H^+ \tag{6.4}$$

$$5Mg_6Si_4O_{10}(OH)_8 + 28SiO_2 + 12Ca^{2+} = 6Ca_2Mg_5Si_8O_{22}(OH)_2 + 2H_2O + 24H^+$$

Mg chlorite + muscovite/illite = clinochlore + microcline + quartz + $H_2O$ (6.5)

$$5Mg_6Si_4O_{10}(OH)_8 + 6KAl_2Si_3AlO_{10}(OH)_2 = 6Mg_5AlSi_3AlO_{10}(OH)_8 + 6KAlSi_3O_8 + 2SiO_2 + 2H_2O$$

Mg chlorite + muscovite/illite + $H^+$ = clinochlore + quartz + $H_2O$ + $K^+$ (6.6)

$$5Mg_6Si_4O_{10}(OH)_8 + 4KAl_2Si_3AlO_{10}(OH)_2 + 4H^+ = 6Mg_5AlSi_3AlO_{10}(OH)_8 + 14SiO_2 + 2H_2O + 4K^+$$

Alternative reactions with Fe end-members, clinochlore and 14 Å amesite or oxidation of daphnite to form epidote and/or magnetite could also be considered. Consideration of these reactions lends no confidence to the simple assumption of $Al^{IV}$ in chlorite as a pure thermometer, because they are divariant equilibria that slide across P-T space and vary with the assemblage. At a fixed $X(CO_2)/X(H_2O)$ the Al content of chlorite is expected to vary in the opposite direction with T for reaction (1) vs reactions (3) and (5). Reaction (1) has such a large ratio of $CO_2$ to $H_2O$ that it will act primarily as a decarbonation reaction when the fluid is mainly $H_2O$, such that small variations in $XCO_2$ will shift its locus dramatically. Reactions (2) and (4) vary with 2pH-pCa but with opposite slopes in T vs 2pH-pCa space and reaction (6) varies with T and pK-pH. Given the reported neoformed assemblages, reactions (5) and (6) would buffer the Al of chlorite in the Salton sea geothermal system. However it may not apply to EMP analyses of chlorite at < 250°C, due to illite mixed in chlorite, the small grain size of authigenic chlorite (Giorgetti et al. 2003) or complexities of corrensite and/or smectite (Jiang et al. 1994a).

Vidal et al. (2001) formulated chlorite solid solutions in terms of clinochlore and daphnite with 14 Å 14 Å amesite, $Mg_4Al_2Si_2Al_2O_{10}(OH)_8$ and sudoite, $Mg_2Al_3Si_3AlO_{10}(OH)_8$ (di/trioctahedral chlorite) and derived their thermodynamic and mutual mixing properties from experimental and natural data. One quilibrium they derived is potentially applicable to low-grade chlorite in many settings. It is:

clinochlore + sudoite = amesite + quartz + $H_2O$ (6.7)

$$2Mg_5AlSi_3AlO_{10}(OH)_8 + 3(Mg_2Al_3\quad)Si_3AlO_{10}(OH)_8 = 4Mg_4Al_2Si_2Al_2O_{10}(OH)_8 + 7SiO_2 + 4H_2O$$

which may be compared to a reaction of Walshe (1986):

Mg-chlorite + Al-chlorite = clinochlore + quartz + $H_2O$ (6.8)

$$5Mg_6Si_4O_{10}(OH)_8 + 3Al_4\quad{}_2Si_4O_{10}(OH)_8 = 6Mg_5AlSi_3AlO_{10}(OH)_8 + 14SiO_2 + 8H_2O$$

The two sets of equilibria (7–8) are closely linked because 2clinochlore = Mg-chlorite + 14 Å amesite and 2sudoite + Mg-chlorite = 2clinochlore + Al-chlorite. They suggest progressive decomposition of the dioctahedral component and a drive toward a trioctahedral chlorite with increasing T. Applications of chlorite-phengite reactions as thermobarometers (Vidal et al. 2001; Augier et al. 2005a, 2005b) seem reasonable. They relied on identifying the sudoite and pyrophyllite components from EMP analyses and they neglected $Fe^{3+}$ in phengite and chlorite. Vidal et al. (2001) concluded that Cathelineau and Nieva's (1985) negative correlation of the vacancy component in chlorite with T and positive correlation of $Al^{IV}$ with T cannot be extrapolated to higher P without correction. The writer wonders whether there may be a solvus between ordered sudoite and ordered trioctahedral clinochlore and whether Mg, Fe and Al may be increasingly disordered between the two VI sites at elevated T.

### 6.2.1.5 Applications of chlorite thermometry

Notwithstanding criticisms of Cathelineau chlorite thermometry, many workers have continued to apply the apply it to low-grade rocks (Bevins et al. 1991; Laverne et al. 1995; Zang and Fyfe 1995; Drennen et al. 1997; FrimmeI 1997; Xie et al. 1997; Gillis et al. 2001; Timpa et al. 2005; Moura et al. 2006; Esteban et al. 2007). Further empirical corrections to chlorite thermometry were proposed for observed variations of Fe/Mg in chlorite (Kranidiotis and MacLean 1987; Zang and Fyfe 1995; Drennan et al. 1997; Xie et al. 1997). Bevins et al. (1991) analysed chlorite from prehnite-pumpellyite and greenschist facies metabasalts from Wales and NE Greenland. They correlated the decreasing amount of smectite in the chlorite with increased metamorphic grade and T from the chlorite thermometer, which they concluded is applicable to low-grade metamafites. Zang and Fyfe (1995) applied their version of chlorite thermometry to chlorite associated with an ore deposit and obtained 220–270°C, seemingly some 50–100°C low for the formation of (unanalysed) biotite and actinolite in adjacent rocks. Laverne et al. (1995) applied the Cathelineau thermometer to altered sea-floor basalts. Drennen et al. (1997) applied it to Witwatersland veins and host sediments, reporting T to the nearest 0.1°C with most in the range 250–350°C. They did not provide chlorite analyses or associated assemblages. Frimmel (1997) also investigated chlorite thermometry in Witwatersland metaclastic rocks without analyses provided. He found assemblages with muscovite and some with epidote-actinolite. Most of his chlorite T are in the range 380–430°C using Cathelineau (1988) but only 280–320°C with Zang and Fyfe's (1995) calibration.

Xie et al. (1997) applied chlorite thermometry in Archean greenstones, veins and host sediments. Their chlorite analyses do not show excess $Al^{VI}$, but the presence of submicroscopic interlayers in the chlorite upon which calibration of Cathelineau (1988) was based still implies that the thermometer used by Xie et al. (1997) involves intergrown chlorite. Their mafic assemblages include unanalysed actinolite and magnetite, one sample has unanalysed epidote and the rest do not contain full buffers for reactions (6.1–6.6). The chlorite in the mafic assemblages of Xie et al. (1997) may be buffered by oxidation reactions:

$$\text{Fe chlorite} + O_2 = \text{quartz} + \text{magnetite} + H_2O \qquad (6.9)$$

$$Fe_6Si_4O_{10}(OH)_8 + O_2 = 4SiO_2 + 2Fe_3O_4 + 4H_2O$$

$$\text{daphnite} + \text{ferroactinolite} + O_2 = \text{epidote} + \text{quartz} + \text{magnetite} + H_2O \qquad (6.10)$$

$$4Fe_5AlSi_3AlO_{10}(OH)_8 + 4Ca_2Fe_5Si_8O_{22}(OH)_2 + 7O_2 = 4Ca_2Al_2FeSi_3O_{12}(OH) + 32SiO_2 + 12Fe_3O_4 + 18H_2O$$

Progress of reactions (6.9–6.10) will indirectly change the clinochlore by increased dilution or concentration. Walshe (1986) discussed reaction (6.9) and computed its locus. The presumably magnetite-poor rocks of Xie et al. (1997) imply little progress of reactions (6.9–6.10) to the right, i.e. the reduced and hydrated low-T side with chlorite dominates. Alternatively magnetite in the greenstones may be of secondary or retrograde origin. No BSE images were provided to show the textural relations of actinolite, epidote, magnetite and chlorite and it is fruitless to speculate further on these rocks.

Timpa et al. (2005) undertook a systematic study of regionally metamorphosed basalts from the prehnite-actinolite through greenschist facies on S Vancouver Island. They did not give assemblages for individual samples but provided chlorite analyses, some with low analytical totals. They reported Cathelineau chlorite thermometry to the nearest 1°C, T varying from 260°C at the prehnite-actinolite/greenschist transition to 300–340°C near the greenschist/amphibolite boundary. The former may be low by 50°C and the latter by 100–150°C compared to experiments on the greenschist/amphibolite transition (Apted and Liou 1983).

Moura et al. (2006) applied Cathelineau chlorite thermometry to an ore deposit in an altered granite from Brazil with six analyses, five of which have analytical totals of < 87 wt%. Most of the analyses have $Al^{VI}$ close to $Al^{IV}$, but three of the analyses have high Mn (3.2–5.7 wt% MnO). Cathelineu chlorite thermometry was reported to 0.01°C, a mind-boggling precision given the 20–40°C scatter in the original calibration. Moura et al. (2006) estimated the pressure of their ore deposits by intersecting presumed pressure-independent chlorite thermometry with fluid inclusion thermobarometry. Although their T estimates are generally reasonable for their deposits, it is simply a statement of faith to rely on presumed pressure-independent chlorite thermometry with other thermometry for baric estimates.

Esteban et al. (2007) applied chlorite thermometry to chlorite schists found on the margins of the Ronda peridotite. They argued that their analytical and XRD data exclude the possibility of corrensite or expandable clays, but that doesn't address the chlorite on which the thermometer was based. The schists are comprised mostly of chlorite and are depleted in silica, with a small amount of epidote but no quartz. Extensive metasomatism is marked by high variance assemblages, as in these chloritites, which seem related to the metasomatic "blackwall" chloritites found on margins of serpentinised peridotites. Their T cannot be limited except by the stability of chlorite and/or epidote in the absence of quartz. The stability of clinochlore is expanded by 200–300°C relative to clinochlore-quartz (Chernosky and Berman 1988). Ferroan chlorite has a contracted stability relative to clinochlore and may have formed between 300 and 600°C at whatever P is necessary to stabilise the unanalysed epidote in the absence of quartz.

The low analytical totals for chlorite in many of the above applications may be attributed to beam damage and/or analysis of poorly polished areas. The application of chlorite thermometry based on illite- and quartz-bearing rocks to quite different lithologies, assemblages and pressures is not acceptable. If at all useful the chlorite thermometer likely has a P dependence depending on the reaction and assemblage that buffers its Al content. The failure of most workers to identify a buffering assemblage for Al in chlorite raises doubts to its value even as a comparative chlorite thermometer. Reactions (6.7) or (6.8) may provide a buffering system for chlorite-quartz if sudoite substitution is an equilibrium feature and can be measured by EMP analysis in low-grade chlorite. The thermometry in the above applications is mostly in the range 250–350°C, no great surprise as that was the range in the original calibrations. Many workers faced with chlorite rocks that formed at low T (200–400°C), have applied the chlorite thermometer without addressing its limitations that were raised (Shau et al. 1990; de Caritat et al. 1993; Jiang et al. 1994a; Essene and Peacor 1995). The Cathelineau thermometer was based on correlations of $Al^{IV}$ and in chlorite with T based on just a dozen analyses from two geothermal systems with different bulk compositions. Inclusion of additional chlorite analyses from geothermal occurrences lends no confidence to these parameters as a general thermometer (Figs. 6.1, 6.2). Thermodynamic modelling like that of Vidal et al. (2001, 2006) is the appropriate way to proceed for further evaluation of recrystallised metamorphic rocks even if the specific calibrations have been questioned in this review. Studies of chlorite that formed below 300°C remains problematical: to the extent they have submicroscopic intergrowths they cannot be treated as a single phase with EMP analyses. Strong deformation will tend to remove such intergrowths and aid in a closer approach toward an equilibrium assemblage, which likely will shift the chlorite T.

## *6.2.2 Hornblende Barometry*

The substitutions in hornblende have been considered qualitatively in terms of P-T-X relations for the last several decades, especially in often more enigmatic amphibolites. The Al content of hornblende was proposed as a single mineral barometer (Raase 1976), even though highly aluminous hornblende were found in quartz-undersaturated contact metamorphic rocks at only 1–2 kbar (e.g. Shedlock and Essene 1979). Hammarstrom and Zen (1986) used the phase rule to infer that the Al of hornblende was fixed in the presence of K-feldspar-plagioclase-biotite-quartz-magnetite-ilmenite/sphene-melt-fluid. They chose this assemblage for an empirically calibrated barometer for granitoids (s.l.). The list of coexisting phases, especially including a melt phase of uncertain composition, is so lengthy that serious application of this system as a barometer seemed rather unlikely. Hollister et al. (1987) proposed a specific reaction for hornblende barometry:

$$\text{ferrotschermakite} + \text{sanidine} = \text{annite} + \text{anorthite} + \text{quartz} \qquad (6.11)$$

$$Ca_2Fe_3Al_2Si_6Al_2O_{22}(OH)_2 + KAlSi_3O_8 = KFe_3Si_3AlO_{10}(OH)_2 + 2CaAl_2Si_2O_8 + 2SiO_2$$

It is appealing as it does not require a melt phase or $H_2O$-rich fluid. However it indicates consideration of the compositions of coexisting feldspars and biotite, as well as the presence of quartz at the time the hornblende crystallised. Hollister et al. (1987) did not apply a diluted form of this reaction to granitoids or granitic gneisses but followed Hammarstrom and Zen (1986) in a similar field calibration (Fig. 6.3).

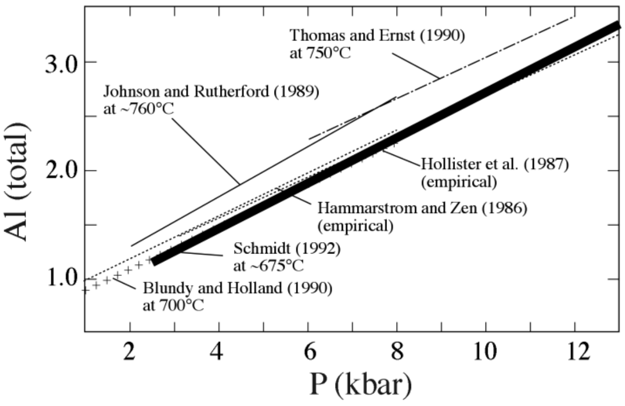

**Fig. 6.3** Various calibrations of the hornblende Al barometer vs P (Anderson and Smith 1995, with permission from Mineralogical Society of America)

### 6.2.2.1 Experimental calibration of the hornblende barometer

Experimental studies of the hornblende barometer followed in several studies (Johnson and Rutherford 1989; Rutter et al. 1989; Thomas and Ernst 1990; Schmidt 1992). Johnson and Rutherford (1989) used a glass + phenocryst starting sample of the Fish Creek tuff in a piston-cylinder and internally heated apparatus at 2–8 kbar, 720–780°C, mixed $H_2O/CO_2$ and variable $fO_2$. They were unable to confirm the presence of quartz or sanidine, but argued for near saturation based on the melt composition. No pressure correction was mentioned for the piston-cylinder experiments at 6.5 and 8.2 kbar. The hornblende contained subequal amounts of ferroan pargasite and ferroan tschermakite at 6.5 and 8.3 kbar and less ferroan magnesiohornblende with more edenite at lower P. From the analyses it is evident that the amphibole solid solution is not well described by Al(tot), $(Al)^{VI}$ or $(Al)^{IV}$. Johnson and Rutherford (1989) concluded that their experiments with hornblende equilibrated with biotite, plagioclase, sanidine, quartz, sphene and magnetite/ilmenite, but they provided analyses only of hornblende.

Rutter et al. (1989) used a starting material of tonalite (plagioclase-biotite-K-feldspar-quartz-hornblende) in piston-cylinder experiments with a 0.5” NaCl cell under conditions of fluid undersaturation. They reported on three runs at 10 kbar and 850, 875 and 950°C, all with neoformed garnet. Only hornblende was analysed and the authors could not confirm sanidine in the run products. The amphibole run product was primarily edenite followed by lesser magnesiohornblende. Thomas and Ernst (1990) undertook experiments on a tonalite at 6–12 kbar and 750°C in a piston-cylinder at UCLA with an NaCl cell for 1 week. They roughly bracketed the Al content by introducing a more aluminous hornblende along with the initial hornblende and analysing rims on each. Their calibration of the hornblende barometer is estimated to have 1 kbar errors. It is similar to the results of Johnson and Rutherford (1989) and was regarded to extend that experimental calibration. It is about 1 kbar lower than the empirical estimates of Hammarstrom and Zen (1987) and Hollister et al. (1988). BSE images of the run products and analyses of the other silicates would have added materially to the phase equilibria in these studies.

Careful experiments were obtained the Al-in hornblende barometer were undertaken by Schmidt (1992) at 2.5–16 kbar and 655–700°C in finely ground tonalite and granodiorite with excess water. The near solidus conditions were chosen so that the matrix assemblage would be close to a granite minimum close to or at saturation with quartz, sodic plagioclase and K-feldspar as well as $H_2O$ vapor. For experiments at and below 13 kbar he confirmed the presence of hornblende, biotite, plagioclase, quartz, sphene, magnetite and melt and in 8 of the 10 runs orthoclase. He obtained some reversals in the Al content of hornblende by initial runs at 720–750°C before continuing the experiment at 645–700°C. Schmidt (1992) assumed a constant $Fe^{3+}/Fe^{2+}$ of 0.3 in the run product hornblende rather than using EMP analysis of the run product to estimate $Fe^{3+}$ with a cation normalisation (e.g. Cosca et al. 1991). He did not analyse biotite, plagioclase or orthoclase in the run products. The amphibole compositions vary from ferroan and ferrian hornblende at low P, with increasing ferroan and ferrian tschermakite, pargasite and barroisite substitution at higher P. The total Al content of the hornblende in the run products (and natural hornblendes) is a complicated summation of $Al_{-1}Al_{-1}Mg_1Si_1$, $Al_{-1}Al_{-1}Fe_1Si_1$, $Na_{-1}Al_{-1}\ {}_1Si_1$, $Na_{-1}Si_{-1}Ca_1Al_1$, $K_{-1}Al_{-1}\ {}_1Si_1$ and $Fe^{3+}{}_{-1}Al_1$ exchanges. Schmidt's (1992) variation of Al in hornblende with P (Fig. 6.3) was very close to the original calibration of Hammarstrom and Zen (1986).

#### 6.2.2.2 Other reactions for the hornblende barometer

Mäder and Berman (1992) evaluated the thermodynamics of hornblende from granulites in terms of several substitutions. They derived a solid-solid reaction with a low P-T slope that could be useful in barometry:

tremolite + phlogopite + anorthite + albite = K-feldspar + quartz + pargasite (6.12)

$$Ca_2Mg_5Si_6Al_2O_{22}(OH)_2 + KMg_3Si_3AlO_{10}(OH)_2 + 2CaAl_2Si_2O_8 + NaAlSi_3O_8 = KAlSiO_8 + 6SiO_2 + 2NaCa_2Mg_4AlSi_6Al_2O_{22}(OH)_2$$

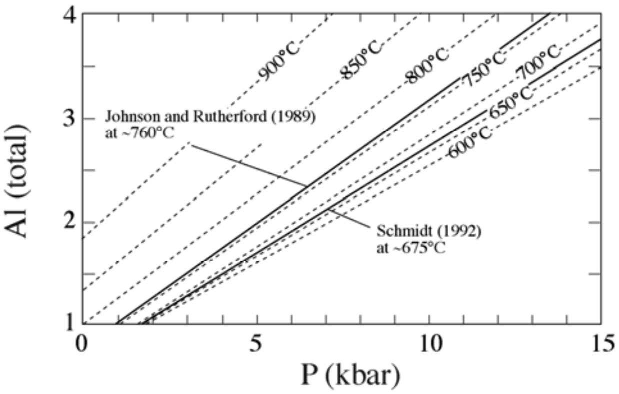

**Fig. 6.4** Inferred T dependence of the hornblende Al barometer (Anderson and Smith 1995, with permission from Mineralogical Society of America)

Anderson and Smith (1995) noted that the hornblende barometer depends on T as well as P (Fig. 6.4), as well as change from $An_{30 \pm 5}$ to more calcic plagioclase, variations in $fO_2$ and $Fe^{3+}/Fe^{2+}$ in the hornblende. They showed that exchange of tschermakite as well as edenite controls the total Al in hornblende. They corrected the hornblende Al barometer for T as P (kbar) = 4.76Al - 3.01 - (T - 675)[0.530Al + 0.005294(T - 675)]85, in T°C with P ±0.6 kbar (2s). Their model (Fig. 6.4) is consistent with the experiments of Johnson and Rutherford (1989) and of Thomas and Ernst (1990) at ca. 750°C, as well as Schmidt (1992) at 675°C and the empirical calibrations (Hammarstrom and Zen 1986; Hollister et al. 1987).

Ague (1997) reconsidered the hornblende barometer as a combination of their reaction (26) and the hornblende-plagioclase thermometer of Blundy and Holland (1990):

tremolite + albite = edenite + quartz (6.13)

$$Ca_2Mg_5Si_8AO_{22}(OH)_2 + NaAlSi_3O_8 = NaCa_2Mg_5Si_7AlO_{22}(OH)_2 + 4SiO_2$$

He used Berman (1988, 1991) to calculate the intersection of (6.12) and (6.13) in P-T space with a fixed $Or_{80}$ in the K-feldspar of reaction (6.12). Fixing the K-feldspar composition is an unnecessary and erroneous approach because the Or content of sanidine varies with P-T-$X_{An}$. The $X_{Or}$ varies considerably in high-grade rocks from 0.30–0.90 (Bohlen and Essene 1977; Hayob et al. 1989). One could specify a preliminary P-T and bootstrap the locus of reactions (6.12–6.13) by selecting $X_{Or}$ consistent with preliminary P-T-$X_{An}$ using SOLVCALC (Wen and Nekvasil 1994), then repeating the calculation until convergence. Bhadra and Bhattacharya (2007) considered several equilibria that might apply for Al in hornblende and selected the following:

tremolite + tschermakite + albite = pargasite + quartz (6.14)

$$Ca_2Mg_5Si_8O_{22}(OH)_2 + Ca_2Mg_3Al_2Si_6Al_2O_{22}(OH)_2 + 2NaAlSi_3O_8 = 2NaCa_2Mg_4AlSi_6Al_2O_{22}(OH)_2 + 8SiO_2$$

They examined a large subset of the experimental literature on hornblende-plagioclase, applied mixing models with site-by-site mixing with intra-site and cross-mixing site parameters. They extracted a linear P equation dependent on T, $a(NaAlSi_3O_8)$ in plagioclase and hornblende composition in the range of 0–16 kbar and 650–950°C. The fit of the equation to the input data is precise to 2 kbar and consideration of data from 20 papers on natural hornblende-plagioclase-quartz assemblages using the reported P and T also gave errors on the order of ±2 kbar for most applications. The thermodynamic model may suffer from failure in experimental and natural assemblages to attain equilibrium and from errors in the P-T estimates of the natural assemblages. However the first-order success of the calculations by Ague (1997) and by Bhadra and Bhattacharya (2007) suggests that a fully thermodynamic approach is a viable approach to hornblende barometry.

## *6.2.3 Ti as a Thermobarometer in Silicates*

Interest has developed in correlating the Ti solubility with T for silicates such as hornblende (Raase 1976), biotite (Henry and Guidotti 2002; Henry et al. 2005), zircon (Watson and Harrison 2005; Ferry and Watson 2007; Ferriss et al. 2008), as well as garnet and orthopyroxene (Kawasaki and Motoyoshi 2007). However Ghent and Stout (1984) offered cautionary views on the subject: "*The solubility of $TiO_2$ in silicate minerals such as biotite and hornblende is not simply a function of the activity of $a(TiO_2)$*". They concluded "*the solubility of $TiO_2$ in biotite and hornblende is a complex function of temperature, pressure, the activities of components in coexisting minerals and crystal chemical constraints in the biotite and hornblende crystal lattices. The solubility of $TiO_2$ in biotite and hornblende does not appear to be strongly dependent upon $a(TiO_2)$ because it is similar for biotite and hornblendes of similar metamorphic grade, no matter what Ti-rich phase is present. Barroisite coexisting with rutile contains a lower Ti concentration than hornblendes coexisting with ilmenite and/or sphene which are inferred to have equilibrated at higher temperatures. The $TiO_2$ content of many metamorphic garnets varies in an irregular manner and does not appear to represent an equilibrium solubility*." These concerns should be taken seriously in any calibration or application of these thermobarometers.

Kawasaki and Motoyoshi (2007) undertook unreversed synthesis experiments on Ti in garnet and orthopyroxene with glass starting materials at 15–20 kbar and 1200–1300°C in a piston-cylinder. They assumed that Ti substituted in IV site of garnet and orthopyroxene with atom correlations, although Ti in IV site cannot be distinguished from VI site in garnet or pyroxene by this approach due to equivalencies: $Mg_3(TiAl)(Si_2Al)O_{12} = Mg_3Al_2(Si_2Al)O_{12}$, $Mg(Ti_{0.5}Mg_{0.5})(SiAl)O_6 = Mg(Mg_{0.5}Al_{0.5})(SiTi_{0.5}Al_{0.5})O_6$. No table of run products and no experimental reversals on the Ti of garnet and orthopyroxene were reported. The analytical data on garnet and pyroxene are highly scattered, leading to uncertainties of at least 100–150°C and therefore in application of the thermometer to ultra-high T (UHT) granulites. Significant fluorescence by Fe Kα X-rays may have contributed to variable Ti derived from matrix rutile rather than necessarily to its substitution in the silicates.

### 6.2.3.1 Biotite Ti thermometry

The Ti content in biotite has been applied as a geothermometer for graphitic aluminous schists and gneisses (Henry and Guidotti 2002; Henry et al. 2005). The thermometer was based empirically using metapelites from New England and includes rather data with rather variable Mg/Fe in biotite (Fig. 6.5). The Ti "saturation" surface (Fig. 6.5) is the basis of the thermometer and although deviations (shown as vertical tails) are present, the fit is quite good. The scatter in the data and in the proposed thermometer was not discussed and no analytical data were provided or reactions considered. The assemblage was considered saturated in Ti when found with either ilmenite or rutile and it was recommended for use only at 5 ± 1 kbar. The failure to distinguish between a buffering and saturation is widespread in petrology. The idea of $Al_2O_3$ saturation in metamorphic systems for instance in quartz-bearing rocks is clearly erroneous. Although $TiO_2$ saturation is obtained in the presence of rutile, if a reaction requires other Ti phases to balance Ti in biotite, their activities clearly also control the Ti substitution in biotite, depending in part on the mechanism by which biotite takes up Ti. The consideration of Al or Ti saturation in a silicate is even more obscure in the absence of metallic Al or Ti and it is recommended that use of these terms be discontinued in petrology. The term saturation should not be casually used without first showing the equilibrium that would saturate that component in a phase. In the case of biotite, Ti reactions depend on the substitution mechanism for Ti substitution, which remains controversial. Even the coordination number of the site preferred by Ti in biotite is not fully resolved.

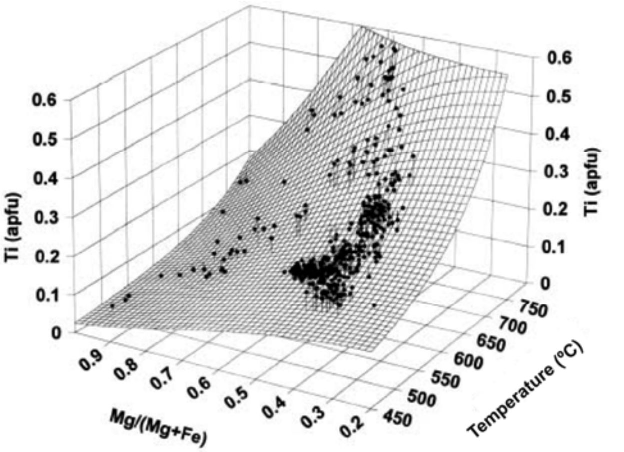

**Fig. 6.5** Empirical calibration of Ti in biotite vs T and Mg #. Although labeled as representing Ti saturation in biotite, at best it is a buffer surface for several reactions such as (6.14–6.17). The surface is remarkably systematic, but individual assemblages were not distinguished. The reactions buffering the Ti content were not evaluated (Henry et al. 2005, with permission from Mineralogical Society of America)

#### 6.2.3.1.1 Ti substitutions in biotite and buffering reactions

Various workers have attempted to identify the major solid solutions of Ti and other exchanges in biotite by correlating analytical data. However Bohlen et al. (1980) showed this approach cannot resolve among several equivalent exchanges in complex mineral biotite, especially in the absence of analytical data for $H_2O$ and $Fe^{3+}$. Bohlen et al. (1980) refined the structure of biotite from a high-grade gneiss and proposed that the most important Ti substitution is a titanium oxy-type, $Ti_{-1}O_{-2}(Fe^{2+})_1(OH)_2$. Cesare et al. (2008) and Sassi et al. (2008) also favoured it as the most important substitution in biotite from high-grade rocks. With this substitution, a simple reaction can be balanced with both ilmenite and rutile:

annite + rutile = Ti-oxy-annite + ilmenite + $H_2O$ (6.14)

$$K_2Fe_6Si_6Al_2O_{20}(OH)_4 + 2TiO_2 = K_2Fe_5TiSi_6Al_2O_{20}(OH)_2O_2 + FeTiO_3 + H_2O$$

Although loss of hydrogen has been described as deprotonation that is only the case when simultaneous oxidation occurs and it is just a dehydration reaction in the case of Ti-oxy substitution. Based on IR measurements in synthetic titanian annite, Robert (1991) argued for substitution of $Ti_{-1}Si_1$ in biotite. That exchange also leads to a simple reaction:

annite + rutile = Ti-Al annite + quartz (6.15)

$$K_2Fe_6Si_6Al_2O_{20}(OH)_4 + TiO_2 = K_2Fe_6Si_5TiAl_2O_{20}(OH)_4 + SiO_2$$

Massonne et al. (1993) also posited this exchange in muscovite even though $K_2Al_4(Si_5TiAl_2)O_{20}(OH)_4$ cannot be distinguished chemically from $K_2(TiAl_3)(Si_5Al_3)O_{20}(OH)_4$. The evidence for significant $Ti^{IV}$ in biotite remains equivocal and its substitution is probably rather limited in micas.

Another mechanism for Ti substitution in biotite is a Ti-Tschermak's type, $Ti_{-1}(Al)^{IV}{}_{-2}(Fe^{2+})_1Si_2$, a substitution favoured by Henry et al. (2005) for biotite in medium- to high-grade metapelites. Balancing the Ti-Tschermak's component requires another aluminous phase such as staurolite, muscovite, garnet or sillimanite. Sillimanite is used in the following reaction:

annite + sillimanite + rutile = Ti-Tschermak's annite + ilmenite + quartz (6.16)

$$K_2Fe_6Si_6Al_2O_{20}(OH)_4 + Al_2SiO_5 + 2TiO_2 = K_2Fe_5TiSi_4Al_4O_{20}(OH)_4 + FeTiO_3 + 3SiO_2$$

Another possibility is a Ti-vacancy substitution in biotite, $Ti_{-1}\;\;{}_{-1}(Fe^{2+})_2$, which leads to the reaction:

annite + rutile = Ti-vacancy annite + ilmenite (6.17)

$$K_2Fe_6Si_6Al_2O_{20}(OH)_4 + 3TiO_2 = K_2Fe_4Ti\;\;Si_6Al_2O_{20}(OH)_4 + 2FeTiO_3$$

Patiño Douce (1993) favoured this substitution by correlating Ti in biotite with VI vacancies, not noticing that the 22 O normalisation procedure for the Ti-oxy exchange automatically produces a false correlation! Many other univariant reactions may be obtained from combination of reactions (6.14–6.17) with equilibria involving staurolite, muscovite and almandine, as well as GRAIL (Bohlen et al. 1983a, 1983b, 1983c), GRIPS (Bohlen and Liotta 1985), GAFS, GAHS, GASP (Essene 1989) or TARK (Manning and Bohlen 1991). Application of such reactions is hampered by failure to distinguish each Ti substitution and lack of a/X relations for Ti exchanges in biotite.

Rutile is involved in reactions (6.14–6.17) yet no $TiO_2$ saturation but only a buffer assemblage is provided for biotite, depending on the reaction mechanism and the other phases (here quartz, rutile, ilmenite, sillimanite, fluid) in the reactions. In reactions (6.14–6.15), more Ti would substitute in biotite of the same Mg-Fe composition from quartz-undersaturated rocks. All four reactions are simultaneously buffered in a metapelite with biotite-sillimanite-quartz-ilmenite-rutile-$H_2O$, yet the progress of each is limited differently depending in part on the substitution mechanism. An advanced solution model is needed to address the activity of titanian biotite adequately. Consideration of assemblages as buffer systems rather than $TiO_2$ saturation may explain why some of biotite (Henry and Guidotti 2002; Henry et al. 2005) with ilmenite has more Ti than in rutile-bearing schists (Henry pers. comm. 2008). One should expect a +P dependence in the biotite thermometer because the reactions will have a +DV due to dense rutile in the reactants and voluminous quartz in the products. The biotite thermometer certainly should not be applied to higher or lower P rocks, e.g. to kyanite schists at >6–8 kbar or to contact metamorphic rocks at 1–4 kbar.

Given a peraluminous biotite with $Al^{VI}$, the substitutions $(Ti)^{VI}{}_{-1}(Al)^{IV}{}_{-2}(Fe^{2+})^{VI}{}_1Si)^{IV}{}_2$ and $Ti_{-1}Si_1$ cannot be resolved by analytical methods because of an equivalency reaction for $Ti^{VI}Al^{IV}$ annite vs $Ti^{IV}Al^{VI}$ annite: $2K_2Fe_{5.5}Ti_{0.5}(Si_5Al_3)O_{20}(OH)_4 = K_2Fe_{5.5}Al_{0.5}(Si_5Al_{2.5}Ti_{0.5})O_{20}(OH)_4$. Peraluminous biotite with Si of ca. 5.2–5.5 is commonplace in metapelites (e.g. Holdaway and Lee 1977). Entrance of Ti may lead to transfer of Al to the IV site and Ti to the octahedral site, whereas on the simple annite-rutile binary this more complex exchange cannot occur because no $Al^{VI}$ is available to partition.

Determination of the Ti formula in a given biotite requires measurement of both FeO and total Fe as well as $H_2O$ and even then one cannot distinguish $Ti_{-1}Si_1$ vs $Ti_{-1}(Al)^{IV}{}_{-2}(Fe^{2+})_1Si_2$ without additional structural information. One cannot simply assume all $Fe^{2+}$ in biotite even in graphitic schists because of the documented significant (8–15%) $Fe^{3+}$ found in Mössbauer in biotite by Guidotti and Dyar (1991). A complex biotite composition means the major mechanism for Ti is ambiguous because reactions can be written among postulated biotite species, including the above Ti exchanges, as well as Al-oxy or $Fe^{3+}$-oxy and substitution of a vacancy as dioctahedral-trioctahedral solid solution $_{-1}(R^{3+})_{-2}(R^{2+})_3$ (Bohlen et al. 1980; Rancourt et al. 2001). The latter substitution is fixed for Al vs Mg + $Fe^{2+}$ in both micas when muscovite coexists with biotite. Patiño Douce (1993) postulated an octahedral site vacancy substitution for Ti, $_{-1}(Ti)_{-1}(R^{2+})_2$, but there is no way to distinguish it from a vacancy engendered by dioctahedral Al or $Fe^{3+}$ substitution. The correlation of octahedral site vacancy with increasing Ti (Patiño Douce 1993) is flawed: a false vacancy in Ti-oxy biotite is generated by a 22 O normalisation. Consider the formula of a Ti-oxy biotite, $K_2TiFe_{4.5}Al_{0.5}Si_{5.5}Al_{2.5}O_{20}(OH)_2O_2$, which must be normalised to 23 O! Erroneously normalising to 22 O yields $K_{1.91}Ti_{0.96}Fe_{4.30}Al_{0.12}\ \ _{0.62}Si_{5.26}Al_{2.74}O_{20}(OH)_4$ on an anhydrous basis, apparently closer to a dioctahedral than a trioctahedral mica, but only because it was misnormalised.

EMP data alone cannot be used to predict the VI occupancy in biotite (Afifi and Essene 1988). The only reliable way to normalise titanian biotite is to measure $Fe^{3+}/Fe^{2+}$ as well as $H_2O$ and apply anion normalisation (Bohlen et al. 1980; Sassi et al. 2008). One cannot evaluate alternative substitutions in biotite or muscovite with an EMP analysis when also granting the possibility of $Fe^{3+}$. Atomic plots such as those shown by Sassi et al. (2008) are not persuasive of a particular substitution even with complete analyses of biotite because they represent projections from multicomponent biotite space onto two dimensions. Thus Ti-oxy substitution cannot be resolved from Al- or Fe-oxy, nor Ti-vacancy from Al- or $Fe^{3+}$-vacancy substitutions. Structure refinements of 10 biotite from medium grade metapelites show 6–24% vacancies ordered into the M1 octahedral site and 0–15% vacancies in the K site of the biotite crystals, as well as 7–12% trioctahedral substitution in four muscovite crystals that coexist with the refined biotite grains (Brigatti et al. 2008). Reasonable crystal-chemical assumptions were made in reaching this result, including placing all Ti and $Al^{VI}$ in the M2 site of biotite. The data indicate limited but significant mutual solid solution of biotite and muscovite in peraluminous metapelites and granites (Brigatti et al. 2000, 2008).

#### 6.2.3.1.2 Applications of the biotite Ti thermometer

Dinklage et al. (2007), Cesare et al. (2008) and Thomson (2008) applied the biotite thermometer of Henry et al. (2005). Dinklage et al. studied schists from the Pequop Mtns, NE Nevada and obtained 607 ± 21°C for the garnet zone and 568 ± 5°C in the biotite zone from the biotite thermometer. The resultant T are 100–150°C too high compared to the expected T of these zones in metapelites (Thompson 1976). Either the particular schists are not sufficiently peraluminous for application of the particular zonal designations or there is a major systematic error in the thermometer. Cesare et al. (2008) obtained >800°C for the Ti-in-biotite thermometer of Henry et al. (2005) applied to aluminous granulites with ilmenite. Although the result is reasonable, quantitative application of this thermometer is hampered by the lack of graphite and higher pressures of the granulites than in the calibration.

Thomson (2008) obtained biotite T from aluminous gneisses with biotite–cordierite–orthopyroxene-quartz ± opaques that were contact metamorphosed beneath the Stillwater intrusion in Montana. She selected the most Ti-rich biotite and obtained 660–760°C from Ti-in-biotite vs 790°C from average P-T calculations with Thermocalc (Holland and Powell 1998). The logic of selecting the most Ti-rich biotite is unclear unless there is clear-cut textural evidence of resetting the other biotite. Much of the biotite is texturally late in the Stillwater hornfelses, which have several complex and incompletely understood textures. Moreover the selected data are still 80 ± 50°C lower than the expected peak T, suggesting a systematic error. Reactions such as (6.14–6.17) buffering Ti in biotite from garnet-sillimanite schists are clearly different than those for Ti in biotite from cordierite and/or hypersthene hornfelses:

biotite + sekaninaite (Fe-cordierite) + ilmenite = TiAl biotite + hypersthene + quartz (6.18)

$$4K_2Fe_6Si_6Al_2O_{20}(OH)_4 + Fe_2Al_4Si_5O_{18} + 2FeTiO_3 = 4K_2Fe_{5.5}Ti_{0.5}Si_5Al_3O_{20}(OH)_4 + 6FeSiO_3 + 3SiO_2$$

biotite + ilmenite + quartz = Ti-oxy biotite + hypersthene + $H_2O$ (6.19)

$$K_2Fe_6Si_6Al_2O_{20}(OH)_4 + FeTiO_3 + 2SiO_2 = K_2TiFe_5Si_6Al_2O_{20}(OH)_2O_2 + 2FeSiO_3 + H_2O$$

Reaction (6.18) is likely to be more of a barometer and (6.19) a thermometer. Both could be applicable to yield P and T in the same assemblage, biotite-cordierite-hypersthene-ilmenite-quartz-melt/$H_2O$, once a comprehensive mixing model is developed for the activity of both Ti substitutions in the same biotite. Thomson (2008) used EDS data to identify the opaques but did not distinguish ferrian ilmenite vs titanian magnetite in the Stillwater aureole. Labotka and Kath (2001) identified ilmenite from several cordierite-hypersthene hornfelses elsewhere in the aureole, so the assumption that it is present seems reasonable, but it should be analysed because the $Fe_2O_3$ solid solution in the Stillwater ilmenite needs to be evaluated. The activity of $TiO_2$ is greatly reduced in pyrrhotite-magnetite-ilmenite

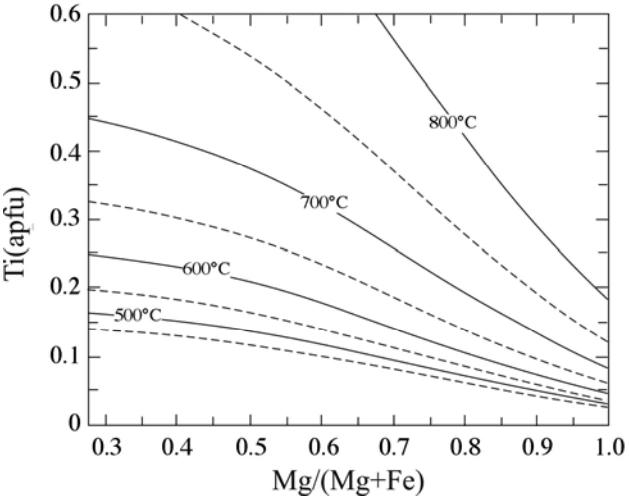

**Fig. 6.6** Empirical calibration of the Ti in biotite vs T. The specific assemblage must also affect the Ti content of the biotite, and the isopleths will kink upon crossing univariant curves separating the different buffering assemblages (Henry et al. 2005, with permission from Mineralogical Society of America)

hornfelses compared to ilmenite-rutile assemblages and amount of $Fe^{3+}$ in both biotite and ilmenite is likely far higher in the Stillwater aureole in the absence of graphite than in New England metapelites.

Each reaction and substitution for Ti in biotite is expected to buffer its Ti content. Isopleths of Ti in biotite are defined with a given buffer assemblage and will kink when crossing a univariant curve that produces new assemblages. Each reaction must be evaluated separately for its P-T-X dependence and each biotite should be analysed for $Fe^{3+}/Fe^{2+}$ and $H_2O$ to correct the equilibria for these more occult substitutions. The simple concept of Ti-saturation for biotite in metapelites with either rutile or ilmenite is flawed: an assemblage may buffer a Ti species without saturation. The biotite thermometer is not recommended in its current form, but the pattern of increasing Ti in biotite with T-X (Fig. 6.6) is encouraging for future work on this system as a thermobarometer.

## *6.2.4 Phengite Barometry*

Phengite barometry was originally based on analyses, XRD measurements and reactions considered by Ernst (1963) and experiments of Velde (1965). Ernst (1963) showed by calculations of the DV of a phengite reaction that it was favoured by increasing pressure. Velde (1965) undertook synthesis experiments that showed an increase in phengite and ferrophengite content with pressure and temperature. Although these efforts were indicative of a pressure effect on phengite, they were seldom applied quantitatively. It was in this framework that Sassi and coworkers first advanced the use of the b cell dimension of phengite in the 1970s.

### 6.2.4.1 Sassi phengite barometry

Sassi (1972), Sassi and Scolari (1974) and Guidotti and Sassi (1976) proposed the average contraction of the b cell dimension (usually referred to incorrectly as $b_0$ barometry) of phengite as an empirical index of increasing pressure presumably due to greater phengite substitution. It will be referred to below as Sassi phengite barometry. They collected XRD data on hundreds of rocks rather than investigating the solid solutions and reactions involving phengite directly. An advantage of this approach is that it can be applied in phyllites to fine-grained phengite, which is very difficult to analyse with the EMP due to beam damage and nearly submicroscopic intergrowths of chlorite and/or paragonite in some cases. Essene (1989) advanced several criticisms of this barometer, chief among them that no reaction was proposed to explain variations in phengite with a buffered assemblage. Another difficulty is that the b cell dimension (if unperturbed by coherent intergrowths) is a complex sum of several simultaneous exchanges in phengite ($Mg_{-1}Si_{-1}Al_2$, $Fe^{2+}{}_{-1}Si_{-1}Al_2$, $Fe^{3+}{}_{-1}Al_1$, $K_{-1}Na_1$, $Mg_{-3}Al_2$, $K_{-1}Al_{-1}\ Si_1$, even $Ba_{-1}Al_{-1}K_1Si_1$: Giorgetti et al. 2000) and it is not a simple guide to a single exchange or phengite content. Zoning from substitutions in phengite will broaden the X-ray peaks in a single sample and when measuring different chemically variable samples it will widen the range of b dimensions in the cumulative plots used in the application of the b cell barometer. Guidotti and Sassi (1986) showed that the b cell dimension in phengite decreases with Na and also with increasing metamorphic grade (i.e. T). Sassi (1972), Sassi and Scolari (1976) and Guidotti and Sassi (1976) recommended exclusion of phengite from K-feldspar bearing rocks for b cell barometry on the ground that those micas have a higher b value. That seems strange given that the phengite content should be *maximised* with K-feldspar and chlorite-quartz-$H_2O$ at low grades and at somewhat higher grade with biotite-quartz-$H_2O$ (Massonne and Schreyer 1987; Essene 1989; Guidotti and Sassi 1998). The b parameter also will vary with oxidation state and T. The latter effect is glossed over by statements that all the rocks "formed essentially at the same temperature", given the variable T (250–450°C) of slates, phyllites, greenschists and blueschists to which it was applied. Massonne and Schreyer (1987) also objected to incautious use of the Sassi barometer when compared with their experiments.

The cause of the shift in the average b cell dimension of phengite with increasing P in unbuffered blueschists is still not well established. The spectrum of data at any one locale (e.g. Sassi 1972; Stone and Merriman 2004) suggests that bulk rock composition is variable or that variable reaction progress was occurring in adjacent rocks, either of which is counter to the stated assumptions in the barometer. Despite comments of Essene (1982, 1989), Frey (1987) and Massonne and Schreyer (1987) on this barometer, about 80 of the 140 current citations to the papers of Sassi (1972) and Sassi and Scolari (1974) were made after 1990 and few that the writer has examined considered or evaluated those criticisms. Ramirez and Sassi (2006) stated that the Sassi barometer "*is based on the increasing celadonite substitution that occurs with P increase in muscovite within the Al-rich portion of the non-limiting assemblage muscovite-albite*" and "*the cautions suggested on the use of this method by Frey (1987) and Essene (1989) are not justified considering that the analytical procedure is such as to prevent the claimed risks*." The cautions that were offered did not address "risks" whatever those might be, but the issue of evaluating a systematic change in a mineral unbuffered by a reaction.

Guidotti and Sassi (1976, 1989, 1992, 1998, 2002) separated four different assemblages with different corresponding b cell dimensions in phengite. None of them is buffered in a straightforward way for phengite substitution (the exchange reactions for $Mg_{-1}Si_{-1}Al_1Al_1$, $Fe^{2+}{}_{-1}Si_{-1}Al_1Al_1$ and $Fe^{3+}{}_{-1}Al_1$ are buffered with chlorite). Those reactions should be primarily dependent on T and not P and moreover the ratios should be sensitive to the rock composition in the absence of other ferromagnesian minerals. Kisch et al. (2006) included an extensive reference list of barometric applications on b of phengite. They wrote "*although the use of the $b_0$ cell parameter as a semiquantitative geobarometer has been criticised, for instance, by Essene (1989), it has been successfully applied in many areas throughout the world, both before Essene's warning ... and after it*." Of course, success should not be judged in the eye of an easily satisfied user, but rather in a critical examination of the system. The role of all substitutions that will control the b dimension need to be evaluated explicitly and when that is accomplished, one might as well use the analytical data to investigate applicable univariant equilibria for thermobarometry. The promise of Sassi phengite barometry in low grade metapelites is simply illusory.

#### 6.2.4.2 Phase equilibria for phengite

Essene (1989) balanced several equilibria for phengite. Their major disadvantage is the infrequence of assemblages with K-feldspar in blueschists except in a few metagranitic rocks (Tropper and Essene 1999). Those reactions would apply to metapelites from the chlorite and the biotite zones with microcline. Sassi (1972), Sassi and Scolari (1976), Guidotti and Sassi (1998, 2002) and Kisch et al. (2006) argued for different levels of Al saturation for various phengite assemblages. However they did not establish Al buffers with balanced reactions ($Al_2O_3$ saturation is obtained only with corundum or diaspore). An Al buffer would apply to pyrophyllite but not phengite substitution. Oberhänsli et al. (1995) and Agard et al. (2001) showed that the phengite component is buffered by a reaction with carpholite and chlorite. A carpholite reaction may be recast as the following:

phengite + magnesiocarpholite = muscovite + clinochlore + quartz + $H_2O$ (6.20)

$$2K_2Al_3MgSi_7AlO_{20}(OH)_4 + 3MgAl_2Si_2O_6(OH)_4 = 2K_2Al_4Si_6Al_2O_{20}(OH)_4 + Mg_5AlSi_3AlO_{10}(OH)_8 + 5SiO_2 + 2H_2O$$

phengite + ferrocarpholite = muscovite + daphnite + quartz + $H_2O$ (6.21)

$$2K_2Al_3FeSi_7AlO_{20}(OH)_4 + 3FeAl_2Si_2O_6(OH)_4 = 2K_2Al_4Si_6Al_2O_{20}(OH)_4 + Fe_5AlSi_3AlO_{10}(OH)_8 + 5SiO_2 + 2H_2O$$

A related version of reaction (6.20) was given in Bousquet et al. (2002). Reactions (6.20–6.21) may provide useful reactions or limits in carpholite blueschists (Makanjuola and Howie 1972; Agard et al. 2001; Bousquet et al. 2002; Bucher and Bousquet 2007).

#### 6.2.4.3 Vidal phengite barometry

Vidal and Parra (2000), Agard et al. (2001) and Vidal et al. (2001) computed phase equilibria for phengite assuming several end-members in phengite including pyrophyllite. This type of thermobarometry, which has become widely used in low-grade rocks is here designated Vidal phengite barometry. Depending on the problem at hand, other ferromagnesian minerals, such as chlorite, chloritoid, glaucophane or garnet may also be used. Agard et al. (2001) identified ca. 10% pyrophyllite solid solution in phengite from HP schistes lustrés and generated a petrogenetic grid for reaction (6.20) as a barometer combined with one involving pyrophyllite as a thermometer (Fig. 6.7). Even though this particular computation is outdated relative to more recent works of Vidal and coworkers, it has been shown here to illustrate some general points in these works. A petrogenetic grid has been constructed using the pyrophyllite component in phengite (vertical lines in Fig. 6.7), the phengite component (numbers associated with slanted lines with a positive slope) and bounding reactions on carpholite and chloritoid stability. Texturally late phengite assemblages (open circles) yield lower P than the texturally earlier associations (close circles), suggestive of a steep decompressive curve. That theme has repeatedly been demonstrated in the subsequent works of Vidal and coworkers.

Vidal and Parra (2001) also calculated and contoured phengite and pyrophyllite compositions in phengite from

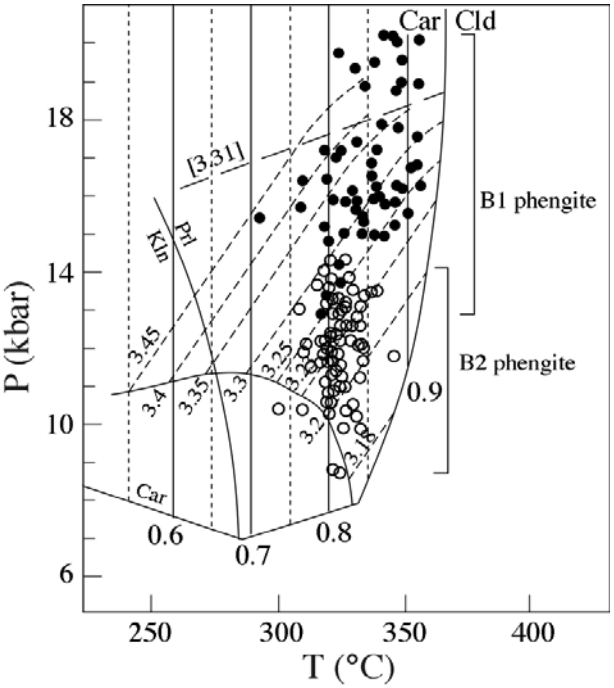

**Fig. 6.7** Phengite barometry. Phengite level is shown by the positively sloped lines and vertical lines represent pyrophyllite substitution. The P-T estimates are for carpholite-chlorite-phengite assemblages with two different sets of phengite grains that were petrographically distinguished as earlier (B1) and later (B2). Bounding equilibria with carpholite are also shown. Vidal et al. (2006, 2007) calculated P-T estimates for chlorite-phengite-quartz-$H_2O$ and other assemblages using updated mixing models for phengite and chlorite. Those papers do not show contours for the phengite composition and involve many unlabeled univariant curves relying on sudoite content in chlorite and pyrophyllite in phengite. This diagram shows the evidence for decompression (modified from Agard et al. 2001, with permission from Blackwell Scientific)

phyllites. The thermodynamic and mixing models in Vidal's papers for phengite, chlorite and carpholite must be viewed critically. Phengite and carpholite equilibria are based on unreversed experiments. The stability of phengite is based on experiments of Massonne and Schreyer (1987) and ferrophengite by those of Massonne and Szpurka (1997) and of Parra et al. (2005). Essene (1989) discussed a number of problems with respect to the experiments of Massonne and Schreyer (1987), chief of which is the failure to obtain experimental reversals and to directly analyse the run products. A similar comment applies to magnesiocarpholite stability, which if reversed likely would place the reaction at lower T than currently assumed. A major concern with EMP data on fine-grained phengite is that pyrophyllite substitution ($K_{-1}Al_{-1}\quad Si_1$) in micas is easily confused with alkali loss from beam damage and submicroscopic intergrowths with chlorite or smectite. In addition, $Fe^{3+}$ is often present at high levels in phengite from HP associations when analysed directly (e.g. van der Plas 1959; Makanjoula and Howie 1972). The effect of neglecting $Fe^{3+}$ is as follows. If ferrimuscovite, $K_2Fe^{3+}{}_4Si_6Al_2O_{20}(OH)_4$ is treated as ferrophengite and normalised to 22 O, it gives $K_{2.11}(Fe^{2+}{}_{4.21}Al_{0.42}\quad{}_{0.37})Si_{6.31}Al_{1.69}O_{20}(OH)_4$. Ferrimuscovite substitution that is ignored generates false VI vacancies, decrease in the K site occupancy and increase in ferroceladonite and ferrophengite. Normalisation of ferriphengite assuming all $Fe^{2+}$ must generate errors that systematically shift P-T estimates (Vidal and Parra 2000; Agard et al. 2001; Parra et al. 2002a) by generating systematic errors in pyrophyllite and celadonite. Furthermore convergence of multisystems reactions is then not a good test of the best estimate, which should be in a divergent zone. Tests should be undertaken to show that pyrophyllite is present in phengite at the levels inferred by EMP and a systematic evaluation of $Fe^{3+}/Fe^{2+}$ in rock-forming phengite is needed.

At higher grades Fe-Mg carpholite is replaced in metapelites by Fe-Mg chloritoid, buffering reactions:

$$\text{ferrophengite + chloritoid = muscovite + almandine + } H_2O \qquad (6.22)$$

$$K_2Al_3FeSi_7AlO_{20}(OH)_4 + 2FeAl_2SiO_5(OH)_2 = K_2Al_4Si_6Al_2O_{20}(OH)_4 + Fe_3Al_2Si_3O_{12} + 2H_2O$$

$$\text{muscovite + daphnite = ferrophengite + chloritoid + quartz + } H_2O \qquad (6.23)$$

$$2K_2Al_4Si_6Al_2O_{20}(OH)_4 + Fe_5AlSi_3AlO_{10}(OH)_8 + 2SiO_2 = 2K_2Al_3FeSi_7AlO_{20}(OH)_4 + 3FeAl_2SiO_5(OH)_2 + H_2O$$

Bousquet et al. (2002) proposed a similar reaction to (6.23). Note that the phengite component changes in the opposite direction to dehydration in reaction (6.22) vs (6.23). Reactions (6.22–6.23) may be useful for chloritoid blueschists (e.g. Makanjoula and Howie 1972; Bousquet et al. 2002) and greenschists (e.g. Mengel and Rivers 1994; Phillips and Law 1994). They should be computed thermodynamically, corrected for solid solutions and compared with other thermobarometers. Although the presence of $Fe^{3+}$ in chlorite and chloritoid is often ignored, chemical analyses of $Fe^{3+}/Fe^{2+}$ of these minerals in HP rocks indicate significant $Fe^{3+}$ (Makanjoula and Howie 1972). An advantage of a phase equilibrium approach is that one can extend applications to rocks at higher metamorphic grades and resolve the effect of T vs P.

#### 6.2.4.4 Applications of phengite barometry

Reactions may be balanced with fewer phases by adding more components in phengite and/or chlorite. Using an

$Al_2Si_4O_{10}(OH)_2$ component with two other muscovite components in KMASH (or one more KMASH component in chlorite) allows reduction in the number of associated phases, e.g. phengite-chlorite-quartz-$H_2O$ instead of reaction (6.20) or ferrophengite-chloritoid-quartz-$H_2O$ instead of reaction (6.23). Confusing beam damage with pyrophyllite substitution is a major concern. Until that is resolved reliance on pyrophyllite in phengite for thermometry (Vidal and Parra 2000; Agard et al. 2001; Parra et al. 2002a; Vignaroli et al. 2008; Yamato et al. 2007) is equivocal. Figure 6.7 shows variation in the phengite and pyrophyllite content of muscovite with PT from Agard et al. (2001). This early treatment of the phengite reactions in a carpholite-chloritoid-quartz schist has been superceded by later work of Vidal et al. (2001, 2006), but it serves to illustrate something of the kinds of reactions that are involved in their papers.

Although widespread in some phyllites and blueschists, paragonite is often avoided in Sassi barometry. Paragonite in low-T eclogites and garnet-epidote blueschists is often recrystallised into coarse grains with coexisting phengite (Ahn et al. 1985). Paragonite in fine-grained blueschists may be preserved as submicroscopic and/or nearly submicroscopic intergrowths with phengite in diagenetic rocks (Li et al. 1994), Franciscan blueschists (Shau et al. 1991) and Cretan phyllites (Manon 2008). Vidal and Parra (2000) analysed phengite in several suites of HP phyllites, but many of their analytical data were obtained with a high analytical current and point beam that probably damaged fine-grained phengite during the analyses, producing low totals and apparent vacancies in the K site. Vidal and Parra (2000) and Agard et al. (2001) identified the assemblage phengite-chlorite-albite-paragonite-quartz in HP phyllites, which buffers the phengite content as follows:

$$\text{phengite + paragonite = muscovite + clinochlore + albite + quartz} + H_2O \qquad (6.24)$$

$$5K_2Al_3MgSi_7AlO_{20}(OH)_4 + 3Na_2Al_6Si_6O_{20}(OH)_4 = 5K_2Al_4Si_6Al_2O_{20}(OH)_4 + Mg_5AlSi_3AlO_{10}(OH)_8 + 6NaAlSi_3O_8 + 2SiO_2 + 2H_2O$$

This assemblage is common in the schistes lustrés of the Alps and reaction (6.24) is worthy of thermodynamic calibration and application. It is appealing as it does not depend on the substitution of a small and uncertain amount of sudoite in chlorite or pyrophyllite in phengite.

Vignaroli et al. (2008) applied the mixing models of Vidal, Parra and coworkers to a series of phengite-chlorite-quartz schists from Sicily using the programmes of Berman (1988, 1991). Their EMP analyses at 15 nA (beam size and counting time were not specified) may well have produced beam damage, in reducing the apparent K and Na content of phengite. They used four components (but not sudoite) for chlorite and four (including pyrophyllite) for phengite. Pyrophyllite is computed by the difference of two large numbers as 1-K-Na-Ca and it assumes no alkali migration during the analyses, so it must be regarded as rather uncertain. Vignaroli et al. (2008) based their thermobarometry on four sets of independent reactions involving 19 univariant reactions. Of these 8 are dehydration reactions that depend on accurate measurement of pyrophyllite in phengite and 11 are solid-solid reactions involving Tschermak's or Mg-$Fe^{2+}$ exchange for chlorite-phengite. The ignored the possibility of $Fe^{3+}$ in phengite and chlorite. Estimates from stoichiometry suggest that a majority to nearly all of the iron in the phengite is 3+, so that the amount of ferroceladonite is small and highly uncertain (Parra et al. 2002a) and the 11 reactions calculated with ferroceladonite likely have major errors. Their calculations showed two sets of P conditions at about 400°C for the schists, one group at 6–8 kbar and the other at 3–4 kbar, with the higher P schists now located in a structurally higher position than those at lower P. Although the P-T results are apparently persuasive, the intersections depend on highly uncertain and unstated assumptions: accuracy of the mixing models, neglect of $Fe^{3+}$ and its impact on the calculations and the implicit assumption that the pyrophyllite component is well determined by EMP. In the writer's opinion, none of the equilibria is reliably located and the agreement of the calculations is an illusion!

Vidal and coworkers have employed phengite barometry in many studies of greenschists and blueschists (Booth-Rea et al. 2002, 2005, 2006; Parra et al. 2002a, 2002b; Trotet et al. 2001; Augier et al. 2005a, 2005b; De Andrade et al. 2006; Vidal et al. 2006; Ganne et al. 2003, 2007; Yamato et al. 2008). The analytical data in these studies mostly were obtained at 15 kV, 10 nA and a 3–5 mm size beam. In several studies no beam size was specified and only Parra et al. (2002b) listed count times per element of 10 s, short for precise analyses. Analytical totals for phengite often are <94 oxide wt% and chlorite <87 oxide wt%. Many of the papers lacked analytical data and alkali migration during analysis was not addressed (Booth-Rea et al. 2002, 2005, 2006; Parra et al. 2002a, 2002b; Trotet et al. 2002; Ganne et al. 2003; Augier et al. 2005a, 2005b). The $Fe^{3+}$ was usually ignored, although it was estimated in chlorite (but *not* in coexisting phengite) by optimising convergence of the phase equilibria while varying $Fe^{3+}$ (Booth-Rea et al. 2006; Vidal et al. 2006). De Andrade et al. (2006) and Vidal et al. (2006) mapped analyses and P-T conditions for phengite-chlorite rocks, but it is not clear despite their tests whether a 100 nA point beam even for just 0.3 ms is quantitative or reliable. Space does not permit a paragraph on each paper, but the concerns raised above for Vignaroli et al. (2008) apply to these studies. It is difficult to evaluate the significance of the P-T convergence and the quality of Vidal phengite barometry. From petrological intuition this writer regards the T estimates as more reliable than the P estimates.

#### 6.2.4.5 Ionic phase equilibria for phengite

Quantitative application of open-system reactions may be considered for phengite, as in the reaction:

$$\text{phengite} + H^+ = \text{muscovite} + \text{clinochlore} + \text{quartz} + H_2O + K^+ \qquad (6.25)$$

$$5K_2Al_3MgSi_7AlO_{20}(OH)_4 + 4H^+ = 3K_2Al_4Si_6Al_2O_{20}(OH)_4 + Mg_5AlSi_3AlO_{10}(OH)_8 + 14SiO_2 + 2H_2O + 4K^+$$

This reaction is buffered in the Salton sea geothermal system for illite-chlorite-quartz, assuming that these phases do not have interlayer complexities (at least at greater depth and higher T) or using AEM analyses for illite and chlorite. The evidence for substantial fluid metasomatism and in some cases the introduction of brines in blueschists and other HP rocks is growing. In such cases ionic equilibria such as reaction (6.25) may explain observed variations in phengite composition in apparently unbuffered rocks. Analysis of the coexisting fluids in geothermal deposits or of syngenetic fluid inclusions could be combined with such equilibria corrected for solid solutions as a function of P, T, pH and pK in order to understand the progress of phengite reactions. Workers should observe buffered reactions for phengite, analyse the assemblages, calibrate the reactions and correct for solid solutions.

### *6.2.5 Transformations in Clay Minerals*

Clay mineral transformations have a long history as a geothermometer (e.g. Frey 1987; Essene and Peacor 1995, 1997). Powder XRD measurements are favoured because bulk clay minerals can be concentrated rapidly by settling and their (00l) peaks can rapidly be scanned by mounting on a glass slide (carefully packed cavities can be used for measurements of non (00l) peaks such as (060). Clay thermometers can be separated into several types: peak width, usually described as "crystallinity" and peak position, selected to measure a compositional change (an example is the b cell dimension of phengite). Several complexities arise with XRD measurements of many clay minerals arising from complex submicroscopic clay mixtures, some of which can be X-ray amorphous especially if they formed from volcanic glass, others producing overlapping peaks or chemical heterogeneities that decrease the measured peak width and finally the effect of coherent intergrowths that may shift the peak position due to strain (Essene and Peacor 1995). The complex textural relations of clay minerals are best addressed with TEM measurements, in which textural relationships can be resolved at scales down to 10 nm (Peacor 2002b). Lattice fringe images obtained parallel to (001) in clays and micas combined with EDS may serve to distinguish different sheet silicates. Clay samples suspended in fluid and energetically vibrated in an ultrasound device during the separation process may break weak hydrogen bonds along (00l), producing anomalous amounts of "fundamental particles", which may reorient turbostratically during settling (Ahn and Peacor 1986; Peacor 1998).

#### 6.2.5.1 TEM observations of clay minerals

Clay crystallinity (peak width in powder XRD measurements) has been correlated with diagenetic T. Direct TEM observations of clay packet thicknesses are preferred to results modeled with the Warren-Averbach model by NEWMOD (Jiang et al. 1997; Merriman et al. 1990). The former are direct measurements whereas the latter computation does not correct for variable interstratifications, chemical heterogeneities or strain effects. Dudek et al. (2002) estimated the sizes of suspended clay packets with XRD and TEM on illite further disaggregated with a polymer. The sizes obtained from XRD modelling had a greater abundance of small (20–30 Å wide) grain compared to TEM and the model failed to simulate the low 2Q region of the XRD pattern in illite from shales. Illite isocysts and other clay mineral crystallinity data are predominantly a measure of grain size and not crystal perfection (Jiang et al. 1997). Although there may be a general correlation of grain size with T in rocks that are not deformed or recrystallised, the advancement of illite crystallinity in low-grade metapelites is retarded by development of strain-reduced subgrain development (Giorgetti et al. 2000). That may explain the anomalously low illite crystallinity on phyllites from the Franciscan Fm. in northernmost California (Merriman pers. comm. 2003). Nadeau et al. (1984) modeled clay diagenesis in terms of "fundamental particles" (dispersed clay packets directly imaged in TEM). The packet size of clay particles was estimated from XRD and low angle X-ray scattering measurements (Shang et al. 2003). However TEM observations on interstratified smectite and rectorite suggest that they did not accumulate from fundamental particles but preserve original structural sequences (Ahn and Peacor 1986; Kasama et al. 2001). Peacor (1998) reviewed the concept of fundamental particles in terms of TEM measurements on less disturbed shales and concluded that the hypothesis was flawed. Clays are best studied in situ with ion-milled samples or focused ion beam (FIB) slicing in order to better select areas of interest with preliminary SEM observations in the FIB (Lee et al. 2003). Thinned samples can be analysed semiquantitatively with EDS with a TEM on selected areas down to a few hundred nm (Peacor 2002a).

### 6.2.5.2 Useful clay mineral thermometers

Useful clay mineral thermometers in deep diagenetic and low-grade metamorphic systems include assemblages of kaolinite-quartz vs pyrophyllite-fluid and diaspore vs corundum-fluid. Phase relations in these systems are reasonably well constrained by experimental and thermodynamic data (e.g. Perkins et al. 1979; Anovitz et al. 1991). El-Shazly (1995) inferred a stability field for kaolinite-microcline and kaolinite-albite, which requires a major adjustment in the entropy of kaolinite, $S°_{298}$ of 187.4 J/mol K. That conclusion is in wild disagreement with Cp measurements on kaolinite, which lead to an $S°_{298}$ of 200.9 ± 0.5 J/mol K (Robie and Hemingway 1991). El-Shazly's model also requires no stability field for paragonite-quartz-$H_2O$ and muscovite-quartz-$H_2O$ at STP, in disagreement with data in self-consistent thermodynamic data bases (e.g. Holland and Powell 1998). Jiang et al. (1994b) described authigenic kaolinite in diagenetic sediments where detrital quartz, K-feldspar and albite was dissolving based on textures. Even when they are found together, kaolinite may not be equilibrated with quartz or feldspars in near-surface environments, which indeed are the breeding grounds for metastable assemblages (Essene 1982). Yang and Steefel (2008) measured dissolution and precipitation rates of kaolinite at 22°C and a pH of 4. They calculated reactive transport conditions on kaolinite and albite at these conditions and they showed that kaolinite can remain stable while albite is greatly undersaturated and far from equilibrium with the fluid. It is concluded that the inferences of El-Shazly (1995) are based on disequilibrium assemblages and that they are incorrect.

The HP stability of diaspore-quartz vs pyrophyllite was calculated thermodynamically (Perkins et al. 1979, 1980; Chatterjee et al. 1984) and determined experimentally (Theye et al. 1997). The field relations of diaspore-quartz may be misconstrued if textures are not carefully considered. Diaspore has been reported in veins cutting low-grade sediments where it is mantled from adjacent quartz by sheaths of pyrophyllite. This observation suggests gradients in $a(SiO_2)$ and $a(Al_2O_3)$ rather than equilibrium of diaspore and quartz (Essene unpublished). Careful high magnification BSE images of diaspore-quartz associations should be obtained before accepting it as an equilibrium assemblage.

## 6.2.6 *Transformations in Carbonaceous Materials*

At diagenetic grades, organic materials may transform to oil by melting processes that can be modeled by successive minimisation of free energy in the metastable assemblages (Helgeson et al. 2008). Raman studies on the transformation of carbonaceous materials on low-grade rocks include recent work on the subject by Beyssac and coworkers (Beyssac et al. 2002a, 2002b, 2003, 2004, 2007; Augier et al. 2005b). The Raman technique is impressive in an analytical volume on the order of 1 $mm^3$, an ability to focus below the surface to avoid perturbations induced by the polishing process and its seemingly high precision. However natural carbonaceous materials from the greenschist facies and below are clearly variably disordered and not fully degassed to pure carbon. Essene (1989) wrote: "*The process of graphitisation of vitrinite produces coexisting carbonaceous phases with different ordering and structure states. Progressive variations in bulk properties, such as powder XRD measurements or reflectance, will reflect modal variations in the coexisting phases rather than a homogeneous, monotonic transformation to ordered graphite. The degree of graphitisation is accelerated by deformation at low temperatures, retarded in contact aureoles relative to regional metamorphites and is correlated with modal carbon, methane fugacity and permeability*." Those concerns remain today. Anthracite contains two-dimensional layers of aromatic hydrocarbons that may exhibit turbostratic ordering (e.g. Pusz et al. 2003). It must undergo further ordering and dehydrogenation in transforming to graphite and kinetics will inhibit the transformation. The presence of aromatics in carbonaceous material vs graphite requires that the transformation is non-isochemical and thus must depend on the associated fluid and its composition. The transformation of carbonaceous material may depend on the deformation history and once transformed, the material may survive a later transient thermal event. Observations of Dunn and Valley (1992) and Rathmell et al. (1999) on graphitic marbles are consistent with early isotopic equilibration of graphite surviving through a later regional metamorphic event. Another concern is the orientation effect, in which graphitic materials not oriented with the c axis in the plane of the section give anomalously high T, on the range of 600–650°C (Katagiri et al. 1988; Wang et al. 1989; Compagnini et al. 1997; Yong 2008). In the writer's experience graphite is often not oriented relative to foliation or bedding plane in marbles and one would therefore expect anomalous high T. In applying Raman thermometry to randomly oriented carbonaceous materials (Yong 2008).

Beyssac et al. (2007) studied carbonaceous materials from Taiwan slates and marbles with Raman thermometry, which yielded 350–500°C across a transect from west to east. The T in the east are 100–200°C higher than previous estimates of Cenozoic metamorphism in the slate belt (Ernst 1983; Ernst and Jahn 1987). The writer agrees with the assessment of Beyssac et al. (2007) that metamorphic T was not well established in the Taiwan slate belt but still regards 500°C as at least 100°C too high for biotite-chlorite-phengite slates. Reaction progress in the carbon compounds may have been accelerated by strong early deformation rather than by a thermal event. Alternatively the orientation of the carbonaceous material may not correspond to current foliation in these units (Wiltschko pers. comm. 2008), which could also produce anomalously high Raman T. The metastability of carbonaceous material relative to graphite requires that the transformation is irreversible. Reaction progress will depend strongly on transformation mechanisms and time/temperature relations in nature (Essene 1982, 1989). Powerful information is enclosed in such transformations, but unraveling the contributions from various parameters is a challenge that has not succeeded quantitatively.

## 6.3 Thermobarometers in the System CaO-$ZrO_2$-$TiO_2$-$SiO_2$ (CazrtiQ)

Several thermobarometers have been proposed in the system, CaO-$ZrO_2$-$TiO_2$-$SiO_2$, named CazrtiQ by analogy with TitaniQ (titanium in quartz). These include Zr in rutile (Zack et al. 2004a), Ti in zircon (Watson and Harrison 2005), Ti in quartz (Wark and Watson 2006) and Zr in sphene (Hayden et al. 2008). All of these would simultaneously apply in zircon-rutile-sphene-quartz assemblages. The first three systems were regarded as pure thermometers in the original works, although the substitution would suggest a DV and a P dependence of the buffering reaction, given the involvement of voluminous quartz vs dense rutile and zircon. The P dependence of Zr in rutile (Tomkins et al. 2007) and Ti in zircon (Ferry and Watson 2007) was subsequently evaluated. At lower T the amount of Ti or Zr is reduced so much (<100 ppm substitution) that these systems become trace-element thermobarometers. Precise analytical data of trace elements on a scale of ca. 10 mm require special analytical techniques such as an UV laser ICP-MS, synchrotron micro-XRF with WDS, SIMS or heroic measurements with an EMP in order to determine the amount of Zr or Ti. The diffusion of Ti was investigated in zircon (Cherniak and Watson 2007) and quartz (Cherniak et al. 2007b), as well as Zr in rutile (Cherniak et al. 2007a) and sphene (Cherniak 2006). These high-field strength elements diffuse slowly enough that moderate to high T information can be retrieved from natural assemblages depending on cooling rate. Core-rim zoning in Ti and/or Zr should be sought to establish the possibility of partial resetting in any slowly cooled high-grade rock when undertaking application of these systems as a thermobarometer. Despite the complexity (which is shared by most thermobarometers), these systems are appealing and are gaining considerable use in recent studies of thermometry of metamorphic and igneous rocks. However the lack of reversed experiments with initially high-Zr or high-Ti starting materials is disturbing. Although rutile, zircon and sphene may be judged as too refractory for reversals, Hayob et al. (1993) recrystallised rutile and ilmenite and reversed experiments with orthopyroxene and quartz at 12–26 kbar and 800–1100°C. This suggests that experiments on these thermobarometers could be reversed at 10–20 kbar and above 800°C.

### *6.3.1 Rutile Thermobarometer*

Zack et al. (2004a) evaluated an empirical geothermometer based on the Zr content of rutile; it is referred to below as the rutile thermometer. They posited the reaction:

$$\text{zircon} = \text{Zr-rutile} + \text{quartz} \tag{6.26}$$

$$ZrSiO_4 = ZrO_2 + SiO_2$$

Substitution of Zr in rutile is not as baddeleyite but involves a rutile structure. Zack et al. (2004a) correlated the reported P-T conditions of various rutile-bearing assemblages equilibrated at 10–30 kbar and 400–1100°C with the Zr levels in the rutile. Application of reaction (6.26) requires equilibration with zircon as well as quartz (Zack et al. 2004a). One would expect these reactions to have a significant DV given the involvement of voluminous quartz relative to the much denser zircon and rutile. Reaction (6.26) is likely to be thermobarometer with a P dependence rather than a pure geothermometer. Zack et al. (2004a) concluded from the empirical data that there was no measurable P dependence of reaction (6.26). Their data are so scattered, however that it is difficult to see much more than a trend from ca. 40 ppm at the lowest T to 4000–5000 ppm (0.4–0.5 wt% Zr) in rutile at the highest T. They emphasised the potential applicability of their system to UHT granulites and that is worthy of investigation, as well as the potential of both rutile and zircon to take up other significant substitutions at such high temperatures. The DV of the reaction should be evaluated to estimate its P dependence. Zack et al. (2004a) argued that rutile is not reset below 650°C from diffusion data (Cherniak et al. 2007a) and that it will preserve compositions from much higher T with rapid cooling. However if rutile is recrystallised during retrogression it would be reset and during replacement of peak metamorphic ilmenite (Ghent and Stout 1984; Baldwin et al. 2007).

Watson et al. (2006) recalibrated the rutile thermometer of Zack et al. (2004a) by combining unpublished experiments at 1000–1400°C and 0–20 kbar of Degeling (2003). Those data were combined with data on rutile from a Sifnos blueschist (Spear et al. 2006), a greenschist from Vermont (Spear et al. 2002), migmatites from the Adirondacks (Storm and Spear 2005) and from Santa Catalina Island, California (Sorensen and Grossman 1989), as well as an aluminous schist from Stillup Tal, Tauern Window, Switzerland (Selverstone et al. 1991), the same rocks used by Watson and Harrison (2005) in calibrating the zircon thermometer. No indication was given that zircon equilibrated with rutile in the greenschist and blueschist samples. Watson et al. (2006) noted that Zack et al. (2004a) used rutile inclusions in garnets for their empirical calibration and suggested that their rutile may not have equilibrated with zircon. They also attributed differences between their calibration and that of Zack et al. (2004a) to P differences in the calibrations. Tomkins et al. (2007) experimentally evaluated the P dependence of the rutile thermometer at 0–30 kbar and 1000–1400°C including data of Degeling (2003) with additional experiments. They stated in the abstract that "*the expected volume change as a result of substitution of the larger* $Zr^{4+}$ *cation for* $Ti^{4+}$ *suggests that the Zr content of rutile should decrease with increasing pressure*". The logic of statement is a commonly held view but is incorrect. The pressure change of the reaction is controlled by the volume change of the heterogeneous equilibrium, not by the volume change of one solid solution in the reaction. One could consider the effect of partial molar volume in zirconian rutile, but the driving force for pressure change is the overall volume change in the reaction, not that of a single solid solution. The experimental data were extrapolated to lower T modelling the W parameter for Zr in rutile. Tomkins et al. (2007) re-evaluated applications with an explicit P dependence (their isopleths are the solid lines in Figs. 6.9, 6.10) and their results are remarkably reasonable for a wide range of parageneses. This version of the rutile thermobarometer is the best one to employ at present.

Recent studies of rutile involve the provenance of detrital rutile as well as its use as a thermometer. Zack et al. (2004b) analysed clastic rutile found in glacial sands from New York that was likely sourced in Grenville granulites. Minor element analyses of rutile distinguish metamafic rutile (high Cr/Nb) from rutile in metapelites and metamafites (low Cr/Nb) and the Cr/Nb in the rutile grains suggests both mafic and metapelitic source rocks. The authors argued that most of the likely source rocks crystallised in the presence of zircon. Although found in some metapelitic gneisses, rutile is not abundant in the Highlands but is widespread in the Major Paragneiss of the Lowlands in the Adirondacks (Edwards and Essene 1988). It is also possible that the source of the glacial sands was in Ontario rather than New York. Treibold et al. (2007) examined detrital rutile from sands proximal to the Erzgebirge massif in east Germany. They compiled a very large amount of minor element analytical data for rutile and distinguished different sources from Cr/Nb in rutile. In addition they compared thermometry from Zack et al. (2004a) with Watson et al. (2006) and concluded that the latter provided low T. Meinhold et al. (2008) studied detrital rutile in Carboniferous to Permo-Triassic sandstones of Chios Island, Greece, identifying the source as mostly metamafic from Cr/Nb and obtaining scattered T from 500–900°C for Zr-in-rutile T. In a clastic system it is difficult to show equilibration of zircon and quartz and lacking both the T are unconstrained. Chronological study of clastic zircon grains from the same clastic units may provide further insights to the above studies. It may be too optimistic to hope for rutile inclusions in clastic zircon grains.

Applications of the rutile thermometer have focused on HP assemblages. Spear et al. (2006) examined rutile from Sifnos blueschists, all of which are stated to contain zircon and quartz. They also noted that rutile occurs mostly as inclusions in garnet whereas sphene is found in the matrix. Whether zircon also forms as inclusions in the garnet or just in the matrix is not clear. Applying the calibration of Watson et al. (2006) they reported T to ±2°C with SIMS and ±10°C with EMP, contouring slightly zoned retiles with an interval of 10°C. The implied precision seems unlikely given expected errors in the calibration as well as disagreements among different versions of the thermometer. Spear et al. (2006) stated that sample SPH-149d contains zircon and cited their Fig. 5 in support, but no zircon is evident in that figure. The authors attribute formation of rutile to progress of GRAIL or a related reaction and rather vaguely apply that barometer to obtain geothermal gradients, neglecting the lack of kyanite in the rocks. Zack and Luvizottow (2006) applied rutile thermometry to rutile in different eclogites that were estimated to have formed between 400–900°C and 18–35 kbar. Zircon is illustrated in only one sample from Lippersdorf, Erzegebirge and there is no mention of zircon in the other 7 samples, but rutile T using Zack et al. (2004a) give reasonable results. Bauer et al. (2007) applied rutile and zircon thermometry to HP eclogites and metapelites from the Rhodopes in Greece. They found rutile only in garnet cores but no zircon, so the somewhat low T may be expected.

Racek et al. (2008) applied rutile thermometry to granulites from the UHT Bohemian massif. They showed BSE images of rutile as inclusions in garnet and in matrix associations, No zircon was identified in the images, so the T must be regarded as minima in its absence. Their Zr thermometry (Tomkins et al. 2007) yields remarkably high values: 810–960°C with average T of 950°C for rutile grains in sieve garnet and matrix rutile and an average of 830°C from rutile inclusions in massive garnet. The high T is supported by the presence of exsolved ternary feldspar. It is unclear whether the rutile inclusions in the massive garnet equilibrated either with quartz or zircon, as none is illustrated in the garnet; the authors granted this as a problem. The rutile thermometer does not apply even as a lower limit in the absence of quartz. Their graph of the diffusion rate (Cherniak et al. 2007a) vs observed grain size and cooling rates show 10,000°C/Ma for Zr data in rutile, which the authors described as >1,000°C/Ma, such high rates that one wonders about the quality of the analytical data on which they are based. Racek et al. (2008) did not provide analytical techniques, tables of analytical data for rutile or precision of Zr analyses (reported to 4 significant digits, rutile thermometry to 0.1°C on the figures).

Carefully establishing the textural relations of zircon and quartz to rutile is imperative before using rutile thermobarometry. Quoting Tomkins et al. (2007), "*Petrographic interpretation of the evolution of the mineral assemblage may be more difficult for accessory minerals such as rutile and zircon. When did the minerals grow? Did the rutile grow in the presence of zircon and quartz, as required for use of the normal formulation of the Zr–in-rutile thermometer? Did the rutile reequilibrate on cooling?*" These cogent concerns deserve careful consideration rather than neglect in future studies.

## *6.3.2 Zircon Thermobarometer*

Watson and Harrison (2005) proposed the use of the Ti in zircon as a geothermometer using the reaction $TiO_2$(Ru) = $TiO_2$(Zc). The activity coefficient of $TiO_2$ in zircon was assumed to be constant in the Henry's Law region, although that may not be the case for variations between 50 and 1300 ppm Ti. The reaction is not clear because Ti will partition between the VI and IV sites in zircon. By empirical calibration of natural assemblages and experiments at 1025–1400°C and 10–20 kbar, the thermometer was related to the equation $\log_{10}(Ti) = 6.01 \pm 0.03 - (5080 \pm 30)/T$ (K), where Ti is in ppm. This was proposed as a pure thermometer without pressure dependence. The difficulty with this model is that Ti does not substitute into zircon as $TiO_2$ (or $Ti_2O_4$), which would imply equal substitution of Ti for Zr and Si. One must consider the site partitioning of Ti between the Zr and the Si site in zircon, which has implications for the univariant equilibria in the system $ZrO_2$-$TiO_2$-$SiO_2$ (Ferry and Watson 2006). Watson and Harrison (2005) corrected experimental natural data on ilmenite-bearing and silica-deficient assemblages with estimated activities of $TiO_2$ and $SiO_2$. The $a(TiO_2)$ was estimated at 0.6–1.0 with citation of Ghent and Stout (1984), a study based on garnet phase equilibria in midcrustal rocks.

### 6.3.2.1 $TiO_2$ activity in metamorphic rocks

Ghent and Stout (1984) calculated $a(TiO_2)$ from metamorphic assemblages by dilution of (a) ilmenite + kyanite/sillimanite + quartz = almandine + rutile (GRAIL: Bohlen et al. 1983a), (b) anorthite + sphene = grossular + rutile + quartz (thermodynamic data from Robie et al. 1978) and (c) anorthite + quartz + ilmenite = almandine + grossular + rutile (calculated by Ghent from GRAIL + GASP). They corrected for a/X relations in the natural plagioclase and garnet and obtained $a(TiO_2)$ close to unity with reaction (a) in metapelites at peak P-T of 3.7–8.0 kbar and 460–620°C. Reaction (c) was later called GRIPS and was experimentally determined for $Alm_{0.67}Grs_{0.33}$ (Bohlen and Liotta 1986). The locus of GRIPS for the unmixed garnet is ca. 0.35 kbar higher (Essene 1989, following Moecher et al. 1988) than in Ghent and Stout (1984), decreasing the calculated $a(TiO_2)$ in reaction (c) by ca. 0.06. Although four ilmenite analyses from metamafites have 5–18% $MgTiO_3$ and 5–8% $Fe_2O_3$, Ghent and Stout (1984) concluded that their ilmenite has $X(FeTiO_3)$ of > 0.95, although it is only 0.73–0.89. Correcting for the additional dilution in reaction (c) reduces $a(TiO_2)$ by another 0.06–0.16, for a total of 0.1–0.2, ranging in an adjusted $a(TiO_2)$ of 0.3–0.5. The ilmenite in the other metamafic samples of Ghent and Stout (1984) was not analysed, so they assumed $a(FeTiO_3) = 1$, but reduction in the $a(FeTiO_3)$ of ilmenite drops the calculated $a(TiO_2)$ correspondingly. The $a(TiO_2)$ from the other ten mafic samples in Ghent and Stout (1984) calculated from reaction (c) is only an upper limit. The Mg/Fe of ilmenite in high-grade metamorphic rocks is rapidly reset during retrogression by reactions with ferromagnesian silicates and only occasionally is preserved by ilmenite inclusions in plagioclase or quartz (Hayob et al. 1993). The $Fe_2O_3$ in ferrian ilmenite is easily exsolved and can migrate to grain boundaries and be lost during slow cooling in metamorphic (e.g. Bohlen and Essene 1977) and granitic rocks (Core 2004). The $a(TiO_2)$ was derived for bulk rock compositions, mineral assemblages and P-T conditions nowhere close to those likely for Archean zircon that likely originated in granitoid intrusions (Wilde et al. 2005). These $a(TiO_2)$ are not applicable to low P granitoids lacking garnet and containing sodic rather than plagioclase.

### 6.3.2.2 $TiO_2$ activity in volcanic rocks

The activity of $TiO_2$ [$a(TiO_2)$] was calculated from the reaction $2FeTiO_3 = Fe_2TiO_4 + TiO_2$ for pure ulvöspinel and ilmenite (Fig. 6.8). Wark et al. (2007) calculated an average $a(TiO_2)$ of 0.63 ± 0.03 from coexisting ilmenite and magnetite in the Bishop tuff (Hildreth and Wilson 2007). The activity product of the reaction is erroneous in the supplemental data, although calculations did not employ that formula (Wark and Spear, pers. comm. 2008). Spear (pers. comm. 2008) subsequently identified an error in his calculations, which means the $a(TiO_2)$ in Wark et al. (2007) should be reduced by 0.12–0.15. For pure ilmenite and ulvöspinel, the equilibrium constant $K = a(TiO_2)$ at 1 bar and is 0.12 at 600°C to 0.32 at 1000°C, reduced by about 20% at 10 kbar (Fig. 6.7). Calculation of $a(TiO_2)$ using natural magnetite-ilmenite pairs is $a(TiO_2) = a(TiO_2) \times [a(FeTiO_3)]^2/a(Fe_2TiO_4)$. Calculations from analyses of magnetite and ilmenite from the Bishop tuff were undertaken in this work at 1 atm and 2 kbar using thermodynamic data from Robie and Hemingway (1995). Correcting with a mixing model for the oxides (Anderson and Lindsley 1981, 1988; Ghiorso and Sack 1991) reduces the $a(TiO_2)$ by another 0.02 and by another 0.03 if the oxides equilibrated

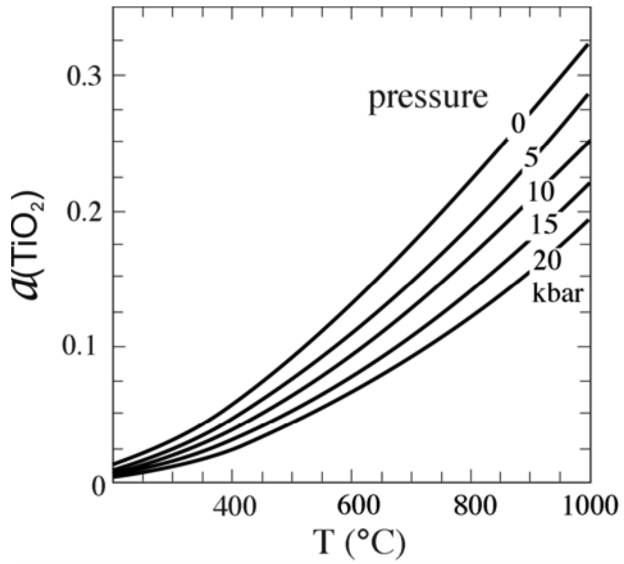

**Fig. 6.8** Calculated $a(\mathrm{TiO_2})$ vs T for pure ulvöspinel and ilmenite at 0–20 kbar. The $a(\mathrm{TiO_2})$ from coexisting oxides changes systematically with T and P. In volcanic rocks microphenocrysts of magnetite and ilmenite may have crystallised in the magma chamber at 1–2 kbar, shifting the $a(\mathrm{TiO_2})$ by -0.01 to 0.03. These calculations are combined with those for dilution of ilmenite and ulvöspinel, which double the $a(\mathrm{TiO_2})$ shown here for magnetite-ilmenite from the Bishop tuff at 750–800°C

in a magma chamber at 2 kbar instead of 1 atm. The estimate of this study from coexisting ilmenite and magnetite for the Hildreth and Wilson (2007) samples of the Bishop tuff indicate an $a(\mathrm{TiO_2})$ of 0.40 ± 0.02 rather than the 0.63 ± 0.03 in Wark and Watson (2006). The $a(\mathrm{TiO_2})$ varies over a wider range at least from 0.3–1.0, in crustal rocks than was previously considered (Watson and Harrison 2005; Ferry and Watson 2006; Watson et al. 2006; Wark and Watson 2006; Hayden et al. 2008).

### 6.3.2.3 Other calibrations of the zircon thermometer

Watson et al. (2006) recalibrated the zircon thermometer (referred to below as the zircon thermometer) with experiments at 10–14 kbar and 1000–1500°C, supplemented by additional data on natural assemblages at lower P-T. They retained the form of the approach used by Watson and Harrison (2005). They used SIMS data to obtain values of 1–10 ppm on zircon in igneous and metamorphic rocks in order to extrapolate their experiments from 1000°C down to 600°C. Zircon and rutile grains were analysed in two migmatites and an aluminous schist (cf. section above on the zircon thermobarometer). Although their calibrations are reasonable they neglected to evaluate its P dependence.

Ferry and Watson (2007) re-evaluated the zircon thermometer on a thermodynamic basis. They considered the substitution of Ti and concluded from several lines of evidence that Ti favours the Si over the Zr site. When Ti is substituted for Si in zircon it is buffered by the following equilibria:

ZrTi zircon + quartz = zircon + rutile (6.27)

$$\mathrm{ZrTiO_4(Zc) + SiO_2 = ZrSiO_4(Zc) + TiO_2}$$

Ferry and Watson (2007) applied zircon-rutile-quartz assemblages to calibrate this reaction. Although still referring to it as a thermometer they evaluated and corrected for the P dependence of the system (dashed lines in Fig. 6.9). They estimated the DV of reaction (6.27) using the oxide compound $\mathrm{ZrTiO_4}$ (Troitsch et al. 2005) and corrected all the T data to 10 kbar with a 5°C/kbar slope. Applications to low P assemblages in volcanic and many granitic rocks that equilibrated at low P thus require a further correction, -50°C at 1 atm, -40°C at 2 kbar. Ferry and Watson (2007) argued from reaction (6.27) that reduction in the $a(\mathrm{TiO_2})$ is largely offset by similar reduction in $a(\mathrm{SiO_2})$. This assumption needs further testing in rock systems to which the zircon thermometer is being applied.

Page et al. (2007b) used an ionic model for zircon solid solution to estimate the $V°_{298}$ of $\mathrm{ZrTiO_4}$(zircon) of 43.6 $\mathrm{cm^3}$/mol, considerably greater than the 39.6 $\mathrm{cm^3}$/mol of Ferry and Watson (2007). Ferriss et al. (2008) undertook quantum mechanical calculations of Ti partitioned into the Si and Zr sites of zircon. They obtained an average volume estimate at STP from density-functional theory of 44.2 ± 0.5 $\mathrm{cm^3}$/mol for $\mathrm{ZrTiO_4}$(zircon), similar to that of Page et al. (2007b). That modification in the $V°_{298}$ of $\mathrm{ZrTiO_4}$(zircon) leads a DV of 9.0 $\mathrm{cm^3}$/mol for reaction (6.27) and a pres-

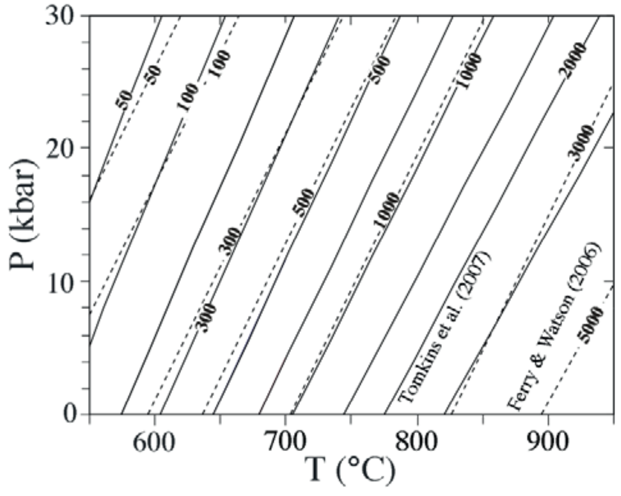

**Fig. 6.9** Isopleths in ppm Zr of rutile (Tomkins et al. 2007) and ppm Ti in zircon Ti in zircon, (Ferry and Watson 2006). Dashed lines represent the $K_D$ for the reaction of Ti/Zr between rutile and zircon. With permission from Blackwell Scientific

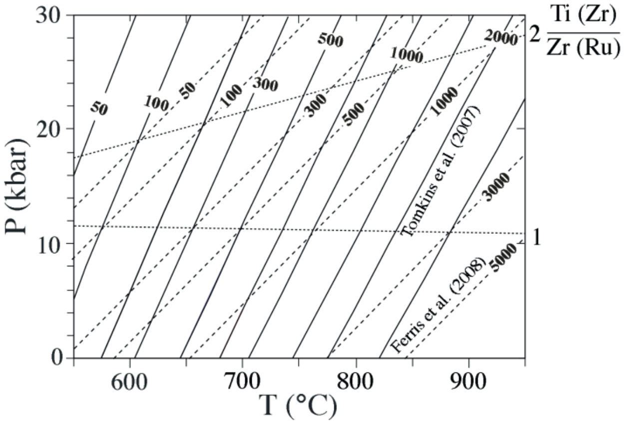

**Fig. 6.10** Isopleths in ppm Zr of rutile (Tomkins et al. 2007) and ppm Ti in zircon in zircon from Ferriss et al. (2008). Dashed lines represent the $K_D$ for the reaction of Ti/Zr between rutile and zircon. with permission from Blackwell Scientific

sure correction for reaction (6.28) that is twice as large as Ferry and Spear (2007). The latter isopleths are shown as the dashed lines in Fig. 6.10. Applications of the zircon barometer with the Ferriss et al. (2008) requires a substantial negative T correction, -100°C at 1 atm and -80°C at 2 kbar. Those corrections place many of the zircon T of Watson and Harrison (2005) below the solidus for $H_2O$ saturated granite. They need correction back to higher T by an $a(TiO_2)$ that is well reduced from unity, i.e. in the range of 0.3–0.5.

Ferriss et al. (2008) also showed that substitution of Ti for Zr is important in zircon above 40 kbar; it implies an alternative reaction of $TiSiO_4$ in zircon:

$$\text{TiSi zircon} = \text{rutile} + \text{quartz} \tag{6.28}$$

$$TiSiO_4(Zc) = TiO_2 + SiO_2$$

Consideration of that reaction is indicated for application of zircon thermobarometry in diamond zone metamorphic rocks and diamond-bearing xenoliths from the mantle.

### 6.3.2.4 Applications of the zircon thermometer

Watson and Harrison (2005) applied their calibration of the zircon thermometer to detrital zircons of Archean age in the Jack Hills, Australia. They obtained zircon T of 650–760°C and argued for their origin in wet, cold granitoids. They noted that the T would increase by ca. 50°C for a reduction of 0.5 in $a(TiO_2)$. Harrison et al. (2007) applied the zircon thermometer to the Dala granodiorite complex in the Himalayas. They did not consider the emplacement pressure of the Dala complex or apply a pressure correction to their zircon T. Bea et al. (2006) obtained 680–770 ± 40°C for the zircon thermometer applied to a migmatite/gabbro complex in central Spain that does not contain quartz or rutile. Baldwin et al. (2007) applied the zircon thermometer to UHT granulites from the Neoproterozoic Anápolis-Itauçu Complex in Brazil and deep crustal xenoliths from the Kaapvaal craton in South Africa. Both sets of rocks were estimated to have equilibrated at ca. 10 kbar and therefore no P correction is indicated. It is not clear why they did not employ the rutile thermobarometer of Tomkins et al. (2007) as well. They recovered T of 900 ± 50°C for the Brazil granulites and 880–1020°C and 840–940°C for two phases of zircon growth in the xenoliths. Although they emphasise the presence of rutile, only BSE image showing zircon with rutile is a zircon associated with Ilmenite being replaced with rutile.

Baldwin et al. (2007) described prograde Ti zoning in zircon and found no evidence of resetting, surprising results given the diffusion data on Ti in zircon. They applied the zircon thermometer to Miocene eclogites from the D'Entrecasteaux Islands east of New Guinea. They cited Ferry and Watson (2007) but applied no P correction in extending the zircon thermometer to 17–25 kbar. Applying a +80°C correction from Ferriss et al. (2008) would raise the zircon T from 670 to 750°C, in somewhat better agreement with results from the rutile thermobarometer (Tomkins et al. 2007).

Fu et al. (2008) did SIMS analyses of Zr in zircon and applied the zircon thermometer of Watson et al. (2006) to a wide range of samples mainly plutonic rocks. They obtained mostly <25 ppm Ti, corresponding to T of 500–850°C, often low compared to other thermometers. The T variation was also large to very large, typically ±30–80°C and sometimes 150–200°C. A P correction will further reduce the zircon T and increase discrepancies with other thermometers. Hofmann et al. (2008) undertook nanoSIMS measurements of trace elements in zircon and found submicron domains of high Ti, as well as enrichment in P, Y and Ce in zircon from several granitoid and granulite localities. They concluded that the zircon thermometer may be perturbed along cracks, local recrystallisation, local epitaxial growth and/or by nanoscale inclusions. To date the applications of the zircon thermometer are unexpected, with intermediate T rocks often recording low to somewhat low values and UHT rocks preserving near-peak T without evidence of resetting. Additional experiments involving compositional reversals on Ti in zircon are indicated at 20–30 kbar and 1000–1200°C.

## *6.3.3 Quartz Ti Thermometer (TitaniQ)*

Wark and Watson (2006) investigated the Ti in quartz thermometer (naming it TitaniQ) and calibrated it at 10 kbar and 700–1100°C in a piston-cylinder (Fig. 6.11a). The

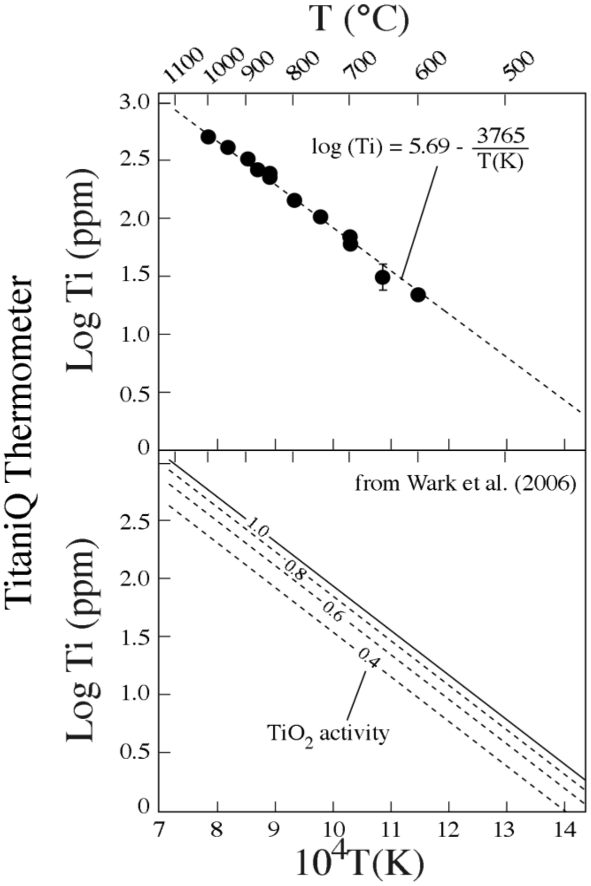

**Fig. 6.11** TitaniQ thermometer. (a) $\mathrm{Log}_{10}$Ti in ppm for quartz vs T (b) reducing $a(\mathrm{TiO_2})$ to 0.4 raises the T by ca. 180°C at 1000°C and by 80°C at 600°C (Wark and Watson 2006, with permission from Springer-Verlag)

reaction may be considered as $TiO_2$(rutile) = $TiO_2$(quartz). The Ti in quartz is saturated when found in natural assemblages with rutile. Rutile in most metamorphic rocks is 98–99.5% pure, so the system quartz-rutile is nearly a binary in crustal metamorphic rocks. They were interested particularly in applications to quartz phenocrysts in volcanic rocks where rutile is not present and therefore corrected the thermometer for reduced $a(\mathrm{TiO_2})$ (Fig. 6.11b).

### 6.3.3.1 Pressure dependence of TitaniQ

Wark and Watson (2006) concluded from indirect lines of evidence that TitaniQ is a pure thermometer, independent of P. However the TitaniQ reaction is $TiO_2$(rutile) = $TiO_2$(quartz) and one would expect a significant positive DV and DS of reaction and therefore a P dependence with a positive slope of the isopleths. The DV may be estimated from the change in volume from stishovite (which is isostructural to rutile) to quartz, which is 8.7 $cm^3$/mol (Robie and Hemingway 1995). This is equivalent to setting the volume change of the reaction V[$TiO_2$(rutile)] + V[$SiO_2$(quartz)] - V[$SiO_2$(stishovite)] - V[$TiO_2$(quartz)] = 0, so DV = V[$TiO_2$(rutile)] + V[$SiO_2$(quartz)] = V[$SiO_2$(stishovite)] - V[$TiO_2$(quartz)]. The volume change of isostructural materials vary systematically with composition whereas different polymorphs do not (Hazen and Finger 1982). The $TiO_2$ polymorph with a quartz structure must be more voluminous and less stable than rutile, which explains the limited amounts of Ti in quartz. A similar isostructural approximation (Helgeson et al. 1978) for the DS of the reaction assuming S[$TiO_2$(rutile)] + S[$SiO_2$(quartz)] - S[$SiO_2$(stishovite)] - S[$TiO_2$(quartz)] = 0, leads to DS of the TitaniQ reaction equal to that for stishovite = quartz, 13.7 J/mol K. A zeroth-order estimate of the slope of the end-member TitaniQ reaction hence is dP/dT = DS/DV = 13.7/0.87 = 15.7 bar/°C = 1.57 kbar/100°C, equivalent to 635°C per 10 kbar, i.e. a flat slope in P-T space, i.e. a barometer. Isopleths can rotate and may steepen with great dilution but they should not approach vertical starting from a nearly flat slope for the end-member reaction.

### 6.3.3.2 Applications of TitaniQ

Wark and Watson (2006) and Wark et al. (2007) applied the TitaniQ thermometer to quartz phenocrysts from the Bishop tuff, which have spectacular zoning and bright CL rims related to an abrupt increase in Ti content. They inferred a rapid T increase of 100°C and dissolution of older zoned quartz (ca. 50 ppm Ti) followed by rapid growth of more titanian and brightly cathodoluminescent quartz rims (ca. 100 ppm) modeled the $TiO_2$ of the glass to correct for reduced $a(\mathrm{TiO_2})$ in applications of the thermometer to volcanic rocks lacking rutile. However the experiments were undertaken only at 10 kbar, requiring extrapolation down to the 1–2 kbar expected for volcanic quartz phenocrysts. If the isopleths are as flat as suggested by the above calculations, extrapolation down to low P would suggest very low T for Ti of 50–100 ppm in the quartz phenocrysts. The approximate thermodynamic slope calculations are inconsistent with the experimental locus of TitaniQ. One could point to the absence of experimental reversals as the cause, but that may be too glib a defense of only what is only a “back-of-the-envelope” calculation.

Wark and Watson (2006) also observed small dark haloes of non-CL quartz around rutile needles in UHT granulites, strongly suggesting derivation of the needles from loss of Ti from quartz in the immediate haloes. They obtained 516 ppm of Ti in quartz from the UHT granulites with broad beam analysis for TitaniQ T > 990°C. Left unaddressed was scatter in the data, reproducibility from grain to grain and fluorescence of Ti from visible subjacent rutile needles producing a systematic error in the Ti analyses.

Sato and Santosh (2007) showed two boules of quartz from veins in UHT rocks, one with large hematite blades and one with rutile needles. They reintegrated BSE images of heterogeneous quartz-rutile domains (their Fig. 3a) to obtain 4 wt% $TiO_2$ in the quartz. However in Table 1 they report a mean of 0.4 wt% $TiO_2$, equivalent to T > 1190°C, seemingly confirming the UHT status of the host country rocks. The T estimates in their Fig. 7 range to over 1400°C, impossibly high for quartz-bearing granulites. Even 1190°C would require bone-dry conditions, surely incompatible with the mixed $H_2O$-$CO_2$ fluid inclusions interpreted as primary by Sato and Santosh (2007). A BSE image shows rutile is heterogeneously distributed in host quartz, not the homogeneous distribution expected from cooling and internal reaction of an original UHT $(Si,Ti)O_2$ phase. The erratic presence of rutile suggests that reintegration has no value because shifting the image by 100 mm would change the Ti content by a large amount. The erratic distribution of the rutile needles in quartz strongly suggest mobilisation of Ti and precipitation elsewhere in the quartz, which is not well modeled as a solid state diffusive process or in terms of reintegration of a few cross-sections. It remains unclear whether the samples are synmetamorphic or whether they may late veins of hydrothermal quartz with topotactical rutile or hematite. The latter origin is surely suggested for the quartz with large plates of hematite (why was hematite not reintegrated as well?). The relation of the quartz veins to the deformation of the country rocks was not documented. The pressure correction (if any) of the TitaniQ thermometer may not have an effect on these rocks, which equilibrated at P similar to that of the experimental calibration. The presumption that the transparent quartz crystals underwent slow cooling from UHT conditions can be tested by studies of Dauphiné twinning. The a–b transition in quartz should have produced Dauphiné twins that could be identified by TEM or by production and examination of etch pits on an SEM. The author remains unconvinced of validity of TitaniQ thermometry in this study.

#### 6.3.3.3 Future research on quartz thermometry

Additional experiments are needed to evaluate the P dependence if any for TitaniQ at 5 and 15 kbar. In addition experiments involving compositional reversals on Ti in quartz coexisting with rutile are indicated to be certain that the original T dependence of TitaniQ obtained by Wark and Watson (2006) at 10 kbar is correct. Additional study is indicated to evaluate the striking disagreement in the slope of the isopleths assumed to be a pure thermometer vs the flat slope estimate made in this paper.

The observation of Ti-depleted haloes around a quartz host is important. It needs further study with a nanoSIMS to evaluate the scale of diffusion more accurately and whether the Ti lost from the quartz halo provides sufficient Ti to produce the rutile needle. NanoSIMS measurements may provide data on diffusive transfer and the cooling rate. That technique would provide a better analytical resolution and avoid the Bremsstrallung fluorescence inferred by Wark and Watson (2006). Ultra-high pressure (UHP) rutile-coesite assemblages, especially those in the diamond stability field, should also be evaluated for minor stishovite solid solution in the rutile.

### 6.3.4 Sphene Thermobarometer

Substitution of Zr in sphene in the presence of zircon + quartz is controlled by the reaction:

sphene + zircon = Zr-sphene + rutile + quartz (6.29)

$$CaTiSiO_5 + ZrSiO_4 = CaZrSiO_5 + TiO_2 + SiO_2$$

Hayden et al. (2008) investigated this reaction experimentally at 800–1000°C and 10–12 kbar, using sphene, rutile and quartz as starting materials and analysing run products with an EMP. One could argue that the best approximation of the locus of reaction (6.29) is the experimental sphene with the highest Zr since that represents the most reaction progress in the experiment. However Hayden et al. (2008) described the development of sector zoning in coarsely recrystallised sphene, attributing high Zr in sphene to that process. They constructed a P-T diagram for Zr in rutile and Zr in sphene, having strong P dependence and providing a nice petrogenetic grid for sphene-zircon-rutile-quartz assemblages (Fig. 6.12, steep solid lines from Tom-

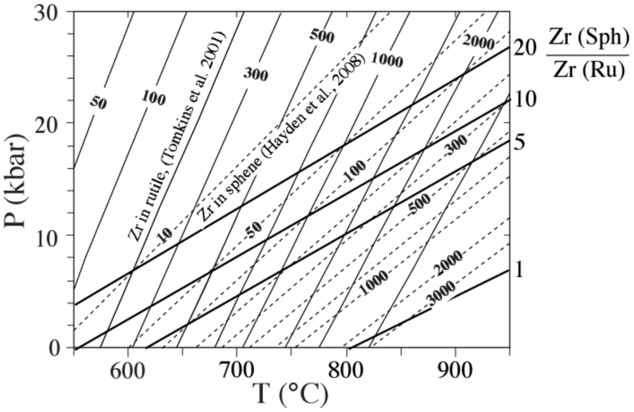

**Fig. 6.12** Isopleths in ppm Zr for rutile (Tomkins et al. 2007) and in ppm Zr for the sphene thermobarometer (Hayden et al. 2008). Lines representing the $K_D$ for the exchange of Ti/Zr between sphene and rutile are added as black lines (reaction 6.30). The flat $K_D$ lines indicate a significant DV of the reaction or error in one of the isopleth sets upon which it is based. The $K_D$ lines compare the locus of reaction (6.30) with the other two thermobarometers (modified from Hayden et al. 2008). with permission from Blackwell Scientific

kins et al. 2007, dashed lines from Hayden et al. 2008). Differential effects of diffusional resetting of Zr in rutile vs zircon must be considered in natural assemblages (Cherniak 2006; Cherniak and Watson 2007). The sphene thermobarometer may also be perturbed by significant solid solution of $CaAlSiO_4F$, $CaAlSiO_4OH$ and $CaFeSiO_4OH$ as has been reported in eclogitic and diagenetic parageneses (e.g. Tropper et al. 2002). In the absence of quartz and rutile, sphene may take up more Zr. Chakhmouradian (2004) found sphene with 26 mol% $CaZrSiO_5$ in a carbonatite from the Kola Peninsula, indicating great reduction in the $a(TiO_2)$ and $a(SiO_2)$ in that assemblage. That example also illustrates that reaction (6.29) is a buffer system not saturating the Zr in sphene.

## 6.3.5 Partition of Ti and Zr Between Sphene and Rutile

Combination of reaction (6.26) with (6.29) yields an exchange reaction for Zr/Ti in sphene/rutile:

sphene + $ZrO_2$(rutile) = Zr sphene + rutile (6.30)

$CaTiSiO_5 + ZiO_2(Ru) = CaZrSiO_5(Sph) + TiO_2$

For nearly pure sphene and rutile the $K_D = X_{Zr}(Sph)/X_{Zr}(Ru)$. Flatter lines of constant $K_D$ are easily calculated from intersections of the isopleths for reactions (6.26) and (6.29); the $K_D$ lines are flatter (thickest lines in Fig. 6.12). The $K_D$ is for X, not activity: the other two lines are in Zr (ppm) and there is no change in converting $K_D$ computed on a weight basis to a mole fraction product. The equation for reaction (6.30) also can be computed from the equations for the two thermobarometers. The flatness of the $K_D$ lines is surprising and indicates a large DV for reaction (6.30) or an error in one of the calibrated curves. Careful textural study is required before proceeding with applications because sphene often overgrows rutile at a different stage of metamorphism. Careful characterisation of rutile and sphene inclusions in garnet porphyroblasts would help judge whether they formed coevally in garnet-bearing rocks (Page et al. 2003, 2007a). Measurements of Zr in rocks with large crystals of rutile and sphene may expand the T range over which the Zr may preserve high-T information with minimal diffusive loss (Hayden et al. 2008).

## 6.3.6 Partition of Si and Ti Between Quartz and Zircon

Partition of Ti vs Si in zircon and quartz is represented by the exchange equilibrium $TiO_2(Qz) + ZrSiO_4(Zc) = SiO_2(Qz) + ZrTiO_4(Zc)$. Its $K_D$ is $X_{Ti}(Qz)(X_{Si}(Zc)/X_{Ti}(Qz)X_{Ti}(Zc)$, assuming Ti substitutes for Si in zircon (Fig. 6.11). If both quartz and zircon are close to end-member, $X_{Si}(Qz) = 1$ and $X_{Si}(Zc) = 1$, reducing the $K_D$ to $X_{Ti}(Qz)X_{Ti}(Zc)$. The $K_D$ may be computed from the intersections of the two sets of isopleths in the diagram as a function of P-T. The result is strongly dependent on the slope of TitaniQ isopleths and it is not considered further here in light of the concerns raised here about that assumption. The reaction would be directly applicable to zircon-quartz assemblages in the absence of quartz, useful for igneous rocks, which usually lack rutile. This reaction could be undertaken experimentally running titanian zircon and titanian quartz in the absence of rutile to test the isopleths of Ti in zircon.

## 6.3.7 Partition of Zr and Ti Between Zircon and Rutile

Although the exchange of Zr and Ti between zircon and rutile seems reasonable, Ti substitutes mainly for Si not Zr in zircon (Ferry and Watson 2006). The exchange of Ti for Zr in zircon may occur HP conditions, where it exchanges with Zr in zircon as $ZrO_2(Ru) + TiSiO_4(Zc) = TiO_2(Ru) + ZrSiO_4(Zc)$, but only computational estimates are available for $TiSiO_4$ in zircon at UHP (Ferriss et al. 2008). Combination of reactions (6.26) and (6.27) yields a heterogeneous equilibrium for $TiZrO_4$ in zircon in the absence of quartz:

ZrTi zircon = rutile + Zr rutile (6.31)

$ZrTiO_4 = TiO_2 + ZrO_2$(rutile)

The mole fraction product, $K_D = X_{Zr}(Ru)X_{Ti}(Ru)/X_{Ti}(Zc)$, reduces to $X_{Zr}(Ru)/X_{Ti}(Zc)$ when $X_{Ti}(Ru) = 1$. The $K_D$ is obtained by intersection of the Zr isopleths in rutile (Tomkins et al. 2007) with those in zircon (Fig. 9, Ferry and Watson 2006; Fig. 10, Ferriss et al. 2008). The two sets of isopleths are nearly parallel with Ferry and Watson (2006) and their intersections are nearly the same curve as the two others. Using Ferry and Watson (2006), reaction (6.26) is nearly parallel to the other curves and offers no additional insights as to P-T conditions. However the isopleths (Fig. 6.10) for ppm Ti in zircon from Ferriss et al. (2008) intersect with ppm Zr in rutile from Tomkins et al. (2007) and the isopleths of reaction (6.31) are flatter than (6.26) or (6.27). Reaction (6.31) could also be explored experimentally for rutile-zircon assemblages in the absence of quartz and would provide a direct test of the Ferry and Watson (2006) vs the Ferriss et al. (2008) P dependence of Ti in zircon compared with Zr in rutile (Tomkins et al. 2007). It could be useful in amphibolites and eclogites where quartz is not texturally part of the assemblage.

## 6.4 Other Empirical Thermometers for Trace Elements

Trace element thermobarometers have focused on mantle assemblages with olivine and garnet, using the minor to trace elements Cr and Ni. One crustal thermometer was proposed by Pyle and Spear (2000), who empirically calibrated a Y in garnet thermometer using the yttrium concentration of natural garnet in equilibrium with xenotime from New England metapelites where P-T conditions are well established. Their results indicate a strong negative dependence of Y content in garnet with T and a P effect was also inferred. However an understanding of this system is hampered in the absence of a buffering reaction. Pyle and Spear (2000) balanced complex heterogeneous reactions for both Y and P using apatite, plagioclase, the grossular component of garnet or a hypothetical phosphorian garnet and a fluid phase, but none of them is very satisfactory. The partitioning of Y in garnet vs xenotime is explained much more easily in terms of a simple $K_D$ exchange of Y for a MREE to HREE, e.g. Er:

$$\text{Er(xenotime)} + \text{Y(garnet)} = \text{Y(xenotime)} + \text{Er(garnet)} \quad (6.32)$$

$$3\text{ErPO}_4 + \text{Y}_3\text{Al}_5\text{O}_{12} = 3\text{YPO}_4 + \text{Er}_3\text{Al}_5\text{O}_{12}$$

One must consider the amount of Er and Y in both xenotime and garnet and not rely on the Y garnet alone as a single mineral thermometer. Such $K_D$ reactions are expected to have small volume changes and therefore often act as thermometers with only a small P dependence. Reaction (6.32) suggests that xenotime in Pyle and Spear (2000) is depleted in Er (and other HREE) and enriched in Y with increasing T relative to garnet. Direct measurement of Y and REE should be undertaken in the coexisting xenotime and garnet, which should be evaluated for zoning and xenotime inclusions. The partition coefficients ($K_D$s) then may be calculated for the HREE vs Y in garnet vs xenotime. Variation of such data as a function of grade may constrain a/X relations for HREE and Y in garnet and xenotime. Partitioning of HREE and Y between garnet and xenotime is accessible to direct experimental calibration at high P-T. Another concern is the effect of Ca in garnet on the Y/HREE partitioning. Changing Ca in garnet systematically shifts the M-O bond length of the VIII site, which affects the partitioning of REE and Y in garnet due to change in the ionic radius (Blundy and Wood 1994; Green et al. 2000). Fortunately, ordinary metapelitic garnets are not rich in Ca and in that case the effect should be minor. It may be important in metagranitoids where garnet has higher and more variable Ca that may also be zoned.

## 6.5 Discussion

The construction and application of many empirically based thermobarometers was evaluated and most of them have significant problems. Many of the empirical thermobarometers are effectively single mineral thermobarometers, with the buffering assemblage left unidentified. At best most of these systems are buffered but not maximised by the postulated assemblages for a given P-T. Ignoring the requirement of a buffering phase such as rutile for Ti in zircon thermometry or Ti in biotite thermometry is a dangerous oversight. The Zr content of rutile is not saturated but only buffered in the presence of zircon-quartz. Similarly, application of Ti in zircon or Ti in biotite thermometry, while ignoring the pressure effect, the mechanism of Ti substitution and the nature of buffering as opposed to a saturated assemblage is flawed. Nearly all single mineral thermobarometers cannot work as proposed because the effect of solid solution of the coexisting mineral was not considered, the nature of the buffering assemblage not evaluated and even their presence not required, e.g. in many applications of zircon and rutile thermometry. The situation is rather like trying to apply garnet-biotite Mg/Fe $K_D$ thermometry by analysing only the garnet or only the biotite. A single mineral thermobarometer may work for a strictly fixed bulk composition and in the few cases where only one phase in a buffered assemblage has significant solid solution. The approach of a fixed composition is indeed applied in pseudosection analysis, in which the bulk composition is considered along with the equilibrium compositions of the required associated assemblage. However even small variations in bulk chemistry may affect substitution in single mineral, especially if the element is a minor species in the rock, e.g. Ti. Doubling or halving (or even greater change) in the level of a minor to trace element is to be expected in metasediments, which may alter the Ti-buffering assemblage (rutile, ilmenite and/or sphene) and substitution of Ti in minerals like biotite, garnet, zircon and quartz. Exploration of different bulk compositions for the blueschist facies or low-grade diagenetic systems may provide additional insights to phengite barometry or chlorite thermometry. However such applications are pushing the capabilities of the extant mixing models for complex rock-forming minerals with solid solutions at low T where few hard data are available.

Ultimately, application of a bootstrapping process, in which well-calibrated phase equilibria are combined with solution of additional a/X data on more complex and less well known minerals, will advance the knowledge of solid solutions in rock-forming minerals from metamorphic rocks. Holland and Powell (1998) employed this procedure in cleverly elucidating metamorphic assemblages and thermodynamic properties of rock-forming minerals. However continued reliance on unreversed experiments, such as those for phengite, carpholite and glaucophane, may lead to significant systematic errors and perturb other thermodynamic data derived from those data. Extrapolation of the mixing properties for plagioclase and garnet below ca. 500–600°C may erroneous in the absence of experimental data at this range and low T miscibility gaps for plagioclase (Essene et al. 2005) and garnet (Wang et al. 2000). Rather than accepting old derivations of mixing properties, heat capacity and phase equilibria for these minerals, the wise worker will update such data with new measurements in field and laboratory.

**Acknowledgments:** The author is grateful for continuing insights provided by his former and present graduate students. Ongoing discussions with O Breyssac, M Cathelineau, LA Hayden, DJ Henry, MR Manon, DR Peacor, M Santosh, FS Spear, O Vidal, DA Wark and Wenjun Yong were helpful in preparation of this paper. The figures were prepared with the generous help of Dale Austin and the writer also benefited from computing skills of JL Magiera. This work was supported by a grant from NSF (EAR 05-37068) and the W.C. Kelly Professorship at the University of Michigan to EJE.

## 6.6 References

Afifi AM, Essene EJ (1988) Minfile: a microcomputer programme for storage and manipulation of chemical data on minerals. Am Mineral 73: 446–448

Agard P, Vidal O, Goffé B (2001) Interlayer and Si content of phengite in HP-LT carpholite-bearing metapelites. J Metam Geol 19: 477–493

Ague JJ (1997) Thermodynamic calculation of emplacement pressures for batholithic rocks, California: implications for the aluminum-in-hornblende barometer. Geology 25: 563–566

Ahn JH, Peacor DR (1985) Transmission electron microscope study of diagenetic chlorite in Gulf Coast argillaceous sediments. Clays Clay Minerals 33: 228–236

Ahn JH, Peacor DR (1986) Transmission electron microscope data for rectorite: implications for the origin and structure of "fundamental particles". Clays Clay Minerals 34: 180–186

Ahn JH, Peacor DR, Essene EJ (1985) Coexisting paragonite-phengite in blueschist eclogite: a TEM study. Am Mineral 70: 1193–1204

Andersen DJ, Lindsley DH (1981) A valid Margules formulation for an asymmetric ternary solution: revision of the olivine-ilmenite thermometer, with applications. Gcochim Cosmochim Acta 45: 847–853

Andersen DJ, Lindsley DH (1988) Internally consistent solution models for Fe-Mg-Mn-Ti oxides: Fe-Ti oxides. Am Mineral 73: 714–726

Anderson JL, Smith DR (1995) The effects of temperature and $fO_2$ on the Al-in-hornblende barometer. Am Mineral 80: 549–559

Anovitz LM, Essene EJ (1990) Thermobarometry and pressure-temperature paths in the Grenville Province of Ontario. J Petrol 31: 197–241

Anovitz LM, Essene EJ, Perkins, D (1991) On the metastability in near-surface rocks of minerals in the system $Al_2O_3$–$SiO_2$–$H_2O$. Clays Clay Minerals 39: 225–233

Apted MJ, Liou JG (1983) Phase relations among greenschist, epidote amphibolite and amphibolite in a basaltic system. Am J Sci 283A: 328–354

Augier R, Agard P, Monie P, Jolivet L, Robin C, Booth-Rea G (2005a) Exhumation, doming and slab retreat in the Betic Cordillera, SE Spain: in situ $^{40}Ar/^{39}Ar$ ages and P-T-d-t paths for the Nevado-Filabride Complex. J Metam Geol 23: 357–381

Augier R, Booth-Rea G, Agard P, Martinez-Martinez JM, Jolivet L, Azanon JM (2005b) Exhumation constraints for the lower Nevado-Filabride Complex (Betic Cordillera, SE Spain): a Raman thermometry and Tweequ multiequilibrium thermobarometry approach. Bull Soc Geol France 176: 403–416

Baldwin JA, Brown M, Schmitz MD (2007) First application of titanium-in-zircon thermometry to ultrahigh-temperature metamorphism. Geology 35: 295–298

Baldwin SL, Webb LE, Monteleone BD (2008) Late Miocene coesite-eclogite exhumed in the Woodlark Rift. Geology 36: 735–738

Bauer C, Rubatto D, Krenn K, Proyer A, Hoinkes G (2007) A zircon study from the Rhodope metamorphic complex, N Greece: time record of a multistage evolution. Lithos 99: 207–228

Bea F, Montero P, Gonzalez-Lodeiro F, Talavera C, Molina JF, Scarrow JH, Whitehouse MJ, Zinger T (2006) Zircon thermometry and U-Pb ion-microprobe dating of the gabbros and associated migmatites of the Variscan Toledo anatectic complex, central Iberia. J Geol Soc 163: 847–855

Berman RG (1988) Internally consistent thermodynamic data set for minerals in the system $Na_2O$-$K_2O$-$CaO$-$MgO$-$FeO$-$Fe_2O_3$–$Al_2O_3$–$SiO_2$–$TiO_2$–$H_2O$-$CO_2$. J Petrol 29: 445–522

Berman RG (1991) Thermobarometry using multi-equilibrium calculations: a new technique with petrological applications. Can Mineral 29: 833–855

Bevins RE, Robinson D, Ropwbotham G (1991) Compositional variations in mafic phyllosilicates from regional low-grade metabasites and application of the chlorite thermometer. J Metam Geol 9: 711–721

Beyssac O, Bollinger L, Avouac J-P, Goffé B (2004) Thermal metamorphism in the Lesser Himalaya of Nepal determined from Raman spectroscopy of carbonaceous material. Earth Planet Sci Lett 225: 233–241

Beyssac O, Brunet F, Petitet J-P, Goffé B, Rouzad J-N (2003) Experimental study of the microtextural and structural transformations of carbonaceous materials under pressure and temperature. Eur J Mineral 15: 937–951

Beyssac O, Goffé B, Chopin C, Rouzaud J-N (2002a) Raman spectra of carbonaceous material in metasediments: a new geothermometer. J Metam Geol 20: 858–871

Beyssac O, Rouzaud J-N, Goffé B, Brunet F, Chopin C (2002b) Graphitisation in a high-pressure, low-temperature metamorphic gradient: a Raman microspectroscopy and HRTEM study. Contr Mineral Petrol 143: 19–31

Beyssac O, Simoes M, Avouac JP, Farley KA, Chen Y-G, Chan Y-C, Goffé B (2007) Late Cenozoic metamorphic evolution and exhumation of Taiwan. Tectonics 26

Bhadra S, Bhattacharya A (2007) The barometer tremolite + tschermakite + 2albite = 2pargasite + 8quartz: constraints from experimental data at unit silica activity, with application to garnet-free natural assemblages. Am Mineral 92: 491–502

Blundy JD, Holland TJB (1990) Calcic amphibole equilibria and a new amphibole-plagioclase geothermometer. Contr Mineral Petrol 104: 208–224

Blundy JD, Wood BJ (1994) Prediction of crystal-melt partition coefficients from elastic moduli. Nature 372: 452–454

Bohlen SR, Essene EJ (1977) Feldspar and oxide thermometry of granulites in the Adirondack Highlands. Contr Mineral Petrol 62: 153–169

Bohlen SR, Liotta JJ (1986) A barometer for garnet amphibolites and garnet granulites. J Petrol 27: 1025–1056

Bohlen SR, Peacor DR, Essene EJ (1980) Crystal chemistry of a metamorphic biotite and its significance in water barometry. Am Mineral 65: 55–62

Bohlen SR, Wall VJ, Boettcher AL (1983a) Experimental investigations and geologic applications of equilibria in the system FeO-$TiO_2$–$Al_2O_3$–$SiO_2$–$H_2O$. Am Mineral 68: 1049–1058

Bohlen SR, Wall VJ, Boettcher AL (1983b) Experimental investigation and application of garnet granulite equilibria. Contr Mineral Petrol 8: 52–61

Bohlen SR, Wall VJ, Boettcher AL (1983c) Geobarometry in granulites. In: Saxena SK (ed) Kinetics and Equilibrium in Mineral Reactions, Adv Phys Geochem 3: 141–172. Springer-Verlag, NY

Booth-Rea G, Azanón JM, Goffé B, Vidal O, Martinez-Martinez JM (2002) High-pressure, low-temperature metamorphism in Alpujarride units of southeastern Betics (Spain). Comptes Rendus Acad Sci Geosci 334: 857–865

Booth-Rea G, Azanon JM, Martinez-Martinez JM, Vidal O, Garcia-Duenas V (2005) Contrasting structural and P-T evolution of tectonic units in the SE Betics: key for understanding the exhumation of the Alboran Domain HP/LT crustal rocks (W Mediterranean). Tectonics 24

Booth-Rea G, Simancas JF, Azor A, Azanón JM, González-Lodeiro F, Fonseca P (2006) HP–LT Variscan metamorphism in the Cubito-Moura schists (Ossa-Morena Zone, southern Iberia). Comptes Rendus Geosci 338: 1260–1267

Bousquet R, Goffé B, Vidal O, Oberhänsli R, Patriat M (2002) The tectono-metamorphic history of the Valaisan Domain from the Western to the Central Alps: new constraints on the evolution of the Alps. Geol Soc Am Bull 114: 207–225

Brigatti MF, Frigieri P, Ghezzo C, Poppi l (2000) Crystal chemistry of Al-rich biotites coexisting with muscovites in peraluminous granites. Am Mineral 85: 436–448

Brigatti MF, Guidotti CV, Malferrari A (2008) Single-crystal X-ray studies of trioctahedral micas coexisting with dioctahedral micas in metamorphic sequences from western Maine. Am Mineral 93: 396–408

Bucher S, Bousquet R (2007) Metamorphic evolution of the Brianconnais units along the ECORSCROP profile (Western Alps): new data on metasedimentary rocks. Swiss J Geosci 100: 227–242

Cathelineau M (1988) Cation site occupancy in chlorites and illites as a function of temperature. Clay Minerals 23: 471–485

Cathelineau M, Nieva D (1985) A chlorite solid solution geothermometer. The Los Azufres (Mexico) geothermal system. Contr Mineral Petrol 91: 235–244

Cesare B, Satish-Kumar M, Cruciani G, Pocker S, Nodari L (2008) Mineral chemistry of Ti-rich biotite from pegmatite and metapelitic granulites of the Kerala khondalite belt (southeast India): petrology and further insight into titanium substitutions. Am Mineral 93: 327–338

Chakhmouradian AR (2004) Crystal chemistry and paragenesis of compositionally unique (Al-, Fe-, Nb- and Zr-rich) titanite from Afrikanda, Russia. Am Mineral 89: 1752–1762

Chatterjee ND, Johannes W, Leistner H (1984) The system CaO-$Al_2O_3$–$SiO_2$–$H_2O$: new phase equilibrium data, calculated phase relations and petrological applications. Contr Mineral Petrol 88: 1–13

Cherniak DJ (2006) Zr diffusion in titanite. Contr Mineral Petrol 152: 639–647

Cherniak DJ, Manchester J, Watson EB (2007a) Zr and Hf diffusion in rutile. Earth Planet Sci Lett 261: 267–279

Cherniak DJ, Watson EB (2007) Ti diffusion in zircon. Chem Geol 242: 473–483

Cherniak DJ, Watson EB, Wark DA (2007b) Ti diffusion in quartz. Chem Geol 236: 65–74

Chernosky JV, Berman RG (1988) The stability of Mg-chlorite in supercritical $H_2O$-$CO_2$ fluids. Am J Sci 288A: 393–420

Cho M, Liou JG, Bird DK (1988) Prograde phase relations in the State 2–14 Well metasandstones, Salton sea geothermal field, California. J Geophys Res 93: 13,081–13,103

Compagnini G, Puglisi O, Foti G (1997) Raman spectra of virgin and damaged graphite edge planes. Carbon 35: 1793–1797

Core DP (2004) Oxygen and sulfur fugacities of granitoids: implications for ore-forming processes. PhD thesis, Univ. Michigan, Ann Arbor MI

Cosca MA, Essene EJ, Bowman JR (1991) Complete chemical analyses of metamorphic hornblendes: implications for normalisations, calculated H2O activities and thermobarometry. Contr Mineral Petrol 108: 472–484

Dasgupta S, Sengupta P, Guha D, Fukuoka MA (1991) A refined garnet-biotite Fe-Mg exchange geothermometer and its application in amphibolites and granulites. Contr Mineral Petrol 109: 130–137

De Andrade V, Vidal O, Lewin E, O'Brien P, Agard P (2006) Quantification of electron microprobe compositional maps of rock thin sections: an optimised method and examples. J Metam Geol 24: 655–668

de Caritat P, Hutcheon I, Walshe JL (1993) Chlorite geothermometry: a review. Clays Clay Minerals 41: 219–239

Degeling HS (2003) Zr equilibria in metamorphic rocks. PhD thesis, Australian National University

Dinklage WS, Calder WJ, St Clair T (2007) Using the Ti-in-biotite geothermometer to investigate the thermal structure of the crust during the Sevier Orogeny. Geol Soc Am Abstr Progr 39: 581

Donohue CL, Essene EJ (2005) Granulite facies conditions preserved in vanadium- and chromium-rich metapelites from the Wind River Range, WY. Can Mineral 41: 495–511

Drennan GR, Boiron M-C, Cathelineau M, Robb LJ (1997) Characteristics of post-depositional fluids in the Witwatersrand Basin. Mineral Petrol 66: 83–109

Dudek T, Srodon J, Eberl DD, Elsass F, Uhlik P (2002) Thickness distribution of illite crystals in shales. I. XRD vs high-resolution TEM measurements. Clays Clay Minerals 50: 562–577

Dunn SR, Valley JW (1992) Calcite-graphite isotope thermometry: a test for polymetamorphsim in marble, Tudor gabbro aureole, Ontario, Canada. J Metam Geol 10: 487–501

Edwards RL, Essene EJ (1988) Pressure, temperature and C-O-H fluid fugacities across the amphibolite - granulite facies transition, NW Adirondack Mtns, NY. J Petrol 29: 39–73

El-Shazly AEDK (1995) On the thermodynamic data of kaolinite. Am Mineral 80: 1048–1053

Ernst WG (1963) Significance of phengitic micas from low-grade schists. Am Mineral 48: 1357–1373

Ernst WG (1983) Mineral paragenesis in metamorphic rocks exposed along Tailuko Gorge, Central Mountain range, Taiwan. J Metam Geol 1: 305–329

Ernst WG, Jahn BM (1987) Crustal accretion and metamorphism in Taiwan, a post-Paleozoic mobile belt. Phil Trans Roy Soc Ser A 321: 129–161

Essene EJ (1982) Geologic thermometry and barometry. In: Ferry J (ed) Characterisation of metamorphism through mineral equilibria, Rev Mineral 10: 153–206

Essene EJ (1989) The current status of thermobarometry in metamorphic rocks, In: Daly SR, Cliff R, Yardley BWD, (eds) Evolution of Metamorphic Belts, Geol Soc Spec Paper 43

Essene EJ, Peacor DR (1995) Clay mineral thermometry: a critical perspective. Clays Clay Minerals 43: 728–745

Essene EJ, Peacor DR (1997) Illite and smectite: metastable, stable, or unstable? Clays Clay Minerals 45: 116–122

Essene EJ, Clavlin C, Giorgetti G, Mata P, Peacor, DR, Arkai P (2005) Two-, three- and four-feldspar assemblages with hyalophane: implications for phase equilibria in the system $BaAl_2Si_2O_8$–$KAlSi_3O_8$–$NaAlSi_3O_8$–$CaAl_2Si_2O_8$. Eur J Mineral 17: 515–535

Esteban JJ, Cuevas J, Tubia, JM, Liati A, Seward D, Gebauer D (2007) Timing and origin of zircon-bearing chlorite schists in the Ronda peridotites (Betic Cordilleras, S Spain). Lithos 99: 121–135

Ferriss BE, Essene EJ, Becker U (2008) Computational study of Ti substitution in zircon. Eur J Mineral, in press

Ferry JM, Spear FS (1978) Experimental calibration of the partitioning of Fe and Mg between biotite and garnet. Contr Mineral Petrol 66: 113–117

Ferry JM, Watson EB (2007) New thermodynamic models and revised calibrations for the Ti-in-zircon and Zr-in-rutile thermometers. Contr Mineral Petrol 154: 429–437

Frey M (1987) Low Temperature Metamorphism, Blackie, Glasgow

FrimmeI HE (1997) Chlorite thermometry in the Witwatersrand Basin: constraints on the Paleoproterozoic geotherm in the Kaapvaal Craton, South Africa. J Geol 105: 601–615

Frost BR, Chacko T (1989) The granulite uncertainty principle: limitations on thermobarometry in granulites. J Geol 97: 435–450

Fu B, Page FZ, Cavosie AJ, Fournelle J, Kita NT, Lackey JS, Wilde SA, Valley JW (2008) Ti-in-zircon thermometry: applications and limitations. Contr Mineral Petrol 156: 197–215

Fulignati P, Malfitano G, Sbrana A (1975) The Pantelleria caldera geothermal system: data from the hydrothermal minerals. J Volc Geothermal Res 75: 251–270

Ganne J, Bertrand J-M, Fudral S, Marquer Di, Vidal O (2007) Structural and metamorphic evolution of the Ambin Massif (W Alps): toward a new alternative exhumation model for the Brianconnais Domain. Bull Soc Geol France 178: 437–458

Ganne J, Bussy F, Vidal O (2003) Multi-stage garnet in the internal Brianconnais Basement (Ambin Massif, Savoy): new petrological constraints on the blueschist-facies metamorphism in the Western Alps and tectonic implications. J Petrol 44: 1281–1308

Ghent ED, Stout MZ (1984) $TiO_2$ activity in metamorphosed pelitic and basic rocks: principles and applications to metamorphism in southeastern Canadian Cordillera. Contr Mineral Petrol 86: 248–255

Ghiorso MS, Sack RO (1991) Fe-Ti oxide geothermometry; thermodynamic formulation and the estimation of intensive variables in silicic magmas. Contr Mineral Petrol 108: 485–510

Gillis KM, Muehlenbachs K, Stewart M, Karson J, Gleeson T (2001) Flud flow patterns in fast-spreading East Pacific Rise crust exposed at Hess Deep. J Geophys Res 106: 26311–26329

Giorgetti G, Mata MP, Peacor DR (2003) Evolution of mineral assemblages and textures from sediment through hornfels in the Salton sea geothermal field: direct crystallisation of phyllosilicates in a hydrothermal-metamorphic system. Clay Minerals 38: 113–126

Giorgetti G, Memmi I, Peacor DR (2000) Retarded illite crystallinity caused by stress-induced sub-grain boundaries in illite. Clay Minerals 35: 693–708

Giorgetti G, Tropper P, Essene EJ, Peacor DR (2000) Characterisation of coexisting non-equilibrium and equilibrium paragonite/muscovite intergrowths in an eclogite from the polymetamorphic Sesia-Lanzo Zone (Western Alps, Italy). Contr Mineral Petrol 138: 326–336

Ghiorso MS, Sack RO (1991) Fe-Ti oxide geothermometry: thermodynamic formulation and the estimation of intensive variables in silicic magmas. Contr Mineral Petrol 108: 485–510

Goldman DS, Albee AR (1977) Correlation of Mg/Fe partitioning between garnet and biotite with $^{18}O/^{16}O$ partitioning between quartz and magnetite. Am J Sci 277: 750–767

Green TH, Blundy JD, Adam J, Yaxley GM (2000) SIMS determination of trace element partition coefficients between garnet, clinopyroxene and hydrous basaltic liquids at 2–7.5 GPa and 1080–1200°C. Lithos 53: 165–187

Guidotti CV, Dyar MD (1991) Ferric iron in metamorphic biotite and its petrologic and crystallochemical implications. Am Mineral 76: 161–175

Guidotti CV, Sassi FP (1976) Muscovite as a petrogenetic indicator mineral in pelitic schists. N Jb Mineral Abh 127: 97–142

Guidotti CV, Sassi FP (1986) Classification and correlation of metamorphic facies series by means of muscovite b data from low-grade metapelites. N Jb Mineral Abh 153: 363–380

Guidotti CV, Sassi FP (1998) Petrogenetic significance of Na-K white mica mineralogy: recent advances for metamorphic rocks. Eur J Mineral 10: 815–854

Guidotti CV, Sassi FP (2002) Constraints on studies of metamorphic K-Na white micas: state of the art and suggestions for future research. In: Mottana A, Sassi FP, Thompson JB, Guggenheim S (eds) Micas: crystal chemistry and metamorphic petrology, Rev Mineral Geochem 46: 413–448

Hammarstrom JM, Zen E (1986) Aluminum in hornblende: an empirical igneous geobarometer. Am Mineral 71: 1297–1313

Harley SL (1989) The origins of granulites: a metamorphic perspective. Geol Mag 126: 215–247

Harrison TM, Watson EB, Aikman AB (2007) Temperature spectra of zircon crystallisation in plutonic rocks. Geology 35: 635–638

Hayden LA, Watson EB, Wark DA (2008) A thermobarometer for sphene (titanite). Contr Mineral Petrol 155: 529–540

Hayob JL, Bohlen SR, Essene EJ (1993) Experimental investigation and application of the reaction rutile + pyroxene = quartz + ilmenite. Contr Mineral Petrol 115: 18–37

Hayob JL, Essene EJ, Ruiz J, Ortega-Gutierrez F (1989) Young high-temperature granulites from the base of the crust in central Mexico. Nature 342: 265–268

Hazen RM, Finger LW (1982) Comparative Crystal Chemistry. Wiley-Interscience, NY

Helgeson HC, Delaney JM, Nesbitt HW, Bird DK (1978) Summary and critique of the thermodynamic properties of rock-forming minerals. Am J Sci 278A

Helgeson HC, Richard L, McKenzie WF, Norton DL, Schmitt A (2008). A chemical and thermodynamic model of oil generation in hydrocarbon source rocks. Geochim Cosmochim Acta in press, doi: 10.1016/j.gca2008.03.004

Henry DJ, Guidotti CV (2002) Titanium in biotite from metapelitic rocks: temperature effects, crystal-chemical controls and petrologic applications. Am Mineral 87: 375–382

Henry DJ, Guidotti CV, Thomson JA (2005) The Ti-saturation surface for low-to-medium pressure metapelitic biotites: implications for geothermometry and Ti-substitution mechanisms. Am Mineral 90: 316–328

Hildreth W, Wilson CJN (2007) Compositional zoning of the Bishop Tuff. J Petrol 48: 951–999

Hofman A, Valley JW, Watson EB, Cavoise AJ, Eiler JM (2008) Submicron-scale correlated distributions of Ti, P, Y and Ce in zircon. Contr Mineral Petrol, in press

Holdaway MJ (2000) Application of new experimental and garnet Margules data to the garnet-biotite geothermometer. Am Mineral 85: 881–892

Holdaway MJ, Lee SM (1977) Fe-Mg cordierite in high grade pelitic rocks based on experimental and natural observations. Contr Mineral Petrol 63: 175–198

Holland TJB, Powell R (1998) An internally consistent thermodynamic data set for phases of petrological interest. J Metam Geol 16: 309–343

Hollister LS, Grissom GC, Peters EK, Stowell HH, Sisson VB (1987) Confirmation of the empirical correlation of Al in hornblende with pressure of solidification of calc-alkaline plutons. Am Mineral 72: 231–239

Hower J, Eslinger EV, Hower ME, Perry EA (1976) Mechanism of burial metamorphism of argillaceous sediment. 1. Mineralogical and chemical evidence. Geol Soc Am Bull 87: 727–737

Jiang W-T, Peacor DR (1994) Prograde transitions of corrensite and chlorite in low-grade pelitic rocks from the Gaspé Peninsula, Quebec. Clays Clay Minerals 42: 497–517

Jiang W-T, Peacor DR, Arkai P, Toth M, Kim JW (1997) TEM and XRD determination of crystallite size and lattice strain as a function of illite crystallinity in pelitic rocks. J Metam Geol 15: 267–281

Jiang W-T, Peacor DR, Buseck PR (1994a) Chlorite geothermometry? Analytical contamination and apparent octahedral vacancies. Clays Clay Minerals 42: 593–605

Jiang W-T, Peacor DR, Essene EJ (1994b) Clay minerals in the McAdams sandstone, California: implications for substitution of $H_3O^+$ and $H_2O$ and metastability of illite. Clays Clay Minerals 42: 35–45

Johnson MC, Rutherford MJ (1989) Experimental calibration of the aluminum-in-hornblende geobarometer with application to Long Valley Caldera (CA) volcanic rocks. Geology 17: 837–841

Kasama T, Murakami T, Kohyama N, Watanabe T (2001) Experimental mixtures of smectite and rectorite: re-investigation of "fundamental particles" and "interparticle diffraction". Am Mineral 86: 105–114

Katagiri G, Ishida H, Ishitani A (1988) Raman spectra of graphite edge planes. Carbon 26: 565–571

Kawasaki T, Motoyoshi Y (2007) Solubility of $TiO_2$ in garnet and orthopyroxene: Ti thermometer for ultrahigh-temperature granulites. US Geol Surv Open File Rept 2007–1047, doi:10.3133/2007-1047SRP038

Kisch HJ, Sassi R, Sassi FP (2006) The $b_0$ lattice parameter and chemistry of phengites from HP/LT metapelites. Eur J Mineral 18: 207–222

Kleemann U, Reinhardt J (1994) Garnet-biotite thermometry revised: the effect of $Al^{VI}$ and Ti in biotite. Eur J Mineral 6: 925–941

Kranidiotis P, MacLean WH (1987) Systematics of chlorite alteration at the Phelps Dodge massive sulphide deposit, Matagami, Quebec. Econ Geol 82: 1898–1911

Labotka TC, Kath RL (2001) Petrogenesis of the contact-metamorphic rocks beneath the Stillwater Complex, Montana. Geol Soc Am Bull 113: 1312–1323

Laverne C, Vanko DA, Tararotti P, Alt JC (1995) Chemistry and geothermometry of secondary minerals from the deep sheeted dyke complex, Hole 504B. Proc Ocean Drill Prog Sci Res 137/140: 167–190

Lee MR, Bland PA, Graham G (2003) Preparation of TEM samples by focused ion beam (FIB) techniques: applications to the study of clays and phyllosilicates in meteorites. Mineral Mag 67: 581–592

Li G, Peacor, DR, Merriman RJ, Roberts B (1994) The diagenetic to low-grade metamorphic evolution of matrix white micas in the system muscovite-paragonite in a mudrock from central Wales, UK. Clays Clay Minerals 42: 369–381

Lonker SW, Fitzgerald JD, Hedenquist JW, Walshe JL (1990) Mineral-fluid interactions in the Broadlands ± Ohaaki geothermal system, New Zealand. Am J Sci 290: 995–1068

Lonker SW, Franzson H, Kristmannsdottir H (1993) Mineral-fluid interactions in the Reykjanes and Svartsengi geothermal systems, Iceland. Am J Sci 293: 605–670

Mäder UK, Berman RG (1992) Amphibole thermobarometry, a thermodynamic approach. Geol Surv Can Pap 92–1E: 393–400

Makanjuola AA, Howie RA (1972) The mineralogy of the glaucophane schists and associated rocks from Ile de Groix, Brittany, France. Contr Mineral Petrol 35: 83–118

Manning CE, Bohlen SR (1991) The reaction titanite + kyanite = anorthite + rutile and titanite-rutile barometry in eclogites. Contr Mineral Petrol 109: 1–9

Manon MR (2008) Heat capacity of high pressure minerals and phase equilibria of Crete blueschists. PhD thesis, Univ. Michigan, Ann Arbor MI

Martıñez-Serrano RG, Dubois M (1998) Chemical variations in chlorite at the Los Humeros geothermal system, Mexico. Clays Clay Minerals 46: 615–628

Mas A, Guisseau D, Patrier Mas P, Beaufort D, Genter A, Sanjuan B, Girard JP (2006) Clay minerals related to the hydrothermal activity of the Bouillante geothermal field (Guadeloupe). J Volc Geothermal Res 158: 380–400

Massonne H-J, Schreyer W (1987) Phengite geobarometry based on the limiting assemblage with K-feldspar, phlogopite and quartz. Contr Mineral Petrol 96: 212–224

Massonne H-J, Szpurka Z (1997) Thermodynamic properties of white micas on the basis of high-pressure experiments in the systems $K_2O$-MgO-$Al_2O_3$–$SiO_2$–$H_2O$ and $K_2O$-FeO-$Al_2O_3$–$SiO_2$–$H_2O$. Lithos 41: 229–250

Massonne H-J, Grosch U, Willner A (1993) Geothermobarometrie mittels Ti-Gehalten in Kalihellglimmern. Ber Deutsch Mineral Gesell 1993: 1–85

McDowell SD, Elders WA (1980) Authigenic layer silicate minerals in borehole Elmore 1. Salton sea Geothermal Field, California, USA. Contr Mineral Petrol 74: 293–310

McDowell SD, Elders WA (1983) Allogenic layer silicate minerals in borehole Elmore 1. Salton sea Geothermal Field, California. Am Mineral 68: 1146–1159

Meinhold G anders B, Kostopoulos D, Reischmann T (2008) Rutile chemistry and thermometry as provenance indicator: an example from Chios Island, Greece. Sed Geol 203: 98–111

Mengel F, Rivers T (1994) Metamorphism of pelitic rocks in the Paleoproterozoic Ramah Group, Saglek area, N Labrador: mineral reactions, P-T conditions and influence of bulk composition. Can Mineral 32: 781–801

Merriman RJ, Roberts B, Peacor DR (1990) A transmission electron microscope study of white mica crystallite size distribution in a mudstone to slate transitional sequence, North Wales, UK. Contr Mineral Petrol 106: 27–40

Moecher DP, Essene EJ, Anovitz LM (1988) Calculation and application of clinopyroxene-garnet-plagioclase-quartz geobarometers. Contr Mineral Petrol 100: 92–106

Moura MA, Botelho NF, Olivo GR, Kyser TK (2006) Granite-related Paleoproterozoic, Serrinha gold deposit, southern Amazonia, Brazil: hydrothermal alteration, fluid inclusion and stable isotope constraints on genesis and evolution. Econ Geol 101: 585–605

Nadeau PH, Wilson MJ, McHardy WJ, Tait JM (1984) Interstratified clays as fundamental particles. Science 225: 923–925

Negro F, Beyssac O, Goffe B, Saddiqi O, Boubaouene ML (2006) Thermal structure of the Alboran Domain in the Rif (northern Morocco) and the western Betics (southern Spain): constraints from Raman spectroscopy of carbonaceous material. J Metam Geol 24: 309–327

Newton RC (1986) Metamorphic temperatures and pressures of group B and C eclogites. Geol Soc Am Mem 164: 17–30

Oberhänsli R, Goffé B, Bosquet R (1995) Record of a HP-LT metamorphic evolution in the Valais zone: geodynamic implications. In: Lombardo B (ed) Studies of Metamorphic Rocks and Minerals of the Western Alps: a Volume in Memory of Ugo Pognante. Bolletino del Museo Regionale di Science Naturali, Torino

Page FZ, Armstrong LS, Essene EJ, Mukasa SB (2007a) Prograde and retrograde history of the Junction School eclogite and an evaluation of garnet-phengite-clinopyroxene thermobarometry. Contr Mineral Petrol 153: 533–555

Page FZ, Essene EJ, Mukasa SB (2003) Prograde and retrograde history of eclogites from the Eastern Blue Ridge, North Carolina. J Metam Geol 21: 685–698

Page FZ, Fu B, Kita NT, Fournelle J, Spicuzza MJ, Schulze DJ, Viljoen F, Basei MAS, Valley JW (2007b) Zircons from kimberlite: new insights from oxygen isotopes, trace elements and Ti in zircon thermometry. Geochim Cosmochim Acta 71: 3887–3903

Pandarinath K, Dulski P, Torres-Alvarado IS, Verma SP (2006) Element mobility during the hydrothermal alteration of rhyolitic rocks of the Los Azufres geothermal field, Mexico. Geothermics 37: 53–72

Parra T, Vidal O, Agard P (2002a) A thermodynamic model for Fe-Mg dioctahedral K white micas using data from phase-equilibrium experiments and natural pelitic assemblages. Contr Mineral Petrol 143: 706–732

Parra T, Vidal O, Jolivet L (2002b) Relation between deformation and retrogression in blueschist metapelites of Tinos Island (Greece) evidenced by chlorite-mica local equilibria. Lithos 63: 41–66

Parra T, Vidal O, Theye T (2005) Experimental data on the Tschermak substitution in Fe-chlorite. Am Mineral 90: 359–370

Patiño Douce AE (1993) Titanium substitution in biotite: an empirical model with applications to thermometry, $O_2$ and $H_2O$ barometries and consequences for biotite stability. Chem Geol 108: 133–162

Peacor DR (1992a) Analytical electron microscopy: X-ray analysis. Rev Mineral 27: 113–140

Peacor DR (1992b) Diagenesis and low-grade metamorphism of shales and slates. Rev Mineral 27: 335–380

Peacor DR (1998) Implication of TEM data for the concept of fundamental particles. Can Mineral 36: 1397–1408

Perkins D III, Essene EJ, Westrum EF Jr, Wall VJ (1979) New thermodynamic data for diaspore, a-AlO(OH) and its application to the system $Al_2O_3$–$SiO_2$–$H_2O$. Am Mineral 64: 1080–1090

Perkins D III, Westrum EF Jr., Essene EJ (1980) The thermodynamic properties and phase relations of some minerals in the system CaO-$Al_2O_3$–$SiO_2$–$H_2O$. Geochim Cosmochim Acta 44: 61–84

Phillips NG, Law JDM (1994) Metamorphism of the Witwatersrand gold fields: a review. Ore Geol Rev 9: 1–31

Powell R, Holland TJB (2008) On thermobarometry. J Metam Geol 26: 155–179

Pusz S, Kwiecinska BK, Duber S (2003) Textural transformation of thermally treated anthracites. Int J Coal Geol 54: 115–123

Pyle JM, Spear FS (2000) An empirical garnet (YAG)-xenotime thermometer. Contr Mineral Petrol 138: 51–58

Raase P (1976) Al and Ti contents of hornblende, indicators of pressure and temperature of regional metamorphism. Contr Mineral Petrol 45: 231–236

Racek M, Stipska, P, Powell R (2008) Garnet-clinopyroxene intermediate granulites in the St. Leonhard massif of the Bohemian Massif: ultrahigh-temperature metamorphism at high pressure or not? J Metam Geol 26: 253–271

Ramirez E, Sassi R (2001) The baric character of the Patagonian basement as deduced from the muscovite $d_{060,331}$ spacing: a first contribution from eastern Andean metamorphic complex (Andes, Chile). Eur J Mineral 13: 1119–1126

Rancourt DG, Mercier PHJ, Cherniak DJ, Desgreniers, S, Kodama H, Robert JL, Murad E (2001) Mechanisms and crystal chemistry of oxidation in annite: resolving the hydrogen-loss and vacancy reactions. Clays Clay Minerals 49: 455–491

Rathmell MA, Streepey MM, Essene EJ, van der Pluijm BA (1999) Comparison of garnet-biotite, calcite-graphite and calcite-dolomite thermometry in the Grenville Orogen, Canada. Contr Mineral Petrol 134: 217–231

Robert JL (1991) Substitution of $Ti^{4+}$ in potassic micas: a reappraisal. Terra Abstr 3: 69

Robie RA, Hemingway BS (1991) Heat capacities of kaolinite from 7 to 380 K and of DMSO-intercalated kaolinite from 20 to 310 K: the entropy of kaolinite $Al_2Si_2O_5(OH)_4$. Clays Clay Minerals 39: 362–368

Robie RA, Hemingway BS (1995) Thermodynamic properties of minerals and related substances at 298.15 K and 1 bar ($10^5$ Pascals) pressure and at higher temperatures. US Geol Surv Bull 2131

Robie RA, Hemingway BS, Fisher JR (1978) Thermodynamic properties of minerals and related substances at 298.15 K and 1 bar ($10^5$ Pascals) pressure and at higher temperatures. US Geol Surv Bull 1452

Rutter MJ, van der Laan SR, Wyllie PJ (1989) Experimental data for a proposed empirical igneous geobarometer: aluminum in hornblende at 10 kbar pressure. Geology 17: 897–900

Sassi FP (1972) The petrologic and geologic significance of $b_0$ value of potassium white micas in low-grade metamorphic rocks. An application to the Eastern Alps. Tschermaks Mineral Petrogr Mitt 18: 105–113

Sassi FP, Scolari A (1974) The $b_0$ value of the potassium white micas as a barometer in low-grade metamorphism of pelitic schists. Contr Mineral Petrol 45: 143–152

Sassi R, Cruciani G, Mazzoli C, Nodari L, Craven J (2008) Multiple titanium substitutions in biotites from high-grade metapelitic xenoliths (Euganean Hills, Italy): complete crystal chemistry and appraisal of petrologic control. Am Mineral 93: 339–350

Sato K, Santosh M (2007) Titanium in quartz as a record of ultrahigh-temperature metamorphism: the granulites of Karur, southern India. Mineral Mag 71: 143–154

Schiffman P, Fridleifsson GO (1991) The smectite-chlorite transition in drillhole NJ-15, Nesjavellir geothermal field, Iceland: XRD, BSE and EMP investigations. J Metam Geol 9: 679–696

Schmidt MW (1992) Amphibole composition in tonalite as a function of pressure: an experimental calibration of the Al-in-hornblende barometer. Contr Mineral Petrol 110: 304–310

Selverstone J, Morteani G, Staude J-M (1991) Fluid channelling during ductile shearing: transformation of granodiorite into aluminous schist in the Tauern Window, Eastern Alps. J Metam Geol 9: 419–443

Shang C, Rice JA, Eberl DD, Lin J-S (2003) Measurement of illite particle thickness using a direct Fourier transform of small-angle X-ray scattering data. Clays Clay Minerals 51: 293–300

Shau Y-H, Feather ME, Essene EJ, Peacor DR (1991) Genesis and solvus relations of submicroscopically intergrown paragonite and phengite in a blueschist from California. Contr Mineral Petrol 106: 367–378

Shau Y-H, Peacor DR, Essene EJ (1990) Corrensite and mixed-layer chlorite-corrensite in metabasalt from northern Taiwan: TEM/AEM, EMPA, XRD and optical studies. Contr Mineral Petrol 105: 123–142

Shedlock RJ, Essene EJ (1979) Mineralogy and petrology of a tactite near Helena, Montana. J Petrol 20: 71–97

Sorensen SS, Grossman JN (1989) Enrichment of trace elements in garnet amphibolites from a paleo-subduction zone: Catalina Schist, southern California. Geochim Cosmochim Acta 53: 3155–3177

Spear FS, Kohn MJ, Cheney JT, Florence F (2002) Metamorphic, thermal and tectonic evolution of central New England. J Petrol 43: 2097–2120

Spear FS, Wark DA, Cheney JT, Schumacher JC, Watson EB (2006) Zr-in-rutile thermometry in blueschists from Sifnos, Greece. Contr Mineral Petrol 152: 375–385

Stone P, Merriman RJ (2004) Basin thermal history favours an accretionary origin for the Southern Uplands Terrane, Scottish Caledonides. J Geol Soc 161: 829–836

Storm LC, Spear FS (2005) Pressure, temperature and cooling rates of granulite facies migmatitic pelites from the southern Adirondack Highlands, New York. J Metam Geol 23: 107–130

Theye T, Chopin C, Grevel KD, Ockenga E (1997) The assemblage diaspore+quartz in metamorphic rocks: a petrological, experimental and thermodynamic study. J Metam Geol 15: 17–28

Thomas WM, Ernst WG (1990) The alumium content of hornblende in cell-alkaline granitic rocks: a mineralogic barometer calibrated experimentally to 12 kbar. In: Fluid-Mineral Interactions: A Tribute to H.P. Eugster, Spencer RJ, Chou I-M, eds, Geochem Soc Spec Pub 2: 59–63

Thompson AB (1976) Mineral reactions in metamorphic rocks I, II. Am J Sci 276: 401–454

Thomson JA (2008) Beneath the Stillwater Complex: petrology and geochemistry of quartz-plagioclase-cordierite (or garnet)-orthopyroxene-biotite ± spinel hornfels, Mountain View area, Montana. Am Mineral 93: 438–450

Timpa S, Gillis KM, Canil D (2005) Accretion-related metamorphism of the Metchosin igneous complex, southern Vancouver Island, British Columbia. Can J Earth Sci 42: 1467–1479

Tomkins HS, Powell R, Ellis DJ (2007) The pressure dependence of the zirconium-in-rutile thermometer. J Metam Geol 25: 703–713

Tracy RJ (1982) Compositional zoning and inclusions in metamorphic minerals. In: Ferry J (ed) Characterisation of metamorphism through mineral equilibria, Rev Mineral

Triebold S, von Eynatten H, Luvizotto GL, Zack T (2007) Deducing source rock lithology from detrital rutile geochemistry: an example from the Erzgebirge, Germany. Chem Geol 244: 421–436

Troitzsch U, Christy AG, Ellis DJ (2005) The crystal structure of disordered (Zr,Ti)$O_2$ solid solution including srilankite: evolution towards tetragonal $ZrO_2$ with increasing Zr. Phys Chem Minerals 32: 504–514

Tropper P, Essene EJ, Sharp ZD, Hunziker JC (1999) New pressure constraints in high pressure rocks: applications of K-feldspar-jadeite-quartz barometry to eclogite facies metagranites and metapelites in the Western Alps. J Metam Geol 17: 195–209

Tropper P, Manning CE, Essene EJ (2002) The substitution of Al and F in titanite at high pressure and temperature: experimental constraints on phase relations and solid solution properties. J Petrol 43: 1787–1814

Trotet F, Vidal O, Jolivet L (2001) Exhumation of Syros and Sifnos metamorphic rocks (Cyclades, Greece): new constraints on the P-T paths. Eur J Mineral 13: 901–920

van der Plas L (1959) Petrology of the northern Adula region, Switzerland. Leidse Geol Med 24: 415–602

Velde B (1965) Phengite micas: synthesis, stability and natural occurrence. Am J Sci 263: 886–913

Velde B, El Moutaouakkil N, Iijama A (1991) Compositional homogeneity in low-temperature chlorites. Contr Mineral Petrol 107: 21–26

Vidal O, Parra T (2000) Exhumation paths of high-pressure metapelites obtained from local equilibria for chlorite-phengite assemblages. Geol J 35: 139–161

Vidal O, De Andrade V, Lewin E, Munoz M, Parra T, Pascarelli S (2006) P-T-deformation-$Fe^{3+}/Fe^{2+}$ mapping at the thin section scale and comparison with XANES mapping. Application to a garnet-bearing metapelite from the Sambagawa metamorphic belt. J Metam Geol 24: 669–683

Vidal O, Parra T, Trotet F (2001) A thermodynamic model for Fe-Mg aluminous chlorite using data from phase equilibrium experiments and natural pelitic assemblages in the 100–600°C,1–25 kbar range. Am J Sci 301: 557–592

Vignaroli G, Rossetti F, Theye T, Faccenna, C (2008) Styles and regimes of orogenic thickening in the Peloritani Mountains (Sicily, Italy): new constraints on the tectono-metamorphic evolution of the Apennine belt. Geol Mag 145: 552–569

Walshe JL (1986) A six-component chlorite solid solution model and the conditions of chlorite formation in hydrothermal and geothermal systems. Econ Geol 81: 681–703

Walshe JL, Solomon M (1981) An investigation into the environment of formation of the volcanic hosted Mt Lyell copper deposits using geology, mineralogy, stable isotopes and a six component chlorite solid solution model. Econ Geol 76: 246–284

Wang A, Dhamelincourt P, Duvessy J, Guerard D, Landais P, Lelaurain M (1989) Chacterisation of graphite alteration in an uranium deposit by micro-Raman spectroscopy, X-ray diffraction, transmission electron microscopy and scanning electron microscopy. Carbon 27: 209–218

Wang L, Essene EJ, Zhang Y (2000) Direct observation for immiscibility in pyrope-almandine-grossular garnet. Am Mineral 85: 41–46

Wark DA, Watson EB (2006) TitaniQ: a titanium-in-quartz geothermometer. Contr Mineral Petrol 152: 743–754

Wark DA, Hildreth W, Spear FS, Cherniak DJ, Watson EB (2007) Pre-eruption recharge of the Bishop magma system. Geology 35: 235–238

Watson EB, Harrison TM (2005) Zircon thermometer reveals minimum melting conditions on earliest Earth. Science 308: 841–844

Watson EB, Wark DA, Thomas JB (2006) Crystallisation thermometers for zircon and rutile. Contr Mineral Petrol 151: 413–433

Welch MD, Barras J, Klinowski J (1995) A multinuclear NMR study of clinochlore. Am Mineral 80: 441–447

Wen S, Nekvasil H (1994) SOLVCALC: an interactive graphics programme package for calculating the ternary feldspar solvus and for two-feldspar geothermometry. Comp Geosci 20: 1025–1040

Wilde SA, Valley JW, Peck WH, Graham CM (2001) Evidence from detrital zircons for the existence of continental crust and oceans on the Earth 4.4 Gyr ago. Nature 409: 175–178

Wu C-M, Cheng B-H (2006) Valid garnet-biotite (GB) geothermometry and garnet-aluminum silicate-plagioclase-quartz (GASP) geobarometry in metapelitic rocks. Lithos 89: 1–23

Xie X, Byerly GR, Ferrerl RE Jr (1997) IIb trioctahedral chlorite from the Barbeton greenstone belt: crystal structure and rock composition constraints with implications to geothermometry. Contr Mineral Petrol 126: 275–291

Yamato P, Agard P, Goffé B, de Andrade V, Vidal O, Jolivet L (2007) New, high-precision P-T estimates for Oman blueschists: implications for obduction, nappe stacking and exhumation processes. J Metam Geol 25: 657–682

Yang L, Steefel CI (2008) Kaolinite dissolution and precipitation kinetics at 22°C and pH 4. Geochim Cosmochim Acta 72: 99–116

Yau Y-C, Peacor DR, Beane RJ, Essene EJ, McDowell SD (1988) Microstructures, formation mechanisms and depth-zoning of phyllosilicates in geothermally altered shales, Salton sea, CA. Clays Clay Minerals 36: 1–10

Yong W (2008) Thermodynamic studies of minerals under mantle conditions. PhD thesis, Univ. Michigan, Ann Arbor MI

Zack T, Luvizottow GL (2006) Application of rutile thermometry to eclogites. Mineral Petrol 88: 69–85

Zack T, Moraes R, Kronz A (2004a) Temperature dependence of Zr in rutile: empirical calibration of a rutile thermometer. Contr Mineral Petrol 152: 471–488

Zack T, von Eynatten H, Kronz A (2004b) Rutile geochemistry and its potential use in quantitative provenance studies. Sed Geol 171: 37–58

Zang W, Fyfe WS (1995) Chloritisation of the hydrothermally altered bedrock at the Igarapé Bahia gold deposit, Carajás, Brazil. Mineral Dep 30: 30–38

7

# On Fluids in the Dynamic Earth

M. Santosh

**Abstract:** Plate, plume and anti-plate tectonics drive the fluid factories in the earth. Whereas water plays a dominant role in subduction zones, collision and rift zones witness the activity of $CO_2$-rich fluids. Paleo-fluid channels can be traced from geologic, petrologic, fluid inclusion and geochemical signature; ongoing fluid activity is defined by seismogenic zones in subduction boundaries. Superplumes, both upwelling and downwelling, exert a major control on the nature and distribution of fluids within the earth. They act as pumps to take water to depth and as gigantic pipes connecting the core to the surface of the earth to transfer volatiles. The entrance of huge volumes of water from late Proterozoic triggered the return flow of $CO_2$ back to the surface by the partial melting or subsolidus decarbonation of the subcontinental carbonated mantle. When a plume hits a carbonated tectosphere, the keel on which continents float, even small amounts of melts generated will be rich in $CO_2$. Rising plumes also bring about thermal and chemical erosion. The magmatic, metasomatic and metamorphic fluid factories have played a major role in the geochemical and tectonic evolution of the earth.

---

M. Santosh (✉)
Department of Earth Science, Faculty of Science, Kochi University, Akebono-cho 2-5-1, Kochi 780-8520, Japan
e-mail: santosh@cc.kochi-u.ac.jp

## 7.1 Introduction

The role of fluids and melts in crustal processes, crust-mantle interaction and mantle dynamics has been investigated in several studies. Recent models on melt and fluid processes at the bottom of the mantle have led to the proposal of an anti-crust at the core-mantle boundary (CMB) similar to the continental crust on the surface of the earth (Maruyama et al. 2007). Fluids and melts play a critical role in the geochemical differentiation and element distribution in the earth. Fluid movements and fluid-induced alternations have been studied from field characteristics, petrology, geochemistry and isotopes. Ongoing fluid processes in tectonically active regions have been evaluated from seismological investigations (Zhao et al. 1996; Sun et al. 2008).

In this brief overview, I attempt to synthesise the distribution and activity of fluids on a whole-earth scale within the perspective of plate, plume and anti-plate tectonics. The various fluid factories in the solid earth are evaluated and the major distinctions between fluids in constructive and destructive plate margins are also considered.

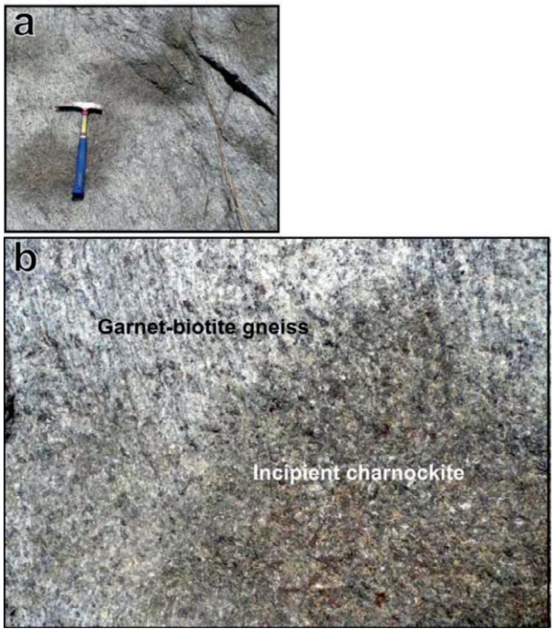

**Fig. 7.1** Field photographs of ‘incipient charnockites’ illustrating an example for paleo-fluid pathways at mid to lower crustal levels. (a) Inicipient charnockites occurring as patches and veins at Kottavattom quarry, southern India. (b) A close-up view of the conversion of garnet- and biotite-bearing foliated gneisses to dark greenish coarse recrystallised patches of incipient charnockite containing brownish orthopyroxene. The dry mineral assemblage in the charnockite was stabilised by the infiltration of $CO_2$-rich fluids at granulite facies condition

## 7.2 Evidence for Ancient Fluid Pathways

Models on fluids in the earth’s crust propose a general fluid stratification with the upper crust rich in $H_2O$, followed by $CO_2 + H_2O$ at intermediate levels and dominantly $CO_2$ in the lower crust (Touret 1985; Santosh 1992). Variable amounts of $CH_4$, $N_2$ and other volatiles may also be present, mostly in the upper and intermediate crustal levels, and rarely at depth. Crustal evidence for fluid activity is varied and includes fluid-induced wall rock alternations, copious fluid flushing along shear/fault zones, fluid-rich melts and magmas, fluid-present metamorphic transformations, among others. One of the typical examples for structurally controlled influx of $CO_2$-dominated anhydrous fluids has been demonstrated in the case of the prograde transformation of upper amphibolite facies gneisses to orthopyroxene-bearing anhydrous granulites on a decimetre scale termed as ‘incipient charnockites’ (Fig. 7.1). Patches, veins and lenses of such ‘arrested charnockites’ have been reported from various localities in southern and eastern India, Sri Lanka and Madagascar (Newton [1992]; Santosh [1992]; Santosh and Omori [2008a]). Petrologic, fluid inclusion and stable isotope studies on the gneiss-charnockite association suggest that the transformation from gneiss to charnockite was a result of the advection of $CO_2$-rich fluids along shears/faults from sub-lithospheric sources. The occurrence of high density $CO_2$-rich fluid inclusions in many granulite facies rocks (Fig. 7.2), most of which formed within continental collision zones, suggest that the formation of hot and ultra-hot orogens witnessed $CO_2$-rich fluids as a buffer to stabilise the anhydrous mineral assemblages (Santosh and Omori [2008a, 2008b]; Santosh et al. [2008]; Tsunogae et al. [2008]). The origin of $CO_2$ is linked to sub-lithospheric sources and the sources are varied including fluids exsolved from plumes or underplated magmas, or fluids released by decarbonation reactions of deep-subducted carbonates. Evidence for mantle-derived $CO_2$ invasion into crustal litholo-

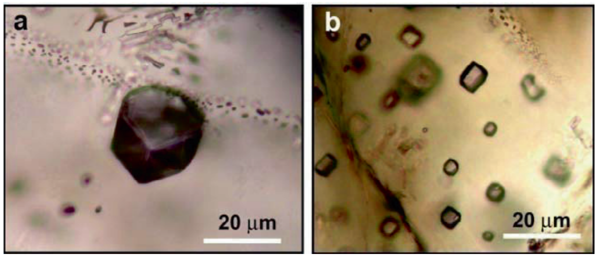

**Fig. 7.2** Photomicrographs of fluids inclusions in garnet (a) from an anhydrous granulite in Sri Lanka and feldspar (b) in a granulite from southern India. These monophase inclusions contain high density pure $CO_2$-rich fluids trapped during peak P-T conditions of metamorphism. The $CO_2$-rich fluids are considered to have influxed from sub-lithospheric sources

gies have also been documented from copious precipitation of graphite crystals as well as extensive carbonation of shear zones resulting in the formation of calcite and ankerite with mantle-like isotopic values. Deep crustal shear zones, often rooted in the mantle are prime locales for focused flow of $CO_2$ such as the giant Himalayan strike-slip system of southern Asia, the crustal scale shear zone network of western Australia, the central African shear zone and the Pan-African shear zones in southern India, Sri Lanka, Madagascar and elsewhere.

## 7.3 Evidence for Ongoing Fluid Processes

One of the important examples for ongoing fluid processes is provided by the seismogenic zone in subducting plate margins, occurring at depths equivalent to a temperature range of 150–350$^{o}$C (clay-illite transition to brittle-ductile transition for quartz and feldspar) (e.g Hyndman et al. 2006). Great earthquake ruptures initiated at this temperature range may propagate with decreasing slip to where the temperature is around 450°C. At deeper levels, double or triple seismic zone develops within the subducting slab characterised by fluid-producing dehydration reactions (Peacock and Wang 1999). The numerous splay faults typically demonstrated in the case of the Nankai trough in south-west Japan (Park et al. 2002) are the channels of fluid flow along which dehydrated $H_2O$-dominated volatiles propagate sealing the fractures, generating fresh cracks and triggering earthquakes. Thus ongoing fluid processes provide a key to understand the mechanism of earthquakes. In south-west Japan, tremor or micro-earthquakes have been correlated to subsurface fluid flow in the three-dimensional space immediately above the seismogenic zone and extensive recrystallisation of the overlying units (Sun et al. 2008).

The main channel flow along the cross section of the subduction zone may be related to the distribution of seismicity. The concept of “bright spot” or “layer” identifies a seismologically remarkable reflection plane immediately below the boundary between the upper and lower crust (Hyndman and Shearer 2008), and has been considered to indicate the presence of fluids or aqueous melts at the bottom of the upper crust (e.g Wei et al. 2001). The mechanism to supply water underneath is presumably through subducting slab. In order to accumulate the fluid in this zone, a strong mechanical barrier is required, which can presumably be generated by silica-enriched fluid. The sealing of the porous grain boundaries of rocks by water-dominated fluids might be the major cause for the origin of the bright layer. If this is the case, then the bright layer can be considered as an underground dam site to store water-rich fluids which migrated below the upper crust. The irregular topography of this layer would allow preferential storage of large volumes of fluid. When the dam is cracked, fluid propagation occurs instantaneously, a mechanism that possibly triggered big earthquakes such as the Kobe earthquake (Zhao et al. 1996). Cooling down and precipitation of quartz veins along the fracture with complete sealing of the crack occurs within a short period of time. It is also believed that spot concentration of micro-earthquakes on the bright layer is a precursor for future big earthquakes.

During subduction, hydrous silicates decompose to release metasomatic fluid against the hanging wall which depresses the melting temperature of the mantle wedge resulting in the formation of arc magmas (Tatsumi et al. 1983). When sub-arc mantle releases arc magma near the Moho, it separates into two liquid phases: one is arc magma and the other is water-enriched fluid, each of which may move upward independently. Such phase separation has been experimentally demonstrated to occur at around 800–1000$^{o}$C near Moho depths. Micro-earthquakes often occur near Moho underneath active volcanoes which may be related to the phase separation and fluid activity.

## 7.4 Plumes as Gigantic Pipes to Transport Fluids

The surface geology of the earth including the presence of topographic superswells, and the present day thermal structure, suggest that the major convection pattern in our planet is controlled by two super-upwellings (superplumes) and one super-downwelling (Fig. 7.3) (Maruyama et al. 2007). The upwellings are termed as Pacific and African superplumes following their first definition by Maruyama (1994). If super-upwelling is present, then downwelling is necessary to counter-balance the material circulation. The

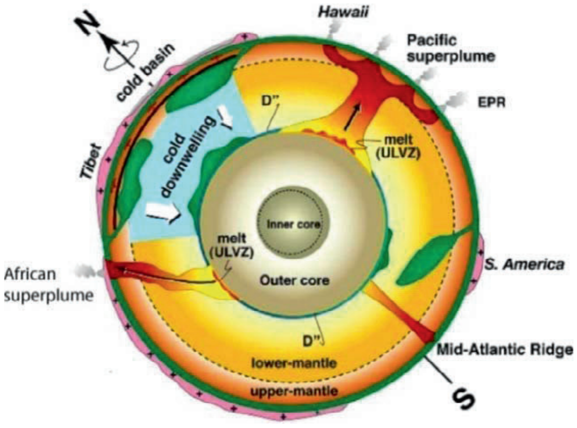

**Fig. 7.3** A schematic cross-section of the earth showing two major upwellings (Pacific superplume and African superplume) and one downwelling (Asian cold plume) (after Maruyama et al. 2007, with permission from Elsevier)

distribution of high velocity anomalies is restricted to the circum-Pacific and Tethyan domains over the world (Zhao 2004) suggesting the presence of subducted lithosphere. The strongest high velocity anomaly within the mantle, both in terms of intensity and in size, occurs in the western Pacific and eastern Asia coinciding with the circum-Pacific subduction zone where it meets with the Tethyan domain, forming an overlapping mega-scale subduction zone. Maruyama (1994) named this zone as a super-downwelling zone or Asian cold superplume. Such cold plumes are gigantic water pumps that push water into the deep earth.

Since superplume is connected to the bottom of the mantle and perhaps rooted to the core, the core heat is effectively transferred by superplume which also transports high temperature and fertile materials from lower mantle to the upper mantle, ultimately driving the plate tectonics on the surface of the earth (Fig. 7.4). Thus the superplume acts as a pipe connecting the CMB with the surface to transfer core heat and volatiles. Super-upwellings trigger the break-up of supercontinents. On the other hand the whirlpool-like super-downwelling functions as a gigantic “black hole” which swallows continental material and drag the dispersed continents together close-packing them into a tight assembly, and thus leading to the formation of supercontinents (Santosh et al. 2009a).

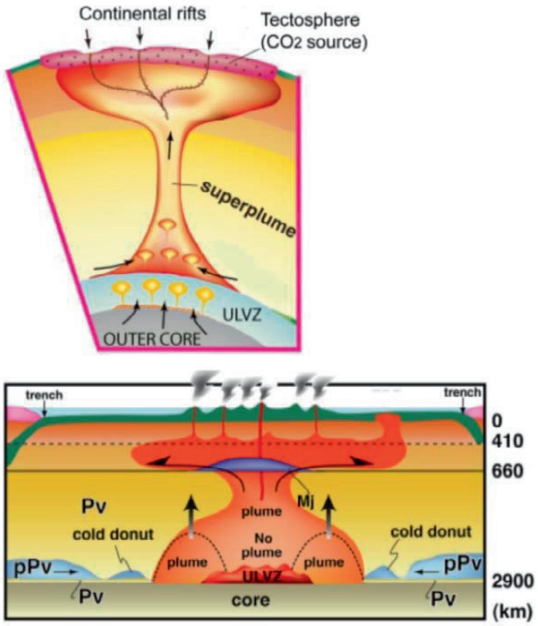

**Fig. 7.4** Plumes as gigantic pipes which transfer volatiles from the CMB to the surface (after Maruyama et al. 2007; Santosh et al. 2009b). The top figure shows rising small plumes from the CMB which amalgamate into a large upwelling. When the superplume hits the tectosphere (carbonated continental keel), huge amounts of $CO_2$ are liberated and flushed out through continental rifts either through magmatic conduits or through hot and ultra-hot metamorphic orogens. The bottom figure shows the birth of a superplume from heating from the core, and heat liberated through the exothermic reactions of perovskite (Pv) to post-perovskite (pPv). Abbreviations: ULVZ–ultra-low velocity zone, indicating melt layer on top of the CMB, designated as ant-crust by Maruyama et al. (2007). Mj – majorite. With permission from Elsevier

Superplumes both upwelling and downwelling, exert a major control on the fluid history and fluid distribution within the earth. The Pacific superplume is a thermal plume which means the higher temperature is the cause for its buoyancy. In the case of chemical plumes, temperature is nearly constant and the plumes are driven by volatiles. Although thermal and chemical plumes are considered as two end-members, it is possible that plume transport involves both thermal and fluid control. In the early history of the earth, juvenile volatiles such as C-H-O-S were trapped in the outer core and by the increasing volume of the solid inner core, these volatiles were released. An over-saturation of these volatiles may promote the extraction of lighter elements and their transport through superplume. In this case the superplume can be driven by the over-saturation of C-O-H-S fluids in the outer core. These light elements have long been trapped when the earth was formed and fractionated. Since they are not stable in the outer core, and must find their way to the atmosphere and ocean, the major driving force of the superplume has been considered to be the gravitationally unstable components at the centre of the earth (Maruyama 1994). Plume acts as a huge pipe that transfers the lighter elements from the CMB to the surface (Fig. 7.4).

## 7.5 Entrance and Exit of Fluids

How do fluids enter into the deeper portions of the earth and where do they exit? Perhaps the only entrance is the subduction zone in consuming plate boundaries. It has been proposed that during the early half of the earth history, the felsic continental crust on the surface which formed in an intra-oceanic environment has mostly been subducted into the deep mantle, except in the rare case of parallel arc collision (Santosh et al. 2009a). The growth history of continental crust shows that simultaneous with its formation, a considerable amount must have also been subducted. Such ongoing subduction process can be seen in the western Pacific region, through tectonic erosion, arc subduction and sediment-trapped subduction (Yamamoto et al. 2009). The process of Archean subduction aided in the sequestration of $CO_2$ from the ocean-atmosphere system to the mantle. Computations demonstrate that about a hundred to ten thousands times of the present atmospheric $CO_2$ level was subducted and was fixed in the Archean mantle (Santosh and Omori 2008a, 2008b).

The transportation of volatiles is controlled by the thermal history of the earth. In the early history of the hot earth, surface water could not penetrate deep into the upper mantle and water circulation was probably restricted to <100 km depth. A time integrated change of fluid input (entrance) into the earth can be traced. In order to understand the fluid circulation history within the earth, it is important to investigate the role of water, and when and how water entered the deep earth. Recent studies show that water began to enter into the mantle transition zone by subduction from the late Proterozoic (Maruyama and Okamoto 2007). Water penetration into the 410 km zone occurred possibly around 600 Ma. The entrance of huge volumes of water triggered the return flow of $CO_2$ back to the surface by the partial melting or subsolidus decarbonation of the subcontinental carbonated mantle (Fig. 7.5). Extensive $CO_2$ flushing in the late Proterozoic and its transfer into the ocean-atmosphere system possibly contributed to the greenhouse effect in the melting of snowball earth (Santosh and Omori 2008b). This also resulted in a drastic reduction of the carbonated upper mantle, a possible reason for the scarcity of $CO_2$-enriched ultra-high temperature granulite facies rocks in the Phanerozoic. Water acts as an effective lubricant and extensive water subduction in the young earth aided the smooth extrusion of deep subducted orogens, a possible reason for the common occurrence of ultrahigh-pressure rocks in Phanerozoic terrains and their near-absence in older terranes (Santosh et al. 2009b).

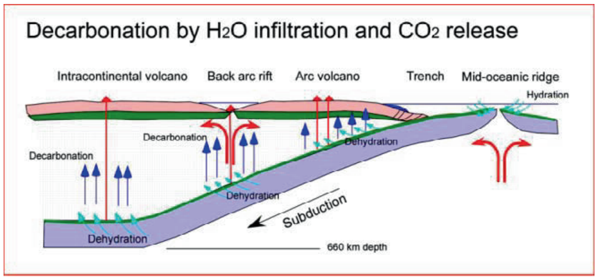

**Fig. 7.5** A schematic model showing $CO_2$ circulation mechanism from ocean-atmosphere through carbonated MORB to the metasomatised mantle wedge through subduction processes in the Archean (after Santosh and Omori 2008b). Carbonated MORB at spreading axes subduct along consuming plate boundary and undergo decarbonation. However the decreased $p(CO_2)$ in the Proterozoic and beginning of sedimentation of massive carbonate rock after 2.5 Ga resulted in the formation of hydrated MORB crust without any carbonate, marking the culmination of carbonation in the mantle wedge. The entrance of huge volumes of water triggered the return flow of $CO_2$ back to the surface by the partial melting or subsolidus decarbonation of the subcontinental carbonated mantle. The active role of both water and $CO_2$ are illustrated in this case. With permission from Elsevier

Whereas fluids enter through subduction zones, their exit is varied and occurs differently at different depth levels. The major exit from the deep mantle is perhaps through Ocean Island Basalt (OIB); in the early Archean fluids were transferred through OIB channels in aluminium depleted komatiites which mark the highest mantle potential temperature related to majorite (Komiya 2007). The shallow exits are dominantly plume-related or through divergent plate boundary zones.

The Archean OIB must have brought juvenile volatiles from deep mantle to the surface. Geochemists have long postulated a hidden juvenile and volatile bearing lower mantle (Jahn et al. 2001). On the other hand Komiya (2007) discussed substantial re-circulation of the earth's lithosphere, and that the whole mantle was melted to extract the basaltic component through geologic time to produce 500 km thick mid ocean ridge basalt (MORB) on the bottom of the mantle, now observed as 250–300 km D" prime layers as a fractionated portion of the mantle (Maruyama et al. 2007). Also seismic tomography shows slab graveyards back to 1 billion years related to Rodinia supercontinent assembly (Zhao et al. 2007). These findings may cast doubt on the existence of a juvenile primitive primordial lower mantle, and suggest that the volatile-enriched juvenile materials must have been ultimately derived from the outer core.

## 7.6 Movement of Volatiles

The global material circulation in our planet from the surface to the bottom of the mantle is controlled by a combination of plate, plume and anti-plate tectonics (Maruyama et al. 2007; Santosh et al. 2009b), with fluids and melts playing an active role. Whereas crustal fluids are dominated by $CO_2$ and $H_2O$ with subordinate $CH_4$ and $N_2$, the volatiles in the lower mantle are predominantly $CO_2$, although in future due to extensive water subduction, the scenario may be altered. A consideration of the availability and distribution of fluids in the earth shows that free fluid circulation may be restricted to specific zones, mostly along the plate boundaries and particularly along subduction zones where there is whole upper mantle-scale fluid circulation. Here the fluid is mostly water-dominated and the mantle transition zone from 410–660 km serves as a huge water tank where about 5 times the volume of all the water in the surface oceans can be stored in the dense hydrous silicates (Maruyama and Okamoto 2007). Fluid circulation within the dynamic earth is thus mostly limited to plate boundaries and plumes – both upwelling and downwelling. All other zones should generally be fluid absent. This also implies that all the other regions remain thermally stable through time, with no pronounced recrystallisation.

How many fluid factories exist within the earth? The major one is certainly related to subduction at shallow level, where sometimes methane-rich 'cold seep' and associated biological community occur as in the Nankai trough pf south-west Japan (Reed et al. 2002). The gas hydrates in these zones might constitute one of the future important sources for fuel. Fluids also transport chemical nutrients and heat which account for the biological community. The second major one is the metasomatic factory associated with subduction process, such as the jadeite-albitite rocks enriched in large ion lithophile elements (LILE) and high field strength elements (HFSE), formed through metasomatic fluid circulation (Morishita et al. 2007). Rodingites, ophicarbonates and other typical mineral assemblages indicate fluid infiltration, such as in the case of $CO_2$-metasomatism of a metabasite block within serpentine melange in south-west Japan where the $CO_2$-rich fluids were generated by devolatilisation reactions between serpentinite and graphite-bearing metasediments (Nishiyama 2004). The above cases illustrate fluids derived from subducting oceanic slab. Blueschist facies metamorphic rocks have long been considered as Na-metasomatised rocks; although this might be true in some sense, these rocks characterise the high P and low T metamorphism associated with oceanic plate subduction and subsequent exhumation through extrusion tectonics.

The third factory is the magma factory, essentially controlled by volatiles. In subduction zones no magmas can be formed in the absence of fluids. The major component in this tectonic setting is the volcanic front which can be generated by volatile driven mantle convection or secondary convection derived by the downgoing slab. Within the mantle wedge, melts can be generated by volatiles and extraction of TTG (tonalite-trondhjemite-granite) components occurs through arc magmatism.

The fourth factory is the 'big mantle wedge' proposed by Zhao et al. (2007), including whole upper mantle above subduction zone down to 660 km as documented in eastern Asia. Old slab can transport surface water into mantle transition zones generating a huge water storage at depths from 410–660 km. Back arc basin or small ocean basins can be formed by episodic mantle avalanche triggered by the collapse of stagnant slabs.

The region between the mantle transition zone and the CMB is a generally 'dull' area. The topmost mantle and the bottom mantle are the only two places where geotherms are intersected, and therefore these zones constitute the thermal boundary layers. The mid mantle is perhaps a very boring place with no vigorous fluid activity. Locally minor melts may be stable by increased water content on the top of the 410 km boundary. Bercovici and Karato (2003) proposed a transition-zone water-filter model where slabs subducting from cold lithosphere force up a broad background of passively upwelling ambient mantle which gets hydrated while passing through the high-water-solubility transition zone. When leaving the transition zone at the 410 km boundary, partial melting occurs thereby extracting water and filtering off the incompatible elements into the melt phase. The wet, enriched melt gathers into the high-melt fraction layer trapped above the 410 km and the residual solid portion of the upwelling ambient mantle which is buoyant, dry and depleted of incompatible elements, provides the MORB source region. In the case of mantle plumes the water-filtering mechanism is suppressed due the higher temperatures and velocities which result in reduced water-solubility and shorter residence times in the transition zone. Thus, little or no melting occurs while passing through the 410 km boundary and plumes arrive at the surface still relatively wet and enriched in compatible elements. Slabs efficiently entrain the melted material, returning water to the transition zone and incompatible elements to the deeper mantle.

CMB is the cooking place of recycled MORB where heating occurs from the core (Maruyama et al. 2007). However melts do not rise up because of the density cross over; instead they pool and spread across on the CMB and increase the volume of anti-crust through time. The volume of total crust on the CMB is speculated to be ten times more than the volume of total crust on the surface of the earth. Tomographic images indicate the origin of the superplume at the bottom of the mantle (Zhao et al. 2007). Volatile-driven buoyancy is one of the important requirements for the plumes to rise up. If this is model is valid, where did the volatiles come from? One potential source is the light elements in the outer core which promote buoyancy of superplume as a chemical plume. Rising plume enriched in volatiles heats the mantle transition zone at 660 km. If temperature is high enough to make majorite as a stable phase, plume cannot remain stagnant and enters more easily into the mantle transition zone from where it diverges horizontally into different directions such as seen in the case of the Pacific superplume (Zhao et al. 2007). In the mantle transition zones, hydrous ringwoodite and hydrous wudsleyite containing calcium, sodium, potassium, titanium, water and other minor elements metasomatise the rising plume (Maruyama et al. 2007). Finally, several independent plumes originate at 410 km penetrating up to the surface. Plumes are thus important carriers of volatiles and constitute the major fluid factory in the earth.

Plume interaction with the lithosphere causes dramatic fluid activity. When a plume hits a carbonated tectosphere, the keel on which old continents float, even small amounts of melts generated will be rich in $CO_2$ (Fig. 7.4) (Santosh and Omori [2008a, 2008b], Santosh et al. [2009b]). Rising plumes also bring about thermal and chemical erosion. All of these 'cooking' mechanisms bring about metasomatic alternations to the original geochemical signature of the plume formed at the CMB. This causes difficulties in geochemically differentiating the depth and origin of plumes and has led to the debate on whether plumes represent components from the earth's core, bottom of the 'juvenile' mantle or recycled material from different sources.

The curtain-like mantle upwelling ongoing at divergent plate boundaries are also significant in terms of volatile circulation in the earth (Zhao 2004). Although these are simple mantle convection and are not plumes, with only small amounts of volatiles such as those in the MORB magma, the volatiles may act as potential components in magma generation and dynamics. In general the volatile content is around 2 wt% for subduction zone magma and 0.2 wt% for MORB magma. $CO_2$ is extremely enriched in plumes associated with continental rift zones. The occurrence of carbonatites, kimberlites and other rock suites in rift zones may suggest systematic difference in the nature and proportion of volatile species at different sources in the mantle. The fundamental difference in the nature of volatiles between subduction zones and rift zones is that water dominates in the former and $CO_2$ dominates in the latter. In the case of collision zones, which are in fact paleo-subduction zones, passive margin sediments which commonly contain carbonate packages, liberate $CO_2$ and $H_2O$, mostly at shallow depths. At progressively deeper regions where eclogites and garnetites form, fluids are mostly anhydrous.

**Acknowledgements:** I thank Prof. Shigenori Maruyama for valuable discussion and suggestions. I am thankful to Prof. Somnath Dasgupta for kindly inviting me to contribute this article.

## 7.7 References

Bercovici D, Karato S (2003) Whole-mantle convection and the transition-zone water filter. Nature 425: 39–44

Hyndman RD, Shearer PM (2008) Water in the lower continental crust: modelling magnetotelluric and seismic reflection results. Geophys J International 98: 343–365

Hyndman RD, Yamano M, Oleskevich DA (2006) The seismogenic zone of subduction thrust faults. Island Arc 6: 244–260

Jahn BM, Wu F, Capdevila R, Martineau F, Zhao Z, Wang Y (2001) Highly evolved juvenile granites with tetrad REE patterns: the Woduhe and Baerzhe granites from the Great Xing'an Mountains in NE China. Lithos 59: 171–198

Komiya T (2007) Material circulation through time: Chemical differentiation within the mantle and secular variation of temperature and composition of the mantle. In: Yuen DA, Maruyama S, Karato S, Windley BF (eds) Superplumes: Beyond Plate Tectonics, Springer, Netherlands

Maruyama S (1994) Plume tectonics. Geological Society of Japan 100: 24–49

Maruyama S, Okamoto K (2007) Water transportation from the subducting slab into the mantle transition zone. Gondwana Res 11: 148–165

Maruyama S, Santosh M, Zhao D (2007) Superplume, supercontinent, and post-perovskite: Mantle dynamics and anti-plate tectonics on the Core-Mantle Boundary. Gondwana Res 11: 7–37

Morishita T, Arai S, Ishida Y (2007) Trace element compositions of jadeite (+omphacite) in jadeitites from the Itoigawa-Ohmi district, Japan: Implications for fluid processes in subduction zones. Island Arc 16: 40–56

Newton RC (1992) Charnockitic alteration: evidence for $CO_2$ infiltration in granulite facies metamorphism. J Metamorphic Geol 10: 383–400

Nishiyama T (2004) CO2-metasomatism of a metabasite block in a serpentine melange from the Nishisonogi metamorphic rocks, southwest Japan. Contrib Mineral Petrol 104: 35–46

Park J-O, Tsuru T, Kodaira S, Cummins PR, Kaneda Y (2002) Splay fault branching along the Nankai subduction zone. Science 297: 1157–1160

Peacock SM, Wang K (1999) Seismic Consequences of Warm Versus Cool Subduction Metamorphism: Examples from Southwest and Northeast Japan. Science 286: 937–939

Reed DW, Fujita Y, Delwiche E, Blackwelder DB, Sheridan PP, Uchida T, Colwell FS (2002) Microbial communities from methane hydrate-bearing deep marine sediments in a forearc basin. Applied and Environmental Microbiology 68: 3759–3770

Santosh M (1992) Carbonic fluids in granulites: cause or consequence? J Geol Soc India 39: 375–399

Santosh M, Omori S (2008a) $CO_2$ flushing: a plate tectonic perspective. Gondwana Res 13: 86–102

Santosh M, Omori S (2008b) $CO_2$ windows from mantle to atmosphere: Models on ultrahigh-temperature metamorphism and speculations on the link with melting of snowball earth. Gondwana Res 14: 82–96

Santosh M, Tsunogae T, Ohyama H, Sato K, Li JH, Liu SJ (2008) Carbonic metamorphism at ultrahigh-temperatures: Evidence from North China Craton. Earth Planet Sci Lett 266: 149–165

Santosh M, Maruyama S, Yamamoto S (2009a). The making and breaking of supercontinents: Some speculations based on superplumes, super downwelling and the role of tectosphere. Gondwana Res (under review)

Santosh M, Maruyama S, Komiya T, Yamamoto S (2009b) Orogens in the evolving earth: From surface continents to "lost continents" on the Core-Mantle Boundary. (submitted)

Sun A, Zhao D, Ikeda M, Chen Y, Chen Q (2008) Seismic imaging of southwest Japan using P and PmP data: Implications for arc magmatism and seismotectonics. Gondwana Res 14: 535–542

Tatsumi Y, Sakuyama M, Fukuyama H, Kushiro I (1983) Generation of arc basalt magmas and thermal structure of the mantle wedge in subduction zones. J Geophys Res 88: 5815–5825

Touret JLR (1985) Fluid regime in Southern Norway: the record of fluid inclusions. In: Tobi AC, Touret JLR (eds) The Deep Proterozoic Crust in the North Atlantic Provinces. Reidel, Dordrecht

Tsunogae T, Santosh M, Dubessy J (2008) Fluid characteristics of high- to ultrahigh-temperature metamorphism in southern India: a quantitative Raman spectroscopic study. Precambrian Res 162: 198–221

Wei W, Unsworth M, Jones A, Booker J, Tan H, Nelson D, Chen L, Li S, Solon K, Bedrosian P, Jin S, Deng M, Ledo J, Kay D, Roberts B (2001) Detection of Widespread fluids in the Tibetan crust by magnetotelluric studies. Science 292: 716–719

Yamamoto S, Senshu H, Rino S, Maruyama S (2009) Granite subduction, arc subduction, tectonic erosion and sediment subduction. Gondwana Res (under review)

Zhao D (2004) Global tomographic images of mantle plumes and subducting slabs: insight into deep earth dynamics. Phys Earth Planet Interiors 146: 3–34

Zhao D, Kanamori H, Negishi H, Wiens D (1996) Tomography of the source area of the 1995 Kobe earthquake: Evidence for fluids at the hypocenter? Science 274: 1891–1894.

8

# Laboratory Measurements of Ultrasonic Wave Velocities of Crustal Rocks at High Pressures and Temperatures: Petrological Structure of Izu-Bonin-Mariana Arc Crust

Masahiro Ishikawa and Makoto Arima

**Abstract:** To construct petrological model for island arc crusts having relatively higher geothermal gradient, we developed experimental techniques capable for simultaneous measurement of P- and S-wave velocities of an encapsulated rock specimen up to 1 GPa and 1000°C. In this paper we introduce our experimental methods and discuss petrological models of the Izu-Bonin-Mariana (IBM) island arc architecture. The models are constructed on the basis of our velocity measurement data at high temperatures and pressures and the seismic velocity profiles of the IBM arc crust previously reported (Suyehiro et al. 1996; Takahashi et al. 1998). These seismic velocity profiles clearly defined a stratified four-layered crustal structure for the IBM arc crust. Our ultrasonic laboratory measurements reveal that the IBM crust consists of a 5 km thick basaltic upper crust underlain by a 5 km thick tonalitic middle crust (Vp = 6.2–6.3 km/s) while the lower crust consist of a 3 km thick hornblende-bearing gabbro (Vp = 6.7–6.8 km/s) succeeded below by a 8 km thick pyroxenite or gabbroic rocks (Vp = 7.1–7.3 km/s). The more recent seismic experiments of the IBM arc further highlighted the relatively low-velocity (Vp = 7.4–7.7 km/s) domains located within the upper mantle immediately below the lower crust (Vp = 7.1–7.3 km/s) (Kodaira et al. 2007a, 2007b). Seismic reflectors were observed within and near the base of these low-velocity domains. Our data suggest that the low-velocity domains probably represent mixtures of various garnet-pyroxene-rich ultramafic rocks of crustal origin (restites after lower crustal anatexis and/or cumulates after magmatic differentiation) and mantle peridotites components.

---

Masahiro Ishikawa (✉) · Makoto Arima
Graduate School of Environment and Information Sciences, Yokohama National University, Tokiwadai,
Hodogaya-ku, Yokohama 2408501, Japan
e-mail: ishikawa@ynu.ac.jp

Makoto Arima
e-mail: arima@ed.ynu.ac.jp

## 8.1 Introduction

Evaluating elastic properties of rocks at high pressures and temperatures is a crucial approach for understanding the composition, structure and dynamics of the continental crusts. Successful petrological modelling of architecture of the continental crusts based on seismic velocity profiles requires experimental determination of seismic velocities of deep-seated crustal conditions. McSkimin (1950) first developed the ultrasonic interferometry techniques. This ultrasonic techniques have been used extensively to measure the elastic properties of rocks and minerals until today (e.g. Birch 1961; Anderson et al. 1968; Liebermann and Schreiber 1968; Kumazawa and Anderson 1969; Christensen and Fountain 1975; Jackson et al. 1981; Matsushima 1981; Gwanmesia et al. 1990; Spetzler at al. 1993; Miller and Christensen 1994; Ito and Tatsumi 1995; Li et al. 1996, 2004; Kern et al. 1997; Mueller and Massonne 2001; Shingai et al. 2001; Aizawa et al. 2001; Kitamura et al. 2003; Kono et al. 2004; Kung et al. 2004; Nishimoto et al. 2005; Higo et al. 2006; Irifune et al. 2008; Ishikawa et al. 2008).

Numerous attempts have been made to evaluate the composition of the earth's continental crust on the basis of velocity profiles derived from seismic refraction experiments and laboratory measurements of the elastic velocities of various crustal rocks (e.g. Christensen and Mooney 1995; Rudnick and Fountain 1995). Island arcs are the building blocks of continental crust and coalescence of island arcs along convergent margins is a fundamental process related to the growth of continental crusts (e.g. Taira et al. 1992; Condie 1997). Island arcs have been a special focus of numerous studies challenging the long-standing question, whether the bulk composition of island arc crust is andesitic or basaltic (e.g. Suyehiro et al. 1996; Taira et al. 1998; Fliedner and Klemperer 1999; Holbrook et al. 1999). In these studies, the petrological and chemical evaluations of arc crust are based on the velocity measurement at relatively low temperature (<600°C) or the velocity values obtained by extrapolation of those low-temperature data toward higher temperature conditions optimal to the island arc lower crustal regime. However the recent ultrasonic velocity measurements for the island arc rocks up to 800°C demonstrated a non-linear behaviour of temperature derivatives of P- and S-wave velocities at temperatures above 400°C and cast a critical question about reliability of such data extrapolations (e.g. Kono et al. 2004, 2006).

For last 10 years, we have developed experimental techniques to measure ultrasonic velocities of deep crustal rocks at high pressures and temperatures with a piston cylinder apparatus. Our initial research interest is focused on measurements of ultrasonic velocity of lower crustal rocks exposed in various Precambrian terrains, we conducted ultrasonic velocity measurements at pressures up to 1 GPa and temperatures up to 400°C by the pulse transmission technique with pure mode P- or S- transducers (Shingai et al. 2001; Kitamura et al. 2001; Ishikawa et al. 2008). Although these experimental studies provided valuable data sets to assess petrological characteristics of lower continental crust having relatively lower geothermal gradient, the temperature range of this experimental method (up to 400°C) is not applicable to the lower crust of modern volcanic island arc having a relatively higher thermal regime.

To understand elastic properties of rocks at lower crustal conditions of the present-day island arcs, we developed new experimental methods capable for P- and S-wave ultrasonic velocities measurement of rocks up to 1 GPa and 1000°C. High temperature measurement of elastic velocity over 400°C required modification of the high-pressure cell assembly of the piston cylinder apparatus. We have used the buffer rod technique that allows us to conduct ultrasonic velocities measurement up to 1000°C. The combination of the buffer rod technique and the pulse reflection method employing high resolution of MHz frequency makes it possible to measure the travel time precisely, thereby providing very accurate measurements of P- and S-wave velocities and thus Poisson's ratios, the bulk and shear modulus over 700°C at high pressure up to 1 GPa for various types of lower crustal rocks (Kono et al. 2004, 2006, 2008; Nishimoto et al. 2008).

The aims of this paper is to introduce our experimental techniques of ultrasonic wave velocity measurements with a piston cylinder type apparatus and to discuss petrological structure models of the island arc crusts such as Izu-Bonin-Mariana (IBM) arc in the western Pacific ocean regions.

## 8.2 Experimental Techniques of Ultrasonic Wave Velocity Measurements

Our experimental system consists of a high pressure temperature cell assembly, a piston-cylinder apparatus having a bore-hole of 34 mm diameter and 80 mm length, an arbitrary waveform generators (Tektronix: AWG2021) and a digital oscilloscopes (Hewlett-Packard: 54110A). Talc, pyrophyllite and boron nitride (BN) were used as the solid pressure-transmitting media to generate high pressure up to 1 GPa. The pressure scale was calibrated employing the phase transformation of quartz (high-low quartz transition; Groos and Heege 1973). The phase transformation of quartz results in a change in travel time of compressional waves through quartz crystal (Kono et al. 2004, 2008). The uncertainties in the pressure and temperature maxima are estimated to be 0.02 GPa (Kono et al. 2004; Kozai and Arima 2005; Nishimoto et al. 2005). High temperatures were achieved using a graphite heater and were monitored by a Pt–$Rh_{13}$ thermocouple. A thermocouple junction was placed upon the top end of the core rock sample. The temperature difference between the thermocouple junction and the top of the sample was ±15°C at the run temperature of 800°C and 1.0 GPa. The temperature differences between the thermocouple junction and several parts of the cylindrical rock sample were also measured. The maximum temperature difference within the cylindrical rock sample is about 54°C at 1000°C. Accuracy of the temperature is estimated to be less than ±7°C at 400°C, ±14°C at 700°C and ±27°C at 1000°C (Kono et al. 2004). The rock sample length was measured with a micrometre and the uncertainty is estimated to be about ±0.05 mm. We made velocity measurement after keeping each run for ~30–180 minutes at a given experimental P-T condition to confirm a steady travel time (Kono et al. 2004; Nishimoto et al. 2005). The waveforms were stored in the digital oscilloscope, which were sampled 4096 times for each run at a given P-T condition. The velocity value reported at a given P-T condition represents the average value. The maximum uncertainty in the measured Vp and Vs values are ±0.4%. After the high P-T experiments, all the run products were quenched and examined by an optical microscope and SEM-EDS.

### 8.2.1 *Pulse Transmission Technique*

We employed the pulse transmission technique and conducted high-pressure and high temperature ultrasonic velocity measurements for deep crustal rocks at pressures up to 1 GPa and temperature up to 400°C with a 34 mm borehole piston-cylinder apparatus (Shingai et al. 2001; Kitamura et al. 2003; Nishimoto et al. 2005; Ishikawa et al. 2008). The pulse transmission method has been described by Shingai et al. (2001), Nishimoto et al. (2005) and Ishikawa et al. (2008) (Fig. 8.1). Rock samples were cut into a 14 mm diameter core of length 12 mm. Both faces of the core sample were diamond-polished. The 24 hours-oven-dried core samples are loaded into a BN sleeve, which was then placed in the talc-pyrophyllite high-pressure cell. Pure-mode P- or S-wave lithium niobate ($LiNbO_3$) transducers were placed on both the upper and lower faces of the core cylinder. Travel times through a core sample of known length are measured using the pulse transmission technique.

### 8.2.2 *Pulse Reflection Technique with Pure-Mode Transducers*

Nishimoto et al. (2008) developed a new high pressure cell assembly to perform simultaneous measurements of Vp and Vs of a rock sample by the pulse reflection technique under high temperature and pressures (up to 1.0 GPa and 800°C), which are relevant to the lower crust of the modern volcanic arc (Fig. 8.2). The P- and S-wave travel times through a rock sample of known length have been measured simultaneously using the pulse reflection technique employing the buffer rod technique and pure-mode P- and S-transducers.

A core rock sample with a diameter of 14 mm and length 12 mm are used. A nickel tube with a diameter of 18 mm and of length 19.5 mm was directly placed at the top and bottom of a graphite heater (18 mm in diameter and 24 mm in length). The rock sample was placed in the BN sleeve, which is in turn was placed between an upper Pt-buffer rod and a lower Pt-buffer rod (length: 20 mm). A P-wave $LiNbO_3$ transducer with a diameter of 6 mm (36° Y-cut) was

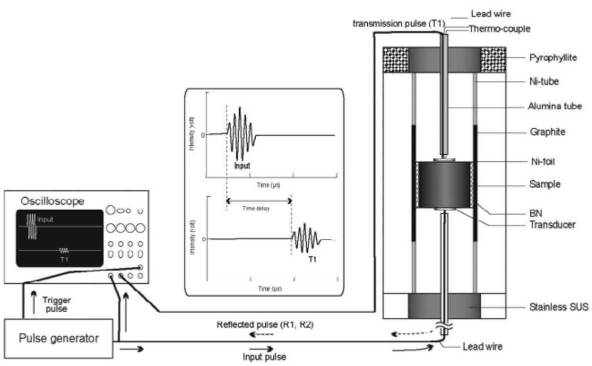

**Fig. 8.1** Schematic diagram of high pressure cell for pulse transmission technique with pure mode transducers. Schematic illustration of cell assembly and electrical circuit for the velocity measurements. The rock samples are loaded into a BN sleeve, which was then placed in the talc-pyrophyllite high-pressure cell. Pure-mode P- or S-wave lithium niobate transducers were placed on both front faces of a core sample

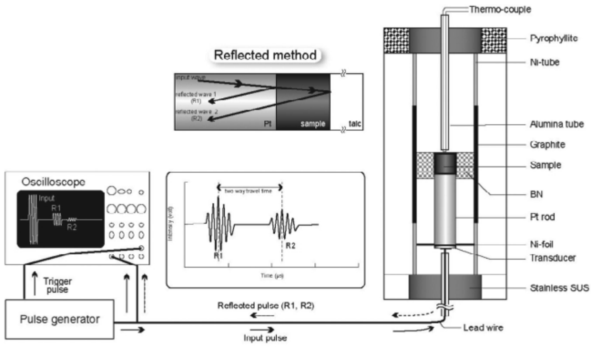

**Fig. 8.2** Schematic diagram of high pressure cell for pulse reflection technique with pure mode transducers. A rock sample was directly surrounded by a BN sleeve, which is in turn placed between an upper Pt-buffer rod and a lower Pt-buffer rod. A P-wave transducer was placed on the bottom end of the Pt-buffer rod and a S-wave lithium niobate transducer was placed on the top end of the other Pt-buffer rod. Arrows in cell assembly indicate reflected signals (R1 and R2) at both front faces of a core sample

placed on the top end of the Pt-buffer rod and a S-wave $LiNbO_3$ transducer of the same diameter (X–Z cut) was placed on the bottom end of the other Pt-buffer rod (Fig. 8.1). The Vp and Vs values of the rock sample were calculated using received sine waveform pulse with frequencies of 8 MHz and 4 MHz, respectively. This method allows us to obtain simultaneously P- and S-wave ultrasonic velocities of a rock up to 800°C and 1 GPa.

### *8.2.3 Pulse Reflection Technique with Dual Mode Transducers*

We developed new experimental methods employing pulse reflection technique with dual mode transducers, which enable us to measure simultaneously P- and S-wave ultrasonic velocities of an encapsulated rock up to 1 GPa and 1000°C. Employing this method, we carried out P- and S-wave measurements of a partially molten amphibolite, sealed in a Pt-capsule, up to 1000°C and 1.0 GPa (Kojo et al. 2007). In the high pressure talc-media cell assembly, an encapsulated specimen (5.7 mm diameter and 6.0 mm length) was placed in a BN sleeve to minimise the effect of $H_2O$ released from dehydration reaction of talc and pyrophyllite on rock velocities (Fig. 8.3). The cylindrical rock specimen was welded in to a Pt-capsule to avoid direct contact between the rock sample and the BN sleeve. Although hydrogen dissociated from $H_2O$ might diffuse through a Pt-capsule wall and might reach to the rock sample, a BN sleeve surrounding the Pt-capsule might suppress the hydrogen diffusion through Pt-capsule wall (Eggler et al. 1974). Kono et al. (2004) considered that hydrogen diffusion into the rock sample did not give significant effect on Vp measurements. A Pt-buffer rod of 20 mm length was placed between a rock sample and a 10°Y-cut $LiNbO_3$ transducer of dual mode, which simultaneously generate P and S waves (Fig. 8.1). No glue was used at interfaces between $LiNbO_3$ transducers, Pt-buffer rods and a Pt-capsule. Vp is determined with the pulse reflection technique by measuring of two-way travel time through the rock sample. As shown in Fig. 8.3, R1 is pulse reflected from the interface between the bottom of the rock sample and the base-wall of the Pt-capsule and R2 is the pulse reflected from the top of the rock sample and the top-wall of the Pt-capsule. The two-way travel time was determined by comparison with the arrival times of each pulse (R1 and R2).

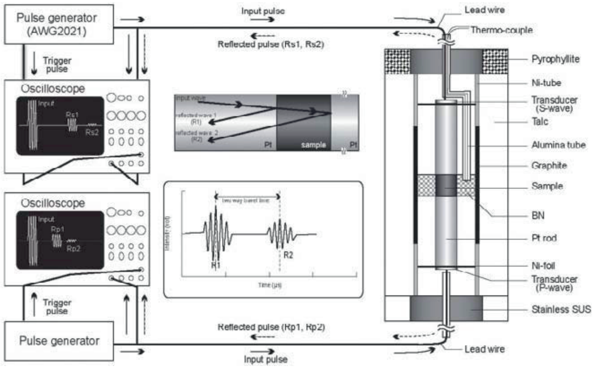

**Fig. 8.3** Schematic diagram of high pressure cell for pulse reflection technique with dual mode transducers. Schematic illustration of the piston-cylinder apparatus, cell assembly and electrical circuit for the Vp measurements. Arrows in cell assembly indicate reflected signals at lower Pt-rock (R1), upper Pt-rock (R2) and Pt-talc interfaces (R3)

## 8.3 Constraints on Crustal Composition of IBM Island Arc

Volcanic arcs are formed by subduction of an oceanic plate beneath an adjacent plate and magmatism in volcanic arc settings plays an important role of growth of the continental crust (Davidson and Arculus 2005). There are two types of volcanic arc systems: intra-oceanic arc system and continental arc system. In the former, fan oceanic plate has been subducted beneath an adjacent oceanic plate and an intra-oceanic arc crust has been developed on the adjacent plate, while in the latter case an oceanic crust has been subducted beneath an adjacent continental crust, on which a continental arc has been developed. In the western Pacific region, the subducting Pacific Plate has generated these two typed arc systems: (1) the IBM intra-oceanic arc system has been developed at the eastern margin of the Philippine sea plate, where the Pacific plate has been subducting beneath the Philippine sea plate along the Izu-Ogasawara-Mariana trench system and (2) the NE Honshu continental arc has been developed at the eastern margin of the North American plate, where the Pacific plate has been subducting beneath the North American plate along the Japan trench system. In the subduction zones along both trench systems, water released from dehydration of the subducted Pacific plate slab induced partial melting of the wedge mantle and generates basaltic magmas that buoyantly ascended and provided new materials for the arc crusts.

Whereas we collect the upper crustal rocks by geological sampling and deep drilling, the deeper portions of the crust are inaccessible to collect samples directly. Nevertheless, these deep portions of the island arc crust contain important information related to the bulk composition of the island arc crust as well as how it forms. Numerous studied have been carried out on exposed sections of ancient arc crusts such as the Kohistan terrain, Pakistan (e.g. Searle et al. 1999) and the Hidaka mountain, Japan (e.g. Osanai et al. 1992) and on lower crustal rock fragments (xenoliths) incorporated in

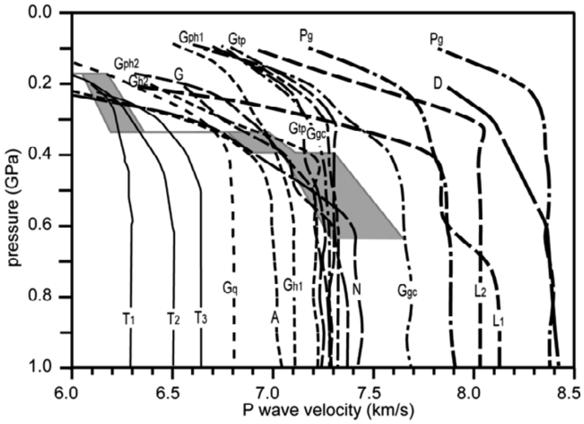

**Fig. 8.4** Comparison of the laboratory measurements of P-wave velocity of Tanzawa rocks with the P-wave velocity profile of northern IBM arc (Takahashi et al. 1998). Solid and dotted line: Measured P-wave velocity of Tanzawa plutonic rocks and other island arc rocks (the Ichinomegata xenoliths in the north-east Japan, the Takashima xenoliths in the south-west Japan and the Cretaceous Kohistan arc in Pakistan) at 25°C as a function of pressure. Shaded zone: Range of P-wave velocity profile of the northern IBM arc (Takahashi et al. 1998) adjusted to 25°C. Vp conversions are based on a temperature derivative of $\partial Vp/\partial T = 4.0 \times 10^{-4}$ km $s^{-1}$ °$C^{-1}$ (Rudnick and Fountain 1995) adopting various thermal gradients (0–40°C/km). Data are after Kitamura et al. (2003), Nishimoto et al. (2005) and Kono et al. (submitted). Details of petrography and/or chemical characteristics are described in these papers. T1: tonalite ($SiO_2$ = 71.1 wt%) from Tanzawa, T2: tonalite (64.1 wt%) from Tanzawa, T3: tonalite (56.4 wt%) from Tanzawa, Gq: quartz gabbro (53.7 wt%) from Tanzawa, A: amphibolite (36.3 wt%) from Ichinomegata, Gh1: hornblende gabbro (3.3 wt%) from Tanzawa, Gh2: hornblende gabbro (41.3 wt%) from Ichno-megata, Gph1: pyroxene hornblende gabbro (47.7 wt%) from Tanzawa, Gph2: pyroxene hornblende gabbro (43.8 wt%) from Ichinomegata, G: gabbro from Takashima, N: norite from Takashima, Gtp: two pyroxene granulite from Kohistan, Ggc: garnet-clinopyroxene granulite from Kohistan, Pg: garnet pyroxenite from Kohistan, D: dunite from Takashima, L1: lherzolite (46.2 wt%) from Ichinomegata, L2: lherzolite (47.2 wt%) from Ichinomegata

mantle derived magmas (e.g. Rudnick 1992). These studies collectively suggest that deeper portions of some island arc crusts would be composed mainly of anhydrous mafic plutonic (gabbroic) or granulite-facies mafic rocks. In contrast amphibolite and hornblende-bearing gabbroic xenoliths have been reported from Ichinomegata, north-eastern Japan (Aoki 1971) and from exposed middle crustal sections at Tanzawa mountain, central Japan (Kawate and Arima 1998). These hydrous mafic lower crustal rocks suggest a relatively high water activity at the middle and lower crustal portions of the arcs due to dehydration of hydrous oceanic plate subducted beneath the arcs. In addition to these geological and petrological investigations of lower crustal rocks, we have increasing understanding of the deeper portion of island arc crust over the last decade as a result of detailed seismological studies and high temperature-pressure measurements of ultrasonic wave velocity of lower crustal rocks. In this section we highlight our recent knowledge of the IBM island arc crust by integrating recent seismic velocity experimental data and laboratory measurements of ultrasonic velocity of arc rocks (Fig. 8.4).

### *8.3.1 Parent Magma Paradox*

Magmatism of intra-oceanic island arcs (subduction factory) has been recognised as one of crucial elements in crustal growth processes (Tatsumi and Eggins 1995; Tatsumi and Kogiso 2003; Tatsumi 2005; Davidson and Arculus 2005) and coalescence of island arcs along convergent margins is a fundamental process related to the growth of continental crusts (e.g. Taira et al. 1992; Condie 1997). The subduction factory has played an important role in chemical differentiation of the earth's crust and island arcs are thought to be the major sites of the generation of tonalitic magma throughout the earth's history. Bulk chemical composition of the continental crust has been estimated to be andesitic (e.g. Taylor and McLennan [1985]; Rudnick [1995]; Rudnick and Fountain [1995]; Wedepohl [1995]; Christensen and Mooney [1995]). One of the simple models to explain chemical characteristics of the continental crust is the arc-accretion model (Taylor 1967; Arculus 1981), which suggests the bulk chemical composition of island arcs is originally andesitic and all the materials of the island arcs are added to continental crusts. This model is probably applied to continental growth processes during Archean because magma generation of TTG in Archean greenstone belts could be related to slab melting processes (Martin 1986; Rollinson 2005). However the parental magmas in present day intra-oceanic arcs are basaltic. Present day intra-oceanic island arcs have been a special focus of such studies to solve the long-standing issue of mantle–crust material flux and its role of continental growth.

### *8.3.2 Velocity Structure*

Seismic experiments carried out at the northern IBM arc (Suyehiro et al. [1996]; Takahashi et al. [1998, 2007]; Kodaira et al. [2007a, 2007b]) and at the eastern Aleutian arc (Fliedner and Klemperer 1999; Holbrook et al. 1999) provide important constraints to understand the structure and composition of intra-oceanic arc crusts. The seismic studies of the northern IBM arc defined that the middle crust has seismic characteristics typical of felsic plutonic rocks (Vp = 6.0–6.3 km/s) at a depth ranging from 7 to 12 km (about 30% of the arc crust) overlying a mafic lower crustal layer

(Vp = 7.1–7.3 km/s; Suyehiro et al. 1996; Takahashi et al. 1998). Based on these velocity structures, Taira et al. (1998) suggest that $SiO_2$ composition of the arc is 56 wt%. These results clearly distinguish the northern IBM arc from the Aleutian arc in which such a 5 km thick ''continental crust-like'' layer is absent (Holbrook et al. 1999; Fliedner and Klempere 1999, 2000). This suggests that bulk chemical composition of the Aleutian arc crust is basaltic, in contrast to the andesitic composition of the northern IBM arc (Holbrook et al. 1999).

### *8.3.3 Linking Seismic Velocity to Lithology*

The Tanzawa mountains, central Japan, provide a unique opportunity to examine the felsic middle crust of the northern IBM arc. Collision of the northern IBM arc with the Honshu arc has been taking place since the middle Miocene (Soh et al. 1991). One manifestation of this collision is uplift and exposure of a Miocene (~7 Ma K–Ar ages; Saito et al. 1991) plutonic complex covering 140 km$^2$ in the Tanzawa mountains. The Tanzawa plutonic complex intruded into the Miocene (17–11 Ma) Tanzawa Group, which consists of submarine volcanic rocks with volcaniclastic and haemipelagic sediments metamorphosed up to pumpellyite–actinolite facies (Arai 1987). The complex consists predominantly of tonalite with subordinate hornblende gabbro and it has been interpreted as exposed deep crust of the northern IBM arc. The Tanzawa plutonic rocks are calc-alkaline and exhibit a wide variety of chemical compositions, ranging from 43–75 wt% $SiO_2$ (Kawate and Arima 1998). In order to develop a petrological model of the northern IBM arc crust, P-wave velocities of Tanzawa plutonic rocks and mafic/ultramafic rocks from Cretaceous Kohistan Arc were compared with the seismic velocity profile of the northern IBM arc.

### *8.3.4 Arc Crustal Lithology*

We have conducted ultrasonic velocity measurement of the crustal rocks of IBM arc at high pressures and high temperatures. Our early experiments were carried out at P <1.0 GPa and T <400°C using pulse transmission method (e.g. Kitamura et al. 2003). The more recent experiments have been made at P <1.0 GPa and T <800°C (Katsune et al. 2007). Kitamura et al. (2003) compared ultrasonic velocities of the Tanzawa plutonic rocks with the seismic velocity profile of the northern IBM arc (Suyehiro et al. 1996; Takahashi et al. 1998) assuming a geothermal gradient of 40°C/km as the maximum value of the northern IBM arc crust (Nakajima and Arima 1998). The temperature derivative of the P-wave velocity ($\partial Vp/\partial T =$ 0.3 to 0.5 × 10$^{4}$ km s$^{-1}$ °C$^{-1}$) obtained by the study is one order of magnitude lower than those reported by Rudnick and Fountain (1995) for an average of crustal rocks ($\partial Vp/\partial T =$ 4.0 × 10$^{-4}$ km s$^{-1}$ °C$^{-1}$). Since measurements of Kitamura et al. (2003) were limited up to 400°C, they could not confirm this relationship. Therefore, they converted the seismic P-wave velocity profile of the IBM arc defined by Suyehiro et al. (1996) and Takahashi et al. (1998) to P-wave velocity profiles at 25°C using a temperature derivative of 4.0 × 10$^{-4}$ km s$^{-1}$ °C$^{-1}$. Subsequent experiments on the Tanzawa hornblende gabbros combining the buffer rod technique and the pulse reflection method were carried out at higher temperatures up to 800°C by Katsune et al. (2007). The P-wave velocity measurements at 1.0 GPa in the hornblende gabbros yielded the temperature derivative of the P-wave velocity ($\partial Vp/\partial T$) = 4.2 to 4.8 × 10$^{-4}$ km s$^{-1}$ °C$^{-1}$. The experimental results support the early assumption of $\partial Vp/\partial T =$ 4.0 × 10$^{-4}$ km s$^{-1}$ °C$^{-1}$ and the interpretation of crustal structure of Kitamura et al. (2003).

Because of a wide range of measured heat flow values for the IBM arc (Yamazaki 1992), we adopted various thermal gradients which ranges from a typical island arc thermal gradient of 25°C km$^{-1}$ (Furukawa 1993) to the maximum value of 40°C km$^{-1}$ (Nakajima and Arima 1998) to infer the thermal structure of the IBM arc. The measured P-wave velocities of the Tanzawa tonalites well correspond to the middle crust (Vp = 6.1–6.3 km/s) defined by the seismic velocity profiles by Suyehiro et al. (1996) and Takahashi et al. (1998). Velocities of the hornblende gabbro are equivalent to the upper portion of lower crust (Vp = 6.7–6.8 km/s) of the profiles. Although Taira et al. (1998) interpreted that the top layer of lower crust (Vp = 6.7–6.8 km/s) consists of tonalitic rocks; our rock velocity data suggest that this layer is better modeled by the hornblende gabbro than tonalitic rocks. The more recent ultrasonic wave velocity measurements of the Tanzawa hornblende gabbros yielded Vp = 7.1 km/s at 25°C and 6.6 km/s at 800°C at 1.0 GPa (Katsune et al. 2007). These data also suggest that the uppermost layer of lower crust may consist of hornblende gabbro. In addition, the Vp-density relations of the Tanzawa rocks show a large difference in acoustic impedance between the tonalities (16.6–17.8 × 10$^6$ kg m$^{-2}$ s$^{-1}$) and the hornblende gabbro (21.1 × 10$^6$ kg m$^{-2}$ s$^{-1}$) (Fig. 8.5). This high impedance contrast is consistent with the seismic experimental results of Takahashi et al. (1998), which reported a strong reflector between the middle and lower crust layers.

The P-wave velocities measured for the Tanzawa gabbroic rocks at 800°C and 1 GPa (Vp = ~6.6 km/s) are significantly lower than those of the lowermost layer of low crust (Vp = 7.1–7.3km/s) defined by Suyehiro et al. (1996) and Takahashi et al. (1998). On the basis of the melting experiments of hydrous low-K tholeiite composition, Nakajima and Arima (1998) suggested that the lowermost crust of the northern IBM arc is probably composed of pyroxenite-restites. On the basis of mineral velocity data, Kitamura and

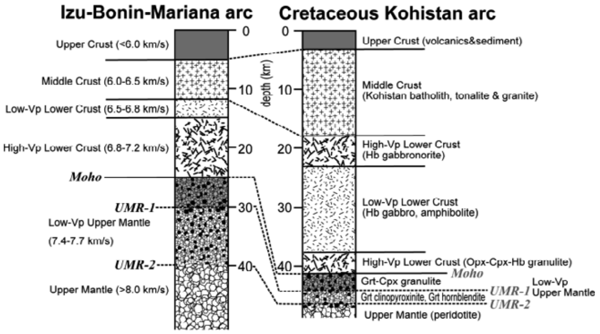

**Fig. 8.5** Comparison of the IBM arc and the Kohistan arc. (a) Seismic velocity structure in the IBM arc, which Tatsumi et al. (2008) generalised using seismic velocity structure and seismic reflectors after Suyehiro et al. (1996), Takahashi et al. (2007, 2008) and Kodaira et al. (2007b). Seismic data of the IBM arc shows the presence of a middle crust with a P-wave velocity (Vp) of 6.0–6.5 km/s, a 6.5–6.8 km/s Vp layer at the upper layer of the lower crust, a high-velocity (Vp = 6.8–7.2 km/s) lower crust and an uppermost mantle exhibiting rather low velocities (Vp = 7.4–7.7 km/s). The Moho of the IBM arc is identified as velocity jump from 6.8–7.2 to 7.4–7.7 km/s. Sub-Moho seismic reflectors are also recognised within and near the base of the low-velocity domains in the uppermost mantle (UMR-1 and UMR-2). (b) Unit volume of each layer of the Cretaceous Kohistan arc crust across the Karakorum highway. Volumes of each layer are calculated on the basis of the observed volume in the field and previous data (Miller and Christensen 1994; Yamamoto and Yoshino 1998). The seismically determined sub-IBM Moho might correspond to the mafic restite/cumulate layer at the basal part of the Kohistan arc. The basal part of the Kohistan arc is much thinner than that of the low-Vp upper mantle layer of the IBM arc although middle crust of the Kohistan arc is much thicker than that of the IBM arc

Ishikawa (1998) suggest that the lower crust (Vp = 7.1–7.3 km/s) is composed of norite, troctolite or orthopyroxenite.

Kono et al. (2004) measured the compressional wave velocities (Vp) of mafic and ultramafic rocks from the Kohistan arc terrain, which is considered as an exposed intra-oceanic island arc of Cretaceous age separating the Indian plate to the south from the Karakoram (Asian) plate to the north within the Indus suture zone of north Pakistan (Searle et al. 1999). The ultrasonic experiments at 1.0 GPa and 800°C yielded Vp = 7.0 km/s for the Kohistan two pyroxene granulite (plagioclase 62%, clinopyroxene 13%, orthopyroxene 22%, hornblende 2%), Vp = 7.1 km/s for the Kohistan pyroxene granulite (plagioclase 61%, clinopyroxene 13%, orthopyroxene 19%, hornblende 2%), Vp = 7.5km/s for the Kohistan websterite (olivine 8%, clinopyroxene 63%, orthopyroxene 17%, spinel 2%) and Vp = 7.6 km/s for the Kohistan wehrlite (olivine 75%, clinopyroxene 21%, orthopyroxene 1%, hornblende 2%, spinel 1%), respectively. These results also support the view that the IBM lower crust may consist of gabbronorite, norite and/or orthopyroxene-rich rocks. The similar lower crustal lithology is also suggested by the petrological modelling of arc magma generation and differentiation in the IBM arc by Tatsumi et al. (2008).

### *8.3.5 Sub-moho Lithology*

On the basis of the recent seismic velocity profiles defined for the IBM arc (Suyehiro et al. [1996]; Takahashi et al. [1998]; Takahashi et al. [2007, 2008]; Kodaira et al. [2007a, 2007b]). Tatsumi et al. (2008) proposed petrological models for arc magma generation and differentiation and discussed the petrological characteristics of the sub-arc Moho and the uppermost sub-arc mantle of the IBM arc. They highlighted the relatively low-velocity (Vp = 7.4–7.7 km/s) domains typically distributed within the upper mantle immediately below the lower crust (Vp = 7.1–7.3 km/s) and the seismic reflectors observed within and near the base of the low-velocity domains in the uppermost mantle (Fig. 8.5). Generally the Moho discontinuity is a sharp seismological boundary that separates lower crust layer with Vp of 6–7 km/s from sub-arc mantle with velocities of about 8 km/s. The sub-Moho ‘‘mantle’’ beneath the IBM arc, however possesses relatively lower Vp = 7.4–7.7 km/s than the typical mantle. Their model suggests that the volume of mafic restite and cumulates that are “crustal residues” resulting from the evolution of middle and upper arc crust is estimated to be at least 3–9 times greater than that of the seismically defined IBM lower crust (Vp = 7.1–7.3 km/s). In order to explain this ‘‘excess crustal residues’’ in the IBM arc, they proposed that the mafic to ultramafic components produced by crustal anatexis (restites) and magma differentiation (cumulates) exist within the evolving arc crust, which were largely transformed into the uppermost mantle. They further suggested that the sub-arc Moho could be the boundary between the remaining initial basaltic arc crust and melting residues or restites, which represents the former melting front during crustal anatexis. The transformed crustal component distributed in the sub-arc low-velocity (Vp = 7.4–7.7 km/s) domains is estimated to be ultramafic rocks of garnet + clinopyroxene ± orthopyroxene + plagioclase assemblage distinct from the sub-arc mantle harzburgite. These uppermost garnet-clinopyroxene-plagioclase rocks may be separated from the arc lithosphere and descend to the deep mantle. Since this ‘‘crustal delamination’’ may take place necessarily during the process of arc crust growth or arc evolution, accumulation of crustal components somewhere in the deep mantle could play a key role in the evolution of mantle geochemical reservoirs.

Garnet-bearing rocks are not exposed in the Tanzawa mountain of the Izu Collision zone but widely exposed in the Kohistan arc terrane (Yamamoto and Yoshino 1998). Along the southern margin of Kohistan arc terrane, originally magmatic lower crustal rocks of garnet + clinopyroxene ± orthopyroxene ± hornblende ± plagioclase association are exposed along with mantle peridotite in the Jijal complex (dunites, harzburgites and websterites) (Yamamoto and Yoshino 1998). Kono et al. (2003) measured the compressional wave velocities of a garnet granulite, a garnet pyroxenite and a dunite from the lowest structural portion of the Kohistan arc terrain. The experiments at 1.0 GPa and 900°C yielded Vp = 7.2 km/s for the garnet granulite, Vp = 7.5 km/s for the garnet pyroxenite and Vp = 8.0 km/s for the dunite, respectively. These results support the view that the relatively low-velocity (Vp = 7.4–7.7 km/s) sub-arc mantle domains of the IBM arc, which typically distributed within the upper mantle immediately below the lower crust (Vp = 7.1–7.3 km/s) are not composed of mantle peridotite (Tatsumi et al. 2008). The low-velocity domains (Vp = 7.4–7.7 km/s) probably represent a mixture of garnet-pyroxene-rich ultramafic restite derived from lower crustal anatexis and/or cumulate generated by magmatic differentiation and peridotite component of mantle origin.

**Acknowledgements:** We thank Professor Alok K. Gupta for inviting us to the Special Platinum Jubilee Issue of the Indian National Science Academy. This study was supported by the Grant-in-Aid for Scientific Research provided by the Japanese Society for the Promotion of Science to M.A. (19340160) and M.I. (19540502).

## 8.4 References

Aoki K (1971) Petrology of mafic inclusions from Ichino-megata, Japan, Contributions to Mineralogy and Petrology 30: 314–331

Aizawa Y, Ito K, Tatsumi Y (2001) Experimental determination of compressional wave velocity of olivine aggregate up to 1000°C at 1 GPa. Tectonophysics 339: 473–479

Anderson OL, Schreiber E, Liebermann RC, Soga N (1968) Some elastic constant data on minerals relevant to geophysics. Rev Geophys 6: 491–524

Arai T (1987) Tectonics of Tanzawa mountains: constraints from metamorphic petrology. J Geological Society Japan 93: 185–200

Arculus RJ (1981) Island arc magmatism in relation to the evolution of the crust and mantle. Tectonophysics 75: 113–133

Birch F (1961) The velocity of compressional waves in rocks at 2–10 kbar. J Geophys Res 66: 2199–2224

Christensen NI, Fountain DM (1975) Constitution of the lower continental crust based on experimental studies of seismic velocities in granulite. Bull Geolo Soc Am 86: 227–236

Christensen NI, Mooney WD (1995) Seismic velocity structure and composition of the continental crust: A global view. J Geophys Res 100: 9761–9788

Condie KC (1997) Plate Tectonics and Crustal Evolution, Butterworth-Heinemann, Oxford

Davidson JP, Arculus RJ (2005) The significance of Phanerozoic arc magmatism in generating continental crust. In: Brown M, Ruchmer T (eds) Evolution and Differentiation of the Continental Crust. Cambridge University Press, Cambridge

Eggler DH, Mysen BO, Hoering TC (1974) Gas species in sealed capsules in solid-media, high pressure apparatus. Year Book 73: 228–232, Carnegie Inst, Washington DC

Fliedner MM, Klemperer SL (1999) Structure of an island-arc: Wide-angle seismic studies in the eastern Aleutian Islands, Alaska. J Geophys Res 104: 10667–10694

Fliedner MM, Klemperer SL (2000) Crustal structure transition from oceanic arc to continental arc, eastern Aleutial Islands and Alaska Peninsula. Earth Planet Sci Lett 179: 567–579

Furukawa Y (1993) Magmatic processes under arc and formation of the volcanic front. J Geophys Res 98: 8309–8319

Groos AF, Heege JP (1973) The high-low quartz transition up to 10 kbars pressure. J Geology 81: 717–724

Gwanmesia GD, Rigden SM, Jackson I, Liebermann RC (1990) Pressure dependence of elastic wave velocity for β-Mg2SiO4 and the composition of the earth's mantle. Science 250: 794–797

Higo Y, Inoue T, Li B, Irifune T, Liebermann RC (2006) The effect of iron on the elastic properties of ringwoodite at high pressure. Phys Earth Planet Inter 159: 276–285

Holbrook WS, Lizarralde D, McGeary S, Bangs N, Diebold J (1999) Structure and composition of the Aleutian island arc and implications for continental crustal growth. Geology 27: 31–34

Irifune T, Higo Y, Inoue T, Kono Y, Ohfuji H, Funakoshi K (2008) Sound velocities of majorite garnet and the composition of the mantle transition region. Nature 451: 814–817

Ishikawa M, Kanao M (2002) Structure and collision tectonics of Pan-African orogenic belt -Scientific significance of the geotransect for a supercontinent: Gondwanaland. Bulletin of the Earthquake Research Institute, Tokyo University 77: 287–302 (in Japanese with English abstract)

Ishikawa M, Shingai E, Arima M (2008) Elastic properties of high-grade metamorphosed igneous rocks from Enderby Land and eastern Dronning Maud Land, Antarctica: evidence for biotite-bearing mafic lower crust. In: Satish-Kumar et al. (eds) Geodynamic Evolution of East Antarctica: A Key to the East–West Gondwana Connection. Geological Society London, Special Publications, 308: 183–194.

Ito K, Tatsumi Y (1995) Measurement of elastic wave velocities in granulite and amphibolite having identical $H_2O$-free bulk compositions up to 850°C at 1 GPa. Earth Planet Sci Lett 133: 255–264

Jackson I, Niesler H (1982) The elasticity of periclase to 3 GPa and some geophysical implications. In: Manghnani M, Syono Y (eds) High Pressure Research: Application to Earth and Planetary Sciences. Terra Scientific Publishing Co and American Geophysical Union, Tokyo and Washington DC

Kanao M, Ishikawa M (2004) Origins of the lower crustal reflectivity in the Lutzow-Holm Complex, Enderby Land, East Antarctica. Earth Planets Space 56: 151–162

Katsune G, Ishikawa M, Arima M (2007) Laboratory measurements of elastic wave velocities in the Tanzawa hornblende gabbro at high pressure and temperatures. Abstract of the Geological Society of Japan 114: 264 (in Japanese)

Kawate S, Arima M (1998) Petrogenesis of the Tanzawa plutonic complex, central Japan: exposed felsic middle crust of the Izu–Bonin–Mariana arc. Island Arc 7: 342–358

Kern H, Liu B, Popp T (1997) Relationship between anisotropy of P and S-wave velocities and anisotropy of attenuation in serpentinite and amphibolite. J Geophys Res 102: 3051–3065

Kitamura K, Ishikawa M (1998) Rock velocities at atmospheric pressure and room temperature in Tanzawa plutonic rocks from central Japan. In: Motoyoshi Y, Shiraishi K (eds) Origin and Evolution of Continents. Memoirs of National Institute of Polar Research Spec Issue 53

Kitamura K, Ishikawa M, Arima M, Shiraishi K (2001) Laboratory measurements of P-wave velocity of granulites from Lützow-Holm Complex, East Antarctica: Preliminary report. Polar Geoscience 14: 180–194

Kitamura K, Ishikawa M, Arima M (2003) Petrological model of the northern Izu–Bonin–Mariana arc crust: constraints from high-pressure measurements of elastic wave velocities of the Tanzawa plutonic rocks, central Japan. Tectonophysics 371: 213–221

Kodaira S, Sato T, Takahashi N, Ito A, Tamura Y, Tatsumi Y, Kaneda Y (2007a) Seismological evidence for variable growth of crust along the Izu intraoceanic arc. J Geophys Res 112: B05104, doi: 10.1029/2006JB004593

Kodaira S, Sato T, Takahashi N, Miura S, Tamura Y, Tatsumi Y, Kaneda Y (2007b) New seismological constraints on growth of continental crust in the Izu-Bonin intra-oceanic arc. Geology 35: 1031–1034

Kono Y, Ishikawa M, Nakajima T, Khan S R, Arima M (2003) Strong decrease in ultrasonic Vp in lower crustal rocks at high temperature. Eos Trans. AGU 84 (46) Fall Meet Suppl Abstract F1441

Kono Y, Ishikawa M, Arima M (2004) Discontinuous change in temperature derivative of Vp in lower crustal rocks. Geophys Res Lett 31: L22601, doi: 10.1029/2004GL020964

Kono Y, Ishikawa M, Arima M (2006) Laboratory measurements of P- and S-wave velocities in polycrystalline plagioclase and gabbronorite up to 700°C and 1 GPa: Implications for the low velocity anomaly in the lower crust. Geophys Res Lett 33: L15314, doi: 10.1029/2006GL026526

Kono Y, Ishikawa M, Arima M (2007) Effect of $H_2O$ released by dehydration of serpentine and chlorite on compressional wave velocities of peridotites at 1 GPa and up to 1000°C. Physics of the Earth and Planetary Interiors doi: 10.1016/j.pepi.2007.02.005

Kono Y, Miyake A, Ishikawa M, Arima M (2008) Temperature derivatives of elastic wave velocities in plagioclase ($An_{51\pm1}$) above and below the order-disorder transition temperature. Am Mineralogist 93: 558–564

Kono Y, Ishikawa M, Harigane Y, Michibayashi K, Arima M (2008) P- and S-wave velocities of the lowermost crustal rocks from the Kohistan arc: Implications for seismic Moho discontinuity attributed to abundant garnet (submitted)

Kojo S, Arima M, Ishikawa M (2007) Elastic wave velocities and Poisson's ratios of amphibolite up to 900°C at 1.0 GPa: Effect of dehydration melting on Poisson's ratio of mid- to lower crustal rock. EOS Trans. 88 (52) MR31C-0530, 2

Kozai Y, Arima M (2005) Experimental study on diamond dissolution in kimberlitic and lamproitic melts at 1300–1420°C and 1 GPa with controlled oxygen partial pressure. Am Mineralogist 90: 1759–1766

Kumazawa M, Anderson OL (1969) Elastic moduli, pressure derivatives and temperature derivatives of single-crystal olivine and single-crystal forsterite. J Geophys Res 74: 5961–5972

Kung J, Li B, Uchida T, Wang Y, Neuville D, Liebermann RC (2004) In situ measurements of sound velocities and densities across the orthopyroxene->high-pressure clinopyroxene transition in MgSiO3 at high pressure. Phys Earth Planet Interiors 147: 27–44

Li B, Rigden SM, Liebermann RC (1996) Elasticity of stishovite at high pressure. Phys Earth Planet Inter 96: 113–127

Li B, Kung J, Liebermann RC (2004) Modern techniques in measuring elasticity of earth materials at high pressure and high temperature using ultrasonics in conjunction with synchrotron X-radiation. Phys Earth Planet Interiors 143–144: 559–574

Liebermann RC, Schreiber E (1968) Elastic Constants of Polycrystalline Hematite as a Function of Pressure to 3 Kilobars. J Geophys Res 73: 6585–6590

Martin H (1986) Effects of steeper Archean geothermal gradient on geochemistry of subduction-zone magmas. Geology 139: 753–756

Matsushima S (1981) Compressional and shear wave velocities of igneous rocks and volcanic glasses to 900°C and 20 kbar. Tectonophysics 75: 257–271

McSkimin HJ (1950) Ultrasonic measurement techniques applicable to small solid specimens. J Acoust Soc Am 22: 413–418

Miller DJ, Christensen NI (1994) Seismic signature and geochemistry of an island arc: A multidisciplinary study of the Kohistan accreted terrane, northern Pakistan. J Geophys Res 99: 11623–611642

Mueller HJ, Massonne H-J (2001) Experimental high pressure investigation of partial melting in natural rocks and their influence on Vp and Vs. Physics and Chemistry of the Earth Part A: Solid Earth and Geodesy 26: 325–332

Nakajima K, Arima M (1998) Melting experiments on hydrous low-K tholeiite: implication for the genesis of tonalitic crust in the Izu–Bonin–Mariana arc. Island Arc 7: 359–373

Nishimoto S, Ishikawa M, Arima M, Yoshida T (2005) Laboratory measurement of P-wave velocity in crustal and upper mantle xenoliths from Ichino-megata, nort-east Japan: ultrabasic hydrous lower crust beneath the NE Honshu arc. Tectonophysics 396: 245–259

Nishimoto S, Ishikawa M, Arima M, Yoshida T, Nakajima J (2008) Simultaneous high P-T measurements of ultrasonic compressional and shear wave velocities in Ichino-megata mafic xenoliths: Their bearings on seismic velocity perturbations in lower crust of northeast Japan arc. J Geophys Res doi: 10.1029/2008JB005587, in press

Osanai Y, Owada M, Kawasaki, T (1992) Tertiary deep crustal ultrameta- morphism in the Hidaka metamorphic belt, northern Japan. J Metamor Geology 10: 401–414

Rudnick LR (1992) Xenoliths-samples of the lower continental crust. In: Fountain DM, Arculus R, Kay RW (eds) Continental Lower Crust, Elsevier, Amsterdam

Rudnick LR (1995) Making continental crust. Nature 378: 571–578

Rollinson H (2005) Crustal genaration in the Arachean. In: Brown M, Ruchmer T (eds) Evolution and Differentiation of the Continental Crust, Cambridge University Press, Cambridge

Rudnick RL, Fountain DM (1995) Nature and composition of the continental crust: A lower crustal perspective. Review of Geophysics 33: 267–309

Saito K, Otomo I, Takai T (1991) K–Ar dating of the Tanzawa tonalitic body and some restrictions on the collision tectonics in the South Fossa Magna, central Japan. J Geomagn Geoelectr 43: 921–935

Searle MP, Khan MA Fraser JE, Gough SJ, Jan MQ (1999) The tectonic evolution of the Kohistan-Karakoram collision belt along the Karakoram Highway transect, north Pakistan. Tectonics 18: 929–949

Shingai E, Ishikawa M, Arima M (2001) P-wave velocity in ultrahigh temperature granulites from the Archean Napier Complex, East Antarctica. Polar Geoscience 14: 165–179

Soh W, Pickering TK, Taira A, Tokuyama H (1991) Basin evolution in the arc–arc Izu Collision Zone, Mio–Pliocene Miura Group, central Japan. J Geol Soc Lond 148: 317–330

Spetzler HA, Chen G, Whitehead S, Getting IC (1993) A new ultrasonic interferometer for the determination of equation of state parameters of sub-millimeter single crystals. In: Liebermann RC, Sondergeld CH (eds) Experimental Techniques in Mineral and Rock Physics. Pure Applied Geo Phy 141: 341–377

Suyehiro K, Takahashi N, Ariie Y, Yokoi Y, Hino R, Shinohara M, Kanazawa T, Hirata N, Tokuyama H, Taira A (1996) Continental crust, crustal underplating and low-Q upper mantle beneath an oceanic island arc. Science 272: 390–392

Taira A, Pickering TK, Windley BF, Soh W (1992) Accretion of Japanese Island arcs and implications for the origin of Archean greenstone belts. Tectonics 11: 1224–1244

Taira A, Saito S, Aoike K, Morita S, Tokuyama H, Suyehiro K, Takahashi N, Shinohara M, Kiyokawa S, Naka J, Klaus A (1998) Nature and growth rate of the Northern Izu–Bonin (Ogasawara) arc crust and their implication for continental crust formation. Island Arc 7: 395–407

Takahashi N, Suyehiro K, Shinohara M (1998) Implications from the seismic crustal structure of the northern Izu–Bonin arc. Island Arc 7: 383–394

Takahashi N, Kodaira S, Klemperer S, Tatsumi Y, Kaneda Y, Suyehiro K (2007) Structure and evolution of Izu-Ogasawara (Bonin) - Mariana oceanic island arc crust. Geology 35: 203–206

Takahashi N, Kodaira S, Tatsumi Y, Kaneda Y, Suyehiro K (2008) Structure and growth of the Izu-Bonin-Mariana arc crust: 1. Seismic constraint on crust and mantle structure of the Mariana arc–back-arc system. J Geophys Res 113: B01104, doi: 10.1029/2007 JB005020

Tatsumi Y, Eggins S (1995) Subduction Zone Magmatism. Blackwell Sci, Boston

Tatsumi Y (2005) The subduction factory: How it operates in the evolving earth. GSA Today 15: 4–10

Tatsumi Y, Kogiso T (2003) The subduction factory: Its role in the evolution of the earth's crust and mantle. In: Larter RD, Leat PT (eds) Geological Soc of London, Special Publication, Geologcal Society London

Tatsumi Y, Shukuno H, Tani K, Takahashi N, Kodaira S, Kogiso T (2008) Structure and growth of the Izu-Bonin-Mariana arc crust: 2. Role of crust-mantle transformation and the transparent Moho in arc crust evolution. J Geophys Res 113: B02203, doi: 10.1029/2007JB005121

Taylor RN (1967) The origin and growth of continents. Tectonophysics 4: 17–34

Taylor SR, McLennan SM (1985) The Continental Crust: Its Composition and Evolution, Blackwell, Boston

Webb SL (1989) The elasticity of the upper mantle orthosilicates olivine and garnet to 3 GPa. Phys Che Miner 16: 684–692

Wedepohl KH (1995) The composition of the continental crust. Geochimica Cosmochimica et Acta 59: 1217–1232

Yamazaki T (1992) Heat flow in the Izu-Ogasawara (Bonin) -Mariana Arc. Bulletin of Geological Survey Japan 43: 207–235

Yamamoto H, Yoshino T (1998) Superposition of replacements in the mafic granulites of the Jijal complex of the Kohistan arc, northern Pakistan: dehydration and rehydration within deep arc crust. Lithos 43: 219–234.

# 9

# Seismic Imaging of the Mantle Discontinuities Beneath India: From Archean Cratons to Himalayan Subduction Zone

Shyam S. Rai, K. Suryaprakasam and V. K. Gaur

**Abstract:** We image the mantle discontinuities in the depth from ~200–800 km beneath India from its southernmost Archean and Proterozoic cratons, Proterozoic mobile belts to the Himalayan subduction zone using P to S converted phases in the 1957 teleseismic waveforms recorded over 54 broadband seismograph locations. These phases are generated from the velocity contrast at the layer boundary. Our results show presence of Lehmann discontinuity at a depth of 220–250 km beneath southern part of India. The 410 discontinuity is sharp and at its normal depth beneath Precambrian terrains and is elevated by ~ 10–15 km in the Ganges basin and the Himalaya. This suggests progressive cooling or thickening of the Indian lithosphere towards its northern margin. We observe a complex 660 km discontinuity with a broad double peak beneath the Himalaya and southern India that may be due to presence of non-olivine component in the deep mantle. Apart from the above mentioned global discontinuities a velocity interface is mapped at 475 km depth beneath the Ladakh. The mantle transition zone show ~ 10 km thickening beneath the Ganges basin, suggestive of the presence of cold material within. The elevated 410 discontinuity beneath the Ganges basin and the Himalaya is interpreted as the signature of north-east subducting Indian slab and perhaps part of the Tethyan oceanic lithosphere in front of it. The Tethyan subducted slab broke off from the overlying Indian slab and rolled back southward, crossed the mantle transition zone discontinuity and lies presently beneath the Ganges basin. This relict Tethyan slab is possibly responsible for the thickened transition zone beneath the Ganges basin and the complex 660 km discontinuity beneath the Himalaya.

---

Shyam S. Rai (✉)
National Geophysical Research Institute, Uppal Road, Hyderabad - 500007, India
e-mail: shyamsrai@gmail.com

K. Suryaprakasam
National Geophysical Research Institute, Uppal Road, Hyderabad - 500007, India

V. K. Gaur
Indian Institute of Astrophysics, Koramangala, Bangalore - 560037, India

## 9.1 Introduction

Knowledge of the present day state and dynamics of the earth's interior is critical to model the early day's conditions of the solid earth and the environment in its neighbourhood. Despite significant effort made to understand the making and working of the earth, it remains a mystery. For half a century earth is known to be made up of a number of concentric shells of distinct elastic property within each of them. Some of the prominent discontinuities defining the shell boundaries are at the inner core boundary, at the core-mantle boundary (CMB), then mid mantle discontinuities at 410, 520 and 660 km referred as mantle transition zone (MTZ), at 220 km and at a depth of about 35–40 km at the crust-mantle boundary (Moho). Precise characterisation of the heterogeneity within and interaction across the shell is the frontier of modern inter-disciplinary research involving seismology, mineral physics and geodynamics (Van der Hilst 2004).

The mantle discontinuities are marked by increase in compressional and shear wave seismic velocity at depths of ~ 220, 410, 520 and 660 km by ~2%, ~5%, ~1–2% and ~5% (Masse 1973; Wajeman 1988; Hales et al. 1991; Revenaugh and Jordan 1991; Zhang and Lay 1993; Owens et al. 2000; Deuss and Woodhouse 2002). The region between 400 and 800 km is referred as the transition zone from upper to lower mantle and the discontinuities in this zone are associated with phase transformation within the olivine dominated peridotite system (Agee 1993). Phase transitions in olivine from olivine to wadsleyite mark the 410 discontinuity – a reaction with a positive Clapeyron (dP/dT) slope, and from the breakdown of ringwoodite to pervoskite plus magnesiowusitite at the 660 km discontinuity – a reaction which has a negative Clapeyron slope (Bina and Helffrich 1994). The MTZ bounded by these two discontinuities plays a central role in controlling the mantle flow (Yuen et al. 1994). Global seismological studies (Lawrence and Shearer 2006) suggest an average thickness of the transition zone of 242 ± 2 km with long wavelength variations: thickening beneath the subduction zones and parts of continent and thinning beneath oceanic plates and above regions affected by plumes (Collier and Helffrich 2001). Figure 9.1 depicts schematics of the physico-chemical status of the transition zone (Lebedev et al. 2002). Accurate constraint on the properties of the transition zone discontinuities are therefore, necessary to understand some of the important issues/questions like: if convection occurs within separate layers or over the whole mantle, nature of large-scale compositional inhomogeneity of the mantle in different geological domains.

The discontinuity at depth of 220 km was first observed in seismic refraction measurements in Europe and North America (Lehmann 1959, 1961) and is referred as Lehmann discontinuity. Using long period SS precursors Gu et al. (2001), Deuss and Woodhouse (2002) performed a global survey of the 220 km discontinuity and suggest that it is observed below both continents and oceans, though the largest amplitude appear beneath the continents. One of the mechanisms responsible for the occurrence of this discontinuity could be due to change in deformation mechanism from dislocation creep to diffusion creep, corresponding to a change from anisotropic to isotropic structure (Karato 1992; Gaherty and Jordan 1995), compositional difference or the onset of partial melting. The depth at which this occurs is also dependent on temperature and water content in the upper mantle.

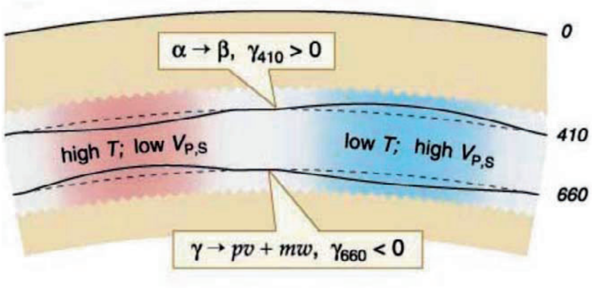

**Fig. 9.1** Schematic depiction of the transition zone in an olivine-dominant mantle. The α ↔ β and γ ↔ pv+mw phase transformations give rise to the 410 and 660 km discontinuities, and the effective Clapeyron slopes $\gamma_{410}$ and $\gamma_{660}$ have opposite signs. Relatively low temperatures (*T*) cause thickening of the TZ and increase in seismic velocities ($V_P$, $V_S$); high temperatures cause thinning of the TZ and decrease in $V_{P,S}$ (after Lebedev et al. 2002, with permission from Elsevier)

We investigate the nature of mantle discontinuities at a depth from ~200–800 km beneath India comprising of varied geological terrains like Archean and Proterozoic cratons, Proterozoic mobile belts and basins, and the Himalayan subduction zone. Seismic characterisation of these discontinuities at various locations has been attempted using teleseismic P to S converted phases from the corresponding layers boundaries. The methodology used is widely referred as common depth point stacking of the receiver function. We demonstrate here (a) the presence of a sharp 410 discontinuity in most parts of India with its depth decreasing from south (415 km) to the north (392 km) suggestive of progressive cooling or thickening of lithosphere; (b) a complex 660 km discontinuity across India showing double peak in certain geological segments like Himalaya and southern India, pointing towards the importance of non-olivine component in the deep mantle; (c) evidence for thickening of the MTZ beneath the Ganges basin; and (d) presence of a velocity contrast in shallower mantle at depth of 220–260 km restricted primarily to the peninsular India.

## 9.2 Geological and Geophysical Framework

Geology of India (Fig. 9.2) could broadly be classified as Archean and Proterozoic domain that forms the region south of the Ganges basin; and the Himalayan orogenic belt evolved in response to the Indo-Asian convergence forming the northern boundary of India.

Precambrian domain: India contains almost 10% of the total (exposed and buried) preserved Archean crust of the world (Goodwin 1996) and is composed primarily of Precambrian cratons and Proterozoic basins. The basements rocks are covered in the north along the Himalayan front by thick deposits of the Indo-Gangetic alluvium and in the west central region by the Deccan flood basalt of 60–65 Ma. Most of the Precambrian basement is predominantly of the Archean age (>2.5 Ga) and exposed in the southern two thirds of the country. Peninsular India is composed of various Precambrian terrains assembled between mid Archean and Neo-Proterozoic. Of these western and the eastern Dharwar cratons form the centrepiece of the Indian shield, with Bastar craton on its northern edge and the granulite terrains to its southern and eastern edges. Other major cratonic assemblages include Bastar, Singhbhum, Bundelkhand and Aravalli. The central part of India is covered with Precambrian Vindhyan sediments that lie in contact with Aravalli and Bundelkhand cratons in the north. Vindhyan basin and Deccan basalt are separated by Narmada-Son Lineament (NSL), a paleo-rift evolved during mid-late Archean and reactivated several times in geological past. The other important feature is the presence of diamond bearing kimberlite fields on the eastern margins of the western Dharwar and Bundelkhand cratons suggestive of a thick lithosperic root beneath them.

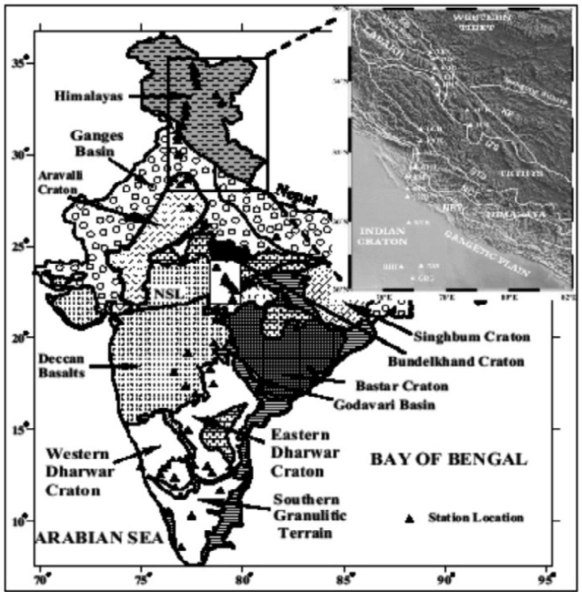

**Fig. 9.2** Important geological terrains of India and location of broadband seismographs

The upper mantle structure of Precambrian India has been investigated using long period surface wave (Mitra et al. 2006; Priestley et al. 2006) and teleseismic receiver function (Saul et al. 2000; Kumar and Mohan 2005; Jagdeesh and Rai 2008; Kiselev et al. 2008). These studies suggest that the lithospheric thickness increasing progressively from ~165 km beneath the eastern Dharwar craton to 190 km beneath Ganges basin and ~200 km beneath the Himalaya. Also a discontinuity with positive velocity contrast was mapped across India at a depth of ~90–110 km. This was suggested to be the signature of Hales discontinuity. Though the Archean cratons are characterised by the existence of thick, cold and depleted lithosphere, the thickness of lithosphere remain unresolved due to poor depth of resolution in seismic tomography. Alternately the limit has been constrained by studying the topography of the 410 km discontinuity because the thermal effects of a thick keel should result in an elevated discontinuity. Using a large network of broadband seismographs (Li et al. 1998) observed a flat 410 km discontinuity beneath the eastern margin of North America and concluded that the mantle downwellings associated with the cold cratonic keel must be confined within the mantle above the transition zone. In a similar study beneath the Kaapvaal craton, Niu et al. (2004) showed the presence of a flat 410 discontinuity and placed limits on the thickness of this chemical boundary layer between ~160 and ~370 km. Beneath the Deccan volcanic province, Kumar and Mohan (2005) mapped the MTZ discontinuities at their normal global depths.

Himalayan domain: The collision of India with southern Asia which started in the mid Eocene (~50 Ma), resulted in the crustal thickening and uplift of southern Tibet and the stacking of thrust sheets to its south forming the Himalaya. Along the northwestern collision boundary, three major terranes are distinguished. The northernmost is the Ladakh-Karakoram, the western section of a 2400 km long stretch of southern Tibet. To its south lies the Tethys zone, a thick pile of essentially conformable Palaeozoic and Mesozoic sediments deposited on the previously formed passive margin of India. The southernmost terrane of the collision zone is the Himalaya formed by successive stacking of crustal slivers, shaved from the penetrating edge of the Indian plate that continues to underthrust the Himalaya and Tibet.

Two end-member models have been proposed for the thickened crust and high elevation of the Himalaya and Tibet: (a) sub-horizontal underthrusting of the Indian plate (Argand 1924; Barazangi and Ni 1982) and (b) intracontinental subduction and delamination of the Indian plate (Bird 1978; Houseman et al. 1981; Molnar 1988) beneath the Himalaya and Tibet. These two end-member models imply different upper mantle and transition zone velocity structures. The first model would likely show high velocities in the shallow upper mantle across Himalaya and most or all of Tibet with little perturbation of the MTZ discontinuities except for a possible upwarp because of the overlying high velocity slab. The second model would likely show low velocities in the shallow upper mantle overlying the dipping, high velocity subducted or delaminated lithosphere. If the cool higher velocity sinking slab was to reach transition zone depths, its thermal affects could result in the significant transition zone topography.

Analysis of surface wave propagation through northern India, the Himalaya and Tibet indicates existence of a continuous high velocity layer across the region (Ritzwoller et al. 2002; Priestley et al. 2006) whereas body wave travel time tomography (Van der Voo et al. 1999; Replumaz et al. 2004; Li et al. 2006) suggests a pronounced high velocity upper mantle (upto a depth of ~300 km) beneath the Precambrian Indian terranes that appears to dip northward with flexure starting from the Ganges basin and continuing beneath the Himalaya and parts of Tibet. This velocity anomaly rolls back southward on crossing the 660 km discontinuity and continue till Ganges basin. The shallower upper mantle anomaly is interpreted as the signature of subducted Indian lithospheric slab along with the part of Tethyan oceanic lithosphere, while the anomaly in the MTZ and lower mantle is interpreted as the relict of broken off part of the Tethys. Kind et al. (2002) investigated the structure of the MTZ beneath eastern Tibet at 90ºE using Ps converted phases in receiver functions. Their results point to the existence of well-defined flat transition zone discontinuities at 400–415 and at 660 km depth. Wittlinger et al. (2004) found similar flat transition zone discontinuities from their receiver function study across western Tibet. These observations indicate that the real structure in the region is more complex than that predicated by the two simple end-member models.

## 9.3 Data and Methodology

During 1999–2004, we operated 54 broadband seismographs in India from southern part of India to Ladakh-Karakoram in north in phased manner covering most of the geological provinces. Each station consisted of a Guralp CMG-3T or 3ESP sensor with a flat velocity response between 0.008 and 50 Hz, and a refraction technology data logger continuously recording waveforms at 20 samples per second. Earlier we used data from this network to map the crustal structure of India (Rai et al. 2003, 2006; Gupta et al. 2003; Jagdeesh and Rai 2008). The inferred Moho depth varies from 32–40 km in most part of the Precambrian terrains except in western Dharwar craton where it is 42–55 km. In the Himalaya, crustal thickness increases from ~45 km in the lesser Himalaya to ~70 km beneath Ladakh.

We have used receiver function analysis (Langston 1979) to map the seismic discontinuities in the mantle. The technique utilises the waves converted at velocity discontinuities to study the nature of the earth directly beneath the receiver (Fig. 9.3). We have used P-Sv conversions that appear in the coda of P arrival which are mainly sensitive to the shear velocity discontinuity at a boundary. The arrival time and amplitude of the converted phase provides us the information related to the depth location, width and the possible causal mechanisms of the discontinuity.

Receiver functions for all high S/N seismograms of events within the distance range 30º and 90º were calculated using the time domain deconvolution method of Ligoria and Ammon (1999). Since our interest is in the structure of the deep mantle, we filtered the waveforms in a low frequency band with a Gaussian width of 0.6 corresponding to a frequency of <0.2 Hz. Thus we obtained 1957 receiver functions with good signal to noise ratio for our analysis.

To image the 3D mantle structure, we followed the ‘Common Depth Point’ stacking approach of Dueker and Sheehan (1997) and Owens et al. (2000), which involves the following steps:

(a) Computation of geographical locations of the piercing points of all P to S conversions for each source-receiver

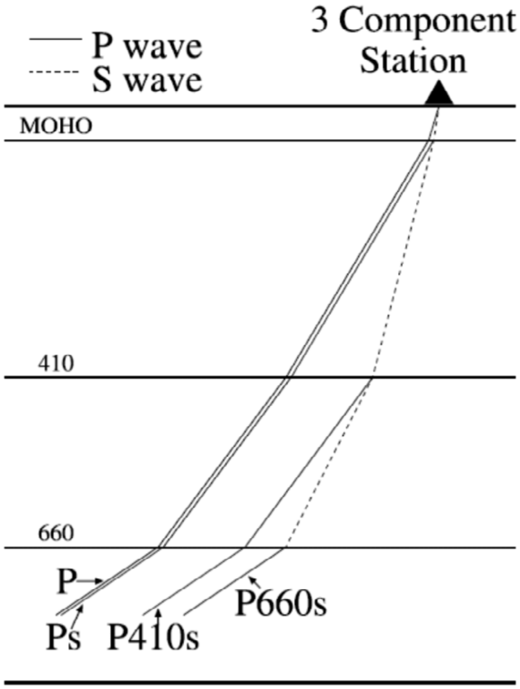

**Fig. 9.3** Cartoon-diagram showing generation of P to S converted phases from a discontinuity. At each discontinuity some of the direct P wave energy is converted from P (solid line) to SV type (dashed line), generating a weak amplitude signal for each discontinuity, arriving after main P peak

pair at 5 km depth increments between 20–800 km, using the IASP91 reference velocity model (Kennet and Engdahl 1991);

(b) Calculation of the travel times of P to S converted phases from various depths using the relation:

$$T_{pds} = \int_{-d}^{0} \sqrt{V_s(z)^{-2} - p^2} - \sqrt{V_p(z)^{-2} - p^2}\, dz \qquad (9.1)$$

where $p$ denotes the ray parameter for the P wave, $d$ the depth of the discontinuity and $V_p(z)$ and $V_s(z)$ are the P and S wave velocities at depth z (Gurrola et al. 1994; Dueker and Shehan 1997);

(c) Discretisation of the region into non-overlapping rectangular blocks of varying width (1°–2°) in latitude depending on the data availability (Fig. 9.4);

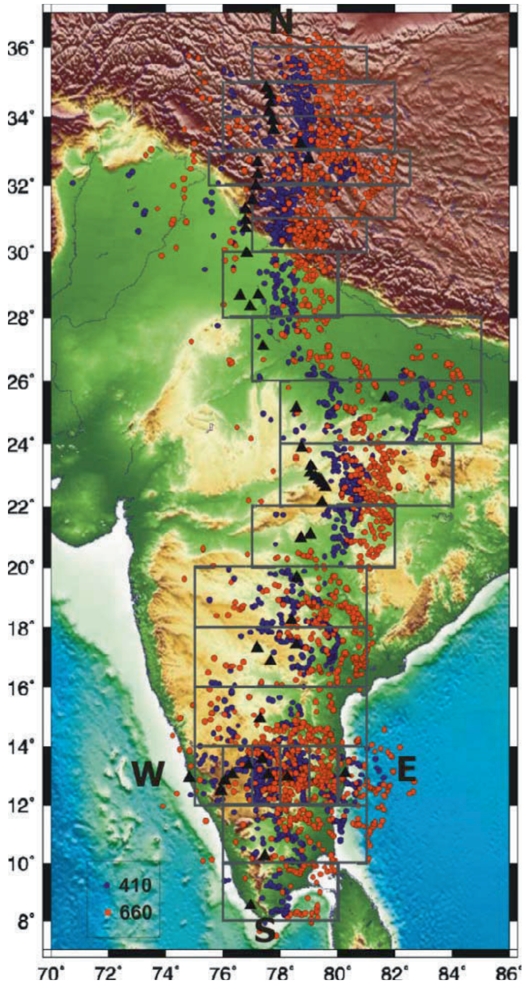

**Fig. 9.4** Piercing points of Ps phase at 410 and 660 km depth. Rectangular grids show the block for which receiver functions are stacked and presented at its mid-point

(d) Stacking of moveout corrected receiver functions within each rectangular region and conversion to depth series using the relation

$$A(d) = \frac{1}{N} \sum_{i=1}^{N} A_i\left(T_{pds}\right)$$

where $A(d)$ is the stacking amplitude for the depth $d$, $N$ the number of piercing points at a depth $d$, $T_{pds}$ the $PdS$ moveout time of the corresponding receiver function for depth $d$ computed using equation (9.1) and $A_i(T_{pds})$ is the amplitude of the $i^{\text{th}}$ receiver function.

Figure 9.4 show the piercing points of rays at 410 and 660 km depths. Since the time of the Ps conversion is translated to a depth using a velocity model, its actual position is dependent on the nature of the overlying velocity structure. Ai et al. (2003) and Gilbert et al. (2003) experimented with varying sets of 1-D and 3-D velocity model to compute the depth of discontinuities. They inferred that the modelled depth of discontinuities are not very sensitive to the velocity model and vary by only ~ 1%. We used here IASP91 reference velocity model (Kennet and Engdahl 1991) for the mantle, while the crustal velocity model of Rai et al. (2003, 2006) obtained by joint inversion of the P-receiver functions and surface wave group velocity measurements was used to account for the thickened crust from 40 km below Delhi to 75 km beneath Ladakh and the Karakoram. Because both the P410s and P660s discontinuities are similarly affected by lateral variation in crust and upper mantle velocities, differences between their depths (i.e. the thickness of the MTZ) are more accurate than the absolute depth of either discontinuity. Figure 9.5 shows the stacked receiver function along the longitude of 80°E (section S-N) from southern tip of India to Ladakh-Karakoram in the north. Also presented is a longitudinal section of the stacked receiver

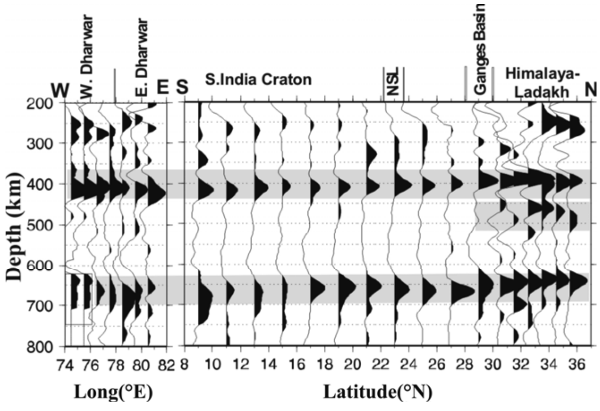

**Fig. 9.5** The stacked receiver functions (a) along the longitude of 80°E shown as S-N, and (b) along the latitude of 13°N shown as W-E

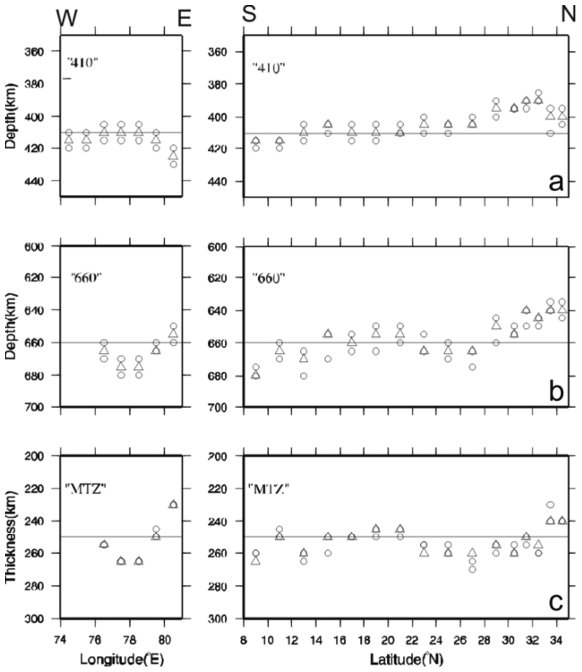

**Fig. 9.6** Depth of (a) 410 km discontinuity, (b) 660 km discontinuity and (c) thickness of MTZ along north-south (N-S) and east-west (E-W) profiles

function along ~13°N (section W-E) to study the mantle stratigraphy beneath the early-late Archean Dharwar craton.

To assess the robustness of the modelled stacked receiver functions in Fig. 9.5 and estimate the depth of 410, 660 km discontinuities and the MTZ thickness, we carried out boot strap analysis on the corresponding receiver function data set for each piercing depth in each block with 100 random replications with replacement (Efron and Tibshirani, 1991). The depth of the 410 and 660 km discontinuities is estimated by examining the peaks of the Ps amplitudes in the depth ranges of 380–430 km and 630–680 km from the data images generated from bootstrap resampling. The depth with maximum amplitude is the candidate depth. Also we computed the depths corresponding to 90% of the peak value. These three computed depths for each discontinuity along the latitude is shown in Fig. 9.6. The uncertainty in computing the depths of individual discontinuity is ±5 km.

## 9.4 Discussion

Notable results of our experiment described above, suggest following inferences about the mantle layering beneath India covering Precambrian terrains and the Himalayan subduction zone.

### 9.4.1 *Lehmann Discontinuity*

At a depth of about 250 km a weak but well defined P to S conversion is observed in the stacked receiver function (Fig. 9.5) across Dharwar craton and along the N-S profile from 10°–19°N covering the southern part of the peninsula. Further north we do not observe the signature of the velocity contrast at this depth. In a global study, Gu et al. (2001) also inferred the presence of Lehmann discontinuity reflection at depth of ~220 km beneath India.

### 9.4.2 *410 km Discontinuity*

This is one of the most well defined discontinuities along the S-N and W-E profiles (Fig. 9.5). Beneath the Dharwar craton the discontinuity is at its namesake depth. However along the S-N receiver function stack the depth of discontinuity decreases progressively towards the Himalaya. In the southernmost part (9°–13°N) of the profile that represents the southern granulite terrain, the discontinuity is deepest at ~415 km. The granulite terrain has impression of major tectono-thermal event coincident with ~550 Ma Pan African Orogeny and is marked by thinnest lithosphere (120 km). Between 14° and 24°N latitudes characterising several Archean cratons (eastern Dharwar, Bastar and Bundelkhand) and Proterozoic basins (Godavari and Vindhyan) the discontinuity is at a depth of 410 km. This is at variance with observations in other Archean cratons (e.g. Kaapvaal, Slave), where due to thermal effects of a thick keel the 410 discontinuity is elevated. This suggests that Indian Archean cratons are underlain by thinner lithosphere or its mantle velocity is lower than the usually observed Vs >4.7 km/s over most of the cratons. Similar situation is observed in eastern Australia where the cratonic root exists only to a depth of 175–200 km. Further north beneath the Ganges basin and Himalaya, the 410 is systematically elevated to depth of 400–390 km suggestive of thickened high velocity lithosphere as also seen in the tomographic images discussed earlier.

### 9.4.3 *475 km Discontinuity*

The other notable result of our experiment is the appearance of an unexpected strong converted phase from an interface at ~475 km beneath Ladakh and Karakoram north of the Indus Suture, but not seen to the south beneath the Himalaya and the Gangetic plain or the peninsular India. This structure is significantly shallower than the 520 km discontinuity which is thought to represent the wadselyite to ringwoodite phase transition or variation in the olivine content and hydrated mantle condition (Gu et al. 1998; Inoue et al. 1998), but corresponds well with the ~500 km depth interface in western Tibet observed by Wittlinger et al. (2004) from coherent but discontinuous P to S conversions. The high velocity layer at depth of ~475 km inferred by us beneath Ladakh and the Karakoram is most likely a relic of the subducted Indian slab, whose northern extension in Tibet may be identified with the north dipping high velocity layer inferred through travel time tomography as discussed earlier. This sinking slab possibly disrupted the 410 discontinuity beneath Ladakh-Karakoram.

### *9.4.4 660 km Discontinuity*

This discontinuity though well defined in both the receiver function profiles; show complex behaviour in its amplitude as well the depth. The velocity contrast across the 660 km depth appear more stronger as compared to the 410 km as reflected in the larger amplitude of the P to S conversion. To the north of 16°N latitude the 660 shows a single peak whereas in south beneath the Dharwar craton it is broad and two peaked. Similar observation can be made in the part of Himalaya where it has two peaks; the second peak though weak is well separated. In general the 660 km discontinuity is interpreted as a result of the breakdown of the $\gamma$ spinel phase of olivine to magnesium-perovskite and magnesiowustite. Recent experimental works point to the important role played by non-olivine components in modifying the nature of the 660 km discontinuity. A computational study show that because of the presence of garnet minerals, multiple discontinuities might exist near a depth of 660 km. Presence of garnet at the base of MTZ has been suggested as a consequence of transformation of subducted oceanic crust that accumulated at the 660 km depth (Ringwood 1994). In the lower MTZ, ilmenite appears at the expense of garnet and at greater depth, it transforms into perovskite plus a small amount of garnet, thereby creating a strong seismic discontinuity at 660 km and a weaker one below it (Vacher et al. 1998). The discontinuity at 650–670 km could result from a phase change from garnet to ilmenite and the lower interface at ~700–715 km could result from a transformation from ilmenite to pervoskite. Similar associations of the 660 km discontinuity have been observed in southern California (Simmons and Gurrola 2000) and northeast China (Ai et al. 2003).

### *9.4.5 Mantle Transition Zone Thickness*

While the depth of 410 and 660 km discontinuities individually could be affected by the presence of velocity in overlying layer, the difference in their depths (*d660–d410*), widely referred as the transition zone thickness is dependent only on the physical property of the material within this zone. As discussed earlier in subduction zones the MTZ is thickened, while the thin transition zone is observed over regions affected by mantle plumes. Along the N-S receiver function profile, generally the depth pattern of 660 follows the 410 except in the Ganges basin where they are opposite to each other: elevated 410 and depressed 660. This is brought out more clearly in the transition zone thickness profile (Fig. 9.6) that shows a well defined 10 km increase in thickness below Ganges basin compared to an average of ~252 km elsewhere beneath India suggesting the presence of colder material in the MTZ beneath it. Global average of the transition zone is 242 km.

## 9.5 Conclusion

The results presented above have been distilled from the most reliable broadband seismograms recorded at 54 broadband seismic stations in India operated during 1999–2004. Two stacked profile of the mantle RF were created using common mid-point approach. These include (a) across the Dharwar craton from west to east and (b) from the southernmost part of India through the Gangetic plain and the western Himalaya to Ladakh-Karakoram. The most significant new results gleaned from this analysis include: (a) evidence for weak mantle discontinuity at a depth of ~220–250 km confined primarily to the southern part of India below the latitude of 19°N; (b) existence of a sharp 410 discontinuity all over, that is at its namesake depth at most places, except beneath Ganges basin and Himalaya-Ladakh where it is elevated to a depth of 390–400 km; (c) the appearance of a high velocity interface just beneath the 660 discontinuity that leads to broadening of the receiver function beneath southern India, whereas in the north beneath the Ganges basin, Himalaya and Ladakh two peaked discontinuity exists; (d) signature of a high velocity interface at ~475 km within the MTZ beneath Ladakh; and (e) thickened MTZ (by 10 km) beneath Ganges basin. These observations suggest that the Indian cratons have thinner root or underlain by lower velocity in mantle compared to other cratons like Kaapvaal and Slave. In context of the Himalayan orogeny, nature of the mantle discontinuities as discussed above alongwith the tomographic results (Van der Voo et al. 1999; Replumaz et al. 2004; Koulakov and Sobolov 2006; Li et al. 2006) suggest the following explanation.

The western Indian continental margin collided with the accreted Ladakh terrane of southern Asia at ~55 Ma terminating the 50 Ma long subduction of the Tethys ocean but continued to drive the Indian continental lithosphere beneath it. Thereupon followed brittle failure of the penetrating upper Indian crust and rapid obduction of the crustal slivers shaved off its under-thrusting front from a depth of ~100 km as seen between the Indus suture zone and the Himalayan (Zanskar) thrust sheets to the south. One can thus visualise the existence somewhere beneath this region of a long sinking oceanic slab which upon continental collision was decoupled from its northward pushing source and its advancing front sequentially sever itself and sink in the mantle. The complex 660 km discontinuity and the existence of another one at 715 km beneath the region most likely represent the first of such broken segments that was rolled progressively southward as it sank and now lies beneath the 660 km discontinuity. The 475 km high velocity interface marked by our results, together with possibly the north dipping high velocity layer inferred by tomography results now lying within the MTZ beneath Ladakh-Tibet, would then appear to represent a later segment that broke off the decoupled oceanic slab. The rolled back material crossed the MTZ beneath Ganges basin has left its signature in terms of thickened transition zone due to presence of cold subducted slab. In this construction of possible past events of oceanic subduction at the IZS followed by continental underthrusting, it is tempting to identify the 715 and 475 km discontinuities, each specific to the Himalayan and the Ladakh-Karakoram, respectively and displaced both horizontally and vertically, as marking the two segments of the pre-Tethyan oceanic slab that were broken off sequentially, the former rolling southward as it sunk because of an expected relative reduction in its northward velocity in the mantle. The modified velocity structure of the overlying MTZ as revealed by the analysis of receiver functions is possibly due to sunken slab rather than any real difference with that across the suture zone as would be normally expected if as in our interpretation, the Indian lithosphere continues to plough through the suture zone. These findings indicate a complex interplay of oceanic subduction followed by unabated underthrusting by a remarkably stolid continental plate that creates not only a wide continental collision zone of high mountains and a large plateau with diverse deformation rheologies, but also leave their impress in the structure of the underlying mantle. A test to the hypothesis requires better data acquisition and imaging of the deep structure of the Ganges basin which is a subject of another investigation in progress.

**Acknowledgements:** We sincerely thank Prof. Alok Gupta for inviting us to write this paper. Data in this work came from several research grants supported by the Department of Science and Technology, New Delhi.

## 9.6 References

Agee C (1993) Petrology of the mantle transition zone. Ann Rev Earth Planet Sci 21: 19–41

Ai Y, Zheng T, Xu W, He Y, Dong D (2003) A complex 660 km discontinuity beneath northeast China. Earth Planet Sci Lett 212: 63–71

Argand E (1924) La Tectonique de l' Asie Int Geol Cong Rep Sess 13: 170–372

Barazangi M, Ni J (1982) Velocities and propagation characteristics of Pn and Sn beneath the Himalayan arc and Tibetan Plateau: possible evidence for underthrusting of Indian lithosphere beneath Tibet. Geology 10: 179–185

Bina C, Helffrich G (1994) Phase transition Clapeyron slopes and transition zone seismic discontinuity topography. J Geophys Res 99: 15853–15860

Bird P (1978) Initiation of intracontinental subduction in the Himalaya. J Geophys Res 83: 4975–4987

Collier JD, Helffrich G (2001) The thermal influence of the subducting slab beneath South America from 410 and 660 km discontinuity observation. Geophys J Int 147: 319–329

Deuss A, Woodhouse JH (2002) A systematic search for mantle discontinuities using SS-precursors. Geophys Res Lett 29. doi: 10.1029/2002GL014768

Dueker KG, Sheehan AF (1997) Mantle discontinuity structure from midpoint stacks of converted P to S waves across the Yellowstone hotspot track. J Geophy Res 102: 8313–8327

Efron B, Tibshirani R (1991) Statistical data analysis in the computer age. Science 253: 390–395

Gilbert HJ, Sheehan AF, Dueker KG, Molnar P (2003) Receiver functions in western United States, with implications for upper mantle structure and dynamics. J Geophys Res 108. doi: 10.1029/2001JB 001194

Goodwin AM (1996) Principles of Precambrian geology, Academic Press

Gu Y, Dziewonski AM, Agee CB (1998) Global de-correlation of the topography of the transition zone discontinuities. Earth Planet Sci Lett 157: 57–67

Gu Y, Dziewonski AM, Ekstrom G (2001) Preferential detection of the Lehmann discontinuity beneath continents. Geophys Res Lett 28: 4655–4658

Gaherty JB, Jordan TH (1995) Lehmann discontinuity as the base of an anisotropic layer beneath continents. Science 268: 1468–1471

Gupta S, Rai SS, Prakasam KS, Srinagesh D, Bansal BK, Priestley K, Chadha RK, Gaur VK (2003) Nature of the south Indian crust: implications for Precambrian crustal evolution. Geophys Res Lett 30: 1419. doi: 101029/2002/GL 016770

Gurrola H, Minster JB, Owens TJ (1994) The use of velocity spectrum for stacking receiver functions and imaging upper mantle discontinuities. Geophys J Int 117: 427–440

Hales AL, Muirhead KJ, Rynn JMW (1991) A compressional wave velocity distribution for the upper mantle. Tectonophysics 63: 309–348

Houseman GA, McKenzie DP, Molnar P (1981) Convective instability of a thickened boundary layer and its relevance for the thermal evolution of the continental convergent belts. J Geophys Res 86: 6115–6132

Inoue T, Weidner DJ, Northrup PA, Parise JB (1998) Elastic properties of hydrous ringwoodite in Mg2SiO4. Earth Planet Sci Lett 160: 107–113

Jagadeesh S, Rai SS (2008) Thickness, composition and evolution of the Indian Precambrian crust. Precambrian Res 162: 4–15

Karato S (1992) On the Lehmann discontinuity. Geophys Res Lett 19: 2255–2258

Kennet B, Engdahl E (1991) Travel times for global earth location and phase identification. Geophys J Int 105: 429–465

Kind R, Yuan X, Saul J, Nelson D, Sobolev SV, Mechie J, Zhao W, Kosarev G, Ni J, Achauer U, Jiang M (2002) Seismic images of crust and upper mantle beneath Tibet: evidence for Eurasian plate subduction. Science 298: 1219–1221

Kiselev S, Oresin S, Vinnik L, Gupta S, Rai SS, Singh A, Kumar RM (2008) Lithosphere of the Dharwar craton by joint inversion of P and S receiver functions. Geophys J Int 173: 1106–1118

Kumar MR, Mohan G (2005) Mantle discontinuities beneath the Deccan volcanic province. Earth Planet Sci Lett 237: 252–263

Koulakov I, Soboloev SV (2006) A tomographic image of Indian lithosphere break-off beneath the Pamir-Hindukush region. Geophys J Int 164: 425–440

Langston CA (1979) Structure under mount Rainier, Washington, inferred from teleseismic body waves. J Geophys Res 84: 4749–4762

Lawrence JF, Shearer PM (2006) A global study of transition zone thickness using receiver functions. J Geophys Res 111. doi: 10.1029/2005JB003973

Lebedev S, Chevrot S, van der Hilst RD (2003) Correlation between the shear-speed structure and thickness of the mantle transition zone. Phys Earth Planet Int 136: 25–40

Lehmann I (1959) Velocity of longitudinal waves in the upper part of the earth's mantle. Ann Geophys 15: 93–113

Lehmann I (1961) S and the structure of the upper mantle. Geophys J R Ast Soc 4: 124–138

Li A, Fisher KM, Wysession ME, Clarke TJ (1998) Mantle discontinuties and temperature under the North America. Nature 395: 160–163

Li C, van der Hilst RD, Toksoz MN (2006) Constraining P-wave velocity variations in the upper mantle beneath Southeast Asia. Phys Earth Planet Int 154: 180–195

Liggoria JP, Ammon CJ (1999) Iterative deconvolution and receiver-function estimation. Bull Seism Soc Am 89: 1395–1400

Masse RP (1973) Compressional wave velocity distribution beneath central and eastern North America. Bull Seis Soc Am 63: 911–935

Mitra S, Priestley K, Gaur VK, Rai SS (2006) Shear-Wave structure of the south Indian Lithosphere from Rayleigh wave phase velocity measurements. Bull Seism Soc Am 96: 1551–1559

Molnar P (1988) A review of geophysical constraints on the deep structure of the Tibetan Plateau, the Himalaya and the Karakoram and their tectonic implications. Phil Trans R Soc Lond Ser A 326: 33–88

Niu F, Lavender A, Cooper CM, Lee CA, Lenardic A, James DE (2004) Seismic constraints on the depth and composition of the mantle keel beneath the Kaapvaal craton. Earth Planet Sci Lett 224: 337–346

Owens TJ, Nyblade A, Gurrola H, Langston CA (2000) Mantle Transition Zone structure beneath Tanzania, East Africa. Geophys Res Lett 27: 827–830

Priestley K, Dabayle E, McKenzie D, Pilidou S (2006) Upper mantle structure of eastern Asia from multimode surface waveform tomography. J Geophys Res 111.doi: 10.1029/2005JB004082

Rai, SS, Priestley K, Prakasam KS, Srinagesh D, Gaur VK, Du Z (2003) Crustal Shear velocity structure of the south Indian shield. J Geophys Res 108: 2088. doi:1029/2002JB001776

Rai SS, Priestley K, Gaur VK, Mitra S, Singh MP, Searle MP (2006) Configuration of the Indian Moho beneath the NW Himalaya and Ladakh. Geophys Res Lett 33: L15308. doi: 10.1029/2006GL 026076

Revenaugh J, Jordan TH (1991) Mantle layering from ScS reverberations: 3. The upper mantle. J Geophys Res 96: 19781–19810

Replumaz A, Karson H, van der Hilst RD, Besse J, Tapponier P (2004) 4-D evolution of SE Asia's mantle from geological reconstruction and seismic tomography. Earth Planet Sci Lett 221: 103–115

Ringwood AE (1994) Role of transition zone and 660 km discontinuity in the mantle dynamics. Phys Earth Planet Int 86: 5–24

Ritzwoller MH, Shapiro NM, Barmin MP, Levshin AL (2002) Global surface wave diffraction tomography. J Geophys Res 107. doi: 10.1029/2002JB001777

Saul J, Kumar MR, Sarkar D (2000) Lithospheric and upper mantle structure of the Indian shield, from teleseismic receiver function. Geophys res Lett 27: 2357–2360

Simmons NA, Gurrola H (2000) Multiple seismic discontinuities near the base of the transition zone in the earth's mantle. Nature 405: 559–562

Vacher P, Mocquet A, Sotin C (1998) Computation of seismic profiles from mineral physics: the importance of the non-olivine components for explaining the 660 km discontinuity. Phys Earth Planet Int 106: 275–298

Van der Hilst DR (2004) Changing views on the earth's mantle. Science 306: 817–818

van der Voo R, Spakman W, Bijwaard H (1999) Tethyan subducted slab under India. Earth Planet Sci Lett 171: 7–20

Wajeman N (1988) detection of underside reflections at mantle discontinuities by stacking broadband data. Geophys Res Lett 15: 669–672

Wittlinger G, Vergne J, Tapponier P, Farra V, Poupinet G, Jiang M, Su H, Herquel G, Paul A (2004) Teleseismic imaging of subducting lithosphere and Moho offsets beneath western Tibet. Earth Planet Sci Lett 221: 117–130

Yuen DA, Reuteler DM, Balachander S, Steinbach V, Smedsmo JJ (1994) various influences on three-dimensional mantle convection with phase transition. Phys Earth Planet Inter 86: 185–203

Zhang Z, Lay T (1993) Investigation of upper mantle discontinuities near northwestern Pacific subduction zones using precursors to sSH. J Geophys Res 98: 4389–4405.

# 10

# Models for Constraining Thermal Structure of the Indian Crust

R. N. Singh

**Abstract:** Knowledge of the thermal structure of the Indian crust is needed to unravel its geological history. The present thermal structure of the crust can be constructed using the available heat flow and radiogenic heat data with steady state heat conduction models. We have summarised several steady state heat conduction models with temperature dependent thermal conductivity and depth dependent radiogenic heat. Thermal models are also needed to study the influences of heat addition to the crust, reordering of heat sources, increase in the mantle heat flux and temperature, uplift and erosion and fluid transport in the Indian crust. We have also summarised several thermal models useful in constraining above processes. Applications of these models to the Indian shield have been done in some special cases which are also reviewed. It is emphasised that progress in deciphering actions of geological processes from signatures embedded in the Indian crust requires confronting thermal models of the processes with the geophysical data.

---

R. N. Singh (✉)
National Geophysical Research Institute (Council of Scientific and Industrial Research), Hyderabad - 500606, India
e-mail: rnsingh@ngri.res.in

## 10.1 Introduction

Model building is an essential scientific activity. Over the years, there have been three paradigms in model building: modelling with differential equations (Newtonian paradigm), qualitative theory and algorithmic modelling paradigm. In the Newtonian paradigm, obtaining closed form solution is aimed using analytical and increasingly now by numerical approaches. In the second paradigm, qualitative aspects of the solution are sought. In the last case the experimental/observation data are used to construct working models. In the case of knowing the thermal structure of the Indian crust and lithosphere, we shall be working within the Newtonian paradigm focusing on closed form solutions of heat conduction equation. The available observations for thermal structure determinations are not yet ripe enough for model building by later two paradigms.

Thermal structure of the Indian crust is obtained using heat conduction equation with given values of thermal parameters such as thermal conductivity and diffusivity; heat sources and boundary conditions such as surface temperature and heat flows. Thermal parameters are obtained by measuring them in the laboratory on rocks which constitute the crust. Such measurements have been done for lithosphere forming rocks and general forms of variation of the thermal conductivity with temperature and composition have been worked out. The distribution of heat sources has also been estimated from measurements of radioactive constituents in rocks and also based on some general geophysical considerations. Measurements of surface temperature and heat flow have been made in several locations and thus the boundary conditions for the heat conduction equations are available. Transient regimes prevalent during its geological history too can be obtained by interpreting the episodes of igneous, metamorphic and sedimentary rock formation. In this chapter we present the heat conduction equation and the solutions of the equation relevant for constraining thermal structure of the Indian crust. Studies conducted in applying these results in understanding the geological environment of the Indian regions are also summarised.

## 10.2 The Heat Conduction Equation

The conservation law of energy and the Fourier constitutive relationship relating heat flux with temperature gradient are used to set up the heat conduction equation. These are respectively

$$\rho \frac{DE}{Dt} = \overline{\overline{\sigma}} \bullet \nabla \vec{v} - \nabla \bullet \vec{q} + A \tag{10.1}$$

and

$$\vec{q} = -k \nabla T \tag{10.2}$$

Here $\rho, E, \vec{v}, \overline{\overline{\sigma}}, \vec{b}, \vec{q}, A$, k and T denote density, internal energy per unit volume, velocity, stress tensor, force per unit mass, heat flux vector, internal energy source, thermal conductivity and temperature, respectively. D/Dt is the material derivative given by

$$\frac{D}{Dt} \equiv \frac{\partial}{\partial t} + \vec{v} \bullet \nabla \tag{10.3}$$

Combining Eqs. (10.1) and (10.2), we get the heat conduction equation. For a stable un-deforming crust $(v = 0)$, we get

$$\rho \frac{\partial E}{\partial t} = \nabla \bullet (k \nabla T) + A \tag{10.4}$$

Further we can write E in terms of T as

$$E = c_p T \tag{10.5}$$

here $c_p$ is the heat capacity. Combining Eqs. (10.4) and (10.5), we get

$$\rho c_p \frac{\partial T}{\partial t} = \nabla \bullet (k \nabla T) + A \tag{10.6}$$

Eq. (10.6) is used to determine the transient thermal state of the lithosphere. For steady state case, we use the following form of the above Eq. (10.6)

$$\nabla \bullet (k \nabla T) = -A \tag{10.7}$$

If thermal fields are function of depth only (z-depth coordinate), Eq. (10.7) reduces to

$$\frac{d}{dz} \bullet \left(k \frac{dT}{dz}\right) = -A \tag{10.8}$$

We can obtain solutions of the equations characterising the thermal structure of the Indian region, given the depth/temperature dependence of k and A and the boundary conditions. Surface condition is taken as

$$T(z = 0) = T_s \tag{10.9}$$

For the second boundary condition, we can take the heat flow value at the surface given by equation

$$k\frac{dT}{dz}(z=0)=Q_s \qquad (10.10)$$

We may also prescribe any of the Eqs. (10.11a), (10.11b) or (10.11c) at the base of the crust instead of Eq. (10.10)

$$T(z = L) = T_L \qquad (10.11a)$$

$$k\frac{dT}{dz}(z=L)=Q_L \qquad (10.11b)$$

$$k\frac{dT}{dz}(z=L)=a+bT_L \qquad (10.11c)$$

a and b are constants and L the thickness of the crust. Surface temperature is taken as 273 K. Values of surface heat flow have been measured at several locations in the Indian regions (Rao et al., 2003).

## 10.3 Steady State Thermal Models

Steady state model is useful after the transient effects have been dissipated. Eq. (10.6) can be used to infer the time scale for a thermal transient to die out. If the length scale of thermal disturbance is ‘l’ then by normalising Eq. (10.6) we can get the time scale $\tau$ as

$$\tau^{-1} = (k/\rho c)l^{-2} = \kappa l^{-2} \qquad (10.12)$$

where $\kappa$ is thermal diffusivity. As an example if we assume that a sill of 100 m thickness at high temperature is emplaced within the crust with $\kappa = 10^{-6}m^{-2}/s$, then its thermal perturbation will be dissipated in about 317 years. We first assume that all thermal disturbances in the Indian crustal regions have dissipated and the steady state regime prevails. We shall consider departure from this approximation in the later sections.

In the simplest steady state case, we take k and A as constants with values as $k_0$ and $A_0$, respectively. We get solution of Eq. (10.8) with boundary conditions Eqs. (10.9) and (10.10) as

$$T(z) = T_s + Q_s z/k_0 - A_0 z^2/2k_0 \qquad (10.13)$$

This equation can be used to find the depth distribution of temperature. We find that the temperature gradient increases with increasing surface heat flow and decreases with increasing radiogenic heat in the crust. It is found that radioactive material will be limited to the upper most layer of about 10–20 km thickness within the crust. So Eq. (10.13) can be used only within this layer. Below this layer the temperature gradient will follow the mantle component of the surface heat flow. It is known that surface heat flow can be partitioned into two components one given by radiogenic heat in the crust and other by mantle convection.

For the model of the radiogenic heat as

$$A(z) = A_0[H(z) - H(z - d)] \qquad (10.14)$$

where H(z) is unit Heaviside function and d is the depth extent of the radiogenic layer, we get the depth distribution of temperature as

$$T(z) = T_s + Q_s z/k_0 - A_0 z^2 / 2k_0 \quad 0 \le z \le d \qquad (10.15a)$$

$$= T_d + Q_d(z-d)/k_0 \qquad (10.15b)$$

where

$$T_d = T_s + Q_s d/k_0 - A_0 d^2/2k_0 \qquad (10.16a)$$

$$Q_d = Q_s - A_0 d \qquad (10.16b)$$

Above model of depth distribution of radiogenic heat (Eq. 10.14) is called step model. Other model which is in use is given by so called exponential model:

$$A(z) = A_0 \exp(-z/d) \qquad (10.17)$$

Solution of Eq. (10.8) with A(z) given by Eq. (10.17) and boundary conditions Eqs. (10.9) and (10.10) is obtained as

$$T(z) = T_s + (Q_s \quad A_0 d)z/k + A_0 d^2(1 \quad \exp(-z/d))/k (10.18)$$

In all above models we have taken thermal conductivity as constant. Experimental and theoretical studies on minerals have shown that thermal conductivity is a function of temperature. It decreases with temperature initially with phonons contributing to heat transport and then increases with temperature due to radiative contributions. In the near surface regions it is given by

$$K(T) = k_0 / (1 + CT) \qquad (10.19)$$

$k_0 = 2.9\ Wm^{-1}K^{-1}$ and C varies within (0.0006–0.0014 $K\ ^{1}$). For such a model of thermal conductivity, the solutions of Eq. (10.8) for the step and exponential models of radiogenic heat Eqs. (10.14 and 10.17) are given respectively by (Singh and Negi 2002)

$$T(z) = \{-1 + M \exp[N(Q_s - A_0 z/2)z]\}/C$$
$$\text{for } z \le d \qquad (10.20a)$$

$= \{-1 + M \exp[N(z(Q_s\text{-}A_0 d) - A_0 d^2/2)]\}/C$
for $z \leq d$ (10.20b)

$T(z) = \{-1 + M \exp[N(z(Q_s\text{-}A_0 d) - A_0 d^2(1\text{-}\exp(\text{-}z/d))]/2\}/C$ for $z \leq d$ (10.20c)

Where

$M = 1 + CT_s$ (10.21a)

$N = C/k_0$ (10.21b)

Another form of temperature dependence of thermal conductivity given below is also used

$$k(T) = 2.264 - \frac{618.2}{T} + k_0\left(\frac{355.6}{T} - 0.3025\right) \quad (10.22a)$$

$$= A + B/T \quad (10.22b)$$

where

$A = 2.264\text{-}0.3025\ k_0$;

$B = \text{-}618.2 - 355.6\ k_0$;

$k_0 = 3.0\ \mathrm{mWm^{-1}K^{-1}}$

The solution for temperature distribution is given as:

$$A(T\text{-}T_s) + B\ln(T/T_s) = (Q_s\text{-}A_s d)z + A_s d^2(1\text{-}\exp(\text{-}z/d)) \quad (10.23)$$

Temperature as a function of depth can be solved from Eq. (10.23) by using a root finding technique such as Newton-Raphson method.

For deeper crustal regions, the temperature dependence of the thermal conductivity is obtained by considering both phonon and radiative contributions. We have the following expression for k(T):

$$k(T) = k_0/(1+C_1 T) + C_2(T\text{-}T^*)\, H(T\text{-}T^*) \quad (10.24)$$

Where $T^*$ is the temperature at which radiative contribution starts. For above thermal conductivity model (Eq. 10.24), we have the following expressions for solution for the temperatures with depth (Singh 1980; Manglik and Singh 1991)

$$\ln\left(\frac{1 + C_1 T}{1 + C_2 T_s}\right) = C_1 Q_s \left(\frac{z}{k_0}\right) + \frac{A_s{}^2 C_1 d\left[1 - \frac{z}{d} - \exp\left(\frac{-z}{d}\right)\right]}{\mathrm{k}_0}$$
for $0 \leq z \leq z^*$ (10.25)

$$\ln\left[\frac{(1+C_1 T)}{(1+C_{21} T^*)}\right] + \frac{C_1 C_2 (T-T^*)^2}{2k_0} = \frac{Q_1^* C_1 (z-z^*)}{k_0} + A_s{}^2 C_1 d^2 \left[\exp\left(\frac{-z}{d}\right) - \exp\left(\frac{-z^*}{d}\right) - (z-z^*)\exp\left(\frac{-z^*}{d}\right)\right]$$
for $z \geq z^*$ (10.26)

In above expressions, $z^*$ is the depth where $T = T^*$ and $Q^*$ is the heat flux at the depth $z^*$ given by

$$Q^* = Q_s\text{-}A_s d(1\text{-}\exp(\text{-}z^*/d)) \quad (10.27)$$

Eq (10.25) and (10.26) are nonlinear in T. Therefore T needs to be determined numerically using for example Newton-Raphson method.

We have so far considered the effects of the depth distribution of radiogenic heat in the crust and temperature dependent conductivity on the crustal temperatures. Thermal conductivity and radiogenic heat in the crust do show random variations. These can be quantified in terms of depth dependence of mean and variance of temperature fields (Srivastava and Singh 1998, 1999a, 1999b).

## 10.4 Transient Thermal Models

Indian crust has been subjected to erosion and uplift and various igneous and metamorphic episodes over its geological history. Characteristics of the transient fields are preserved in the composition and structure of the rocks which have survived till now and are exposed on the surface. Himalayan orogeny, Deccan and other volcanisms, formation of continental margins and sedimentary basins, magma underplatings, high-grade granulites, etc. have signatures of transient thermal events. To model all these episodes, we need to specify their consequences in terms of changes in the initial condition, boundary conditions, source functions or through the addition of new terms in the heat conduction, equation such as adding advection terms for studying uplift and erosion. We shall consider several cases in the sequel.

### *10.4.1 Evolution of Initial Thermal Fields*

Formation of continental margins and sedimentary basins are explained as the thermal evolution of perturbed initial thermal condition. Heat additions into the lithosphere represented by perturbed initial condition decay with time and it leads to contraction of the lithosphere and resulting subsidence.

We shall now consider various forms of T(z, 0) which have been considered in the literature. We consider the lithosphere having a simple thermal structure:

$$T(z,0) = (z/L)T_L \quad (10.28)$$

After stretching the lithosphere-asthenosphere boundary rises and the resulting thermal field becomes:

$$T(z,0) = (z\beta/L)TL \text{ for } 0 \le z \le L/\beta$$
$$= TL \quad \text{for } L/\beta \le z \le L \qquad (10.29)$$

β is a constant and is termed as stretching factor. This perturbed thermal field will evolve finally to equilibrium field given by Eq. (10.28). In the process as the lithosphere will be cooling and densifying, there will be subsidence, forming a basin and sedimentary rocks will be deposited in the basin. The way the basement will deepen can be determined. McKenzie (1978) has derived the thermal model of evolution of stretched lithosphere (Eq. 10.29) and applied to formation of sedimentary basins and also continental margins. Temperature field T(z,t) changes as given below

$$T_L\left\{\frac{z}{L}+\frac{2\beta}{\pi^2}\sum_{n=1}^{\infty}\frac{\sin\left(\frac{n\pi}{\beta}\right)\sin\left(\frac{n\pi z}{L}\right)}{n^2}\exp\left(\frac{-n^2\pi^2\kappa t}{L^2}\right)\right\} \qquad (10.30)$$

For more general stretching model where the perturbed initial thermal structure is given by

$$T(z,0)=\left(\frac{z\beta}{L}\right)T_L \qquad \text{for } 0 \le z \le L/\beta$$

$$= T_L\left\{\frac{\left(\frac{\mathrm{L}}{\beta\text{ - z}}\right)}{\left(\frac{\mathrm{L - L}}{\beta}\right)}\right\} \qquad \text{for } L/\beta \le z \le L \qquad (10.31)$$

the solution for the perturbed temperature distribution is given by Mareschal (1991) as

$$T(z)=\frac{2\beta^2 T_L}{(\beta-1)\pi^2}\sum_{n=1}^{\infty}\frac{\sin\left(\frac{n\pi}{\beta}\right)\sin\left(\frac{n\pi z}{L}\right)}{n^2} * \exp\left(\frac{-n^2\pi^2\kappa t}{L^2}\right) \qquad (10.32)$$

β is the crucial factor which is determined by comparing the heat flow and subsidence histories.

In case the whole lithosphere is perturbed by a uniform temperature, i.e.

$$T(z,0) = T_m \qquad (10.33a)$$

$$T(0,t) = 0 = T(L,t) \qquad (10.33b)$$

we get the following expression for the temperature distribution (Sleep and Snell 1976)

$$T(z,t)=\frac{4T_m}{\pi}\sum_{n=1}^{\infty}\frac{\sin\left[\frac{(2n-1)\pi}{L}\right]\sin\left[\frac{n\pi z}{L}\right]}{(2n-1)} * \exp\left[\frac{-(2n-1)^2\pi^2\kappa t}{L^2}\right] \qquad (10.34)$$

For general initial thermal field:

$$T(z,0) = F(z) \qquad (10.35)$$

and boundary conditions as in Eq. (10.31), we can use the following solution given in Ozisik (1993)

$$T(z,t)=\sum_{n-1}^{\infty}\left(\frac{2}{L}\right)\exp\left(\frac{-\kappa(n\pi)^2 t}{L^2}\right)\mathrm{x}$$

$$\sin\left(\frac{n\pi z}{L}\right)\int_0^L F(z')\sin\left(\frac{n\pi z'}{L}\right)dz \qquad (10.36)$$

Above models can be used to study the thermal structure in case there is addition of heat to the crust and lithosphere.

### 10.4.2 Basal Heating

Crust and mantle thermal interaction can be characterised by enhancing the temperature or heat flow or a combination of both at the base of the crust. For instance we have following case:

$$T(z,0) = 0 \qquad (10.37a)$$

$$T(0,t) = 0 \qquad (10.37b)$$

$$T(L,t) = \nabla T \qquad (10.37c)$$

Here the base of lithosphere is perturbed by ∇T. The solution for this problem has been given in Carslaw and Jaeger (1959) as

$$T(z,t)=\frac{\nabla T z}{L}+\frac{2\nabla T}{\pi}\sum\frac{(-1)^n}{n}\exp\frac{-\kappa n^2\pi^2 t}{L^2}\sin\frac{n\pi z}{L} \qquad (10.38)$$

In case the basal heat flux is perturbed, the following initial and boundary conditions can be used

$$T(z,0) = 0 \tag{10.39a}$$

$$T(0,t) = 0 \tag{10.39b}$$

$$k\frac{dT}{dz}(L,t) = \nabla Q \tag{10.39c}$$

The solution of the problem in this case is (Carslaw and Jaeger 1959)

$$T(z,t) = \frac{(\nabla Q)z}{k} - \frac{8\nabla Q\, L}{k\pi^2}\sum_{n=0}^{\infty}\frac{(-1)^n}{(2n+1)^2} * \exp\left\{\frac{-\kappa(2n+1)^2\pi^2 t}{4L^2}\right\}\sin\left\{\frac{(2n+1)\pi z}{2L}\right\} \tag{10.40}$$

The above formalism of basal heating has been applied by Saltus and Lachenbruch (1991) to explain thermal evolution of Sierra Nevada, USA.

The solution for the following initial and boundary conditions for transient variation in basal heat flux

$$T(z,0) = 0 \tag{10.41a}$$

$$T(0,t) = 0 \tag{10.41b}$$

$$k\frac{dT}{dz}(L,t) = Q_0 t^{m/2} \quad (m = -1,0,1,...) \tag{10.41c}$$

is given as (Carslaw and Jaeger 1959)

$$T(z,t) = \frac{2^{m+1}Q_0\sqrt{\kappa t^{(m+1)}}\,\Gamma(1+m/2)}{k} * \sum_{n=0}^{\infty}(-1)^n \left\{ i^{m+1}erfc\frac{(2n+1)L-z}{2\sqrt{\kappa t}} - i^{m+1}erfc\frac{(2n+1)L+z}{2\sqrt{\kappa t}} \right\} \tag{10.42}$$

### 10.4.3 Reordering of Heat Sources

Due to tectonic deformations it is possible that a layer of high heat producing elements is buried at depth. It would be interesting to know how much increase in the crustal temperatures takes place due to this tectonic process. Sandiford and McLaren (2002) and Sandiford et al. (2004) have shown that for the following model of radiogenic heat:

$$A(z) = \begin{cases} A_1 & 0 \le z \le h_1 \\ A_2 & h_1 \le z \le h_2 \\ 0 & h_2 \le z \end{cases} \tag{10.43}$$

resulting from long-term effect of reordering of radiogenic heat, the solution of the steady heat conduction Eq. 10.8 with boundary conditions as Eqs. (10.9) and (10.11b) is:

$$T(z) - T_s = [Q_m + h_1(A_1 - A_2) + h_2 A_2]\frac{z}{k} - \frac{A_1 z^2}{2k} \qquad (0 \le z \le h_1) \tag{10.44a}$$

$$= \left\{\frac{h^2{}_1(A_1 - A_2)}{2k} + \frac{(Q_m + h_2 A_2)z}{k} - \frac{A_2 z^2}{2k}\right\} \quad h_1 \le z \le h_2 \tag{10.44b}$$

$$T(z) - T_s = [Q_m z + h_1^2(A_1 - A_2) + h_2^2 A_2)/2]/k \qquad h_2 \le z \tag{10.44c}$$

$Q_m$ is the heat flux at $z = h_2$. For the case when $A_1 = 0$, the maximum temperature increase at the base of radiogenic layer is

$$\nabla T(z = h_2) = A_2(h_2^2 - h_1^2)/2k \tag{10.45}$$

With following notation:

$$Q_c = A_2(h_2 - h_1) \tag{10.46a}$$

$$h = h_1 + (h_2 - h_1)/2 = (h_2 + h_1)/2 \tag{10.46b}$$

the thermal perturbation is given by

$$\nabla T = Q_c h/k \tag{10.47}$$

This equation can be used to obtain effects of long-term thermal changes due to burial or exhumation reordering of high radiogenic layer. However for estimating transient effects of reordering of radiogenic heat recourse to numerical method has been taken by Sandiford et al. (2004).

### 10.4.4 Transient Uplift/Erosion Effects

In this case the governing equation changes to

$$\rho c\left(\frac{\partial T}{\partial t} - v\frac{\partial T}{\partial z}\right) = K\frac{\partial^2 T}{\partial z^2} + A(z,t) \tag{10.48}$$

Here v is the rate of uplift/erosion. The source term now becomes also a function of time. For exponential model, we have the source terms as

$$A(z,t) = A_0 \exp(-(z + \nu t)/d) \tag{10.49}$$

This problem has been addressed in Haxby and Turcotte (1980), Lee (1980), Clark (1980), Woodhouse and Birch (1980) and Singh and Negi (1980). According to Woodhouse and Birch (1980) the solution is

$$\begin{aligned} T(z,t) = T_s &+ \frac{\left(\frac{dQ_0}{k}\right)(h+x)}{s} + \left\{\frac{A_0 d^2}{2k}\right\}\left\{2\exp\left(\frac{-h}{2}-\frac{x}{s}\right)\right. \\ &. \mathrm{Re}\left\{\exp(ilh)\, erfc\left[\left(\frac{h}{(4x)^{1/2}}\right)+il(x)^{1/2}\right]\right\} \\ &- erfc\left(\frac{(h+x)}{(4x)^{1/2}}\right) - \exp(-h).erfc\left(\frac{(h-x)}{(4x)^{1/2}}\right) + 2 - \\ &\left. 2\exp\left(\frac{-(h+x)}{s}\right)\right\} + \left(\frac{\kappa}{(2v^\wedge 2)}\right)\left(\frac{Q_0 v}{k}\right)\left\{(h+x)\right. \\ &\left. erfc\left(\frac{(h+x)}{(4x)^{1/2}}\right) - (h-x)\exp(-w)\, erfc\left(\frac{(h-x)}{(4x)^{1/2}}\right)\right\} \end{aligned} \tag{10.50}$$

where

$$x = t\nu^2/\kappa,\ s = d\nu/\kappa,\ h = \nu z/\kappa,\ l = (1/s - ¼)^{1/2} \tag{10.51}$$

Originally Woodhouse and Birch (1980) used Eq. (10.50) to find the effects of uplift and erosion on the nature of the linear surface heat flow and heat generation relationship.

### 10.4.5 *Effects of Fluid Transport*

Though crust is taken as solid continua, we find movement of fluid phases within it. Movement of magma and groundwater and volatile gases like $CO_2$ are known to permeate through crust. Groundwater flows disturb the geotherms in near surface regions. Percolation of $CO_2$ has been used to explain generation of granulites, high-grade metamorphic rocks. In steady state the governing equation for temperature is given by

$$\rho C v \frac{dT}{dz} = K \frac{d^2 T}{dz^2} \tag{10.52}$$

The boundary conditions are

$$T(0) = 0 \tag{10.53}$$

$$T(L) = 0 \tag{10.54a}$$

or

$$K \frac{dT}{dz}(z = 0) = q_m \tag{10.54b}$$

The solutions of the equation for above two cases are:

$$T(z) = T_L \frac{(1-\exp(-\alpha z))}{(1-\exp(-\alpha L)} \tag{10.55}$$

$$T(z) = (qm/K\alpha)\exp(\alpha L)(1 - \exp(-\alpha z)) \tag{10.56}$$

here

$$\alpha = \rho C \nu / K \tag{10.57}$$

In case of transient heat transfer with fluid transport, we need to solve

$$\rho C\left(\frac{\partial T}{\partial t} + v\frac{dT}{dz}\right) = K\frac{d^2T}{dz^2} + A_0 \exp\left(\frac{-z}{d}\right) \tag{10.58}$$

This equation is similar to that considered in the transient uplift and erosion case, except for the source term. The source terms are independent of time. An analytical solution of this equation can be derived (Ganguly et al. 1995) for realistic initial and boundary conditions.

## 10.5 Applications to the Indian Regions

Determination of the thermal structure of the Indian region became possible with the availability of surface heat flow and heat generation data. Rao et al. (1976) presented a summary of previous works and proposed a linear relationship between surface heat flow and heat generation, partitioning Indian region into two geothermal provinces based on the intercept and slope values of this relationship. In the southern part the slope of the relationship, interpreted in terms of the thickness of radiogenic crust, gave a value of 7.5 km while in the northern part it was as high as 14.8 km. The intercept at the heat flow axis yielded the heat flow below this radiogenic crustal layer. In the northern part it was 38 $mWm^{-2}$ and in the southern part of the Indian shield it was 33 $mWm^{-2}$. Rao et al. (1976) gave the value of the Moho temperature for the Indian shield as about 550ºC. Singh and Negi (1982) used their data and several models of temperature dependent thermal conductivity and depth dependence of radiogenic heat in the crust to obtain the Moho temperatures. These Moho temperature values were higher than what was obtained in Rao et al. (1976). For the southern part of the shield, Moho temperatures were in the range 550–600ºC and for the northern part of the shield the values were in the rages of 850–900ºC. Singh (1981, 1985) made further calculations of crustal and lithosphere temperatures by including the radiative part in the thermal conductivity model and obtained the thickness of Indian lithosphere in the northern region which came to be about 100 km. This work was extended for the southern part of the shield for understanding the genesis of Cuddapah basin (Bhattacharji and Singh 1984). A comprehensive model of the thermal structure of the Indian region was constructed for use in the understanding of the rheology of the Indian regions by Manglik and Singh (1991, 1992, 1999 and 2002) and Manglik (1993, 2004). Gupta and Gaur (1984), Gupta et al. (1991) and Gupta (1995) estimated thermal structure within the shield crust and below Deccan traps. Negi et al. (1986, 1987), Pandey et al. (2002) and Agrawal and Pandey (1999, 2004) also estimated the steady state thermal structures at various locations in the Indian region towards understanding various tectonic characteristics of the Indian shield. Singh (1984) obtained paleo-temperatures in southern Indian shield by interpreting metamorphic pressure and temperature data and derived value of the rate of mantle cooling below the Indian region as ~25ºC/Ga.

In present decade the geothermal investigations of Indian shield have made great progress in extending the heat flow values observations and also estimates of the radiogenic heat in the crust. Earlier the linear heat flow and heat generation relationship was used to obtain depth dependence of the radiogenic heat. With larger dataset available now, such a relationship is not so clear, though data does show that surface heat flow increases with increase in the surface heat generation. Investigators looked for other means to obtain depth dependence of radiogenic heat. This became possible with the availability of crustal section from seismic investigations and their translations in terms of rock types combined with new estimates of radiogenic heat in these rock types as exposed on the surface of the Indian regions. In Dhawar craton and other surrounding regions such studies have been undertaken by Roy and Rao (1999, 2003), Kumar and Reddy (2004), Kumar et al. (2007a, 2007b) and Manglik (2006). Indian shield now appears quite similar to other shield areas. For Dharwar craton the Moho temperatures are around 300ºC and for the eastern ghat belts values are ~ 550ºC. Steady state calculations have also been extended to two dimensions by Ramana et al. (1999, 2003), Rai et al. (2003, 2006, 2007), Thiagarajan (2002) and Thiagarajan et al. (2001) for several DSS sections in the Indian region using finite element modelling .

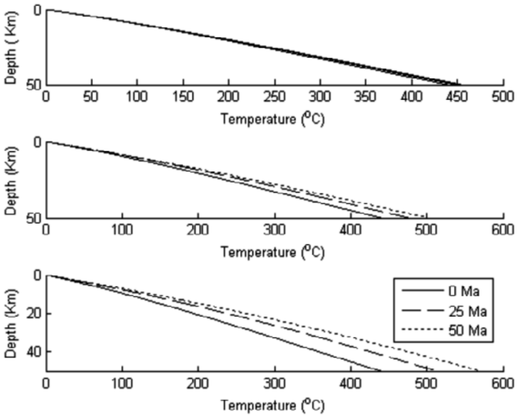

**Fig.10.1** Temperature-depth profiles for various values of erosion rates (top v = 0.05 km/Ma, middle for v = 0.2 km/Ma and bottom v = 0.4 km/Ma) and 0, 25 and 50 Ma for $A_s = 1.0$ μWm$^{-3}$ and $Q_o = 20$ mWm$^{-2}$ (Singh 2007)

There have been numerous transient heat perturbations in the Indian regions as reflected in igneous, metamorphic, tectonic and sedimentation episodes. However only a few transient studies have been undertaken. Ganguly et al. (1996) undertook transient modelling of the generation of charnockitic rocks in southern India. They first constructed a steady state model of the thermal structure prevailing before formation of these rocks. Then they perturbed this profile by invoking $CO_2$ advection. The duration of advection and its amount was estimated by summing transient solution of relevant advection–diffusion equation. They also considered the crustal thickening by overthrusting of a

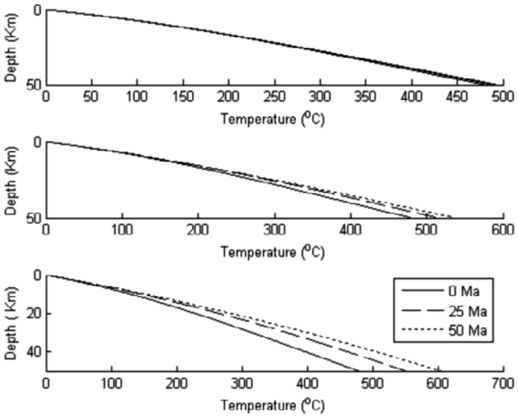

**Fig.10.2** Temperature-depth profiles for various values of erosion rates (top v = 0.05 km/Ma, middle for v = 0.2 km/Ma and bottom v = 0.4 km/Ma) and 0, 25 and 50 Ma for $A_s = 2.0$ μWm$^{-3}$ and $Q_o = 20$ mWm$^{-2}$ (Singh 2007)

thrust sheet for the formation of charnockites and estimated the thicknesses of the thrust sheet which can raise the temperatures necessary for charnockitisation. They concluded that a combination of $CO_2$ advection and crustal thickening by emplacement of a thrust sheet would give requisite temperatures for the formation of charnokckites. This work was further extended by Gliko et al. (1999) to include viscous effects of $CO_2$ solitary wave propagation through lithosphere and associated thermal effects. Another study of the effect of ongoing erosion on the thermal structure of the Indian shield was recently investigated in Singh (2007). Erosion brings up hotter rocks to the surface, but eroded material has higher radiogenic heat. Both these effects control the nature of the geotherms. Figures 10.1 and 10.2 show the evolution of geotherms at two values of surface radiogenic heat representing southern Indian shield. Singh (2007) has discussed implication of these results for tectonics of the Indian shield. There have been interesting discussions about the signatures of plume which led to Deccan volcanism in heat flow and topographic data. No convincing answer to this question has been provided so far. As geological, geochemical and geophysical investigations become more definitive about types of physico-chemical processes which have taken place in the Indian region, above models will shed more light on the working of these processes.

So far role of heat conduction models has been highlighted in the above review. However the temperature dependence of rock properties such as seismic velocities, electrical conductivity, mineralogical and petrological compositions have been measured in high pressure and temperature laboratory experiments. Thermodynamic and kinetic models have been worked out to interpret laboratory data and applied to quantify evolution of earth's interior. Several ab-initio (first-principles) numerical quantum mechanical calculations have been made for estimating physical and chemical properties at high pressures and temperatures using high performance computing. All these results can be used to estimate thermal structure and composition of earth's interior from the joint interpretation of seismic, gravity and electromagnetic responses of the earth. Several studies have been done in the past to estimate the thermal structure of the mantle by such a joint interpretation. Priestley and McKenzie (2006) have obtained a relationship between the shear wave velocity and pressure and temperature distribution in the Pacific oceanic lithosphere and have used this relationship to constrain regional variation of thickness of continental lithosphere from the knowledge of its shear wave velocity structure. Kronrod and Kuskov (2007) have used a combination of the dependence of seismic wave velocities on composition and temperatures using thermodynamic models and steady heat conduction model constrained by surface heat flow values to jointly invert them to estimate the thermal structure of the crust and upper mantle. Khan et al. (2006) have used the temperature dependence of electrical conductivity and composition of the mantle rocks based on laboratory thermodynamic experiments and models to invert earth's electromagnetic sounding data to estimate the thermal structure of the mantle. These ideas have been in the literature in some form earlier also, but current studies have benefited from better laboratory data and theoretical methodologies, such as use of inversion theory. Such studies should also be undertaken to estimate thermal structure of the Indian crust keeping in view its compositional and thermomechanical complexities.

## 10.6 Summary

Indian crust has signatures of interesting geological processes since Archean. In order to decipher these processes it is necessary to build their models and confront them with observations. Thermal models are mostly based on applications of heat conduction theory. Since its formulation by Fourier in early nineteenth century, it has been used to infer quantitative knowledge of the earth. In this endeavor various analytical models have been used. We have summarised several such models which are used frequently in the literature to find the thermal structure of crust. We have also summarised the studies conducted for the Indian continental crust and lithosphere. As more geological, geochemical and geophysical data for the Indian region would become available, these models will find applications in understanding evolution of Indian continental region.

**Acknowledgements:** Author is grateful to Director NGRI for his kind encouragements, Dr. Ajay Manglik for his critical review of the manuscript and CSIR for providing him Emeritus Scientist Scheme.

## 10.7 References

Agrawal PK, Pandey OP (1999) Relevance of hot underlying asthenosphere to the occurrence of Latur earthquake and Indian peninsular shield seismicity. J Geodynamics 28: 303–316

Agrawal PK, Pandey OP (2004) Unusual lithospheric structure and evolutionary pattern of the cratonic segments of the south Indian shield. Earth Planets Space 56: 139–150

Bhattacharji S, Singh RN (1984) Thermo-mechanical structure of the southern part of the Indian shield and its relevance to Precambrian basin evolution. Tectonophys 105: 103–120

Carslaw HS, Jaeger JC (1959) Conduction of heat in Solids, Oxford University Press, New York

Clark SP (1980) Comment on "Erosion, uplift, exponential heat source distribution and transient heat flux" by TC Lee. J Geophys Res 85: 2694–2695

Ganguly J, Singh RN, Ramana DV (1995) Thermal perturbation during charnockitization and granulite facies metamorphism in southern India. J Metamorphic Geology 13: 419–430

Gliko AO, Singh RN, Swathi PS (1999) Physical approach to the problem of origin of charnockitic rocks of southern India: Mechanism of crustal heating and transfer of carbon dioxide. Russian J of Earth Science 1, No 5

Gupta ML (1995) Thermal regime of the Indian shield, In: Gupta ML, Yamano M (eds) Terrestrial heat flow and geothermal energy in Asia, Oxford and IBH Publishing Co

Gupta ML, Sunder A, Sharma SR (1991) Heat flow and heat generation in the Archean Dharwar cratons and implications for the southern Indian shield geotherm and lithospheric thickness. Tectonophysics 194: 107–122

Gupta ML, Gaur VK (1984) Surface heat flow and possible evolution of Deccan volcanism. Tectonophysics 105: 309–318

Haxby WF, TurcotteDL (1976) Stresses induced by addition or removal of overburden and associated thermal effects. Geology 4: 81–184

Khan A, Connolly JAD, Olsen N (2006) Constraining the composition and thermal state of the mantle beneath Europe from inversion of long-period electromagnetic sounding data. J Geophys.Res 111, B10102,doi: 10.1029/2006JB004270

Kronrod VA, Kuskov OL (2007) Modelling of the thrmal structure of continental lithosphere. Izvestia, Physics of the Solid Earth 43: 91–101

Kumar PS, Reddy GK (2004) Radioelemetns and heat production of an exposed Archean crustal cross-section, Dharwar craton, south India. Earth Planet Sci Lett 224: 309–324

Kumar PS, Menon R, Reddy GK (2007a) The radiogenic heat production in the thermal evolution of a proterozoic granulite-facies orogenic belt: Eastern Ghats, Indian shield. Earth Planet Sci Lett 254: 39–54

Kumar PS, Menon R, Reddy GK (2007b) Crustal geotherm in southern Deccan basalt province, India: The Moho is as cold as adjoining cratons. Geol Soc Am Special Paper 430

Lee TC (1980) Erosion, uplift, exponential heat source distribution and transient heat flux. J Geophys Res 84: 585–590

Manglik A (1993) Movement of phase boundaries and thermorheological evolution of lithosphere, PhD Thesis, OU, Hyderabad

Manglik A (2004) Rheological modelling of the Indian continental lithosphere. Himalayan Geology 26: 165–173

Manglik A (2006) Mantle heat flow and thermal structure of the northern block of Southern Granulite Terrain, India. J Geodynamics 41: 510–519

Manglik A, Singh RN (1991) Rheology of Indian continental crust and upper mantle. Proc Ind Acad Sci (Earth Planet Sci) 100: 389–398

Manglik A, Singh RN (1992) Rheological thickness and strength of Indian continental lithosphere. Proc Ind Acad Sci (EPS) 101: 339–345

Manglik A, Singh RN (1999) Rheological stratification of the Indian continental lithosphere: Role of diffusion creep, Proc Indian Acad Sci (EPS) 108: 15–21

Manglik A, Singh RN (2002) Thermomechanical structure of the central Indian shield: Constraints from deep crustal seismicity, Curr Sci 82: 1151–1157

Mareschal JC (1991) Determination of past heat flow from subsidence data in intercratonic basins and passive margins. In: Cermak V, Ryback L (eds) Terrestrial heat flow and lithosphere structure, Springer, Berlin

McKenzie DP (1978) Some remarks on the development of sedimentary basins. Earth Planet Sci Lett 40: 25–32

Negi JG, Agrawal PK, Pandey OP (1987) Large variation of Curie-depth and lithospheric thickness in Indian sub-continent and a case for magnetothermometry. Geophys J Roy Astr Soc 88: 763–775

Negi JG, Agrawal PK, Pandey OP (1986) Super mobility of hot Indian lithosphere. Tectonophysics 131: 147–156

Ozisik MN (1993) Heat conduction, 2nd Edition, John Wiley and Sons

Pandey OP, Agrawal PK (1999) Lithospheric mantle deformation beneath the Indian cratons. J Geology 107: 683–692

Pandey OP, Agrawal PK, Chetty TRK (2002) Unusual lithospheric structure beneath the Hyderabad granite region, Eastern Dharwar craton, South India. Phys Earth Planet Inter 130: 59–69

Priestley K McKenzie D (2006) The thermal structure of the lithosphere from shear wave velocities. Earth Planet Sci Lett 244: 285–301

Rai SN, Thiagarajan S, Ramana DV (2003) Seismically constrained 2-D thermal model of Central India along Hirapur–Mandla Deep Seismic Sounding profile across the Narmada Son Lineament. Curr Sci 85: 208–213

Rai SN, Thiagarajan S (2006) A tentative 2D thermal model of central India across the Narmada-Son Lineament (NSL). J Asian Earth Sci 28: 363–371

Rai SN, Thiagarajan S (2007) 2-D crustal thermal structure along Thuadara-Sindad DSS profile across Narmada-Son Lineament, Central India. J Earth Syst Sci 116: 347–355

Ramana DV, Thiagarajan S, Singh RN (1999) Thermal modelling along the Kavali-Udipi profile in southern Indian shield. Acta Geophysica Polonica 47: 423–433

Ramana DV, Thiagarajan S, Rai SN (2003) Crustal thermal structure of the Godavari graben and coastal basin. Curr Sci 84: 1116–1122

Rao RUM, Rao GV, Narain H (1976) Radioactive heat generation and heat flow in Indian region. Earth Planet Sci Lett 30: 57– 64

Rao RUM, Roy S, Srinivasan R (2003) Heat flow researches in India: Results and Perspectives. In: Mahadevan TM, Arora BR, Gupta KR (eds) Indian Continental Lithosphere: Emerging research Trends. Memoir Geol Soc India 53: 347–391

Roy S, Rao RUM (1999) Geothermal investigations in 1993 Latur earthquake area, Deccan Volcanic Province, India. Tectonophysics 306: 237–252

Roy S, Rao RUM (2003) Towords a crustal thermal model for the Archean Dharwar craton. Phys Chem Earth 28: 361–373

Saltus RW, Lachenbruch AH (1991) Thermal evolution of the Sierra Nevada: Tectonic implications of new heat flow data. Tectonics 10: 325–344

Sandiford M, McLaren S (2002) Tectonic feedback and ordering of heat producing elements within the continental lithosphere Earth Planet Sci Lett 204: 133–150

Sandiford M, van Kranendonk MJ, Bodoros S (2004) Conductive incubation and the origin of dome-andkeel structure in Archaen granite-greenstone terrains: A model based on the eastern Pilbara Craton, Western Australia. Tectonics 23, TC 1009. doi: 10.1029/2002TC001452

Singh RN, Negi JG (1980) Comment on "Erosion, uplift, exponential heat source distribution and transient heat flux" by TC Lee. J Geophys Res 85: 2696–2697

Singh RN (1981) State of stress in the northern part of the Indian plate. In: Gupta HK, Delany FM (eds) Zagros, Hindukush, Himalaya Geodynamic Evolution, AGU, Washington and GSA, Boulder

Singh RN (1984) Thermal evolution of the Indian shield and subjacent mantle. Tectonophys 105: 413–418

Singh RN (1985) Thermal structure of the Indian shield. Ind J Earth Sci 12: 155–158

Singh RN (2007) Modelling erosion induced subsurface thermal changes and tectonic consequences. Jour Geol Soc Ind 70: 489–498

Singh RN, Negi JG (1982) High moho temperature in the Indian shield. Tectonophysics 82: 299–306

Sleep NH, Snell NS (1976) Thermal contraction and flexure of mid-continent and Atlantic marginal basins. Geophys J R Astron Soc 45: 125–154

Srivastava K, Singh RN (1998) A model for temperature variations in sedimentary basins due to random radiogenic heat sources. Geophysical J Int 135: 727–730

Srivastava K, Singh RN (1999a) Influence of random thermal conductivity on the subsurface temperature fluctuations. J Geophysics 20: 89–92

Srivastava K, Singh RN (1999b) A stochastic model to quantify the steady state crustal geotherms subject to uncertainty in thermal conductivity. Geophy J Int 138: 895–899

Thiagarajan S (2002) Two-dimensional modelling of crustal thermal structure along selected deep seismic sounding profiles with Indian region, Ph D Thesis, OU, Hyderabad

Thiagarajan S, Ramana DV, Rai SN (2001) seismically constrained two-dimensional crustal thermal structure of the Cambay basin. Proc Ind Acad Sci (EPS) 110: 1–8

Woodhouse J, Birch F (1980) Comment on “Erosion, uplift, exponential heat source distribution and transient heat flux” by TC Lee. J Geophys Res 85: 2691–2693.

## 11

# Convection in the Earth's Mantle

Ajay Manglik

**Abstract:** Solid state convection is considered as the main heat transport mechanism in the earth's mantle because of significant temperature difference between the base of lithosphere and core-mantle boundary and the large thickness of the mantle layer. Convective circulations in the mantle, induced by thermal heating are modeled by using fluid dynamical modelling approach. Initially some analytical models were developed to understand the process of convection in the mantle. However the complexity of the structure dependence of rock properties on pressure and temperature and grain-size effects, distribution of plate boundaries, presence of heterogeneous boundary layers, etc. have led to the development of numerical techniques to understand the dynamics of the mantle, plume-lithosphere interaction, flood basalt volcanism, ridge and subduction processes and other related processes. Ever-increasing computing power has helped in the development of more realistic models of the mantle dynamics. A brief overview of mathematical formulation and some of the applications of mantle convection modelling is presented in this chapter.

---

Ajay Manglik (✉)
National Geophysical Research Institute (Council of Scientific and Industrial Research), Hyderabad - 500606, India
e-mail: ajay@ngri.res.in

## 11.1 Introduction

The realisation in the early fifties that the earth's outermost shell of about 100 km thickness, the lithosphere could be divided into a number of plates on the basis of global seismicity and volcanism distribution led to the plate tectonic hypothesis. This hypothesis successfully explained many geotectonic phenomena in terms of interaction of moving plates at accretionary, subducting and transform boundaries. The hypothesis of plate tectonics received wide acceptance because it linked many enigmatic observations to the kinematics of the plates. However an important question remained about the forces necessary to drive the plates. The driving force for the movement of lithospheric plates was inferred as due to the convection in the underlying mantle. The analogy can be drawn from the convection in a fluid layer heated from below. When a layer of fluid is heated from below by external heat sources and/or from within by internal heat sources and cooled from the top the density of the fluid becomes less in the regions of heating because of thermal expansion and temperature dependence of density. The temperature induced density heterogeneities lead to gravitational instability as the cool dense fluid in the upper part of the layer tries to sink and hot less dense fluid tries to rise upward due to its buoyancy. Once the buoyancy becomes strong enough to overcome the viscous resistance, the convection starts. This process is called thermal convection.

In the earth's mantle, a region lying between 100 and 2900 km depth, this situation exists because of significant temperature difference between the base of lithosphere (100 km depth) and core-mantle boundary (2900 km) and the thickness of the mantle layer leading to heat transport by convection. Studies related to convection in the mantle can be grouped into plate-mode and plume-mode convection. In the plate-mode of convection, spreading ridges and subducting slabs are considered to be forming the upwelling and downwelling limbs of a convection cell. Models dealing with this mode of convection are used mainly to analyse the coupling between the plate motion and underlying convection and self-consistent generation of lithospheric plates. Plume-mode of convection is used to explain the occurrence of intraplate volcanism at hotspots, the surface manifestations of hot, narrow upwellings in the mantle, termed as mantle plumes. Largely fixed in space, mantle plumes are considered as representative of a convective style complementary to that of plate tectonics and have been used to relate surface observations to processes in the deep mantle and at the core-mantle boundary. In the absence of direct observations of the deep earth, exception being the inclusions of mantle rocks in diamonds, surface geophysical observables such as geoid and topography, heat flow and seismic images of the mantle and geochemical characteristics of rocks coupled with mathematical models of deep earth processes provide useful insights into the earth's deep interior.

Convective circulations in the mantle induced by thermal heating are modeled by using fluid dynamical modelling approach. The mantle convects in solid state, meaning it behaves as a fluid in geological times but is solid on short time scales. To understand the nature and conditions for onset of thermal convection one needs to solve the Navier-Stokes equation along with the continuity and energy balance equations. Numerical modelling techniques are an integral part of studies related to mantle plumes in particular and mantle convection in general. The convective motions in the mantle induced either by plumes or by plate motions have been analysed by employing numerical techniques in two-dimensional, three-dimensional, Cartesian, cylindrical and spherical geometries. Starting from simple models of convection of a uniform viscosity fluid in a closed box heated from below, later models have grown in complexity and include highly temperature- and pressure-dependent viscosity, internal heating, plate motions and melting in time-dependent convection. These experiments have been performed at the Rayleigh numbers representative of the earth's mantle for both the two-layered and the whole mantle convection. This chapter describes the governing equations, modelling approaches and their application to some of the issues related to mantle dynamics.

## 11.2 Governing Equations

For thermal convection of an incompressible, Boussinesq fluid the Navier-Stokes and continuity equations are given as (Christensen 1992)

$$\rho \frac{D\mathbf{u}}{Dt} = -\nabla P + \nabla : \boldsymbol{\tau} + \rho \mathbf{g} \qquad (11.1)$$

$$\nabla . \mathrm{u} = 0 \qquad (11.2)$$

where P, $\tau$, u, $\rho$ and g are pressure, deviatoric stress, velocity, density and gravity acceleration, respectively. The Boussinesq approximation to the Navier-Stokes equation states that the variation in density may be neglected except in the terms involving pressure. In Eq. 11.1, the left hand side represents the inertial term which, for mantle convection case, can be ignored because of very high viscosity ($\sim 10^{21}$ Pa.s) of the mantle. Thus the Navier-Stokes equation becomes

$$\nabla . \mathrm{P} = \nabla : \tau + \rho \mathrm{g} \qquad (11.3)$$

The energy balance equation for incompressible fluid is written as

$$\rho C_P \frac{\partial T}{\partial t} + \mathbf{u}.\nabla T = \nabla.(k\nabla T) + Q \tag{11.4}$$

where $C_P$, T, **u**, k, Q and t are specific heat, temperature, velocity vector, thermal conductivity, internal heat sources and time, respectively. The heat source term Q includes all the sources of heat such as radiogenic heat sources, viscous dissipation etc. within the mantle. In addition the equation of state

$$\rho = \rho_0[1-\alpha(T_0-T)] \tag{11.5}$$

is also required to compute density difference and hence thermal buoyancy. Here $\rho_0$, $\alpha$ and $T_0$ are reference density, coefficient of thermal expansion and reference temperature, respectively.

An equation analogous to the heat conduction is used to solve for the compositional convection. This can be written as

$$\frac{\partial C}{\partial t} + \mathbf{u}.\nabla C = \nabla.(\kappa_c \nabla C) + S \tag{11.6}$$

where C, S, $\kappa_c$ are concentration of compositional component, source term such as depletion due to partial malting and compositional diffusivity. $\kappa_c$ is more than two orders of magnitude smaller than the thermal diffusivity. The equation of state (Eq. 11.5) is also modified to include the effect of compositional changes. This is expressed as

$$\rho = \rho_0[1-\alpha(T - T_0) - \beta(C - C_0)] \tag{11.7}$$

where $\beta$ is analogous to the coefficient of thermal expansion $\alpha$.

The above set of equations can be simplified depending on the type of the coordinate system and the dimensionality of the problem chosen. As an example, if we select a two-dimensional problem in the Cartesian coordinate system, then Navier-Stokes equation (Eq. 11.3) can be written as (Manglik 2002):

$$\frac{\partial P}{\partial x}\hat{x} + \frac{\partial P}{\partial z}\hat{z} = \left(\frac{\partial \tau_{xx}}{\partial x} + \frac{\partial \tau_{xz}}{\partial z}\right)\hat{x} + \left(\frac{\partial \tau_{xz}}{\partial x} + \frac{\partial \tau_{zz}}{\partial z} + \rho g\right)\hat{z} \tag{11.8}$$

where $\hat{x}$ and $\hat{z}$ are unit normals in x- and z-directions, respectively. The deviatoric stress components $\tau_{ij}$ can be related to the velocity through the deviatoric strain rate components $\dot{\varepsilon}_{ij}$ and the isotropic viscosity $\eta$ as

$$\tau_{ij} = \eta\dot{\varepsilon}_{ij} = \frac{\eta}{2}\left(\frac{\partial u_i}{\partial x_j} + \frac{\partial u_j}{\partial x_i}\right) \tag{11.9}$$

Where i, j represent either of the x- and z-components.

Similarly continuity equation (Eq. 11.2) can be written as

$$\frac{\partial u}{\partial x} + \frac{\partial w}{\partial z} = 0 \tag{11.10}$$

and the energy equation (Eq. 11.4) takes the form

$$\frac{\partial T}{\partial t} + u_x\frac{\partial T}{\partial x} + u_z\frac{\partial T}{\partial z} = \kappa\left(\frac{\partial^2 T}{\partial x^2} + \frac{\partial^2 T}{\partial z^2}\right) + \frac{Q}{\rho C_P} \tag{11.11}$$

under the assumption that the thermal diffusivity $\kappa$ ( = k/$\rho$C) of the medium is constant and isotropic.

In order to solve the Navier-Stokes and the energy equation along with the continuity equation and the equation of state, appropriate boundary conditions suitable to a geodynamic scenario are required. For the Navier-Stokes equation, free-slip, no-slip or open boundary conditions are most commonly used and prescribed temperature, prescribed flux or mixed boundary conditions are used for the energy equation. An initial condition is required for the energy equation to initiate the convection.

These equations are solved in non-dimensional form with the two important control parameters characterising the nature of thermal convection. These are the Rayleigh number and the Nusselt number. Rayleigh number (R*a*) in the classical case of heating at the base and no internal heat sources, is defined as

$$Ra = \frac{\rho_0 \alpha g \Delta T h^3}{\kappa \eta_0} \tag{11.12}$$

where $\rho_0$, $\alpha$, g, $\kappa$, $\eta_0$ are reference density, coefficient of thermal expansion, gravity acceleration, thermal diffusivity and reference viscosity, respectively. $\Delta$T, h are temperature difference across the layer of thickness h. Other variants of the Rayleigh number corresponding to the prescribed basal heat flux ($Ra_q$) and internal heating ($Ra_H$), respectively are:

$$Ra_q = \frac{\rho_0 \alpha g q_b h^4}{k\kappa\eta_0}, \quad Ra_H = \frac{\rho_0 h^2 H}{k\Delta T} Ra \tag{11.13}$$

where $q_b$, k, H are basal heat flux, thermal conductivity and concentration of internal heat sources, respectively. The pattern and the vigor of convection depends on the Rayleigh number. Extensive research work has been carried out to analyse the convective motions for a range of Rayleigh numbers (Tackley 1995; Jackson 1998). Similarly a Rayleigh number can be defined for compositional convection also. Nusselt number (Nu) provides an estimate of convective heat transport. In fluid dynamics as well as in mantle convection studies a lot of emphasis has been put on establishing a relation between the Rayleigh and the Nusselt numbers. This relationship is represented in the following form for a classical thermal convection case

$$Nu = cRa^b \qquad (11.14)$$

Some other control parameters used in convection studies are Prandtl number, Peclet number and buoyancy flux. Prandtl number is very large for mantle convection. Therefore Prandtl number is assumed to be infinite in mantle convection studies.

## 11.3 Analytical Solutions

Complexity of the lithosphere and mantle viscosity structure, temperature- and pressure-dependence of material properties and non-uniform nature of the heat flow into the mantle from the core inhibits any simple solution of the convective flows in the mantle. Therefore numerical techniques are used to solve the system of equations discussed in the previous section. However a number of analytical solutions were developed for simple cases to gain insight into the dynamics of the mantle. Linear stability analysis provided a constraint on the critical value of the Rayleigh number required for the onset of convection in a layer (Turcotte and Schubert 1982). For the convection to initiate in a layer of thickness h heated from below and having free-slip boundary conditions the minimum value of $Ra$ should be $27\pi^4/4$. The Rayleigh number, however is significantly larger than the critical Rayleigh number for the convection in the earth's mantle. As an example for the earth's upper mantle $\eta = 10^{21}$ Pa.s, $\rho = 4000$ kg/m$^3$, $\alpha = 3.0 \times 10^{-5}$ K$^{-1}$, g = 10 m/s$^2$, h = 700 km and $\delta T = 1300$ºC. Substituting these values into Eq. 11.12 the value of $Ra$ is $5.4 \times 10^5$. This is much larger than the value of the critical Rayleigh number implying that strong convection in the mantle. Therefore boundary layer approach was used in early models of mantle convection. In this approach, analytical solutions were obtained for the flow in upwellings and downwellings and in thermal boundary layers for simplified cases at moderate Rayleigh numbers (Turcotte and Oxburgh 1967; Yuen and Schubert 1976; Olson et al. 1993). These solutions provided useful insights into the structure of the convection cells and were used in testing numerical simulations.

## 11.4 Numerical Modelling

Numerical modelling techniques are an integral part of studies related to mantle convection due to the complexities in the structure of the boundary layers, rheology of the mantle, presence of phase transitions and compositional heterogeneities as imaged by seismic tomography experiments. For example, viscosity one of the important parameters in the Navier-Stokes equation is not constant. It has exponential relationship with temperature for mantle-like rheology, implying a drastic reduction in viscosity for a small change in the temperature. This viscosity reduction increases the value of the Rayleigh number and, hence facilitates strong convection. The difficulty in obtaining analytical solutions for such a complex fluid dynamical system has led to the development of various numerical techniques for the simulation of thermal convection for mantle-like conditions (Torrance and Turcotte 1971; Parmentier et al. 1975; Brooks and Hughes 1982; Christensen 1984; King et al. 1990; Christensen 1992; Schubert et al. 2001). Two popularly used methods are the finite difference and finite element methods. However other approaches like combination of the spectral methods in space and finite difference in time domain or finite volume method have also been used. These techniques have been applied to simulate convection in 2-D, 3-D Cartesian, axisymmetric cylindrical and spherical geometries incorporating phase transitions, melting, compositional convection, convection with moving and rigid lithosphere and faulted plates (Tackley 1995, 1998; Jackson 1998; Lowman and Jarvis 1999; Manglik and Christensen 1997, 2006). The technical details of these techniques are beyond the scope of this chapter. A detailed review is of these techniques is presented in Schubert et al. (2001). Application of finite difference technique to the solution of 2-D Navier-Stokes equation applicable to mantle convection is described in Manglik (2002).

## 11.5 Applications to Mantle Dynamics

Numerical techniques have been extensively used to understand the dynamics of the mantle, plume-lithosphere interaction, flood basalt volcanism, ridge and subduction processes, etc. Ever-increasing computing power has helped in the development of more realistic models of the mantle dynamics. Some of the applications of mantle convection modelling are given below after describing various viscosity laws used to simulate lithospheric plates.

### *11.5.1 Effect of Viscosity Variations*

Viscosity is one of the most important parameters controlling the nature of convection in the mantle. Initial models of mantle convection were analysed for the systematic relationship between the Rayleigh number, Nusselt number, thicknesses of boundary layers and up- and downwellings assuming the mantle as a constant viscosity fluid ($\eta(x, z) =$

$\eta_0$, where $x$ and $z$ are spatial coordinates) (McKenzie et al. 1973; Jarvis 1984; Schubert and Anderson 1985). These models provided useful insight into the efficiency of heat transport, flow velocity and thickness of thermal boundary layers as a function of the Rayleigh number. Models of mantle convection, however require inclusion of lithospheric plates of varying thickness and plate velocities. Therefore many different types of viscosity laws were used to simulate lithosphere, asthenosphere and sub-asthenospheric mantle. Some of these viscosity laws are as following:

**Depth-dependent viscosity**

$$\eta = \eta_0 \exp(a z^b) \text{ and also } \eta = \eta_i \text{ for } z_i \leq z \leq z_i \qquad (11.15)$$

where $a$, b are material parameters and $z_i$ is the depth to the i<sup>th</sup> interface.

**Temperature-dependent viscosity**

$$\eta = \eta_0 \exp\left[A\left({}^{T_m}\!/_{T}\right)\right] \qquad (11.16)$$

where A, $T_m$ are material parameter and reference temperature, respectively.

**Temperature- and depth-dependent viscosity**

$$\eta = \eta_0 \exp\left[\frac{E + \rho_0 g(d - z)V}{R(T + T_{abs})} - \frac{E + \rho_0 g d V}{R(T_0 + T_{abs})}\right] \qquad (11.17)$$

where E, V, $\rho_0$, g, d, R, $T_0$, $T_{abs}$ are activation energy, activation volume, reference density, gravity acceleration, length scale, universal gas constant, reference temperature and absolute temperature, respectively.

**Power-law non-Newtonian rheology**

$$\eta = A\dot{\varepsilon}^{-(n-1)/n} \exp\left[(E + PV)/nR(T + T_{abs})\right] \qquad (11.18)$$

where $\dot{\varepsilon}$, P, n are strain rate, pressure and coefficient of power law rheology, respectively. E, V, R, $T_{abs}$ are defined above.

**Damage rheology (Plate-like structures)**

$$\begin{aligned} \eta &= \frac{2}{1 + d^m} e^{-\gamma T} \\ \frac{\partial d}{\partial t} &+ \mathbf{u}.\nabla d = a\sigma\dot{\varepsilon} - b e^{\gamma T} d \end{aligned} \qquad (11.19)$$

where $a$, b, $\gamma$ are material parameters, **u**, $\sigma$, $\dot{\varepsilon}$, d are velocity, stress tensor, strain rate and damage parameter, respectively. Among these laws very strongly non-linear viscosities, such as described by Eqs. 11.18 and 11.19 can mimic plate-like behaviour (Bercovici 1993; Auth et al. 2003).

## 11.5.2 Whole Versus Layered Mantle Convection

Whether the mantle convects as a single layer or in a layered mode separated by phase transition boundary between the upper and the lower mantle at 660 km has been extensively studied through numerical modelling . These models included the effects of density difference across a phase boundary either by modifying the effective thermal expansion coefficient

$$\alpha'(z) = \alpha(z) + \sum_{j=1}^{n} f_i(z) \qquad (11.20)$$

or by including a density difference

$$\delta\rho(z) = \frac{\delta\rho_d}{2}\left[1 + \tanh\left(\frac{P - P_d - \gamma(T - T_d)}{\rho g d}\right)\right] \qquad (11.21)$$

at the phase boundary (Christensen and Yuen 1985). Here $n$ is the number of phase transitions, $f_i$ is a function similar to delta function, $\delta\rho_d$, $\gamma$, d, p, g, $P_d$, $T_d$ are density jump across the phase boundary, Clapeyron slope, depth of the transition zone, gravity acceleration, pressure and temperature at the transition zone, respectively.

These numerical modelling experiments helped in understanding the nature of this transition zone and its influence on the dynamics of the mantle. These experiments, mainly focused on the ability of plumes rising from the core-mantle boundary to penetrate the phase boundary or subducting slabs sinking through the transition zone, brought out some interesting insights into the nature of convection. The modelling results indicated that the vigor of convection and its tendency to become strongly layered increases with the increase in the Rayleigh number (Christensen and Yuen 1985; Zhao et al. 1992). This implies that as the velocity of flow of mantle material increases with the increase in the Rayleigh number, the 660 km phase boundary opposes the flow of rising mantle material across it more strongly, favouring a two-layered convection. Thus numerical modelling of mantle convection incorporating the transition zone provided constraints on the dynamics of the mantle.

Numerical modelling studies brought out another interesting scenario of episodic changes in the mode of convection from layered to whole mantle convection and vice versa. These numerical modelling studies incorporating mainly subducting slabs supported a mantle overturn model (Machetel and Weber 1991; Davies 1995). In this type of model, subducting slabs play an important role. Modelling results indicated accumulation and buckling of cold subducted slab material just above the transition zone at 660 km during the layered convection mode. The rate of accumulation of slab material depended on the velocity of trench migration and the age of the subducting lithosphere (Christensen 1996, 1997). Once the slab material became large enough to remain stable at this depth, it started sinking into the lower mantle like avalanche, initiating large pulses of plume activity. These models also provided the constraints on the velocity of trench migration needed for mantle overturning. Slow velocity of trench migration resulted in direct penetration of subducting slab across the transition zone whereas slab accumulation occurred for high velocity of trench migration. These numerical results also corroborated seismic tomography mapping of subducting slabs (van der Hilst 1995; Widiyantoro and van der Hilst 1996) suggesting alternation of the mantle between the two-layer and single-layer mode of convection. Geological observations of increased global volcanic activity during the Cretaceous have been inferred as a consequence of such mode overturns (Stein and Hofmann 1994).

### 11.5.3 Effect of Boundary Layers

Early models of mantle convection considered the lithosphere as a rigid layer, with thickness variation as a function of square root of its age, signifying an oceanic-type lithosphere (Parsons and Sclater 1977) and included it in numerical models by employing temperature dependent rheology thereby increasing the viscosity of the boundary layer excessively. The continental lithosphere, however is very complex, both compositionally and in terms of its thermo-rheological properties and consists of thick cratonic roots (Polet and Anderson 1995). Earlier models of mantle convection considered continental lithosphere as an aged oceanic lithosphere. The continental lithosphere is, however distinct in terms of its thermal insulation effect and concentration of radiogenic heat sources in the crust. Numerical models evolved in complexity to include more realistic heterogeneous boundary layers mimicking continental lithosphere embedded in an oceanic lithosphere (Guillou and Jaupart 1995; Gurnis 1988; Zhong and Gurnis 1993; Lowman and Gable 1999; Lowman and Jarvis 1999; Manglik and Christensen 2006). Some of the important effects obtained through numerical modelling of mantle convection are preferential heating of sub-continental mantle and promotion of mantle upwelling beneath a super-continent. These models have been used to understand the mechanism of continental breakup and close temporal and spatial proximity of continental rifting and large-scale magmatism.

### 11.5.4 Plume Mode of Convection

Mantle plumes are narrow upwellings of hot mantle rocks that owe their origin to the instabilities of the thermal boundary layers at the transition zone and core-mantle boundary. These upwellings convectively bring deep mantle material to the base of lithosphere and are considered as the source for intraplate flood volcanism. Plume mode of mantle convection has been extensively studied using fluid dynamical approach discussed above to understand the lithospheric deformation and flood volcanism in terms of deep mantle processes. Earlier models tried to explain geoid, topography and heat flow variations over mantle plumes and subduction zones (e.g. Parsons and Daly 1983; Richards and Hager 1984; Courtney and White 1986) in terms of convective flows in the mantle. These earlier models, however did not include the effect of variable lithospheric structure and the role of plate boundaries. Enormous amount of work has been done ever since to analyse the effect of viscosity variations on plume flow, role of imposed plate boundaries at different geological times into convection models to study the evolution of convection pattern in presence of segmented top boundary layer (Karpychev and Fleitout 1996; Tackley 1998; Lithgow-Bertelloni and Gurnis 1997), effect of moving continental cratonic roots on plume flow and melting (Manglik and Christensen 2006), etc.

Decompression melting of upwelling mantle material at hotspots has been an important process providing constraint on the physical properties and dynamics of the mantle. The volume, composition and isotope patterns of basalts erupted at hotspots locations have been used to constrain models of plume-lithosphere interaction (McKenzie and Bickle 1988). The higher than normal mantle temperature of plume material yielding formation of mushroom shaped structure (Griffith and Campbell 1990) has been successful in explaining the origin of many large flood basalt provinces and intraplate volcanic ridges (White and McKenzie 1989). Earlier, McKenzie and Bickle (1988) parameterised the results of laboratory experiments on partial melting of garnet peridotite to quantify the amount of partial melt generated in an adiabatically ascending mantle material. This parameterisation was incorporated into the numerical mantle convection model by Watson and McKenzie (1991) to quantify the volume and geochemical composition of partial melt generated by mantle plume during its initiation and subsequently. These studies provided additional constraints for the dynamics of the mantle by integrating geochemical data (White and McKenzie 1995) and geophysical deep crustal mapping studies. Watson and McKenzie (1991) used simple isoviscous axisymmetric cylindrical model of mantle convection and computed melting by including the latent heat effect. More refined models of this process have ever since been developed. Farnetani and Richards (1995) used a layered viscosity model and discussed the nature of thermal entrainment in the presence of melting. The effect of melting, in the form of density reduction of the residue, on the dynamics of the plume flow has been discussed by Dupeyrat et al. (1995) for an isoviscous 2-D case. Manglik and Christensen (1997) analysed the effect of buoyant residue on plume flow for a 2-D case considering highly pressure- and temperature-dependent viscosity given. Ribe and Christensen (1999) have studied the effect of plume melting on the nature of convection beneath a moving oceanic plate through 3-D numerical modelling of thermal convection with variable viscosity and used the results to explain the presence of two zones of melting for Hawaiian plume; one at the plume axis and the other about 300–500 km downstream of the plume axis. More recent models include interaction of a starting plume with a moving lithospheric root (Manglik and Christensen 2006).

An example of interaction of a mantle plume with a moving continental lithosphere is shown in Figs. 11.1–11.3. In this 3-D model a moderate size plume blob is considered and the nature of its flow beneath the lithosphere is analysed to show the effect of the presence of a lithospheric root on the nature of flow. Results were computed using a 3-D finite volume thermo-chemical convection code (Manglik and Christensen 2006). A pressure- and depth-dependent viscosity [Eq. 11.17] was considered and a lithospheric root was imposed in the model as a high viscosity block. Three scenarios have been considered. In the first case, the plume reaches the base of the lithosphere after the root has passed over the hotspot. In this case (Fig. 11.1), the plume material initially spreads in the up-stream direction and the plume stem also tilts in the up-stream direction (Fig. 11.1a). The presence of the lithospheric root in the vicinity of the rising plume blob inhibits the flow of plume material in the direction of plate motion. After the root has gone sufficiently far away, the plume stem becomes vertical and the flow starts in the direction of plate motion (Fig. 11.1d). Intermediate stages of plume flow are shown in Figs. 11.1b, c.

In the second case, the root is just at the hotspot location when the plume reaches the base of the lithosphere (Fig. 11.2a). The plume material spreads beneath the root and it tends to flow in the down-stream direction towards the thin lithosphere (Figs. 11.2b, c). Once the root has moved sufficiently away down-stream from the location of the hotspot, the flow becomes similar to that observed beneath an oceanic lithosphere. In the third scenario, the lithospheric root lies in the up-stream direction when the plume reaches the asthenospheric depths (Fig. 11.3a). In this case the root considerably drags the plume in the down-stream direction

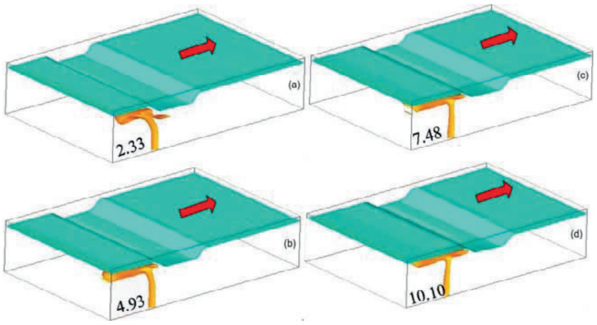

**Fig. 11.1** Flow of a moderate-sized plume head beneath a moving lithosphere at different times (a) 2.33 Myr, (b) 4.93 Myr, (c) 7.48 Myr and (d) 10.10 Myr. In this model, the thick root has already passed over the hotspot location (centre of plume upwelling projected on the horizontal surface) before the plume head reached the base of the lithosphere. The lithosphere moves towards right side at a moderate speed of 5 cm/yr. Pressure- and temperature-dependent viscosity is considered

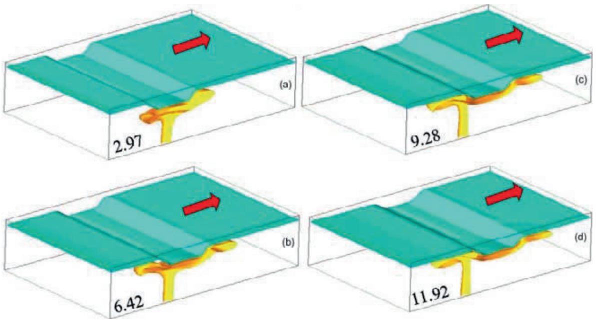

**Fig. 11.2** Flow of plume head beneath a moving lithosphere at different times (a) 2.97 Myr, (b) 6.42 Myr (c) 9.28 Myr and (d) 11.92 Myr. In this model, the plume head hits at the centre of the root. Other details are the same as given in Fig. 11.1

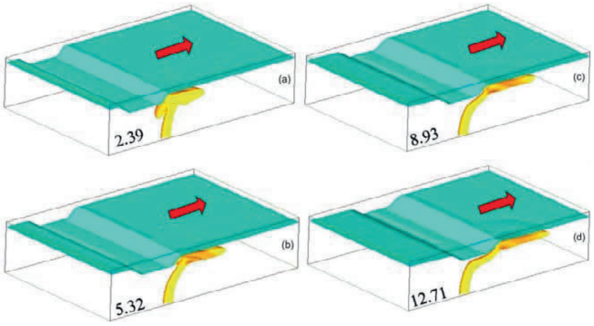

**Fig. 11.3** Flow of plume head beneath a moving lithosphere at different times (a) 2.39 Myr, (b) 5.32 Myr (c) 8.93 Myr and (d) 12.71 Myr. In this model, the plume head reaches the base of the thin lithosphere in front of the root. Other details are the same as given in Fig. 11.1

(Figs. 11.3b, c) and the plume-stem remains strongly tilted towards the down-stream direction even after a long time (Fig. 11.3d). In terms of decompression melting of the plume material, first model supports initial melting in the up-stream side of the hotspot whereas third model implies melting in front of the root. Second model yields initial small amount of melting in front of the root followed by melting at the hotspot location once the root has shifted to the right of the hotspot. These model results imply that the location of a continental root relative to the hotspot location at the time of impingement of a mantle plume has significant control over the volume and spatial distribution of volcanism.

## 11.6 Summary

The solid state convection is considered as the main heat transport mechanism in the earth's mantle. The study of mantle convection requires besides fluid dynamics, inputs from geophysics and mineral physics, geochemistry and geochronology, gravity and topography, rock mechanics, etc. to constrain various models of global mantle convection and plume induced convection. Compositional heterogeneities present in the mantle and complex rheological behaviour of mantle rocks add further complications to simple thermal models of mantle convection. With the availability of rapidly increasing computing power it is possible to develop sophisticated three-dimensional models of mantle convection incorporating above complications.

**Acknowledgements:** Computations presented in this chapter were carried out at the Institute for Geophysics, Goettingen, Germany. The permission of the Director, NGRI, to publish this work is gratefully acknowledged. The Author is thankful to Prof. Alok K. Gupta and Dr. R.N. Singh for their encouragement and support.

## 11.7 References

Auth C, Bercovici D, Christensen UR (2003) Two-dimensional convection with a self-lubricating, simple-damage rheology. Geophys J Int 154: 783–800

Bercovici D (1993) A simple model of plate generation from mantle flow. Geophys J Int 114: 635–650

Brooks AN, Hughes TJR (1982) Streamline upwind/Petrov-Galerkin formulations for convection dominated flows with particular emphasis on the incompressible Navier-Stokes equations. Compu Methods Appl Mech Eng 32: 199–259

Christensen U (1984) Convection with pressure- and temperature- dependent non-Newtonian rheology. Geophy J Ast Soc 77: 343–384

Christensen U (1992) An Eulerian technique for thermomechanical modelling of lithospheric extension. J Geophy Res 97: 2015–2036

Christensen UR (1996) The influence of trench migration on slab penetration into the lower mantle. Earth Planet Sci Lett 140: 27–39

Christensen UR (1997) Influence of chemical buoyancy on the dynamics of slabs in the transition zone. J Geophys Res 102: 22435–22443

Christensen UR, Yuen DA (1985) Layered convection induced by phase transitions. J Geophys Res 90: 10291–10300

Courtney RC, White RS (1986) Anomalous heat flow and geoid across the Cape Verde Rise: Evidence for dynamic support from a thermal plume in the mantle. Geophys J R Astron Soc 87: 815–867

Davies GF (1995) Penetration of plates and plumes through the mantle transition zone. Earth Planet Sci Lett 133: 507–516

Dupeyrat L, Sotin C, Parmentier EM (1995) Thermal and chemical convection in planetary mantles. J Geophys Res 100: 497–520

Farnetani CG, Richards MA (1995) Thermal entrainment and melting in mantle plumes. Earth Planet Sci Lett 136: 251–267

Griffith RG, Campbell IH (1990) Stirring and structure in mantle starting plumes. Earth Planet Sci Lett 99: 66–78

Guillou L, Jaupart C (1995) On the effect of continents on mantle convection. J Geophys Res 100: 24217–24238

Gurnis M (1988) Large-scale mantle convection and the aggregation and dispersal of supercontinents. Nature 332: 695–699

Jackson I (1998) The earth's mantle: Composition, structure and evolution. Cambridge Univ. Press

Jarvis GT (1984) Time-dependent convection in the earth's mantle. Phys Earth Planet Int 36: 305–327

Karpychev M, Fleitout L (1996) Simple considerations on forces driving plate motion and on the plate-tectonic contribution to the long-wavelength geoid. Geophys J Int 127: 268–282

King SD, Raefsky A, Hager BH (1990) ConMan: vectorising a finite element code for incompressible two-dimensional convection in the earth's mantle. Phys Earth Planet Int 59: 195–207

Lithgow-Bertelloni C, Gurnis M (1997) Cenozoic subsidence and uplift of continents from time-varying dynamic topography. Geology 25: 735–738

Lowman JP, Gable CW (1999) Thermal evolution of the mantle following continental aggregation in 3D convection models. Geophys Res Lett 26: 2649–2652

Lowman JP, Jarvis GT (1999) Effects of mantle heat source distribution on supercontinent stability. J Geophys Res 104: 12733–12746

Machetel P, Weber P (1991) Intermittent layered convection in a model with an endothermic phase change at 670 km. Nature 350: 55–57

Manglik A (2002) Rheological modelling and deformation of continental lithosphere. In: Rai SN, Ramana DV, Manglik A (eds) Dynamics of earth's Fluid Systems, Oxford and IBH Pub. Co., New Delhi

Manglik A, Christensen UR (1997) Effect of mantle depletion buoyancy on plume flow and melting beneath a stationary plate. J Geophys Res 102: 5019–5028

Manglik A, Christensen UR (2006) Effect of lithospheric root on decompression melting in plume-lithosphere interaction models. Geophys J Int 164: 259–270

McKenzie D, Bickle MH (1988) The volume and composition of melt generated by extension of the lithosphere. J Petrol 29: 625–679

McKenzie D, Roberts J and Weiss N (1973) Numerical models of convection in the earth's mantle. Tectonophysics 19: 89–103

Olson P, Schubert G and Anderson C (1993) Structure of axisymmetric mantle plumes. J Geophys Res 98: 6829–6844

Parmentier E\M, Turcottte DL, Torrance KE (1975) Numerical experiments on the structure of mantle plumes. J Geophys Res 80: 4417–4424

Parsons B, Daly S (1983) The relationship between surface topography, gravity anomalies and temperature structure of convection. J Geophys Res 88: 1129–1144

Parsons B, Sclater JG (1977) An analysis of the variation of ocean floor bathymetry and heat flow with age. J Geophys Res 82: 803–827

Polet J anderson DL (1995) Depth extent of cratons as inferred from tomographic studies. Geology 23: 205–208

Ribe NM, Christensen UR (1999) The dynamical origin of Hawaiian volcanism. Earth Planet Sci Lett 171: 517–531

Richards MA, Hager BH (1984) Geoid anomalies in a dynamic earth. J Geophys Res 89: 5987–6002

Schubert G, Turcotte DL, Olson P (2001) Mantle convection in the earth and planets. Cambridge Univ. Press

Schubert G anderson CA (1985) Finite element calculations of very high Rayleigh number thermal convection. Geophys J R Astron Soc 80: 575–601

Stein M, Hofmann AW (1994) Mantle plumes and episodic crustal growth. Nature 372: 63–68

Tackley PJ (1995) Mantle dynamics: Influence of transition zone. Rev Geophys 33 (Suppl): 275–282

Tackley PJ (1998) Self-consistent generation of tectonic plates in three-dimensional mantle convection. Earth Planet Sci Lett 157: 9–22

Torrance KE, Turcotte DL (1971) Thermal convection with large viscosity variations. J Fluid Mech 47: 113–125

Turcotte DL, Oxburgh ER (1967) Finite amplitude convective cells and continental drift. J Fluid Mech 28: 29–42

Turcotte DL, Schubert G (1982) Geodynamics. John Wiley, NY

van der Hilst RD (1995) Complex morphology of subducted lithosphere in the mantle beneath Tonga trench. Nature 361: 699–704

Watson S, McKenzie D (1991) Melt generation by plumes: A study of Hawaiian volcanism. J Petrol 32: 501–537

White RS, McKenzie DP (1989) Magmatism at rift zones: The generation of volcanic continental margins and flood basalts. J Geophys Res 94: 7685–7729

White RS, McKenzie D (1995) Mantle plumes and flood basalts. J Geophys Res 100: 17543–17585

Widiyantoro S, van der Hilst R (1996) Structure and evolution of lithospheric slab beneath the Sunda arc, Indonesia. Science 271: 1566–1570

Yuen DA, Schubert G (1976) Mantle plumes: A boundary layer approach for Newtonian and non-Newtonian temperature-dependent rheologies. J Geophys Res 81: 2499–2510

Zhao W, Yuen DA, Honda S (1992) Multiple phase transitions and the style of mantle convection. Phys. Earth Planet Int 72: 185–210

Zhong S, Gurnis M (1993) Dynamic feedback between a continent like raft an thermal convection. J Geophys Res 98: 12219–12232.

# 12

# Post-perovskite Phase: Findings, Structure and Property

Takehiko Yagi

**Abstract:** Experimental study by Lin (1994) on natural garnets in a laser-heated diamond-anvil under 30 GPa showed transformation of this phase to a new mineral having a perovskite like structure. Subsequently mineral physicists observed that all essential mantle minerals transformed to an assemblage comprising perovskite or rock salt like structure. While studying pyrolitic assemblage under lower mantle conditions, Hirose et al. observed that between 110 and 120 GPa a new phase appeared. It had a structure with Cmcm space group and was isostructural with $UFeS_3$. It had a layered structure made up of two types of layers. One layer had a two-dimensional network of $SiO_6$ octahedra, connected by edge or corner sharing along the direction of a and c axis. The other layer is formed by Mg cation.

The P-T condition or depth of transformation of perovskite to post-perovskite structure coincides with the D” layer of the earth. As this layer shows seismic anisotropy, it has been postulated that materials with post-perovskite structure may have lattice preferred orientation (LOP). This paper also describes deformation experiments related to development of LOP in the material with post-perovskite structures.

---

Takehiko Yagi (✉)
Institute for Solid State Physics, University of Tokyo, Japan
e-mail: yagi@issp.u-tokyo.ac.jp

## 12.1 Introduction

This is a short review describing the findings of a post-perovskite phase and various studies to clarify its structure and property. The first reports of the findings of the post-perovskite phase were made in 2004. This transition was really unexpected for almost all the earth scientists but once it was found, it affected considerably to our understandings of the structure and property of the D” layer which is located at the bottom of the lower mantle and just above the core. Since its discovery, numerous studies have started worldwide to clarify its various properties such as structure, elastic and plastic properties and transport properties. Because it is believed that this mineral may play a key role in understanding various complexities observed in the D” layer; in this article, I am going to review very briefly the story from the finding to the various studies of post-perovskite phase.

## 12.2 Stability of Silicate Perovskite and the Discovery of Post-perovskite Phase

The first report of the synthesis of silicate perovskite was made in 1974 (Liu 1974). He heated a natural garnet at around 30 GPa using laser-heated diamond-anvil and found that it has transformed into a phase having perovskite structure. He also clarified that, other major minerals in the upper mantle like olivine and pyroxene, all transforms into phases with perovskite structure or the assemblage of perovskite plus rocksalt structures. By that time many scientists have anticipated this silicate perovskite as a strong candidate of high-density mineral in the lower mantle. Therefore, soon after this discovery, it was widely believed that the silicate perovskite is the most abundant mineral in the lower mantle. Figure 12.1 shows the perovskite structure with a composition of $ABO_3$. It can be seen from this figure that the structure of perovskite is formed by a fcc close-packing of both oxygen ions and large “A” cations. Small “B” cations are distributed among them. In other words, most of the close packing silicates are formed by the close packing of oxygen alone and cations are distributed among them. In perovskite structure, on the other hand, large cations are also joining the close packing network. Because of this, perovskite has an unusually high efficiency of packing among various $ABO_3$-type structures, particularly when the size of the “A” cation is close to that of oxygen anion. As a result many $ABO_3$-type compounds transform into phases having perovskite like structure at high pressures. However for a long time, no further pressure-induced phase transformation from perovskite was known and no one could think of a structure which has higher efficiency of packing than perovskite.

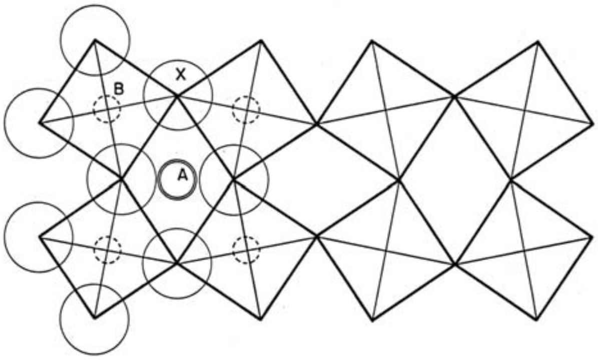

**Fig. 12.1** Crystal structure of $ABX_3$ perovskite (modified from Yagi et al. 1978). All the corners of $BX_6$ octahedrons are connected by corner shearing and forms three-dimensional network. If we take X anions and large A cations, they form fcc close packing

To clarify the high pressure stability limit of silicate perovskite was a subject of great interest from the beginning of its findings. Experimental studies were made possible by the development of diamond-anvil apparatus. During the 1980s the pressure range was extended beyond 100 GPa. Knittle and Jeanloz (1987) made high-pressure in situ X-ray studies for olivine samples heated at 127 GPa and concluded that “silicate perovskite is stable throughout the lower mantle”. Kesson et al. (1998) performed a transmission electron microscopy (TEM) study of the sample synthesised at 135 GPa and concluded that “Mg-perovskite was found to be present and no additional phases or disproportionations were encountered”. As is clear from these statements, it was widely believed that perovskite is an ultimate stable form of silicate in the lower mantle and is stable all the way down to the core-mantle boundary.

In spite of this, efforts were made to extend the pressure limit of the high-pressure and high-temperature in situ X-ray observation to clarify the possible new unquenchable high-pressure phases in the lower mantle. High-pressure and high-temperature in situ X-ray observations under deep lower-mantle conditions became possible by the use of a laser-heated diamond-anvil apparatus combined with synchrotron radiation. Various systems were developed and constructed at the synchrotron radiation facilities worldwide and in 1990s there were three places, ESRF (France), APS (USA) and Photon Factory (Japan) where such experiments were made successful. The laser-heating system developed at the Photon Factory (Yagi et al. 2001) was duplicated in SPring-8 (Watanuki et al. 2001), the third-generation synchrotron source in Japan. Combined with the high brightness and small divergence of the X-ray beam at SPring-8, this system made it possible to obtain very high quality X-ray diffraction patterns even above 100 GPa. However no one had seriously pursued the possibility to clarify further transitions in $MgSiO_3$ perovskite, because no one expected the existence of such a transition.

In 2002, Hirose and his colleagues started a systematic study of the lower mantle mineralogy using a laser-heated diamond-anvil system at SPring-8, which was further improved by that time. Through the study of complicated pyrolitic composition, they found new unidentified diffraction lines above about 120 GPa. They had no idea what component in the pyrolite caused these new lines and repeated the experiments using simpler compositions. Through these experiments they found that the same change in diffraction pattern occurs even in pure $MgSiO_3$ perovskite. They found that the pattern changes completely and reversibly between 110 and 125 GPa and they were convinced the existence of a new phase transition from perovskite into another structure. Still, they had no idea about the new structure which must have higher density than perovskite. From the powder diffraction pattern alone, it was almost impossible to solve the unknown crystal structure and theoretical calculations played important role to solve this problem.

## 12.3 Structure of Post-perovskite

Although the experiments were made at extremely high pressure and temperature conditions, the quality of X-ray diffraction patterns of Hirose's group obtained was very high as shown in Fig. 12.2. With the aid of powder diffraction indexing programme, they succeeded in determining the unit cell parameter which satisfies this X-ray data almost unambiguously. Since the atoms in the unit cell were well fixed (Z = 4, $MgSiO_3$), they performed molecular dynamic calculations using this unit cell and tried to find the possible structures. They synthesised powder X-ray diffraction patterns for each possible structure and compared them with the observation. Through these analyses, they succeeded in finding that this new phase had a structure with a Cmcm space group and was isostructural with $UFeS_3$ (Murakami et al. 2004). This new phase had a layered structure made up of a stacking of two kinds of layers; one layer formed by a two-dimensional network of $SiO_6$ octahedrons connected by the edge shearing and corner shearing in a direction of a-axis and c-axis, respectively. The other layer is formed by Mg cations (Fig. 12.3). This structure is quite different from the structure of perovskite which is formed by a three-dimensional network of $SiO_6$ octahedrons connected by corner shearing. In most of the pressure-induced phase transitions, the dimensionality of structure increases with increasing pressure, like a transition from graphite to diamond. Therefore, the pressure induced transition form three-dimensional perovskite into a layered structure was really a surprise and the result was not easily accepted at the beginning.

The same structure was, however also obtained by other theoretical simulations and experiments. Oganov and Ono (2004) reported that $MgSiO_3$ transforms into the same

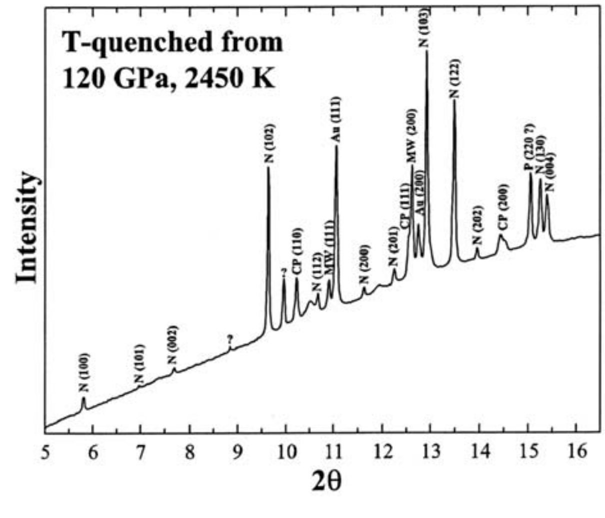

**Fig. 12.2** High-pressure in situ X-ray diffraction pattern of post-perovskite phase of $MgSiO_3$ (Murakami 2004). Diffraction pattern of $MgSiO_3$ observed after the heating at 120 GPa. Diffractions from the perovskite phase have disappeared and many new diffractions (N) appeared which were later explained by the post-perovskite structure

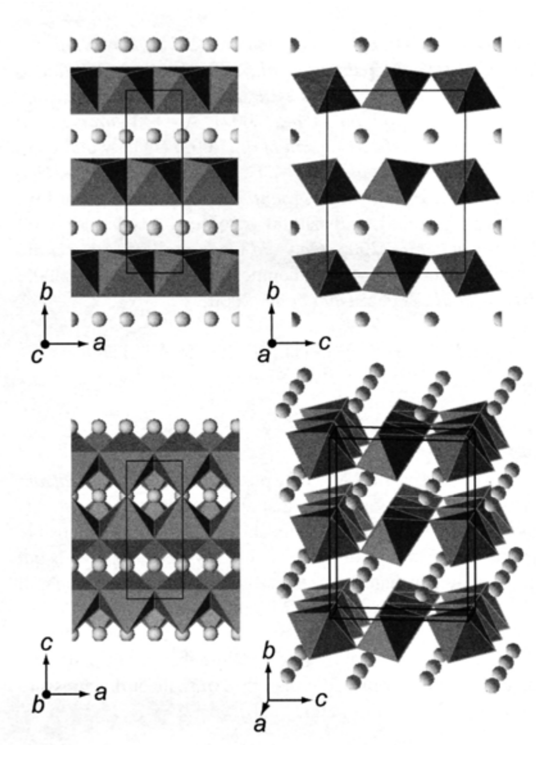

**Fig. 12.3** Crystal structure of the post-perovskite phase of $MgSiO_3$ (Hirose and Kawamura 2004)

structure at about 118 GPa, which was predicted by their first principle calculations based on the observation of the transition in $Al_2O_3$. Tsuchiya et al. (2004) made a first principle calculation of the structure using the unit cell parameter observed by Murakami et al. and concluded that the same structure was stabilised. Iitaka et al. (2004) also performed a first principle calculation and confirmed the stability of this new phase relative to the perovskite phase above about 100 GPa. Although the ways of calculations were quite different, the same conclusion was obtained by all these workers.

At the beginning, it was reported that other than $UFeS_3$, some sulfides and selenides, such as $AgTaS_3$, $UMnSe_3$ and $ThMnSe_3$, take the same structure while $CaIrO_3$ was the only oxide known to take the same structure. Many people tried to find other oxides with the same structure, as an analog material. Through these studies, it became clear that $MgGeO_3$, a classical germanate analogue material of $MgSiO_3$, also transforms from perovskite into the same structure at a much lower pressure of around 60 GPa (Hirose et al. 2005). Experiments in this pressure range are much easier and scientists could have recognised the possibility of the post-perovskite transition much earlier had someone studied it seriously. $MnGeO_3$ (Tateno et al. 2005) and $NaMgF_3$ (Liu et al. 2005) were also found to transform into a post-perovskite structure but they are all unquenchable to ambient condition and thus the study of its property were very difficult. Efforts were made to find oxides having post-perovskite structure and are quenchable to ambient condition. Kojitani et al. (2007) and Ohgushi et al. (2008) found $CaRuO_3$ and $CaPtO_3$, respectively and various studies are now carried out using these compounds.

As is clear from Fig. 12.3, $ABO_3$ type post-perovskite structure is formed by the stacking of “A” layer and $BO_6$ layer and from this layered nature, strong elastic anisotropy was expected. Based on the first principle calculation Iitaka et al. (2004) and Tsuchiya et al. (2004) showed that a strong elastic anisotropy do exist in $MgSiO_3$. This is quite important to explain various unsolved problems of the D” layer.

## 12.4 Properties of Post-perovskite

Seismic observation clarified the existence of strong elastic anisotropy in the D” layer and many arguments were made to explain the origin of this anisotropy, although no convincing explanation was obtained until recently. After the discovery of the post-perovskite phase, mineral physicists tried to explain the anisotropy in D” layer by the anisotropy of the post-perovskite phase itself. However in order that the bulk D” layer shows elastic anisotropy, proper lattice preferred orientation (LPO) of the component mineral must be understood. Therefore various studies were started to clarify the LPO of the post-perovskite phase under the condition of simple flow. Because the bottom of the lower mantle is the area where the subducted slab arrives from the upper mantle and hot plume migrate to the surface, it is believed that some kind of horizontal flow exist between them just like a plate motion at the surface of the earth.

Some experiments were made using $CaIrO_3$ as a model material because it is stable at ambient condition and many existing techniques to study the deformation texture could be used for this material. Yamazaki et al. (2006) made a simple shear deformation experiments at 1 GPa and 1173 K and observed that the a- and b-axis were aligned in the shear direction and perpendicular to it, respectively. Niwa et al. (2007) made a simple compression experiment using diamond-anvil and observed the LPO by radial X-ray diffraction technique. They clarified that strong LPO was developed in post-perovskite phase accompanied with a deformation while in perovskite, no meaningful LPO was formed under the same condition. In this experiment, the b-axis of the post-perovskite phase was aligned parallel to the compression axis. All these results on $CaIrO_3$ are in harmony with the idea that it has a strong layered structure and the plane parallel to the layer becomes slip plane during deformation.

On the other hand the result on $MgGeO_3$ is quite contradictory. Since the post-perovskite phase of $MgGeO_3$ is unquenchable to ambient condition, experiments can be made only above 60 GPa using radial X-ray diffraction technique. Merkel et al. (2006) reported that the planes close to (100) were aligned perpendicular to the compression axis, contrary to (010) in $CaIrO_3$. They also studied $(Mg,Fe)SiO_3$ post-perovskite and reported very similar results (Merkel et al. 2007). However Okada et al. (2008) showed that the LPO of $MgGeO_3$ observed by Merkel et al. (2006) is not a deformation texture but the transformation texture, because the LPO changes completely depending on the phase from which the post-perovskite was formed, that is either ilmenite phase or perovskite phase. Okada et al. (2008) further tried to observe the real deformation texture by increasing sample thickness. The result is not yet convincing but they suggest that the plane close to (001) may be aligned perpendicular to the compression axis. The results of the theoretical calculations (Oganov et al. [2005]; Carrez et al. [2007]) are also quite contradictory to each other, depending on the method of calculation. All these results indicate that more systematic study using various model materials or the development of new experimental technique is required to clarify the LPO of $MgSiO_3$ post-perovskite in the D” layer.

Other than the LPO, numerous studies have been made to clarify various properties of post-perovskite, because of its importance in understanding the nature of the D” layer. Among them are the wave velocity measurements using Brillouin scattering technique (Murakami et al. 2007), static compression experiments using diamond-anvil (Ono et al.

[2006]; Shieh et al. [2006]) and electrical conductivity measurements (Ohta et al. 2008).

Discovery of the post-perovskite phase in $MgSiO_3$ has been one of the most unexpected events in high-pressure mineral physics. It was not a simple addition of a new high pressure mineral in the lower mantle but was a discovery of key material to understand various unsolved problems of the D” layer. It is the area near the boundary between the lower mantle and the core, the biggest discontinuity inside the earth. Many properties such as temperature, seismic velocity, chemical composition and electrical conductivity changes discontinuously in this region and much more studies are needed on post-perovskite to properly understand this area.

## 12.5 References

Carrez P, Ferre D, Cordier P (2007) Implications for plastic flow in deep mantle from modelling dislocations in $MgSiO_3$. Nature 446: 68–70

Hirose K, Kawamura K (2004) Discovery of post-perovskite phase transition in $MgSiO_3$ and the earth’s lowermost mantle (in Japanese) Rev High Press Sci Tec 14: 265–274

Hirose K, Kawamura K, Ohishi Y, Tateno S, Sata N (2005) Stability and equation of state of $MgGeO_3$ post-perovskite phase. Am Mineral 90: 262–265

Iitaka T, Hirose K, Kawamura K, Murkami M (2004) The elasticity of $MgSiO_3$ post-persovskite phase in the earth’s lowermost mantle. Nature 430: 442–445

Kesson SE, Fitz Gerald JD, Shelly JM (1998) Mineralogy and dynamics of a pyrolite lower mantle. Nature 393: 252–255

Knittle E, Jeanloz R (1987) Synthesis and equation of state of $(Mg,Fe)SiO_3$ perovskite to over 100 gigapascals. Science 235: 668–670

Kojitani H, Shirako Y, Akaogi M (2007) Post-perovskite phase transition in $CaRuO_3$. Phys Earth Planet Inter 165: 127–134

Liu L (1974) Post oxide phases of Forsterite and Enstatite. Geophys Res Lett 2: 417–419

Liu HZ, Chen J, Hu J, Martin CD, Weidner DJ, Hausermann D, Mao HK (2005) Octahedral filing evolution and phase transition in orthorhombic $NaMgF_3$ perovskite under pressure. Geophys Res Lett 32.L04304

Merkel S, Kubo A, Miyagi L, Speziale S, Duffy TS, Mao HK, Wenk HR (2006) Plastic deformation of $MgGeO_3$ post-perovskite at lower mantle pressures. Science 311: 644–646

Merkel S, McNamara AK, Kubo A, Speziale S, Miyagi L, Meng Y, Dyffy TS, Wenk HR (2007). Deformation of $(Mg,Fe)SiO_3$ post-perovskite and D” anisotropy. Science 316: 1729–1732

Murakami K (2004) Phase Transitions of Lower Mantle Minerals and Its Geophysical Implications, Ph.D thesis, Tokyo Institute of Technology

Murakami K, Hirose K, Kawamura K, Sata N, Ohishi Y (2004) Post-perovskite phase transition in $MgSiO_3$. Science 304: 855–858

Murakami M, Sinogeikin SV, Bass JD, Sata N, Ohishi Y, Hirose K (2007) Sound velocity of $MgSiO_3$ post-perovskite phase: A constraint on the D”discontinuty. Earth Planet Sci Lett 259: 18–23

Niwa K, Yagi T, Ohgushi K, Merkel S, Miyajima N, Kikegawa T (2007) Lattice preferred orientation in $CaIrO_3$ perovskite and post-perovskite formed by plastic deformation under pressure. Phys Chem Minerals 34: 679

Okada T, Yagi T, Niwa K, Kikegawa T (2008) Phys Earth Planet Inter. submitted

Oganov AR, Ono S (2004) Theoritical and experimental-evidence for a post-perovskite phase of $MgSiO_3$ in earth’s D” layer. Nature 430: 445–448

Oganov AR, Martonak R, Laio A, Raiteri P, Parrinello M (2005) Anisotropy of earth’s D” layer and stacking faults in the $MgSiO_3$ post-perovskite phase. Nature 438: 1142–1144

Ohgushi K, Matsushita Y, Miyajima N, Katsuya Y, Tanaka M, Izumi F, Goto H, Ueda Y, Yagi T (2008) $CaPtO_3$ as novel post-perovskite oxide. Phys Chem Minerals 35: 189

Ohta K, Onoda S, Hirose K, Sinmyo R, Shimizu K, Sata N, Ohishi Y, Yasuhara A (2008) The electrical conductivity of post-perovskite in earths D” layer. Science 320: 89–91

Ono S, Kikegawa T, Ohishi Y (2006) Structural properties of $CaIrO_3$-type $MgSiO_3$ up to 144 GPa. Am Minera l 9: 475–478

Shieh SR, Duffy TS, Kubo A, Shen G, Prakapenka VB, Sata N, Hirose K, Ohishi O (2006) Equation of state of the post-perovskite phase synthesised from a natural $(Mg,Fe)SiO_3$ and $CdGeO_3$ perovskite and the post-perovskite phase transition. Proc Natl Acad Sci 103: 3039–3043

Tateno S, Hirose K, Sata N, Ohishi Y (2005) High-pressure behavior of $MnGeO_3$ and $CdGeO_3$ perovskite and the post-perovskite phase transition. Phys Chem Mineral 32: 721–725

Tsuchiya T, Tsuchiya J, Umemoto K, Wentzcovitch RM (2004) Phase transition in $MgSiO_3$ perovskite in the earth’s lower mantle. Earth Planet Sci Lett 224: 241–248

Watanuki T, Shimomura O, Yagi T, Kondo T, Isshiki M (2001) Construction of laser-heated diamond-anvil cell system for in-situ X-ray diffraction study at Spring-8. Rev Sci Instrum 72: 1289–1292

Yamazaki D, Yoshino T, Ohfuji H ando J, Yoneda A (2006) Origin of seismic anisotropy in the D” layer inferred from shear deformation experiments on post-perovskite phase. Earth Planet Sci Lett 252: 372–378

Yagi T, Mao HK, Bell PM (1978) Structure and crystal chemistry of post-perovskite type $MgSiO_3$. Phys Chem Mineral 3: 97–110

Yagi T, Kondo T, Watanuki T, Shimomura O, Kikegawa T (2001) Laser heated diamond-anvil apparatus at the photon factory and SPring-8: Problems and improvements. Rev Sci Instrum 72: 1293–1296.

# Important Images of the Volume

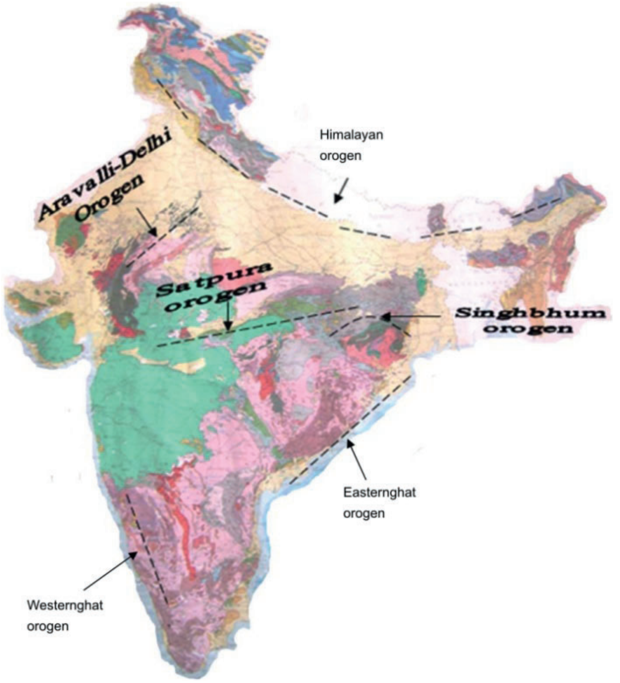

**Fig. 3.1** Distribution of orogenic belts in Indian craton (after GSI published geological maps, with permission from Geological Survey of India) *(referred on page 42)*

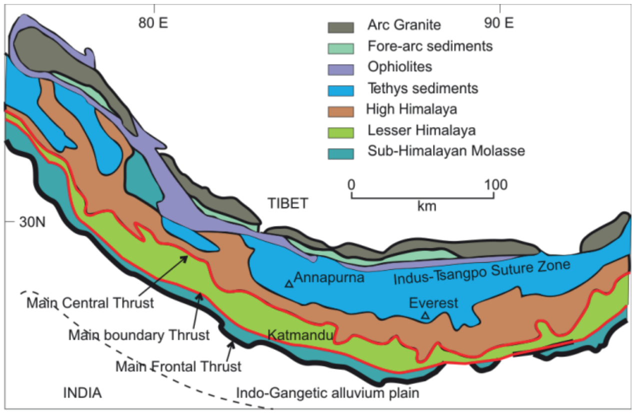

**Fig. 3.6** A generalised map showing the principal tectonic divisions and different geological units of the Himalayan mountain belt (after Avouac 2007, with permission from Elsevier) *(referred on page 45)*

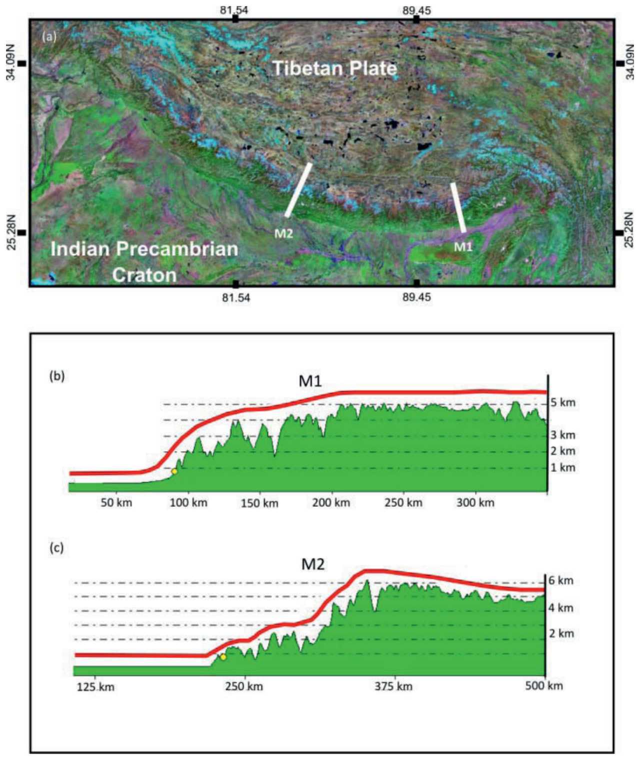

**Fig. 3.4** (a) A panoramic view of the Himalaya-Tibet mountain system. (b) and (c) Topographic profiles (prepared from a digital elevation map) of the Himalayan belt lying the Indo-Tsango stuture zone and the Indo-Gangetic Alluvium Plain. Location of these sections are shown in (a) *(referred on page 44)*

**Fig. 3.7** Field examples of ductile deformational structures from the Darjeeling-Sikkim Himalaya. (a) Hinterland-dipping weakly deformed sandstone of Lower Siwalik. (b) Superposition of later upright folds on earlier subhorizontal schistosity in Daling Group. (c) Intra-folial tight and isoclinals folds in Daling. (d) Pinch-and-swell structures in Gneissic rocks, west Sikkim *(referred on page 45)*

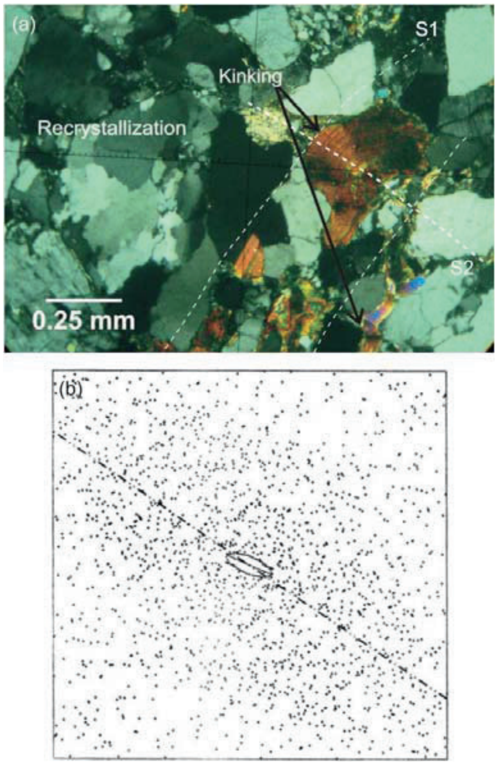

**Fig. 3.9** (a) Micro-scale tectonic fabrics in Siwalik rocks. Note superposition of folds on the fabric. (b) Estimation of strain, based on the Fry Method for Lower Siwalik rocks *(referred on page 46)*

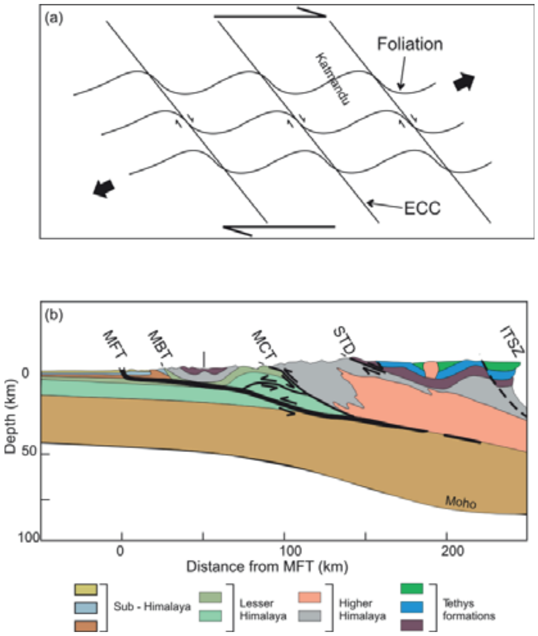

**Fig. 3.21** (a) Foreland-vergent extensional crenulation cleavage developed under top-to-hinterland horizontal shear. (b) Large-scale hinterland-dipping extensional zone (STDZ) in the hinterland part of the Himalayan orogen (after Avouac 2007, with permission from Elsevier) *(referred on page 51)*

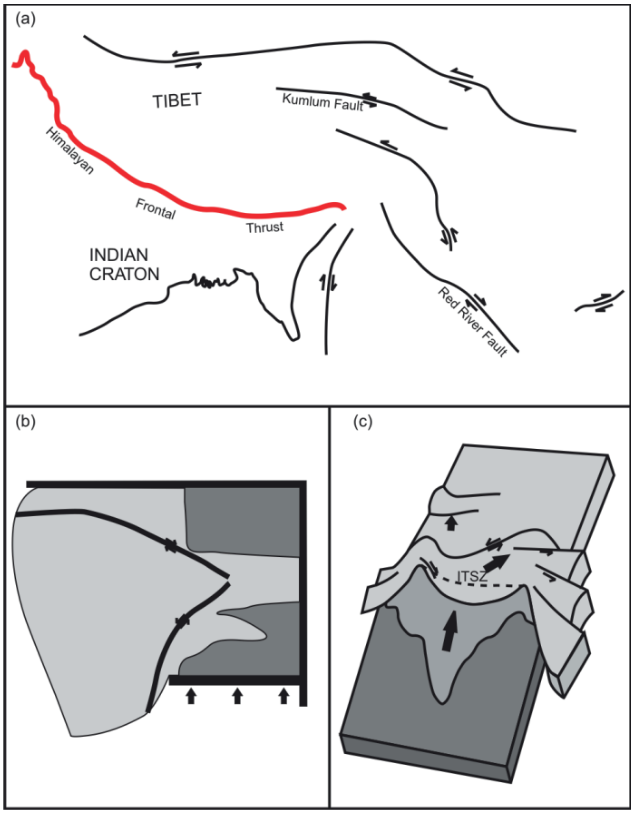

**Fig. 3.22** (a) Major strike-slip faults in the Himalaya-Tibet system (after Molnar et al. 1981). (b) Formation of strike-slip faults associated with lateral extrusion tectonics in models. (c) A schematic sketch of strike-slip movement on the eastern flank of the Tibetan plateau (after Avouac 2007, with permission from Elsevier) *(referred on page 51)*

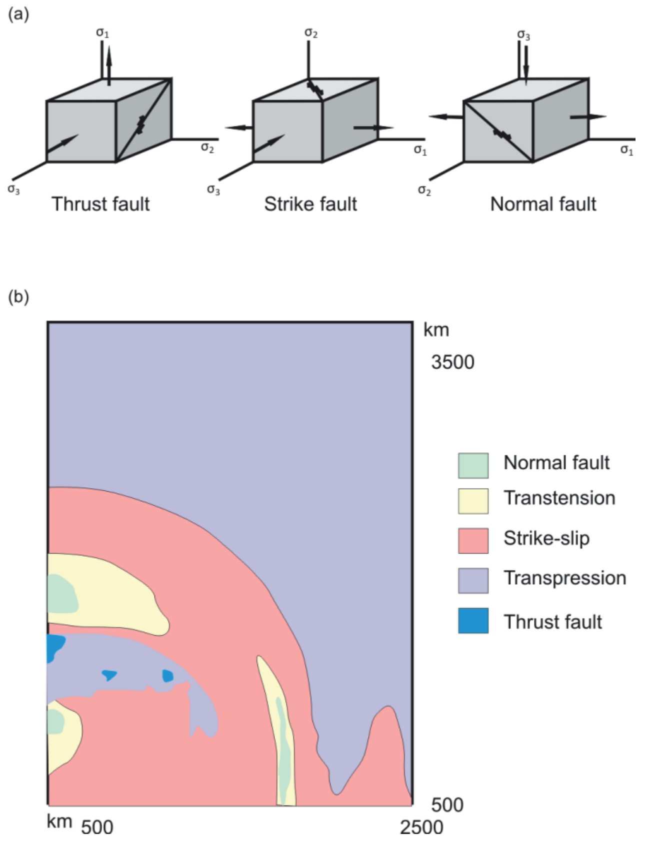

**Fig. 3.23** (a) Stress conditions for thrust, strike-slip and normal faulting in the crust. (b) Distribution of different types of faults in the Himalaya-Tibet system predicted from finite difference numerical model (after Jimenez-Munt and Platt 2006, with permission from Elsevier) *(referred on page 52)*

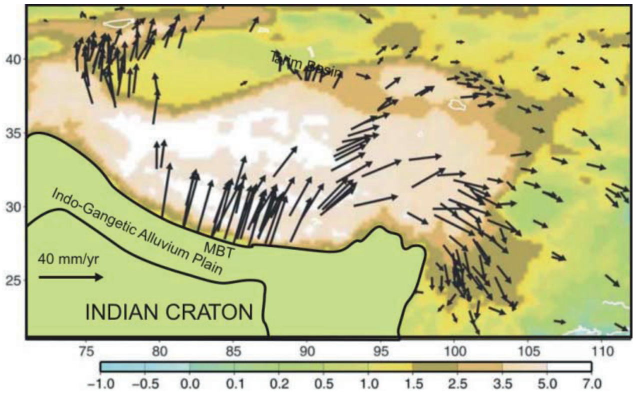

**Fig. 3.24** Surface velocity pattern in the Himalaya-Tibet convergent zone. The velocity is relative to the Eurasian plate (after Wang et al. 2001, with permission from American Association of Advancement of Science) *(referred on page 52)*

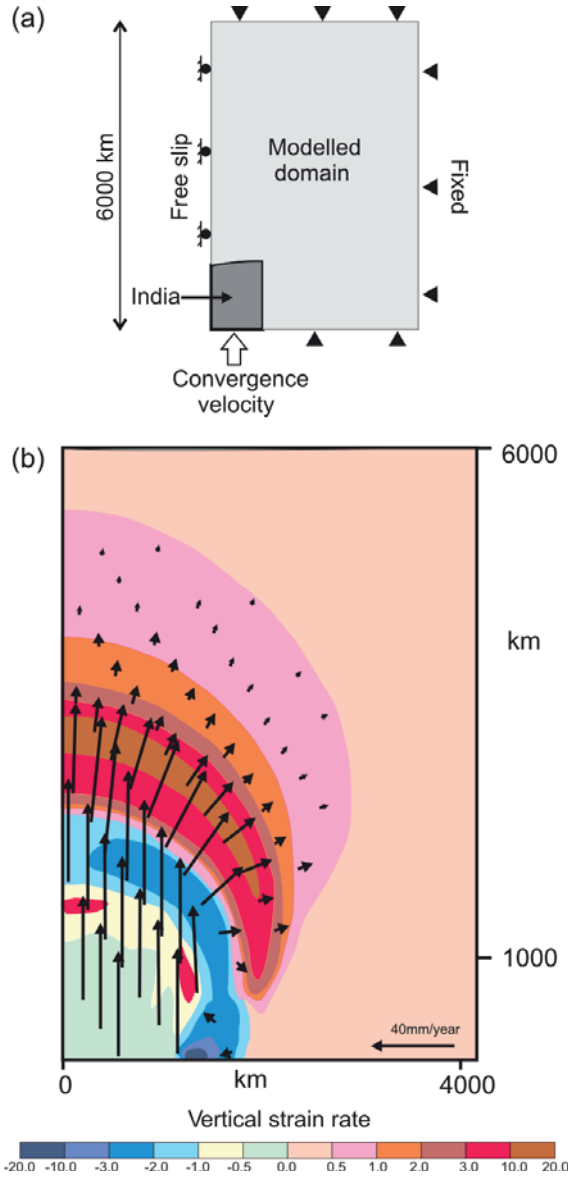

**Fig. 3.25** Consideration of boundary conditions for crustal flow modelling using finite difference method (after Jimenez-Munt and Platt 2006, with permission from Elsevier) (b) Model results showing flow pattern in the Himalaya-Tibet system *(referred on page 53)*

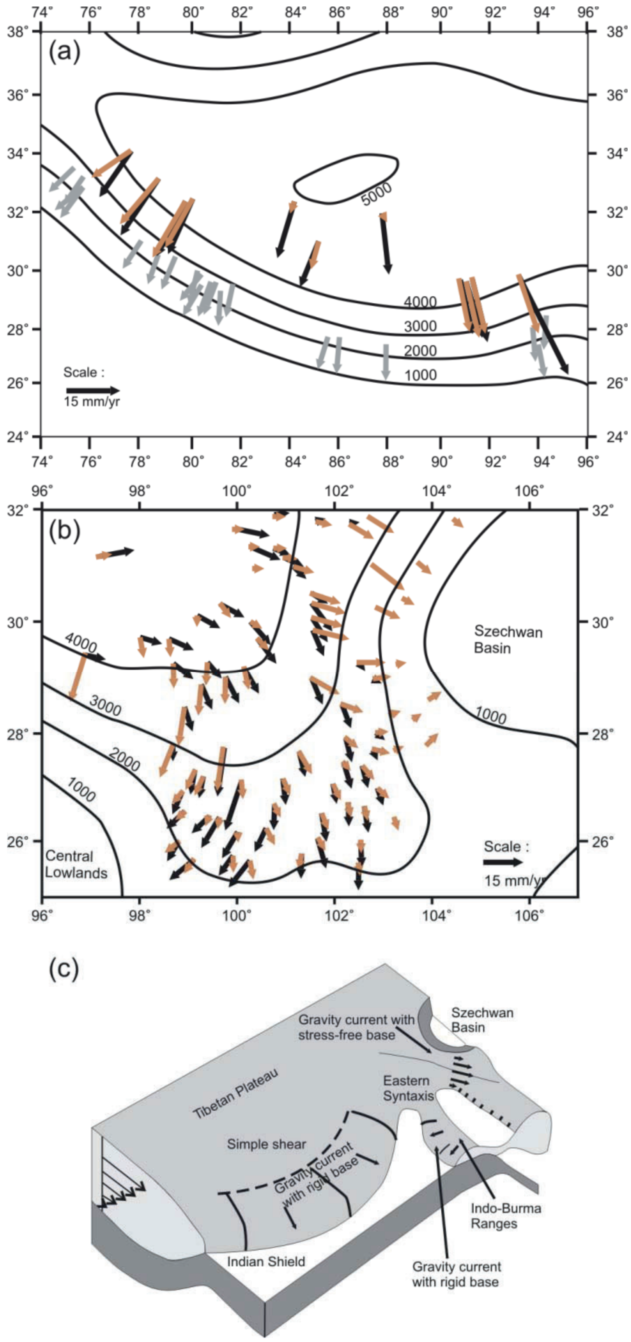

**Fig. 3.26** Modelling of topography-driven crustal flow under topography controlled pressure gradients in (a) south Tibet and (b) south-eastern Tibet. Black and brown arrows show velocity from GPS data and model results respectively. Gray shaded arrows indicate motion obtained from fault slip data. (c) An overall view of topography controlled flow in the Himalaya-Tibet system. (after Copley and McKenzie 2007, with permission from Blackwell Scientific) *(referred on page 54)*

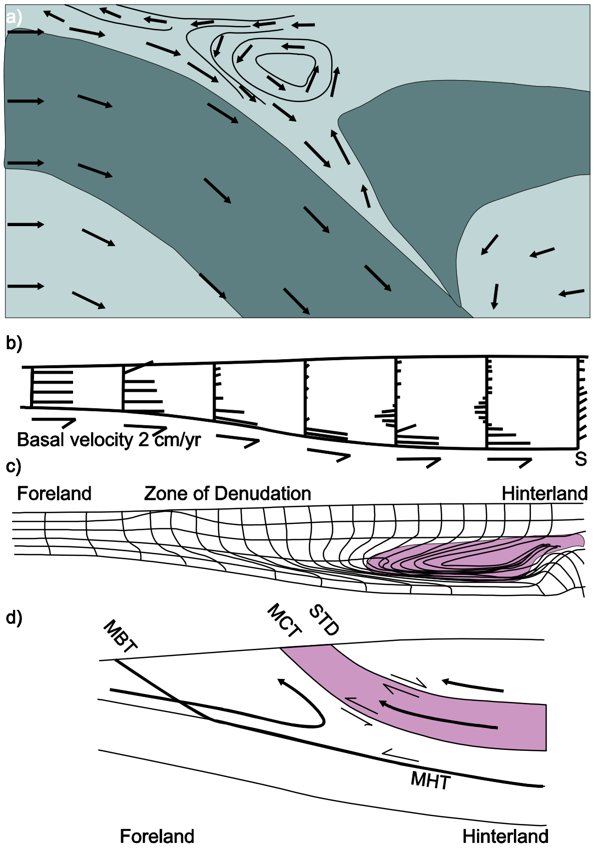

**Fig. 3.28** (a) Numerical models showing the crustal flow pattern in a subduction zone (after Gerya et al. 2002, with permission from American Geophysical Union). (b)-(c) Numerical simulation of lower crustal flow beneath the Tibetan plateau and (d) Exhumation of low-viscous deep-crustal rocks (pink shaded) in the form of channel in the higher Himalaya (after Beaumont et al. 2001, with permission from Nature Group of Publishers) *(referred on page 55)*

**(a)** ***$V_s$=2 cm/yr***

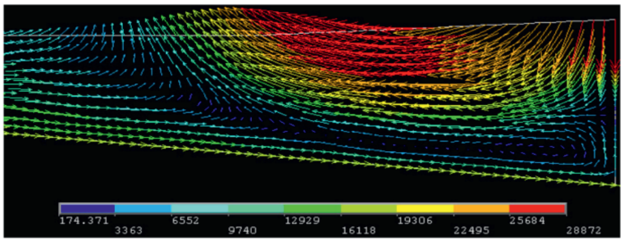

**(b)** ***$V_s$=4 cm/yr***

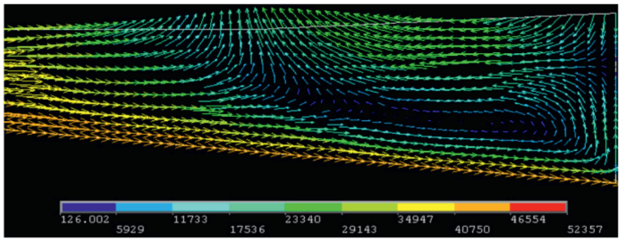

**(c)** ***$V_s$=6 cm/yr***

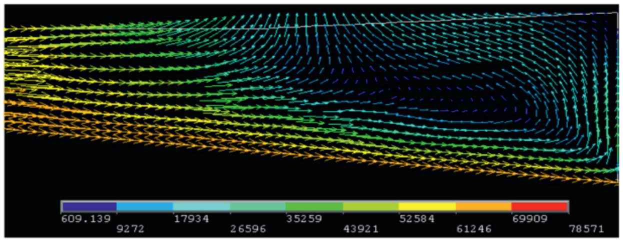

**(d)** ***$V_s$=8 cm/yr***

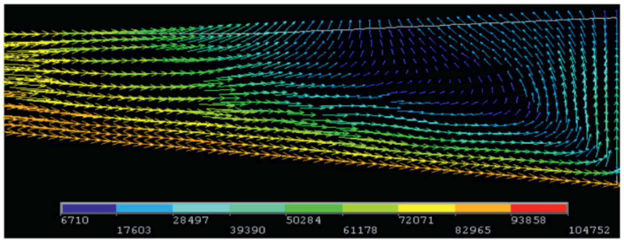

**Fig. 3.30** Finite element models showing flow patterns in convergent zones as a function of subduction rate ($V_s$) *(referred on page 56)*

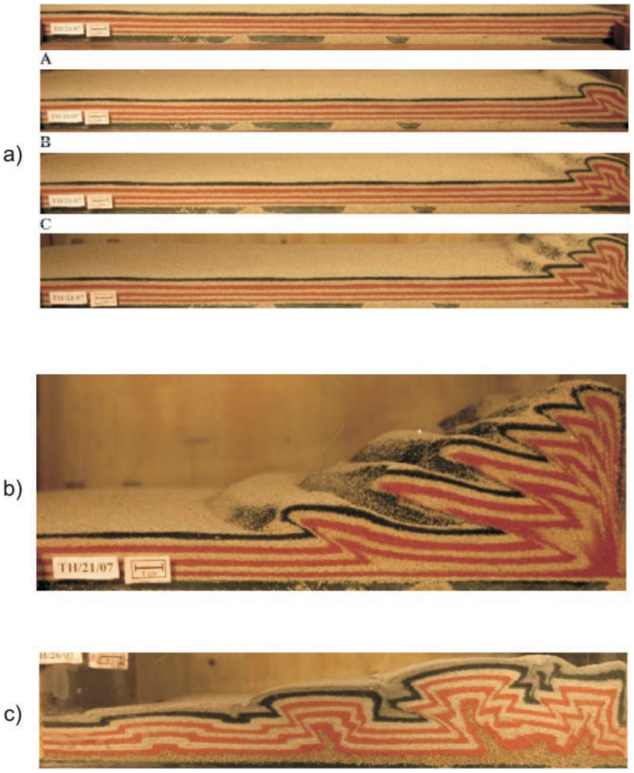

**Fig. 3.33** (a) Sequential thrusting in sandbox experiments. (b) and (c) Thrust wedges with high basal (0.46) and low (0.3) basal friction *(referred on page 58)*

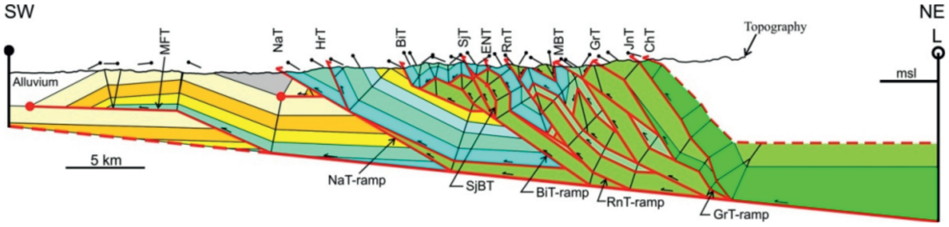

**Fig. 3.32** Imbircate thrust sequence in Nahan Salient, western Himalaya (Mukhopadhyay and Mishra 2005, with permission from Elsevier) *(referred on page 58)*

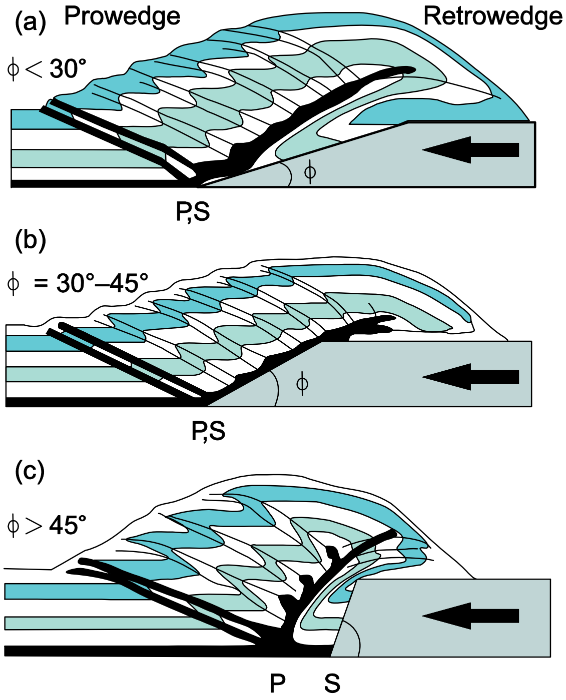

**Fig. 3.35** Development of a bi-vergent Coulomb wedge against a rigid indentor (after Persson and Sokoutis 2002, with permission from Elsevier) *(referred on page 59)*

**Fig. 3.37** Effects of surface erosion on localisation of exhumation in experimental thrust wedges. (a) High and (b) low basal friction *(referred on page 60)*

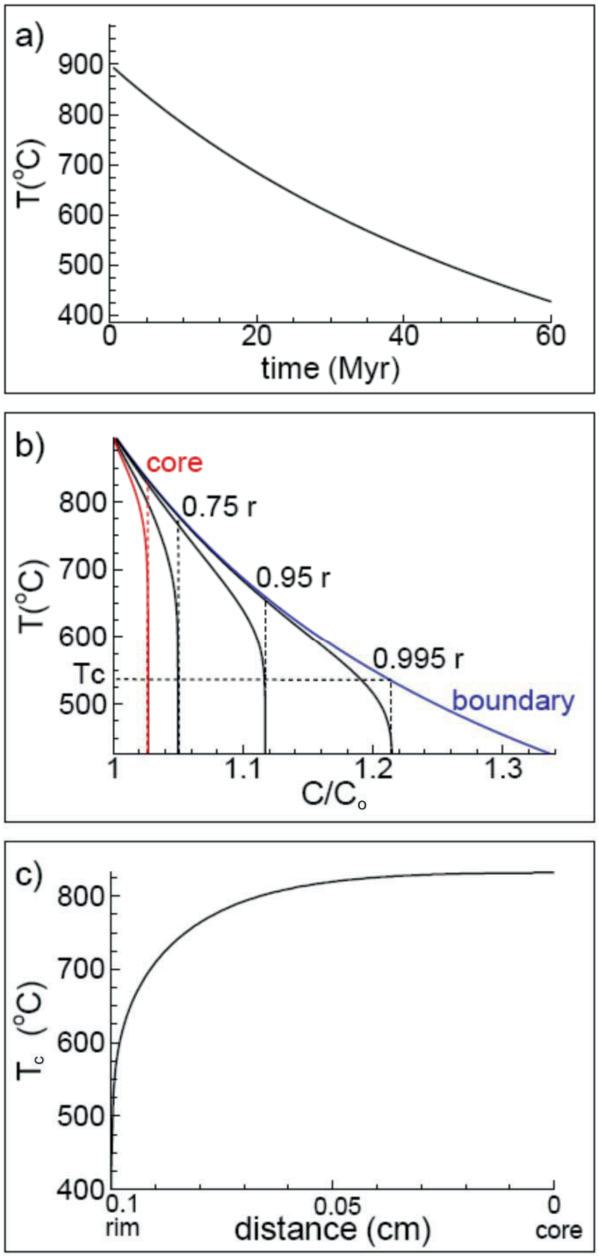

**Fig. 5.2** Numerical simulation of (a) cooling of a system following an asymptotic T-t relation (Eq. 5.1a) with $\eta = 9.6 \times 10^{-6}$ $\mathrm{Myr}^{-1}\mathrm{K}^{-1}$, (b) spatial variation of change of concentration of a species during cooling within a spherical grain of 1 mm radius and (c) corresponding closure temperature profile within the crystal. The diffusion coefficient of the species is given by $D = 7.22 \times 10^{-4}\exp(-E/RT)$ with E(activation energy) = 266 kJ/mol. The panel (b) illustrates the formal definition of closure temperature ($T_c$) at any radial distance within the crystal. $C_o$ stands for the initial concentration that is established at the peak temperature *(referred on page 91)*

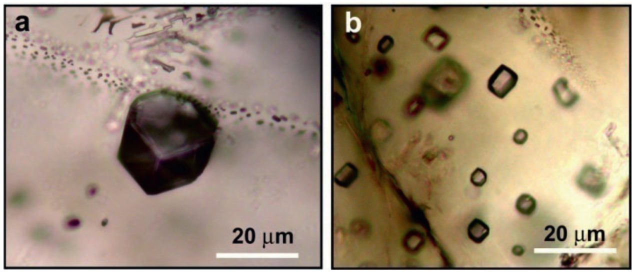

**Fig. 7.2** Photomicrographs of fluids inclusions in garnet (a) from an anhydrous granulite in Sri Lanka and feldspar (b) in a granulite from southern India. These monophase inclusions contain high density pure $CO_2$-rich fluids trapped during peak P-T conditions of metamorphism. The $CO_2$-rich fluids are considered to have influxed from sub-lithospheric sources *(referred on page 136)*

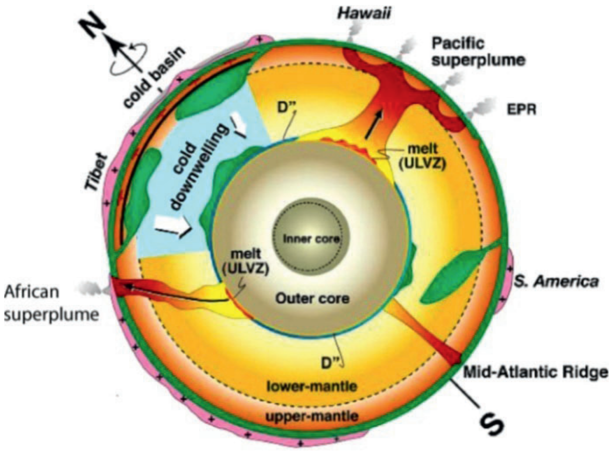

**Fig. 7.3** A schematic cross-section of the earth showing two major upwellings (Pacific superplume and African superplume) and one downwelling (Asian cold plume) (after Maruyama et al. 2007, with permission from Elsevier) *(referred on page 137)*

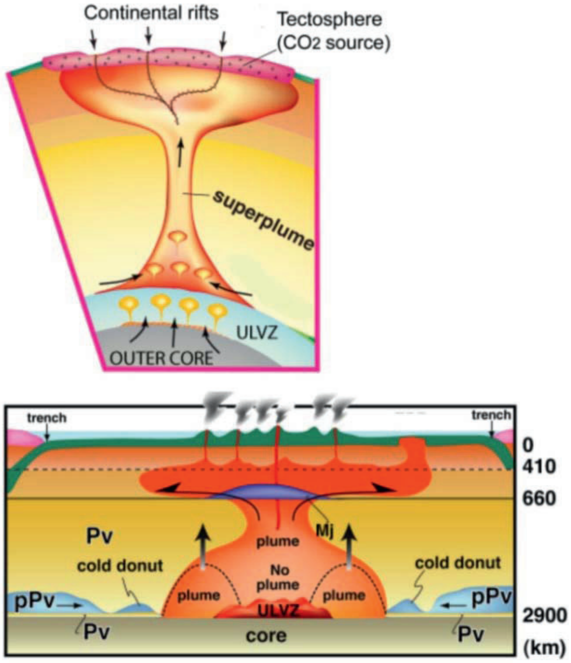

**Fig. 7.4** Plumes as gigantic pipes which transfer volatiles from the CMB to the surface (after Maruyama et al. 2007; Santosh et al. 2009b). The top figure shows rising small plumes from the CMB which amalgamate into a large upwelling. When the superplume hits the tectosphere (carbonated continental keel), huge amounts of $CO_2$ are liberated and flushed out through continental rifts either through magmatic conduits or through hot and ultra-hot metamorphic orogens. The bottom figure shows the birth of a superplume from heating from the core, and heat liberated through the exothermic reactions of perovskite (Pv) to post-perovskite (pPv). Abbreviations: ULVZ–ultra-low velocity zone, indicating melt layer on top of the CMB, designated as ant-crust by Maruyama et al. (2007). Mj – majorite. With permission from Elsevier *(referred on page 138)*

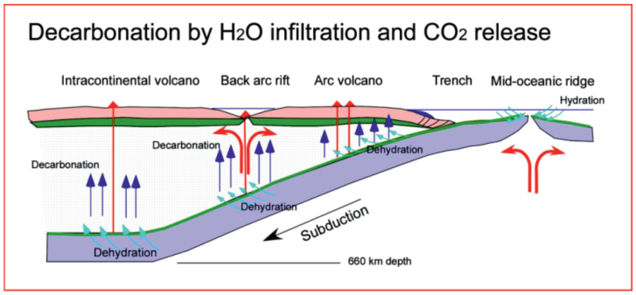

**Fig. 7.5** A schematic model showing $CO_2$ circulation mechanism from ocean-atmosphere through carbonated MORB to the metasomatised mantle wedge through subduction processes in the Archean (after Santosh and Omori 2008b). Carbonated MORB at spreading axes subduct along consuming plate boundary and undergo decarbonation. However the decreased $p(CO_2)$ in the Proterozoic and beginning of sedimentation of massive carbonate rock after 2.5 Ga resulted in the formation of hydrated MORB crust without any carbonate, marking the culmination of carbonation in the mantle wedge. The entrance of huge volumes of water triggered the return flow of $CO_2$ back to the surface by the partial melting or subsolidus decarbonation of the subcontinental carbonated mantle. The active role of both water and $CO_2$ are illustrated in this case. With permission from Elsevier *(referred on page 139)*

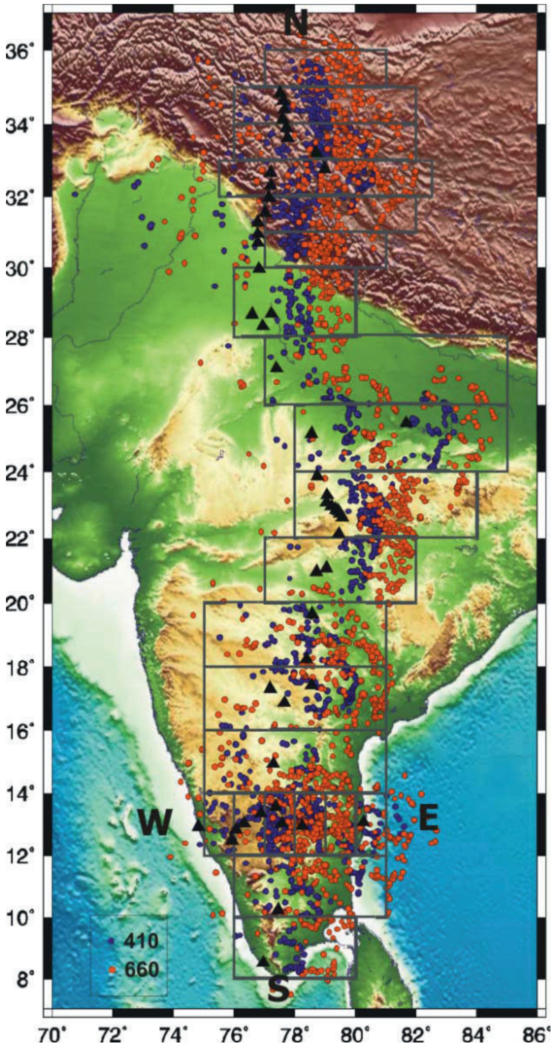

**Fig. 9.4** Piercing points of Ps phase at 410 and 660 km depth. Rectangular grids show the block for which receiver functions are stacked and presented at its mid-point
*(referred on page 157)*